LECTURE NOTES ON

CONFIGURATION AERODYNAMICS

WILLIAM H. MASON

EDITED BY PRADEEP RAJ



"This course, as far as I know, produced some of the most experienced and capable aerodynamic design practitioners in the US today."

–Dr. Russell Cummings, USAFA

Practical applications of aerodynamic theory are critically important for aerodynamic design of aircraft configurations, but are often omitted from aerospace engineering curricula. *Lecture Notes on Configuration Aerodynamics* is an incredible resource for educating the next generation of aerospace engineering students who aspire to engage in the aerodynamic design of aircraft configurations. It shows how aerodynamic theory is applied in practice, giving students insight into what a career in aerodynamics entails. This book offers a design-oriented perspective of the development and analysis of aircraft aerodynamics.

Based on his academic experience as a professor and his industrial experience at Grumman, Mason presents decades of relevant knowledge and wisdom of a large number of exceptional researchers and practicing engineers. Extensive references throughout the book encourage further study of configuration aerodynamics.

This book encompasses the aerodynamic design of flight vehicles with emphasis on flow fields and configuration concepts. Mason covers methodologies for aerodynamic analysis and design for flows ranging from low speed to high speed and includes case studies of classic configurations.

COLLEGE OF ENGINEERING
KEVIN T. CROFTON DEPARTMENT OF AEROSPACE AND OCEAN ENGINEERING
VIRGINIA TECH

VIRGINIA TECH PUBLISHING

BY-NC-SA

Licensed with a Creative Commons Attribution NonCommercial-ShareAlike 4.0 license

DOI: https://doi.org/10.21061/configurationaerodynamics

ISBN: 978-1-962841-52-8

Lecture Notes on Configuration Aerodynamics

Similar Titles in the Open Education Series

Series Editor: Anita Walz

Aerodynamics and Aircraft Performance

Aerospace Structures

Conducting Mixed-Methods Research:

From Classical Social Sciences to the Age of Big Data and Analytics

Electromagnetics, Volume 1

Electromagnetics, Volume 2

Introduction to Biosystems Engineering

Radio Systems Engineering, Revised First Edition

Lecture Notes on
Configuration Aerodynamics

William H. Mason

Edited by Pradeep Raj

PDF and EPUB free online at: https://doi.org/10.21061/configurationaerodynamics





This work is published by the Kevin T. Crofton Department of Aerospace and Ocean Engineering in association with Virginia Tech Publishing

Blacksburg, VA

© **Estate of William H. Mason and Pradeep Raj, 2026.** *Lecture Notes on Configuration Aerodynamics* by William H. Mason and Pradeep Raj is licensed under a Creative Commons Attribution-NonCommercial-ShareAlike 4.0 International License, except where otherwise noted.

You are free to copy, share, adapt, remix, transform, and build on the material for any primarily noncommercial purpose as long as you follow the terms of the license: https://creativecommons.org/licenses/by-nc-sa/4.0.

You must:

- Attribute—You must give appropriate credit, provide a link to the license, and indicate if changes were made. You may do so in any reasonable manner, but not in any way that suggests the licensor endorses you or your use.
- ShareAlike—If you remix, transform, or build on the material, you must distribute your contributions under the same license as the original.

You may not:

- NonCommercial—You may not use the work for primarily commercial use.
- Additional restrictions—You may not add any legal terms or technological measures that legally restrict others from doing anything the license permits.

Suggested citation: William H. Mason and Pradeep Raj, *Lecture Notes on Configuration Aerodynamics* (2026). CC BY-NC-SA 4.0. https://doi.org/10.21061/configurationaerodynamics.

Publisher: This work is published by the Kevin T. Crofton Department of Aerospace and Ocean Engineering in association with Virginia Tech Publishing.

Kevin T. Crofton Department of Aerospace and Ocean Engineering
Virginia Tech Swing Space, Room 241
1600 Innovation Drive
Blacksburg, VA 24061

Virginia Tech Publishing
University Libraries at Virginia Tech
560 Drillfield Drive
Blacksburg, VA 24061
https://publishing.vt.edu | publishing@vt.edu

Peer review: This book has undergone single-anonymous peer review by five reviewers.

Accessibility statement: Virginia Tech is committed to making its publications accessible in accordance with the Americans with Disabilities Act of 1990. The text, images, and links in the PDF versions of this text are tagged structurally and include alternative text, which allows for machine readability. Virginia Tech Publishing is continuously working to improve accessibility and welcomes any feedback from readers.

Disclaimers: Data and information appearing in this book are for informational purposes only. Virginia Tech, the author's estate, editors, and contributors are not responsible for any injury or damage resulting from use or reliance on the information contained within. Contents or reliance thereon are not guaranteed to be free from owned trademarks or patents.

This work may contain components (e.g., illustrations or quotations) not covered by the license. Every effort has been made to clearly identify these components but ultimately it is your responsibility to independently evaluate the copyright status of any work or component part of a work you use, in light of your intended use. Please check the references at the end of each chapter before redistributing.

Use of AI: This publication was developed without the use of generative artificial intelligence.

Funding: This project was made possible in part through financial support from the University Libraries' Open Education Initiative and the Kevin T. Crofton Department of Aerospace and Ocean Engineering.

Cataloging-in-Publication Data
Mason, William H., & Raj, Pradeep
Lecture Notes on Configuration Aerodynamics / William H. Mason and Pradeep Raj
Pages cm
ISBN 978-1-962841-52-8 (PDF)
ISBN 978-1-962841-51-1 (EPUB)
ISBN 978-1-962841-53-5 (Pressbooks; https://pressbooks.lib.vt.edu/configurationaerodynamics)
ISBN 978-1-962841-50-4 (Print)
URI: https://hdl.handle.net/10919/139932
DOI: https://doi.org/10.21061/configurationaerodynamics

Airplanes--Aerodynamics--Textbooks.
Airplanes--Design and construction--Textbooks.
TL570 .M37 2026

Cover image: NASA (1990). Public domain. Retrieved from Wikimedia Commons.
Cover design: Kindred Grey

Contents

Preface ix

Instructor Resources xii

1. Introduction to Configuration Aerodynamics 1

1.1 Purpose of Configuration Aerodynamics 1

1.2 Examples of Innovative Configuration Concepts 1

1.3 Decision Issues 8

1.4 Design Approaches 9

1.5 The Role of Aerodynamicists Within the Overall Design Process 9

1.6 What's Left Out? 10

2. Foundations of Fluid Mechanics: Governing Equations 15

2.1 Governing Equations of Fluid Mechanics 15

2.2 Derivation of Governing Equations 17

2.3 Boundary Conditions 29

2.4 Standard Forms and Terminology of Governing Equations 30

2.5 The Gas Dynamics Equation and the Full-Potential Equation 35

2.6 Special Cases 39

2.7 Examples of Zones of Application 44

2.8 Mathematical Classification of Partial Differential Equations (PDEs) 45

2.9 Requirements for a Complete Problem Formulation 49

3. Fundamentals of Aerodynamic Drag 53

3.1 The Importance of Drag 53

3.2 Drag—Numerous Viewpoints and Basic Concepts 54

3.3 Theoretical Analysis of Drag Components Based on Momentum Balance 60

3.4 Important Aspects of Lift-Induced Drag 66

3.5 Predicting Drag 83

3.6 Accurate Drag Prediction: State of the Art 99

3.7 Drag Reduction Possibilities 101

3.8 Some Issues for Drag Calculation Using Computational Aerodynamics 103

4. Configuration Aerodynamic Design: Use of Computational Aerodynamics 111

4.1 Configuration Aerodynamic Layout: Key Considerations 112

4.2 Aircraft Configuration Architecture Options 115

4.3 Configuration Sizing: Aerodynamic Considerations 122

4.4 Overview of the Specific Aerodynamic Design Tasks 124

4.5 Use of Computational Aerodynamics in Aerodynamic Design 125

4.6 A Review of Detailed Computational Aerodynamic Design Approaches 127

4.7 Summary of the Status of Aerodynamic Design 136

5. Subsonic Aerodynamics: Airfoils and Wings 141

5.1 Airfoils 142

5.2 Wings 158

6. Transonic Aerodynamics: Airfoils and Wings 187

6.1 Physical Aspects of Flowfield Development With Mach Number 187

6.2 Technology Issues and Developments 189

6.3 Airfoils 193

6.4 Wings 199

7. High-Lift Aerodynamics 211

7.1 Characteristics of High-Lift Systems 211

7.2 Examples of High-Lift Devices 213

7.3 Aerodynamics of Leading- and Trailing-Edge Devices 216

7.4 Physics of High Lift: A. M. O. Smith's Analysis of the High-Lift Aerodynamics 222

7.5 Computational Methods for High Lift 224

7.6 Passive and Active Boundary Layer Control 225

7.7 Powered Lift 226

7.8 Configuration Integration Issues 226

8. High-Angle-of-Attack (High-α) Aerodynamics 229

8.1 Basic Aerodynamics of High-α 230

8.2 Flight Mechanics of High-α 233

8.3 Control Effectiveness With Angle of Attack 237

8.4 The F-22: Putting It All Together (An Example) 238

8.5 Some Configuration Issues: Amazing Stories 241

9. Supersonic Aerodynamics 245
9.1 Supersonic "Cruise" Airplanes 245
9.2 The Challenge for Supersonic Airplane Design 250
9.3 Wave Drag 252
9.4 Wings: Lift and Drag Due to Lift 258
9.5 The Aerodynamic Center Shift 266
9.6 The Oblique-Wing Concept 270
9.7 Aeropropulsion Integration 272
9.8 Computational Methods and Supersonic Aerodynamic Design 273
9.9 Supersonic Airplane Configuration Design Examples 281
10. Hypersonic Aerodynamics 307
10.1 Surface Pressure Estimation 308
10.2 Aerodynamic Stability and Control 311
10.3 Aerodynamic Heating 316
10.4 Additional Considerations for Gas Dynamics 320
10.5 Considerations for High-Temperature Gas Dynamics 323
10.6 Hypersonic Vehicle Design 327
11. End Note 335

Appendix A: Geometry for Aerodynamicists 337
A.1 Airfoil Geometry 337
A.2 Classic Bodies of Revolution 352
A.3 Cross-Section Geometries for Bodies 359
A.4 Planform Analysis 360
A.5 Conical Camber 364
A.6 Three-Dimensional Wing Geometry 365
Appendix B: Fifteen Minutes of Stealth in Aircraft Design 367
B.1 How RCS Works 368
B.2 Computations 372
Appendix C: Government Regulations Affecting Configuration Aerodynamics 375
C.1 Light Sport Aircraft (LSA) 379

Appendix D: Examples of Aerodynamic Design 381
D.1 Overview of Case Studies 381
D.2 The B-2 Study 381
D.3 Comparison of the Beech Starship and X-29 406
D.4 Term Project: Examine the YF-22 and YF-23 415
D.5 Discussion 416
Appendix E: Software for Aerodynamic Analysis and Aircraft Design 419
Important Note 419
E.1 Aerodynamic Relations 420
E.2 Airplane Design and Sizing 421
E.3 Geometry 423
E.4 Lifting-Line Theory 424
E.5 Drag 424
E.6 Vortex Lattice Methods 427
E.7 Airfoil Aerodynamics 428
E.8 Supersonic Aerodynamics 430
E.9 Stability and Control 431
E.10 Cryogenic Wind Tunnel Testing 433
Appendix F: Configuration Aerodynamics Reading List 435
Appendix G: The Configuration Aerodynamicist's Bookshelf 437
Acknowledgments 441
About the Author 443

Preface

William H. Mason, Professor Emeritus in the Kevin T. Crofton Department of Aerospace and Ocean Engineering at Virginia Tech, painstakingly prepared a comprehensive set of lecture notes while teaching the one-of-a-kind Configuration Aerodynamics course for more than two decades before he unexpectedly passed away in March 2019. The department is pleased to honor his notable contributions by offering *Lecture Notes on Configuration Aerodynamics* (an edited version of Mason's manuscript of the lecture notes) as an online open access book to the aerospace engineering community at large and to the students and practitioners of aerodynamics in particular.

Bill Mason—a self-described lifelong student of airplanes and aerodynamics—developed the Configuration Aerodynamics course from scratch to serve as a much-needed companion to the capstone Aircraft Design courses that he began teaching in 1989 when he joined Virginia Tech after 15 years at Grumman. The original manuscript outlined his motivation for creating this course in a draft preface that is included below. Bill thoroughly enjoyed teaching the "ConfigAero" course every spring, and the students who elected to enroll enjoyed learning the use of engineering tools and processes for configuration aerodynamic design. More importantly, the students learned the *thought processes* that are essential to effectively applying basic aerodynamics theories in creating aircraft configurations that best meet customer needs. He made the draft version of his notes widely available through his personal website, ensuring that students at Virginia Tech and many other universities as well as professional aerodynamicists worldwide benefited from his insights.

It is unfortunate that the manuscript Mason left behind had a few blank sections with just topic captions that he intended to populate. However, even without these topics, the manuscript had more than enough material to warrant publication as a book. I, as the editor, made a good faith attempt to populate some of the blank sections using suitable material. For example, we added material on aircraft buffeting, AIAA Drag Prediction Workshops, and aircraft drag reduction technologies. Having known Bill for several decades, including our time as esteemed colleagues at Virginia Tech for seven years starting in 2012, I believe he would have approved of these additions. It is worth mentioning that we deliberately retained the conversational style of the entire manuscript to ensure that it remains Mason's book!

The primary purpose of the book is to be a resource for educating the next generation of aerospace engineering students who aspire to engage in aerodynamic design of aircraft configurations. Although all aerospace engineering curricula include basic aerodynamics theory courses that students are required to take, several topics are often omitted out of necessity. Many of these topics relate to practical applications of aerodynamic theory, and they need to be reinforced due to their critical importance for practical aerodynamic design. This book bridges the gap between theory and practice by offering a design-oriented perspective of the development and analysis of aircraft aerodynamics typical of what a career in aerodynamics might entail.

Every time Mason taught the course, he added more relevant material to his lecture notes! We strongly recommend that anyone who wishes to adopt this book for teaching a course on Configuration Aerodynamics should consider adding examples of the latest developments in the aerodynamic design of aircraft because this book mainly covers ideas and configurations until and including the spring of 2019.

Completing a course based on this book will help students achieve the following key objectives:

- *Develop the flow physics insight.* Learn to form a "mental model" of each flow field or concept against which to gauge computational/experimental "reality."
- *Understand strengths and shortcomings of computational aerodynamics methods.* Computational and experimental tools must be used together. Both have highly complementary strengths and weaknesses.
- *Value analytical theory.* Airplanes were built before computational aerodynamics methods became available. Analytical aerodynamics provides valuable insights into the role of key flow and configuration shape parameters.
- *Answer the question based on physics.* "What configuration do I want to develop to do this job?"

The scope of the book encompasses the aerodynamic design of flight vehicles with emphasis on nonlinear flow fields and configuration concepts. Mason's manuscript covers methodologies for aerodynamic analysis and design for flows ranging from low speed to high speed. In addition, it includes case studies of classic configurations. The main body of the book is organized into ten chapters grouped in two parts. In addition, there are 7 appendices.

Part 1: Foundational Elements (Chapters 1 through 4)

Chapter 1 provides an overview of configuration aerodynamics, including its purpose and role in the design of innovative configurations. Chapter 2 reviews the physical description of flow fields in the mathematical terms that are used in modern computational aerodynamics. Those familiar with the equations and their derivations may skip this chapter altogether. Chapter 3 discusses fundamentals of aerodynamic drag, providing more depth on the topic than an entry-level aerodynamics course. Airplane drag is covered upfront as a foundational element since it is a crucial driver of configuration aerodynamic design. Chapter 4 provides an overview of the configuration aerodynamic design process and the increasingly important role of computational aerodynamics.

Part 2: Practical Considerations (Chapters 5 through 10)

Chapters 5 through 10 address practical considerations that are specific to the aerodynamic design of aircraft for operations in different flight regimes from subsonic through hypersonic. Subsonic flows are covered in Chapter 5 and transonic flows in Chapter 6. These are followed by Chapter 7 on aerodynamics of high-lift devices and Chapter 8 on aerodynamic considerations for flight with a high angle of attack. Supersonic flows are discussed in Chapter 9 and hypersonic flows in Chapter 10. To emphasize practical considerations and retain engagement, Mason made an attempt to integrate case histories and "amazing stories" to the extent possible.

Each chapter ends with a set of exercises. Most of the exercises have a specific learning objective spelled out at the beginning. For example, the first exercise in Chapter 3, Exercise 3.1, explains that it is targeted at demonstrating "the importance of streamlining." In some of the exercises, Mason asks students to "comment on your results." This reinforces the idea of open-ended problems having multiple possible results, and it helps students develop critical thinking skills to assess the "goodness" of their results by choosing appropriate metrics. In some exercises, a classic technical paper is assigned to the class and students write an essay on what they learned from reading it, sharing their findings in classroom discussion afterward. Such an exercise is a great way to help students develop two-way communication skills and an appreciation of how challenging it is to capture all ideas and concepts in a classic paper. In Mason's own words: "The importance of working the exercises cannot be overstated."

In addition to the ten chapters, there are seven appendices. Appendix A details pertinent information about geometric shapes of interest to aerodynamicists. This is followed by appendix B, which highlights a few key aspects to be considered in shaping a stealth aircraft design, and appendix C, which presents regulatory requirements that affect configuration aerodynamics. Appendix D provides examples of aerodynamic design studies conducted by students using aerodynamic design procedures and computational aerodynamic tools. A list of useful software tools for aerodynamic analysis and aircraft design is presented in appendix E. As is often the case with software, many of the tools have become dated, but the intention is to offer a set of tools that have proven applications for practical problems. Students/readers should not feel restricted to using only these tools. To the contrary, Mason encouraged students to use modern software tools as long as they fully understood what was required to obtain accurate and useful results. In appendix F, Mason's recommended reading list points to several key papers that perfectly align with the primary themes of the book. The last appendix, appendix G, includes a short list of books and reports that Mason considered essential for any configuration aerodynamicist's bookshelf.

Publication of Mason's lecture notes as an online, open access book ensures that countless future students and professionals involved in aircraft design will have the opportunity to benefit from his insights. The book offers them the requisite information for applying the fundamentals of aerodynamics they have learned in standard textbooks. The present book, combined with *Applied Computational Aerodynamics* (which Mason coauthored with Cummings, Morton, and McDaniel), clearly attests to the rich legacy Mason has left behind. For me, it has been a great pleasure and a distinct privilege to serve as the editor and thereby play a small role in preserving Bill Mason's legacy.

I want to thank Carol Bland, executor of the William H. Mason estate, for wholeheartedly supporting this endeavor aimed at perpetuating Mason's legacy. I am truly grateful to Anita Walz of Virginia Tech for bringing her extensive planning and execution expertise to bear on this project and for patiently coaching and guiding me through the publication process. Special thanks go to Kindred Grey, Pranay Patel, Sullivan Madden, and Joseph Brooks for their invaluable assistance in converting Mason's manuscript into a quality publication. We are extremely thankful to Russ Cummings of USAF Academy, Jason Merret of UIUC, and Jason Riopelle of Gulfstream (plus two others who wish to remain anonymous) for devoting their time and effort to critically reviewing a draft of the book and for providing numerous constructive suggestions that made the final version so much more impactful. We are particularly appreciative of the support and encouragement of Eric Paterson, Bob Canfield, and Ella Atkins, who were AOE Department Heads when this book was produced.

Pradeep Raj
Blacksburg, Virginia

This text is based on the notes for the Configuration Aerodynamics course I've given for 20 years at Virginia Tech. I started giving the class because it seemed to me that the students needed an aircraft aerodynamics–oriented course that elaborated on the fundamentals usually taught in such courses. It is an elective, generally taken by seniors and graduate students. However, second semester juniors can take the class without undo difficulty. They should have a basic text such as Bertin and Cummings or Anderson available to refresh their recollection of the fundamental aerodynamic theory. If possible, it would be desirable to take the class before their senior design project.

This is a text in "why" as opposed to a book on "how." That part ["how"] of the education foundation is addressed in the companion volume, Applied Computational Aerodynamics, *that was published in 2015, spearheaded by Russ Cummings, with Scott Morton, Dave McDaniel, and myself as collaborators. There is some overlap. Ideally students would take both classes at the same time. However, their course load doesn't allow for this. With the powerful computational tools now available, students need to understand what they should be doing with them!*

The importance of working the exercises cannot be overstated. They have been developed to bring out key points. Students learn much more by working the exercises than if they just sit in class passively listening. If the book is being studied independently, the exercises should not be overlooked. In addition, the text is integrated with a number of resources available on the web (a truly phenomenal development providing access to information). This includes both additional text material and software. In terms of the use of computational aerodynamics tools, the exercises try to strike a balance between emphasizing the validation of the tools (and the student's skill in using them) and using them to explore aerodynamics ideas.

A configuration aerodynamicist straddles the artificial academic divide between fluid mechanics–oriented "aerodynamics" and classical flight mechanics, which has become less a class in bare airframe aerodynamics for the stability characteristics and the ability to generate moments with (primarily) aerodynamic control forces; now, classical flight mechanics is more of a class in electrical engineering–oriented control theory. My experience with fighter configurations was that it was easier to achieve performance goals than to make the airplane fly (i.e., good high-angle-of-attack characteristics, which we try to address).

W. H. Mason (1947–2019)
Blacksburg, Virginia

Instructor Resources

Available formats and helpful links

Navigate to the book's main landing page to access:

- Links to multiple electronic versions of the textbook (PDF, EPUB, HTML)
- A link to Amazon for ordering a print copy
- A link to the errata document
- A link for reporting errors

If you are interested in making your own version of this book, check out the book's license and information on recommended practices for attribution.

Instructors reviewing, adopting, or adapting this book are encouraged to register their interest. This assists the Open Education Initiative at Virginia Tech in assessing the impact of the book and allows us to more easily alert instructors of additional resources, features, and opportunities.

About Open Educational Resources (OER)

OER are free teaching and learning materials that are licensed to allow for revision and reuse. They can be fully self-contained textbooks, videos, quizzes, learning modules, and more. OER are distinct from free online resources in that they permit others to use, copy, distribute, modify, or reuse the content. The legal permission to modify and customize OER to meet the specific learning objectives of a particular course make them a useful pedagogical tool.

About Pressbooks

Pressbooks is an open source, web-based authoring tool based on WordPress. Virginia Tech personnel use it to create and adapt openly licensed course materials. Pressbooks offers an intuitive editing environment for educators interested in customizing this book.

About This Book



Lecture Notes on Configuration Aerodynamics is an open textbook. You are welcome to freely use, adapt, and share this book with attribution according to the Creative Commons Attribution NonCommercial ShareAlike 4.0 (CC BY-NC-SA 4.0) license. This license allows customization and redistribution that is "not primarily intended for or directed toward commercial advantage or monetary compensation." All figures in this book are licensed under Creative Commons licenses or used under fair use. Please see the end-of-chapter references for license information for each figure before reuse.

URLs

License: https://creativecommons.org/licenses/by-nc-sa/4.0/deed.en
Instructor interest form: https://bit.ly/interest_configurationaerodynamics
Book's main landing page: https://doi.org/10.21061/configurationaerodynamics
View known errata: https://bit.ly/errata_configurationaerodynamics
Report an error: https://bit.ly/reporterror_configurationaerodynamics
Recommended practices for attribution: https://wiki.creativecommons.org/wiki/Recommended_practices_for_attribution

1. Introduction to Configuration Aerodynamics

The field of configuration aerodynamics encompasses the role of aerodynamics in aircraft configuration design. Even though all aerospace engineering students take the basic aerodynamics theory classes, several topics related to applying the theory to aircraft design are usually omitted due to lack of time, and some other topics need additional reinforcement. This book serves as a bridge between theory and practical applications. The target audience is engineering students who wish to engage in the aerodynamic design of aircraft configurations.

1.1 Purpose of Configuration Aerodynamics

Experience has shown that the basic, analysis-oriented aerodynamics class doesn't provide an understanding of how to approach the configuration aerodynamic design process. Although many of the classical approaches to aircraft design are now highly refined, we frequently have to investigate innovative designs, some examples of which are presented in section 1.2. We need to be able to understand these innovative designs and predict their performance potential. To develop an appreciation of these concepts, we must assess them using first principles. Many times, concepts are proposed that don't obey the laws of physics. *A successful design must*!

To get some insight into aerodynamic thinking, it is worthwhile to read about the experience of one of the more successful aerodynamic designers, Irving Waaland, whose 1991 Wright Brothers Lecture shows how an aerodynamicist approaches design.[1]

1.2 Examples of Innovative Configuration Concepts

This section includes three innovative aircraft concepts to illustrate the type of configurations that aerodynamicists are called upon to investigate. Two of the concepts, covered in sections 1.2.1 and 1.2.2, have the potential to reduce the cost of subsonic commercial transportation. The third, in section 1.2.3, has the potential to increase the efficiency of supersonic flight. In section 1.2.4, we present additional examples of a range of proposed concepts, many developed by student design teams. Some of these are impractical for aerodynamic or other reasons. Yet all have required an aerodynamic assessment, and several could benefit from a better understanding of the aerodynamic design principles based on the physics of flow fields.

1.2.1 The Blended-Wing Body

The blended-wing body (BWB) concept, shown in figure 1-1, combines the fuselage and wing into a concept that offers the potential aerodynamic advantages of the flying wing while providing the volume required for commercial transportation. This configuration offers the potential for a large increase in aerodynamic efficiency characterized by the lift-to-drag ratio, L/D, and an associated large reduction in fuel use and in maximum takeoff gross weight (MTOGW). The major overview was given by Robert Liebeck,[2] who predicted that the BWB has an 18% reduction in MTOGW and 32% in fuel burn per seat compared to the then-proposed A380-700. This Robert Liebeck paper is an archival publication of Liebeck's Wright Brothers Lecture at the 40th Aerospace Sciences Meeting and Exhibit, Reno, Nevada, in January 2002.

Note that the BWB does not have large moment arms for generating control moments and also requires a nontraditional passenger compartment. That is why the design is more difficult than traditional designs and requires the use of multidisciplinary design optimization methods to obtain the predicted benefits.[3] Roman et al. have demonstrated a significant speed advantage over other commercial transports.[4] Because of the advantages of this concept, it has been extensively studied by many design groups. More references on the BWB concept are available on one of my websites.[5]



Figure 1-1: The blended-wing body (BWB) concept. From NASA/Boeing. Public domain.

1.2.2 The Strut-Braced Wing

In the early 1950s, Dr. Werner Pfenninger, Swiss-born aerodynamicist, suggested the truss-braced wing as a promising concept for long-range transport missions. His extensive research in laminar flow control (LFC) using suction demonstrated significant reductions in skin friction drag on wings, even at high subsonic Mach numbers and high Reynolds numbers. LFC prevented laminar separation, and it extended laminar flow up to 100% on some wings. To take full advantage of the reduced skin friction (or parasite) drag, the induced drag needs to be significantly reduced as well; this is because the maximum L/D occurs when the induced and parasite drag are equal.[6] In the mid 1970s, Pfenninger shared his research on design considerations for LFC-enabled large global-range high subsonic speed transport aircraft at a special course organized by AGARD.[7] This research formed one part of a comprehensive lecture on Laminar Flow Control Laminarization that he gave at this special course. In 1992, Pfenninger and Vemuru shared their insights into the design philosophy of long-range LFC transports with advanced LFC airfoils.[8] The key observations and issues may be summarized as:

- The tight coupling between structures and aerodynamics requires the use of modern multidisciplinary design optimization (MDO) methodology to make it work.
- The strut allows a thinner wing without a weight penalty, with a higher aspect ratio, and with less induced drag.
- Reduced thickness-to-chord ratio (t/c) allows less sweep without a drag penalty.
- Reduced sweep leads to *even lower* wing weight.
- Reduced sweep allows for some natural laminar flow and thus reduced skin friction drag.



Figure 1-2: The strut-braced wing concept. From NASA. Public domain.

The benefits of this concept are similar to the benefits cited for the BWB configuration in section 1.2.1. This concept has the advantage that it doesn't have to be used on a large airplane. The key issue is the need to provide a mechanism to relieve the compression load on the strut under negative *g* loads. Work on this concept was done at Virginia Tech.[9,10] Figure 1-2 shows the design resulting from a joint Virginia Tech–Lockheed Martin study. More references on strut-based concepts are available on one of my websites.[11]

1.2.3 The Oblique Wing



Figure 1-3: The oblique-wing concept. From NASA. Public domain.

Supersonic airplanes are especially difficult to architect for efficient flight. In addition to the issue of spanloading for low induced drag, the designer has to contend with supersonic wave drag associated with the volumetric distribution and the wave drag due to lift. One unique concept proposed by R. T. Jones[12] helps resolve the aerodynamic dilemma. Jones points out that using an obliquely swept wing allows the lift to be distributed longitudinally in an elliptic distribution as well as laterally. At the same time, the maximum cross-sectional area can be reduced and the area distribution can be very smooth. Aerodynamically this is the right configuration for supersonic flight. Of course, the unusual asymmetric configuration introduces other challenges that must be overcome. Numerous models were built and flown to demonstrate that these configurations could, in fact, fly. One small manned aircraft, the AD-1, was built and flown successfully, as shown in figure 1-3.[13,14,15]

Because of the possible adverse wing-body interference associated with this configuration, the natural choice for the oblique wing is a flying wing configuration. This has been the focus of further configuration studies.[16,17] More references on oblique-wing concepts are available on one of my websites.[18]

1.2.4 Additional Examples

Figure 1-4 shows an example of the strut-braced wing (SBW) concept implemented on an A-7 for possible demonstration in 2000 by a Virginia Tech student team, Team REVCON, consisting of Chad Leigh, Josh Frommer, Conor Haines, Eric Kromer, Chris Lampman, Adam Lessey, Todd Norell, Chris Rourke, Joe Vasquez, Kurt Werner, and Han Woo. The team derived their motivation from ongoing SBW studies, as mentioned in section 1.2.2. This model was included as one of the examples in a Virginia Tech report[19] prepared for NASA LaRC under contract.



Figure 1-4: The strut-braced wing concept as it might be demonstrated on an A-7. From Ko, Mason, Grossman, & Schetz. CC BY-NC-SA 4.0.



Figure 1-5: The innovative arch-shaped strut concept by VT AOE "Imagineering." From J. M. Grasmeyer. Reproduced with permission.

The arch-shaped strut concept, presented in figure 1-5, illustrates the result of some imagineering. (Imagineering is an American English word that is a combination of imagine plus engineering. Collins dictionary defines this word to mean *the implementing of creative ideas into practice*.) It is a concept by Prof. Joe Schetz of Virginia Tech. The model was made using rapid prototyping.

Figure 1-6 shows a concept that is the result of a collaborative senior design project between Loughborough University (in the UK) and Virginia Tech. This concept draws on the idea of increased efficiency made possible by the use of the box-plane concept.

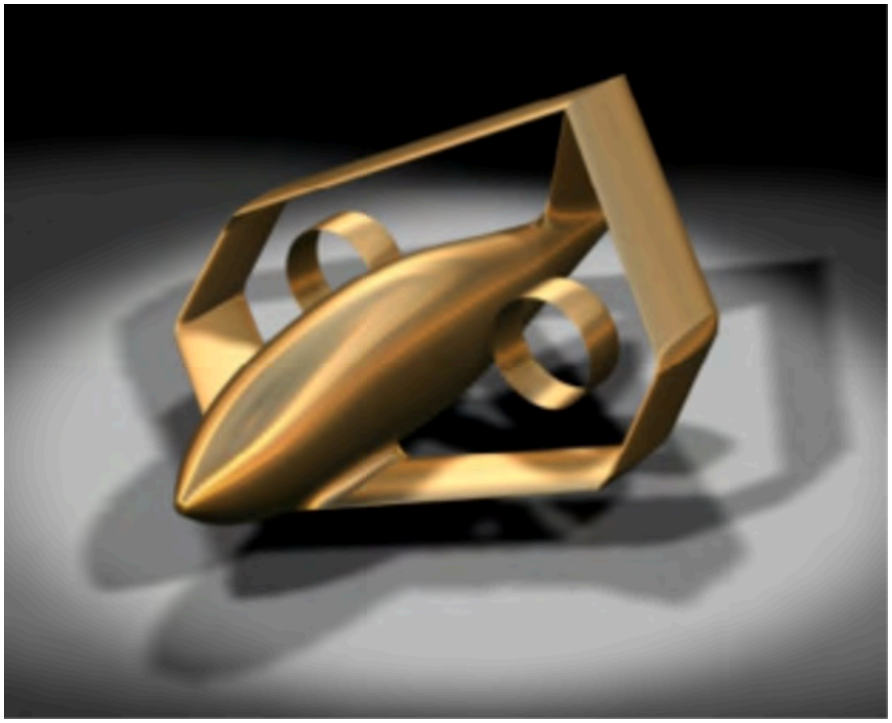


Figure 1-6: Ikelos—a box-wing concept. Result of a senior design project between Loughborough University and Virginia Tech. From D. Etchells. CC BY-NC-SA 4.0. J. F. Marchman, III.

Figure 1-7 is also from a senior design project.[20] It is a roadable aircraft, sometimes called a flying car. There has been additional study into some of the details of this concept and its further refinement.[21]

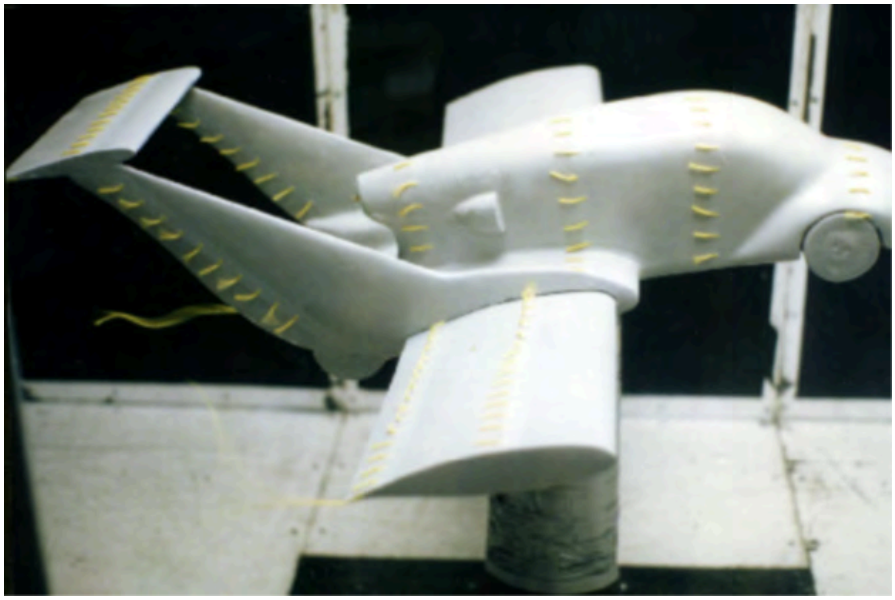


Figure 1-7: Pegasus—a dual-mode personal vehicle concept in the Virginia Tech Stability Wind Tunnel. From J. F. Marchman, III. CC BY-NC-SA 4.0.

The next example is Askin Isikveren's innovative X-Wing concept[22] known as TOLS (Twin Oblique Lifting Surfaces). Shown in figure 1-8, this concept is intended to take advantage of the strut-braced wing concept by using the engine pylons to reduce wing weight and to employ the advantages of an oblique/forward-swept wing to reduce drag (described in more detail in Isikveren's AIAA paper).



Figure 1-8: The X-Wing TOLS concept by Askin T. Isikveren. Fair use.

Figure 1-9 is an example of the so-called inboard wing configuration[23] based on the concept initially proposed by Leroy Spearman.[24] This concept is intended to address the needs of very large aircraft. Spearman expected to reduce, or even eliminate, induced drag by having the fuselages act as endplates to the wing. An assessment of the viability of this concept requires the aerodynamicist to test the validity of Spearman's flow hypothesis. Note that although we don't show it, there is another variation of the twin-fuselage concept due to Houbolt with wings extending outboard of each fuselage.[25] That concept may have a stronger basis in physics.

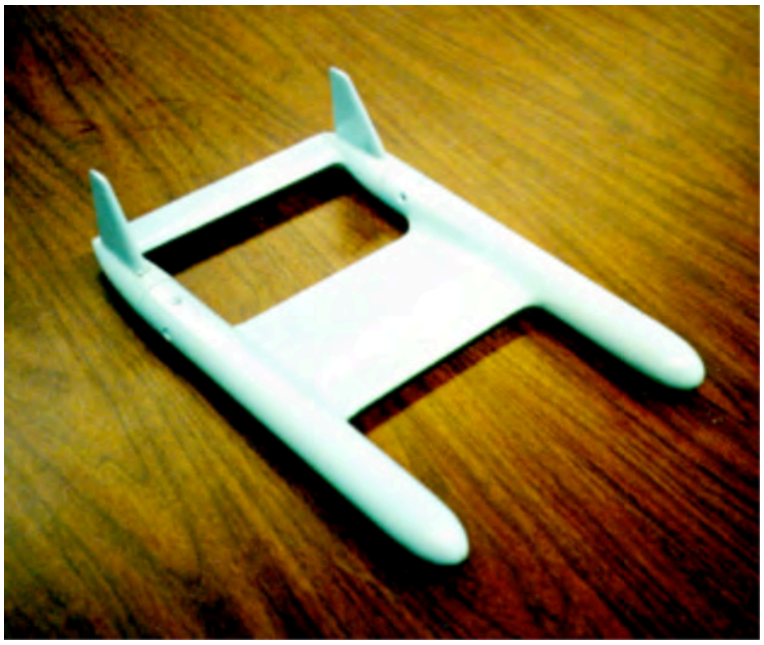


Figure 1-9: The inboard wing concept. From James F. Marchman III. CC BY-NC-SA 4.0.

Figure 1-10 shows the Boeing Sonic Cruiser studied by Boeing as a potential new aircraft concept in 2001 and 2002. Hepperle[26] performed independent analysis of this configuration. Boeing dropped the Sonic Cruiser from further development in 2003.[27]

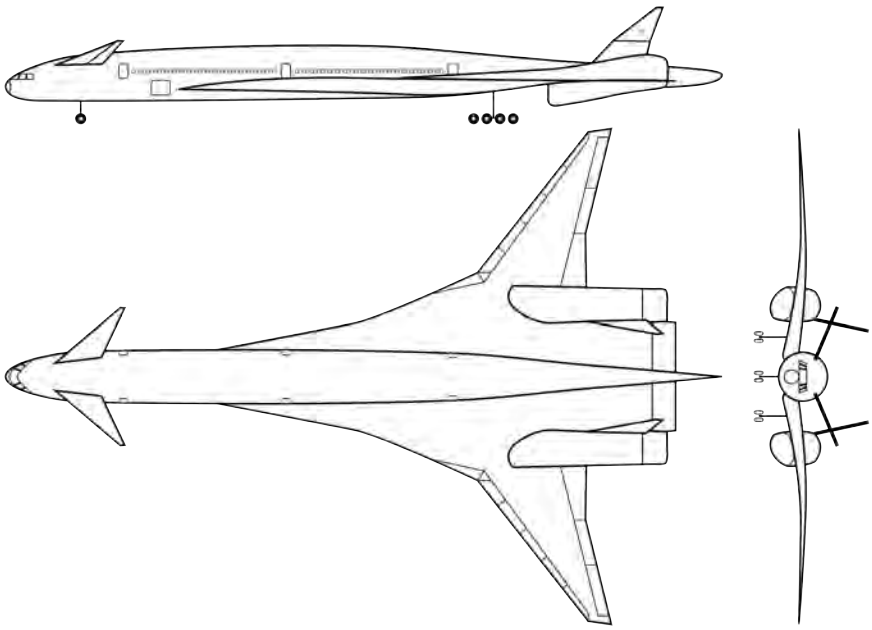


Figure 1-10: The Boeing Sonic Cruiser. From Mliu92. Wikimedia. CC BY-SA 4.0.

Figure 1-11 shows the Bird of Prey, a concept built and flown by the Boeing Phantom Works in the 1990s, presumably as a stealth concept.[28]



Figure 1-11: The Bird of Prey by Boeing Phantom Works. From unknown author. Copyright undetermined. Fair use.

There are myriad other examples, including UAVs, from micro UAVs to Global Hawk. Figure 1-12 shows one of them: the AeroVironment Black Widow micro UAV.[29] This concept is remarkable, as it has flown for nearly an hour while sending a video feed back to a base station.



Figure 1-12: The AeroVironment Black Widow. *Copyright undetermined. From AeroVironment. Fair use.*

Figure 1-13 is an artist's rendering of the X-65 technology demonstrator being developed by Defense Advanced Research Projects Agency (DARPA) under its Control of Revolutionary Aircraft with Novel Effectors (CRANE) program.[30] Virtually every aircraft since the Wright Flyer of 1903 has used a system of movable, external control surfaces for flight control. The X-65 breaks this design paradigm by using jets of air from a pressurized source to shape the flow of air over the aircraft surface, with active flow control (AFC) effectors embedded in several flying surfaces to control the plane's roll, pitch, and yaw moments. The elimination of external moving parts is expected to reduce weight and complexity and to improve performance of future operational aircraft.

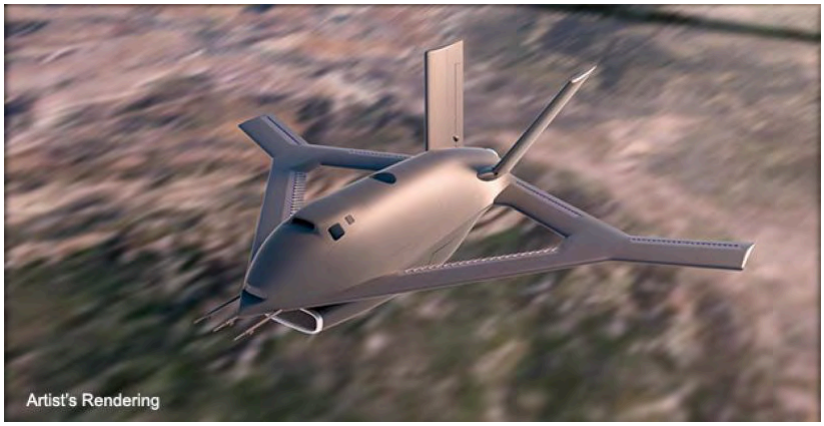


Figure 1-13: The X-65 technology demonstrator being developed by Aurora for DARPA's CRANE program. *From DARPA. Public domain.*

The X-65 is being developed by Aurora Flight Sciences under a DARPA contract. The aircraft has a unique design with a distinctive joined tandem wing in a diamond configuration. The wingspan is around 9 meters (30 feet). It has twin vertical tails, and is powered by a single turbojet engine. Its weight is targeted to be around 3,200 kilograms (7,000 pounds), and its cruise speed is targeted to reach up to Mach 0.7. It will have modular construction so that the AFC effectors and wing shapes can be changed relatively easily for test purposes. The aircraft will initially be equipped with both traditional flaps and rudders, as well as the AFC effectors, to provide a baseline for performance comparison. Flight testing is expected to start in late 2025. Anyone interested in learning about the fundamentals of modern flow control technologies and their applications may check out the book by Joslin and Miller.[31]

This brief survey of current unconventional concepts being investigated illustrates the wide range of shapes that have garnered interest. All require an aerodynamic assessment of their potential performance.

1.2.5 Morphing Airplanes

We've seen that specific airplane configurations are related to specific requirements. What if an airplane could change its shape in flight to respond to different flight requirements? The oblique wing configuration shown in figure 1-3 is one example with a variable-sweep wing that changes sweep to best meet the flight performance requirements. There is considerable interest in possibly using advances in structures, actuators, sensors, and controls to design an airplane that can achieve significantly increased performance by changing its shape in flight; this process is called *morphing*.[32] This is a true multidisciplinary design activity, and a number of different advanced concept investigations fall within this general category, including recent work at Virginia Tech.[33]

Although a wide range of configuration options are discussed in this section, there is still room for dreamers. We don't yet know what the ultimate airplane concept is! Concerning the configurations described here, all of them are appropriate in the right circumstance. After all, they always say, *There is a time and place for everything*.

1.3 Decision Issues

With the airplane's mission requirements and configuration options discussed above in mind, designers create a configuration that best satisfies the requirements. The following list summarizes the possibilities that have to be considered.

- Should it be a canard? aft tail? tailless? three-surface? sensitivity to CG travel?
- Should the wings be swept? forward or aft?
- Should it be a high aspect ratio, low aspect ratio, or slender wing?
- What is the control concept? Should it be stable or unstable?
- Should thrust vectoring be used as a control? How is the propulsion system integrated?

Designers make decisions about the specific options to incorporate into their configuration based on an understanding of the connection between the mission requirements and the strengths and weaknesses of the various configuration concepts.

Knowledge of previous designs is important in making these decisions. As an example, consider the Joint Strike Fighter (JSF) competition of the 1990s. Back in the 1960s, the US had tried to design a plane to be used by both the Air Force and Navy. The result was the F-111, which proved to be too heavy for use on a carrier. The JSF project stipulated a requirement that the new plane should be designed to meet the needs of the Navy, Air Force, and Marines. As it turned out, the resulting F-35 is not a single airframe, but comes in different versions for each service, with considerable amount of commonality among them. Anyone interested in learning more about the F-35 project should consider reading a book published by AIAA in 2019 titled “The F-35 Lightning II: From Concept to Cockpit” authored by Jeffrey W. Hamstra.

Another example of a key design constraint is the eighty-meter gate box-based span limit that affects the A380's design. If you simply scale up previous Airbus, designs you discover that the wingspan would be much larger than 80 meters. So it is clear that aerodynamic efficiency has been compromised to meet the span limit constraint.

1.4 Design Approaches

1.4.1 Traditional approach

A matrix of concepts is usually defined by the designers in trying to create the best concept to satisfy a design requirement. The concepts are then evaluated against each other. There is not usually enough time to make a thorough evaluation of each design concept, and often not much detail is used. Relatively crude approximate analyses are used to choose "the configuration." Once the concept is selected, more detailed design studies begin.

At this point, the disciplinary specialists (including the aerodynamicists) on the design team are given the basic design parameters such as the wing planform (sweep, aspect ratio, etc.) and maximum t/c, among others. At this stage, there is usually limited opportunity to change the basic design parameters. The aerodynamicist defines the detailed airfoil shapes, twist and camber, high lift system, and for supersonic aircraft, the area ruling.

1.4.2 Multidisciplinary Design Optimization (MDO) Approach

This is a new approach to computational design technology that seeks to use the more detailed analyses and design methods typical of preliminary and detail design much earlier in the design process. This allows the configuration to be defined using much more accurate information, with less uncertainty and risk. This approach has become known as MDO. A classic example that can be addressed using MDO is the aerostructures trade-off:

- A thinner wing is better for aerodynamics, worse for structures (fuel weight versus structural weight).
- More sweep reduces transonic wave drag, increases wing weight.

Numerous airplane design research studies using MDO have been done recently. We refer interested readers to two representative examples.[34,35]

1.5 The Role of Aerodynamicists Within the Overall Design Process

Aerodynamicists play a pivotal role throughout the entire aircraft design process because they "own" the outer mold line (OML), as asserted by Nicolai and Carty.[36] If you are an aerodynamicist on the design team, you have to be the advocate for your discipline by considering the following:

- Which aerodynamic concepts are appropriate?
- Consider the appropriate uses and risks of advanced technology.

To be effective, you must:

- Show the aerodynamic benefits of the configuration very clearly.
- Accommodate other team members.
- Be ready to change.

Finally, the best airplane is not the one with the highest $(L/D)_{max}$, but most likely the one with the lowest cost. There are many costs that should be estimated. Ultimately there is the life cycle cost (LCC), but other costs are frequently more important. Examples include the direct operating cost (DOC) and the acquisition cost.

Once the concept is selected, many more details of the aerodynamic configuration will still have to be determined. The material in the remainder of the book addresses many of these details.

1.6 What's Left Out?

In this book, we have omitted discussion of numerous aspects of configuration aerodynamics in favor of the absolute essentials. Even the concepts discussed aren't necessarily covered in depth, and the interested reader can use the book's references and appendices as a start toward more detailed studies of the concepts. Omitted topics include:

- Aeropropulsion integration
- Unsteady flows (which may in fact become important in design and aeroelastic effects)
- Helicopter aerodynamics
- Missile aerodynamics

Chapter 1 Exercises

1.1 What characteristic controls induced drag?

Consider four rectangular wings:

Wing	Span	Chord
1	10 ft	1.00 ft
2	10 ft	2.00 ft
3	9 ft	0.90 ft
4	9 ft	1.11 ft

Table 1.1: Four wings and their characteristics

Explicitly stating your assumptions,

a. What is the wing area of each wing?
b. What is the aspect ratio of each wing?
c. At q = 40 psf and a lift of 200 lbs,

- What are the lift coefficients for each wing?
- What are the induced drag coefficients for each wing?
- What are the values of the induced drags for each wing?

d. Explain your results.

1.2 Key aerodynamic relationships

Assuming:

$$C_D = C_{D_0} + \frac{C_L^2}{\pi ARE}$$

a. Derive an expression for L/D_{max}.
b. What is the corresponding C_L?
c. Comment on the implications for aerodynamic design (i.e., provide a physical statement of the L/D_{max} condition).

1.3 Developing a feel for key design parameters

Find the wing loading, W/S, and cruise C_L for one of the variants of the A380 and B737 transports and for the F-22 and F-35 fighters. Compare these values with typical values for a classic general aviation airplane, the Cessna 172. What can you say about these results?

1.4 A start toward thinking like an aerodynamic designer

a. Read Irv Waaland's Wright Brothers Lecture ("Technology in the Lives of an Aircraft Designer") and write one page describing what you learned.

b. Read the paper on the DC-9 development by Shevell and Schaufele ("Aerodynamic Design Features of the DC-9," Journal of Aircraft, Vol. 3, No. 6, Nov-Dec 1966, pp 515-523) and discuss their experiences with aerodynamic pitchup.

c. Summarize the aerodynamic configuration issues for the Black Widow micro UAV.

d. Summarize the aerodynamic configuration issues for SpaceShipOne, the Scaled Composites Model 316.

e. Summarize the aerodynamic configuration issues for CAC Boomerang aircraft.

f. Summarize the aerodynamic configuration issues for the low-strength sonic boom supersonic flight demonstrator (https://www.nasa.gov/directorates/armd/iasp/lbfd).

Figure References

Figure 1-1: NASA/Boeing. Blended-wing body concept. Public domain. https://www.nasa.gov/aeronautics/new-ideas-sharpen-focus-for-greener-aircraft

Figure 1-2: NASA. The strut-braced wing concept. Public domain. https://www.nasa.gov/centers/ames/orgs/aeronautics/windtunnels/multimedia/truss-braced-wing

Figure 1-3: NASA. AD-1 in flight at 60 degree wing sweep. Public domain. https://web.archive.org/web/20250309005849/https://www.dfrc.nasa.gov/Gallery/Photo/AD-1/HTML/ECN-13302B.html

Figure 1-4: Ko, A., Mason, W. H., Grossman, B., and Schetz, J. A. "A-7 Strut Braced Wing Concept Transonic Wing Design," WPI-AOE-275, Jul. 12, 2002. Prepared for NASA LaRC under contract. https://archive.aoe.vt.edu/mason/Mason_f/AOE275SBW.pdf

Figure 1-5: Grasmeyer, J. M., Naghshineh-Pour, A., Tetrault, P.-A., Grossman, B., Haftka, R. T., Kapania, R. K., Mason, W. H., and Schetz, J. A. "Multidisciplinary Design Optimization of a Strut-Braced Wing Aircraft with Tip-Mounted Engines," MAD Center Report 98-01-01, Virginia Tech, AOE Dept., Blacksburg, VA, Jan. 1998.

Figure 1-6: Etchells, D. Ikelos. Loughborough University.

Figure 1-7: Virginia Polytechnic Institute and State University and Longhborough University. "Pegasus: The First Successful Roadable Aircraft," AGATE General Aviation Design Competition 2000, p. 327. https://archive.aoe.vt.edu/design/pegasus/reports/MainDoc.pdf. Figure released under CC BY-NC-SA 4.0 by James F. Marchman, III.

Figure 1-8: Isikveren, A. T. "High-Performance Executive Transport Design Employing Twin Oblique Lifting Surfaces," Paper 2001-01-3031, 2001 SAE World Aviation Congress and Exposition, Seattle, WA, Sept. 2001. Fair use. https://www.researchgate.net/publication/274706798_High_Performance_Executive_Transport_Design_Employing_Twin_Oblique_Lifting_Surfaces

Figure 1-9: Model of inboard wing concept. Courtesy of James F. Marchman III. CC BY-NC-SA 4.0.

Figure 1-10: Mliu92. Boeing Sonic Cruiser 3-view. 2019. CC BY-SA 4.0. https://commons.wikimedia.org/wiki/ File:Boeing_Sonic_Cruiser_3-view.svg

Figure 1-11: Unknown author. Retrieved from multiple sources. Copyright undermined. Fair use.

Figure 1-12: AV AeroVironment. Copyright undetermined. Fair use. https://www.avinc.com/innovative-solutions/small-uas

Figure 1-13: DARPA. Artist's rendering of X-65. 2024. Public domain. https://www.darpa.mil/news/2024/x-65-demonstrator

Notes

1. Waaland, I. T., "Technology in the Lives of an Aircraft Designer," AIAA Wright Brothers Lecture, Aircraft Design and Operations Meeting, Baltimore, MD, Sept. 23-25, 1991. https://doi.org/10.2514/6.1991-3069
2. Liebeck, R. H., "Design of the Blended Wing Body Subsonic Transport," Journal of Aircraft, Vol. 41, No. 1, Jan.-Feb. 2004, pp. 10–25.
3. Wakayama, S., "Multidisciplinary Design Optimization of the Blended-Wing-Body," AIAA Paper 98-4938, 7th AIAA/USAF/NASA/ISSMO Symposium on Multidisciplinary Analysis and Optimization, St. Louis, MO, Sept. 2-4, 1998.
4. Roman, D., Gilmore, R., and Wakayama, S., "Aerodynamics of High-Subsonic Blended-Wing-Body Configurations," AIAA 2003-0554, 41st Aerospace Sciences Meeting and Exhibit, Reno, NV, Jan. 6-9, 2003.
5. Mason, W. H., "Blended Wing Body Concept." https://archive.aoe.vt.edu/mason/Mason/ACiADblended.html
6. Pfenninger, W., and Bacon, J. W., "Design Studies of Long Range Laminar Suction Airplanes at High Subsonic Speeds," WADC TR-56-111, US Air Force, Apr. 1957, pp. 294–328.
7. Pfenninger, W., "Design Considerations of Large Global Range High Subsonic Speed LFC Transport Airplanes," AGARD-R-654, Special Course on Concepts for Drag Reduction, von Karman Institute, Rhode-Saint-Genese, Belgium, Mar. 28–Apr. 1, 1977, pp. 3-63 to 3-75.
8. Pfenninger, W., and Vemuru, C. S., "Design Philosophy of Large Global Range LFC Transports with Advanced Supercritical LFC Airfoils," *Natural Laminar Flow and Laminar Flow Control*, edited by R. W. Barnwell and M. Y. Hussaini (eds.), Springer-Verlag, New York, 1992.
9. Grasmeyer, J. M., Naghshineh, A., Tetrault, P.-A., Grossman, B., Haftka, R. T., Kapania, R. K., Mason, W. H., Schetz, J. A., "Multidisciplinary Design Optimization of a Strut-Braced Wing Aircraft with Tip-Mounted Engines," MAD 98-01-01, Virginia Tech MAD Center Report, Jan. 1998.
10. Gundlach, J. F., Tetrault, P.-A., Gern, F. H., Naghshineh-Pour, A., Ko, A., Schetz, J. A., Mason, W. H., Grossman, B., Kapania, R. K., and Haftka, R. T., "Multidisciplinary Design Optimization of a Strut-Braced Transonic Transport," AIAA Paper 2000-0420, 36th Aerospace Sciences Meeting and Exhibit, Reno, NV, Jan. 2000.
11. Mason, W. H., "Strut and Truss-Braced Wing Concepts." https://archive.aoe.vt.edu/mason/Mason/ACiADtbw.html
12. Jones, R. T., and Nisbet, J. W., "Transonic Transport Wings-Oblique or Swept?" AIAA Astronautics and Aeronautics, Jan. 1974, pp. 40–47.
13. McMurtry, T. C., Sim, A. G., and Andrews, W. H., "AD-1 Oblique Wing Aircraft Program," AIAA Paper 81-2354, AIAA/SETP/SFTE/ASE/ITEA/IEEE 1st Flight Testing Conference, Las Vegas, NV, Nov. 11-13, 1981.
14. Curry, R. E., and Sim, A. G., "Unique Flight Characteristics of the AD-1 Oblique-Wing Research Airplane," AIAA Paper 82-1329, AIAA Atmospheric Flight Mechanics Conference, San Diego, CA, Aug. 9-11, 1982.

15. Kroo, I., "The Aerodynamic Design of Oblique Wing Aircraft," AIAA 86-2624, AIAA/AHS/ASEE Aircraft Systems Design and Technology Meeting, Dayton, OH, Oct. 20-22, 1986.
16. Van der Velden, A. J. M., and Torenbeek, E., "Design of a Small Supersonic Oblique-Wing Transport Aircraft," Journal of Aircraft, Vol. 26, No. 3, Mar. 1989, pp.193–197.
17. Seebass, R., "Oblique Flying Wing Studies," New Design Concepts for High Speed Transport, edited by H. Sobieczky, CISM Courses and Lectures, Vol. 366, Springer-Verlag, Vienna/New York, 1997, pp. 317–336.
18. Mason, W. H., "Oblique Wing Concepts." http://archive.aoe.vt.edu/mason/Mason/ACiADoblique.html
19. Ko, A., Mason, W. H., Grossman, B., and Schetz, J. A., "A-7 Strut Braced Wing Concept Transonic Wing Design," VPI-AOE-275, Jul. 12, 2002.
20. Gassler, R., Anderson, W., Bosen, T., Carr, A., Cramer, K., Gray, D., Leasure, D., Lueltinger, S., Pattersson, H., Prem, G., Skinner, G., Stevens, A., Sale, G., Apps, T., Batchelor-Wylan, C., Birtwhistle, J., Downey, M., Goodwin, R., Hodkinson, S., Kalyan, G., Luxmore, J., Panteny, D., Phillippo, D., Smyth, R., and Warren, J. "Pegasus, A Report to the AGATE NASA/FAA General aviation design Competition," Dept. of Aerospace and Ocean Engineering, Virginia Tech, Blacksburg, VA, May 2000.
21. Marchman, J. F., III, Intaratep, N. and Mason, W. H., "A Design for a Dual-Mode Personal Vehicle," AIAA Paper 2002-5877, 2002 AIAA Aircraft Technology, Integration, and Operations Forum, Los Angeles, CA, October 1-3, 2002.
22. Isikveren, A. T., "High-Performance Executive Transport Design Employing Twin Oblique Lifting Surfaces," Paper 2001-01-3031, 2001 SAE World Aviation Congress and Exposition, Seattle, WA, Sept. 2001.
23. Orr, M., Magill, S., Schetz, J., Marchman, J. F., III, Mason, W. H., and Grossman, B., "An Experimental Study of the Aerodynamics of the Inboard Wing Concept," AIAA Paper 2001-0577, 39th AIAA Aerospace Sciences Meeting and Exhibit, Reno, NV, Jan. 8-11, 2001. https://doi.org/10.2514/6.2001-577
24. Spearman, M. L., and Feigh, K., "An Airplane Configuration with an Inboard Wing Mounted Between Twin Fuselages," AIAA Paper 98-0440, 36th AIAA Aerospace Sciences Meeting and Exhibit, Reno, NV, January 12-15, 1998. https://doi.org/10.2514/6.1998-440
25. Houbolt, J. C., "Why Twin-Fuselage Aircraft?" AIAA Astronautics and Aeronautics, Apr. 1982, pp. 26–35.
26. Hepperle, M., "The Sonic Cruiser – A Concept Analysis," International Symposium "Aviation Technologies of the XXI Century: New aircraft Concepts and Flight Simulation," 7-8 May 2002, Aviation Salon ILA-2002, Berlin. http://www.mh-aerotools.de/company/paper_7/astec_2002.htm
27. March, D. J., "Boeing's Failed Concept: Demise of the Sonic Cruiser," Flightpath: The International Journal of Commercial Aviation, Fall 2003, pp. 14–16.
28. Sweetman, B., "First Look," Popular Science, Oct. 18, 2002.
29. Grasmeyer, J., and Keennon, M., "The development of the Black Widow Micro Air Vehicle," AIAA Paper 2001-0127, Jan. 2001.
30. DARPA, "DARPA Moves Forward on X-65 Technology Demonstrator." https://www.darpa.mil/news/2024/x-65-demonstrator
31. Joslin, R. N., and Miller, D. N., "Fundamentals and Application of Modern Flow Control," Progress in Aeronautics and Astronautics, AIAA, Sept. 30, 2009.
32. Wlezien, R. W., Horner, G. C., McGowan, A. R., Padula, S. L., Scott, M. A., Silcox, R. J., and Simpson, J. O., "The Aircraft Morphing Program," AIAA Paper 98-1927, Apr. 1998.
33. Johnston, C. O., Neal, D. A., Wiggins, L. D., Robertshaw, H. H., Mason. W. H., and Inman, D. J., "A Model to Compare the Flight Control Energy Requirements of Morphing and Conventionally Actuated Wings," AIAA Paper 2003-1716, 11th AIAA/ASME/AHS Adaptive Structures Conference, Norfolk, VA, Apr. 7-10, 2003.
34. Alexandrov, N. M., and Hussaini, M. Y. (eds.), *Multidisciplinary Design Optimization: State of the Art*, SIAM, Philadelphia, 1997.
35. Giunta, A. A., Golovidov, O., Knill, D. L., Grossman, B., Mason, W. H., Watson, L. T., and Haftka, R. T., "Multidisciplinary Design Optimization of Advanced Aircraft Configurations," Fifteenth International Conference on Numerical Methods in Fluid Dynamics, edited by P. Kutler, J. Flores, and J.-J. Chattot, in Lecture Notes in Physics, Vol. 490, Springer-Verlag, Berlin, 1997, pp. 14–34.
36. Nicolai, L. M., and Carty, A., "Role of the Aerodynamicist in a Concurrent Multidisciplinary Design Process," Symposium on Aerodynamic Design and Optimisation of Flight Vehicles in a Concurrent MultiDisciplinary Environment, NATO RTO AVT MP-35, Ottawa, Canada, 18-21 Oct. 1999.

2. Foundations of Fluid Mechanics: Governing Equations

In this chapter, we review the governing equations of fluid mechanics that describe flow fields in mathematical terms. Modern computational aerodynamic methods are based on the particular governing equations that they solve. Since computational aerodynamics is now a necessity, not a luxury, for many aspects of configuration aerodynamics, it is crucially important for aerodynamicists to have a good understanding and appreciation of the underlying assumptions and approximations behind an equation before using its associated computational aerodynamic method. We will see that developments in computational methods have resulted in a slightly different approach to fundamental conservation statements compared with presentations before the digital computing age. This chapter also defines the nomenclature and terminology used in current aerodynamics practice. **If you are fully conversant with the derivation and characteristics of the governing equations of fluid mechanics, you might consider skipping the remainder of this chapter and going straight to Chapter 3.**

The presentation of material in this chapter presumes that the reader has previously had a course in fluid mechanics or aerodynamics. Many excellent discussions of the foundations of fluid mechanics for aerodynamics application are available in books by Karamcheti,[1] Bertin,[2] Anderson,[3] and Moran.[4] The best formal derivation of the equations was assembled by Grossman.[5] Indeed, an entire book has been written on the equations of fluid mechanics by Hoffman et al.[6]

2.1 Governing Equations of Fluid Mechanics

Fluid is assumed to be a continuum. For virtually all aerodynamics work, this is a valid assumption. One case where this may not be true is when fluid density is so low that the actual molecular motion must be analyzed, which is the purview of the field of rarefied gas dynamics. This may be important for vehicles in hypersonic flight. Aeroassisted orbital transfer vehicles (AOTV's) are examples of the vehicles requiring noncontinuum flow field analysis.

The fluid is defined by an equation of state and by the thermodynamic and transport properties, namely, the ratio of specific heats, γ, viscosity, μ, and the coefficient of heat conduction, k. Governing equations and boundary conditions control the motion of the fluid. The governing equations are given by conservation laws listed in table 2-1.

Governing equations	
Mass	Continuity
Momentum	Newton's Second Law, $\boldsymbol{F} = m\boldsymbol{a}$
Energy	First Law of Thermodynamics

Table 2-1: Conservation laws for governing equations

Coordinate systems are also important in aerodynamics. The general equations of fluid motion are independent of the coordinate system. However, simplifying assumptions frequently introduce *directional bias* into approximate forms of the equations; they must be used with a specific coordinate system orientation relative to the flow field.

Traditionally, Cartesian coordinates were used to describe vehicle geometry. In this chapter, we will work entirely in the Cartesian coordinate system. It is frequently desirable to make calculations in non-Cartesian coordinate systems that are distorted to fit a particular shape. In general, these are non-orthogonal curvilinear coordinates. Even when using Cartesian coordinates, the *x*-, *y*-, and *z*-coordinates are oriented differently depending on whether the flow is two- or three-dimensional. Figure 2-1 shows the usual two-dimensional coordinate system.

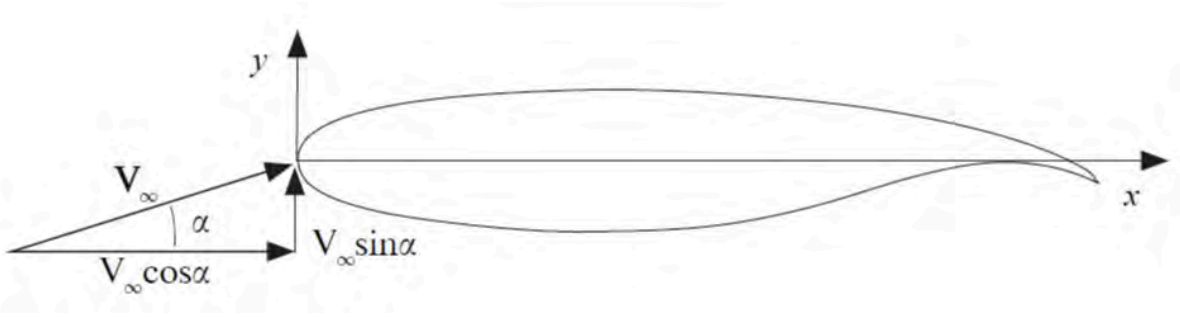


Figure 2-1: Body-fixed Cartesian coordinate system for two-dimensional flow. From W. H. Mason. Adapted by S. Madden.

The standard coordinate system used in three dimensions is illustrated in figure 2-2. Note the different orientation of the *y* coordinate in figures 2-1 and 2-2. In three dimensions, *x* is chordwise, much like it is in 2D, but *y* is spanwise instead of being normal to the chord. The right-hand rule determines the direction of the *z* coordinate. Figure 2-2 also shows the components of the freestream velocity vector, $\boldsymbol{V}_\infty$, in *x*, *y*, and *z* directions. The wing is flying at an angle of attack of α and a sideslip angle of β. The unit vectors in *x*, *y*, and *z* directions are denoted by $\boldsymbol{i}$, $\boldsymbol{j}$, and $\boldsymbol{k}$, respectively.

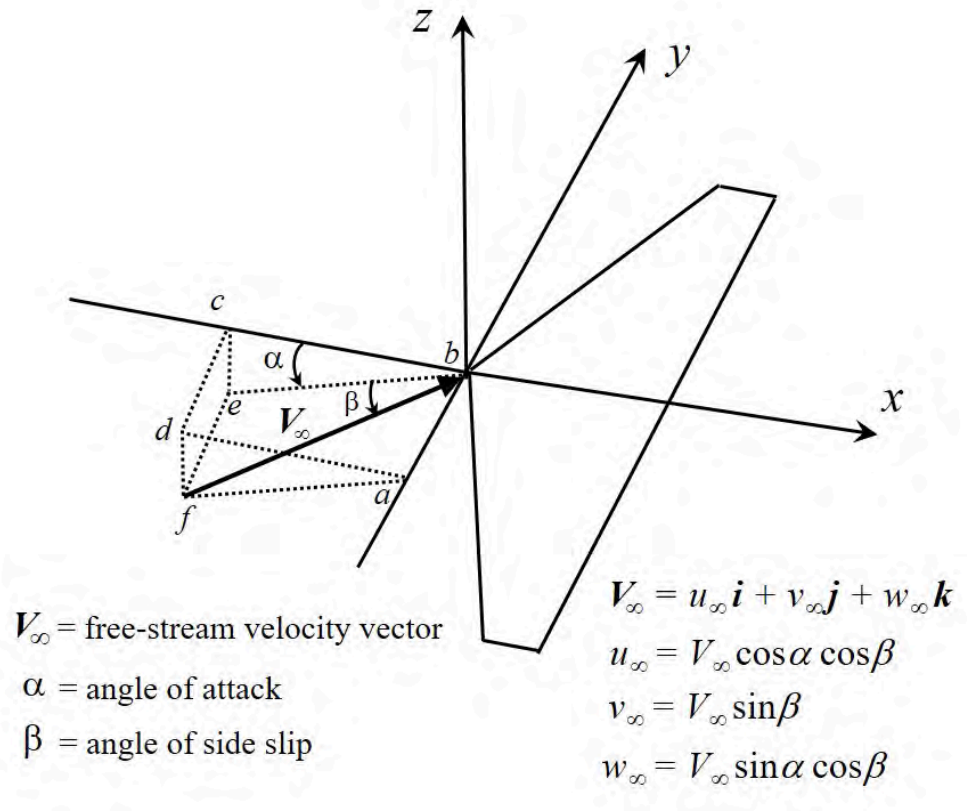


Figure 2-2: Standard body-fixed Cartesian coordinate system for three-dimensional flows. From W. H. Mason. Adapted by S. Madden.

In Cartesian coordinates, the independent variables are x, y, z, and t. Here t denotes time. We want to know the velocities (u, v, w) and the fluid properties (p, ρ, T). (Note that u, v, and w are the components of the flow velocity in the x, y, and z directions, respectively.) These six unknowns require six equations which are shown in table 2-2.

Six equations	
Continuity	1 equation
Momentum	3 equations
Energy	1 equation
Equation of state	1 equation

Table 2-2: Six equations of fluid mechanics

Assumptions frequently reduce the number of equations required; for example, incompressible, inviscid, and irrotational flow can be described by a single equation, as shown below in section 2.5. Prior to the 1980s, almost all aerodynamics work used a single partial differential equation, possibly coupled with another equation. An example of this approach is the calculation of potential flow for the inviscid portion of the flow field, which is used in combination with the boundary layer equations to compute the flow field where an estimate of the viscous effects is required.

2.2 Derivation of Governing Equations

Governing equations of fluid motion are mathematical models based on the conservation laws (for mass, momentum, and energy) and the fluid properties as listed in section 2.1. For most of the practical aerodynamic applications, the governing equations are numerically solved to determine the density, velocity, pressure, and temperature distributions. To develop the governing equations themselves, we can use two approaches, Lagrangian and Eulerian.

1. **Lagrangian:** In this approach, we observe the trajectory of an individual fluid particle as it moves in time through the space surrounding a body. The space itself is defined by a coordinate system fixed to the body, commonly referred as a body-fixed coordinate system. Figures 2-1 and 2-2 show body-fixed coordinates systems in two and three dimensions, respectively. Note that the motion of every fluid particle is described in terms of a "fixed reference configuration" which could be (but isn't necessarily) the position in space occupied by each fluid particle at an initial time, $t = 0$. The Lagrangian approach may be considered as the conventional application of Newton's Second Law to each fluid particle. Even in steady flow, the forces encountered by the particle are a function of the time history of its motion.
2. **Eulerian:** In contrast to the Lagrangian approach, the Eulerian approach considers the entire space around the body as a field, also called a flow field, and determines flow properties such as velocity and pressure at a given point in the field through which the fluid particles move. The space itself is defined by a body-fixed coordinate system. We essentially ignore the motion of individual fluid particles and instead consider the distribution of velocity and pressure throughout the space around a body. This approach imitates wind tunnels, in which fluid particles flow past a body and flow properties are measured at various points in the space surrounding the body.

It is worth noting that the Lagrangian and Eulerian approaches describe the same physical phenomena. Therefore, they are mathematically related. Karamcheti[7] provides a particularly good explanation of the underlying ideas in his Chapters 4 through 7.

The Eulerian approach is almost universally used to develop the governing equations of fluid motion. The use of this approach requires careful attention in the application of the conservation concepts and of Newton's Second Law in particular. Computational aerodynamic methods have been developed to numerically solve the resulting equations. Newton's Law governs the motion of every fluid particle. To apply this law in the Eulerian approach, we define a control volume that maintains a fixed location relative to the coordinate system but through which fluid particles traverse. The connection between the rate of change of the properties of a fluid particle (e.g., velocity, density, pressure) and the rate of change of fluid properties flowing through the control volume* requires special consideration. The substantial derivative, discussed in section 2.2.2, is employed to define the rate of change of the properties of the fluid particle as it moves through the flow field relative to the fixed coordinate system. An integral approach to the description of the change of properties of a fluid particle relative to the fixed coordinate system is available through the use of the Reynolds transport theorem, which is described in Owczarek[8] and section 1.2 of Grossman.[9]

The conservation equations of fluid motion can be expressed in either a differential or integral viewpoint. The differential form of the equations is found in most aerodynamics books. However, the integral form is preferred for numerically solving the equations since integrals are more accurately computed than derivatives. The integral form is also better suited for simulating discontinuities (shocks) in the flow field than the differential form, which assumes fluid properties to be continuous. We will use aspects of each approach in this book.

*The concept of a "control volume" arose as an engineering requirement for a means to formulate the physical description to allow calculations to be made. It differs from the viewpoint adopted by physicists. An explanation of the concept's origins is contained in Walter G. Vincenti's 1990 book *What Engineers Know, and How They Know It: Analytical Studies from Aeronautical History*, published by John Hopkins University Press. The relevant chapter is entitled "A Theoretical Tool for Design: Control Volume Analysis 1912–1953."

2.2.1 Conservation of Mass: The Continuity Equation

In this section, we derive the continuity equation from a control volume viewpoint (in 2D), and then we look at the equivalent integral statement and the use of the Gauss divergence theorem to establish the connection. Other derivations are given by Moran (sections 2.2, 2.3, 2.4),[10] Anderson (Chapters 2 and 6),[11] and Bertin and Smith (Chapter 2).[12]

From a control volume viewpoint, the statement of conservation of mass is in words simply:

Net outflow of mass through the surface surrounding the volume = decrease of mass within the volume.

To translate this statement into a mathematical form, consider the control volume given in figure 2-3. Here, *u* is the velocity in the *x*-direction, *v* is the velocity in the *y*-direction, and ρ is the density. The following represents the net mass flow rate, or flux,* out of the volume, as illustrated in figure 2-3:

$$[\mathrm{X}-\mathrm{out}]-[\mathrm{X}-\mathrm{in}]+[\mathrm{Y}-\mathrm{out}]-[\mathrm{Y}-\mathrm{in}]=\text{change of mass (decrease)}=-\frac{\partial \rho}{\partial t}\Delta X\Delta Y \qquad (2\text{-}1)$$

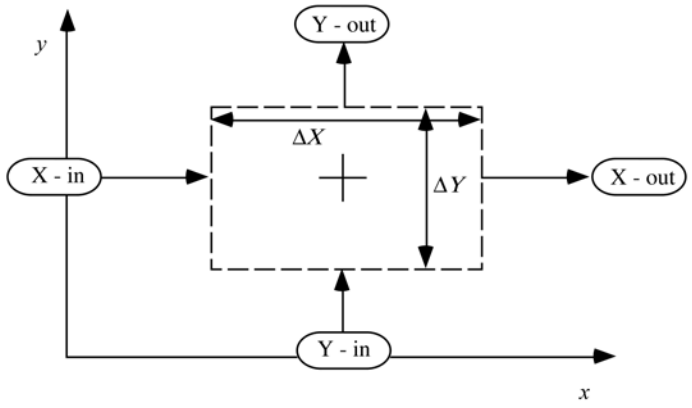


*Figure 2-3: Control volume for conservation of mass.***

*A flux is a quantity that flows across the boundary of a defined surface. Typically we think of mass, momentum, and energy fluxes.

** Note that convention requires that control volumes be described using dashed lines to illustrate that the boundaries are fictitious and that fluid flows freely across them.

We use a Taylor series expansion of the mass fluxes into the volume around the origin of the volume. The flux per unit length through the surface is multiplied by the length of the surface.

$$\begin{aligned}
[\mathrm{X}-\mathrm{out}] &= \left[\rho u+\frac{\partial \rho u}{\partial x}\cdot\frac{\Delta X}{2}\right]\Delta Y \\
[\mathrm{X}-\mathrm{in}] &= \left[\rho u-\frac{\partial \rho u}{\partial x}\cdot\frac{\Delta X}{2}\right]\Delta Y \\
[\mathrm{Y}-\mathrm{out}] &= \left[\rho v+\frac{\partial \rho v}{\partial y}\cdot\frac{\Delta Y}{2}\right]\Delta X \\
[\mathrm{Y}-\mathrm{in}] &= \left[\rho v-\frac{\partial \rho v}{\partial y}\cdot\frac{\Delta Y}{2}\right]\Delta X
\end{aligned} \qquad (2\text{-}2)$$

Substituting these terms in equation (2-1), we arrive at equation (2-3) below.

$$\begin{aligned}
&\left[\rho u+\frac{\partial \rho u}{\partial x}\cdot\frac{\Delta X}{2}\right]\Delta Y-\left[\rho u-\frac{\partial \rho u}{\partial x}\cdot\frac{\Delta X}{2}\right]\Delta Y \\
&+\left[\rho v+\frac{\partial \rho v}{\partial y}\cdot\frac{\Delta Y}{2}\right]\Delta X-\left[\rho v-\frac{\partial \rho v}{\partial y}\cdot\frac{\Delta Y}{2}\right]\Delta X=-\frac{\partial \rho}{\partial t}\Delta X\Delta Y
\end{aligned} \qquad (2\text{-}3)$$

Summing up and canceling $\Delta X \Delta Y$, we obtain

$$\frac{\partial \rho u}{\partial x} + \frac{\partial \rho v}{\partial y} = -\frac{\partial \rho}{\partial t} \qquad (2\text{-}4)$$

or, in three dimensions,

$$\frac{\partial \rho}{\partial t} + \frac{\partial \rho u}{\partial x} + \frac{\partial \rho v}{\partial y} + \frac{\partial \rho w}{\partial z} = 0. \qquad (2\text{-}5)$$

This is the differential form of the continuity equation. The more general vector form of the equation is

$$\frac{\partial \rho}{\partial t} + \nabla \cdot (\rho \mathbf{V}) = 0 \qquad (2\text{-}6)$$

where $\mathbf{V} = u\boldsymbol{i} + v\boldsymbol{j} + w\boldsymbol{k}$ with $\boldsymbol{i}$, $\boldsymbol{j}$, and $\boldsymbol{k}$ denoting unit vectors in *x*-, *y*-, and *z*-coordinate directions, respectively.

Alternately, consider the arbitrary control volume shown in figure 2-4. The conservation of mass can then be written in an integral form quite simply. The surface integral of the flow out of the volume Ω with surface area *S* simply equals the change of mass in the volume as given in equation (2-7):

$$\oiint \rho \mathbf{V} \cdot \mathbf{n} dS = -\frac{\partial}{\partial t} \iiint \rho \mathrm{d}\Omega \qquad (2\text{-}7)$$

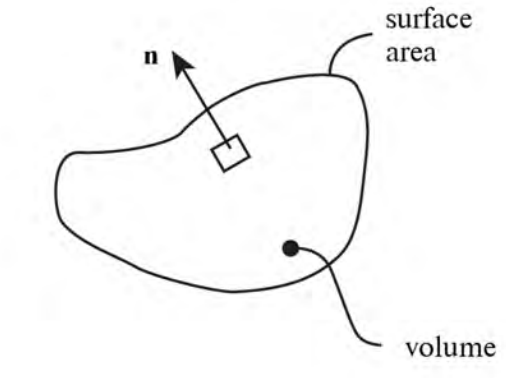


Figure 2-4: Arbitrary fluid control volume. From W. H. Mason. Adapted by S. Madden.

This is true without making any assumption requiring continuous variables and differentiability. It holds for all flows—viscous or inviscid, compressible or incompressible. To relate this expression to the differential form, we make use of the Gauss divergence theorem, which assumes continuous partial derivatives. It is given by

$$\oiint \mathbf{A} \cdot \mathbf{n} dS = \iiint \nabla \cdot \mathbf{A} \mathrm{d}\Omega. \qquad (2\text{-}8)$$

The equivalent statement for a scalar is

$$\oiint \phi \mathbf{n} dS = \iiint \mathrm{grad}\, \phi \mathrm{d}\Omega. \qquad (2\text{-}9)$$

Using the divergence theorem, equation (2-8), the differential and integral forms can be shown to be the same. First, rewrite the surface integral in the conservation of mass, equation (2-7), as

$$\oiint \rho \mathbf{V} \cdot \mathbf{n} dS = \iiint \nabla \cdot (\rho \mathbf{V}) \mathrm{d}\Omega. \qquad (2\text{-}10)$$

Substituting it in equation (2-7), the continuity equation in integral form is written as equation (2-11).

$$\iiint \nabla \cdot (\rho \mathbf{V}) \mathrm{d}\Omega = -\frac{\partial}{\partial t} \iiint \rho \mathrm{d}\Omega \qquad (2\text{-}11)$$

Since Ω refers to a fixed volume, we can move ∂/∂*t* inside the integral and rewrite equation (2-11) as

$$\iiint \left[\nabla \cdot (\rho \mathbf{V}) + \frac{\partial \rho}{\partial t} \right] \mathrm{d}\Omega = 0. \qquad (2\text{-}12)$$

For this to be true in general, the integrand must be zero, which is just the differential form! Further discussion and other derivations are available in Moran (sections 2.2, 2.3, and 2.4),[13] Anderson (section 2.6),[14] and Bertin and Smith (Chapter 2).[15]

2.2.2 Conservation of Momentum and the Substantial Derivative

In this section, we derive the general equations for the conservation of momentum. This is a statement of Newton's Second Law: *The time rate of change of momentum of a body equals the net force exerted on it.* For a fixed mass, this is the famous equation

$$\mathbf{F} = m\mathbf{a} = m\frac{D\mathbf{V}}{Dt}. \qquad (2\text{-}13)$$

Notice a new term, *D*/*Dt*, called the substantial derivative, on the right-hand side of equation (2-13). It is the consequence of the need to apply Newton's Law to a moving fluid element (the "body" in the Second Law statement given above) in our fixed coordinate system, which introduces some extra complications. We discuss the substantial derivative next.

2.2.2.1 Substantial Derivative

Let us look at what *D*/*Dt* means in a body-fixed coordinate system. Figure 2-5 shows a moving fluid particle at two instances of time.[16] In this figure, *Q*(**r**,*t*) represent any fluid property associated with the fluid particle at position ***r*** at time *t*; *Q* could be density or pressure or velocity. The change in the property *Q* between the position **r** at time *t* and **r**+Δ*s* at *t*+Δ*t* is

$$\Delta Q = Q(\mathbf{r} + \Delta s, t + \Delta t) - Q(\mathbf{r}, t\ ). \qquad (2\text{-}14)$$

The space change Δ*s* is simply equal to **V**Δ*t*. Thus we can write

$$\Delta Q = Q(\mathbf{r} + \mathbf{V}\Delta t, t + \Delta t) - Q(\mathbf{r}, t\ ). \qquad (2\text{-}15)$$

Equation (2-15) is in a form that can be used to find the rate of change of *Q*:

$$\frac{DQ}{Dt} = \lim_{\Delta t \to 0} \frac{\Delta Q}{\Delta t} = \lim_{\Delta t \to 0} \frac{Q(\mathbf{r} + \mathbf{V}\Delta t, t + \Delta t) - Q(\mathbf{r}, t)}{\Delta t} \qquad (2\text{-}16)$$

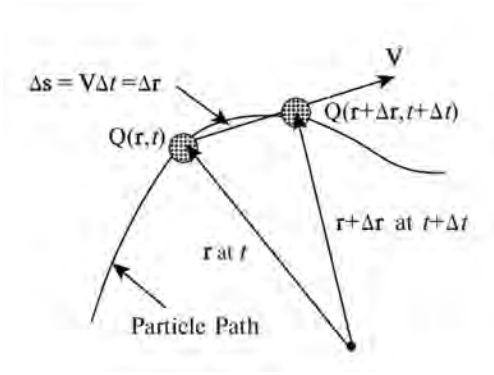


Figure 2-5: Moving particle viewed from a fixed coordinate system. From W. H. Mason. Adapted by S. Madden.

Note that the rate of change is in two parts, one for a change in time and the other for a change in position. Thus we write the change of Q as a function of both time and space using the Taylor series expansion as

$$Q(\mathbf{r}+\mathbf{V}\Delta t, t+\Delta t) = Q(\mathbf{r},t) + \left.\frac{\partial Q}{\partial t}\right|_{\mathbf{r},t} \Delta t + \ldots + \left.\frac{\partial Q}{\partial s}\right|_{\mathbf{r},t} V\Delta t + \ldots \qquad (2\text{-}17)$$

where the direction of *s* is understood from figure 2-5. Substituting into equation (2-16) and taking the limit, we obtain equation (2-18) below.

$$\lim_{\Delta t \to 0} \frac{\Delta Q}{\Delta t} = \frac{\partial Q}{\partial t} + \frac{\partial Q}{\partial s} V \qquad (2\text{-}18)$$

The noteworthy outcome of applying Newton's Law for a moving particle in a stationary coordinate system is that the rate of change of Q at a point in space is the sum of two terms shown on the right-hand side of equation (2-18). The first term, *local derivative,* represents the temporal change or the instantaneous rate of change of Q at its location. The second term, *convective derivative*, represents the rate at which Q is convected to that location by the fluid motion. This term has the unknown velocity**,** *V*, multiplying a term containing the unknown Q. This is important as it introduces a fundamental nonlinearity into the system, as shown next.

We now put this result into a specific coordinate system:

$$\frac{\partial Q}{\partial s} = \mathbf{e}_V \cdot \nabla Q \qquad (2\text{-}19)$$

where $\mathbf{e}_V$ denotes the unit vector in the direction of V. Thus, $\mathbf{V} = V\mathbf{e}_V$ and

$$\frac{\partial Q}{\partial s} V = \mathbf{V} \cdot \nabla \mathrm{Q}. \qquad (2\text{-}20)$$

Thus, we use equations (2-18) and (2-20) to write the substantial derivative, equation (2-16), as

$$\frac{D}{Dt} = \frac{\partial}{\partial t} + (\mathbf{V} \cdot \nabla) \qquad (2\text{-}21)$$

which can be applied to either a scalar as

$$\frac{DQ}{Dt} = \frac{\partial Q}{\partial t} + (\mathbf{V} \cdot \nabla) Q \qquad (2\text{-}22)$$

or to a vector quantity as

$$\frac{D\mathbf{V}}{Dt} = \frac{\partial \mathbf{V}}{\partial t} + (\mathbf{V} \cdot \nabla)\mathbf{V}. \qquad (2\text{-}23)$$

In Cartesian coordinates, *u*, *v*, and *w*, are the components of **V** in the *x*, *y*, and *z* directions, respectively. The substantial derivative becomes equation (2-24).

$$\begin{aligned}\frac{Du}{Dt} &= \frac{\partial u}{\partial t} + u\frac{\partial u}{\partial x} + v\frac{\partial u}{\partial y} + w\frac{\partial u}{\partial z} \\ \frac{Dv}{Dt} &= \frac{\partial v}{\partial t} + u\frac{\partial v}{\partial x} + v\frac{\partial v}{\partial y} + w\frac{\partial v}{\partial z} \\ \frac{Dw}{Dt} &= \frac{\partial w}{\partial t} + u\frac{\partial w}{\partial x} + v\frac{\partial w}{\partial y} + w\frac{\partial w}{\partial z}\end{aligned} \qquad (2\text{-}24)$$

To solve equations containing these nonlinear terms, we generally have to employ numerical methods. There are only a very few special cases where you can obtain analytic solutions to the nonlinear equations explicitly.

2.2.2.2 Forces

Next we need to find the net forces acting on the fluid element. The forces are:

- Body forces
- Pressure forces
- Shear forces

Each of these forces applies to the control volume. Surface forces are shown in figure 2-6, with **τ** as a commonly used symbol for stresses. [Note that the orientation of axes in figure 2-6 is different from that in figure 2-3. However, both systems follow the right-hand rule. Therefore, the conclusions are equally valid in both systems.] In the figure, the first subscript for **τ** indicates the direction normal to the surface, and the second subscript defines the direction in which the force acts. Fluids of interest in aerodynamics are isotropic (i.e., properties are uniform in all directions). Therefore, the following expressions hold to satisfy equilibrium of moments about each axis:

$$\begin{aligned}\tau_{xy} &= \tau_{yx} \\ \tau_{xz} &= \tau_{zx} \\ \tau_{yz} &= \tau_{zy}\end{aligned} \qquad (2\text{-}25)$$

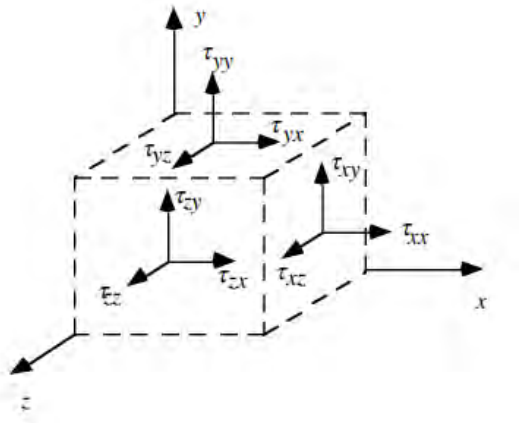


Figure 2-6: Control volume showing the surface forces.

The connection between pressure and stress is defined more specifically when the properties of a fluid are prescribed. Figure 2-7 shows the details of the forces, with the surface forces expanded about the center of the control volume using a Taylor series and the body force per unit mass denoted by *f* acting at the center.

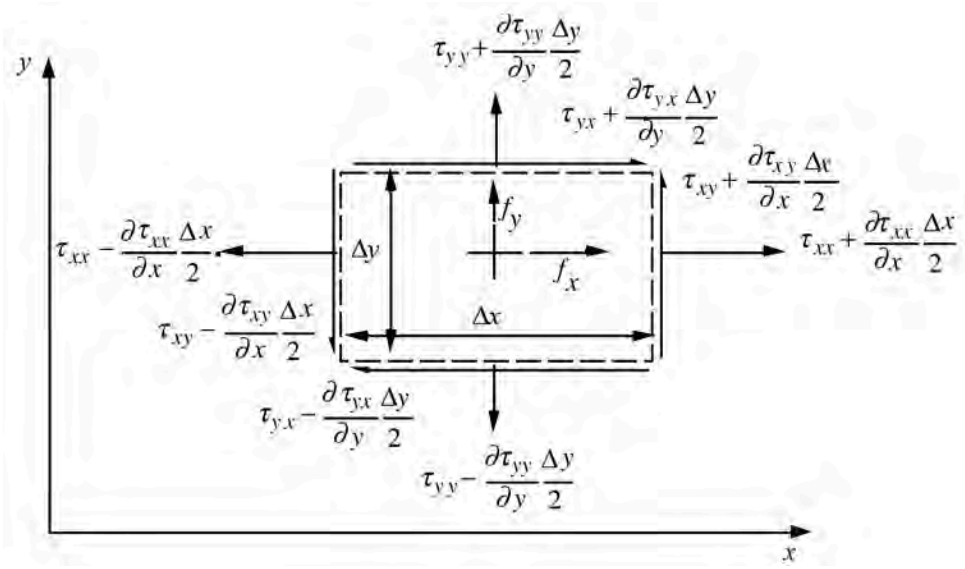


Figure 2-7: Details of forces acting on a two-dimensional control volume.

Considering the *x*-direction as an example and using the Taylor series expansion shown in figure 2-7, the net forces are found in a manner exactly analogous to the approach used in the derivation of the continuity equation. Thus, the net force in the *x*-direction is found to be

$$\rho \cdot \Delta x \Delta y f_x + \frac{\partial}{\partial x}(\tau_{xx})\Delta x \Delta y + \frac{\partial}{\partial y}(\tau_{yx})\Delta y \Delta \mathrm{x}. \qquad (2\text{-}26)$$

Now we combine the forces, including the *z*-direction terms, and use them to substitute for the force term **F** in the original statement, **F** = m**a**, as seen in equation (2-13). Using the substantial derivative and the definition of the mass, m = ρΔ*x*Δ*y*Δ*z*, the *x*-momentum equation is equation (2-13) written as m**a**=**F**, the usual fluid mechanics convention; considering the *x* component, $ma_x = F_x$,

$$\rho \Delta x \Delta y \Delta z \frac{Du}{Dt} = \rho \Delta x \Delta y \Delta z f_x + \frac{\partial}{\partial x}(\tau_{xx})\Delta x \Delta y \Delta z + \frac{\partial}{\partial y}(\tau_{yx})\Delta y \Delta x \Delta z + \frac{\partial}{\partial z}(\tau_{zx})\Delta y \Delta x \Delta \mathrm{z}. \quad (2\text{-}27)$$

Dividing both sides by Δ*x*Δ*y*Δ*z*, we obtain the final set of three equations by appending the *y*- and *z*-momentum equations that can be easily derived by applying the approach used for equation (2-27):

$$\begin{aligned}
\rho\frac{Du}{Dt} &= \rho f_x + \frac{\partial \tau_{xx}}{\partial x} + \frac{\partial \tau_{yx}}{\partial y} + \frac{\partial \tau_{zx}}{\partial z} \\
\rho\frac{Dv}{Dt} &= \rho f_y + \frac{\partial \tau_{xy}}{\partial x} + \frac{\partial \tau_{yy}}{\partial y} + \frac{\partial \tau_{zy}}{\partial z} \qquad (2\text{-}28) \\
\rho\frac{Dw}{Dt} &= \rho f_z + \frac{\partial \tau_{xz}}{\partial x} + \frac{\partial \tau_{yz}}{\partial y} + \frac{\partial \tau_{zz}}{\partial z}
\end{aligned}$$

These are general conservation of momentum relations, *valid for anything!*

To make equation (2-28) more specific for fluid flow problems, we need to relate the stresses to the motion of the fluid. For gases and water, stress is a linear function of the rate of strain. Such a fluid is called a Newtonian fluid, and equation (2-29) shows the expression for stress as

$$\tau = \mu \frac{\partial u}{\partial y} \qquad (2\text{-}29)$$

where μ is the coefficient of viscosity. In our work, we consider μ to be a function of temperature only. Note that in air, the viscosity coefficient increases with increasing temperature, and in water, the viscosity coefficient decreases with temperature increases.

To complete the specification of the relationship between stress and rate of strain, we need to define precisely the relation between the stresses and the motion of the fluid. This can become complicated. In general, the fluid description requires two coefficients of viscosity. The coefficient of viscosity arising from the shear stress is well defined. The second coefficient of viscosity is not. This coefficient depends on the normal stress and is only important in computing the detailed structure of shock waves. Various assumptions relating the coefficients of viscosity are made. The set of assumptions that leads to the equations known as the Navier–Stokes equations are:

- The stress-rate-of-strain relations must be independent of coordinate system.
- When the fluid is at rest and the velocity gradients are zero (the strain rates are zero), the stress reduces to the hydrostatic pressure.
- Stoke's hypothesis is used to eliminate the issue of mean pressure versus thermodynamic pressure. This is the assumption between viscosity coefficients.

Details of the theory associated with these requirements can be found in Schlichting[17] and Grossman.[18] Using the set of assumptions listed above leads to the following relations:

$$\begin{aligned}
\tau_{xx} &= -p - \frac{2}{3}\mu\nabla\cdot V + 2\mu\frac{\partial u}{\partial x} \\
\tau_{yy} &= -p - \frac{2}{3}\mu\nabla\cdot V + 2\mu\frac{\partial v}{\partial y} \qquad (2\text{-}30) \\
\tau_{zz} &= -p - \frac{2}{3}\mu\nabla\cdot V + 2\mu\frac{\partial w}{\partial z}
\end{aligned}$$

and

$$\begin{aligned}
\tau_{xy} &= \tau_{yx} = \mu\left(\frac{\partial u}{\partial y} + \frac{\partial v}{\partial x}\right) \\
\tau_{xz} &= \tau_{zx} = \mu\left(\frac{\partial u}{\partial z} + \frac{\partial w}{\partial x}\right) \qquad (2\text{-}31) \\
\tau_{yz} &= \tau_{zy} = \mu\left(\frac{\partial v}{\partial z} + \frac{\partial w}{\partial y}\right)
\end{aligned}$$

If we combine equations (2-28), (2-30), and (2-31) and we neglect the body force term (which is very small compared to the other terms since the air is so light), we get the standard set of equations for aerodynamics:

$$\begin{aligned}
\rho\tfrac{Du}{Dt} &= -\tfrac{\partial p}{\partial x} + \tfrac{\partial}{\partial x}\left(2\mu\tfrac{\partial u}{\partial x} - \tfrac{2}{3}\mu\nabla\cdot V\right) + \tfrac{\partial}{\partial y}\left[\mu\left(\tfrac{\partial u}{\partial y} + \tfrac{\partial v}{\partial x}\right)\right] + \tfrac{\partial}{\partial z}\left[\mu\left(\tfrac{\partial w}{\partial x} + \tfrac{\partial u}{\partial z}\right)\right] \\
\rho\tfrac{Dv}{Dt} &= -\tfrac{\partial p}{\partial y} + \tfrac{\partial}{\partial x}\left[\mu\left(\tfrac{\partial u}{\partial y} + \tfrac{\partial v}{\partial x}\right)\right] + \tfrac{\partial}{\partial y}\left(2\mu\tfrac{\partial v}{\partial y} - \tfrac{2}{3}\mu\nabla\cdot V\right) + \tfrac{\partial}{\partial z}\left[\mu\left(\tfrac{\partial w}{\partial y} + \tfrac{\partial v}{\partial z}\right)\right] \qquad (2\text{-}32) \\
\rho\tfrac{Dw}{Dt} &= -\tfrac{\partial p}{\partial z} + \tfrac{\partial}{\partial x}\left[\mu\left(\tfrac{\partial w}{\partial x} + \tfrac{\partial u}{\partial z}\right)\right] + \tfrac{\partial}{\partial y}\left[\mu\left(\tfrac{\partial v}{\partial z} + \tfrac{\partial w}{\partial y}\right)\right] + \tfrac{\partial}{\partial z}\left(2\mu\tfrac{\partial w}{\partial z} - \tfrac{2}{3}\mu\nabla\cdot V\right)
\end{aligned}$$

These are the classic Navier–Stokes equations written in the standard aerodynamics form. Note that the equations are (i) non-linear (remember that superposition of solutions is not allowed—D/Dt!); (ii) second order; (iii) highly coupled, and (iv) long! As written above, it's easy to identify **F** = m**a**, written in the fluid mechanics form m**a** = **F**.

When the viscous terms are small and thus ignored, the flow is termed inviscid. The resulting equations are known as the Euler equations.

There are also alternate integral formulations of the equations. Consider the momentum flux through an arbitrary control volume in a manner similar to the integral statement of the continuity equation pictured in figure 2-4 and given in equation (2-7). Here, the rate of momentum change is proportional to the force. The integral statement is

$$\oiint \rho \mathbf{V}(\mathbf{V}\cdot\mathbf{n})dS + \frac{\partial}{\partial t}\iiint \rho \mathbf{V} \mathrm{d}\Omega = \mathbf{F} = \mathbf{F}_{\text{volume}} + \mathbf{F}_{\text{surface}}, \qquad (2\text{-}33)$$

and this statement can also be converted to the differential form using the Gauss divergence theorem. Note that we use the partial derivative notation ∂/∂*t* to denote the change in the fixed "porous" control volume with fluid moving across the boundaries. The derivation of the Navier–Stokes equations is for general unsteady fluid motion. Because of limitations in our computational capability (for some time to come), these equations are directly applicable to solve for laminar flows. When the flow is turbulent, the usual approach is to Reynolds-average the equations, with the result that additional Reynolds stresses appear in the equations. Clearly, the addition of new unknowns requires additional equations. This problem is treated through turbulence modeling and is discussed, for example, in Tannehill, et al.[19]

2.2.3 The Energy Equation

The equation for the conservation of energy is required to complete the system of equations. This is a statement of the First Law of Thermodynamics: *The sum of the work and heat added to a system will equal the increase of energy*. Following the derivation given by White:[20]

$$\underbrace{dE_t}_{\substack{\text{change of total energy}\\ \text{of the system}}} = \underbrace{\delta Q}_{\text{change of heat added}} + \underbrace{\delta W}_{\substack{\text{change of work done}\\ \text{on the system}}} \qquad (2\text{-}34)$$

For our control volume in a fixed coordinate system, the rate of change is

$$\frac{DE_t}{Dt} = \dot{Q} + \dot{W} \qquad (2\text{-}35)$$

where

$$E_t = \rho\left(e + \frac{1}{2}V^2 - \mathbf{g}\cdot\mathbf{r}\right) \qquad (2\text{-}36)$$

and *e* is the internal energy per unit mass. The last term is the potential energy (i.e., the body force). In aerodynamics, this term is neglected. E_t can also be written in terms of specific energy as

$$E_t = \rho e_0 \qquad (2\text{-}37)$$

where

$$e_0 = e + \frac{1}{2}V^2. \qquad (2\text{-}38)$$

To obtain the energy equation, we need to write the right-hand side (RHS) of equation (2-35) in terms of flow properties. Consider first the

heat added to the system.* The heat flow into the control volume is found in the identical manner to the mass flow. Using figure 2-8 for reference, we obtain the expression for the net heat flow.

*We neglect heat addition due to radiation. See Grossman[21] for the extension to include this contribution.

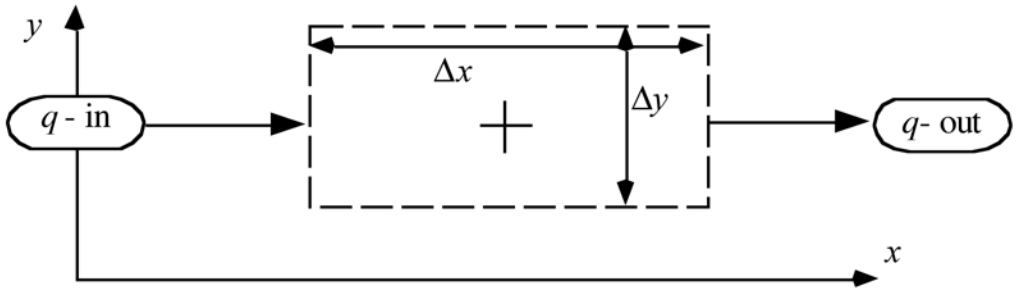


Figure 2-8: The x-component of heat flux into and out of the control volume. From W. H. Mason. Adapted by S. Madden.

The heat fluxes are:

$$\begin{aligned} q_{x_{\text{in}}} &= \left(q_x - \frac{\partial q}{\partial x} \frac{\Delta x}{2} \right) \Delta y \\ q_{x_{\text{out}}} &= \left(q_x + \frac{\partial q}{\partial x} \frac{\Delta x}{2} \right) \Delta y \end{aligned} \qquad (2\text{-}39)$$

and the net heat flow into the control volume in the *x*-direction is $q_{x\text{in}} - q_{x\text{out}}$, or

$$-\frac{\partial q}{\partial x} \Delta x \Delta \mathrm{y}.$$

Using the same analysis in the *y*– and *z*-directions, we obtain the net heat flux into the control volume (realizing that the $\Delta x \Delta y \Delta z$ terms will cancel):

$$\dot{Q} = -\left(\frac{\partial q_x}{\partial x} + \frac{\partial q_y}{\partial y} + \frac{\partial q_z}{\partial z} \right) = -\nabla \cdot \mathbf{q} \qquad (2\text{-}40)$$

Now relate the heat flow to the temperature field. Fourier's law provides this connection:

$$\mathbf{q} = -k \nabla T \qquad (2\text{-}41)$$

where *k* is the coefficient of thermal conductivity. Combining equation (2-41) with equation (2-40), we get the heat conduction in terms of the temperature gradient in the flow field as

$$\dot{Q} = -\nabla \cdot \mathbf{q} = +\nabla \cdot (k \nabla T\ ). \qquad (2\text{-}42)$$

Next we find the work done on the system. Using the definition of *work = force × distance*, the rate of work is

$$\dot{W} = \text{force} \times \text{velocity}. \qquad (2\text{-}43)$$

Using the control volume again, we find the work, which is equal to the velocity times the stress. The work associated with the *x*-face of the control volume (for two-dimensional flow) is

$$w_x = u\tau_{xx} + v\tau_{xy}. \qquad (2\text{-}44)$$

The complete description of the work on the control volume is shown in figure 2-9.

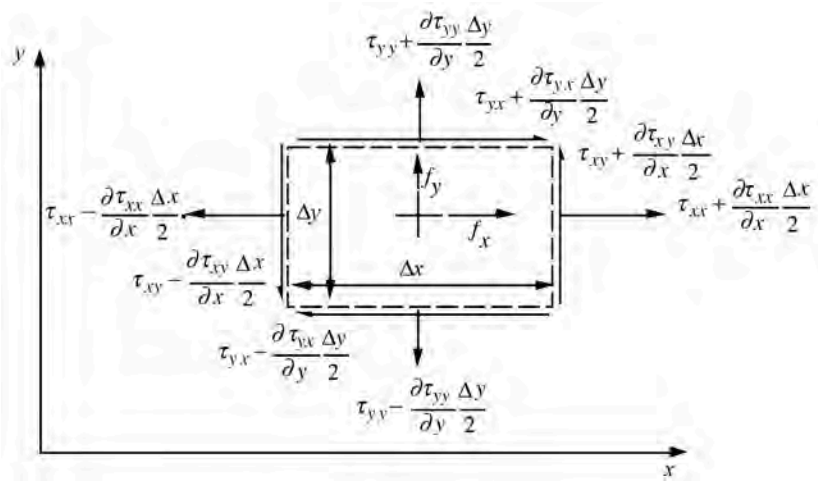


Figure 2-9: Work done on a control volume.

Using the *x*-component of net work as an example again, the work done on the system is $w_{x\text{in}}$ or $w_{x\text{out}}$, or

$$\left(w_x - \frac{\partial w_x}{\partial x}\frac{\Delta x}{2}\right)\Delta y - \left(w_x + \frac{\partial w_x}{\partial x}\frac{\Delta x}{2}\right)\Delta y = -\frac{\partial w_x}{\partial x}\Delta x\Delta \mathrm{y}. \qquad (2\text{-}45)$$

Including the other two directions, namely *y* and *z*, and dropping the $\Delta x\Delta y\Delta z$ terms, which cancel out, we get

$$\dot{W} = -\operatorname{div}\mathbf{w} = \frac{\partial}{\partial x}(u\tau_{xx} + v\tau_{xy}) + \frac{\partial}{\partial y}(u\tau_{yx} + v\tau_{yy}\ ).^{*} \qquad (2\text{-}46)$$

*Here we are using White's notation. Realize there is a difference between W and **w**.

Substituting equations (2-37) and (2-38) into (2-35) for E_t, equation (2-42) for the heat, and equation (2-46) for the work, we obtain

$$\frac{D\rho\left(e + \frac{1}{2}V^2\right)}{Dt} = \nabla\cdot(k\nabla T) - \operatorname{div}\mathbf{w}. \qquad (2\text{-}47)$$

Many, many equivalent forms of the energy equation are found in the literature. Often the equation is thought of as an equation for the temperature. We now describe how to obtain one specific form. Substituting equation (2-46) into (2-47) and using the expressions for the τ's in terms of μ and the velocity gradients in equations (2-29) and (2-30), we obtain the following lengthy expression (see Bertin and Smith,[22] pp. 40–42). After making use of the momentum and continuity equations to simplify and finally introducing the definition of enthalpy, $h = e + p/\rho$, we obtain a frequently written form of the classical energy equation given as:

$$\rho\frac{Dh}{Dt} - \frac{Dp}{Dt} = \underbrace{\nabla\cdot(k\nabla T)}_{\text{heat conduction}} + \underbrace{\Phi}_{\substack{\text{viscous dissipation}\\ \text{(always positive)}}} \qquad (2\text{-}48)$$

where

$$\Phi = \mu \left\{ \begin{array}{c} 2\left[\left(\frac{\partial u}{\partial x}\right)^2 + \left(\frac{\partial v}{\partial y}\right)^2 + \left(\frac{\partial w}{\partial z}\right)^2\right] + \left(\frac{\partial v}{\partial x} + \frac{\partial u}{\partial y}\right)^2 + \left(\frac{\partial w}{\partial y} + \frac{\partial v}{\partial z}\right)^2 \\ + \left(\frac{\partial u}{\partial z} + \frac{\partial w}{\partial x}\right)^2 - \frac{2}{3}\left(\frac{\partial u}{\partial x} + \frac{\partial v}{\partial y} + \frac{\partial w}{\partial z}\right)^2 \end{array} \right\}. \qquad (2\text{-}49)$$

The energy equation can be written in numerous forms, and many different but entirely equivalent forms are available. In particular, the energy equation is frequently written in terms of the total enthalpy, *H*, to good advantage in inviscid and boundary layer flows. A good discussion of the energy equation is also given by White.[23]

There is also an integral form of this equation:

$$\oiint \rho\left(e + V^2/2\right)(\mathbf{V}\cdot\mathbf{n})dS + \frac{\partial}{\partial t}\iiint \rho\left(e + V^2/2\right)d\Omega = \dot{Q} + \dot{W} \qquad (2\text{-}50)$$

Here again note that we use the partial derivative notation ∂/∂*t* to denote the change in the fixed "porous" control volume with fluid moving across the boundaries.

2.3 Boundary Conditions

If all flow fields are governed by the same equations, what makes flow fields different? Boundary conditions are the means through which the solution of the governing equations produce different results for different shapes. For aerodynamic solutions, the specification of the arbitrarily shaped configuration geometry and of the boundary conditions constitutes the major part of any effort.

2.3.1 Boundary Conditions on the Surface

The boundary condition on the surface of the configuration is the most straightforward and most obvious physically. However, the statement of the boundary conditions is tightly connected to the flow field model in use and the type of surface (e.g., solid or porous).

For an inviscid steady flow over a solid surface, the statement of the boundary condition is

$$\mathbf{V}_R \cdot \mathbf{n} = 0. \qquad (2\text{-}51)$$

In this equation, $\mathbf{V}_R$ is the relative velocity defined as the difference between fluid (or freestream) velocity **V** and the surface velocity $\mathbf{V}_S$, and **n** is the unit vector normal to the surface. Therefore, this boundary condition simply stipulates that the component of the relative velocity normal to the surface must be zero and is known as the no-normal-flow or nonpenetration condition. In other words, the flow must be parallel to the surface at every point on the surface. Equation (2-51) may be written as

$$(\mathbf{V} - \mathbf{V}_S)\cdot\mathbf{n} = 0. \qquad (2\text{-}52)$$

If the surface is fixed, $\mathbf{V}_S = 0$, and equation (2-52) becomes

$$\mathbf{V}\cdot\mathbf{n} = 0. \qquad (2\text{-}53)$$

For a viscous flow over a solid surface, the statement becomes even simpler: **V** = 0, known as the no-slip condition. If the surface is porous and there is mass flow, the values of the surface velocity must be specified as part of the problem definition. Numerical solutions of the

Euler and Navier–Stokes solutions require that other boundary conditions be specified. In particular, conditions on pressure and temperature are required.

Let us next review how to compute the unit normal vector, **n**. Recall that to obtain the unit normal, the body is defined (in 2D) in the form $F(x,y) = 0$, which is the traditional analytic geometry nomenclature.

In the usual two-dimensional notation, the body shape is given by $y = f(x)$, which is written as

$$F(x, y) = 0 = y - f(x) \qquad (2\text{-}54)$$

and the unit normal is

$$\mathbf{n} = \frac{\nabla F}{|\nabla F|}. \qquad (2\text{-}55)$$

2.3.2 Boundary Conditions Away From the Surface

Conditions also must be specified away from the body. For most of the external flows, the most commonly used condition is that at large distances (approaching infinity) from the body, the flow field must approach the freestream conditions. In numerical computations, the question of the farfield boundary condition can become troublesome. How far away is infinity? Exactly how should you specify the farfield boundary condition numerically? How to best handle these issues is the basis for many papers in the literature, such as Thomas and Salas,[24] Verhoff,[25] and the survey by Colonius.[26]

Another important use of boundary conditions arises as a means of modeling physics that would be neglected otherwise. When an approximate flow field model is used, the boundary conditions frequently provide a means of including key elements of the physics in the problem without having to include the physics explicitly. The most famous example of this is the Kutta condition, wherein the viscous effects at the trailing edge can be accounted for in an inviscid calculation without treating the trailing-edge problem explicitly. Karamcheti[27] discusses boundary conditions in more detail.

2.4 Standard Forms and Terminology of Governing Equations

To understand the literature in computational aerodynamics, several other aspects of the terminology must be discussed. This section provides several of these considerations.

2.4.1 Nondimensionalization

The governing equations should be nondimensionalized. Considering fluid mechanics theory, nondimensionalization reveals important similarity parameters. In practice, many different nondimensionalizations are used, and for a particular computer program, care must be taken to understand exactly what nondimensionalization is used.

Sometimes the dimensional quantities are defined by *'s or ~'s. In other schemes, the nondimensionalized variables are designated by the

special symbols. In the example given here, the nondimensionalized values are denoted by an asterisk (*). In this system, once the quantities are defined, the *'s are dropped and the nondimensionalization is understood.

Many different values can be used for nondimensionalization. We give an example here using the freestream velocity (V_∞), flow properties (ρ_∞, T_∞, etc.), and a reference length, L, as follows:

$$\begin{array}{llll} x^* = \frac{x}{L} & y^* = \frac{y}{L} & z^* = \frac{z}{L} & t^* = \frac{tV_\infty}{L} \\ u^* = \frac{u}{V_\infty} & v^* = \frac{v}{V_\infty} & w^* = \frac{w}{V_\infty} & p^* = \frac{p}{\rho_\infty V_\infty^2} \\ T^* = \frac{T}{T_\infty} & \rho^* = \frac{\rho}{\rho_\infty} & \mu^* = \frac{\mu}{\mu_\infty} & e_o^* = \frac{e_o}{U_\infty^2} \end{array} \qquad (2\text{-}56)$$

Each code will have a set of reference nondimensionalizations similar to these. A specific example is given in section 2.4.3. Frequently, the speed of sound is used as the reference velocity. Making sure that you understand the nondimensionalization used in a particular program is an important part of using computational aerodynamics programs to solve aerodynamic problems.

2.4.2 Use of Divergence Form of Governing Equations

The classical forms of the governing equations (shown in the preceding sections) that are normally given in textbooks are not used for computations. Instead, the divergence, or conservation, form* is preferred.

> *Be careful to clearly distinguish between conservation equations and conservation forms, as the terminology can be confusing. The continuity, momentum, and energy equations are all conservation equations. "Conservation form" refers to the formulation where the variables are inside the derivatives. That's why I prefer the use of "divergence form" to describe this mathematical arrangement. Conservation form is the more widely used terminology. They are both the same.

This form is found to be required for reliable numerical calculation. If discontinuities in the flow field exist, this form must be used to account for discontinuities correctly. It is a way to improve the capability of the differential form of the governing equations. For example, across a shock wave, the density and velocity both jump in value. However, the product of these quantities, the mass flow, is a constant. Thus we can easily see why it is better numerically to work with the product rather than the individual variables. In this section, we show how the divergence forms are obtained from the standard classical form. We use the 2D steady x-momentum equation as the example:

$$\rho u \frac{\partial u}{\partial x} + \rho v \frac{\partial u}{\partial y} = -\frac{\partial p}{\partial x} \qquad (2\text{-}57)$$

This equation is written using the following identities:

$$\frac{\partial \rho u u}{\partial x} = \rho u \frac{\partial u}{\partial x} + u \frac{\partial \rho u}{\partial x} \qquad (2\text{-}58)$$

or

$$\rho u \frac{\partial u}{\partial x} = \frac{\partial \left(\rho u^2\right)}{\partial x} - u \frac{\partial \rho u}{\partial x} \qquad (2\text{-}59)$$

Similarly the second term on the left-hand side of equation (2-57) may be written as

$$\frac{\partial \rho v u}{\partial y} = \rho v \frac{\partial u}{\partial y} + u \frac{\partial \rho v}{\partial y} \qquad (2\text{-}60)$$

or

$$\rho v \frac{\partial u}{\partial y} = \frac{\partial \rho v u}{\partial y} - u \frac{\partial \rho v}{\partial y}. \qquad (2\text{-}61)$$

Substituting (2-59) and (2-61) into (2-57), we get

$$\frac{\partial \rho u^2}{\partial x} - u \frac{\partial \rho u}{\partial x} + \frac{\partial \rho v u}{\partial y} - u \frac{\partial \rho v}{\partial y} + \frac{\partial p}{\partial x} = 0 \qquad (2\text{-}62)$$

which can be written as

$$\frac{\partial \rho u^2}{\partial x} + \frac{\partial \rho v u}{\partial y} - u(\underbrace{\frac{\partial \rho u}{\partial x} + \frac{\partial \rho v}{\partial x}}_{= 0 \text{ from continuity}}) + \frac{\partial p}{\partial x} = 0. \qquad (2\text{-}63)$$

Finally, the *x*-momentum equation written in divergence form for 2D steady flow is given in equation (2-64).

$$\frac{\partial \left(\rho u^2 + p \right)}{\partial x} + \frac{\partial (\rho v u)}{\partial y} = 0 \qquad (2\text{-}64)$$

The equations must be written in divergence form to be valid when shock waves are present.

2.4.3 Standard Form of the Equations

Even after writing the governing equations in divergence form, the equations that you see in the literature won't look like the ones we've been writing down. A standard form is used in the literature for numerical solutions of the Navier–Stokes equations. In this section, we provide one representative set used in the NASA Langley codes **CFL3D** and **CFL3DE.**[28] Professors Walters and Grossman (of Virginia Tech) and their students have made contributions to these codes. The Navier–Stokes equations (and the other equations required in the system) are written in vector divergence form as follows:

$$\frac{\partial \mathbf{Q}}{\partial t} + \frac{\partial \left(\mathbf{F} - \mathbf{F}_v \right)}{\partial x} + \frac{\partial \left(\mathbf{G} - \mathbf{G}_v \right)}{\partial y} + \frac{\partial \left(\mathbf{H} - \mathbf{H}_v \right)}{\partial z} = 0 \qquad (2\text{-}65)$$

where the conserved variables are

$$\mathbf{Q} = \begin{Bmatrix} \rho \\ \rho u \\ \rho v \\ \rho w \\ E_t \end{Bmatrix} = \begin{Bmatrix} \text{density} \\ \text{x– momentum} \\ \text{y– momentum} \\ \text{z– momentum} \\ \text{total energy per unit volume} \end{Bmatrix} \qquad (2\text{-}66)$$

There are two sets of flux vectors in equation (2-65), inviscid and viscous. The inviscid flux vectors are **F**, **G**, and **H** in *x*-, *y*-, and *z*-directions, respectively, and the viscous flux vectors are $\mathbf{F}_v$, $\mathbf{G}_v$, and $\mathbf{H}_v$ in *x*-, *y*-, and *z*-directions, respectively.

The flux vectors in the *x*-direction are described in (2-67) below.

$$\mathbf{F} = \begin{bmatrix} \rho u \\ \rho u^2 + p \\ \rho uv \\ \rho uw \\ (E_t + p)u \end{bmatrix} \quad \mathbf{F}_v = \begin{bmatrix} 0 \\ \tau_{xx} \\ \tau_{xy} \\ \tau_{xz} \\ u\tau_{xx} + v\tau_{xy} + w\tau_{xz} - \dot{q}_x \end{bmatrix} \qquad (2\text{-}67)$$

Similar expressions can be written down for the *y*- and *z*-direction fluxes, with the *y*-direction given as

$$\mathbf{G} = \begin{bmatrix} \rho v \\ \rho vu \\ \rho v^2 + p \\ \rho vw \\ (E_t + p)v \end{bmatrix} \quad \mathbf{G}_v = \begin{bmatrix} 0 \\ \tau_{yx} \\ \tau_{yy} \\ \tau_{yz} \\ u\tau_{yx} + v\tau_{yy} + w\tau_{yz} - \dot{q}_y \end{bmatrix} \qquad (2\text{-}68)$$

and with the *z*-direction given as

$$\mathbf{H} = \begin{bmatrix} \rho w \\ \rho wu \\ \rho wv \\ \rho w^2 + p \\ (E_t + p)w \end{bmatrix} \quad \mathbf{H}_v = \begin{bmatrix} 0 \\ \tau_{zx} \\ \tau_{zy} \\ \tau_{zz} \\ u\tau_{zx} + v\tau_{zy} + w\tau_{zz} - \dot{q}_z \end{bmatrix}. \qquad (2\text{-}69)$$

The equation of state (perfect gas) is written in this formulation as

$$p = (\gamma - 1)\left[E_t - \rho\left(u^2 + v^2 + w^2\right)/2\right]. \qquad (2\text{-}70)$$

To complete the flow equations, we need to define (i) nondimensional variables using the freestream values of the flow properties like density, pressure, temperature, speed of sound, etc., and (ii) the shear stress and heat transfer nomenclature. In the following equations, the tilde (~) superscript denotes a dimensional quantity and the infinity (∞) subscript denotes evaluation at freestream conditions.

Equations (2-71) and (2-72) below show how nondimensional shear stress and heat transfer terms are written in indicial (or index*) notation.

*Index notation is a shorthand notation. x_i denotes *x*, *y*, *z* for *i* = 1, 2, 3.

$$\tau_{x_i x_j} = \frac{M_\infty}{\mathrm{Re}_L}\left[\mu\left(\frac{\partial u_i}{\partial x_j} + \frac{\partial u_j}{\partial x_i}\right) + \lambda \frac{\partial u_k}{\partial x_k}\delta_{ij}\right] \qquad (2\text{-}71)$$

and

$$\dot{q}_{x_i} = -\left[\frac{M_\infty \mu}{\mathrm{Re}_L \,\mathrm{Pr}(\gamma - 1)}\right]\frac{\partial\left(a^2\right)}{\partial x_i} = -\left[\frac{M_\infty \mu}{\mathrm{Re}_L \,\mathrm{Pr}(\gamma - 1)}\right]\frac{\partial T}{\partial x_i} \qquad (2\text{-}72)$$

The nondimensional molecular viscosity is found using Sutherland's law:

$$\mu = \tilde{\mu}/\tilde{\mu}_\infty = \left(\frac{\tilde{T}}{\tilde{T}_\infty}\right)^{3/2} \left[\frac{\tilde{T}_\infty + \tilde{c}}{\tilde{T} + \tilde{c}}\right] = (T)^{3/2} \left[\frac{\left(1 + \tilde{c}/\tilde{T}_\infty\right)}{\left(T + \tilde{c}/\tilde{T}_\infty\right)}\right] \qquad (2\text{-}73)$$

where Sutherland's constant (defined by the symbol c with a tilde (~) superscript) has a value of 198.6°R = 110.4°K.

Below are the definitions of the other quantities.

Reynolds number:

$$\mathrm{Re}_L = \tilde{\rho}_\infty \tilde{q}_\infty \tilde{L}/\tilde{\mu}_\infty$$

Mach number:

$$M_\infty = \tilde{q}_\infty/\tilde{a}_\infty$$

Prandtl number:

$$\mathrm{Pr} = \tilde{\mu}\tilde{c}_p/\tilde{k}$$

Stoke's hypothesis for bulk viscosity is used, meaning

$$\lambda + 2\mu/3 = 0$$

and the freestream velocity magnitude is

$$\tilde{q}_\infty = \left[\tilde{u}_\infty^2 + \tilde{v}_\infty^2 + \tilde{w}_\infty^2\right]^{1/2}.$$

The nondimensional velocity components are given by

$$\begin{array}{ll} u = \tilde{u}/\tilde{a}_\infty & u_\infty = M_\infty \cos\alpha \cos\beta \\ v = \tilde{v}/\tilde{a}_\infty & v_\infty = -M_\infty \sin\beta \\ w = \tilde{w}/\tilde{a}_\infty & w_\infty = M_\infty \sin\alpha \cos\beta \end{array} \qquad (2\text{-}74)$$

and the thermodynamic variables are given by

$$\begin{array}{rr} \rho = \tilde{\rho}/\tilde{\rho}_\infty, & \rho_\infty = 1 \\ p = \tilde{p}/\tilde{\rho}\tilde{a}_\infty^2, & p_\infty = 1/\gamma \\ T = \tilde{T}/\tilde{T}_\infty = \gamma p/\rho = a^2 & T_\infty = 1 \end{array} \qquad (2\text{-}75)$$

$$E_t = \tilde{E}_t/\tilde{\rho}_\infty \tilde{a}_\infty^2 \quad E_{t_\infty} = 1/[\gamma(\gamma - 1)] + M_\infty^2/2. \qquad (2\text{-}76)$$

This completes the nomenclature for one typical example of the application of the Navier–Stokes equations in an actual computer code, **CFL3D**. Note that these equations are for a Cartesian coordinate system. The general non-orthogonal curvilinear coordinate generalization is considerably more complicated.

2.5 The Gas Dynamics Equation and the Full-Potential Equation

For inviscid flow problems (and even some viscous flows), it is useful to combine the equations in a special form known as the gas dynamics equation. In particular, the gas dynamics form of the equation is used to obtain the complete or "full" nonlinear potential flow equation in section 2.5.3. Many valuable results can be obtained in computational aerodynamics using the potential flow approximation. When compressibility effects are important, a special form of the governing equation can be obtained based on the gas dynamics equation, which we derive here. The gas dynamics equation is valid for any flow assumed to be inviscid. The starting point for the derivation is the Euler equations, the continuity equation, and the equation of state.

2.5.1 The Gas Dynamics Equation

We demonstrate the derivation using two-dimensional steady flow. This is not required but is used for simplicity. Furthermore, the index notation x_i is used where the index $i = 1, 2, 3$, denote x-, y-, z-axes, respectively. To start, we make use of a thermodynamic definition to rewrite the pressure term in the momentum equation as equation (2-77).

$$\frac{\partial p}{\partial x_i} = \frac{\partial p}{\partial \rho}\bigg)_s \frac{\partial \rho}{\partial x_i} \qquad (2\text{-}77)$$

Using the definition of the speed of sound assuming isentropic or constant entropy flow,

$$a^2 = \frac{\partial p}{\partial \rho}\bigg)_s \qquad (2\text{-}78)$$

allowing $\partial p/\partial x_i$ to be written as

$$\frac{\partial p}{\partial x_i} = a^2 \frac{\partial \rho}{\partial x_i}. \qquad (2\text{-}79)$$

We next write the x-momentum equation multiplied by u- and y-momentum equation multiplied by v:

$$\begin{aligned} u^2\frac{\partial u}{\partial x} + uv\frac{\partial u}{\partial y} &= -\frac{u}{\rho}\frac{\partial p}{\partial x} = -u\frac{a^2}{\rho}\frac{\partial \rho}{\partial x} \\ vu\frac{\partial v}{\partial x} + v^2\frac{\partial v}{\partial y} &= -\frac{v}{\rho}\frac{\partial p}{\partial y} = -v\frac{a^2}{\rho}\frac{\partial \rho}{\partial y} \end{aligned} \qquad (2\text{-}80)$$

We use the continuity equation by expanding it from

$$\frac{\partial \rho u}{\partial x} + \frac{\partial \rho v}{\partial y} = 0 \qquad (2\text{-}81)$$

to

$$u\frac{\partial \rho}{\partial x} + \rho\frac{\partial u}{\partial x} + v\frac{\partial \rho}{\partial y} + \rho\frac{\partial v}{\partial y} = 0 \qquad (2\text{-}82)$$

or

$$u\frac{\partial \rho}{\partial x} + v\frac{\partial \rho}{\partial y} = -\rho\frac{\partial u}{\partial x} - \rho\frac{\partial v}{\partial y}. \qquad (2\text{-}83)$$

We now add the modified x- and y-momentum equations, equation (2-80), which gives us equation (2-84) below.

$$u^2\frac{\partial u}{\partial x}+uv\frac{\partial u}{\partial y}+vu\frac{\partial v}{\partial x}+v^2\frac{\partial v}{\partial y}=-u\frac{a^2}{\rho}\frac{\partial \rho}{\partial x}-v\frac{a^2}{\rho}\frac{\partial \rho}{\partial y}$$
$$=-\frac{a^2}{\rho}\left(u\frac{\partial \rho}{\partial x}+v\frac{\partial \rho}{\partial y}\right) \qquad (2\text{-}84)$$

We substitute the rewritten continuity equation, equation (2-83), into equation (2-84), resulting in

$$u^2\frac{\partial u}{\partial x}+uv\frac{\partial u}{\partial y}+vu\frac{\partial v}{\partial x}+v^2\frac{\partial v}{\partial y}=-\frac{a^2}{\rho}\left(-\rho\frac{\partial u}{\partial x}-\rho\frac{\partial v}{\partial y}\right)$$
$$=a^2\frac{\partial u}{\partial x}+a^2\frac{\partial v}{\partial y}. \qquad (2\text{-}85)$$

Finally, we rearrange the terms in equation (2-85) to obtain the following gas dynamic equation in two dimensions:

$$\left(u^2-a^2\right)\frac{\partial u}{\partial x}+uv\left(\frac{\partial u}{\partial y}+\frac{\partial v}{\partial x}\right)+\left(v^2-a^2\right)\frac{\partial v}{\partial y}=0 \qquad (2\text{-}86)$$

Extension to three dimensions is straightforward, creating the corresponding gas dynamic equation:

$$\left(u^2-a^2\right)\frac{\partial u}{\partial x}+\left(w^2-a^2\right)\frac{\partial w}{\partial z}+\left(v^2-a^2\right)\frac{\partial v}{\partial y}+uv\left(\frac{\partial u}{\partial y}+\frac{\partial v}{\partial x}\right)+vw\left(\frac{\partial v}{\partial z}+\frac{\partial w}{\partial y}\right)+wu\left(\frac{\partial w}{\partial x}+\frac{\partial u}{\partial z}\right)=0 \qquad (2\text{-}87)$$

2.5.2 Derivation of the Classical Gas Dynamics-Related Energy Equation

The special form of the energy equation that is used to close the system (in two dimensions or 2D) is given below.

$$a^2=a_0^2-\left(\frac{\gamma-1}{2}\right)\left(u^2+v^2\right) \qquad (2\text{-}88)$$

We next show exactly how this relation is obtained. Let us start with the energy equation for inviscid, adiabatic flow expressed in the form of

$$\frac{DH}{Dt}=0 \qquad (2\text{-}89)$$

where *H* is the total enthalpy, defined (in 2D) by

$$H=h+\frac{1}{2}\left(u^2+v^2\right). \qquad (2\text{-}90)$$

Equation (2-89) yields *H* = constant. Thus, we have a purely algebraic statement of the energy equation instead of a partial differential equation. This is an important reduction in complexity.

For a thermally and calorically perfect gas, $h = c_p T$ and c_p = constant. Substituting for the enthalpy, we get equation (2-91).

$$c_pT_0=c_pT+\frac{1}{2}\left(u^2+v^2\right) \qquad (2\text{-}91)$$

Recalling that $a^2 = \gamma RT$ and $R = c_p - c_v$, with $\gamma = c_p/c_v$, we write

$$a^2=\frac{c_p}{c_v}(c_p-c_v)T=\left(\frac{c_p-c_v}{c_v}\right)c_pT \qquad (2\text{-}92)$$

or

$$c_p T = \left(\frac{c_v}{c_p - c_v}\right) a^2 = \left(\frac{1}{\gamma - 1}\right) a^2. \qquad (2\text{-}93)$$

Using equation (2-93), we can rewrite the total energy equation (*H* = constant), equation (2-91), as

$$\frac{a_0^2}{\gamma - 1} = \frac{a^2}{\gamma - 1} + \frac{1}{2}\left(u^2 + v^2\right) \qquad (2\text{-}94)$$

or

$$a_0^2 = a^2 + \left(\frac{\gamma - 1}{2}\right)\left(u^2 + v^2\right). \qquad (2\text{-}95)$$

The two-dimensional form shown in equation (2-88) is readily obtained by solving equation (2-95) for *a*. Extension to three dimensions is straightforward, and the equation in 3D is

$$a^2 = a_0^2 - \left(\frac{\gamma - 1}{2}\right)\left(u^2 + v^2 + w^2\right). \qquad (2\text{-}96)$$

2.5.3 Full Potential Equation

The gas dynamics equation is converted to the classical nonlinear potential equation when we make the irrotational flow assumption. The potential flow assumption requires that the flow be irrotational. This is valid for inviscid flow when the onset flow is uniform and there are no shock waves. However, we often continue to assume that the flow can be represented approximately by a scalar potential Φ when the Mach number normal to any shock wave is close to one (for example, $M_n < 1.25$). Recall that the irrotational flow assumption is stated mathematically as curl **V** = 0. When this is true, **V** can be defined as the gradient of a scalar potential, **V** = ∇Φ. Using the common subscript notation to represent partial derivatives, the velocity components are *u* = Φ*x* ,*v* = Φ*y*, and *w* = Φ*z*. Using the gas dynamics equation, equation (2-87), the nonlinear or "full-potential" equation is written as

$$\left(\Phi_x^2 - a^2\right)\Phi_{xx} + \left(\Phi_y^2 - a^2\right)\Phi_{yy} + \left(\Phi_z^2 - a^2\right)\Phi_{zz} + 2\Phi_x\Phi_y\Phi_{xy} + 2\Phi_y\Phi_z\Phi_{yz} + 2\Phi_z\Phi_x\Phi_{zx} = 0. \qquad (2\text{-}97)$$

This is the classic form of the equation. This single nonlinear partial differential equation has been extensively used to obtain physical insights into a wide variety of flows. Note that, as written above, it is not in divergence (or conservation) form.

2.5.4 Equivalent Divergence Form and Energy Equation

The equivalent equation written in conservation form makes use of the continuity equation. This is the form that is used in most computational fluid dynamics codes. Equation (2-98) shows how it is written in two dimensions.

$$\frac{\partial}{\partial x}(\rho\Phi_x) + \frac{\partial}{\partial y}(\rho\Phi_y) = 0 \qquad (2\text{-}98)$$

The relation between ρ and the potential is given by

$$\rho = \left[1 - \left(\frac{\gamma - 1}{\gamma + 1}\right)\left(\Phi_x^2 + \Phi_y^2\right)\right]^{\frac{1}{\gamma - 1}} \qquad (2\text{-}99)$$

which is a statement of the energy equation (see section 2.5.5). Note that the full-potential equation is still nonlinear when the density varies, and ρ must be considered a dependent variable.

2.5.5 Derivation of Another Form of the Related Energy Equation

It is informative to demonstrate the derivation of the energy equation, equation (2-99), in section 2.5.4. To get this standard form, understand the specific nondimensionalization employed with this form:

$$\rho = \frac{\tilde{\rho}}{\rho_0}, \quad \Phi_x = \frac{\tilde{u}}{a^*}, \quad \Phi_y = \frac{\tilde{v}}{a^*}, \qquad (2\text{-}100)$$

where a^* denotes the sonic value. Start with the previous energy equation and work with dimensional variables for the moment:

$$a^2 = a_0^2 - \left(\frac{\gamma - 1}{2}\right)\left(u^2 + v^2\right) \qquad (2\text{-}101)$$

or

$$\frac{a^2}{a_0^2} = 1 - \left(\frac{\gamma - 1}{2}\right)\left(\frac{u^2 + v^2}{a_0^2}\right). \qquad (2\text{-}102)$$

Now, let us get a relation for a_0 in terms of the eventual nondimensionalizing velocity a^*.

When the velocity is equal to the speed of sound, we can write

$$a_0^2 = a^2 + \left(\frac{\gamma - 1}{2}\right)\underbrace{\left(u^2 + v^2\right)}_{=a^2}. \qquad (2\text{-}103)$$

Since $a = a^*$ when the velocity is equal to the speed of sound, we obtain either

$$a_0^2 = a^{*2} + \left(\frac{\gamma - 1}{2}\right)a^2 = \left(1 + \frac{\gamma - 1}{2}\right)a^{*2} \qquad (2\text{-}104)$$

or

$$a_0^2 = \left(\frac{\gamma + 1}{2}\right)a^{*2}. \qquad (2\text{-}105)$$

Using $a^2 = \gamma RT$, the left-hand side of equation (2-102) becomes

$$\left(\frac{a}{a_0}\right)^2 = \frac{T}{T_0}. \qquad (2\text{-}106)$$

In addition, replacing ${a_0}^2$ with ${a^*}^2$ in the denominator of the last term on the right-hand side of equation (2-102), we can rewrite the energy equation, equation (2-102), as

$$\frac{T}{T_0} = 1 - \frac{\gamma - 1}{2}\frac{u^2 + v^2}{\frac{\gamma+1}{2}a*^2} \qquad (2\text{-}107)$$

or

$$\frac{T}{T_0} = 1 - \left(\frac{\gamma - 1}{\gamma + 1}\right)\left[\left(\frac{u}{a^*}\right)^2 + \left(\frac{v}{a^*}\right)^2\right]. \qquad (2\text{-}108)$$

Recall that entropy, *s*, is constant for isentropic flows (a consistent assumption if the use of Φ is valid):

$$s = \text{const} \qquad (2\text{-}109)$$

and

$$\frac{p}{\rho^\gamma} = \text{const} = \frac{p_0}{\rho_0^\gamma} \qquad (2\text{-}110)$$

Now, we introduce (~) to denote dimensional quantities and convert to the desired nondimensional form:

$$\left(\frac{\tilde{p}}{p_0}\right) = \left(\frac{\tilde{\rho}}{\rho_0}\right)^\gamma = \left(\frac{\tilde{T}}{T_0}\right)^{\frac{\gamma}{\gamma-1}} \qquad (2\text{-}111)$$

or

$$\frac{\tilde{T}}{T_0} = \left(\frac{\tilde{\rho}}{\rho_0}\right)^{\gamma-1} \qquad (2\text{-}112)$$

Using equation (2-112) we write the energy equation, equation (2-108), as

$$\left(\frac{\tilde{\rho}}{\rho_0}\right)^{\gamma-1} = 1 - \left(\frac{\gamma - 1}{\gamma + 1}\right)\left[\left(\frac{\tilde{u}}{a^*}\right)^2 + \left(\frac{\tilde{v}}{a^*}\right)^2\right]. \qquad (2\text{-}113)$$

Using the nondimensionalizing definition given in section 2.4.3, we finally obtain equation (2-114) below.

$$\rho = \left[1 - \left(\frac{\gamma - 1}{\gamma + 1}\right)\left(\Phi_x^2 + \Phi_y^2\right)\right]^{\frac{1}{\gamma-1}} \qquad (2\text{-}114)$$

This is an energy equation in ρ to use with the divergence form of the full-potential equation. It is also an example of how to get an energy equation in a typical nondimensional form used in the literature.

2.6 Special Cases

In this section, we present a number of special, simplified forms of the equations described above. These simplified equations are entirely adequate for many of the problems of computational aerodynamics, and until recently they were used nearly exclusively. The ability to obtain simpler relations that provide explicit physical insight into the flow field process has played an important role in the development of aerodynamic concepts. One key idea is the notion of small disturbance equations. The assumption is that the flow field is only slightly disturbed by the body. We expect this assumption to be valid for inviscid flows over streamlined shapes. These ideas are expressed mathematically by small perturbation or asymptotic expansion methods and are elegantly described in the book by Van Dyke.[29] Figure 2-10 summarizes the theoretical path required to obtain these equations.

2.6.1 Small Disturbance Form of the Energy Equation

The expansion of the simple algebraic statement of the energy equation provides an example of a small disturbance analysis. In this case, the square of the speed of sound (or equivalently the temperature) is linearly related to the velocity field. Start with the energy equation:

$$a^2 = a_0^2 - \left(\frac{\gamma - 1}{2}\right)\left(u^2 + v^2\right) \qquad (2\text{-}115)$$

and

$$a_0^2 = \text{const} = a^2 + \left(\frac{\gamma - 1}{2}\right)\left(u^2 + v^2\right) = a_\infty^2 + \frac{\gamma - 1}{2}U_\infty^2 \qquad (2\text{-}116)$$

Assuming the freestream velocity, U_∞, is aligned with the *x*-direction and letting the velocity components be $u = U_\infty + u'$, $v = v'$ (where u' and v' are disturbance velocities in *x*- and *y*-directions, respectively), we can write equation (2-116) as

$$a^2 = a_\infty^2 + \frac{\gamma - 1}{2}U_\infty^2 - \left(\frac{\gamma - 1}{2}\right)\left[U_\infty^2 + 2U_\infty u' + u'^2 + v'^2\right]. \qquad (2\text{-}117)$$

Combining terms, we obtain equation (2-118).

$$a^2 = a_\infty^2 - \left(\frac{\gamma - 1}{2}\right)\left[2U_\infty u' + u'^2 + v'^2\right] \qquad (2\text{-}118)$$

At this point, the relation is still exact, but now it is written in a form that can be easily simplified. The basic idea is to take advantage of the small perturbation assumption:

$$u' < U_\infty, \quad v' < U_\infty \qquad (2\text{-}119)$$

and thus,

$$\frac{u'}{U_\infty} < 1 \Rightarrow \left(\frac{u'}{U_\infty}\right)^2 \approx 0. \qquad (2\text{-}120)$$

Equation (2-120) is applicable to v' as well. The implications of the small disturbance assumption for equation (2-118) are

$$a^2 = a_\infty^2 - \left(\frac{\gamma - 1}{2}\right)[2U_\infty u' + \underbrace{u'^2 + v'^2}_{\substack{\text{neglect as small} \\ \text{henceforth}}}\ ]. \qquad (2\text{-}121)$$

This is a linear relation between the disturbance velocity and the speed of sound. It is a heuristic example of the procedures used in a more formal approach known as perturbation theory.

2.6.2 Small Disturbance Expansion of the Full Potential Equation

We now use an approach similar to that in section 2.6.1 to show how to obtain a small disturbance version of the full-potential equation. Again consider the situation where we assume that the disturbance to the freestream is small. Now we examine the full-potential equation. First, we rewrite the full-potential equation, equation (2-97), in 2D for simplicity as

$$\left(\Phi_x^2 - a^2\right)\Phi_{xx} + 2\Phi_x\Phi_y\Phi_{xy} + \left(\Phi_y^2 - a^2\right)\Phi_{yy} = 0. \qquad (2\text{-}122)$$

Now write the velocity as a difference from the freestream velocity. Introduce a disturbance potential, φ, defined by

$$\begin{aligned}\Phi &= U_\infty x + \phi(x,y)\\ \Phi_x &= u = U_\infty + \phi_x \qquad (2\text{-}123)\\ \Phi_y &= v = \phi_y\end{aligned}$$

where we have introduced a directional bias. The *x*-direction is the direction of the freestream velocity. We next assume that φ_x and φ_y are small compared to U_∞. Using the idea of a small disturbance to the freestream, simplified (and even linear) forms of a small disturbance potential equation and an energy equation can be derived.

As an example of the expansion process, consider the first term in equation (2-122). Use the definition of the disturbance potential and the simplified energy equation as shown in equation (2-124) below.

$$\begin{aligned}\left(\Phi_x^2 - a^2\right) &\cong \left(U_\infty + \phi_x\right)^2 - \left\{a_\infty^2 - \left(\frac{\gamma-1}{2}\right)\left[2U_\infty u'\right]\right\}\\ &\cong U_\infty^2 + 2U_\infty\phi_x + \phi_x^2 - a_\infty^2 + \frac{\gamma-1}{2}2U_\infty \underbrace{u'}_{=\phi_x'}\end{aligned} \qquad (2\text{-}124)$$

Regroup and drop the square of the disturbance velocity as small:

$$\begin{aligned}\left(\Phi_x^2 - a^2\right) &\cong U_\infty^2 - a_\infty^2 + 2U_\infty\phi_x + (\gamma-1)U_\infty\phi_x\\ &\cong U_\infty^2 - a_\infty^2 + \underbrace{[2+(\gamma-1)]}_{\gamma+1}U_\infty\phi_x\\ &\cong U_\infty^2 - a_\infty^2 + (\gamma+1)U_\infty\phi_x\end{aligned} \qquad (2\text{-}125)$$

Dividing by a_∞^2,

$$\begin{aligned}\left(\frac{\Phi_x^2}{a_\infty^2} - \frac{a^2}{a_\infty^2}\right) &\cong \frac{U_\infty^2}{a_\infty^2} - 1 + (\gamma+1)\frac{U_\infty}{a_\infty}\frac{\phi_x}{a_\infty}\\ &\cong M_\infty^2 - 1 + (\gamma+1)M_\infty \underbrace{\frac{U_\infty}{a_\infty}}_{\frac{U_\infty}{U_\infty}\frac{\phi_x}{a_\infty}}\frac{\phi_x}{U_\infty}\\ &\cong \left(M_\infty^2 - 1\right) + (\gamma+1)M_\infty^2\left(\frac{\phi_x}{U_\infty}\right)\end{aligned} \qquad (2\text{-}126)$$

Rewrite the potential equation, equation (2-122), by first dividing by a_∞^2 and then replacing the coefficient of the first term using equation (2-126):

$$\underbrace{\left(\frac{\Phi_x^2}{a_\infty^2} - \frac{a^2}{a_\infty^2}\right)}_{\left[(M_\infty^2-1)+(\gamma+1)M_\infty^2\left(\frac{\phi_x}{U_\infty}\right)\right]}\Phi_{xx} + 2\frac{\Phi_x}{a_\infty}\frac{\Phi_y}{a_\infty}\Phi_{xy} + \left(\frac{\Phi_y^2}{a_\infty^2} - \frac{a^2}{a_\infty^2}\right)\Phi_{yy} = 0 \qquad (2\text{-}127)$$

Now, by definition,

$$\Phi_{xx} = \phi_{xx}, \quad \Phi_{yy} = \phi_{yy}, \quad \Phi_{xy} = \phi_{xy} \qquad (2\text{-}128)$$

while

$$\frac{\Phi_x}{a_\infty} = M_\infty \left(1 + \frac{\phi_x}{U_\infty}\right), \quad \frac{\Phi_y}{a_\infty} = M_\infty \frac{\phi_y}{U_\infty}. \qquad (2\text{-}129)$$

Using the same approach demonstrated above, we can write

$$\left(\frac{\Phi_y^2}{a_\infty^2} - \frac{a^2}{a_\infty^2}\right) \cong -1 + (\gamma - 1) M_\infty^2 \left(\frac{\phi_y}{U_\infty}\right). \qquad (2\text{-}130)$$

Putting these relations all into the potential equation, we obtain

$$\left[M_\infty^2 - 1 + (\gamma + 1) M_\infty^2 \frac{\phi_x}{U_\infty}\right] \phi_{xx} + 2M_\infty^2 \left(1 + \frac{\phi_x}{U_\infty}\right) \frac{\phi_y}{U_\infty} \phi_{xy} + \left[-1 + (\gamma - 1) M_\infty^2 \frac{\phi_y}{U_\infty}\right] \phi_{yy} = 0 \qquad (2\text{-}131)$$

where the ϕ_x^2, ϕ_y^2 terms are neglected in the coefficients. This equation is still nonlinear but is in a form ready for further simplifications described below.

2.6.3 Transonic Small Disturbance Equation

Transonic flows contain regions with both subsonic and supersonic flows. Any equation describing this flow must simulate the correct physics in the two different flow regimes. As we show below, this makes the problem difficult to solve numerically. Indeed, the numerical solution of transonic flows was one of the primary thrusts of research in CFD over the decades of the '70s and '80s. A small disturbance equation can be derived that captures the essential nonlinearity of transonic flow, which is the rapid streamwise variation of flow disturbances in the *x*-direction, including normal shock waves. Therefore, in transonic flows, we assume

$$\frac{\partial}{\partial x} > \frac{\partial}{\partial y}. \qquad (2\text{-}132)$$

The transonic small disturbance equation retains the key term in the convective derivative, $u(\partial u/\partial x)$, which allows the shock to occur in the solution. Retaining this key nonlinear term, the small disturbance equation given above becomes

$$\left[\left(1 - M_\infty^2\right) - (\gamma + 1) M_\infty^2 \frac{\phi_x}{U_\infty}\right] \phi_{xx} + \phi_{yy} = 0. \qquad (2\text{-}133)$$

Using the definition of the potential from equation (2-123), we can identify the nonlinear term, $u(\partial u/\partial x)$, which appears as the product of the second term in the bracket, $u = \phi_x$, and the φ_{xx} term, which is $\partial u/\partial x$.

This is one version of the transonic small disturbance equation. It is still nonlinear and can change mathematical type (to be discussed in section 2.8). This means that the sign of the coefficient of ϕ_{xx} can change in the flow field, depending on the value of the nonlinear term. It is valid for transonic flow, and as written, it is not in a divergence form. Transonic flows occur for Mach numbers from 0.6 to 1.2, depending on the degree of flow disturbance. They also occur under other circumstances. At high-lift conditions, the flow around the leading edge may become locally supersonic at freestream Mach numbers as low as 0.20 or 0.25. Transonic flow occurs on rotor blades and propellers. At hypersonic speeds, the flow between the bow shock and the body will frequently be locally subsonic. These are also transonic flows. The transonic small disturbance equation can be numerically solved on your personal computer.

2.6.4 Prandtl–Glauert Equation

When the flow field is entirely subsonic or supersonic, all terms involving products of small quantities can be neglected in the small disturbance equation. When this is done, we obtain the Prandtl–Glauert equation:

$$\left(1 - M_\infty^2\right)\phi_{xx} + \phi_{yy} = 0 \qquad (2\text{-}134)$$

This is a linear equation valid for small disturbance flows that are either entirely supersonic or subsonic. For subsonic flows, this equation can be transformed to Laplace's equation, while at supersonic speeds, this equation takes the form of a wave equation. The difference is important, as described below in the section on the mathematical type of partial differential equations (PDEs). This equation requires that the onset flow be in the *x*-direction, an example of the importance that coordinate systems assume when simplifying assumptions are made. Thus, use of simplifying assumptions introduced a directional bias into the resulting approximate equation.

The extension to three dimensions is shown in equation (2-135).

$$\left(1 - M_\infty^2\right)\phi_{xx} + \phi_{yy} + \phi_{zz} = 0 \qquad (2\text{-}135)$$

2.6.5 Incompressible, Irrotational Flow: Laplace's Equation

Assuming that the flow is incompressible, ρ is a constant and can be removed from the modified continuity equation, equation (2-98), given above. Alternately, divide the full-potential equation by the speed of sound, a^2, and take the limit as a goes to infinity. Either way, the following equation is obtained:

$$\Phi_{xx} + \Phi_{yy} = 0 \qquad (2\text{-}136)$$

This is Laplace's equation. Frequently people call this equation the potential equation. For that reason, the complete potential equation, equation (2-97), is known as the full-potential equation. Do not confuse the true potential flow equation with Laplace's equation, which requires the assumption of incompressible flow. When the flow is incompressible, this equation is exact when using the inviscid irrotational flow model and does not require the assumption of small disturbances.

2.6.6 The Boundary Layer Equations

The last special case retains a viscous term, while assuming that the pressure is a known function and independent of the *y*-coordinate value. These are Prandtl's boundary layer equations that describe the flow immediately adjacent to the body surface. In a 2D, steady flow context, the boundary layer equations are detailed below.

$$\frac{\partial \rho u}{\partial x} + \frac{\partial \rho v}{\partial y} = 0 \qquad (2\text{-}137)$$

$$\rho u\frac{\partial u}{\partial x} + \rho v\frac{\partial u}{\partial y} = -\frac{\partial p}{\partial x} + \frac{\partial}{\partial y}\left(\mu\frac{\partial u}{\partial y}\right) \qquad (2\text{-}138)$$

$$0 = -\frac{\partial p}{\partial y} \qquad (2\text{-}139)$$

The related energy equation must also be included if compressibility effects are important.

All the equations presented in this section provide physical models of classes of flows that, under the right circumstances, are completely adequate to obtain an accurate representation of the flow. Many, many other approximate flow models have been proposed. Those presented in this section represent by far the majority of methods currently used. Numerous versions of the Navier–Stokes equations (taken here to include the time-averaged Reynolds equations) have also been used. These equations are discussed as appropriate in subsequent chapters. Figure 2-10 summarizes the connection between the mathematical models of various types of flow fields.

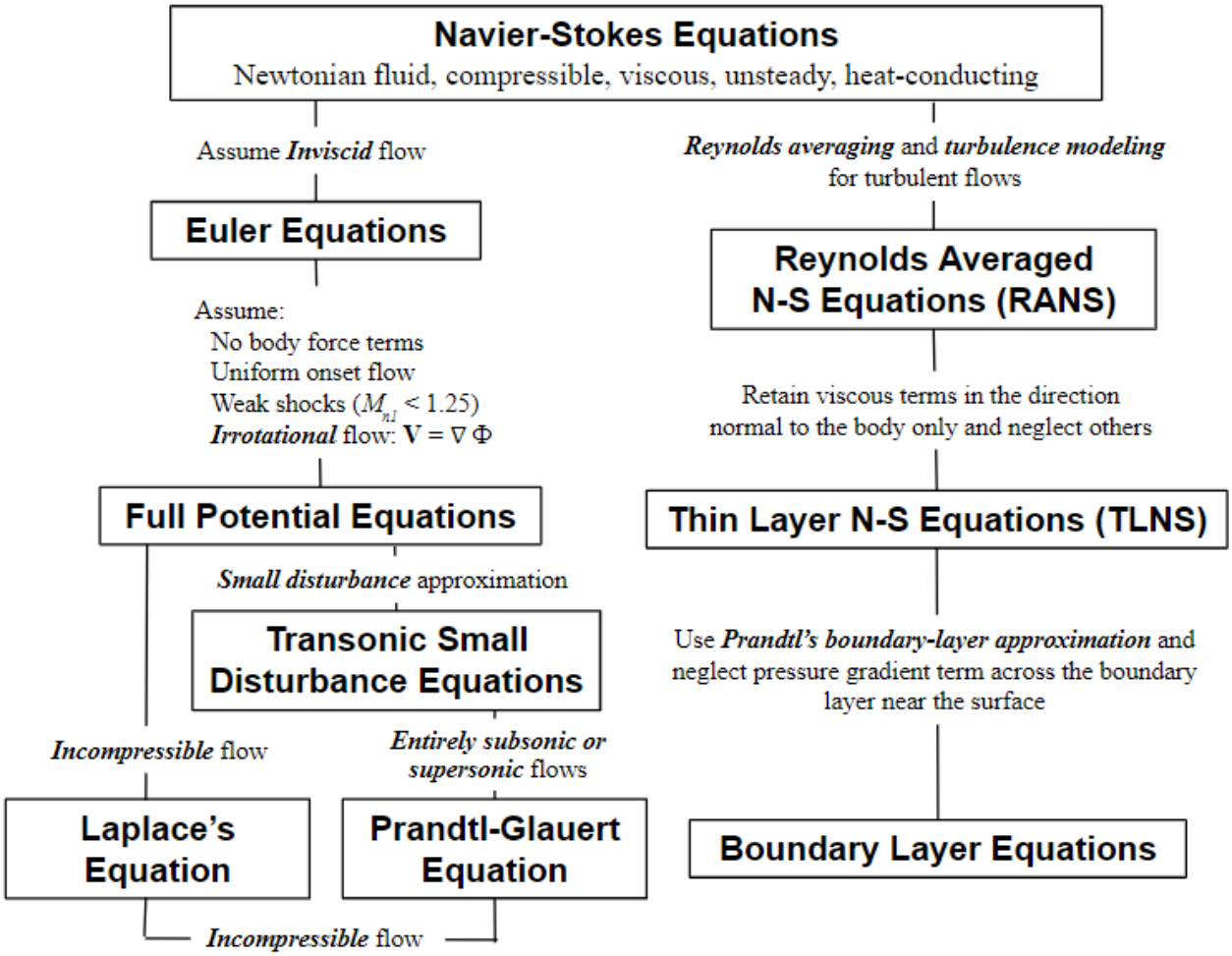


Figure 2-10: Connection between various approximations to the Navier–Stokes equations. From W. H. Mason. Adapted by P. Raj.

2.7 Examples of Zones of Application

The appropriate version of the governing equation depends on the type of flow field being investigated. For high Reynolds number attached flow, the pressure can be obtained very accurately without considering viscosity. Recall that the use of a Kutta condition provides a simple way of enforcing key physics associated with viscosity by specifying this feature as a boundary condition on an otherwise inviscid solution. If the onset flow is uniform and any shocks are weak (characterized by Mach number normal to the shock, M_n, to be < 1.25 or 1.3), then the potential flow approximation is valid. If a slight flow separation exists, a special approach using the boundary layer equations can be used interactively with the inviscid solution to obtain a solution. As speed increases, shocks begin to get strong and are curved. Under these circumstances, the solution of the complete Euler equations is required.

When significant separation occurs or when you cannot figure out the preferred direction to apply a boundary layer approach, the Navier–Stokes equations are used. Note that many different "levels" of the N–S equations are in use.

To avoid having many different codes, some people would like to have just one code that does everything. While this may be a worthy goal, most applications are more effective using a variety of methods. A step in the right direction is the use of a system that employs a common geometry and grid processing system and a common output/graphics systems.

2.8 Mathematical Classification of Partial Differential Equations (PDEs)

A key property of any system of PDEs is the "type" of the equations. In mathematics, an equation type has a very precise meaning. Essentially, the type of the equation determines the domain on which boundary or initial conditions must be specified. The mathematical theory has been developed over a number of years for PDEs and is given in books on PDEs. Two examples include Sneddon[30] (pp. 105–109) and Chester[31] (Chapter 6). Discussions from the computational fluid dynamics viewpoint are available in Tannehill, Anderson, and Pletcher,[32] (Chapter 2), Fletcher[33] (Chapter 2), and Hoffman[34] (Chapter 1).

To successfully obtain the numerical solution of a PDE, you must satisfy the "spirit" of the theory for the type of a PDE. Usually the theory has been developed for model problems, frequently linear. For PDEs describing physical systems, the type will be related to the following categorization:

1. **Equilibrium problems.** Examples include steady-state temperature distributions and steady incompressible flow. These are similar to boundary value problems for ordinary differential equations (ODEs).
2. **Marching or propagation problems.** These are transient or transient-like problems. Examples include transient heat conduction and steady supersonic flow. These are similar to initial value problems for ODEs.

The three types of PDEs are elliptic, parabolic, and hyperbolic. A linear equation will be of one type. The nonlinear equations of fluid flow can change type locally depending on the local values of the variables. This "mixed-type" feature has had a profound influence on the development of methods for computational aerodynamics. A mismatch between the type of the PDE and the prescribed boundary conditions dooms any attempt at numerical solution.

The standard mathematical illustration of PDE type uses a second-order PDE:

$$A\phi_{xx} + B\phi_{xy} + C\phi_{yy} + D\phi_x + E\phi_y + F\phi + G = 0 \qquad (2\text{-}140)$$

where *A*, *B*, *C*, *D*, *E*, *F*, and *G* can be constants or functions of *x*, *y*, and ϕ. Depending on the values of *A*, *B*, and *C*, the PDE will be of different type. The specific type of the PDE depends on the characteristics of the PDE. One of the important properties of characteristics is that the second derivative of the dependent variables are allowed, although there can be no discontinuity of the first derivative. The slopes of the characteristics can be found from *A*, *B*, and *C*. From mathematical theory, the characteristics are found depending on the sign of determinant as shown in table 2-3.

Sign of determinant	Characteristics	Type
$(B^2 - 4AC) > 0$	real	hyperbolic
$(B^2 - 4AC) = 0$	real, equal	parabolic
$(B^2 - 4AC) < 0$	imaginary	elliptic

Table 2-3: Sign of the determinant classifies the type of governing PDE

2.8.1 Hyperbolic

The basic property is a limited *domain of dependence*. Initial data are required on a curve or a plane, which does not coincide with a characteristic curve. Figure 2-11 illustrates this requirement.

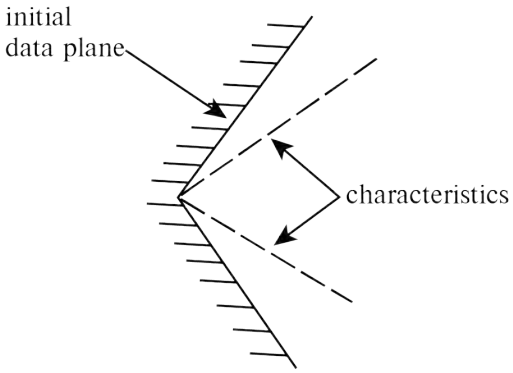


Figure 2-11: Connection between characteristics and initial condition data planes. From W. H. Mason. Adapted by S. Madden.

Classical linearized supersonic aerodynamic theory is an example of a hyperbolic system.

2.8.2 Parabolic

This is associated with a diffusion process. Data must be specified at an initial plane, marching forward in a time or time-like direction. There is no limited region of influence equivalent to the hyperbolic case. Data are required on the entire time-like surface. Figure 2-12 illustrates the requirement.

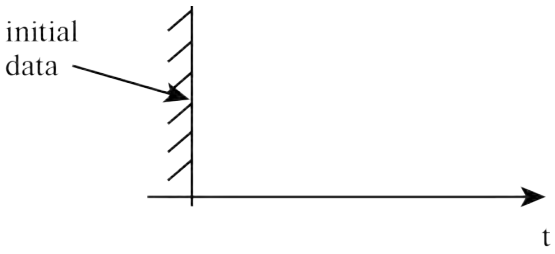


Figure 2-12: Initial data plane for parabolic equation. From W. H. Mason. Adapted by S. Madden.

In aerodynamics, boundary layers have a parabolic type.

2.8.3 Elliptic

These are equilibrium problems. They require boundary conditions everywhere, as shown in figure 2-13. Incompressible potential flow is an example of a governing equation of elliptic type. The region of influence and the zone of dependence are the same.

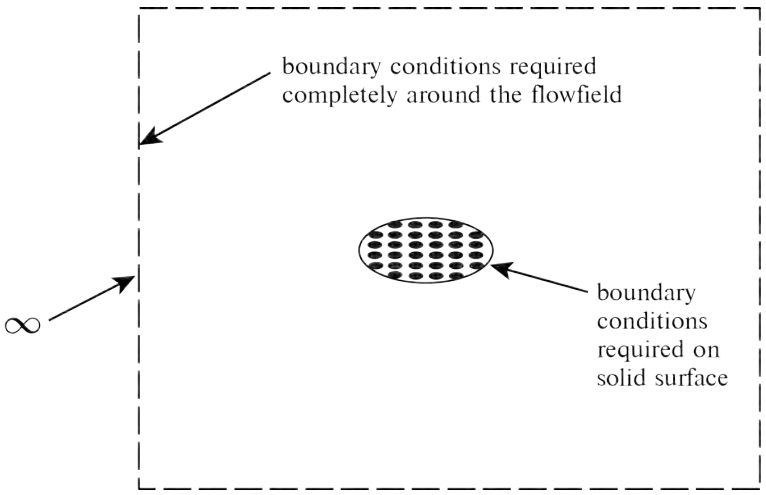


Figure 2-13: Boundary conditions required for elliptic PDEs. *From W. H. Mason. Adapted by S. Madden.*

Consider the following examples. For the Prandtl–Glauert equation,

$$\left(1 - M_\infty^2\right)\phi_{xx} + \phi_{yy} = 0 \qquad (2\text{-}141)$$

and

$$\begin{matrix} M_\infty < 1 \text{elliptic} \\ M_\infty > 1 \text{hyperbolic} \end{matrix}. \qquad (2\text{-}142)$$

For the transonic small disturbance equation,

$$\left(1 - M_\infty^2\right)\phi_{xx} + \phi_{yy} = 0. \qquad (2\text{-}143)$$

This is an equation of mixed type. It is required to treat the physics of transonic flows.

Type plays a key role in computational approaches. The type can be used to advantage. In the case of the Euler equations, the steady state Euler equations are hard to solve. It is standard procedure to consider the unsteady case, which is hyperbolic, and to obtain the steady state solution by marching in time until the solution does not change in time.

Alternate approaches are available for systems of first-order PDEs. Classification is sometimes difficult to determine. The type of an equation is determined with respect to a particular variable. The type of equations with respect to time may be completely different than their type with respect to space. The type of the equation often helps to define the appropriate solution coordinate system. The different types of the equations given above are responsible for the distinct numerical approaches that are adopted to solve different problems.

2.8.4 Elaboration on Characteristics

This section provides additional details that offer some insight into why the determinant of the coefficients of the second derivative terms define the type of the equation.

Consider equation (2-144) below.

$$A\phi_{xx} + B\phi_{xy} + C\phi_{yy} + D\phi_x + E\phi_y + F\phi + G = 0 \qquad (2\text{-}144)$$

- Assume ϕ is a solution describing a curve in space.
- These curves "patch" various solutions, known as characteristic curves.
- Discontinuity of the second derivative of the dependent variable is allowed but no discontinuity of the first derivative.

The differentials of ϕ_x and ϕ_y that represent changes from x, y to $x + dx, y + dy$ along characteristics are

$$d\phi_x = \frac{\partial \phi_x}{\partial x}dx + \frac{\partial \phi_x}{\partial y}dy = \phi_{xx}dx + \phi_{xy}dy \qquad (2\text{-}145)$$

and

$$d\phi_y = \frac{\partial \phi_y}{\partial x}dx + \frac{\partial \phi_y}{\partial y}dy = \phi_{yx}dx + \phi_{yy}\mathrm{d}y. \qquad (2\text{-}146)$$

Express equation (2-144) as

$$A\phi_{xx} + B\phi_{xy} + C\phi_{yy} = H \qquad (2\text{-}147)$$

with

$$H = -\left(D\phi_x + E\phi_y + F\phi + G\right). \qquad (2\text{-}148)$$

Assume equation (2-147) is linear. Solve it together with equations (2-145) and (2-146) for second derivatives of ϕ:

$$\begin{aligned} A\phi_{xx} + B\phi_{xy} + C\phi_{yy} &= H \\ dx\phi_{xx} + dy\phi_{xy} &= d\phi_x \\ dx\phi_{xy} + dy\phi_{yy} &= d\phi_y \end{aligned} \qquad (2\text{-}149)$$

or

$$\begin{bmatrix} A & B & C \\ dx & dy & 0 \\ 0 & dx & dy \end{bmatrix} \begin{bmatrix} \phi_{xx} \\ \phi_{xy} \\ \phi_{yy} \end{bmatrix} = \begin{bmatrix} H \\ d\phi_x \\ d\phi_y \end{bmatrix} \qquad (2\text{-}150)$$

and solve for ϕ_{xx}, ϕ_{xy}, ϕ_{yy}. Since second derivatives can be discontinuous on the characteristics, the derivatives are indeterminate and the coefficient matrix would be singular:

$$\begin{bmatrix} A & B & C \\ dx & dy & 0 \\ 0 & dx & dy \end{bmatrix} = 0 \qquad (2\text{-}151)$$

This expands into

$$A(dy)^2 - Bdxdy + C(dx)^2 = 0, \qquad (2\text{-}152)$$

and the slopes of the characteristics curves are found by dividing by $(dx)^2$:

$$A\left(\frac{dy}{dx}\right)^2 - B\left(\frac{dy}{dx}\right) + C = 0. \qquad (2\text{-}153)$$

Solve for *dy*/*dx*.

$$\left.\frac{dy}{dx}\right|_{\alpha,\beta} = \frac{B \pm \sqrt{B^2 - 4AC}}{2A} \qquad (2\text{-}154)$$

Hence the requirement on $(B^2 - 4AC)$ shown in table 2-3 and discussed above to define the type of the PDE as related to the characteristics of the equation. See the references cited above for more details.

2.9 Requirements for a Complete Problem Formulation

When formulating a mathematical representation of a fluid flow problem, you have to carefully consider both the flow field model equations and the boundary conditions. An evaluation of the mathematical type of the PDEs that are being solved plays a key role in this. Boundary conditions must be properly specified. Either over- or under-specifying boundary conditions will doom your calculation before you start. A proper formulation requires:

- Governing equations
- Boundary conditions
- Coordinate system specification

This is all necessary before even computing the first number! If this is done, then the mathematical problem being solved is considered to be well posed.

Chapter 2 Exercises

2.1 Convert the unsteady 3D Euler equations from classical nonconservative form to divergence form.

2.2 Equation (2-70) is an unusual form of the equation of state. It is from presentation slides defining the equations used in **CFL3D**.

Turn in your derivation of this equation. Is there a typo?

2.3 Show how equation (2-76) can be obtained.

2.4 Why is equation (2-97) not in divergence form?

2.5 Show that point source and point vortex singularities are solutions of Laplace's equation in two dimensions.

Recall that a point source can be expressed as

$$\phi(x, y) = \frac{q}{4\pi}\ln\left(x^2 + y^2\right)$$

and a point vortex as

$$\phi(x, y) = \frac{\Gamma}{2\pi} \tan^{-1}\left(\frac{y}{x}\right).$$

2.6 Consider the point source of problem 2.5.

What is the behavior of the velocity as the distance from the source becomes large?

What is the potential function for a point source?

How does it behave as the distance from the source becomes large?

Comment from the standpoint of having to satisfy the "infinity" boundary condition in a program for a potential flow solution.

2.7 Find the classification type of the following equations:

Laplace equation: $U_{xx} + U_{yy} = 0$

Heat equation : $U_y = \sigma U_{xx}$, σ real

Wave equation: $U_{xx} = c^2 U_{yy}$, c real

Figure References

Figure 2-1: W. H. Mason. Adapted by S. Madden. CC BY-NC-SA 4.0

Figure 2-2: W. H. Mason. Adapted by S. Madden. CC BY-NC-SA 4.0

Figure 2-4: W. H. Mason. Adapted by S. Madden. CC BY-NC-SA 4.0

Figure 2-5: W. H. Mason. Adapted by S. Madden. CC BY-NC-SA 4.0

Figure 2-8: W. H. Mason. Adapted by S. Madden. CC BY-NC-SA 4.0

Figure 2-10: W. H. Mason. Adapted by P. Raj. CC BY-NC-SA 4.0

Figure 2-11: W. H. Mason. Adapted by S. Madden. CC BY-NC-SA 4.0

Figure 2-12: W. H. Mason. Adapted by S. Madden. CC BY-NC-SA 4.0

Figure 2-13: W. H. Mason. Adapted by S. Madden. CC BY-NC-SA 4.0

Notes

1. Karamcheti, K., *Principles of Ideal-Fluid Aerodynamics*, Krieger Publishing Co., Malabar, 1966, chaps. 4, 5, 6, and 7.
2. Bertin, J. J., *Aerodynamics for Engineers*, 4th ed., Prentice-Hall, Inc., Upper Saddle River, 2002.
3. Anderson, J., *Modern Compressible Flow*, 2nd ed., McGraw-Hill Book Company, New York, 1990.
4. Moran, J., An Introduction to Theoretical and Computational Aerodynamics, John Wiley and Sons, New York, 1984. (*Note:* Now available from Dover.)
5. Grossman, B., "Derivation of the Navier-Stokes Equations," Lecture Notes No. 2, AOE 3044, Boundary Layer and Heat Transfer, Virginia Tech, 1992.
6. Hoffman, K. A., Chiang, S. T., Siddiqui, S., and Papadakis, M., *Fundamental Equations of Fluid Mechanics*, Engineering Education Systems, Wichita, 1996.
7. Karamcheti, K., *Principles of Ideal-Fluid Aerodynamics*, Krieger Publishing Co., Malabar, 1966, chaps. 4, 5, 6, and 7.
8. Owczarek, J. A., *Fundamentals of Gas Dynamics*, International Textbook Co., 1964.
9. Grossman, B., "Derivation of the Navier-Stokes Equations," Lecture Notes No. 2, AOE 3044, Boundary Layer and Heat Transfer, Virginia Tech, 1992.
10. Moran, J., *An Introduction to Theoretical and Computational Aerodynamics*, John Wiley and Sons, New York, 1984.
11. Anderson, J., *Modern Compressible Flow*, 2nd ed., McGraw-Hill Book Company, New York, 1990.
12. Bertin, J. J., *Aerodynamics for Engineers*, 4th ed., Prentice-Hall, Inc., Upper Saddle River, 2002.
13. Moran, J., *An Introduction to Theoretical and Computational Aerodynamics*, John Wiley and Sons, New York, 1984.
14. Anderson, J., *Modern Compressible Flow*, 2nd ed., McGraw-Hill Book Company, New York, 1990.
15. Bertin, J. J., Smith, M. L., *Aerodynamics for Engineers*, 4th ed., Prentice-Hall, Inc., Upper Saddle River, 2002.
16. Karamcheti, K., *Principles of Ideal-Fluid Aerodynamics*, Krieger Publishing Co., Malabar, 1966, chaps. 4, 5, 6, and 7.
17. Schlichting, H., *Boundary-Layer Theory*, 6th ed., McGraw-Hill, New York, 1968.

18. Grossman, B., "Derivation of the Navier-Stokes Equations," Lecture Notes No. 2, AOE 3044, Boundary Layer and Heat Transfer, Virginia Tech, 1992.
19. Tannehill, J. C., Anderson, D. A., and Pletcher, R. H., *Computational Fluid Mechanics and Heat Transfer*, 2nd ed., Taylor & Francis, Washington, 1997.
20. White, F. M., *Viscous Fluid Flow*, McGraw-Hill, New York, 1974.
21. Grossman, B., "Derivation of the Navier-Stokes Equations," Lecture Notes No. 2, AOE 3044, Boundary Layer and Heat Transfer, Virginia Tech, 1992.
22. Bertin, J. J., and Smith, M. L., *Aerodynamics for Engineers*, 4th ed., Prentice-Hall, Inc., Upper Saddle River, 2002.
23. White, F. M., *Viscous Fluid Flow*, McGraw-Hill, New York, 1974.
24. Thomas, J. L., and Salas, M. D., "Farfield Boundary Conditions for Transonic Lifting Solutions to the Euler Equation," AIAA Journal, Vol. 24, No. 7, Jul. 1986, pp. 1074–1080.
25. Verhoff, A., "Global Far-Field Computational Boundary Conditions for C- and O-Grid Topologies," AIAA Journal, Vol. 36, No. 2, Feb. 1998, pp. 148–156.
26. Colonius, T., "Modeling Artificial Boundary Conditions for Compressible Flow," Annual Review of Fluid Mechanics, Vol. 36, 2004, pp. 315–345.
27. Karamcheti, K., *Principles of Ideal-Fluid Aerodynamics*, Krieger Publishing Co., Malabar, 1966, chaps. 4, 5, 6, and 7.
28. Rumsey, C. L., Biedron, R. T., and Tomas, J. L., "CFL3D: Its History and Some Recent Applications," NASA TM-112861, May 1997.
29. Van Dyke, M., *Perturbation Methods in Fluid Mechanics*, The Parabolic Press, Stanford, CA,1975.
30. Sneddon, I. N., Elements of Partial Differential Equations, McGraw-Hill, New York, 1957.
31. Chester, C. R., Techniques in Partial Differential Equations, McGraw-Hill, New York, 1971.
32. Tannehill, J. C., Anderson, D. A., and Pletcher, R. H., *Computational Fluid Mechanics and Heat Transfer*, 2nd ed., Taylor & Francis, Washington, 1997.
33. Fletcher, C. A. J., *Computational Techniques for Fluid Dynamics*, Vol. 1, Springer-Verlag, Berlin, 1988.
34. Hoffman, K. A., and Chiang, S. T., *Computational Fluid Dynamics for Engineers*, Vol. 1, Engineering Education System, Wichita, 1993.

3. Fundamentals of Aerodynamic Drag

In this chapter, our primary goal is to discuss drag in more depth than the discussions typical to a introduction course in aerodynamics. We believe drag to be of foundational significance for configuration aerodynamics, and it is an *extremely important* driver of the aerodynamic design of configuration. Therefore, we cover it before addressing other aerodynamic considerations.

Drag is one of the two components of the total aerodynamic force that acts on an aircraft that is moving through air. When the total force is resolved in the plane of symmetry of the aircraft, drag is one component and lift is the other. Lift is perpendicular to the flight path, and drag is parallel to the flight path. Drag opposes the motion of the aircraft, requiring a propulsion system to overcome its retarding effect.

In this chapter, we introduce the key aspects of aerodynamic drag. We first highlight, in section 3.1, some of the main reasons why drag is crucially important for aircraft design. The subsequent sections discuss the concepts and methodologies required to evaluate drag of aircraft configurations. Additional discussions are included in later chapters on subsonic, transonic, and supersonic aerodynamics.

3.1 The Importance of Drag

Drag is at the heart of aircraft aerodynamic design. There are many different contributors to the total drag of an airplane. In three-dimensional flows, drag occurs even when the flow is assumed to be inviscid. This is also true in two-dimensional flows when compressibility becomes important. Before discussing the aerodynamics of lifting systems, the fundamental aspects of aerodynamic drag need to be established.

The subject is complicated. All aerodynamicists secretly hope for negative drag! In practice, however, there is no escaping the downsides of drag. The value of drag is also very important. Even seemingly minor changes in drag can be critical. On the Concorde, a one-count drag increase ($\Delta C_D = 0.0001$) required that two passengers out of the 90–100 passenger capacity be taken off the North Atlantic run.[1] In design studies, a drag decrease is equated to the decrease in aircraft weight required to carry a specified payload a required distance. One advanced fighter study found the drag sensitivity in supersonic cruise to be 90 lb/drag count compared to 48 lb/ct for subsonic/transonic cruise. At the transonic maneuver design point, the sensitivity was 16 lb/ct (drag is very high here). In comparison, the growth factor was 4.1 pounds of takeoff gross weight for every 1 pound of fixed weight added. For one executive business jet, the range sensitivity is 17 miles/drag count. The large long-range advanced supersonic transports studied in the 1990s had range sensitivities of about 100 miles/drag count.

When new aircraft are sold, the sales contract stipulates numerous performance guarantees. One of the most important is range. The aircraft company guarantees a specified range before the aircraft is built and tested. The penalty for failure to meet the range guarantee is severe. Conservative drag projections aren't allowed. The competition is so intense that, in the design stage, aerodynamicists are pressured to make optimistic estimates. In one briefing I attended in the early '80s, an aerodynamicist for a major airframer said that his company was willing to invest $750,000 for each count of drag reduction! Under these conditions, the importance of designing for low drag and the ability to estimate drag can hardly be overstated.

The economic viability and future survival of an aircraft manufacturer depends on minimizing aerodynamic drag (together with incorporating advances in other key technologies of structures, propulsion, and control) while maintaining good handling qualities to ensure flight safety and ride comfort. New designs that employ advanced computational aerodynamics methods are expected to produce vehicles with less drag than the aircraft in service. Designs such as Boeing 777 and Airbus A340 already take advantage of computational aerodynamics, advanced experimental methods, and years of experience. Future improvements in aerodynamic performance present tough challenges requiring both innovative concepts and the very best methodologies possible.

In the early stages of a design effort, initial drag estimates can dictate the selection of a specific configuration concept after comparison with others. The drag predictions have a huge effect on the projected configuration size and cost and thus on the selection of a specific concept and the decision to proceed with the design.

There are two other key considerations in discussing drag. First, drag cannot yet be predicted accurately with high confidence levels[2] (especially for nonconventional configuration concepts) without extensive testing. Second, no one is exactly sure of the minimum possible drag level that can be achieved for a practical configuration. To this extent, aerodynamic designers are the dreamers of the engineering profession.

Because of its importance, AGARD (the NATO Advisory Group for Aerospace Research & Development) has held numerous conferences devoted to drag and its reduction. AGARD publications include CP-124,[3] CP-264,[4] R-723,[5] and R-786.[6] These reports provide a wealth of information. An AIAA Progress Series book has also been devoted primarily to drag,[7] including chapters that discuss the history of drag prediction, typical methods currently used to predict drag, and the intricacies of drag prediction for complete configurations. The most complete compilation of drag information is available due to Hoerner.[8] Because of its importance, techical papers on drag prediction and reduction appear regularly. A good example is the survey by van Dam.[9]

3.2 Drag—Numerous Viewpoints and Basic Concepts

In discussing drag, the numerous viewpoints that people use can create confusion. Here we illustrate the challenge of defining drag from several viewpoints. This also provides an opportunity to discuss various basic drag concepts.

3.2.1 Nearfield Drag Calculation Viewpoint

Consider the distribution of forces over a surface. The forces include a pressure force and a shear stress force due to the presence of viscosity. Many people assume that drag can be accurately calculated through an accurate integration of surface forces. This approach is known as a nearfield drag calculation. However, two problems exist:

- This integration requires extreme precision.
- The results are difficult to interpret for aerodynamic analysis. Exactly where is the drag coming from? Why does it exist, and how do you reduce it?

Thus in most cases, a simple integration over the surface is not satisfactory for use in aerodynamic design. Codes have only recently begun to be fairly reliable for nearfield drag estimation and then only for certain specific types of problems. Though the best success has been achieved for airfoils, even that situation isn't perfect.

3.2.2 Fluid Mechanics Viewpoint

This viewpoint emphasizes the drag resulting from various fluid mechanics phenomena. This approach is important in conceiving a means to reduce drag. It also provides a means of computing drag contributions in a systematic manner. Thinking in terms of contributions from different physical effects in subsonic flow, a typical drag breakdown is shown in figure 3-1.

The key contributors are:

- Friction drag—caused by the action of viscosity in the boundary layer on the surface of a body; it's commonly referred to as skin friction drag.
- Form drag—caused by the net difference between pressure forces acting on the forward-facing and the rearward-facing portions of a body. Note that viscous effects are the principal source of the different pressures that are highly dependent on the shape of the body.
- Wave drag—caused by the energy radiated away from the supersonic flow regions around a body in the form of pressure waves.
- Induced drag—caused by the vorticity shed behind a lifting surface, such as the vortex wake behind a wing.

Drag	=	Friction Drag	+	Form Drag	+	Wave Drag	+	Induced Drag
		Shear force on the body surface due to action of viscosity in boundary layer		*Net difference of pressure on forward and rearward facing portions of a body*		*Resulting from energy radiated away from supersonic flow regions in the form of pressure waves*		*Due to momentum left in the fluid in the form of vorticity shed behind lifting vehicles traveling through the fluid*

Figure 3-1: A simplified drag breakdown from fluid mechanics viewpoint.

Torenbeek's book[10] offers a good discussion of drag and its estimation. That discussion makes a convincing case that the subject can be complicated!

For a highly streamlined, aerodynamically clean shape, the zero-lift drag at subsonic speeds in the absence of shock waves should be mostly due to skin friction. Pressure drag arises from regions of separated flow, which need to be avoided. R. T. Jones[11] has presented a striking figure, shown here as figure 3-2, comparing a 21-percent-thick NACA 64-421 airfoil to a circular wire of diameter equal to only about 0.006 times the airfoil thickness. It is hard to believe, but the two have the same drag at the same speed! It clearly demonstrates the importance of streamlining. Friction drag is the dominant contributor to the streamlined airfoil drag and form drag for the wire.

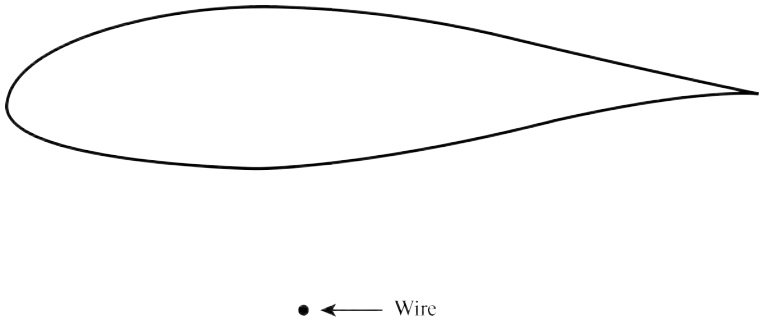


Figure 3-2: Wire and airfoil shown here have the same drag! *From R. T. Jones. Adapted by S. Madden. Fair use.*

3.2.3 Aerodynamic Design Viewpoint

This viewpoint results from combining the fluid mechanics viewpoint with more practical considerations. From the perspective of the aerodynamic design of aircraft, it proves useful to think in terms of contributions from a variety of aircraft features. This includes effects due to the requirement to trim the aircraft and due to interactions between the aerodynamics of the vehicle and both propulsion-induced flow effects and structural deformation effects. Within this context, several other considerations are identified. The basic contributions from each component must be included.

This leads to a drag analysis based on typical configuration features itemized below:

- Individual component contributions to drag
- Base drag
- Inlet drag with spillage
- Boattail drag
- Camber drag
- Trim drag
- Thrust-drag bookkeeping
- Aeroelastic effects on drag

3.2.4 Aircraft Performance Viewpoint

To calculate the performance of an airplane, it is natural to define drag as the sum of the drag at zero lift and the drag due to lift. This is the approach that leads to the typical drag polar equation:

$$C_D = C_{D_0} + \frac{C_L^2}{\pi ARE} \qquad (3\text{-}1)$$

Here each term is a function of Mach number, Reynolds number (which, in practice, is given to the performance group in terms of Mach number and altitude), and the particular geometric configuration (flap deflection, wing sweep, etc.). The drag is not precisely a quadratic function of the lift, and the value of the Oswald efficiency factor, *E*, in equation (3-1) is a function of the lift coefficient and Mach number: $E = E(C_L, M)$.

Note that uppercase *E* in equation (3-1) accounts for additional losses due to the fuselage and viscous effects. We reserve the use of lowercase *e* for span efficiency factor, which is solely a function of the spanload estimated using inviscid flow theories, such as the lifting-line theory. This notation is the most prevalent in use in the US aircraft industry. However, other notations are frequently employed, and care must be taken when reading the literature to make sure that you understand the notation used. The drag also depends on the throttle setting, but that effect is usually included in the thrust table.

There is another drag polar approximation that is seen often. This approximation is more commonly used by aerodynamic designers trying to understand wing performance. It is used to consider the effect of wing camber and twist, which causes the drag polar to be displaced "upward," becoming asymmetrical about the $C_L = 0$ axis, as shown in figure 3-3. It is given as equation (3-2) below.

$$C_D = C_{D_0} + \Delta C_{D_m} + K(C_L - C_{L_m})^2 \qquad (3\text{-}2)$$

In taking into account the effect of camber and twist on displacing, or "shifting," the polar, the term ΔC_{Dm} represents a penalty associated with using twist and camber to achieve good performance at the design lift coefficient. This equation is for a fixed geometry. Note that the effect of ΔC_{Dm} is exaggerated for emphasis in figure 3-3. The value of *K* defines the shape of the polar. C_{D0} represents the minimum drag of the configuration *without camber and twist*. The values of ΔC_{Dm} and C_{Lm} are functions of the design lift coefficient. Sometimes novice aerodynamicists fail to include ΔC_{Dm} properly and obtain incorrect values of *E* when evaluating published drag polars. This type of polar shape is discussed in more detail later in this chapter. Advanced aircraft concepts such as the X-29, as well as the F-16 and F-18, minimize this penalty by defining a device schedule to maximize performance across a broad range of lift coefficients.

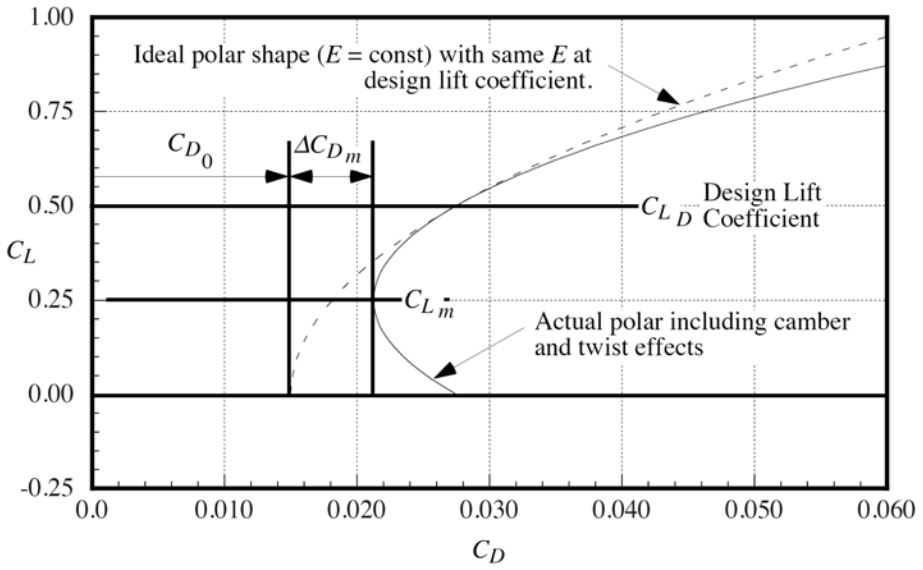


Figure 3-3: A comparison of ideal vs. actual drag polar shapes. From W. H. Mason. Adapted by S. Madden.

3.2.5 Categorization of Drag Concepts

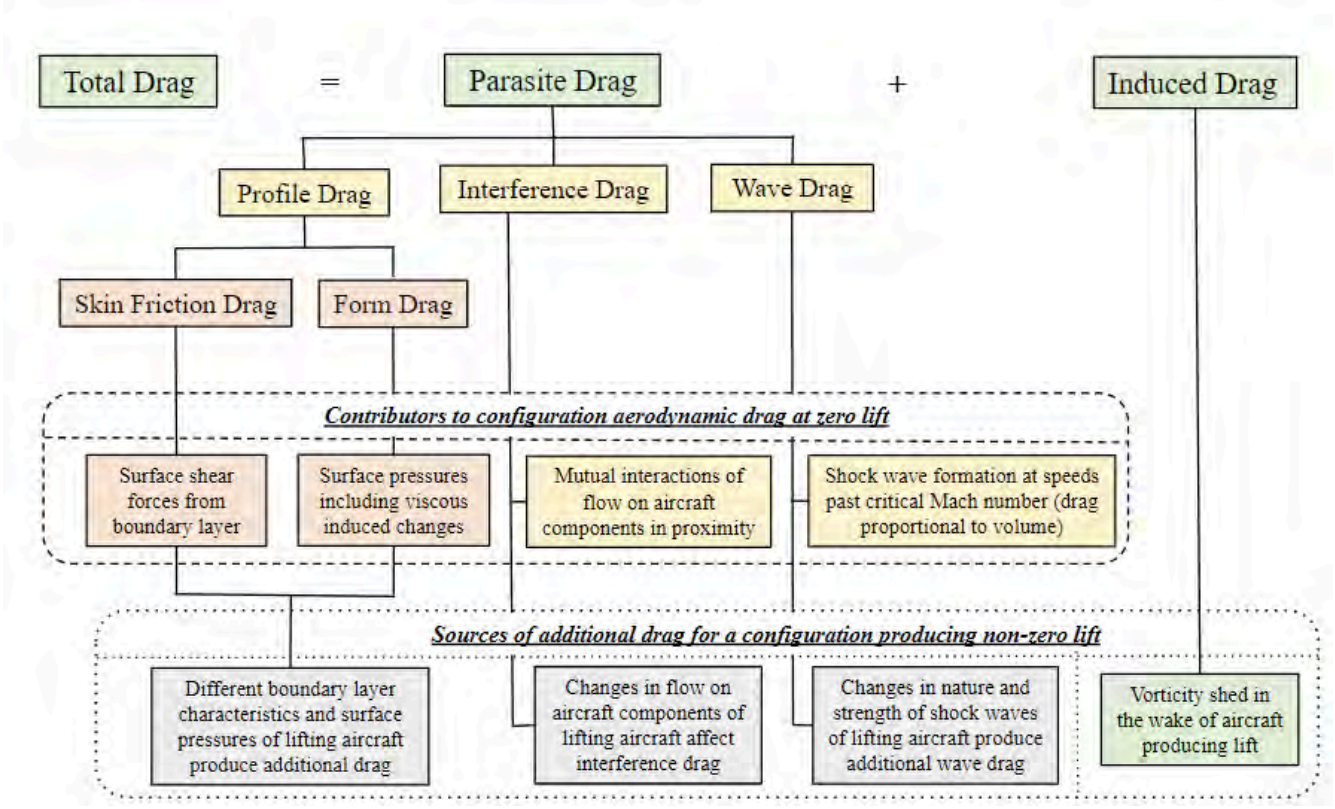


Figure 3-4: A basic categorization of drag concepts for configuration aerodynamics. From P. Raj.

It is apparent that the types of viewpoints outlined above may be confusing, and sometimes they get in the way of technical discussions. To facilitate further discussion in the context of configuration aerodynamics, the chart in figure 3-4 provides a basic categorization of drag concepts. This aerodynamic configuration-focused approach to drag is not covered in fluid mechanics–oriented aerodynamics texts, but it is described in aircraft design books. Two good reference books are by Whitford[12] and by Huenecke.[13] An approach to the evaluation of drag performance, including the efficiency achieved on actual aircraft, was presented by Haines.[14]

We next discuss refinements to several of these concepts in more detail. However, the most important overview of aerodynamic drag for design has been given by Küchemann[15] and should be studied for a complete understanding of drag concepts.

3.2.5.1 A Fluid Mechanics Refinement: *Transonic Wave Drag*

The simplified picture of drag presented in figure 3-1 may suggest that wave drag appears suddenly at supersonic speeds. A more refined examination shows that wave drag arises at subsonic speeds when the flow accelerates locally to supersonic speeds and then returns to subsonic speed through a shock wave. This leads to the presence of wave drag at subsonic (actually, by definition, transonic) freestream speeds, as shown in figure 3-4. This initial drag increase, known as drag rise, is followed by a rapid increase in drag and is an important consideration in the design of wings and airfoils. The Mach number at which the rapid drag increase occurs is known as the drag divergence Mach number, M_{DD}. The increase in drag occurs directly because of the wave drag associated with the presence of shock waves. However, the drag also increases because the boundary layer thickness increases due to the sudden pressure rise on the surface due to the shock wave, which leads to increased profile drag. Lynch[16] has estimated that, at drag divergence, the additional transonic drag is approximately evenly divided between the explicit shock drag and the shock-induced additional profile drag.

Several definitions of the drag rise Mach number are commonly used. The specific definition is usually not important because the drag rises very rapidly at drag divergence and different definitions all result in similar values of M_{DD}.

One standard definition of M_{DD} is the Mach number where

$$\left.\frac{dC_D}{dM}\right|_{C_L=\text{const.}} = 0.1. \qquad (3\text{-}3)$$

Another definition of M_{DD} is the Mach number at which

$$\Delta C_D = 0.0020 \text{ from the subsonic value.} \qquad (3\text{-}4)$$

Commercial transports fly at or close to M_{DD}, and the drag divergence Mach number is a key part of the performance guarantee.

Figure 3.5 (data from Shevell[17]) illustrates the transonic wave drag, a fluid mechanics refinement, as additional drag, ΔC_{Dcomp}, due to compressibility as Mach number increases. Note that the M_{DD} values corresponding the criteria in equations (3-3) and (3-4) are quite close. Together with the definitions associated with the drag rise, this figure also illustrates a common characteristic known as drag creep, which occurs with many transonic designs. Drag creep is characterized by a slow rise in drag with Mach number increase or a small and roughly constant positive slope in the drag versus Mach curve starting well before M_{DD}. This drag increase is attributed to the increasing strength of the forward relatively benign shocks and to the gradual thickening of the boundary layer due to the shocks and the higher adverse pressure gradient from increasing C_p.[18]

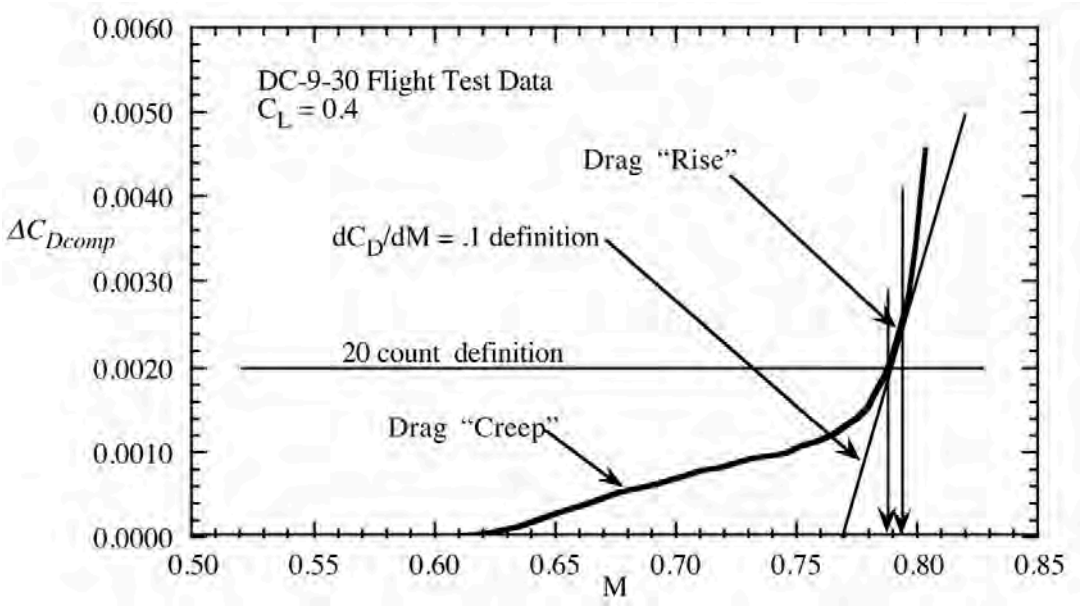


Figure 3-5: Details of wave drag increases at transonic speeds.

3.2.5.2 An Aerodynamics/Flight Mechanics Refinement: *Trim Drag*

A source of drag not directly related to fluid mechanics arises from the need to trim the vehicle (C_m = 0 about the center of gravity) for steady flight. This requirement can lead to control surface deflections that increase (or decrease) the drag. It can be especially important for supersonic aircraft because of the shift in the aerodynamic center location with changing Mach numbers. Other cases with significant trim drag may include configurations with variable wing sweep and the use of airfoils with large values of the zero-lift pitching moment about their aerodynamic center. Section 3.5.6 contains more details about trim drag.

3.2.5.3 An Aeropropulsion Integration Refinement: *Thrust-Drag Bookkeeping*

To determine aircraft performance, the key value is actually not drag but the balance between thrust and drag. The drag of the airframe is affected by the operation of the propulsion system, and care must be taken to understand and define these interactions. The amount of air used by the engine defines the size of the streamtube entering the inlet. If all the air in front of the inlet does not enter the inlet, a spillage drag will result. Similarly, the boattail drag over the external portion of the nozzle will depend on the nozzle setting in the case of engines with afterburners and the pressure of the nozzle flow. The definition of a system to properly account for aeropropulsion interactions on the specification of thrust minus drag values is known as thrust-drag bookkeeping. Since thrust is usually provided by the propulsion group, and drag is provided by the aerodynamics group, significant errors in the estimation of aircraft performance have occurred when the necessary coordination and adjustments were not made. The details of this procedure are described in the article by Rooney.[19]

Generally, the aerodynamics group provides the performance group with a reference drag polar, and all thrust-dependent corrections to the drag polar are accounted for by making adjustments to the thrust values. This is done because it is natural to establish a performance calculation procedure using this approach. The precise details are not important as long as everyone involved in the performance prediction agrees to a specific approach. Usually this requires a specific document defining thrust-drag bookkeeping for each aircraft project.

3.2.5.4 An Aerostructural Interaction Refinement: *Aeroelastic Effects on Drag*

This issue is not strictly a drag consideration, but it can contribute to the drag if it is not addressed. Aircraft structures deform due to air loads. If the design is centered around a single design point, the aerodynamic shape at the design point can be defined, and the structural analysts will adjust for structural deformation, specifying a "jig shape" that will produce the desired aerodynamic shape at the design point and loading. This is harder to do if there are multiple design points. Deformation of wind tunnel models should also be considered when estimating drag.

3.3 Theoretical Analysis of Drag Components Based on Momentum Balance

In this section, we discuss the most accurate estimation of drag on a body by considering the overall momentum balance on a control volume surface well away from the body—a farfield calculation. This approach is particularly useful when our prediction methods are not exact. The results are also much less sensitive compared to the nearfield pressure integration approach, which requires detailed calculations of surface pressure and then the integration of the pressures over the surface to obtain the drag. It also allows the components to be found separately.

3.3.1 Farfield Drag Analysis

The farfield analysis makes use of the momentum theorem. References containing good derivations are Ashley and Landahl,[20] sections 1.6, 6.6, 7.3, and 9.2, and Heaslet and Lomax.[21]

For a surface *S* that encloses the volume containing the body, the force can be determined by balancing the momentum across *S*:

$$\mathbf{F} = -\oiint_S (p - p_\infty) d\mathbf{S} - \oiint_S \rho \mathbf{q} \left[(\mathbf{V}_\infty + \mathbf{q}) \cdot d\mathbf{S} \right] \qquad (3\text{-}5)$$

where **q** is the disturbance velocity vector,

$$\mathbf{V} = \mathbf{V}_\infty + \mathbf{q} \qquad (3\text{-}6)$$

Define a control volume for use in equation (3-5), as shown in figure 3-6.

Consider flows far enough away from the body such that linearized flow relations are valid. Use the small disturbance relations:

$$\rho \cong \rho_\infty \left(1 - M_\infty \frac{u}{V_\infty} \right) \qquad (3\text{-}7)$$

and

$$(p - p_\infty) \cong -\rho_\infty \left[V_\infty u + \frac{1}{2} \left(u^2 + v^2 + w^2 \right) \right] + \frac{1}{2} \rho_\infty M_\infty^2 u^2 \qquad (3\text{-}8)$$

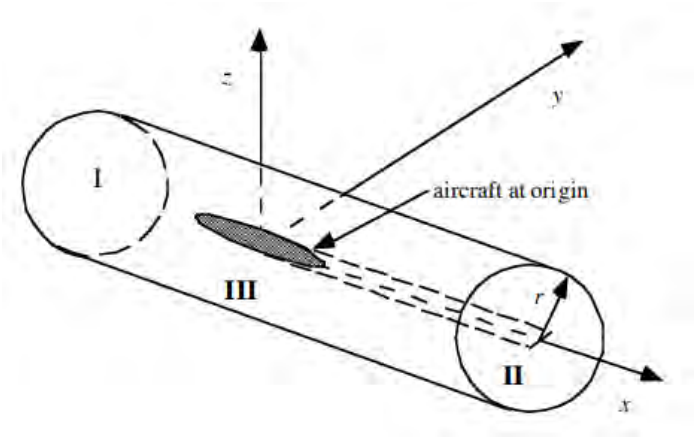


Figure 3-6: Control volume for drag evaluation using farfield analysis.

Now, consider the drag component of equation (3-5), making use of equation (3-7) and equation (3-8):

$$D = \frac{1}{2}\rho_\infty \iint_{I+II} \left[\left(M_\infty^2 - 1\right)u^2 + v^2 + w^2\right] dydz - \rho_\infty \iint_{III} uv_r r d\theta dx \qquad (3\text{-}9)$$

The radial component is v_r,

$$v_r^2 = v^2 + w^2,$$

and

$$r^2 = x^2 + y^2.$$

Considering the control volume shown in figure 3-6, place **I** and **II** far upstream and downstream, respectively, and make *r* large. Then, the integral over **I** is zero as $x \to -\infty$. The integral over **II** as $x \to \infty$, corresponds to the so-called Trefftz plane (see section 3.3.2). The integral over **III** is the wave drag integral, which is zero for subsonic flow and when any embedded shock waves do not reach **III**.

3.3.2 Lift-Induced Drag: The Trefftz plane

Let us first outline the basic concept of the Trefftz Plane (named after a German mathematician and aerodynamicist):

1. Far downstream, the motion produced by the trailing vortices becomes 2D in the *y*-*z* plane (no induced velocity in the *x*-direction).
2. For a wing moving at a speed U_∞ through the fluid at rest, an amount of mechanical work $D_i U_\infty$ is done on the fluid per unit of time. Since the fluid is nondissipative (potential flow), it can store energy in kinetic form only. Therefore, the work $D_i U_\infty$ must show up as the value of kinetic energy contained in a length U_∞ of the distant wake.
3. The vortices in the trailing vortex system far downstream can be used to find the induced drag.

Consider the integral over **II** in figure 3-6. This is the first integral in equation (3-9), the induced drag integral:

$$D_i = \frac{1}{2}\rho_\infty \int_{-\infty}^{\infty}\int_{-\infty}^{\infty} \left[\left(M_\infty^2 - 1\right)u^2 + v^2 + w^2\right] dydz \qquad (3\text{-}10)$$

Note that many supersonic aerodynamicists call this the vortex drag, D_v, since it is associated with the trailing vortex system. However, it is in fact the induced drag. The term vortex drag is confusing in view of the current use of the term "vortex" to denote effects associated with other vortex flow effects. Far downstream, at $u \to 0$, we are left with the v- and w-components of velocity induced by the trailing vortex system. The trailing vortex sheet can be thought of as legs of a horseshoe vortex. Thus the integral becomes

$$D_i = \frac{1}{2}\rho_\infty \int_{-\infty}^{\infty}\int_{-\infty}^{\infty} \left(v^2 + w^2\right) dydz \qquad (3\text{-}11)$$

and relates the induced drag to the kinetic energy of the trailing vortex system.

Now, the flow is governed downstream by the Prandtl–Glauert equation (even if the flow at the vehicle has large disturbances, the perturbations decay downstream):

$$\left(1 - M_\infty^2\right)\phi_{xx} + \phi_{yy} + \phi_{zz} = 0 \qquad (3\text{-}12)$$

As $x \to \infty$, then $u = 0$ and $u_x = \phi_{xx} = 0$. As a result, the governing equation for the disturbance velocities is Laplace's equation for the crossflow velocity:

$$\phi_{yy} + \phi_{zz} = 0 \qquad (3\text{-}13)$$

An interesting result arises here. The induced drag is explicitly independent of Mach number! The analysis is valid for subsonic, transonic, and supersonic flows. The Mach number only enters the problem in an indirect manner through the boundary conditions, as we will see.

We now use Green's theorem to convert the area integral in equation (3-11) to a contour integral. Applying the theorem to the drag integral, we arrive at equation (3-14).

$$\iint_{II} \left(v^2 + w^2\right) dS = -\int_c \phi \frac{\partial \phi}{\partial n} dc \qquad (3\text{-}14)$$

This is a general relation that converts the integral over the entire crossplane into an integral along the contour. It applies to multiple lifting surfaces. To illustrate the application of the integral to the determination of the induced drag, we consider the special case of a planar lifting surface. Here the contour integral is taken over the surface shown in figure 3-7, where the trace of the trailing vortices shed from the wing are contained in the slit between $-b/2$ and $b/2$.

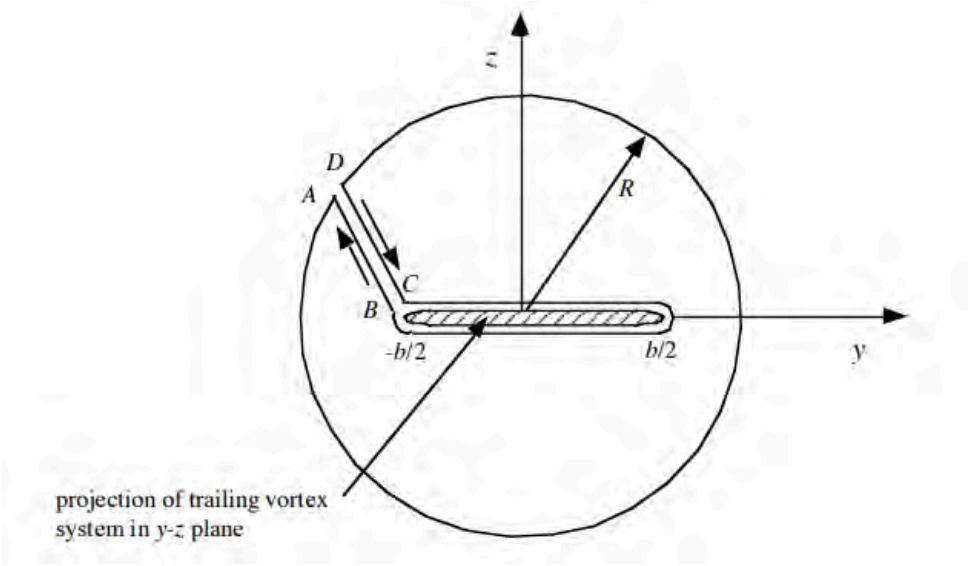


Figure 3-7: Contour integral path for induced drag analysis in the Trefftz plane. From W. H. Mason. Adapted by S. Madden.

In this Trefftz plane, the integral vanishes around the outside contour as $R \to \infty$ and the integrals along *AB* and *CD* cancel. Thus, the only contribution comes from the slit containing the trace of vorticity shed from the wing. The value of ϕ is equal and opposite above and below the vortex sheet. On the sheet, $\partial\phi/\partial n = w$, the downwash velocity.

Thus the integral for a single flat lifting surface can be rewritten as

$$D_i = -\frac{1}{2}\rho_\infty \int_{-b/2}^{b/2} (\Delta\phi)_{x=\infty} w_{x=\infty} dy \qquad (3\text{-}15)$$

where *w* is the velocity induced by the trailing vortex system. The jump in the potential on the slit at infinity can be related to the jump in potential at the trailing edge. To see this, first consider the jump in the potential at the trailing edge. Recall that the circulation is given by the contour integral:

$$\Gamma = \oint \mathbf{V} \cdot d\mathbf{s} \qquad (3\text{-}16)$$

For an airfoil, we illustrate the concept by considering a small disturbance–based argument. However, the results hold regardless of the small disturbance–based illustration. Consider the airfoil given in figure 3-8.

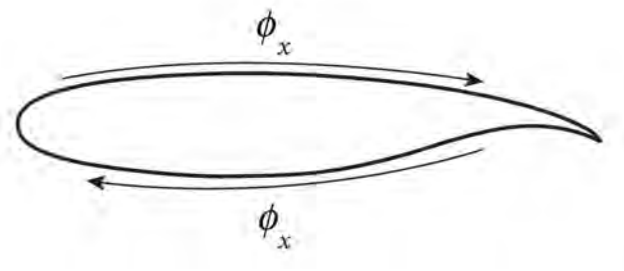


Figure 3-8: Integration path around an airfoil. From W. H. Mason. Adapted by S. Madden.

The dominant velocity is in the *x*-direction, $u = \phi_x$, and the integral around the airfoil, equation (3-16), can be seen to be essentially:

$$\begin{aligned}
\Gamma &= \int_{TE_{\text{lower}}}^{LE} \phi_x dx + \int_{LE}^{TE_{upper}} \phi_x dx \\
&= \phi|_{TE_{\text{lower}}}^{LE} + \phi|_{LE}^{TE_{upper}} \\
&= \phi_{LE} - \phi_{TE_{\text{lower}}} + \phi_{TE_{upper}} - \phi_{LE} \\
&= \phi_{TE_{\text{upper}}} - \phi_{TE_{\text{lower}}} \\
&= \Delta\phi_{TE}
\end{aligned} \qquad (3\text{-}17)$$

The value of the potential jump at infinity can be found by realizing that the circulation is created by the wing, and any increase in the contour of integration will produce the same result. Therefore,

$$\Delta\phi_{x=\infty} = \Delta\phi_{TE} = \Gamma(y\,). \qquad (3\text{-}18)$$

Next, the induced velocity required in equation (3-15) is found from the distribution of vorticity in the trailing vortex sheet by considering the slit to be a sheet of vorticity and using the velocity induced by a distribution of vorticity from the following integral, which is a form of the so-called thin airfoil theory integral shown in equation (3-19).

$$w_{x=\infty}(y) = \frac{1}{2\pi} \int_{-b/2}^{b/2} \frac{\gamma(\eta)}{y-\eta} d\eta \qquad (3\text{-}19)$$

To complete the derivation, we have to connect the distribution of vorticity in the trailing vortex sheet to the circulation on the wing. To do this, consider the sketch of the circulation distribution given in figure 3-9.

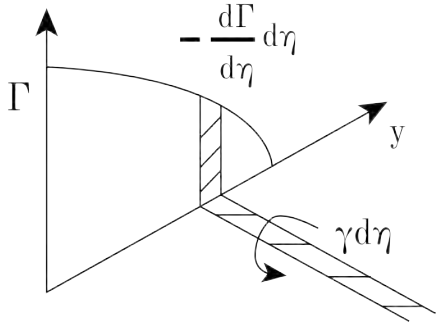


Figure 3-9: Relation between circulation change on the wing and vorticity in the wake. From W. H. Mason. Adapted by S. Madden.

As the circulation on the wing, Γ, changes across the span, circulation is conserved by shedding an amount equal to the local change into the wake. Thus, the trailing vorticity strength is related to the change in circulation on the wing by

$$\gamma(\eta) = -d\Gamma/d\mathrm{y}. \qquad (3\text{-}20)$$

Substituting this into equation (3-19), we obtain

$$w_{x=\infty} = -\frac{1}{2\pi}\int_{-b/2}^{b/2} \frac{d\Gamma/dy}{y-\eta}d\eta. \qquad (3\text{-}21)$$

Substitute equations (3-18) and (3-21) into equation (3-15) and integrate by parts using the conditions that Γ(-*b*/2) = Γ(*b*/2) = 0 (which simply states that the load distribution drops to zero at the tip). This results in equation (3-22).

$$D_i = -\frac{\rho_\infty}{4\pi}\int_{-b/2}^{b/2}\int_{-b/2}^{b/2} \frac{d\Gamma\left(y_1\right)}{dy}\frac{d\Gamma(y_2)}{dy}\ln|y_1-y_2|dy_1dy_2 \qquad (3\text{-}22)$$

Equation (3-22) shows how the spanload distribution is related to the induced drag. Because of the double integral, we can get the total induced drag, but we have lost the ability to get detailed distributions of the induced drag on the body. This is the price we pay for the use of the farfield analysis.

Finally, this result shows that the induced drag is a function of the Γ distribution (spanload) alone. The only impact made by the Mach number is its effect on the circulation distribution on the wing. We will show later how equation (3-22) can be used to obtain the classical result that an elliptic spanload minimizes the induced drag for a planar wing with span *b*.

3.3.3 Supersonic Wave Drag: The Farfield Wave Drag Integral

Consider the integral over **III** in figure 3-6. This is the farfield wave drag integral. The integral corresponds to the last term on the right-hand side of equation (3-9) and can be written as

$$D_w = \lim_{r\to\infty}\left(-\rho_\infty r\int_0^{2\pi} d\theta\int_{-\infty}^{+\infty} uv_r dx\right). \qquad (3\text{-}23)$$

If $u,v_r \to 0$ as $r \to \infty$, then $D_w = 0$. Thus, when the flow is subsonic, there is no wave drag, as we already know. However, if the flow is supersonic and shock waves are generated, the integral is not zero. This integral can be calculated for any solution of the flow field. In this analysis, we assume that the flow is governed by the Prandtl–Glauert equation. Equation (2-135) is reproduced here from Chapter 2 for convenience.

$$\left(1 - M_\infty^2\right)\phi_{xx} + \phi_{yy} + \phi_{zz} = 0$$

This equation implies small disturbance flow. This is valid if the vehicle is highly streamlined, as any supersonic vehicle must be. However, this is not a significant restriction because, far from the body causing the disturbance, this equation can model flows from any vehicle.

To obtain an expression for ϕ that can be used to calculate the farfield integral, assume that the body can be represented by a distribution of sources on the x-axis (making the aircraft look very "slender" from far away). To illustrate the analysis, assume that the body is axisymmetric. Recall that there are different forms for the subsonic and supersonic sources:

$$\phi = \underbrace{-\frac{1}{4\pi}\frac{1}{\sqrt{x^2+\beta^2 r^2}}}_{\substack{\text{subsonic source} \\ \downarrow \\ \phi \to 0 \quad \text{as} \quad r \to \infty}}, \qquad \phi = \underbrace{-\frac{1}{2\pi}\frac{1}{\sqrt{x^2-\beta^2 r^2}}}_{\substack{\text{supersonic source} \\ \downarrow \\ \phi \to 0 \quad \text{as} \quad r \to \infty \\ \text{except as} \quad r \to \frac{x}{\beta}}} \qquad (3\text{-}24)$$

This means that the integral will have a contribution along the Mach wave regardless of how far away the outer control volume is taken. Figure 3-10 illustrates this effect. The resulting force is exactly what is expected in regards to the shock wave contribution to drag—the wave drag.

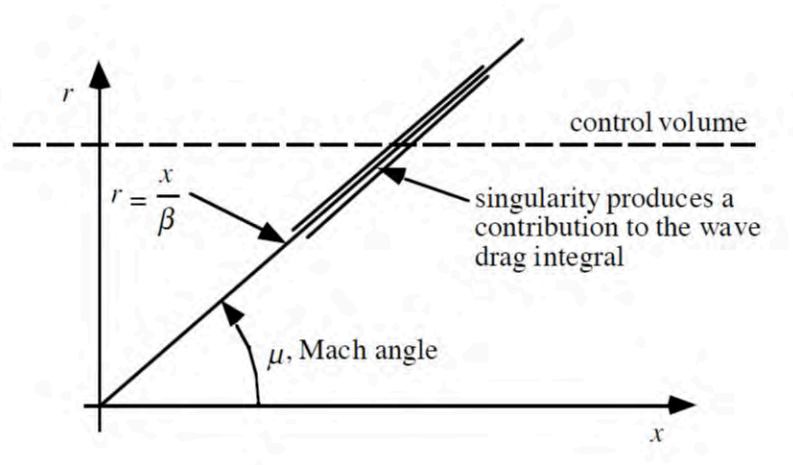


Figure 3-10: Behavior of disturbances along Mach lines in the farfield.

The farfield behavior of the source singularity given in equation (3-24) can be used to obtain an expression for the farfield integral in terms of geometric properties of the aircraft. A complete analysis is given in Ashley and Landahl,[22] sections 1.6, 6.6, 7.3, and 9.2, and in Liepmann and Roshko.[23] The key connection is the assumption relating the supersonic source strength and aircraft geometry. The approximate boundary conditions on the surface equate the supersonic source strength to longitudinal change of cross-sectional area: $\sigma(x) = S'(x)$. One required assumption is that the cross-sectional area distribution, $S(x)$, satisfies $S'(0) = S'(l) = 0$. After some algebra, the following wave drag integral is obtained:

$$\bar{D}(\theta)_w = -\frac{\rho_\infty U_\infty^2}{4\pi}\int_0^l \int_0^l S''(x_1) S''(x_2) \ln|x_1 - x_2| dx_1 dx_2 \qquad (3\text{-}25)$$

Note that it is in the same mathematical form as the induced drag integral in equation (3-22). While the spanload distribution is the key contributor to the induced drag, longitudinal variation of the cross-sectional area distribution controls the volumetric wave drag.

The standard method for evaluation of this integral is available in a program known as the Harris wave drag program.[24] This program determines the cross-sectional area distribution of the aircraft and then evaluates the integral numerically. Note that as given above, the Mach number doesn't appear explicitly. A refined analysis[25] for bodies that aren't extremely slender extends this approach by taking slices, or Mach cuts, of the area through the body at the Mach angle. This is how the Mach number dependence enters the analysis. Finally, for nonaxisymmetric bodies, the area associated with the Mach cuts changes for each angle around the circumferential integral for the cylindrical integration over eegion **III** in figure 3-6. Thus the area distribution must be computed for each angle. The total wave drag is then found from

$$D_w = \frac{1}{2\pi}\int_0^{2\pi} \bar{D}_w(\theta)d\theta. \qquad (3\text{-}26)$$

Examples of the results obtained using this computational method are given in section 3.4.5 and in Chapter 9.

3.4 Important Aspects of Lift-Induced Drag

To establish a technical basis for understanding the drag due to lift of wings, singly and in combination, four important aspects must be discussed: (a) planar wing induced drag in section 3.4.1; (b) nonplanar wing induced drag in section 3.4.2; (c) induced drag of multiple lifting surfaces and Munk's Stagger Theorem in section 3.4.3; and (d) leading edge suction concept in section 3.4.4 that helps us understand additional induced drag due to span efficiency factor "*e*" (see section 3.2.4) being less than 1, and typical variation of E. In addition, supersonic wave drag is discussed in section 3.4.5 where one of the most important concepts in wave drag is addressed: Whitcomb's Area Rule.

3.4.1 Induced Drag—Planar Surfaces

The three-dimensional flow field over a lifting surface (for which a horseshoe vortex system is a very good conceptual model) produces a drag, even if the flow is inviscid. (Before proceeding, it might be worthwhile for the reader to review the Trefftz plane analysis in section 3.3.2.) At the wing, the induced drag can be visualized as an effective change in the angle of attack along the wing span induced by the trailing vortex system. This induced change of angle results in a local inclination of the force vector relative to the freestream, and thus it produces an "induced" drag. It is one part of the total drag due to lift, and its form typically arises naturally, as shown in equation (3-27) below.

$$C_{D_i} = \frac{C_L^2}{\pi ARe} \qquad (3\text{-}27)$$

The small *e* in this equation is known as the span efficiency. In this case, the induced drag is assumed to be *only* a function of the spanload. Additional losses due to the fuselage and viscous effects are included when a capital *E*, known as Oswald's *E*, is used in this expression, as mentioned in section 3.2.4. It is worth reiterating that this notation is the most prevalent in use in the US aircraft industry. However, other notations are frequently employed, and care must be taken when reading the literature to make sure that you understand the notation used.

When designing and evaluating wings, the question becomes *What is* e, *and how large can we make it?* The "conventional wisdom" is that, for a planar surface, $e_{max} = 1$, and for a nonplanar surface or a combination of lifting surfaces, $e_{max} > 1$, where the aspect ratio, AR, is based on the projected span of the wing with the largest span.* However, studies searching for higher *e*'s abound. The quest of the aerodynamicist is to find a fundamental way to increase aerodynamic efficiency.

In the 1970s, increased aerodynamic efficiency, *e*, was sought by exploiting nonplanar surface concepts such as winglets and canard configurations. Indeed, these concepts are now commonly employed on aircraft configurations in service. In the 1980s, a great deal of attention was devoted to the use of advanced wingtip shapes on nominally planar configurations. But it is not clear that the advanced wingtips resulted in theoretical *e*'s above unity. However, in practice, these improved tip shapes help clean up the flow field at the wingtip, reducing viscous effects and resulting in a reduction in drag. Kroo conducted an excellent survey of induced drag and reduction prospects in the *Annual Review of Fluid Mechanics,*[26] which is electronically available for no charge to Virginia Tech students through the library website.

* However, *e* is not *too* much bigger than unity for practical configurations.

In section 3.3, we derived the expression for the drag due to the trailing vortex system in the Trefftz plane. Here we explain the physical basis of the idea of the Trefftz plane following sections 1.6, 6.6, 7.3, and 9.2 in Ashley and Landahl.[27] An alternate and valuable procedure has been described by Sears.[28]

Here we repeat the expression for induced drag, equation (3-22), for convenience:

$$D_i = -\frac{\rho_\infty}{4\pi}\int_{-b/2}^{b/2}\int_{-b/2}^{b/2}\frac{d\Gamma\left(y_1\right)}{dy}\frac{d\Gamma(y_2)}{dy}\ln\left|y_1 - y_2\right|dy_1 dy_2.$$

The usual means of evaluating the integral is to represent Γ as a Fourier series, as shown in equation (3-28).

$$\Gamma = U_\infty b\sum_{n=1}^{\infty}A_n \sin n\theta \qquad (3\text{-}28)$$

The unknown values of the A_n's are found from a Fourier series analysis, where Γ(*y*) is known from an analysis of the configuration. Panel or vortex lattice methods can be used to find Γ(*y*). (See Chapter 5 for a brief description of vortex lattice methods.) Integration of the drag integral using equation (3-28) results in

$$D_i = \frac{\pi\rho_\infty U_\infty^2 b^2}{8}\sum_{n=1}^{\infty}nA_n^2 \qquad (3\text{-}29)$$

and

$$L = \frac{\pi}{4}\rho_\infty U_\infty^2 b^2 A_1 \qquad (3\text{-}30)$$

which are the classical results frequently derived using lifting-line theory. Note that the lift depends only on the first term of the series, whereas all of the components contribute to the drag. Putting the expressions for lift and drag into coefficient form and then replacing the A_1 term in the drag integral by its definition in terms of the lift coefficient leads to the classical result given above by equation (3-27), which is reproduced here:

$$C_{D_i} = \frac{C_L^2}{\pi ARe}$$

In this case,

$$e = \frac{1}{\left[1 + \sum_{n=2}^{\infty} n\left(\frac{A_n}{A_1}\right)^2\right]}. \qquad (3\text{-}31)$$

It is important to understand that the contribution of induced drag to the drag due to lift assumes that the airfoil sections in the wing are operating perfectly, as if in a two-dimensional potential flow that has been reoriented relative to the freestream velocity at the angle associated with the effects of the trailing vortex system. Wings can be designed to operate close to these conditions. It is also noteworthy that, if the wing is twisted and the shape of the spanload changes as the lift changes, then e is not a constant, independent of the lift coefficient.

We conclude from this discussion:

1. Regardless of the wing planform(s), induced drag is a function of circulation distribution alone, independent of Mach number except in the manner which Mach number influences the circulation distribution (a minor effect in subsonic and transonic flows).
2. Given Γ, e can be determined by finding the A_n's of the Fourier series for the simple planar wing case. Other methods are required for nonplanar systems.
3. Extra drag due to the airfoil's inability to create lift ideally must be added over and above the induced drag. Our analysis here assumes that the airfoils operate perfectly in a two-dimensional sense; there is no drag due to lift in two-dimensional flow.

3.4.2 Nonplanar Lifting Surfaces Including Winglets

The expressions given in section 3.4.1 show that $e_{max} = 1$ for a planar lifting surface. However, if the slit representing the trailing vortex system is not a simple flat surface and C_{Di} is based on the projected span, a nonplanar or multiple lifting surface system can result in values of $e > 1$. In this section, we look at the case of nonplanar wings. First, we consider the case of a wing with dihedral. The effect of dihedral on the maximum e is given in figure 3-11, which is recreated from a figure in one of my papers.[29] The symbols (labeled *Numerical Result, Ref. 6*) in the figure are numerical results by Lamar[30] and the curve (labeled *Analytical Result, Ref. 23*) is by Letcher.[31] The figure shows that modest amounts of dihedral lead to modest increases in e_{max} using the projected wingspan. If the running length were used instead of the projected span, the e would not exceed one.

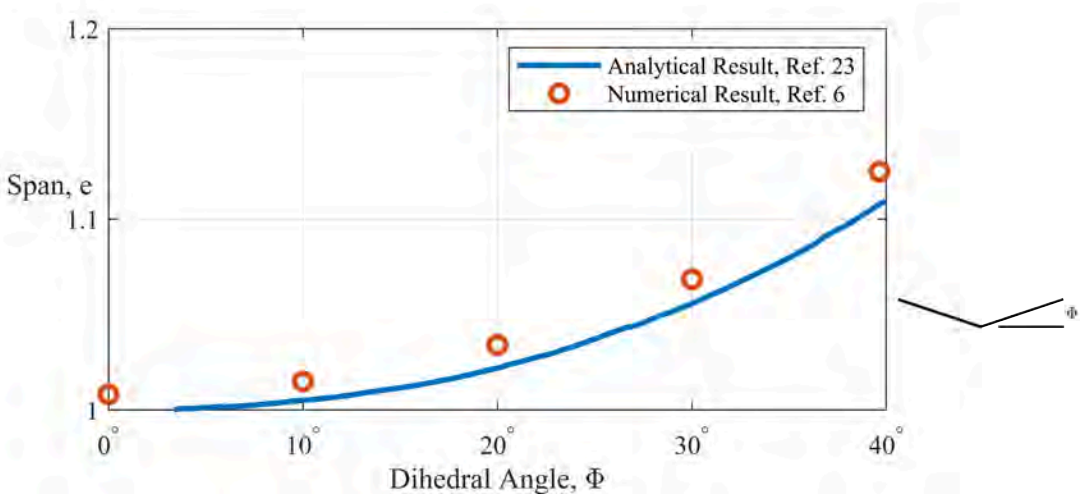


Figure 3-11: Apparent span e of a V-wing configuration. *From W. H. Mason. "Wing-Canard Aerodynamics at Transonic Speeds—Fundamental Considerations on Minimum Drag Spanloads." Adapted by S. Madden. Fair use.*

The other case of considerable interest is the use of winglets to reduce induced drag. Figure 3-12 shows the *e* that can be expected from a winglet that obtains its maximum performance. This figure is recreated from one in a paper by Feifel.[32] The figure shows good agreement between VLM estimates using 25 and 50 spanwise panels with the curve labeled *Exact Solution (Lundry Ref. 8)* from Lundry[33]

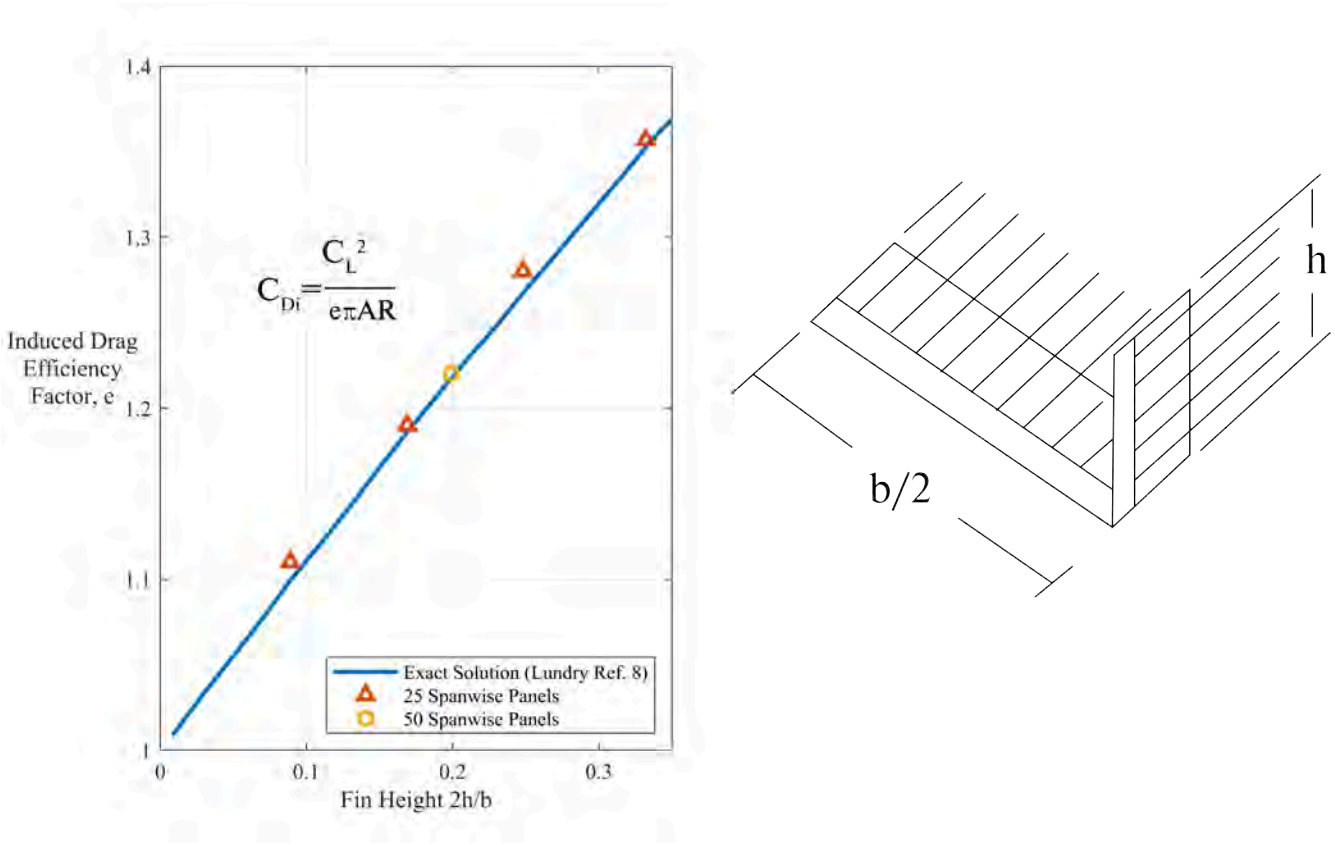


Figure 3-12: The effect of winglet fin height on the induced drag efficiency factor, e. From W. M. Feigel. NASA. Public domain. Adapted by S. Madden.

3.4.3 Multiple Lifting Surfaces and Munk's Stagger Theorem

Biplane theory can be used to investigate the multiple lifting surface case. Thwaites[34] provides a detailed discussion. Figure 3-13, adapted from Thwaites, shows the potential benefit of biplanes obtaining performance improvements in *e* for a given span using two lifting surfaces of spans b_1 and b_2 separated by height *h*. The parameter κ is actually 1/*e*. The figure also contains the associated distribution of lift between the two lifting surfaces using the parameter λ, which is the lift on the smaller span surface as a fraction of the total lift. Two limiting cases can be considered. If the lifting elements are in the same plane, then the sum of the spanloads should be elliptic for minimum drag. If the elements are vertically separated by a large distance, then each component individually needs an elliptic spanload to obtain minimum induced drag.

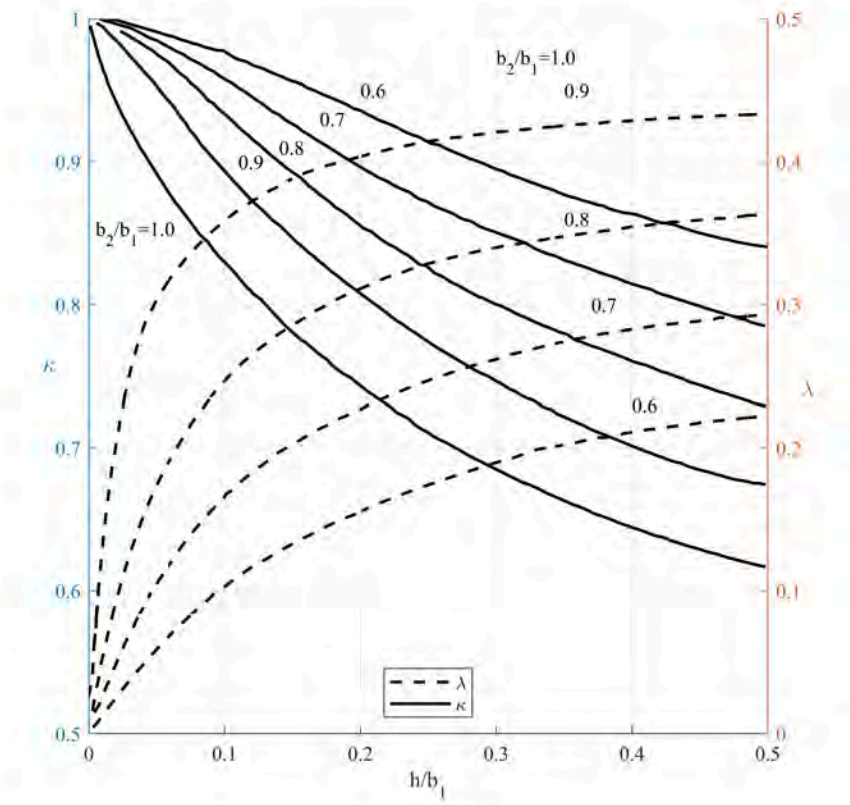


Figure 3-13: Induced drag and lift split for two lifting surface configurations. *From B. Thwaite. Adapted by S. Madden. Fair use.*

An important result in the consideration of multiple lifting surfaces is Munk's stagger theorem. You can find a proof of the theorem in Milne-Thomson.[35] The theorem states that the total induced drag of a multisurface system does not change when the elements of the system are translated parallel to the direction of the flow (as illustrated in the sketch in figure 3-14) *provided that* the circulation distributions on the elements are left unchanged. Thus the drag depends only on the projection of the system in the Trefftz plane. This means that, given the circulation distributions, the Trefftz plane analysis can be used to find the induced drag. This is consistent with the analysis given for the Trefftz plane above and reinforces the concept of using the farfield analysis to determine the induced drag. Naturally, to maintain the circulation distribution of the elements when they are repositioned, their geometric incidence and twist or camber have to be changed.

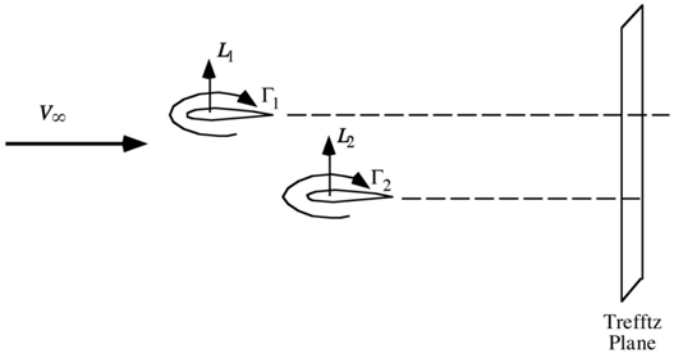


Figure 3-14: Example of Munk's stagger theorem.

We complete this section by presenting a classic table showing the types of values of *e* that can be obtained for a variety of multiple and nonplanar lifting surfaces. Figure 3.15 shows the Trefftz plane trace of the surfaces and the associated values of *e*.[36] In each case, the wing(s) will have to be twisted and cambered to achieve the spanload distribution required to achieve the *e* given in the figure. In terms of analytic estimation techniques for unusual configurations, the NASA CRs by John deYoung[37,38] should be studied. Numerical methods for computing span *e*'s and the associated spanloads are described in section 3.5.3, where several different codes are available for the calculation.

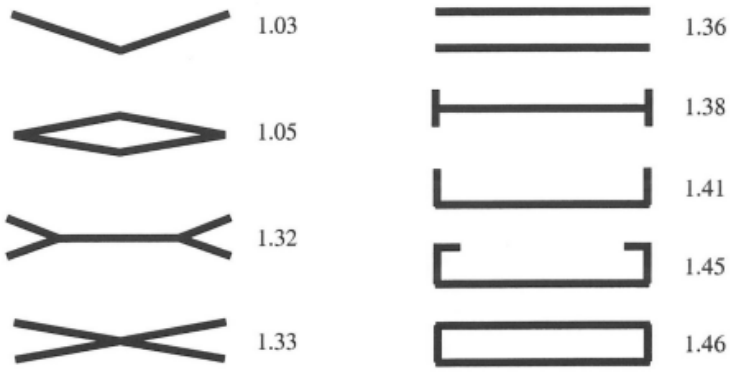


Figure 3-15: Span e's that can be achieved for various nonplanar and multiple surface concepts. From Kroo, I., "Drag Due to Lift: Concepts for Prediction and Reduction," Annual Reviews of Fluid Dynamics, Vol. 33. Used with permission.

3.4.4 The Leading-Edge Suction Concept

Aerodynamicists often evaluate the performance of configurations in term of what is called leading-edge suction. The concept can be explained by considering the inviscid flow over the proverbial thin (zero thickness) flat plate at angle of attack in an incompressible, inviscid flow, as shown in figure 3-16.

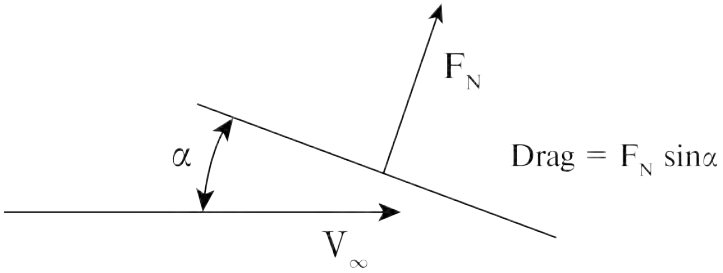


Figure 3-16: Basic relations between aerodynamic forces for an infinitely thin plate in a freestream (V_∞) at an angle of attack (α). From W. H. Mason. Adapted by S. Madden.

What is the drag? According to theory, it must be zero. In the sketch, we see that the force acts in a direction perpendicular to the plate, and this clearly leads to a force component in the drag direction. What's the explanation for the paradox? Consider the sketch of the front portion or leading edge of the thin flat plate in figure 3-17.

There is a low pressure region over the front edge face due to the expansion of the flow around the leading edge. The expansion becomes stronger as the thickness decreases, so that the force on the front face of the plate due to the product of the pressure and plate thickness is

$$F_s = \lim_{\delta \to 0} (\delta \cdot C_{p_s} q_\infty) = \text{finite.} \qquad (3\text{-}32)$$

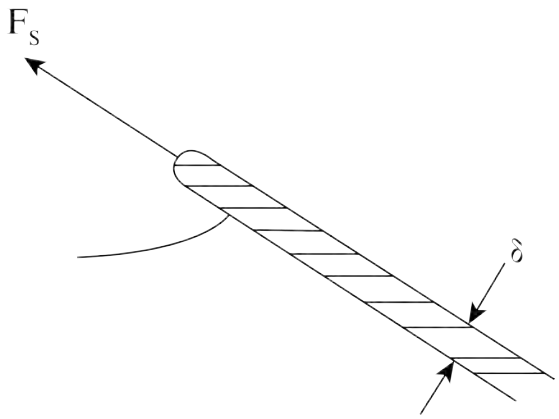


Figure 3-17: Details of the flow near the leading edge of a thin plate. *From W. H. Mason. Adapted by S. Madden.*

The value of F_s is just the amount for the drag of the plate to be zero. Thus the correct model of the flow over the flat plate is actually modified from the sketch given above to include an edge force, as shown in figure 3-18.

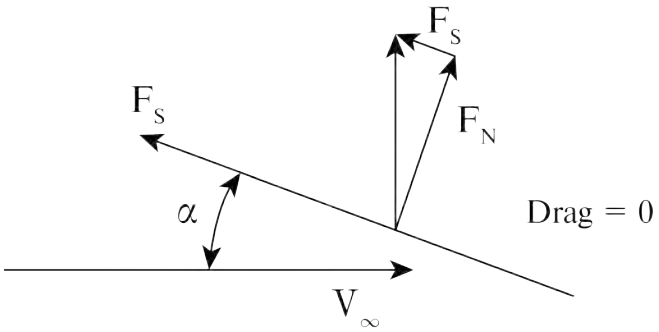


Figure 3-18: Corrected flow model to satisfy inviscid flow theory. *From W. H. Mason. Adapted by S. Madden.*

Of course, a very thin flat plate will realize almost none of the suction force and hence will have a drag component. However, an airfoil section (even a fairly thin one) with a smooth, round nose may in fact achieve nearly all of the suction force, at least at small angles of attack. If the airfoil section in the wing does not achieve the full suction performance, the resulting drag must be added to the induced drag.

The drag due to lift is thus broken up into induced drag and additional profile drag. As described previously, the induced drag is a function of the wing spanload only and is independent of the details of the particular airfoil used in the wing. The additional profile drag is associated with the airfoil used in the wing. At low lift coefficients, this drag should be small, only becoming important as flow separation starts to develop on the airfoil section. The additional profile drag becomes large as wing stall is approached.

Wing performance is evaluated based on the ability to obtain a high value of the lift-to-drag ratio, L/D, relative to the maximum possible for that planform and based on the ability to achieve a high maximum lift coefficient. Essentially, the wing is designed to allow the airfoil to achieve its full performance. Recalling that a two-dimensional airfoil under the assumption of inviscid subsonic flow has no drag due to lift, the maximum performance should occur by adding the induced drag—assuming an elliptic spanload—to the zero-lift drag. This is known as the 100% suction polar since the airfoil section has no additional profile drag due to lift and is thus achieving 100% of the leading-edge suction required to eliminate the drag force in a two-dimensional flow. The drag due to lift may be expressed as

$$C_{D_{L_{100\%}}} \cong C_L^{2/} \pi \mathrm{AR}. \qquad (3\text{-}33)$$

At the other extreme is the 0% leading-edge suction case, in which the airfoil fails to produce any efficient lift, such that the only force is normal to the surface and there is no edge or suction* force. In this case, the entire lifting force on the wing is the normal force, and the polar can be determined by resolving that force into lift and drag components. The equation for the 0% suction drag can be expressed in a variety of forms, starting with

$$C_{D_{L_{0\%}}} \cong C_L \tan(\alpha - \alpha_0) \qquad (3\text{-}34)$$

where a_0 is the zero-lift angle of attack. We also use the linear aerodynamic relation,

$$C_L = C_{L_\alpha}(\alpha - \alpha_0), \qquad (3\text{-}35)$$

which can be solved for the angle of attack:

$$(\alpha - \alpha_0) = \frac{C_L}{C_{L_\alpha}}. \qquad (3\text{-}36)$$

Finally, substitute equation (3-36) into equation (3-34) for the angle of attack as follows:

$$\begin{aligned} C_{D_{L_{0\%}}} &= C_L \tan(\alpha - \alpha_0) \cong C_L(\alpha - \alpha_0) \\ &\cong C_L \frac{C_L}{C_{L_\alpha}} \end{aligned}$$

or

$$C_{D_{L_{0\%}}} \cong \frac{C_L^2}{C_{L_\alpha}} \qquad (3\text{-}37)$$

*On a swept wing, the suction force is normal to the leading edge. The component of the leading edge suction force in the streamwise direction is called the leading-edge thrust.

This equation for the 0% suction polar shows why this polar is often referred to as the "1/$C_{L\alpha}$" polar by aerodynamicists. Using this approach, effective wing performance is quoted in terms of the fraction of suction achieved, based on the difference between the actual drag and the 100% and 0% suction values, as shown in figure 3-19. This figure illustrates how wings typically perform. The wing will approach the 100% level at low lift coefficients, and then as flow separation starts to develop, the performance deteriorates. Eventually, the wing may have a drag substantially higher than the 0% suction value.

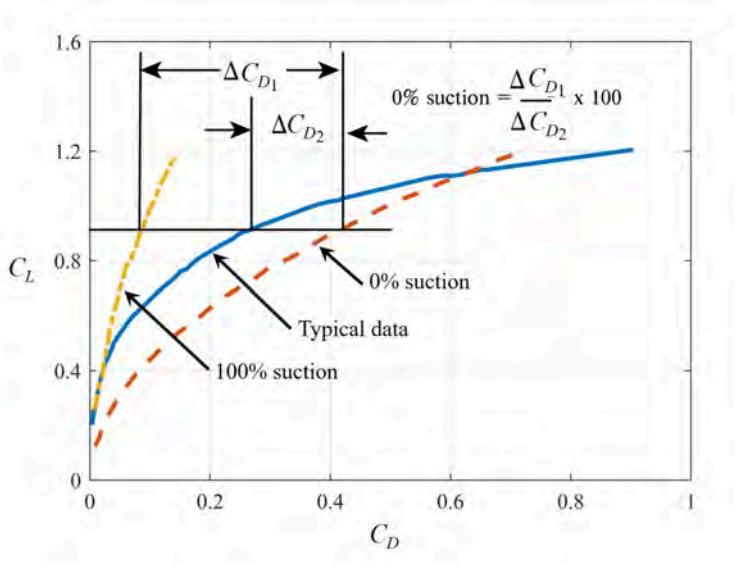


Figure 3-19: Definition of percent leading-edge suction performance. From W. H. Mason. Adapted by S. Madden.

The value of *E* for this level of performance can be found by equating equation (3-37) to the standard form,

$$C_{D_L} = \frac{C_L^2}{\pi ARE} \quad , \qquad (3\text{-}38)$$

which leads to

$$E_{0\%} = \frac{C_{L_\alpha}}{\pi AR} \quad . \qquad (3\text{-}39)$$

Typically, the value of *E* varies with the lift coefficient. By plotting experimental data, typical variations can be obtained for various classes of wings. Figure 3-20 shows a typical variation. This relation was shown in general by McKinney and Dollyhigh.[39]

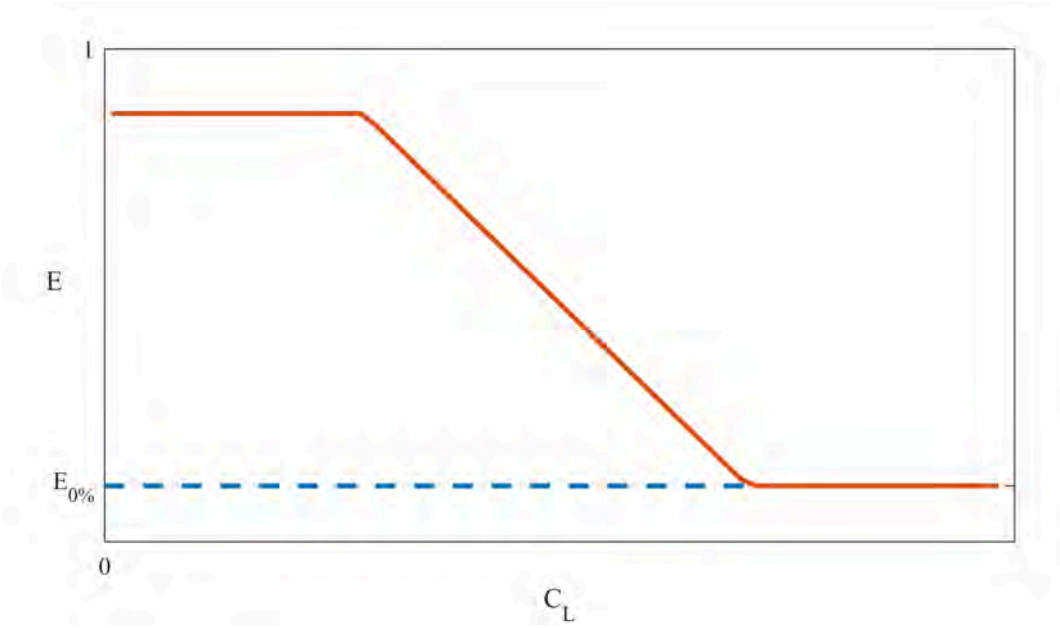


Figure 3-20: Typical variation of E (defined in section 3.2.4) with lift coefficient. From W. H. Mason. Adapted by S. Madden.

Alternately, in supersonic flow, the drag due to lift relation is frequently written as

$$C_{D_L} = KC_L^2 \qquad (3\text{-}40)$$

for uncambered airfoils. For cambered and twisted wings, the polar is shifted, and the minimum drag occurs at a C_L other than zero, as shown previously in figure 3-2 and described by equation (3-2). In practice, we expect the wing to achieve a performance level between the $K_{100\%}$ and $K_{0\%}$ limits. This approach is described in detail by Raymer.[40]

In considering the shift of the polar, a few comments are warranted. First, the wing performance cannot exceed the optimum value, which is $E = 1$ for subsonic flow over a single planar lifting surface. Especially for wings in supersonic flow, it is hard to get 100% of the leading-edge suction. In that case, the approach is to camber the wing to make the drag performance of a wing with less than 100% suction attain the 100% suction level at a specified value of design lift coefficient, C_{Ld}. This uses the polar definition shown in equation (3-41).

$$C_D = \Delta C_{D_m} + K_{xx\%}(C_L - C_{L_m})^2 \qquad (3\text{-}41)$$

where the value of *K* corresponds to the performance of the wing in terms of leading-edge suction (i.e., *xx* is a number between 0 and 100). We find the values of ΔC_{Dm} and C_{Lm} in terms of the design lift coefficient, C_{Ld}. To do this, equate the polar to the 100% suction value at the design lift. This polar must also be tangent to the 100% polar at this point so that the polar will not predict better performance than the optimum at other values of the lift. If we use a 0% leading-edge suction wing as an example, we get equations (3-42) and (3-43).

$$C_D(100\%LES) = C_D(0\%LES)|_{C_L=C_{Ld}} \qquad (3\text{-}42)$$

$$\frac{dC_D(100\%LES)}{dC_L} = \frac{dC_D(0\%LES)}{dC_L}\bigg|_{C_L=C_{L_d}} \qquad (3\text{-}43)$$

The unknown values of ΔC_{Dm} and C_{Lm} in equation (3-41) are

$$C_{L_m} = \left(1 - \frac{K_{100\%}}{K_{0\%}}\right) C_{L_d} \qquad (3\text{-}44)$$

and

$$\Delta C_{D_m} = K_{100\%} C_{L_d}^2 - K_{0\%}(C_{L_d} - C_{L_m})^2. \qquad (3\text{-}45)$$

In any experimental evaluation of wing performance, both the 100% and 0% theoretical polars should be constructed and used to establish bounds on the experimental polar. Thus a typical drag polar would include the 100% and 0% suction polars as well as the predicted or measured performance to establish a basis for evaluating a wing's efficiency. Figure 3-21 presents the actual performance of an unswept rectangular wing at subsonic speed. Here, the performance is very close to the lower drag limit until the wing stalls.

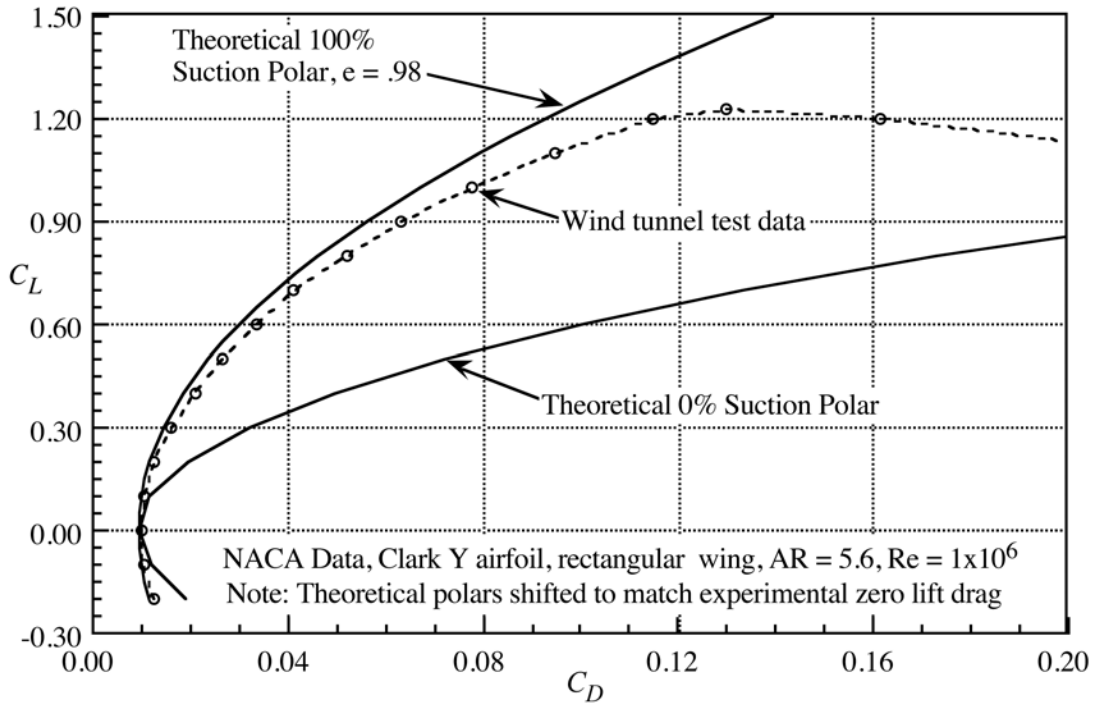


Figure 3-21: Drag performance of simple unswept wing with a Clark Y airfoil.

It is difficult to identify the initial flow breakdown using the drag polar. Often you can identify flow breakdown more clearly by plotting the axial force as a function of normal force. In such a plot, the axial force should initially decrease, as described above. When the airfoil section starts to lose leading-edge suction, the data displays a sharp "break." Figure 3-22 illustrates this approach to the examination of wing efficiency.

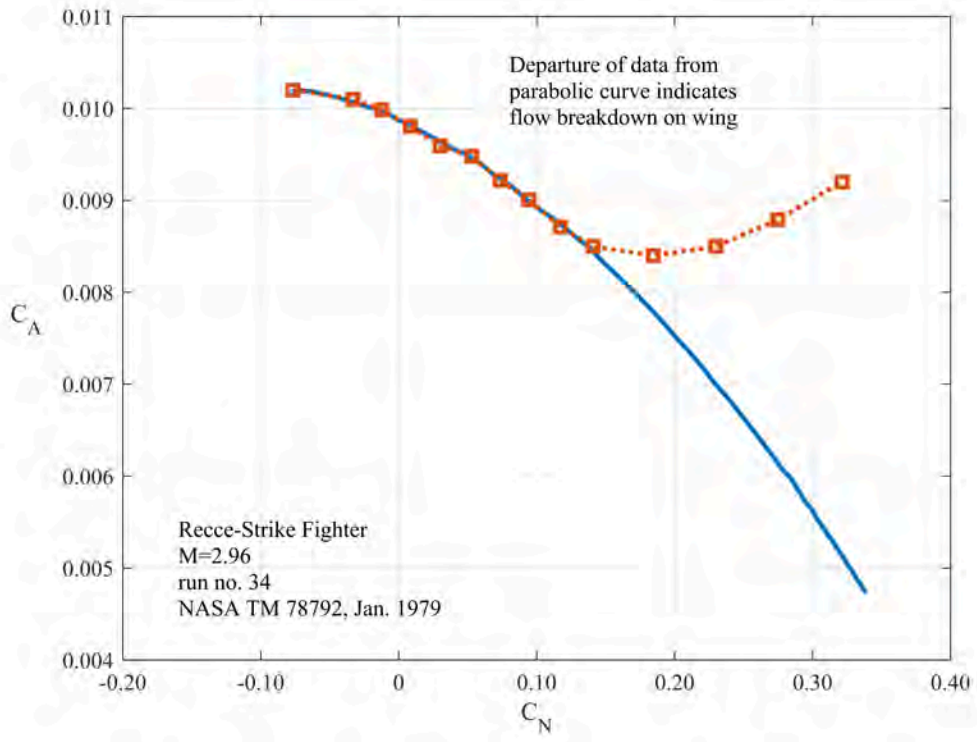


Figure 3-22: Axial force analysis of wing performance.

For configurations with very poor aerodynamic efficiency, the 0% suction force provides a good estimate of the vehicle drag. However, 0% suction levels are so inefficient that this level of performance would be unacceptable and not competitive for most aircraft designs.

To estimate the performance of real configurations, which operate between the two limits, Harry Carlson at NASA's Langley Research Center established the notion of "attainable" leading-edge suction.[41,42] Based on an extensive analysis of 2D airfoil data, Carlson established an empirical correlation which is used to estimate the fraction of the full suction that should be attained for the specified airfoil, planform, and flight condition. Carlson's concepts are based on linear theory.

Nonlinear effects can be important and can be exploited. Although the linear theory–based concepts described here provide a valuable way of looking at wing designs, nonlinear effects can provide a means of improving performance. In considering nonlinear effects, interactions between thickness and lifting effects can be exploited.[43]

3.4.5 Supersonic Wave Drag: The Farfield Wave Drag Integral and Whitcomb's Area Rule

The farfield analysis (see section 3.3) showed us that an aircraft in supersonic flight has wave drag. Not surprisingly, the supersonic wave drag has played a key role in the aerodynamic design of supersonic aircraft.

The equations for estimating the total wave drag, equations (3-25) and (3-26), are repeated here for convenience:

$$\bar{D}_w(\theta) = -\frac{\rho_\infty U_\infty^2}{4\pi} \int_0^l \int_0^l S''(x_1) S''(x_2) \ln|x_1 - x_2| dx_1 dx_2$$

and

$$D_w = \frac{1}{2\pi} \int_0^{2\pi} \bar{D}_w(\theta) d\theta$$

where the *S(x)* values represent the area from an oblique (Mach angle) cut to find the cross-sectional area of the aircraft at a specific roll angle, θ.

The importance of the distribution of the cross-sectional area on the value of wave drag is clear in the integral. To minimize the integral, the area change should be very smooth so that the *S"(x)* is minimized. Thus, the shaping of the design geometry plays a major role in the value of the integral. It has been shown that low drag is achieved by minimizing the maximum cross-sectional area of the design. The key parameter is the fineness ratio, which is the length divided by the maximum diameter. Increasing the fineness ratio decreases the wave drag. A number of minimum drag bodies of revolution have been derived using equation (3-25). The geometric details of these shapes are given in appendix A.

To estimate the wave drag, a theoretical analysis of the integral is available.* Since the integrand is proportional to the second derivative of the area distribution, it is clear even without an analysis that the lowest drag occurs when the distribution is made as smooth as possible. Eminton[44] devised the standard method for the numerical evaluation of the integral. The difficulty in evaluating the integral is that the result depends on the second derivative of the area distribution. This distribution is made up of contributions from numerous components, and it is not known with great precision. Polynomials or other interpolation schemes used to perform the quadrature (i.e., calculate the definite integral) may amplify any imprecision in the data and produce unreasonably high drag predictions. Eminton used a Fourier series for the distribution of the gradient of the area. The coefficients are then found by solving an optimization problem that determines the coefficients that will produce the curve passing through the known values of the area with the least drag. In this sense, the method is also a design method. By specifying a small number of control stations (say, from a designer's configuration layout) with a specified area distribution, the method will provide the complete distribution of area required for minimum drag and to satisfy the imposed control station constraints.

*Advanced CFD calculation methods don't require the aerodynamicist to look at the problem using the area rule diagram. Those approaches don't provide the insight for design available through the area rule diagram.

3.4.5.1 Whitcomb's Area Rule

The principle that aerodynamicists use to achieve low values of wave drag is known as the area rule. Proposed by Richard Whitcomb* at the NACA's Langley Field (now NASA Langley Research Center), the area rule states that the air displaced by the body should develop in a smooth fashion as it moves around and along the body, with no sudden discontinuities. Thus the total aircraft area distribution should form a smooth progression. In particular, when the wing becomes part of the cross-sectional area, the adjacent fuselage area should be reduced to make the total area distribution smooth. This results in the distinctive area ruled, or "coke bottle," fuselage shape.

Whitcomb, who won the National Aeronautics Association's Collier trophy for his work on area rule in 1954, obtained evidence for the validity of this rule experimentally (the computer had not yet become a practical design tool). Figure 3-23 shows the key result obtained by Whitcomb.[45] The increase in drag with increasing transonic Mach number is almost identical for a wing-body combination and a body of revolution with the same cross-sectional area distribution. The wing-body combination has significantly higher subsonic drag because of the increased surface area compared to the body-alone case. All the cases Whitcomb presented weren't as dramatic, but similar trends were found for a number of shapes. Whitcomb's original idea addressed transonic speeds, and the normal area distribution (the area in the plane perpendicular to the flow) was made smooth to obtain low drag. At supersonic speeds, the problem is more complicated. Instead of using the normal area distribution, the supersonic area rule requires smoothness for the area of the so-called Mach cuts that correspond to the area distribution along the Mach angle for each θ angle around the circumference (see equation 3-26 in section 3.3.3).

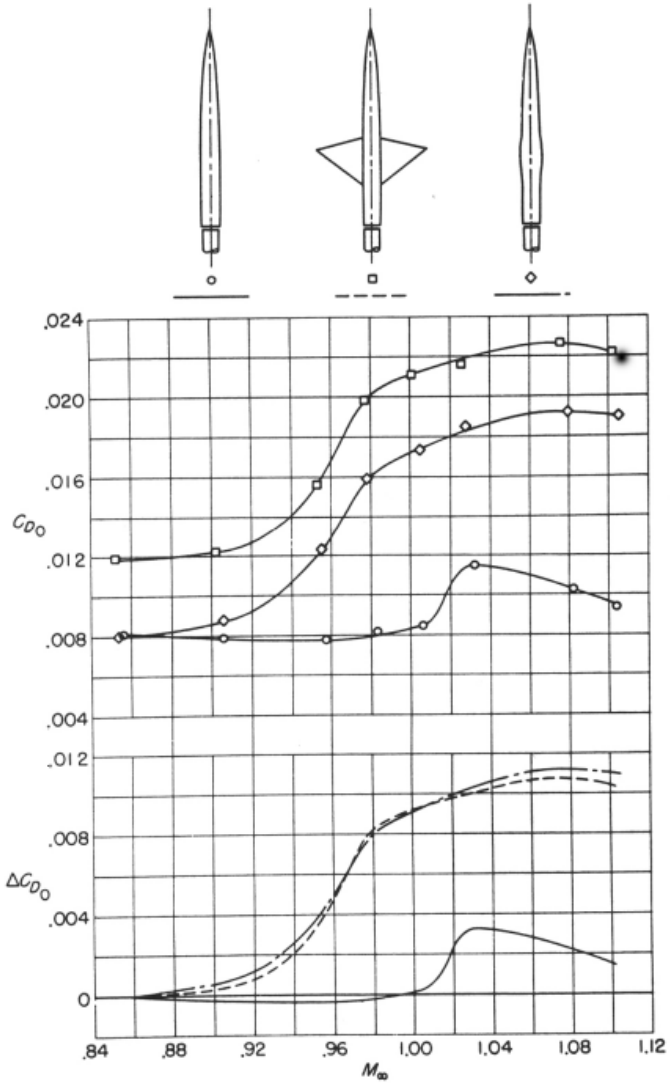


Figure 3-23: Whitcomb's proof of the area rule. *From R. T. Whitcomb. "A Study of the Zero Lift Drag-Rise Characteristics of Wing-Body Combinations near the Speed of Sound." NACA. Public domain.*

3.4.5.2 Practical Applications of Area Rule

Convair F-102 and F-106

The most famous application of the area rule occurred on the Convair F-102 aircraft program.* This airplane was supposed to be supersonic in level flight. When it first flew, the original prototype YF-102 was unable to break the sound barrier and fly supersonically. The nose was lengthened approximately five feet and area was added (with the plane already completed, it was impossible to reduce area) to the fuselage via faired bulges—or bustles—at the intersection of the fuselage and the wing trailing edge. The bulges were faired beyond the engine exhaust nozzle to improve the fineness ratio and area distribution. After these modifications, the prototype YF-102, shown in figure 3-24(a),[46] was capable of penetrating deeper into the transonic region. However, it was still not capable of exceeding Mach 1.0 in level flight. A complete redesign was necessary to continue the contract.

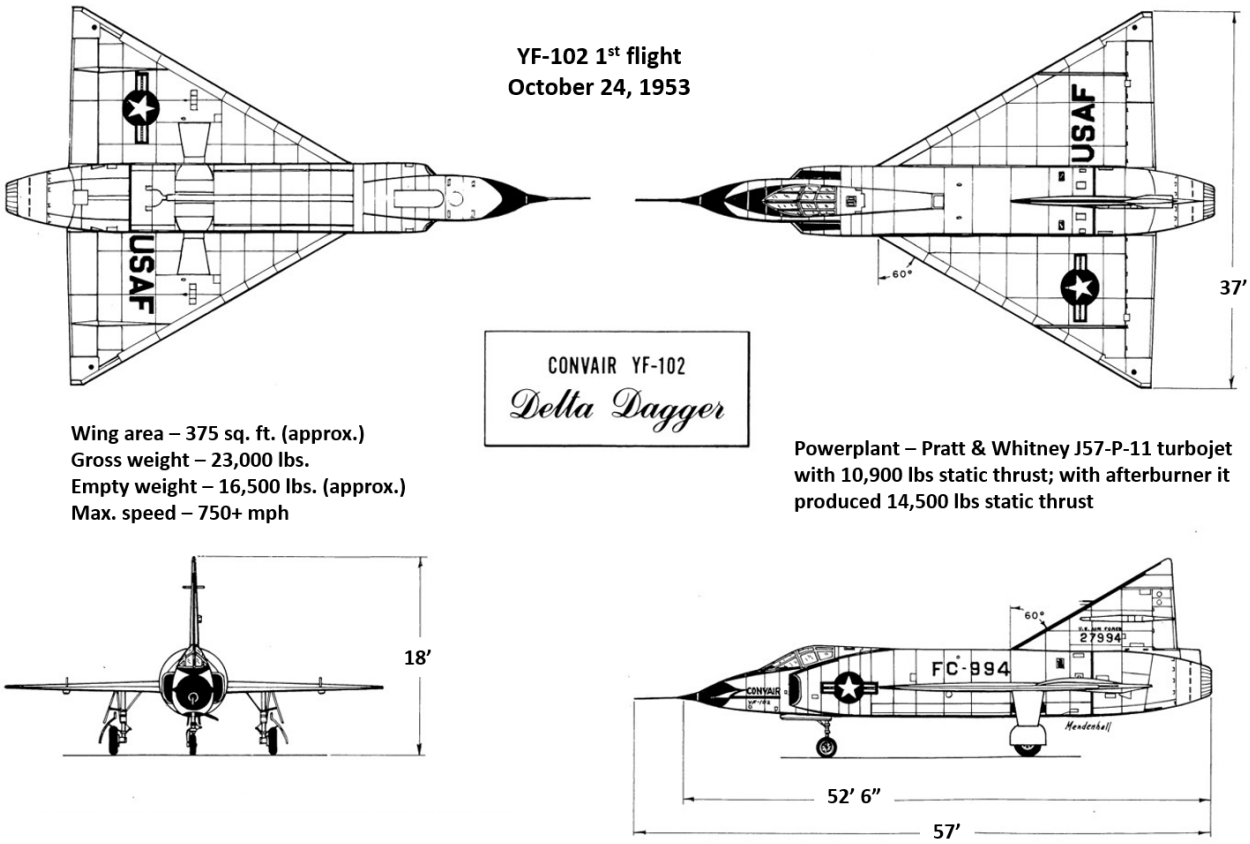


Figure 3-24(a): Convair original YF-102 prototype configuration. From C. A. Mendenhall. Copyright undetermined by Motorbooks International/Quarto, General Dynamics, and Boeing. Fair use.

*Portions of this section were contributed by my colleague, Nathan Kirschbaum, who retired from Grumman in 1989 after thirty-eight years and then joined Virginia Tech as an aircraft design teacher for ten years before retiring for a second time in 2001.

One hundred and seventeen working days later(!), a new, completely redesigned F-102 was ready to fly. The fuselage fineness ratio and area distribution had been increased and refined. The fuselage midsection cross-sectional area had been reduced (cinched-up, wasp-waisted, or coke-bottled) as much as structure and component integration would permit. It was lengthened eleven feet, three inches, with most of the increased length added ahead of the wing. The cockpit canopy was reduced in cross section with a near-triangular cross section and headed by a flat plate, highly swept V-shaped windshield. The cockpit and the side-mounted engine inlets were moved forward to reduce their sudden area buildup, or impact on the fuselage area. The aft fuselage bustles were retained to avoid the rapid collapse of the cross-sectional area at the delta wing trailing edge. Reconfigured in this way, the airplane was able to fly at low supersonic speeds (M = 1.2). Figure 3-24(b) shows the reconfigured F-102A as produced for service use.[47]

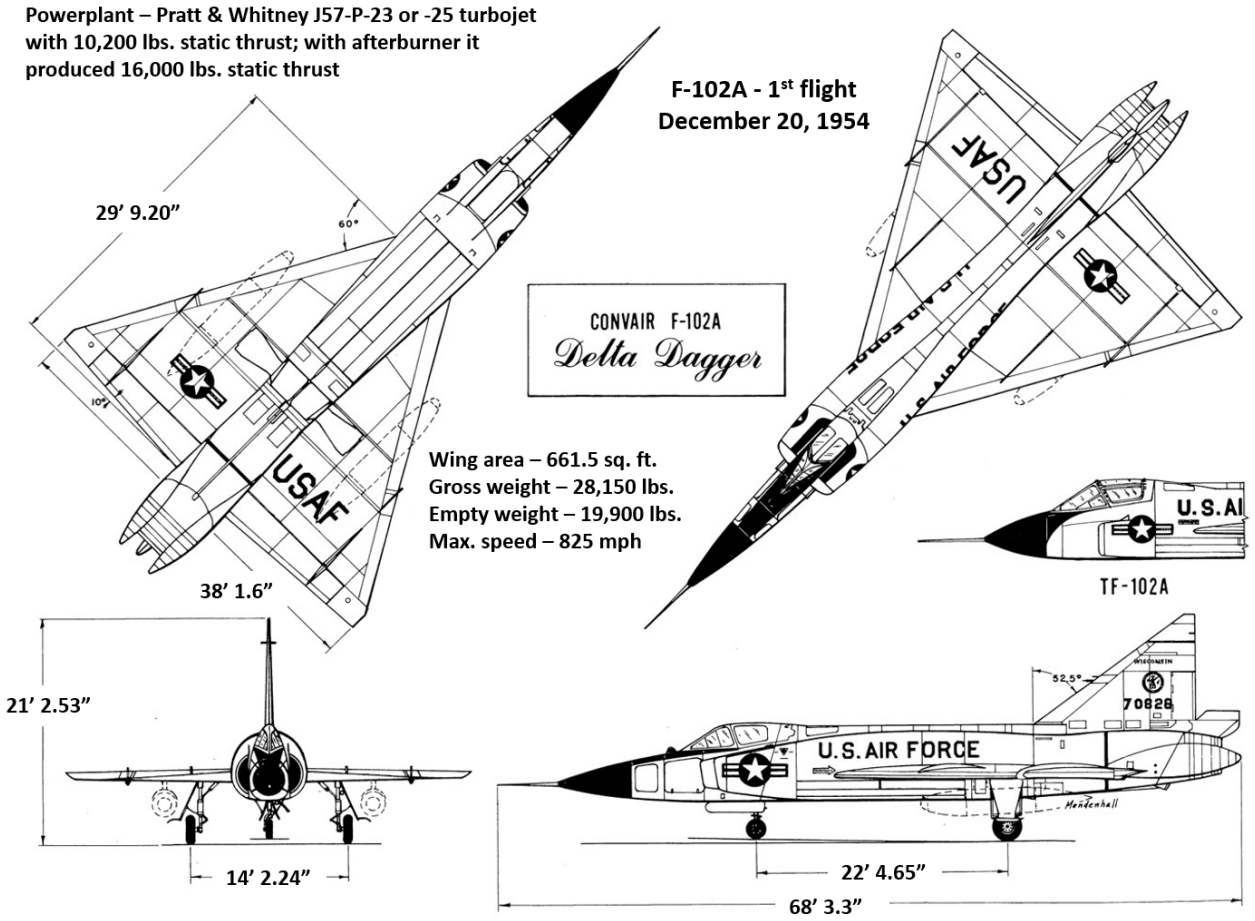


Figure 3-24(b): Convair original F-102A configuration based on reconfigured YF-102. *From C. A. Mendenhall. Copyright undetermined by Motorbooks International/Quarto, General Dynamics, and Boeing. Fair use.*

The resulting change in drag from the YF-102 to the F-102A was about twenty-five counts and is shown in figure 3-24(c), recreated from an original Convair plot. Although the change might not appear dramatic, the reduction in wave drag was sufficient to allow the plane to fly faster then the speed of sound. Notice that the use of conical camber (discussed later), introduced to improve the lift and drag-due-to-lift characteristics of the delta wing, added a significant penalty (camber drag) to the minimum drag.

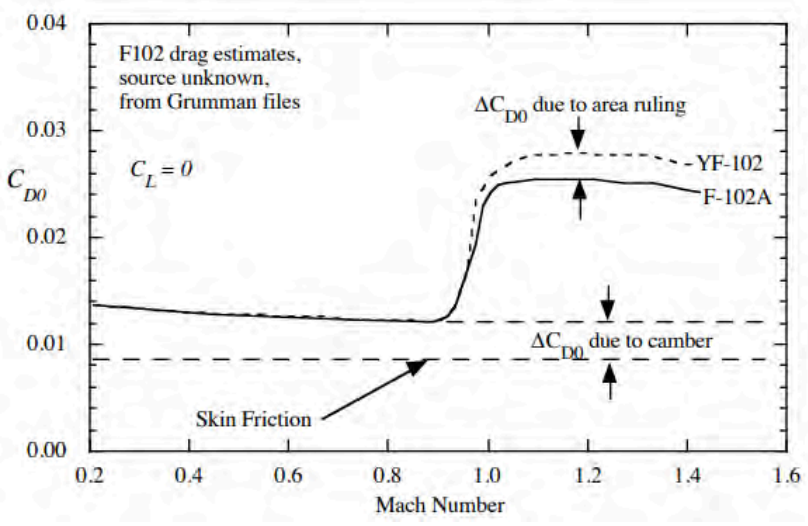


Figure 3-24(c): Zero-lift drag for the YF-102 and F-102A airplanes.

Subsequently, the configuration was completely redesigned to incorporate a more refined, integrated area rule. Further slimmed down by a reduced weapon bay capacity and by shortened and repositioned engine air intake ducts, and powered by a 50% more powerful engine, it was capable of routine Mach 2+ speeds. The designation was then changed to F-106A. This design is shown in figure 3-25. The volume of the increased area of the vertical tail on the F-106A, required to counteract the loss of tail surface effectiveness at the increased operational Mach number, replaced the aft side bustles on the F-102.

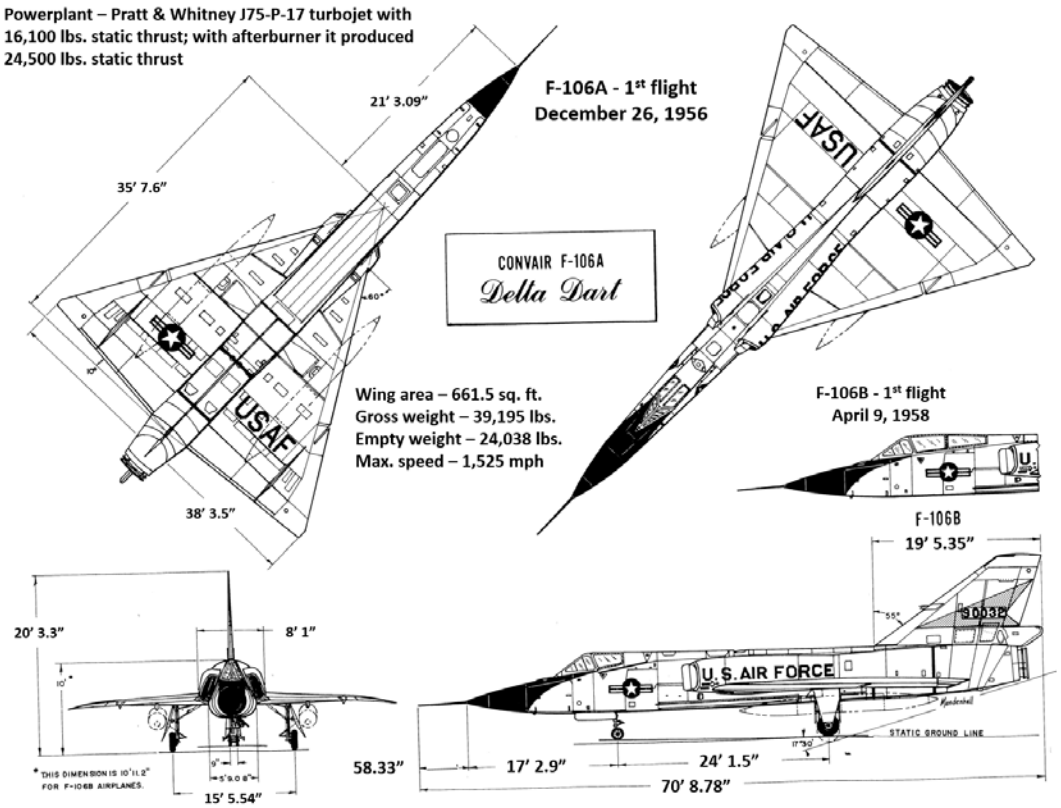


Figure 3-25: Convair original F-106A configuration redesigned by incorporating area rule. *From C. A. Mendenhall. Copyright undetermined by Motorbooks International/Quarto, General Dynamics, and Boeing. Fair use.*

Grumman F-11F and Northrop F-5

As an historical note, the Grumman F-11F (F-11) was the first aircraft designed "from scratch" using the area rule. The result is clearly evident, as shown in figure 3-26(a). Another design employing the area rule in an effective manner was the Northrop F-5A/B (and the T-38 derivative), as shown in figure 3-26(b).[48] This design had essentially unswept wings. Even the wingtip fuel tanks were area ruled, although the inboard localized area reduction could arguably be assigned to Küchemann interface contour theorems.[49]

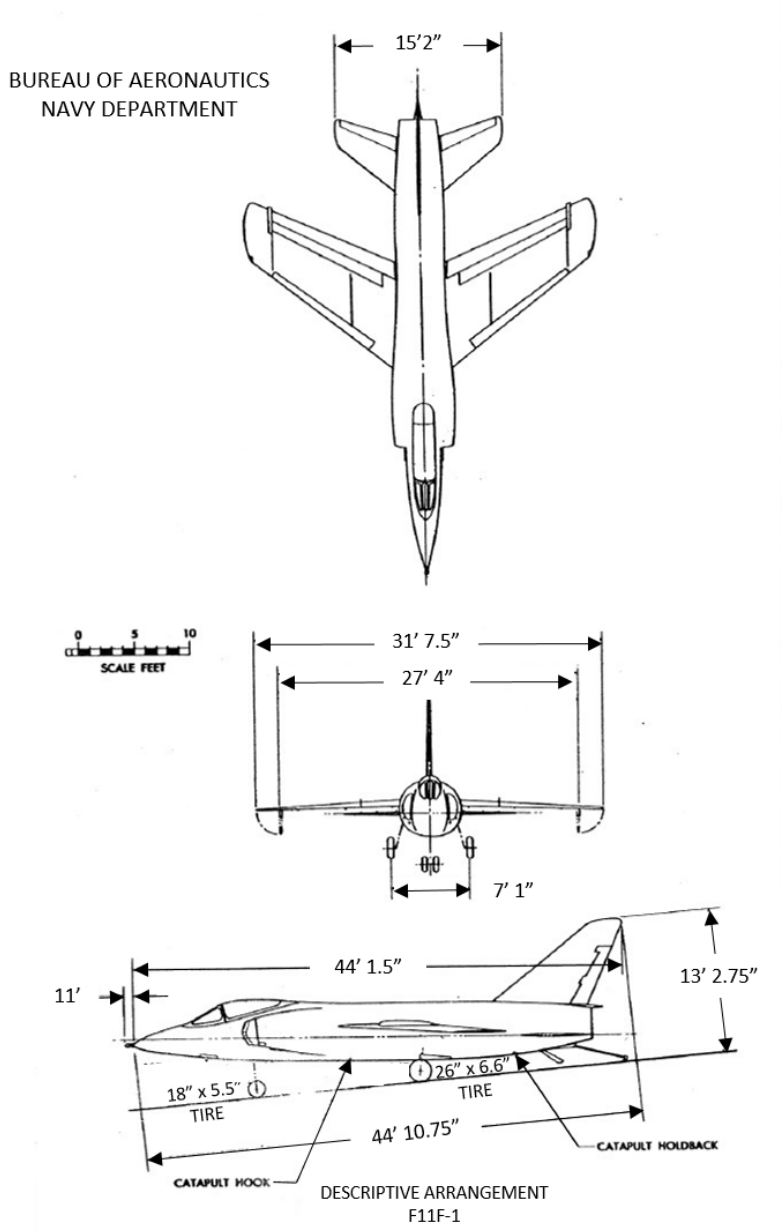


Figure 3-26(a): Other aircraft designs with evident area ruling, Grumman F11F-1. From US Navy. Wikimedia. Public domain.

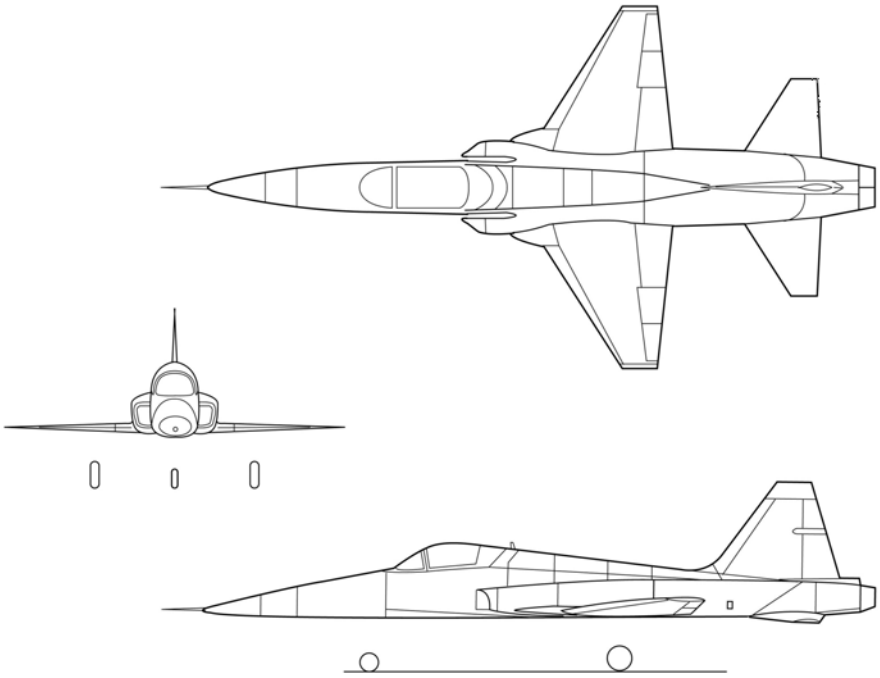


Figure 3-26(b): Other aircraft designs with evident area ruling, Northrop F-5. From NASA. Wikimedia. Public domain.

When considering the area rule, remember that this is only one part of successful airplane design.[50] Moreover, extreme area ruling for a specific Mach number may significantly degrade the performance of the design at other Mach numbers.

3.5 Predicting Drag

Accurate prediction of drag is one of the most important yet most challenging tasks of aircraft design projects for aerodynamicists. Actual flight performance is heavily dependent on the accurate value of drag. For example, if drag is underpredicted (predicted value is less than the actual value), then the actual fuel consumption will be higher than the predicted one. Similarly, if the drag is overpredicted (predicted value is more than the actural value), the aircraft might end up being overdesigned (for example, featuring a higher gross weight due to higher predicted fuel consumption). For the challenges associated with accurate drag prediction, Jobe[51] is a good source. In this section, we discuss the relevant drag prediction methodologies.

3.5.1 Overview of Methodologies

We group aerodynamic drag prediction methodologies into three categories:

i. *semi-empirical correlation curves* based on data from past and present aircraft
ii. *numerical simulations* of flow about an aircraft using computational fluid dynamics (CFD) methods
iii. *physical simulations* of flow about a scale model of an aircraft using ground test facilities, such as the wind tunnels

All three approaches have their own unique strengths and weaknesses. Selection of the best approach(es) depends on the aircraft design stage (see Chapter 4) and the nature and scope of the required drag data. In this book, our focus is on the early stages of design, which are characterized by the evolution of configuration geometry, also known as outer mold line (OML), through frequent modifications. Designers receive inputs from teams of experts from various disciplines such as aerodynamics, structures, stability and control, cost, and manufacturing. The OML is frequently modified to accommodate those inputs. One of the major tasks of the aerodynamics experts on the team is to predict the drag of constantly changing OMLs and to find ways of keeping it as low as possible. Aerodynamics experts are expected to provide accurate drag data at the right time and the right cost to meet the strict scope, cost, and schedule specifications of the design project. The use of semi-empirical correlation curves and numerical simulations with rapid turnaround times provides the right balance between the required accuracy and tight schedules. Physical simulations (wind tunnel testing) are typically too costly and take too long to be effective in the early stages of design. They are better suited for later stages, where they are extensively used. Readers interested in learning more about the semi-empirical correlations can find them in just about any aircraft design book. For state of the art numerical simulations, the *Applied Computational Aerodynamics* book by Cummings et al.[52] is an excellent source of information.

It is worth mentioning that you may find drag components being characterized as "inviscid" or "viscous" drag in the literature. This characterization reflects the fluid mechanics viewpoint discussed in section 3.2.2. For example, lift-induced drag and wave drag are considered inviscid drags, whereas friction drag and form drag are viscous. It is straightforward to see why friction drag is considered viscous. After all, it represents the total force on a body due to surface shear forces caused by viscosity. However, form drag is a bit more nuanced since it represents the net force due to surface pressures. We know from d'Alembert's paradox that the net force on a body is zero in steady, incompressible, inviscid flow. However, when viscous effects modify the surface pressure distributions, the net force is no longer zero. This non-zero net force is the form drag. Friction drag and form drag contribute to the total drag even when a body produces no lift. Methods to predict them are discussed in section 3.5.2. We can estimate lift-induced drag using methods based on inviscid flow approximations, as highlighted in section 3.5.3. Wave drag can also be estimated using inviscid flow methods, as discussed in sections 3.5.5 and 3.5.6.

3.5.2 Zero Lift Drag: Skin Friction and Form Drag Estimation

Estimates of skin friction based on classical flat plate skin friction formulas can be used to provide initial estimates of the friction and form drag portion of the zero-lift drag. These are required for aerodynamic design studies using the rest of the methods described here. These simple formulas are used in conceptual design in place of detailed boundary layer calculations, and they provide good initial estimates until more detailed calculations are made using boundary layer calculations or other methods. They are included here because they appear to have been omitted from current basic aerodynamics textbooks.* An excellent examination of the methods and accuracy of the approach described here was given by Paterson, MacWilkinson, and Blackerby of Lockheed.[53]

> *Expanded details including compressibility effects and mixed laminar-turbulent skin friction estimates are given in appendix E, section E.5.1.

For a highly streamlined aerodynamically clean shape, the zero-lift drag should be mostly due to friction and form drag at subsonic speeds where there are no shock waves and can be estimated using skin friction formulas. However, table 3-1 shows that, for a typical military attack airplane, about two-thirds of the zero-lift drag is associated with skin friction and form drag. This illustrates the serious performance penalties associated with seemingly small details.

Until recently, aerodynamicists assumed the flow on actual airplanes was completely turbulent. However, as a result of work at NASA, some configurations can now take advantage of at least some laminar flow, showing significant reduction in friction drag. Advanced airfoils, such as a natural laminar flow (NLF) airfoil, can have as much as 30% to 50% laminar flow. As an example of this approach, consider a typical turbulent flow skin friction formula (for one side of a flat plate surface only):

$$C_F = \frac{0.455}{[\log \mathrm{Re}_c]^{2.58}} \qquad (3\text{-}46)$$

where "log" means logarithm to the base 10. Note also that the capital C_F denotes an integrated value. Formulas for the local skin friction coefficient customarily use a lowercase *f* subscript.

Numerous form factors are available to help account for effects due to thickness and additional trailing-edge pressure drag; see Hoerner[54] and Covert[55] for summaries. For planar surfaces, one form factor is

$$FF = 1 + 2.7\left(\frac{t}{c}\right) + 100\left(\frac{t}{c}\right)^4 \qquad (3\text{-}47)$$

where *t*/*c* is the maximum thickness-to-chord ratio.

For bodies, the form factor would be

$$FF = 1 + 1.5\left(\frac{d}{l}\right)^{1.5} + 7\left(\frac{d}{l}\right)^3 \qquad (3\text{-}48)$$

where *d*/*l* is the diameter-to-length ratio.

The skin friction coefficient estimate is then converted to aircraft drag coefficient form through equation (3-49) below.

$$C_{D_0} \cong C_F \frac{S_{\text{wet}}}{S_{\text{ref}}} FF \qquad (3\text{-}49)$$

Here S_{wet} is the total area scrubbed by the flow, and S_{ref} is the reference area used in the definition of the force coefficients. For a thin wing, the reference area is usually the planform area and the wetted area is approximately twice the planform area (including the upper and lower surface of the wing).

A computer program FRICTION automates this procedure using slightly improved skin friction formulas that include compressibility effects. The program computes the skin friction and form drag over each component, including regions of laminar and turbulent flow. The user can input either the Mach and Reynolds numbers or the Mach number and altitude. The program and its use are described in an online manual.[56] This analysis assumes that the aircraft is highly streamlined. For many aircraft, this is not the case. As mentioned in section 3.2, table 3-1 provides an example of the significantly increased drag that results when developing an aircraft for operational use. Note that the parasite drag coefficient based on a total wetted area of 1119 ft^2 is 0.00495, whereas it is 0.0213 based on the reference area of 260 ft^2.

> Comment: On a tour of the final assembly lines of the Boeing 747 and 777 on February 29, 1996, I observed that the 777 was much, much smoother aerodynamically than the 747. Clearly, a lot of the advanced performance of the 777 is due to old-fashioned attention to detail. The aerodynamicists have apparently finally convinced the manufacturing engineers of the importance of aerodynamic cleanliness. Think about this the next time you compare a Cessna 182 to the modern homebuilt aircraft exemplified by the Lancair and Glassair.

Component	S_{wet}	S_{π}	C_{Df}	$C_{D\pi}$	ΔC_D	% total
1. Wing						**22.1%**
(a) Affected by slats	262		0.00308		0.00308	
(b) Not affected by slats	150		0.00280		0.00162	
2. Horizontal tail	84.4		0.0033		0.00108	**5.1%**
3. Vertical tail	117		0.00385		0.00173	**8.1%**
4. Fuselage (including inlets)	434		0.00306		0.00512	**24.0%**
5. Enclosure		2.3		0.122	0.00108	**5.1%**
6. Appendages						**33.1%**
(a) Upper avionics bay					0.00069	
(b) Drag-chute fairing					0.00012	
(c) Landing gear fairings					0.00042	
(d) Aero 7A Rack-Pylon @ CL					0.00058	
(e) Arresting hook					0.00058	
(f) Inflight-Fueling probe					0.00092	
(g) Wing-Vortex generators					0.00115	
(h) Boundary layer diverter					0.00042	
(i) Boundary-Layer splitter plate					0.00004	
(j) Inlet vortex fences					0.00023	
(k) Landing spoilers					0.00012	
(l) ECM antenna and chaff dispensers					0.00038	
(m) Pilot tube					0.00004	
(n) Angle-of-attack indicator					0.00004	
(o) Rudder damper					0.00023	
(p) Aileron damper					0.00023	
(q) Barrier detents					0.00008	
(r) Anti-collision lights					0.00008	
(s) Radar altimeter					0.00015	
(t) Fuel dump and vent					0.00023	
(u) Airblast rain removal					0.00008	
(v) Catapult holdback					0.00027	
7. Inlets and exits						**1.6%**
(a) Powerplant (vents, etc.)					0.00027	

Component	S_{wet}	S_{π}	C_{Df}	$C_{D\pi}$	ΔC_D	% total
(b) Air conditioning					0.00008	
8. Miscellaneous					0.00020	**0.9%**
Total zero-lift drag coefficient (based on S_{ref} = 260 ft^2)					0.0213	**100%**

Table 3-1: Drag breakdown on a "dirty" military airplane. Total speed minimum parasite drag breakdown: M < .65, C_L = 0.0.

3.5.3 Computer Programs for Lift-Induced Drag Estimation

The lift-induced drag, as discussed in section 3.4, can be estimated using many computer programs; three are highlighted in this section. Readers should see appendix E for these and many other computer programs that are useful for aerodynamics and aircraft design efforts.

3.5.3.1 Program LIDRAG: *Induced Drag of a Single Planar Wing*

The LIDRAG program computes the span efficiency factor *e* for a single planar lifting surface given the spanload using a fast Fourier transform. For reference, note that the *e* for an elliptic spanload is 1.0 and the *e* for a triangular spanload is about 0.72. LIDRAG was originally written by Dave Ives, who was a research scientist at Pratt & Whitney, and the program is employed in numerous aerodynamics codes.[57]

3.5.3.2 Program LAMDES: *Induced Drag of Simple Nonplanar Lifting Systems with Camber Line Design*

When the lifting system is not limited to a single lifting component, LIDRAG cannot be used to find the span efficiency factor *e*. When the system is composed of two lifting surfaces or a lifting surface with dihedral breaks, including winglets, then the induced drag can be estimated using a code known as LAMDES that was originally developed by John Lamar,[58] who served as an aerospace research scientist at NASA-Langley. As originally developed, this code finds the minimum induced drag and the required spanloads for a prescribed lift and pitching moment constraint. This program is much more elaborate than LIDRAG. For subsonic flow, the program can also estimate the camber and twist of the lifting surfaces required to achieve the spanload for minimum drag. In my work, I extended this code to incorporate, approximately, the effects of viscosity and find the system *e* for a user-supplied spanload distribution.[59]

3.5.3.3 Program IDRAG: *Induced Drag of Nonplanar Lifting Systems*

The IDRAG program can be used to find the induced drag of a system of nonplanar lifting elements. It was written by Joel Grasmeyer while he was a master's student at Virginia Tech. It has both design and analysis capabilities. This means that you either find the spanload required to obtain the minimum induced drag or you can input a spanload and find the induced drag. The program also provides the span efficiency factor *e*. This program does not give you the twist and camber required to generate the spanloads. Three FORTRAN programs are required and must be linked to run the IDRAG program.

3.5.4 Transonic Drag Rise: The Korn Equation

Attempts have been made to estimate the capability of transonic airfoils for the purposes of design studies without performing wind tunnel or detailed computational design work. This is important in the initial stages of aircraft design, where airfoil performance needs to be estimated before the actual airfoil design is completed. Here, we provide an approximate method for estimating the transonic performance of airfoils. It is based on the Korn equation—an empirical relation developed by Dave Korn, who earned a PhD in applied mathematics from the New York University Courant Institute of Mathematical Sciences and contributed to computer simulations of transonic airfoils in the early 1970s. The Korn equation was in use at Grumman when I arrived in 1974.

Based on Dave Korn's experience, it appeared that airfoils could be designed for a variety of Mach numbers, thickness-to-chord ratios, and design lift coefficients. However, in all cases, there seemed to be a limit to the combination of three parameters: drag divergence Mach number (M_{dd}), thickness-to-chord ratio (t/c), and lift coefficient (C_l). In particular, the Korn equation for a 2D airfoil is

$$M_{\mathrm{dd}} + \frac{C_l}{10} + \left(\frac{t}{c}\right) = \kappa_A \qquad (3\text{-}50)$$

where κ_A is an airfoil technology factor with a value of 0.87 for an NACA 6-series airfoil section and a value of 0.95 for a supercritical section. Equation (3-50) provides a simple means of estimating the possible combination of Mach number, lift coefficient, and thickness ratio that can be obtained using modern airfoil design, and variations of it have been explored graphically by many authors; the scales are often left out of public presentations by aircraft companies. Note that the Korn equation is sensitive to the value of the airfoil technology factor.

Mason[60] compares the prediction from the Korn equation with other estimates. Figure 3-27(a) shows a comparison of the performance estimates of both older airfoils and modern supercritical airfoil presented by Shevell.[61] The agreement is good with the exception of being overly pessimistic regarding older conventional airfoils at lower thickness ratios.

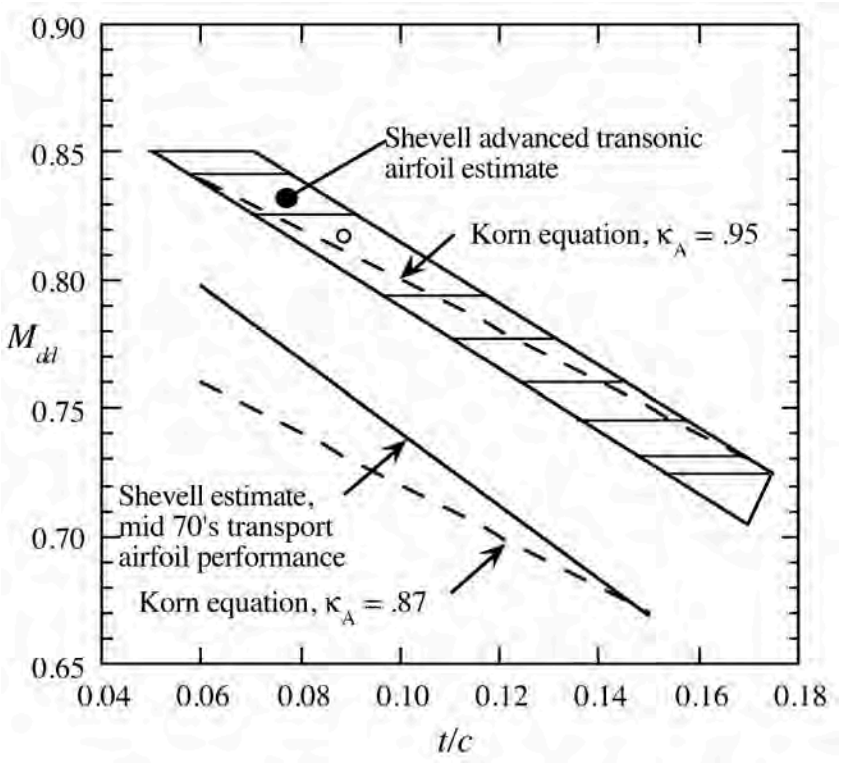


Figure 3-27(a): Comparison of the Korn equation with Shevell's estimates. *From W. H. Mason. "Analytic Models for Technology Integration in Aircraft Design." Reprinted by permission of the American Institute of Aeronautics and Astronautics, Inc.*

Figure 3-27(b) compares the Korn equation with NASA projections[62] for supercritical airfoils based on a wealth of data and experience. In this case, the Korn equation is extremely good at lift coefficients of 0.4 and 0.7, but it is overly optimistic at higher lift coefficients. This type of technology representation is important in developing integrated designs. To develop each point on this type of chart represents a large effort on the part of the designer (in this case, the aerodynamicist).

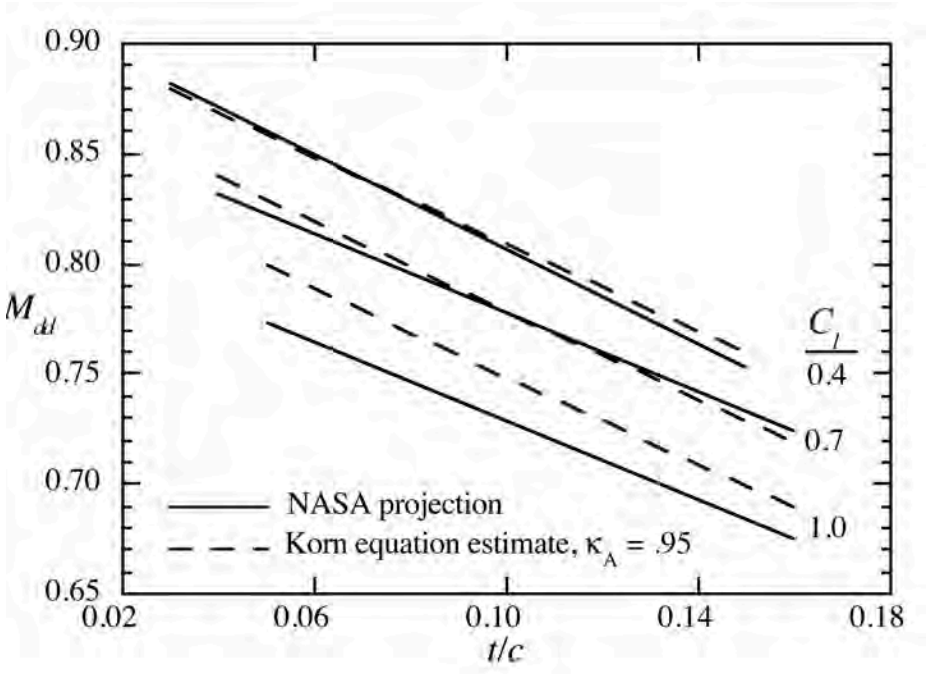


Figure 3-27(b): Comparison of the Korn equation with NASA projections. From W. H. Mason. "Analytic Models for Technology Integration in Aircraft Design." Reprinted by permission of the American Institute of Aeronautics and Astronautics, Inc. Adapted by S. Madden.

The Korn equation has been extended to estimate the drag divergence Mach number for a 3D swept wing by including sweep using simple sweep theory.[63,64] The result for a 3D wing is given by

$$M_{\mathrm{DD}} = \frac{\kappa_A}{\cos\Lambda} - \frac{(t/c)}{\cos^2\Lambda} - \frac{C_L}{10\cos^3\Lambda} \quad . \qquad (3\text{-}51)$$

This model estimates the drag divergence Mach number, M_{DD}, as a function of an airfoil technology factor (κ_A), the thickness-to-chord ratio (t/c), the wing lift coefficient (C_L), and the *effective* sweep angle (Λ). Recall that the airfoil technology factor has a value of 0.87 for a NACA 6-series airfoil section and a value of 0.95 for a supercritical section.

With this approximation for the drag divergence Mach number, we can now calculate the critical Mach number. The definition of the drag divergence Mach number is taken to be

$$\frac{\partial C_D}{\partial M} = 0.1. \qquad (3\text{-}52)$$

(Note that C_d should replace C_D for 2D airfoils.) Next, we make use of Lock's proposed empirically derived shape of the drag rise, resulting in equation (3-53).[65]

$$C_D = 20(M - M_{crit})^4 \qquad (3\text{-}53)$$

The definition of the drag divergence Mach number is equated to the derivative of the drag rise formula given above to produce the following equation:

$$\frac{\partial C_D}{\partial M} = 0.1 = 80(M - M_{crit})^3 \qquad (3\text{-}54)$$

We can then solve this equation for the critical Mach number:

$$M_{crit} = M_{\mathrm{DD}} - \left(\frac{0.1}{80}\right)^{1/3} \qquad (3\text{-}55)$$

where the drag divergence Mach number is given by the extended Korn equation, equation (3-51).

Joel Grasmeyer et al.[66] developed a method to compute wave drag coefficient on a number of spanwise strips of a wing for use in MDO studies of a transonic strut-braced wing concept. The method employs the following relation:

$$C_{d_{\mathrm{wave}}} = 20(M - M_{crit})^4 \frac{S_{\mathrm{strip}}}{S_{\mathrm{ref}}} \quad \text{for} M > M_{crit}, \qquad (3\text{-}56)$$

where the local t/c, C_l, and half-chord sweep angle are specified for a number of spanwise strips along the wing, and the drag of each strip is combined to form the total wave drag. In the equation above, the wave drag for each strip is multiplied by the ratio of the strip area (S_{strip}) to the reference area (S_{ref}). This method has been validated with the Boeing 747-100, as shown in figure 3-28. The curves represent the results of the current model using eight spanwise strips, and the discrete data points represent the Boeing 747 flight test data. The predictions show good agreement with the data over a wide range of Mach numbers and lift coefficients. We reemphasize that the results are sensitive to the value of the airfoil technology factor. A value of 0.89 was used for the Boeing 747 results in figure 3-28. Based on an analysis of the Boeing 777, we used a value of 0.955 to simulate the Boeing 757-100 wave drag characteristics.

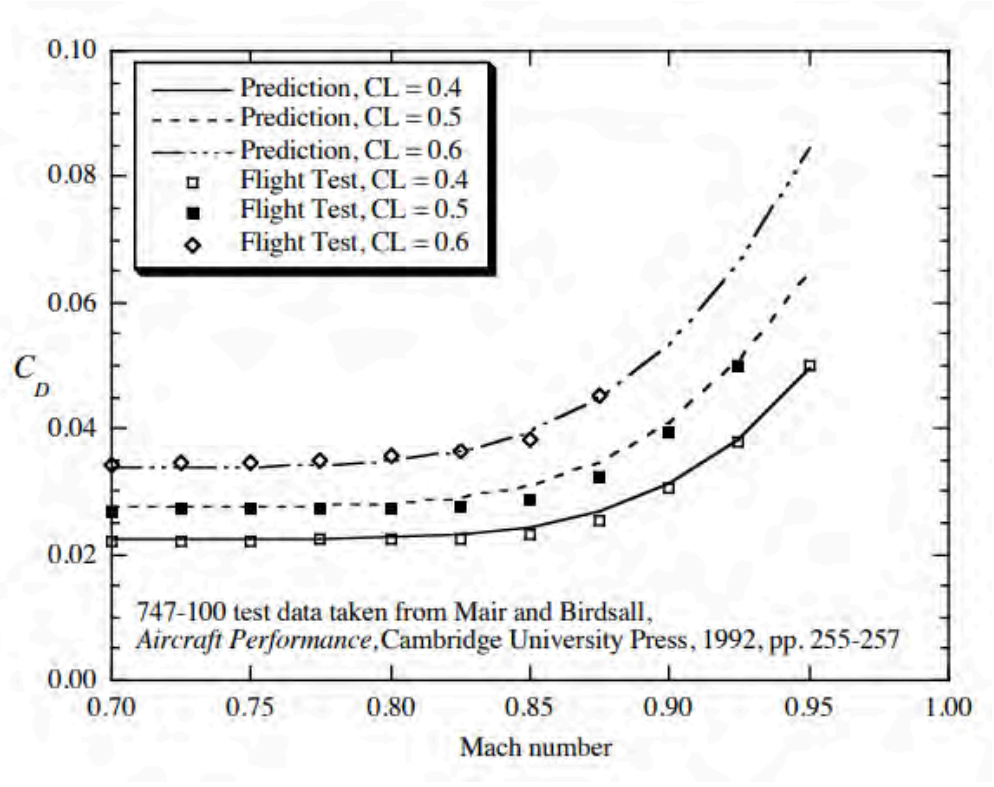


Figure 3-28: Comparison of approximate drag rise methodology with Boeing 747-100 flight test data. From S. Madden. Data: Mair and Birdsall.

3.5.5 Supersonic Wave Drag Estimation

The Harris wave drag program[67] is one of the most widely used methods for estimating wave drag. It is the practical implementation of the concepts described in sections 3.3.3 and 3.4.5. Figure 3-29 illustrates the procedure. At each roll angle θ, a number of *x*-cuts are made to use in evaluating the integral, with the *x*-axis running along the length of the body. Typically, fifty to 100 *x*-cuts are made for each θ; the total number of roll angles typically ranges from twenty-four to thirty-six. In making these calculations, the inlet capture area is removed from the area distribution. The Mach number dependence comes in through the orientation of the cutting plane at Mach angle, μ, which is defined as $\sin^{-1}(1/M)$.

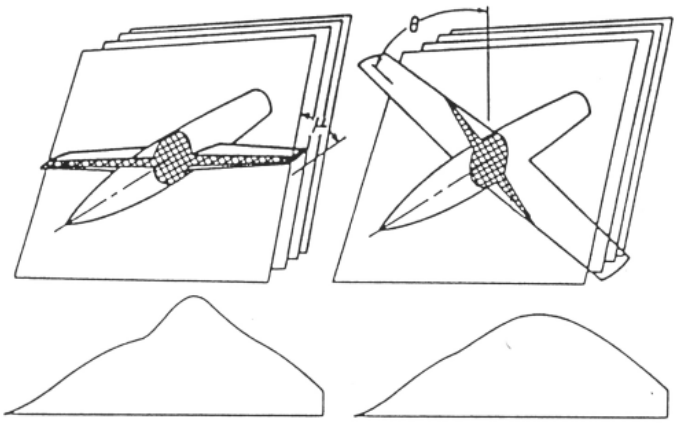


Figure 3-29: Evaluation of the wave drag integral. *From R. V. Harris. NASA. Public domain.*

As previously discussed in section 3.4.5, area ruling plays an important role in supersonic cruise vehicle design. We present the results of our analysis of the NASA AST3I high-speed civil transport (HSCT) concept. Figure 3-30(a) shows the general arrangement of the baseline HSCT configuration—highly blended Mach 3 with a 6,500-mile range.[68]

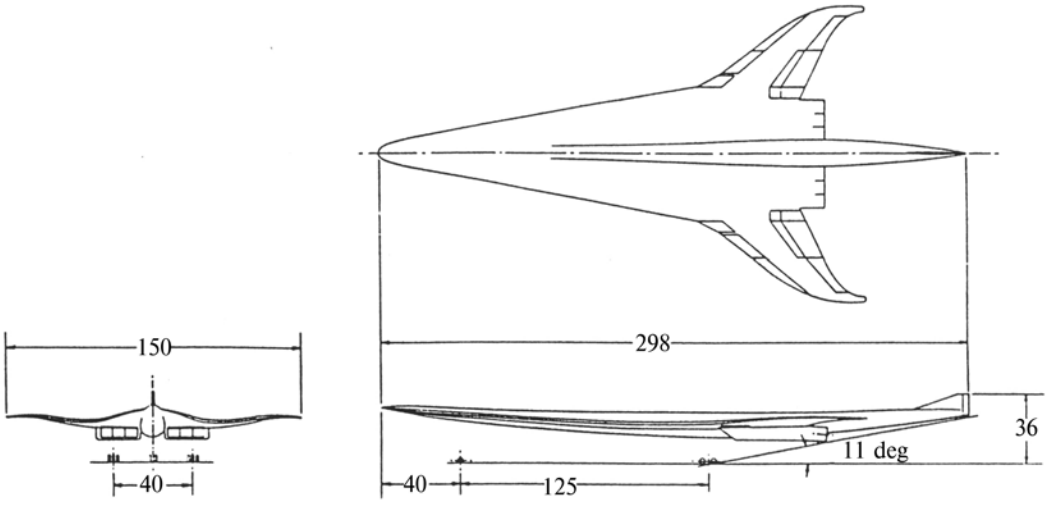


Figure 3-30(a): General arrangement of an advanced concept for a Mach 3 high-speed civil transport by NASA, labeled AST3I. *From Robins, A. W., Dollyhigh, S. M., Beissner, F. L., Jr., Geiselhart, K., Martin, G. L., Shields, E. W., Swanson, E. E., Coen, P. G., Morris, S. J., Jr., "Concept Development of a Mach 3.0 High-Speed Civil Transport," NASA. Public domain. Note: All linear dimensions in feet.*

Figure 3-30(b) shows the variation in drag for the initial NASA concept and our optimized design as the computed results of the integral for several "theta cuts" at Mach 3. The curve titled *Optimized Design* is for a geometry that also contains the results of a combined structural-aerodynamic study to improve this design using systematic advanced design methodology.[69] Note that the drag is presented in terms of *D/q*. This is a traditional approach that eliminates any false impressions produced when configurations with differing reference areas are compared.

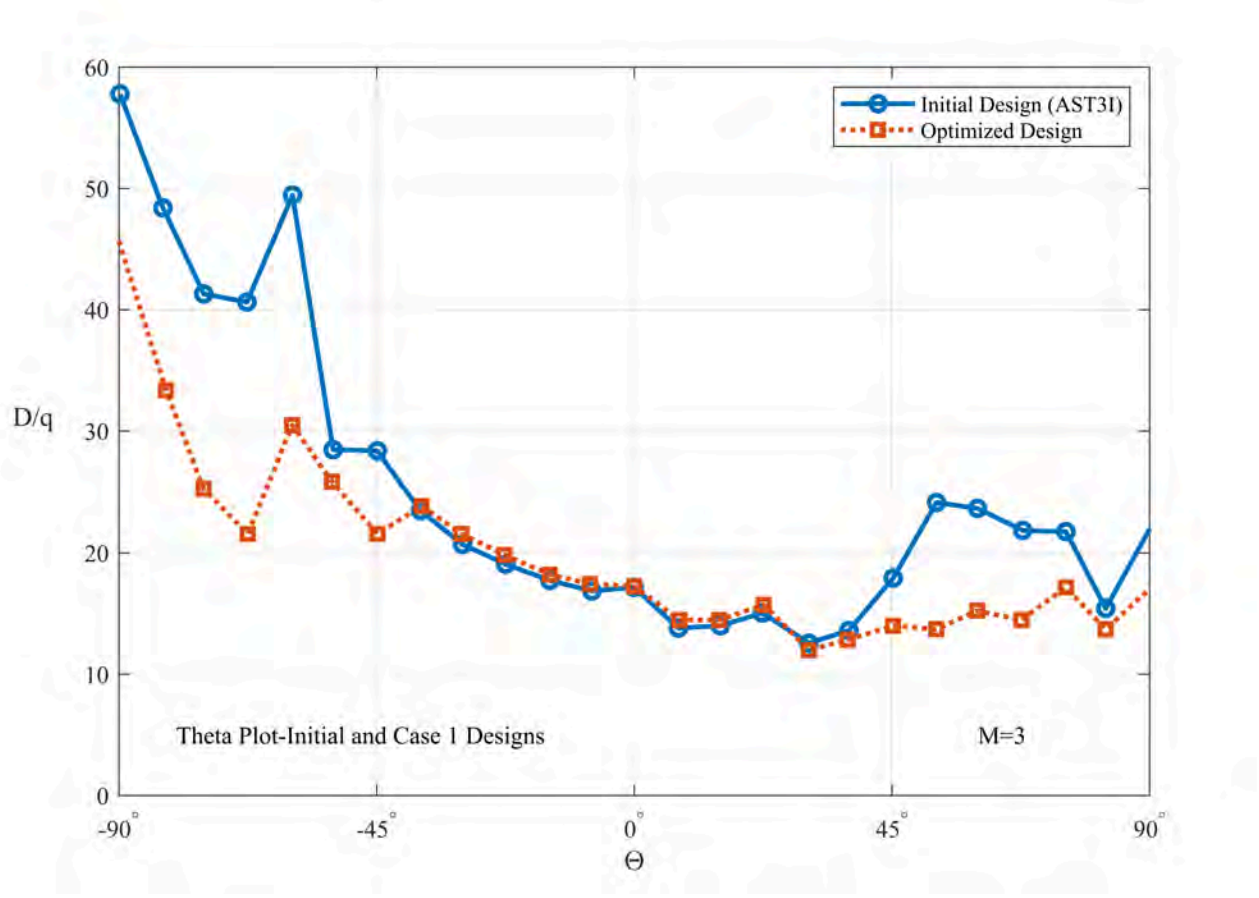


Figure 3-30(b): Distribution of the drag for each circumferential cut for the AST3I configuration at Mach 3.

Figure 3-30(c) shows the normal cross-sectional area distribution. Here, the nacelles are seen to make a large impact on the area distribution. However, the area distribution of interest is for $M = 3.0$. Figures 3-30(d) and 3-30(e) present the area distributions for the $\theta = 0°$ and $\theta = 90°$ cases obtained using the Harris wave drag program. Here, the area distribution is seen to be much smoother. This is especially true for the $\theta = 0°$ case. The $\theta = 90°$ case still involves the problem of integrating the propulsion system into the configuration to obtain a smooth area distribution. Compare the area distributions presented in figures 3-30(d) and 3-30(e) with the change in drag at these two different roll angles, as this will provide some insight into the importance of shaping in producing a smooth area distribution.

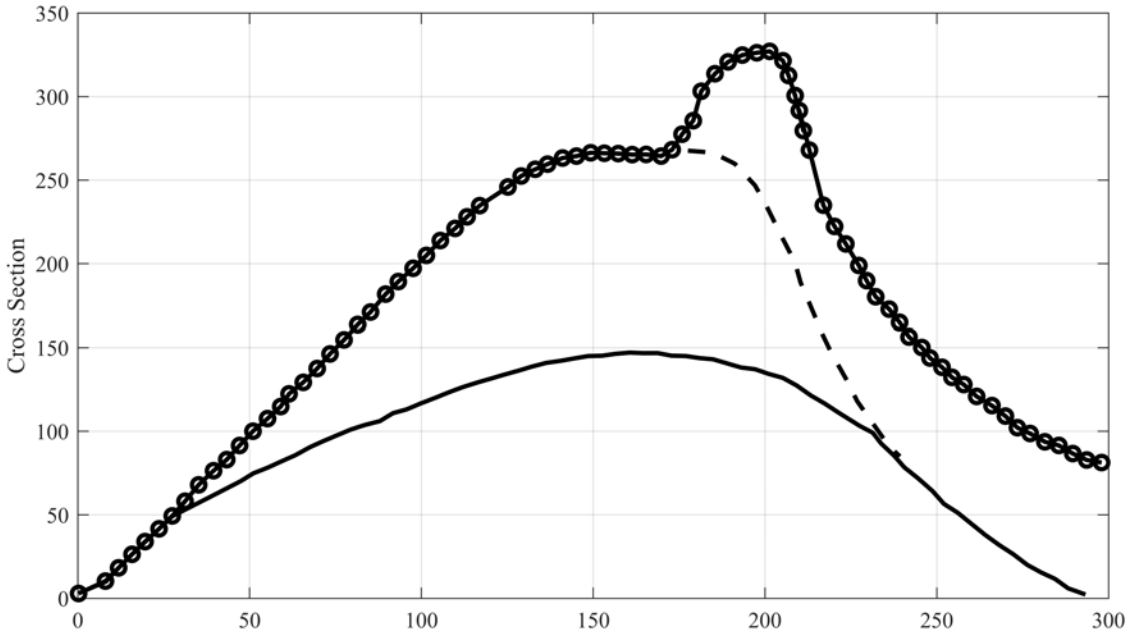


Figure 3-30(c): Normal cross-sectional area distribution (capture area removed).

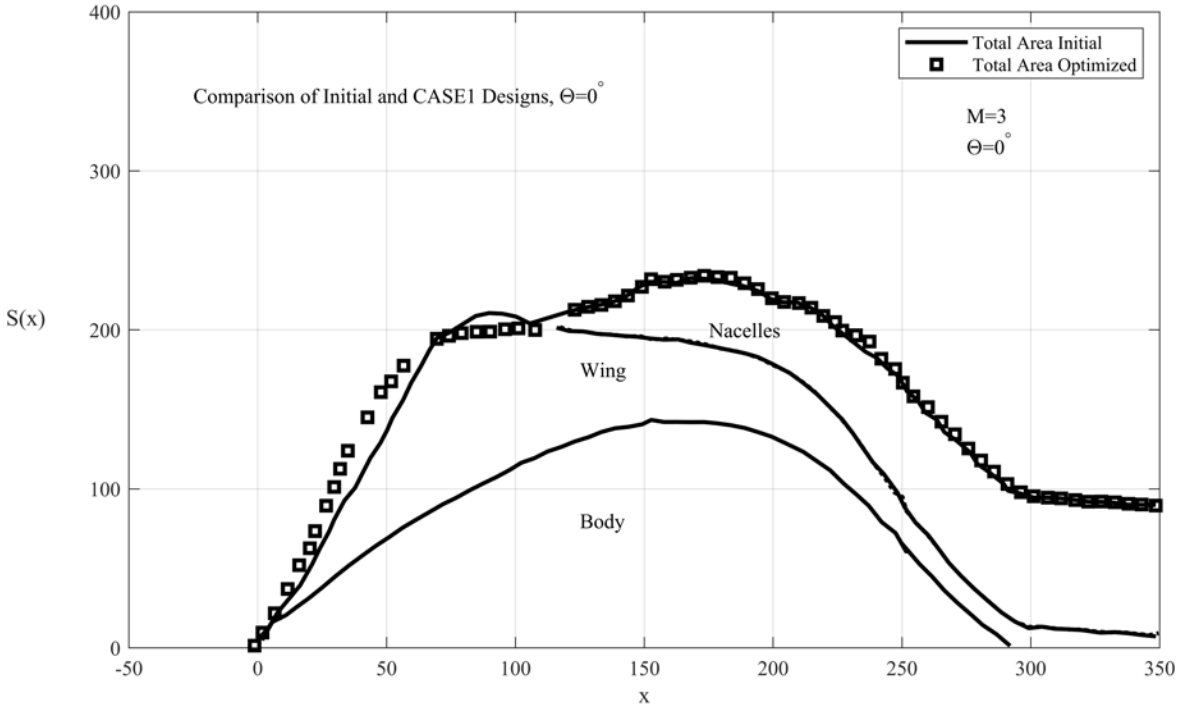


Figure 3-30(d): Mach 3 area distribution, $\theta = 0$ degrees.

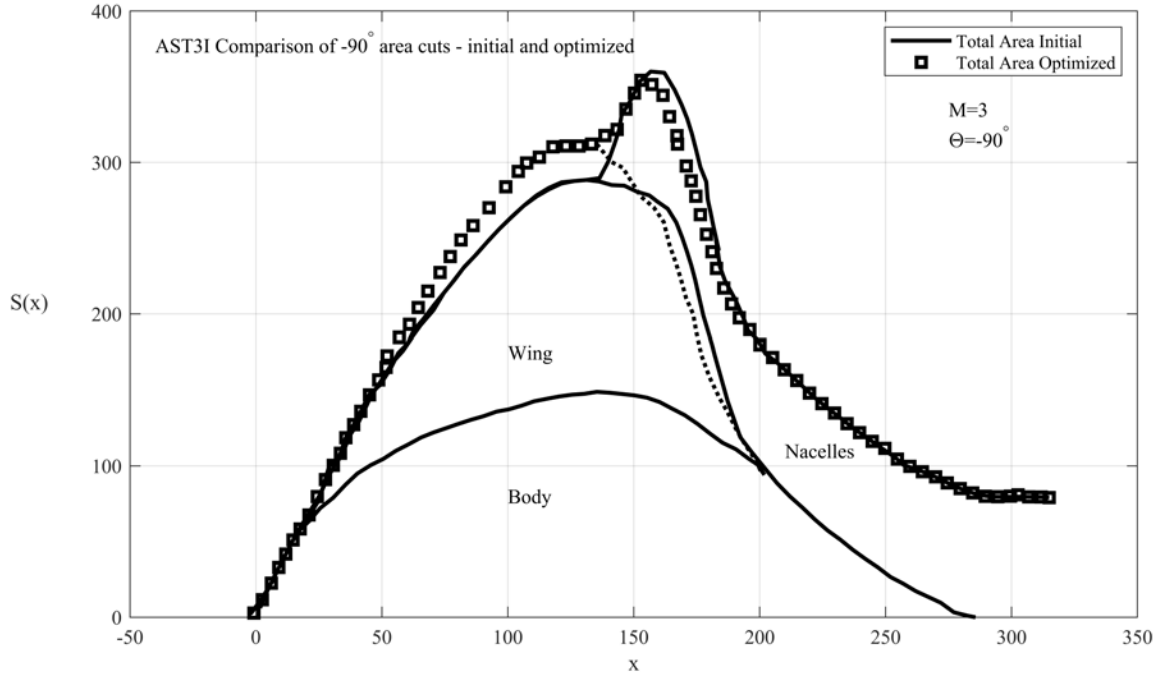


Figure 3-30(e): Mach 3 area distribution, $\theta = 90$ degrees.

Area diagrams for typical fighters are not nearly so streamlined. Figure 3-31(a) shows the original area distribution for the YF-16.[70]

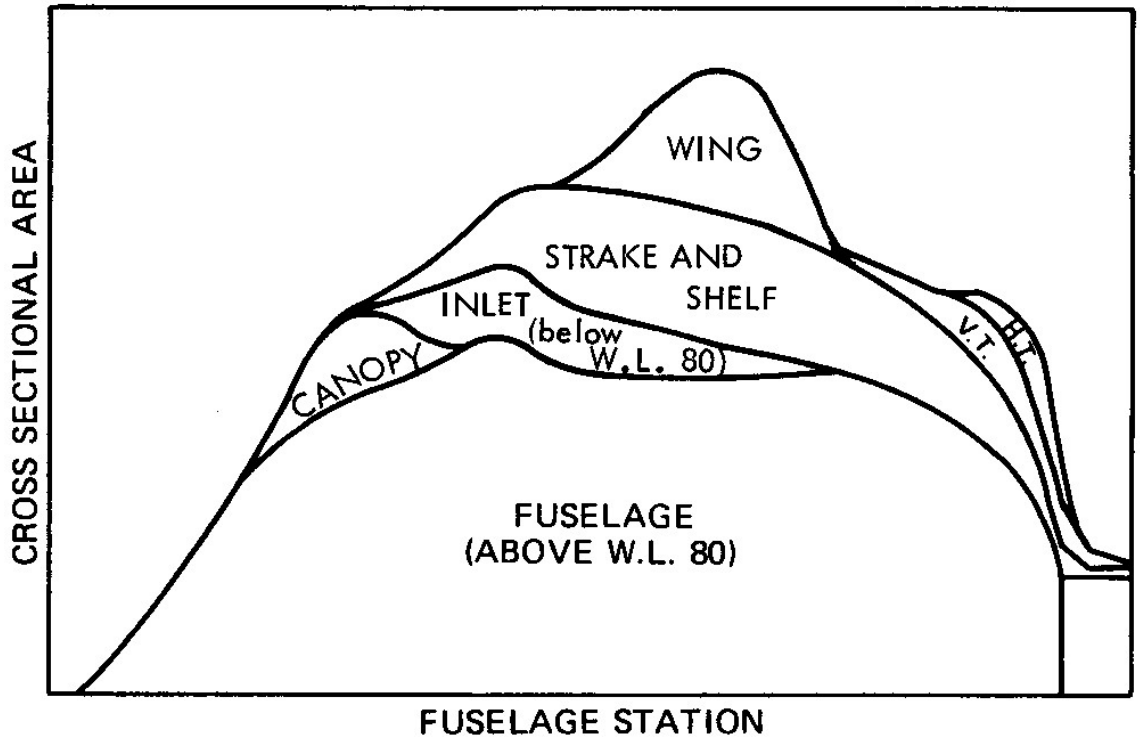


Figure 3-31(a): The YF-16 area rule diagram: Original cross-sectional area. *From J. K. Buckner, D. W. Hill, and D. B. Benepe. "Aerodynamic Design Evolution of the YF-16." Copyright undetermined by AAIA. Fair use.*

Figure 3-31(b) displays the results of refinements on the YF-16. The F-16 was not designed primarily for supersonic flight. It has a low fineness ratio and consequently a relatively high wave drag. Small aircraft are much more difficult to lay out to ensure a smooth distribution of area. Note in figure 3-31(a) that the canopy is placed to help "fill in" the area diagram. Figure 3-31(b) shows the revisions made to improve the contour forward and aft of the maximum cross-sectional area to fill in the shape and also add fuel volume. This curve has no scale. Manufacturers are sensitive about this information.

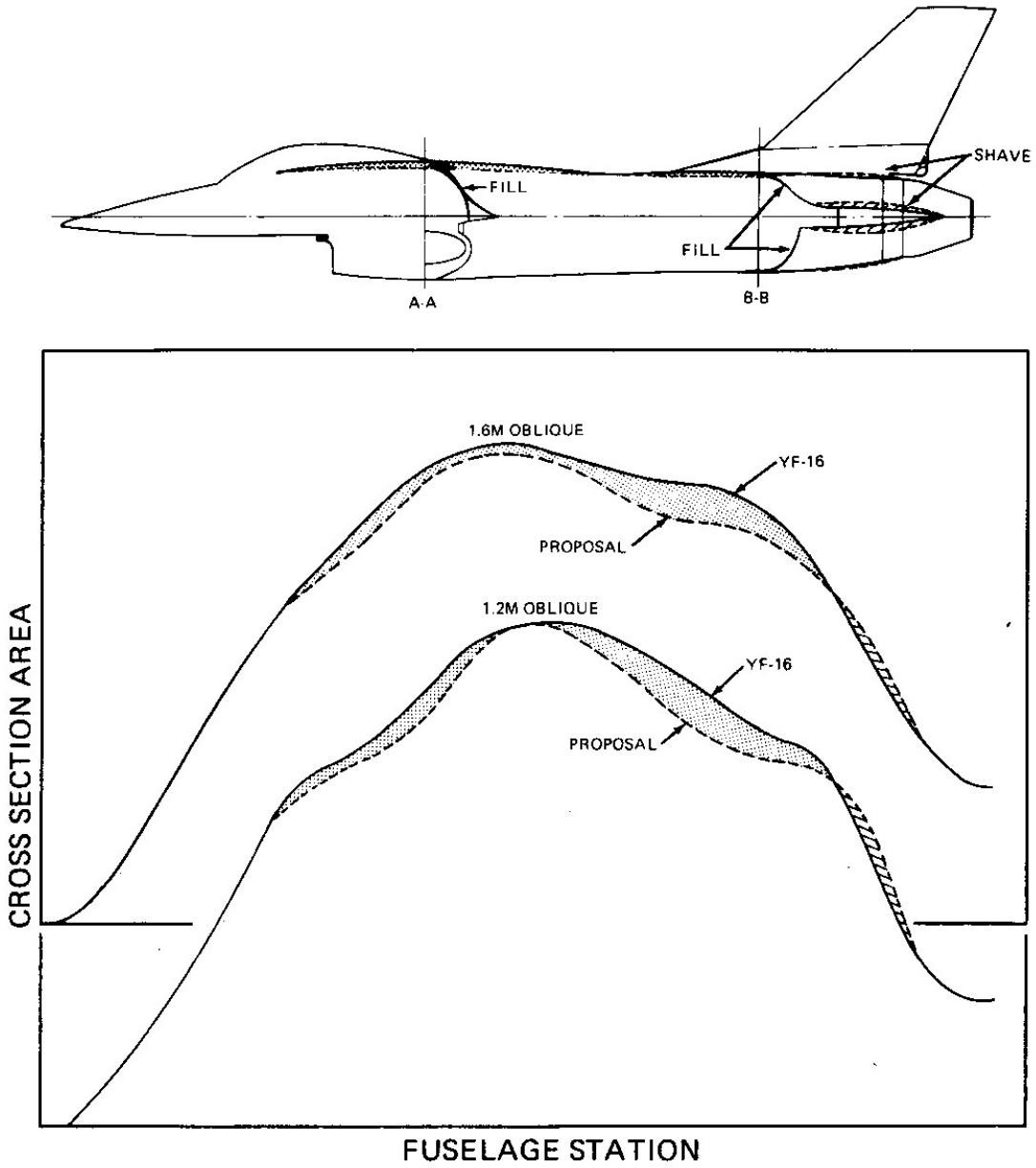


Figure 3-31(b): The YF-16 area rule diagram: Refined area distribution. *From J. K. Buckner, D. W. Hill, and D. B. Benepe. "Aerodynamic Design Evolution of the YF-16." Copyright undetermined by AAIA. Fair use.*

There is also a wave drag due to lift, as discussed by Ashley and Landahl.[71] However, almost all area ruling at supersonic speeds primarily emphasizes the volumetric wave drag.

3.5.6 Trim Drag

For equilibrium flight, the airplane must be trimmed. The forces must be such that the moments about the center of gravity in all axes are zero. To achieve this condition, the control surfaces are usually deflected to generate the required trimming moments.

Figure 3-32 shows a schematic of the requirement. Two typical situations are shown in figure 3-32(a). In one case, the center of gravity is ahead of the wing center of pressure, the aircraft is stable, and a download on the tail is required to balance the moment due to lift of the wing. In the other case, the center of gravity is behind the wing center of pressure, the airplane is unstable, and an upload on the tail is required to balance the moment due to lift of the wing. Other situations are possible, but these two illustrate the key idea.

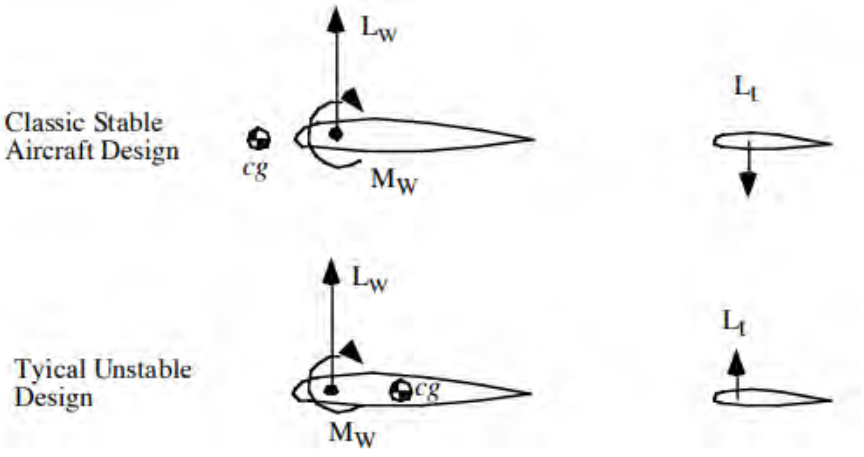


Figure 3-32(a): Surface lift requirements for trim. *From W. H. Mason. Adapted by S. Madden.*

Figure 3-32(b) illustrates the difference between stable and unstable configurations. For a stable airplane, the basic C_{mO} is typically positive, while for an unstable aircraft, the basic C_{mO} is negative. In each case, a control surface has to be deflected over a range of settings to maintain trim over a range of lift coefficients (unless the configuration is neutrally stable). On modern aircraft, the required moment could be provided by the deflection of the thrust through thrust vectoring.

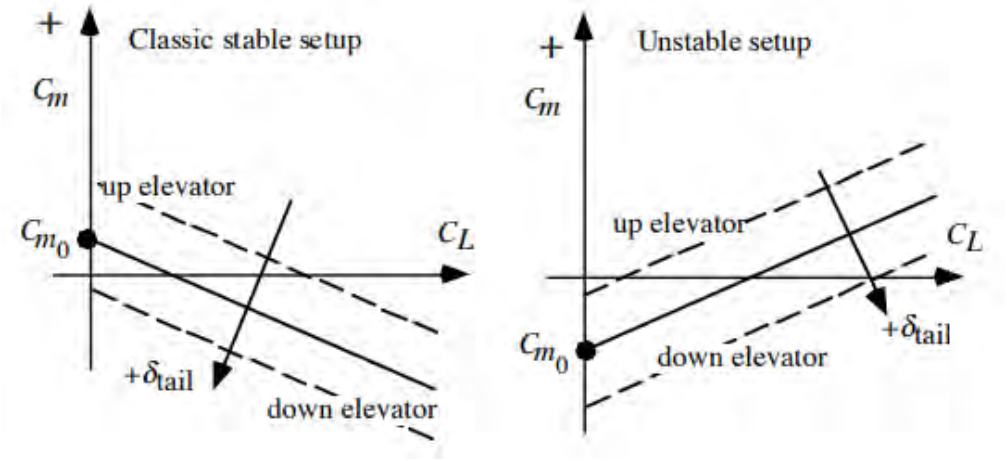


Figure 3-32(b): Idealizations of design requirements for trim.

Control surface deflections change the drag from the undeflected reference value. This difference in drag is known as a trim drag. There are many definitions of trim drag because it is difficult to be precise in defining the term. Some definitions consider only the drag due to the lift of the trimming surface. Some analyses allow for a negative trim drag. However, for a given flight condition, the total lift must be fixed and any change in lift on the trimming surface requires a change in lift and thus drag, on the primary surface. On a well designed aircraft, the trim drag should be small. Canard concepts are often considered advantageous because the canard and wing both supply positive lift to trim, whereas for traditional aft-tail configurations, the tail load is negative and the wing must operate at a higher lift to compensate. However, for modern aft-tail designs, the tail load is near zero, resulting in little trim drag.

Trim drag has always been an important consideration in airplane design. However, trim drag became especially important with the development of stability and control augmentation systems that allowed the designer much greater freedom in choosing a location for the center of gravity. While the static stability condition had frequently made it difficult to obtain minimum trim drag, natural static stability was no longer required. This meant that trim drag could become a key criteria for the placement of the center of gravity in a configuration; this is part of the motivation for so-called control configured vehicle (CCV) concepts.

Trim drag is especially important for several specific classes of aircraft. Supersonic aircraft demand special consideration because of the aerodynamic center shift from subsonic to supersonic flight. To control trim drag as well as stability, fuel is transferred fore and aft between subsonic and supersonic flight to achieve proper balance on supersonic cruise aircraft. Variable-sweep wing aircraft also have aerodynamic center locations that vary with wing sweep, potentially leading to high values of trim drag. Finally, maneuvering aircraft can suffer high trim drag at high lift coefficients, severely limiting sustained turn performance. This was especially true of the first generation of supersonic-capable fighters. Examples of the contribution of trim drag to the total drag are shown in figure 3-33, taken from the aircraft and airship design book by Nicolai and Carichner.[72]

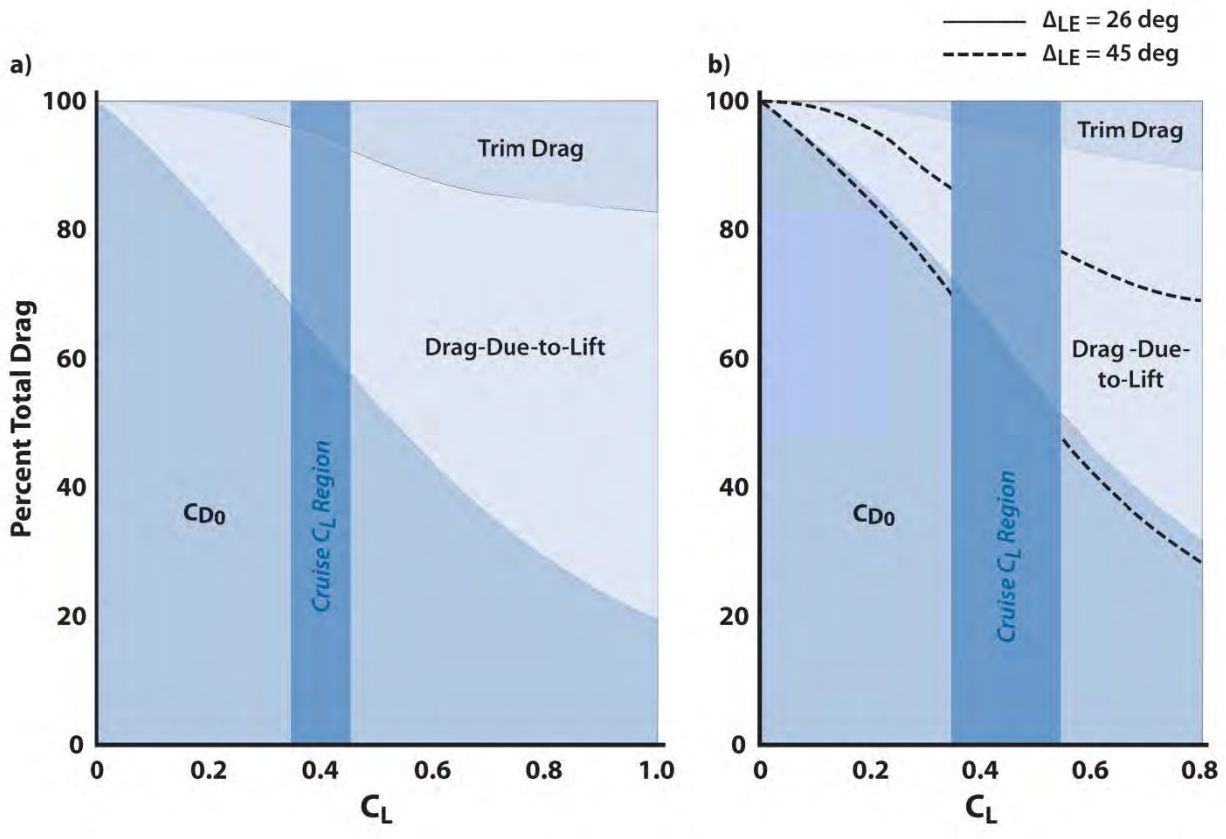


Figure 3-33: Contributions to drag for two configurations: C-141 at M = 0.75 (left) and F-111A (right). *From L. M. Nicolai and G. E. Carichner. "Fundamentals of Aircraft and Airship Design." AIAA. Fair use.*

A more useful approach to the trim drag analysis is to consider the value of trimmed drag. In this approach, it is difficult to define a specific trim drag value. The best way to assess the trim penalty is to define the difference between the minimum drag attainable for the system and the minimum trimmed drag for a specified center of gravity position. This provides the designer with a measurement of the drag penalty being paid for a particular center of gravity location. This approach also demonstrates the direct connection between static margin and minimum trimmed drag. Different configuration concepts lead to different values of static margin to obtain minimum trimmed lift. In general, for aft-swept wings with aft tail configurations, the minimum trimmed drag occurs at a slightly unstable center of gravity (~5%–10%), canard configurations have minimum trim drag at slightly more unstable conditions (~15%), and forward-swept wing canard configurations must be even more unstable to achieve minimum trimmed drag (e.g., the X-29 is about 30%–35% unstable). Many studies of these fundamental properties of various configuration concepts have been made. See the study by Landfield and Rajkovic[73] and the references contained in the study for more information.

Several key papers examining trim drag from a nearfield point of view have been written, including works by McKinney and Dollyhigh,[74] Lutze,[75] and Sachs.[76] In the nearfield, extreme care must be taken to include the downwash incidences and induced angles of attack correctly. Alternately, an analysis can be made in the Trefftz plane. Lamar[77] developed a code for finding the minimum trimmed induced drag for two surfaces, which was extended by Mason[78] to include (approximately) the effects of profile drag. Note that a farfield analysis combining the minimization of induced drag and wave drag due to lift has been presented by Tulinius and Margason.[79] A more general approach to treating multiple surfaces was given by Kuhlman.[80] More recently, three-surface configuration has been introduced, and the three-surface minimum trim drag problem has been solved by Goodrich, Sliwa, and Lallman[81] using a nearfield approach.

An example of the possible dramatic effects of CG location on trimmed drag is presented in figure 3-34.[82] All the results contained in the figure are for the minimum trimmed drag at different values of a specified CG location. These results were obtained during early forward-swept wing configuration studies, illustrating why an aft CG position and resulting highly unstable configuration are required to obtain the full benefits of a forward-swept wing configuration similar to the X-29.* The very high drag values reflect a transonic maneuver condition. Trim drag should be much smaller for the cruise condition (certainly less than 2%–4%). As shown here, modern technology should allow the aircraft to fly with no trim drag. The difference between the minimum trimmed drag at Δx_{cg} = -40% and any other CG could be considered the trim drag. The figure contains both induced and profile drag contributions to the total trimmed drag. As the CG moves forward (x positive in this nomenclature; x = 0 corresponds to neutral stability), the additional load on the canard leads to a rapidly increasing value of the minimum trimmed drag. Because of the increasing load on the canard, the canard airfoil section becomes important. Near the CG for minimum drag, the canard airfoil is not important because the canard is lightly loaded. This figure shows why canard configurations are most efficient when used with unstable configuration concepts. Stable canard configurations are not necessarily the most efficient aerodynamically. Because of the high loads on a stable canard configuration, the canard airfoil section is very carefully selected. Specifically, it is usually highly cambered to achieve the high lift coefficients and has a small leading-edge radius so that it will stall before the main wing.

*The hydraulic power used to activate the canard to achieve apparent stability is obtained from the engine, reducing thrust and resulting in increased fuel flow. Thus, in essence, some trim drag benefits are gained at the expense of increased fuel usage to control the unstable vehicle.

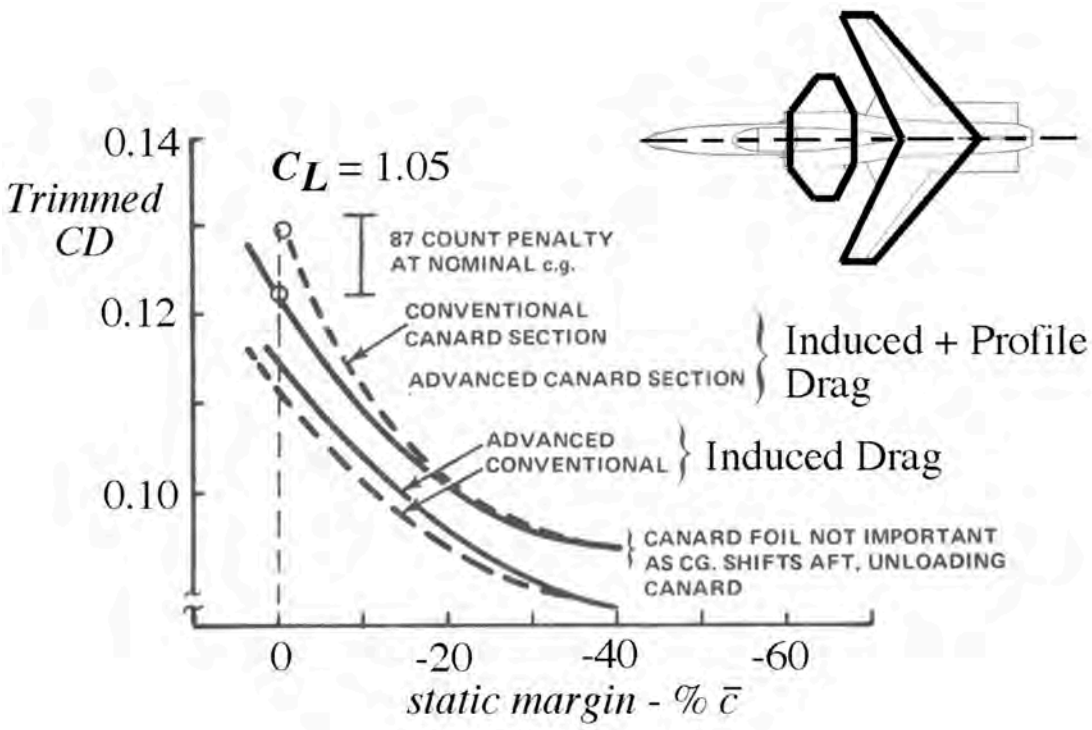


Figure 3-34: Minimum trimmed drag throughout a range of balance locations, including the effect of canard airfoil section. *Adapted from W. H. Mason. "Wing-Canard Aerodynamics at Transonic Speeds—Fundamental Considerations on Minimum Drag Spanloads." Reprinted by permission of the American Institute of Aeronautics and Astronautics, Inc.*

3.6 Accurate Drag Prediction: State of the Art

During the 1990s, significant advances were made in the numerical simulation of viscous flows on complex aircraft configurations using proprietary, commercial, and open source CFD codes based on the Reynolds-averaged Navier–Stokes (RANS) equations with a variety of turbulence models. It goes without saying that RANS codes could compute absolute drag—a quantity of great interest for aerodynamic design of aircraft configurations. Tinoco[83] went so far as to state, "The application of Computational Fluid Dynamics (CFD) to the design of commercial transport aircraft has revolutionized the process of aerodynamic design. Today, CFD stands alongside the wind tunnel in terms of importance." His assertion was, of course, reflective of his extensive experience at Boeing and his awareness of published work of other organizations.

One of the challenges facing the aerodynamics community worldwide was the lack of an impartial assessment of the accuracy of CFD predictions of aerodynamic characteristics in general and of drag in particular. To address this challenge, the AIAA Applied Aerodynamics Technical Committee formed a technical working group (TWG) which recommended conducting an international workshop with the primary goal of assessing state-of-the-art CFD methods as practical aerodynamic tools for the prediction of forces and moments on industry-relevant geometries, with a focus on absolute drag. The motivation was to identify areas needing additional research and development. Several members of the TWG formed the AIAA Drag Prediction Workshop (DPW) organizing committee that hosted a workshop in 2001—the first in a series of workshops discussed next in section 3.6.1.

3.6.1 The Drag Prediction Workshops

In the first AIAA Drag Prediction Workshop in 2001, eighteen international participants using fourteen different codes submitted CFD results for a DLR-F4 wing-body configuration. An AIAA paper by Levy et al.[84] highlights the results, including those of a statistical analysis conducted by Hemsch.[85] Analysis of the results showed a code-to-code scatter of the force and moment predictions that was an order of magnitude larger than anticipated. The CFD drag predictions exhibited a 2-sigma confidence interval of roughly +/- 40 counts (1 count represents a 0.0001 change in drag coefficient). In contrast, the experimental data used for assessing the accuracy of computational predictions exhibited a 2-sigma confidence interval of roughly +/- 8 drag counts.

From these unexpected results, it was easy to conclude that numerical simulations of viscous flows using the then state-of-the-art CFD methods were not accurate enough to earn the trust and confidence of most aerodynamicists. However, the workshop was successful in demonstrating intense interest in the community by bringing together many CFD developers and practitioners, which greatly facilitated the sharing of diverse ideas and best practices. The DPW organizing committee also identified several deficiencies in the quality of the grids supplied to the participants and in the assumption of fully turbulent flow made by many participants. Therefore, the DPW committee decided to organize and host a second workshop, DPW-2, in 2003 with DLR-F6 as the test case. Laflin et al.[86] provide highlights of the important findings.

The DPW-2 established the need and framework for conducting a series of workshops over the subsequent years. Each successive workshop demonstrated improvements in our capabilities for drag prediction while also pointing to the shortcomings to be addressed in the future workshops.

- DPW-3 (2006)—Summary of data and findings compiled in a paper in 2007 by Vassberg et al.[87]
- DPW-4 (2009)—Summary of data and findings compiled in a paper in 2010 by Vassberg et al.[88]
- DPW-5 (2012)—Summary of data and findings compiled in a paper in 2013 by Levy et al.[89]
- DPW-6 (2016)—Summary of data and findings compiled in papers by Roy and Tinoco,[90] Keye and Mavriplis,[91] Tinoco et al.,[92] and Derlaga and Morrison.[93]

Clearly a lot of progress was made in the fifteen years since the first workshop. We encourage interested readers to review the papers cited above to learn about the progress. However, we share three key DPW-6 findings from the paper by Tinoco et al.[94]

1. Computational solutions for a NASA Common Research Model (CRM) wing-body configuration exhibited "tighter" convergence of total drag with a spread of less than ten counts.
2. Results for a NASA CRM wing-body-pylon-nacelle configuration showed that predicted drag increment was within the uncertainty of the test data—a finding of significant importance to aerodynamicists in the industry.
3. Results for NASA CRM wing-body configuration that incorporated static aeroelastic effects showed that lift was overpredicted, whereas the pitching moment was more negative (i.e., nose down) at a given lift coefficient than observed in test data.

The seventh workshop, DPW-7, was held in 2022, with a summary of data and many interesting findings presented in a paper by Tinoco.[95] One of the test cases involved significant shock-induced separation and an assessment of more than thirty different solutions prompted the authors to conclude, "It is obvious from this and prior workshops that there is an interaction between solver, grid, and turbulence model that becomes most prevalent when there is significant shock-induced separation that we don't understand."

In the more than two decades of effort since the first workshop, we have clearly come a long way in terms of developing a comprehensive understanding and assessment of capabilities and shortcomings of the state-of-the-art CFD codes for accurate drag prediction. But we have a long way to go—especially when the flow is complex due to boundary layer separation or dominated by free vortices—to be able to

credibly predict drag. We consider a prediction to be credible if it replicates reality. The state-of-the-art viscous flow simulation methods that are largely based on the RANS equations continue to face serious challenges in providing credible predictions.

3.7 Drag Reduction Possibilities

So far, we have discussed various aspects of aircraft drag prediction because the fuel consumption (or in a broader sense, energy consumption) is heavily dependent on the value of drag. Clearly, the lower the value of drag, the higher the energy efficiency of the aircraft. To explore drag reduction possibilities, it is instructive to assess the relative magnitudes of the drag components. For a typical transport aircraft in the cruise segment of flight that usually dominates its missions, major drag components are skin friction drag and lift-induced drag. The former is about 50%, and the latter about 40%. The remaining 10% is contributed by form drag, interference drag, and wave drag. The challenge for aerodynamicists is quite clear; their main focus ought to be on reducing skin friction and lift-induced drags. We discuss some of the related aspects in this section. Bushnell[96] provides an excellent summary of state-of-the-art drag reduction across the speed range, as well as describing drag reduction approaches.

3.7.1 Skin Friction Drag Reduction

The skin friction drag mainly depends on two factors: (i) wetted area, which depends on the size of the configuration, and (ii) Reynolds number, which is a major determinant as to whether the boundary layer will be laminar or turbulent. It is well known that the boundary layer on a simple flat plate is laminar near the leading edge and transitions to turbulent when the Reynolds number exceeds a critical value. Considerable research has been done over the years on drag reduction technologies based on management of boundary layers. Many researchers have focused their efforts on reducing the skin friction of turbulent boundary layers, while others focus on extending the extent of laminar flow region.

3.7.1.1 Wetted Area Reduction

Since skin friction drag is directly proportional to wetted area, it stands to reason that reducing the wetted area is a straightforward way of reducing the skin friction drag. However, the feasibility of wetted area reduction is rather limited for conventional wing-body-tail configurations (e.g., B-777). Achieving smaller wetted areas requires dramatically different aircraft configuration, as discussed by Torenbeek.[97] Examples of dramatically different aircraft include blended-wing body (figure 1-1) and strut-braced wing (figure 1-2).

3.7.1.2 Turbulent Skin Friction Reduction

Since the boundary layer on nearly the entire surface may be considered to be turbulent in most conventional designs at cruise conditions, many researchers have focused their efforts on devising means of reducing the associated friction drag. Riblets is one of the relatively mature technologies for achieving this. Viswanathan[98] reviews the progress made in the last two decades of the twentieth century. Riblets are small longitudinal striations on the surface that impose spanwise viscous forces to reduce skin friction by 8% to 10%. Riblets can be

applied to the aircraft surface in the form of a self-adhesive film. This technology has been flight tested on the Airbus A320 fuselage. About 75% of the surface was covered with 3M riblet film, which resulted in approximately 1.5% reduction in aircraft drag.

3.7.1.3 Extended Laminar Flow Region

It is well known that skin friction drag of a laminar boundary layer is roughly one order of magnitude less than that of a turbulent boundary layer. Considering the significant impact of the lift-to-drag (L/D) ratio on energy efficiency, let us examine flow on a wing as an example. On most wings, the boundary layer starts out as laminar near the leading edge but transitions to turbulent a short distance downstream. The main contributing factors are (i) Tollmien–Schlichting instability, which amplifies streamwise disturbances to promote transition; (ii) crossflow instabilities that dominate transition for wings with high sweep at high Reynolds number; and (iii) attachment-line instability that is due to disturbances originating in the fuselage boundary layer and propagating along the leading edge. Extensive research has been and is being conducted to develop a comprehensive understanding of these factors and to devise techniques for managing them to increase the extent of the laminar regions. Both passive and active techniques have been devised.

3.7.1.4 Natural Laminar Flow

Natural laminar flow (NLF) is a prime example of a passive technique which relies on shaping the airfoil geometry to extend the laminar-flow region and does not require any extra energy during flight operations. The airfoil geometry is modified to move the maximum thickness point as far aft as possible. This produces favorable pressure gradient on the forward part of the airfoil, which delays transition. Campbell and Lynde[99] and Lynde and Campbell[100] are excellent sources on the advances in and promise of the NLF technique.

3.7.1.5 Laminar Flow Control

Laminar flow control (LFC) encompasses active techniques which rely on either suction to remove small amounts of the boundary layer closest to the surface or blowing to energize the boundary layer. This results in stabilization of the boundary layer that delays transition. Both of these are active techniques because additional energy is required to operate the suction or blowing systems. Torenbeek[101] provides concise descriptions of suction-based LFC techniques in Chapter 4. Researchers have demonstrated that laminar flow can be obtained using LFC on modern airfoil surfaces to midchord and beyond. As Bushnell[102] points out, the major concern is not whether laminar flow can be obtained but rather whether it can be maintained, reliably, in an economic fashion. Some of the real-world challenges hampering the widespread adoption of LFC include surface roughness/waviness, joints and steps (including aeroelastic deformations thereof), flight through ice clouds (visibility under fifty miles can affect LFC system performance), acoustic fields caused by both engine and airframe, and suction-related issues such as plenum acoustics and localized vorticity generation, including clogging effects.

3.7.2 Lift-Induced Drag Reduction

The lift-induced drag is typically about 40% of the total drag in the cruise flight of an aircraft's mission. Therefore, it is highly desirable to reduce it. Increasing the span is the most straightforward approach of reducing it because lift-induced drag is inversely proportional to the square of the span. Reducing lift-induced drag can be quite beneficial for takeoff performance as well. At low speeds, lift-induced

drag can account for up to 90% of the total drag at a critical takeoff condition with a one-engine inoperative. Even a small reduction of lift-induced drag allows the aircraft to take off if an engine fails. However, the designer cannot arbitrarily increase the wingspan without paying a penalty. A larger span increases the structural weight due to the increased bending moment. Aircraft statistical weight equations (that you can find in most aircraft design books) show a strong dependence between wing structural weight and span for all classes of aircraft. Careful tradeoffs must be conducted to determine an optimum span, and this may require the use of modern multidisciplinary design optimization (MDO) methodologies. In addition, practical operational considerations, such as meeting airport gate categories, may limit the span of large transport aircraft.

The strut-braced wing (SBW) is one such configuration which employs a high-aspect-ratio wing and uses a strut to minimize the wing weight penalty that a cantilever long-span wing will pay. The origins of this concept in the 1950s are presented in section 1.2.2. For many years in the 1990s, Virginia Tech conducted extensive concept and technology maturation research.[103,104] You can find more references on the SBW concepts on my websites.[105]

Designers have explored configurations using nonplanar lifting systems (e.g., box wing, joined wing, C-wing, and twin fuselage) that reduce the lift-induced drag. However, design trade studies have not proven significant improvements over the conventional monoplane. For example, wind tunnel tests of a box wing by Miranda and Dougherty[106] verified the predicted low induced drag at high speed. However, flutter analysis revealed both symmetric and antisymmetric instabilities to occur well below the required flutter speed that could not adequately be suppressed. No significant reductions in wing and tail weight were realized for the boxplane relative to a monoplane with the same mission capability. These findings led to the abandonment of boxplane research by Lockheed. However research studies continue, and Salem et al.[107] provide a critical review of design approaches and applications for the box-wing configuration.

3.8 Some Issues for Drag Calculation Using Computational Aerodynamics

Because of the quest for reduced drag and the difficulty in computing and measuring small changes in drag, numerous disputes have arisen in aerodynamics. Confusion introduced by nonstandard drag nomenclature also contributes to these spirited debates. One recent issue was the sheared wingtip drag reduction controversy. Here, it was speculated that wingtip shaping could lead to spans (e's) greater than one for planar planforms.[108] This conclusion arose based on both computations and wind tunnel tests. Refined computational investigations[109] illustrating the need to study computational solution convergence carefully have resulted in the conclusion that e's greater than one were not actually computed. However, it is clear that wingtip planform-shaping can lead to improved aerodynamic efficiency.

Another area is the search for more fundamental understanding of drag. These theories differ significantly from the accepted approach to drag. One key example is found in the work of Yates.[110]

In addition to the efforts to reduce drag due to lift by tip-shaping, use of winglets, tip sails, and canard configurations, among other methods, significant efforts are being made to reduce skin friction drag. They include efforts to obtain laminar flow through passive means (NLF), suction, or a combination known as hybrid natural laminar flow control. Turbulent friction-reduction techniques are also being developed. Riblets are perhaps the most well known means. An AIAA book reviews this area.[111]

3.1 The importance of streamlining

Use experimental data to find the answers for this problem. ("Summary of Airfoil Data," NACA R-824 by Abbott, von Doenhoff, and Stivers is one source of data. It's a free download off the NASA Tech Report Server site at https://ntrs.nasa.gov/citations/19930090976. A version of this report is available as a Dover book, *Theory of Wing Sections*, a standard reference for aerodynamicists.)

Consider an NACA or other symmetrical airfoil. The chord is 2 feet, and the aircraft is flying at 250 mph at sea level.

a. What is the parasite drag?
b. What is the diameter of a wire (circular cylinder) with the same drag? (For an example of circular cylinder drag, look at Anderson's Aero Text for a figure of cylinder drag. Bertin has a similar figure.)
c. What is the ratio of the thickness of the airfoil to the diameter of the wire in this situation?
d. Comment on your findings.

3.2 Compare the test results and the estimated parasite drag for an airfoil.

For the airfoil you used in Exercise 3.1 above:

a. Estimate the parasite drag coefficient for the airfoil using the FRICTION code on my software site or an equivalent program.
b. Compare with the value found in 3.1.
c. Examine the effect of Reynolds number.
d. Examine the effect of transition location. Provide your results through the use of plots that tell the story.
e. Comment on your findings.

3.3 Typical Reynolds number for a transonic transport

Now that we've seen the importance of streamlining, let's develop intuition about Reynolds number values. Estimate the Reynolds of the Boeing 787 flying at a Mach number of 0.85 and at an altitude of 40,000 feet. Comment on your results.

3.4 Drag coefficient versus actual drag

We are used to seeing plots of the skin friction drag coefficients decreasing with increasing Reynolds number. Lets look at a comparison of the skin friction drag coefficient and the actual drag over a range of speeds. Pick a 10-foot chord airfoil at an altitude of 20,000 feet. Plot the results for both the skin friction drag coefficient and the drag from a Mach number of 0.3 to 0.9. Comment on your results.

3.5 Span limitations arising from airport gate requirements

The A380 is subject to the 80-meter gate box limit. What do you think the induced drag penalty is for satisfying this constraint? You could present your solution as a percent comparison with previous Airbus aircraft. Comment on your results.

3.6 Winglet versus span extension

It is often said that a winglet is equivalent to a wingtip extension. Is this true? Küchemann says in his book that a smart endplate (winglet) of height h can increase the aerodynamic efficiency of a wing of span b as

$$e = 1 + \frac{h}{b/2}$$

where

$$C_{D_i} = \frac{C_L^2}{\pi A R e}.$$

Note that Küchemann's approximation is pretty good because vortex lattice studies indicate that

$$e = 1 + 1.06\frac{h}{b/2}.$$

a. What is the difference between an endplate and a winglet?

b. Compare the effect of a winglet with the effect of a simple wingtip extension. Comment on your results.

3.7 Spanload shape effects on the span e

Use LIDRAG or an equivalent program to find the span *e* of an elliptic spanload and a triangular spanload. Comment on your results.

3.8 Insight into the supersonic wave drag of simple axisymmetric bodies

Reference Chapter 9. For a length-to-diameter ratio of 10, what is the difference in the wave drag between a von Karman ogive and a Sears–Haack body? If the answers are different, explain why.

Figure References

Figure 3-2: Figure 1.2 in Jones, R. T. *Wing Theory*. Princeton University Press, Princeton, 1991, p. 6. Adapted by S. Madden. Fair use.

Figure 3-3: W. H. Mason. Adapted by S. Madden. CC BY-NC-SA 4.0

Figure 3-4: P. Raj. CC BY-NC-SA 4.0

Figure 3-7: W. H. Mason. Adapted by S. Madden. CC BY-NC-SA 4.0

Figure 3-8: W. H. Mason. Adapted by S. Madden. CC BY-NC-SA 4.0

Figure 3-9: W. H. Mason. Adapted by S. Madden. CC BY-NC-SA 4.0

Figure 3-11: From Mason, W. H., "Wing-Canard Aerodynamics at Transonic Speeds—Fundamental Considerations on Minimum Drag Spanloads," AIAA Paper 82-0097, Jan. 1982. Adapted by S. Madden under fair use. https://arc.aiaa.org/doi/10.2514/6.1982-97

Figure 3-12: Feifel, W. M., "Optimization and Design of Three-Dimensional Aerodynamic Configurations of Arbitrary Shape by a Vortex Lattice Method," Proceedings of the Vortex Lattice Utilization Workshop, NASA SP-405, 1976, pp. 71–88. Public domain. Adapted by S. Sullivan. https://ntrs.nasa.gov/citations/19760021080

Figure 3-13: Thwaite, B., *Incompressible Aerodynamics*. Oxford University Press. 1960, p. 525. Adapted by S. Madden. Fair use.

Figure 3-15: Kroo, I., "Drag Due to Lift: Concepts for Prediction and Reduction," Annual Review of Fluid Mechanics, Vol. 33, 2001, pp. 587–617. © Used with permission. https://doi.org/10.1146/annurev.fluid.33.1.587

Figure 3-16: W. H. Mason. Adapted by S. Madden. CC BY-NC-SA 4.0

Figure 3-17: W. H. Mason. Adapted by S. Madden. CC BY-NC-SA 4.0

Figure 3-18: W. H. Mason. Adapted by S. Madden. CC BY-NC-SA 4.0

Figure 3-19: W. H. Mason. Adapted by S. Madden. CC BY-NC-SA 4.0

Figure 3-20: W. H. Mason. Adapted by S. Madden. CC BY-NC-SA 4.0

Figure 3-23: From figure 3 in Whitcomb, R. T., "A Study of the Zero Lift Drag-Rise Characteristics of Wing-Body Combinations near the Speed of Sound," NACA TR-1273, 1956, p. 15. Public domain. https://ntrs.nasa.gov/citations/19930092271

Figure 3-24(a): Adapted from Mendenhall, C. A., *Delta Wings: Convair's High Speed Planes of the Fifties and Sixties*, Motorbooks International, Osceola, WI, 1983, pp. 23, 37, and 135. Copyright undetermined by Motorbooks International/Quarto, General Dynamics, and Boeing. Fair use.

Figure 3-24(b): Adapted from Mendenhall, C. A., *Delta Wings: Convair's High Speed Planes of the Fifties and Sixties*, Motorbooks International, Osceola, WI, 1983 Pages 23, 37, 135. Copyright undetermined by Motorbooks International/Quarto, General Dynamics, and Boeing. Fair use.

Figure 3-25: Adapted from Mendenhall, C. A., *Delta Wings: Convair's High Speed Planes of the Fifties and Sixties*, Motorbooks International, Osceola, WI, 1983 Pages 23, 37, 135. Copyright undetermined by Motorbooks International/Quarto, General Dynamics, and Boeing. Fair use.

Figure 3-26(a): US Navy. Official US Navy Standard Aircraft Characteristics (SAC) for the Grumman F11F-1 (F-11A) Tiger Fighter, 1967. Public domain. https://commons.wikimedia.org/wiki/File:Grumman_F11F-1_Tiger_drawings.png

Figure 3-26(b): NASA. Northrop F-5A Freedom Fighter 3. Public domain. https://commons.wikimedia.org/wiki/File:Northrop_F-5_3-view.jpg

Figure 3-27(a): Figure 1 in Mason, W. H., "Analytic Models for Technology Integration in Aircraft Design," AIAA Paper 90-3262, AIAA-AHS-ASEE Aircraft Design, Systems, and Operations Conference, Dayton, OH, Sept. 17-19, 1990. Used with permission. https://doi.org/10.2514/6.1990-3262

Figure 3-27(b): Figure 1 in Mason, W. H., "Analytic Models for Technology Integration in Aircraft Design," AIAA Paper 90-3262, AIAA-AHS-ASEE Aircraft Design, Systems, and Operations Conference, Dayton, OH, Sept. 17-19, 1990. Used with permission. https://doi.org/10.2514/6.1990-3262

Figure 3-28: S. Madden, from data in Mair, W. A., and Birdsall, D. L., *Aircraft Performance*, Cambridge University Press, 1992, pp. 255–257.

Figure 3-29: Figure 1 in Harris, R. V., "An Analysis and Correlation of Aircraft Wave Drag," NASA TM X-947, 1964, p. 3. Public domain. https://www.pdas.com/refs/tmx947.pdf

Figure 3-30(a): Figure 1 in Robins, A. W., Dollyhigh, S. M., Beissner, F. L., Jr., Geiselhart, K., Martin, G. L., Shields, E. W., Swanson, E. E., Coen, P. G., and Morris, S. J., Jr., "Concept Development of a Mach 3.0 HighSpeed Civil Transport," NASA TM-4058, p. 20. Public domain. Labels modified. https://ntrs.nasa.gov/citations/19880017798

Figure 3-31(a): From Buckner, J. K., Benepe, D. B., and Hill, D. W., "Aerodynamic Design Evolution of the F-16," AIAA Paper 74-935, 1974, p. 14. Copyright undetermined by AIAA. Fair use. https://arc.aiaa.org/doi/10.2514/6.1974-935

Figure 3-31(b): From Buckner, J. K., Benepe, D. B., and Hill, D. W., "Aerodynamic Design Evolution of the F-16," AIAA Paper 74-935, 1974, p. 14. Copyright undetermined by AIAA. Fair use. https://arc.aiaa.org/doi/10.2514/6.1974-935

Figure 3-32(a): W. H. Mason. Adapted by S. Madden. CC BY-NC-SA 4.0

Figure 3-33: Figures 3-9 and 3-10 from Nicolai, L. M. and Carichner, G. E., *Fundamentals of Aircraft and Airship Design*, 2010, p. 87. AIAA. Fair use. https://doi.org/10.2514/5.9781600867538.0000.0000

Figure 3-34: Figure 6 in Mason, W. H., "Wing-Canard Aerodynamics at Transonic Speeds—Fundamental Considerations on Minimum Drag Spanloads," AIAA Paper 82-0097, Jan. 1982. Adapted. https://doi.org/10.2514/6.1982-97

Notes

1. Strang, W. J., and McKinlay, R. M., "Concorde in Service," The Aeronautical Journal of the Royal Aeronautical Society, Vol. 83, No. 818, Feb. 1979, pp. 39–52.
2. Sloof, J. W., ed., "Technical Status Review on Drag Prediction and Analysis from Computational Fluid Dynamics: State of the Art," AGARD-AR-256, Jun. 1989.
3. "Aerodynamic Drag," AGARD CP-124, Apr. 1973.
4. "Aircraft Excrescence Drag," AGARD AG-264, 1981.
5. "Aircraft Drag Prediction and Reduction," AGARD-R-723, 1985.
6. "Special Course on Skin Friction Drag Reduction," AGARD R-786, Mar. 1992.
7. Covert, E. E., ed., *Thrust and Drag: Its Prediction and Verification*, AIAA, New York, 1985.
8. Hoerner, S., *Fluid Dynamic Drag*. (*Note*: Originally published by the author and is available from Hoerner Fluid Dynamics, PO Box 21992, Bakersfield, CA 93390.)
9. Van Dam, C. P., "Recent experience with different methods of drag prediction," Progress in Aerospace Sciences, Vol. 35, No. 8, Nov. 1999, pp. 751–798.
10. Torenbeek, E., *Synthesis of Subsonic Airplane Design*, Delft University Press, Delft, 1982.
11. Jones, R. T., *Wing Theory*, Princeton University Press, Princeton, 1991.
12. Whitford, R., Design for Air Combat, Jane's, London, 1987.
13. Huenecke, K., *Modern Combat Aircraft Design*, Naval Institute Press, Annapolis, 1987.
14. Haines, A. B., "Subsonic Aircraft Drag: An Appreciation of the Standards," The Aeronautical Journal of the Royal Aeronautical Society, Vol. 72, No. 687, Mar. 1968, pp. 253–266.
15. Küchemann, D., *The Aerodynamic Design of Aircraft*, Pergamon Press, Oxford, 1978.
16. Lynch, F. T., "Commercial Transports—Aerodynamic Design for Cruise Performance Efficiency," in *Transonic Aerodynamics*, edited by D. Nixon, Progress in Astronautics and Aeronautics, Vol. 181, AIAA, New York, 1982.
17. Shevell, R. S., "Aerodynamic Bugs: Can CFD Spray Them Away?" AIAA Paper 85-4067, Oct. 1985. (*Note*: Also published as "Aerodynamic Anomalies: Can CFD Prevent or Correct Them?" in the *Journal of Aircraft*, Vol. 23, No. 8, Aug. 1986, pp. 641–649.)
18. Shevell, R. S., *Fundamentals of Flight*, 2nd ed., Prentice-Hall, Englewood-Cliffs, 1989.
19. Rooney, E. C., "Thrust-Drag Accounting Methodology," in *Thrust and Drag: Its Prediction and Verification*, edited by E. E. Covert, AIAA, New York, 1985.
20. Ashley, H., and Landahl, M., *Aerodynamics of Wings and Bodies*, Addison-Wesley, Reading, 1965. (Note: Now published by Dover.)
21. Heaslet, M. A., and Lomax, H., "Supersonic and Transonic Small Perturbation Theory," in *General Theory of High Speed Aerodynamics*, edited by W. R. Sears, Princeton University Press, 1954, sec. D-14, pp. 221–229.
22. Ashley, H., and Landahl, M., *Aerodynamics of Wings and Bodies*, Addison-Wesley, Reading, 1965.
23. Liepmann, H. W., and Roshko, A., *Elements of Gasdynamics*, John Wiley, New York, 1957, pp. 235–239. (*Note*: Now published by Dover.)
24. Harris, R. V., "An Analysis and Correlation of Aircraft Wave Drag," NASA TM X-947, 1964.
25. Ashley, H., and Landahl, M., *Aerodynamics of Wings and Bodies*, Addison-Wesley, Reading, 1965.
26. Kroo, I., "Drag Due to Lift: Concepts for Prediction and Reduction," Annual Review of Fluid Mechanics, Vol. 33, 2001, pp. 587–617.
27. Ashley, H., and Landahl, M., *Aerodynamics of Wings and Bodies*, Addison-Wesley, Reading, 1965.
28. Sears, W. R., "On Calculation of Induced Drag and Conditions Downstream of a Lifting Wing," Journal of Aircraft, Vol. 11, No. 3, Mar. 1974, pp.191–192.
29. Mason, W. H., "Wing-Canard Aerodynamics at Transonic Speeds—Fundamental Considerations on Minimum Drag Spanloads," AIAA Paper 82-0097, 20th Aerospace Sciences Meeting, Orlando, FL, Jan. 11-14, 1982.

30. Lamar, J. E., "A Vortex Lattice Method for the Mean Camber Shapes of Trimmed Non-Coplanar Planforms with Minimum Vortex Drag " NASA TN D-8090, June 1976.
31. Letcher, J. S., Jr., "V-wings and Diamond Ring Wings of Minimum Induced Drag," AIAA Journal of Aircraft, Vol. 9, No. 8, Aug. 1972, pp. 605–607.
32. Feifel, W. M., "Optimization and Design of Three-Dimensional Aerodynamic Configurations of Arbitrary Shape by a Vortex Lattice Method," in *Proceeding of the Vortex Lattice Utilization Workshop*, NASA SP-405, 1976, pp.71–88.
33. Lundry, J. L., "A Numerical Solution for the Minimum Induced Drag, and the Corresponding Loading, of Nonplanar Wings," NASA CR-1218, 1968.
34. Thwaites, B. (ed.), *Incompressible Aerodynamics, An Account of the Theory and Observation of the Steady Flow of Incompressible Fluid past Aerofoils, Wings, and Other Bodies*, Dover Publications, 1987, pp. 454–457, 523–527.
35. Milne-Thomson, L. M., *Theoretical Aerodynamics*, Dover, New York, 1973, pp. 218–219.
36. Kroo, I., "Drag Due to Lift: Concepts for Prediction and Reduction," Annual Review of Fluid Mechanics, Vol. 33, 2001, pp. 587–617.
37. DeYoung, J., "Minimization Theory of Induced Drag Subject to Constraint Conditions," NASA CR-3140, June 1979.
38. DeYoung, J., "Induced Drag Ideal Efficiency Factor of Arbitrary Lateral-Vertical Wing Forms," NASA CR-3357, December, 1980.
39. McKinney, L. W., and Dollyhigh, S. M., "Some Trim Drag Considerations for Maneuvering Aircraft," Journal of Aircraft, Vol. 8, No. 8, Aug. 1971, pp. 623–629.
40. Raymer, D. P., *Aircraft Design: A Conceptual Approach*, 3rd ed., AIAA, Reston, 1999.
41. Carlson, H. W., Mack, R. J., and Barger, R. L., "Estimation of Attainable Leading Edge Thrust for Wings at Subsonic and Supersonic Speeds," NASA TP-1500, 1979.
42. Mann, M. J., and Carlson, H. W., "Aerodynamic Design of Supersonic Cruise Wings with a Calibrated Linearized Theory," AIAA Journal of Aircraft, Vol. 31, No. 1, Jan.-Feb. 1994, p. 35; based on Mann, M. J., and Carlson, H. W., "An Assessment of Current Methods for Drag-Due-To-Lift Minimization at Supersonic Speeds," AIAA Paper 91-3302, 9th Applied Aerodynamics Conference, Baltimore, MD, Sep 23-25, 1991.
43. Mason, W. H., and DaForno, G., "Opportunities for Supersonic Performance Gains Through Non-Linear Aerodynamics," AIAA Paper 79-1527, 12th Fluid and Plasma Dynamics Conference, Williamsburg, VA, Jul. 23-25, 1979.
44. Eminton, E., and Lord W. T., "Note on the Numerical Evaluation of the Wave Drag of Smooth Slender Bodies Using Optimum Area Distributions for Minimum Wave Drag," Journal of the Royal Aeronautical Society, Vol. 60, Jan. 1956, pp. 61–63.
45. Whitcomb, R. T., "A Study of the Zero Lift Drag-Rise Characteristics of Wing-Body Combinations Near the Speed of Sound," NACA Report 1273, 1956.
46. Mendenhall, C., *Delta Wings—Convair's High Speed Planes of the Fifties and Sixties*, Motorbooks International, Osceola, WI, 1983.
47. Mendenhall, C., *Delta Wings—Convair's High Speed Planes of the Fifties and Sixties*, Motorbooks International, Osceola, WI, 1983.
48. *Jet Fighters of the World Part 2*, Kantosha Co. Ltd., Tokyo, 1965. (*Note*: In Japanese.)
49. Küchemann, D., *The Aerodynamic Design of Aircraft*, Pergamon Press, Oxford, 1978.
50. Stuart, W. G., "Northrop F-5 Case Study in Aircraft Design," AIAA Professional Study Series, Sept. 1978.
51. Jobe, C. E., "Chapter IV: Thrust and Drag: Its Prediction and Verification" in *Prediction and Verification of Aerodynamic Drag, Part I: Prediction*, edited by E. E. Covert, AIAA, New York, 1985.
52. Cummings, R. M., and Mason, W. H., Morton, S. A., and McDaniel, D. R., *Applied Computational Aerodynamics: A Modern Engineering Approach*, Cambridge University Press, 2015.
53. Paterson, J. H., MacWilkinson, D. G., and Blackerby, W. T., "A Survey of Drag Prediction Techniques Applicable to Subsonic and Transonic Aircraft Design," in "Aerodynamic Drag," AGARD CP 124, Apr. 1973.
54. Hoerner, S., *Fluid Dynamic Drag*. (*Note*: Originally published by the author and is available from Hoerner Fluid Dynamics, PO Box 21992, Bakersfield, CA 93390.)
55. Covert, E. E. (ed.), *Thrust and Drag: Its Prediction and Verification*, AIAA, New York, 1985.
56. FRICTION Online Manual. https://archive.aoe.vt.edu/mason/Mason_f/FRICTman.pdf
57. Mason, W. H., Mackenzie, D., Stern, M., Ballhaus, W. F., and Frick, J., "An Automated Procedure for Computing the Three Dimensional Transonic Flow over Wing-Body Combinations, Including Viscous Effects," AFFDL-TR-77-122, Feb. 1978.
58. Lamar, J. E., "A Vortex Lattice Method for the Mean Camber Shapes of Trimmed Non-Coplanar Planforms with Minimum Vortex Drag," NASA TN D-8090, June 1976.
59. Mason, W. H., "Wing-Canard Aerodynamics at Transonic Speeds-Fundamental Considerations on Minimum Drag Spanloads," AIAA Paper 82-0097, 20th Aerospace Sciences Meeting, Orlando, FL, January 11-14, 1982.
60. Mason, W. H., "Analytic Models for Technology Integration in Aircraft Design," AIAA Paper 90-3262, AIAA/AHS/ASEE Aircraft Design, Systems and Operations Conference, Dayton, OH, September 17-19, 1990.
61. Shevell, R. S., *Fundamentals of Flight*, 2nd ed., Prentice-Hall, Englewood-Cliffs, 1989, p. 223.
62. Harris, C. D., "NASA Supercritical Airfoils," NASA TP-2969, Mar. 1990.
63. Mason, W. H., "Analytic Models for Technology Integration in Aircraft Design," AIAA Paper 90-3262, AIAA/AHS/ASEE Aircraft Design, Systems, and Operations Conference, Dayton, OH, September 17-19, 1990.
64. Malone, B., and Mason, W. H., "Multidisciplinary Optimization in Aircraft Design Using Analytic Technology Models," Journal of Aircraft, Vol. 32, No. 2, Mar.-Apr., 1995, pp. 431–438.
65. Hilton, W. F., *High Speed Aerodynamics*, Longmans, Green, & Co., London, 1952, pp. 47–49.

66. Grasmeyer, J. M., Naghshineh, A., Tetrault, P.-A., Grossman, B., Haftka, R. T., Kapania, R. K., Mason, W. H., and Schetz, J. A., "Multidisciplinary Design Optimization of a Strut-Braced Wing Aircraft with Tip-Mounted Engines," Virginia Tech MAD Center Report MAD 98-01-01, Jan. 1998.
67. Harris, R. V., "An Analysis and Correlation of Aircraft Wave Drag," NASA TM X-947, 1964.
68. Robins, A. W., Dollyhigh, S. M., Beissner, F. L., Jr., Geiselhart, K., Martin, G. L., Shields, E. W., Swanson, E. E., Coen, P. G., and Morris, S. J., Jr., "Concept Development of a Mach 3.0 High- Speed Civil Transport," NASA TM-4058, 1988.
69. Hutchison, M., Unger, E., Mason, W. H., Grossman, B., and Haftka, R., "Variable-Complexity Aerodynamic Optimization of an HSCT Wing Using Structural Wing-Weight Equations," AIAA Paper 92-0212, 30th AIAA Aerospace Sciences Meeting and Exhibit, Reno, NV, Jan. 6-9, 1992.
70. Buckner, J. K., Hill, P. W., and Benepe, D. B., "Aerodynamic Design Evolution of the YF-16," AIAA Paper 74-935, 6th Aircraft Design, Flight Test and Operations Meeting, Los Angeles, CA, Aug. 12-14, 1974.
71. Ashley, H., and Landahl, M., *Aerodynamics of Wings and Bodies*, Addison-Wesley, Reading, 1965, sections 1.6, 6.6, 7.3 and 9.2.
72. Nicolai, L. M., and Carichner, G. E., *Fundamentals of Aircraft and Airship Design, Volume I-Aircraft Design*, AIAA Education Series, AIAA, Reston, VA, 2010.
73. Landfield, J. P., and Rajkovic, D., "Canard/Tail Comparison for an Advanced Variable-Sweep-Wing Fighter," AIAA Paper 84-2401, AIAA/AHS/ASEE Aircraft Design, Systems, and Operations Meeting, San Diego, CA, Oct. 31-Nov. 2, 1984.
74. McKinney, L. W., and Dollyhigh, S. M., "Some Trim Drag Considerations for Maneuvering Aircraft," Journal of Aircraft, Vol. 8, No. 8, Aug. 1971, pp. 623–629.
75. Lutze, F. H., "Trimmed Drag Considerations," Journal of Aircraft, Vol. 14, No. 6, Jun. 1977, pp. 544–546.
76. Sachs, G., "Minimum Trimmed Drag and Optimum c.g. Position," *Journal of Aircraft*, Vol. 15, No. 8, Aug. 1978, pp. 456–459.
77. Lamar, J. E., "A Vortex Lattice Method for the Mean Camber Shapes of Trimmed Non-Coplanar Planforms with Minimum Vortex Drag," NASA TN D-8090, June, 1976.
78. Mason, W. H., "Wing-Canard Aerodynamics at Transonic Speeds—Fundamental Considerations on Minimum Drag Spanloads," AIAA Paper 82-0097, Jan. 1982.
79. Tulinius, J. R., and Margason, R. J., "Aircraft Aerodynamic Design and Evaluation Methods," AIAA Paper 76-15, Jan. 1976.
80. Kuhlman, J. M., "Higher Order Farfield Drag Minimization for a Subcritical Wing Design," Journal of Aircraft, Vol. 17, No. 9, Sept. 1980, pp. 648–655.
81. Goodrich, K. H., Sliwa, S. M., and Lallman, F. J., "A Closed-Form Trim Solution Yielding Minimum Trim Drag for Airplanes with Multiple Longitudinal Control Effectors," NASA TP-2907, May 1989.
82. Mason, W. H., "Wing-Canard Aerodynamics at Transonic Speeds—Fundamental Considerations on Minimum Drag Spanloads," AIAA Paper 82-0097, 20th Aerospace Sciences Meeting, Orlando, FL, Jan. 11-14, 1982.
83. Tinoco, E. N., "The Changing Role of Computational Fluid Dynamics in Aircraft Development," AIAA-98-2512, 16th Applied Aerodynamics Conference, Albuquerque, NM, Jun. 15-18, 1998.
84. Levy, D. W., Zickuhr, T., Vassberg, J., Agrawal, S., Wahls, R. A., Pirzadeh, S., and Hemsch, M. J., "Summary of Data from the First AIAA CFD Drag Prediction Workshop," AIAA-2002-0841, 40th Aerospace Sciences Meeting, Reno, NV, Jan. 14-17, 2002.
85. Hemsch, M., "Statistical Analysis of CFD Solutions from the Drag Prediction Workshop," AIAA-2002-0842, 40th Aerospace Sciences Meeting, Reno, NV, Jan. 14-17, 2002.
86. Laflin, K. R., Vassberg, J. C., Wahls, R. A., Morrison, J. H., Brodersen, O. P., Rakowitz, M., Tinoco, E. N., Godard, J., "Summary of Data from the Second AIAA CFD Drag Prediction Workshop," AIAA-2004-0555, 42nd Aerospace Sciences Meeting, Reno, NV, Jan. 5-8, 2004.
87. Vassberg, J. C., Tinoco, E., Mani, M., Brodersen, O. P., Eisfeld, B., Wahls, R. A., Morrison, J. H., Zickuhr, T., Laflin, K. R., and Mavriplis, D. J., "Summary of the Third AIAA CFD Drag Prediction Workshop," AIAA-2007-0260, 45th Aerospace Sciences Meeting, Reno, NV, Jan. 8-11, 2007.
88. Vassberg, J. C., Tinoco, E. N., Mani, M., Rider, B., Zickuhr, T., Levy, D. W., Brodersen, O. P., Eisfeld, B., Crippa, S., Wahls, R. A., Morrison, J. H., Mavriplis, D. J., and Murayama, M. "Summary of the Fourth AIAA CFD Drag Prediction Workshop," AIAA-2010-4547, 28th Applied Aerodynamics Conference, Chicago, IL, Jun. 28-Jul. 1, 2010.
89. Levy, D. W., Laflin, K. R., Tinoco, E. N., Vassberg, J. C., Mani, M., Rider, B., Rumsey, C., Wahls, R. A., Morrison, J. H., Brodersen, O. P., Crippa, S., Mavriplis, D. J., and Murayama, M., "Summary of Data from the Fifth AIAA CFD Drag Prediction Workshop," AIAA-2013-0046, 51st Aerospace Sciences Meeting, Grapevine, TX, Jan. 7-10, 2013.
90. Roy, C. J. and Tinoco, E. N., "Summary of Data from the Sixth AIAA CFD Drag Prediction Workshop: Case 1 Code Verification," AIAA-2017-1206, 55th Aerospace Sciences Meeting, Grapevine, TX, Jan. 9-13, 2017.
91. Keye, S., and Mavriplis, D., "Summary of Data from the Sixth AIAA CFD Drag Prediction Workshop: Case 5 (Coupled Aero-Structural Simluation)," AIAA-2017-1207, 55th Aerospace Sciences Meeting, Grapevine, TX, Jan. 9-13, 2017.
92. Tinoco, E. N., Brodersen, O. P., Keye, S., Laflin, K. R., Feltrop, E., Vassberg, J. C., Mani, M., Rider, B., Wahls, R. A., Morrison, J. H., Hue, D., Roy, C. J., Mavriplis, D. J., and Murayama, M., "Summary of Data from the Sixth AIAA CFD Drag Prediction Workshop: CRM Cases 2 to 5," AIAA-2017-1208, 55th Aerospace Sciences Meeting, Grapevine, TX, Jan. 9-13, 2017.
93. Derlaga, J. M., and Morrison, J. H., "Statistical Analysis of CFD Solutions from the 6th AIAA CFD Drag Prediction Workshop," AIAA-2017-1209, 55th Aerospace Sciences Meeting, Grapevine, TX, Jan. 9-13, 2017.
94. Tinoco, E. N., Brodersen, O. P., Keye, S., Laflin, K. R., Feltrop, E., Vassberg, J. C., Mani, M., Rider, B., Wahls, R. A., Morrison, J. H., Hue, D., Roy, C. J., Mavriplis, D. J., and Murayama, M., "Summary of Data from the Sixth AIAA CFD Drag Prediction Workshop: CRM Cases 2 to 5," AIAA-2017-1208, 55th Aerospace Sciences Meeting, Grapevine, TX, Jan. 9-13, 2017.
95. Tinoco, E. N., "Summary Data from the Seventh AIAA CFD Drag Prediction Workshop," AIAA-2023-3492, Aviation Forum, San Diego, CA, Jun. 12-16, 2023.

96. Bushnell, D. M. "Aircraft Drag Reduction—A Review." *Proceedings of the Institution of Mechanical Engineers, Part G: Journal of Aerospace Engineering*, Vol. 217, 2003, pp. 1–18. https://doi.org/10.1243/095441003763031789
97. Torenbeek, E., Advanced Aircraft Design, John Wiley & Sons., Ltd., 2013.
98. Viswanathan, P. R., "Aircraft viscous drag reduction using riblets," Progress in Aerospace Sciences, Vol. 38, Nos. 6-7, Aug.-Oct. 2002, pp. 571–600.
99. Campbell, R. L., and Lynde, M. N., "Natural Laminar Flow Design for Wings with Moderate Sweep," AIAA 2016-4326, Jun. 2016.
100. Lynde, M. N., and Campbell, R. L., "Computational Design and Analysis of a Transonic Natural Laminar Flow Wing for a Wind Tunnel Model," AIAA 2017-3058, Jun. 2017.
101. Torenbeek, E., *Advanced Aircraft Design*, John Wiley & Sons., Ltd., 2013.
102. Bushnell, D. M. "Aircraft Drag Reduction—A Review." *Proceedings of the Institution of Mechanical Engineers, Part G: Journal of Aerospace Engineering*, Vol. 217, 2003, pp. 1–18. https://doi.org/10.1243/095441003763031789
103. Grasmeyer, J. M., Naghshineh, A., Tetrault, P.-A., Grossman, B., Haftka, R. T., Kapania, R. K., Mason, W. H., and Schetz, J. A., "Multidisciplinary Design Optimization of a Strut-Braced Wing Aircraft with Tip-Mounted Engines," MAD 98-01-01, Virginia Tech MAD Center Report, Jan. 1998.
104. Gundlach, J. F., Tetrault, P.-A., Gern, F. H., Naghshineh-Pour, A., Ko, A., Schetz, J. A., Mason, W. H., Grossman, B., Kapania, R. K., and Haftka, R. T., "Multidisciplinary Design Optimization of a Strut-Braced Transonic Transport," AIAA Paper 2000-0420, 36th Aerospace Sciences Meeting and Exhibit, Reno, NV, Jan. 2000.
105. Mason, W. H., "Strut- and Truss-Braced Wing Concepts." https://archive.aoe.vt.edu/mason/Mason/ACiADtbw.html
106. Miranda, L. R., and Dougherty, G. L., "Transonic Wind Tunnel Testing of a Low Induced Drag Lifting System," Vols. I and II, Lockheed Aircraft Corp., Burbank, CA, February 1974.
107. Salem, K. A., Palaia, G., Frediani, A., and Carrera, E., "The Box-Wing Configuration: A Critical Review of Design Approaches and Applications," Progress in Aerospace Sciences, Vol. 157. https://doi.org/10.1016/j.paerosci.2025.101108
108. Van Dam, C. P., "Induced-Drag Characteristics of Crescent-Moon-Shaped Wings," Journal of Aircraft, Vol. 24, No. 2, Feb. 1987, pp. 115–119.
109. Smith, S. C., and Kroo, I. M., "A Closer Look at the Induced Drag of Crescent-Shaped Wings," AIAA Paper 90-3063, Flight Simulation Technologies Conference and Exhibit, Dayton, OH, September 17-19, 1990.
110. Yates, J. E., "Prediction of Drag and Lift: A Viscous/Thermodynamic Approach," ARAP Report No. 651, Aug. 1990. (*Note*: Presented at an AIAA Short Course, Portland, OR, Aug. 23-24, 1990).
111. Bushnell, D. M., and Hefner, J. N. (ed.), *Viscous Drag Reduction in Boundary Layers*, AIAA Progress in Astronautics and Aeronautics Series, Vol. 123, AIAA, Washington, 1990.

4. Configuration Aerodynamic Design: Use of Computational Aerodynamics

This chapter provides a brief discussion of several key aspects of aircraft configuration development. As aerodynamicists, we aspire to follow Küchemann, who explained:

> [The] main task that remains is to establish enough confidence to believe that, for the type of aircraft and mission under consideration, there exists regions of no conflict between the various essential characteristics, with which a set of design requirements can be met naturally. What we are really seeking is probably that "harmony" between elements . . . So we are not out for "compromise" in the sense that we can achieve some desirable characteristic only by degrading another and where a "deal" is made at somebody else's expense. We shall endeavor to explain what is meant by this by giving examples of good design concepts. . . . On the other hand such "good design" is not likely to be one where the overall result is an "optimum" with regard to any single parameter at just one point. Instead, all the significant parameters are in harmony and not in conflict for a set of design points and off design conditions, and the final solution is sound and healthy. . . . It was Prandtl who introduced the concept of healthy flows, and we are well-advised to follow him and to search for sound and healthy engineering solutions when designing aircraft.[1]

Küchemann's "healthy flows" include both attached flow and well behaved separated flows. He was apparently the originator of the notion that controlled leading-edge vortex flow could be used to obtain the required low-speed lift for the Concorde. Without exploiting vortex lift for takeoff and landing, the proposed Concorde concept would have been impractical. Thus, his words provide a high standard for us when we start an aerodynamic design.

Our approach in this course is more modest, but we continue to stress the importance of the underlying aerodynamic principles and show how they contribute to configuration development. The details require further study on the part of the reader, and key references are provided. We also emphasize the development of geometry associated with aerodynamic design, particularly in the exercises at the end of the chapter. Another objective is to illustrate the engineering aspects of the process. In terms of the use of computational aerodynamics, a key goal is to define a process for using software in aerodynamic design. Although the literature typically identifies a particular code as being used for the design, the reality is that the design is the result of work of the designer *plus* the code. Just having the code is not sufficient. Mark Maughmer, Professor of Aerospace Engineering at Pennsylvania State University, pointed out that the code isn't everything in airfoil design, explaining that "just having a piano doesn't mean you are a concert pianist." Thus, some skill is required to use the available methods, and we describe a process that helps the aerodynamicist evaluate when a code is giving the "right" answer—the infamous "sanity check" identified by Waaland as an important part of today's engineering using sophisticated codes.[2]

As hard as it might be for the aerodynamicist to imagine, aircraft designs are the result of the integration of several technologies, of which aerodynamics, although key, is only one. Thus the aerodynamicist is responsible as a team member for the overall concept. Traditionally, the other technologies are propulsion, structures, and flight control. For many military aircraft, stealth has become a critical technology impacting the configuration shape. Some notes describing stealth issues for aerodynamic design are given in appendix B. Detailed examples of aerodynamic design are provided in appendix D using the software available on the website as described in appendix E.

To achieve a successful design, the aerodynamicist must be a strong advocate for effective aerodynamic design. If this isn't the case, the team will likely not produce a winning design. If the aerodynamics group fails to persuade the company of the importance of aerodynamics, manufacturing costs will be reduced by eliminating wing camber and twist and the stealth group will be allowed to dominate the design at the expense of aerodynamic maneuvering performance. In one case, enormous development costs were incurred while still resulting in an aircraft with reduced performance. In another case, the proposed design lost to the competition. To be an effective advocate, the aerodynamicist must have a good understanding of several aspects of configuration development that are addressed in this chapter.

In section 4.1, we highlight the key considerations for aircraft configuration aerodynamic layout. This is followed by configuration architecture options and their aerodynamic implications in section 4.2. The discussion in section 4.2 might be characterized as addressing the question, *Why do airplanes look the way they do?* In section 4.3, we define the aerodynamic design problem in terms of wing loading (W/S) and thrust-to-weight (T/W). This is a key part of the initial sizing activity and is important in defining the cruise, takeoff, and landing lift coefficients that are some of the key requirements that aerodynamicists must meet. In section 4.4, we summarize the typical aerodynamic design tasks that occur during configuration design. This is followed in sections 4.5 and 4.6 by a discussion of the use of computational aerodynamics methods in design and explanations of the computational aerodynamic design methodology that has emerged as key to achieving improved designs in practical design cycle times. Section 4.7 provides a brief summary of the present status of aerodynamic design.

4.1 Configuration Aerodynamic Layout: Key Considerations

So where do we start when considering the aerodynamic layout of an airplane? In general, form follows function. We decide on candidate configurations (form) based on what the airplane is supposed to do (function). Generally, this starts with a decision on the type of payload and the mission the airplane is supposed to carry out with this payload. This is expressed generally in terms of the following questions that should be answered first:

- What does it carry?
- How far does it go?
- How fast is it supposed to fly?
- What are the field requirements? (e.g., runway length)
- Are there any maneuvering and/or acceleration requirements?

Another consideration is the specific safety-related regulatory requirements that must be satisfied. For commercial and civilian aircraft in the US, this means satisfying the Federal Aviation Regulations (FARs)* that are managed by the Federal Aviation Administration (FAA). These regulations (https://www.ecfr.gov/current/title-14) define the takeoff and landing distances, engine-out performance requirements, noise limits, icing performance, and emergency evacuation among many others. In the European Union (EU), Joint Aviation Requirements (JARs) were developed by the Joint Aviation Authorities (JAA) to harmonize aviation standards across participating European countries. The European Union Aviation Safety Agency (EASA), created in 2003 and fully functional since 2008, has taken over most of the JAA's functions. JARs are now called JAA Certification Specifications (JAA CS), which form an acceptable basis for showing compliance with national airworthiness codes of any nation. Military aircraft also have numerous requirements which, much like the commercial requirements, emphasize safety, including handling qualities. Appendix C in this book provides a few examples of the regulatory requirements.

*Since 1958, the Federal Aviation Regulations have typically been referred to as FARs. However, FAR is also an acronym for "Federal Acquisition Regulations," which has led to confusion at times. Therefore, the term "14 CFR" has been adopted for the Federal Aviation Regulations since Title 14 of the United States Code of Federal Regulations (14 CFR) contains rules and regulations issued by the US Department of Transportation and Federal Aviation Administration for Aeronautics and Space.

With this start, the aerodynamicist, reluctantly allowing other members of the design team and management to participate, develops a configuration concept and shape that responds to the mission. At the outset, the following list shows the considerations associated with

defining a configuration concept. At this stage, we begin to see that configuration design resembles putting a puzzle together. These components all have to be completely integrated.

Configuration Concept

- Lifting surface arrangement
- Control surface(s) location
- Propulsion system selection
- Payload
- Landing gear

The components listed above must be coordinated in such a fashion that the airplane satisfies the requirements given in the following list. The configuration designer works to satisfy these requirements with inputs from the various team members. This is where the team member that dominates can distort the design in a way that keeps it from responding correctly to the design requirements. For the design to be successful, the following criteria must be met.

Good Aircraft

- Aerodynamically efficient, including propulsion integration (streamlining!)
- Must balance near stability level for minimum drag
- Landing gear must be located relative to CG to allow rotation at takeoff.
- Adequate control authority must be available throughout the flight envelope.
- Design to build easily (cheaply) and have low maintenance costs
- Today, commercial airplanes must be quiet and nonpolluting.

Two books do an especially good job of covering the aerodynamic layout issues, although their titles are slightly misleading. The first of the two books is by Ray Whitford,[3] and the second is by Abzug and Larrabee.[4] There are aircraft design books by Raymer[5] and Roskam[6] that discuss configuration options.

We can translate the desirable properties of a good aircraft into specific aerodynamic characteristics. These desirable properties are outlined below.

Design for Performance

- Reduce minimum drag:
    - Minimize the wetted area (skin friction drag).
    - Streamline to reduce flow separation (pressure drag).
    - Distribute area smoothly, especially for supersonic aircraft (area ruling for wave drag).
    - Consider laminar flow (skin friction drag).
    - Emphasize clean design/manufacture with few protuberances, steps, or gaps (parasitic drag).

- Reduce drag due to lift:
    - Maximize span (must be traded against wing weight).
    - Tailor spanload to get a good span efficiency, e (twist).
    - Distribute lifting load longitudinally to reduce wave drag due to lift (a supersonic requirement according to R. T. Jones' oblique-wing idea).
    - Consider camber as well as twist to integrate airfoils and maintain good 2D characteristics.

- Key constraints:
    - At cruise: buffet and overspeed constraints on the wing (preventing structural damage)
    - Adequate high lift for field performance (simpler is cheaper)
    - Alpha tailscrape: $C_{L\alpha}$ goes down with sweep, *AR*.
    - Airport gate code: limitations on wingspans to fit existing airport gates—e.g., Code A: <15 m (49.2 ft); Code B: 15 m to <24 m (49.2 ft to <78.7 ft); Code C: 24 m to <36 m (78.7 ft to <118 ft); Code D: 36 m to <52 m (118 ft to <170.6 ft); Code E: 52 m to <65 m (170.6 ft to <213.3 ft); and Code F: 65 m to <80 m (213.3 ft to <262.5 ft)

Design for Handling Qualities

- Adequate control power is essential.
    - Nose-up pitching moment for stable vehicles
    - Nose-down pitching moment for unstable vehicles
    - Yawing moment, especially for flying wings and fighters at high-α (high angle of attack)
    - Consider the full range of center of gravity (CG) travel (ensure balanced flight operations).

- This implies you must properly balance the configuration around the CG.

Design for FAA and Military Requirements

- Safety: For the aerodynamic configuration, this means safe flying qualities.
    - FAR Part 25 and some of Part 121 for commercial transports
    - MIL STD-1797 for military airplanes
- Ability to use the airplane as a stable weapons platform
- Noise: Community noise, FAR Part 36, no sonic booms over land (High L/D in the takeoff configuration reduces thrust requirements, making the plane quieter.)

To begin discussion of the various configuration concepts, we use the successful transonic commercial transport configuration, exemplified by the Boeing 747 in figure 4-1, as a starting point. This type of configuration is mature. New commercial transports have almost uniformly adopted this configuration, and variations are minor. An interesting comparison of two different transport configuration development philosophies is available in the papers describing the development of the original Douglas DC-9 and Boeing 737 designs.[7] Note that advances in performance and reductions in cost are typically obtained by improvements in the contributing technologies.

The Boeing 747 layout shown in figure 4-1 meets the criteria cited above. The payload is distributed around the CG. Longitudinal stability and control power comes from the horizontal tail and elevator, which has a very useful moment arm. The vertical tail provides directional stability, using the rudder for directional control. The wing-fuselage-landing gear setup allows the wing to provide its lift near the center of gravity and positions the landing gear so that the airplane can rotate at takeoff speed and also provides for adequate rotation without scraping the tail. This arrangement also results in low trimmed drag. The engines are located on pylons below the wing. This arrangement allows the engine weight to counteract the wing lift, reducing the wing root bending moment, resulting in a lighter wing. This engine location can also be designed so that there is essentially no adverse aerodynamic interference.

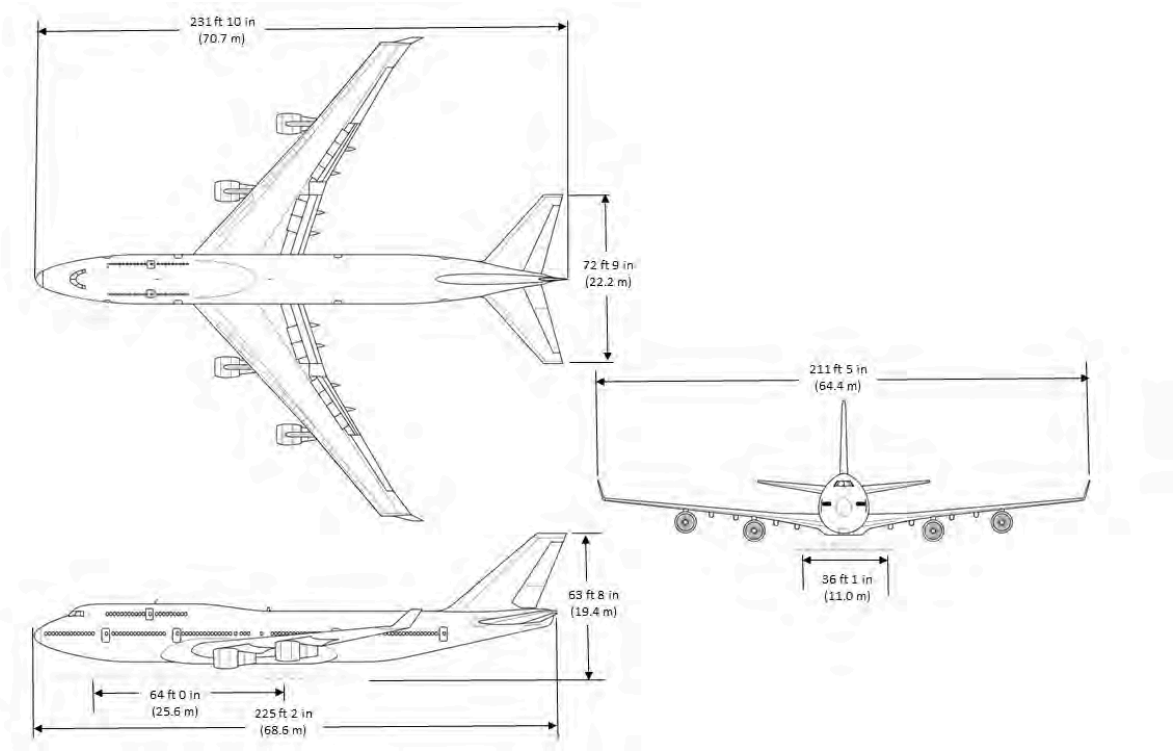


Figure 4-1. The classic commercial transport, the Boeing 747. *From Kaboldy. Wikipedia. CC BY-SA 4.0. Note: Dimensions added.*

Having established the baseline, we next examine features of other configuration concepts that are often considered, giving a summary of the major options. Many, many other innovations have been tried, and we make no attempt to be comprehensive.

4.2 Aircraft Configuration Architecture Options

In this section, we look at a large number of options for architecting an aircraft configuration. In particular, we highlight the issues associated with sweep, including forward sweep, canards, flying wings, three-surface configurations, winglets, and variable sweep.

4.2.1 Why Swept Wings?

Many aircraft wings are swept. Just about all such wings are swept aft, but a small number have been swept forward. Thus aft sweep is part of the classical concept. Aft sweep integrates well into an aft tail configuration, as we saw above with the B-747. Generally the wing is swept to delay transonic drag rise. That's because the compressibility effects can be associated with the Mach number normal to the leading edge on a well designed wing. The swept-wing concept was originated by German aerodynamicists prior to World War II and by R. T. Jones[8] at the NACA during WWII. George Schairer[9] has described the emergence of the swept-wing concept.

Below are the three key aspects of sweep.

- Subsonic (usually small sweep)
  - Adjust wing aerodynamic center relative to CG.
  - On a flying wing, get moment arm length for control.

- Transonic (significant, 20°–35°)
  - Delay drag rise Mach number (i.e., delay undesirable compressibility effects).

- Supersonic (large, 45°–70°)
  - Wing concept changes to slender wing or vortex flow wing—must distribute load longitudinally as well as laterally.
  - Reduce max cross-sectional area, and area variation occurs more gradually.

Sweeping the wing is not without drawbacks. Wing sweep increases the wing weight for a fixed span since the length of the wing spars increases with sweep to reach the specified wingspan. In addition, high-lift devices aren't as effective when the trailing edge is swept. Wing sweep also tends to increase the likelihood of the outboard wing stalling first, leading to pitchup, a situation where the wing stops lifting well aft of the center of gravity while continuing to lift ahead of the center of gravity. This results in a sudden nose-up pitching moment and an unstable slope. Pitchup is discussed in detail in the paper by Shevell and Schaufele.[10] This issue can be alleviated with the appropriate aerodynamic tailoring of the wing critical spanwise location. Finally, for aft sweep, the wing tends to be flutter critical.

4.2.2 Why Sweep the Wing Forward?

Several designs have adopted a forward-swept wing. It was known for some time that a forward-swept wing has the same delayed drag rise benefit as an aft-swept wing. However, forward-swept wings tend to suffer from aeroelastic divergence. This prevented them from being considered for most design concepts. One notable exception was a German bomber, the Junkers JU-287, used in WWII. The wing was swept forward so that the wing carry-through structure would be aft of the bomb that was carried on the CG. After the war, this design team produced a transonic business jet (the HFB-320 Hansa Jet) using the same logic to provide room for passengers.

With the advent of aeroelastic tailoring through the use of composites, forward-swept wing concepts were reconsidered. Studies at Grumman in the late 1970s and 1980s[11,12] identified numerous advantages of forward-swept wings in some applications, and the X-29 shown in figure 4-2 was built and flown.[13]



Figure 4-2: The X-29 designed by Grumman. From NASA. Public domain.

Essentially, for transonic maneuvering using an airfoil concept–based wing, the highly loaded wing will produce a shock wave near the trailing edge. For fighters like the F-15 and F-16, the trailing edge is nearly unswept. However, for a tapered wing, the trailing edge can be highly swept if it is swept forward. This allows a shock near the trailing edge to be highly swept, which will reduce the wave drag. If the trailing-edge sweep is essentially the effective aerodynamic sweep, then the effective structural sweep will be less than the aerodynamic sweep, resulting in a structural weight advantage.

A number of other advantages have been cited in the literature:

- Less twist to attain good spanload
- Wing stalls at the root (outboard ailerons remain effective)
- Better for reduced skin friction from the possibility of achieving some laminar flow because of reduced leading-edge sweep and no fuselage boundary layer contamination
- Integrates with a canard more naturally (less twist required)
- Good high-angle-of-attack performance (root stall, ailerons keep working)

However, there are some drawbacks. The first is the aeroelastic divergence penalty that remains to some degree, even when using composite materials. In addition, these configurations have difficulty in integrating landing gear relative to the center of gravity. They are also more unstable than aft-tail airplanes to achieve good performance (the X-29 was about 30%–35% unstable) and are not easily amenable to stealth because the leading-edge sweep tends to be low. Finally, the supersonic volumetric wave drag is high because the Mach cuts tend to foreshorten the design, resulting in a lower effective fineness ratio.

4.2.3 Why Canards?

Canard aircraft have been the subject of interest ever since the Wright Brothers' first flight. The basic argument is that the trim surface carries positive load for positive g maneuvers, reducing the load required on the wing. Grumman considered a number of canard configurations,[14,15] including the Research Fighter Configuration (RFC) shown in figure 4-3. In general, I think canard configurations should only be considered for designs with stringent requirements for both supersonic cruise and transonic maneuvers. The recent generation of European fighters has adopted canard configurations. The SAAB JAS 39 Grippen is a good example.[16]

Issues related to the use of canards include:

- Reduced subsonic-supersonic aerodynamic center shift
- The need to be balanced unstable to take full advantage of performance
- The downwash from the canard unloads the wing (for forward-swept wing concepts, this is good).
- If balanced stable, C_L on the canard is much higher than the wing.
- If balanced unstable, the control system design is expensive.
- Acceptable high-angle-of-attack lateral/directional characteristics are very hard to obtain.

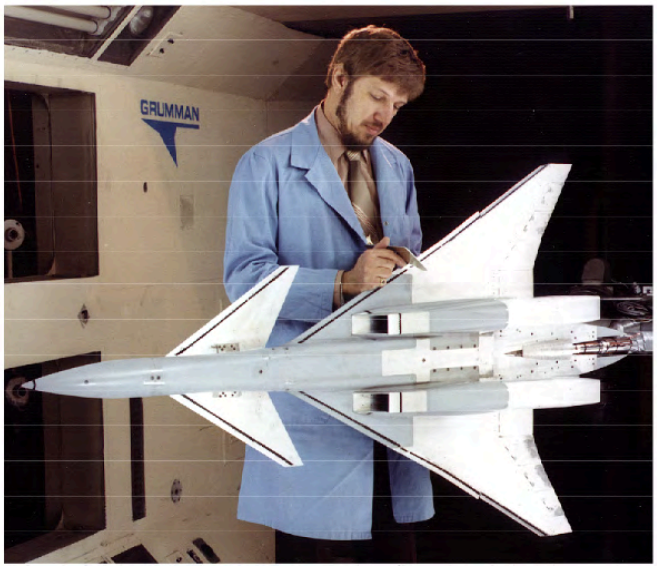


Figure 4-3: The Grumman Research Fighter canard configuration. From Northrop Grumman via W. H. Mason's archive. Copyright undetermined. Fair use.

Canard configurations are more difficult to develop than traditional aft-swept wing configurations. In figure 4-3, note that the inlets are behind the canards. Therefore, it is possible that under some circumstances the wake from the canard could enter the inlets. When balanced stable, the demands on the canard airfoil are quite high. When the airfoils used on the canards of early Rutan designs encountered rain, it appears that the boundary layer transitioned early and as a result didn't produce the required lift to allow level flight. These airplanes had to get out of the rain before they encountered the ground! Garrison has given a particularly cogent discussion of canard configurations, primarily for general aviation designs.[17]

4.2.4 Why a Flying Wing?

Another concept popular with aerodynamicists is the flying wing. The advantage is that eliminating the surface area of the fuselage and control surfaces reduces the parasite drag, hence improving the aerodynamic efficiency. You also eliminate the weight of the tail. This concept can work well if extreme maneuverability is not needed. The volume distribution can be an issue. Jack Northrop devoted much of his career to the development of flying wings, and the XB-35 (first flight, June 1946) and YB-49 (first flight, October 1947) bombers employed this concept. For a variety of reasons, these designs weren't practical at the time. Jack Northrop's excellent paper on flying wings that he presented as the 35th Wilbur Wright Memorial Lecture in London in 1947 is still worth reading.[18]

One particularly important technology not available to Jack Northrop was the modern digital flight control system. The flying-wing concept makes extensive use of augmentation systems for stability and control. For a wing without a vertical tail and rudder, directional stability and control requires special attention. The usual method of producing yawing moments is to use the so-called "drag rudders," which consist of split flaps on the outboard portion of the wings. The flying wing is also synergistic with relaxed static stability. This is because, when the airplane is unstable, the trailing edge will be deflected down to bring the nose up. This means that trailing-edge deflection for control and high lift are both in the same direction.[19] This advantage of being balanced through being unstable was known to the designers of the XB-35, but flight control technology was not developed to the point where this could be achieved. However, the XB-35 did use stability in the form of a yaw damper to improve directional flying qualities.[20]

Another flying wing, the B-2, shown in figure 4-4, was also developed at Northrop (for more on the B-2 development, see Waaland[21]). The B-2 shows that this concept is also well suited for stealth. For use as a passenger transport, a large volume is required, and thus the flying-wing concept is most natural for large airplanes. More references and information on flying wings are available on one of my websites.[22]



Figure 4-4: Northrop Grumman B-2 Spirit flying-wing aircraft. From US Department of Defense. Public domain.

A variation of the flying-wing concept known as the blended-wing body was proposed by the McDonnell Douglas Aircraft design team located in Southern California.[23] See section 1.2.1 for more details.

4.2.5 Why Three-Surface Configurations?

Some aircraft concepts employ a three-surface concept, which is the exact opposite of the flying wing. Since the flying wing doesn't have a significant moment arm for control, the center of gravity must be tightly controlled. With three surfaces, you can trim the airplane with near-minimum drag over wide CG range.[24,25] Sometimes, efficient component integration leads to three surfaces to save weight. However, the argument will typically be made that, if you can do the job with two surfaces, why use three? The third adds cost, weight, and wetted area.

One very good airplane, the Piaggio Avanti shown in figure 4-5, has used this approach quite effectively.[26] In this case, the three-surface concept allows the wing torque box, the aft pressure bulkhead, and the main landing gear to share the same fuselage bulkhead[27] (see also *Roskam's Airplane War Stories*.[28]). Note that the X-29 should also be considered a three-surface configuration since it uses a flap at the end of the aft strake in the control system in addition to the canard.



Figure 4-5: The Piaggio Avanti three-surface configuration. From Tibboh. Wikimedia. CC BY-SA 3.0.

4.2.6 Why Slender Wings?

Highly swept wings appropriate for supersonic flight represent a fundamentally different concept. The Concorde is the primary example. For these wings, the idea of an airfoil embedded in a wing is not appropriate. If anything, the spanwise cross section of the wing can be considered to be the relevant two-dimensional section. Two forces must be at work here to make highly swept slender wings viable. Considering supersonic flight, these wings allow for a smooth area distribution and low maximum cross-sectional area for a given wing area. Additionally, the longitudinal distribution of lift occurs over a long length. To be viable at low speeds, the wings get extra lift due to the presence of an additional low-pressure effect on the wing when a leading-edge vortex forms on the top of the wing at landing and while maneuvering angles of attack. In the US, Polhamus is usually associated with slender-wing concepts.[29] We will discuss these types of vortex flows in a detail in a later chapter. Another key survey on the subject was conducted by Poisson-Quinton.[30]



Figure 4-6: An example of a slender-wing aircraft. From NASA. Public domain.

Figure 4-6 shows the F-16XL, which was an experimental version of the F-16 airplane that employed the highly swept slender-wing concept. This plane was used to study supersonic performance, vortex flow aerodynamics, and laminar flow and transition at supersonic speeds.

4.2.7 Why Variable Sweep?

Variable-sweep wings have been used on a number of military aircraft. The F-14 is one such design and is shown in figure 4-7. Some of the pros and cons of variable-sweep wings are:

- Swept-back position (high-speed flight): low supersonic drag (low maximum cross-sectional area) and good "on-the-deck" ride quality (low $C_{L\alpha}$)
- Unswept position (low-speed flight): low landing speed (carrier suitability), efficient loiter
- Optimum sweep back available over transonic speed range
- Adds weight/complexity, currently unfashionable

Variable-sweep-wing aircraft design has been discussed by Kress[31] and Poisson-Quinton.[32] One of the issues in the design of variable-sweep-wing aircraft is the change of the aerodynamic center and thus the static margin as the wing sweeps.



Figure 4-7: The Grumman F-14. From NASA. Public domain.

4.2.8 Why Winglets?

Winglets have received a lot of attention since Whitcomb developed them. Figure 4-8 shows a typical winglet as used on a regional jet. Although they may not be a major architectural effect, they deserve a few comments. Below are some of the key considerations associated with winglets.

- Almost equivalent to a span extension without increased root bending moment
- Used where span limitations are important
- Good wingtip flow crucial to low drag
- The local flow field is extremely nonuniform, and for winglets to work, their design requires the use of advanced computational aerodynamics methods.



Figure 4-8: Winglet on a Canadair Regional Jet at Roanoke, Virginia, Airport, January 2003. From W. H. Mason.

Essentially, the winglet operates in the highly nonuniform flow where the wingtip trailing vortex is forming. Two effects contribute to the reduction in drag. The local spanload is increased near the tip, reducing the downwash on the main wing near the tip and reducing the local induced drag. The other effect is that the local nonuniform flow rotates the normal force on the winglet so that it produces a thrust component relative to the freestream. We cite two references.[33,34] More references on winglets are available on one of my websites.[35]

4.2.9 Propulsion System Integration Issues

Integrating the propulsion system into the configuration is always a key issue. For jet transports, the engines are either mounted on the aft fuselage or mounted on pylons under the wings. The first jet transport, the de Havilland Comet, which went into service in 1952, mounted the engines inside the wings very near the wing root. The inlets were mounted directly at the leading edge. This propulsion system installation can still be seen in the British Aerospace Nimrod, which is a direct descendant of the Comet. However, today, the preferred location for engines is under the wing, which was initially thought to result in a drag penalty until Boeing was able to demonstrate that this location could be used without penalty. Engines are still fuselage-mounted when the wings are positioned so close to the ground that there is no room for the engine. This is frequently the case for modern regional jets.

Advantages of wing-mounted engines are load relief, with the engine weight countering the lift force; good access to the engines for maintenance; and safety due to the distance from the passenger compartment. One drawback is the need to account for engine-out conditions when the thrust line is far from the centerline, as well as accounting for foreign object debris (FOD) damage when the inlets are so close to the ground. Swan and Sigalla[36] have given an excellent overview of the issues for transport aircraft.

Other installations have also been used. Engines are placed above the wing on short takeoff and landing (STOL) airplanes when the high-lift system incorporates over-the-wing blowing, using the engine exhaust to flow over the deflected flaps, which leads to increased values of maximum lift. On most modern jet fighters, engine(s) are integrated within the fuselage. This type of installation reduces drag and contributes to improving the stealth characteristics.

4.2.10 Controlling the Airplane

Appropriate integration of control surfaces also requires careful consideration. Longitudinal (pitch) control is usually the starting point, with an aft-mounted tail being the standard configuration. Perhaps the chief consideration is controllability at high angles of attack. In particular, when the engines are fuselage-mounted, the horizontal stabilizer and elevator are typically attached to the top of the vertical stabilizer and rudder. This is known as a T-tail configuration. With a T-tail arrangement, the horizontal tail can become immersed in the wake of the wing at high angles of attack, resulting in the loss of effectiveness of the tail both as a stabilizing surface and as a control.

In the worst-case scenario for this pitchup problem, the plane can be caught in a high-angle-of-attack stable trim condition known as a "hung" or "deep stall." The paper by Shevell and Schaufele[37] describes the redesign of the DC-9 when the flight-test crash of a BAC-111 in October 1963 brought this problem to the attention of commercial transport designers. Military aerodynamicists were already familiar with the problem as a result of experiences with airplanes like the McDonnell F-101 Voodoo. Fighter airplanes employing strakes for high lift can also encounter hung stalls. One example is the F-16, which uses an alpha limiter (limiting the angle of attack, α) in the control system to avoid the problem. The C-17 also uses an alpha limiter in the control system.

Another aspect of the longitudinal control is the use of all-flying tails in place of the conventional horizontal stabilizer and elevator to increase the control effectiveness. This is especially important at high transonic and supersonic speeds. Yeager attributes the discovery of the all-flying-tail approach on the X-1 program to the eventual incorporation of the all-flying-tail approach on the F-86 and its subsequent outstanding high-speed performance.

The choice of the wing-planform sweep (Λ), taper ratio (λ), and aspect ratio is also critical in establishing the basic pitching moment characteristics. Typically, an aft-swept wing stalls near the tip and the forward inboard portion of the wing continues to lift, leading to a change in the slope of the pitching moment curve and to pitchup. The allowable boundaries for these parameters were developed experimentally in the 1950s and are summarized in figure 4-9, which was reproduced from a NACA report.[38] This figure provides an indication of the allowable design space, although detailed design may allow acceptable characteristics to be obtained outside the region labeled "stable."

The same report also includes data to show the influence of flaps, slats, and fences on expanding the stable region, which is also included in the USAF Stability and Control DATCOM.[39]

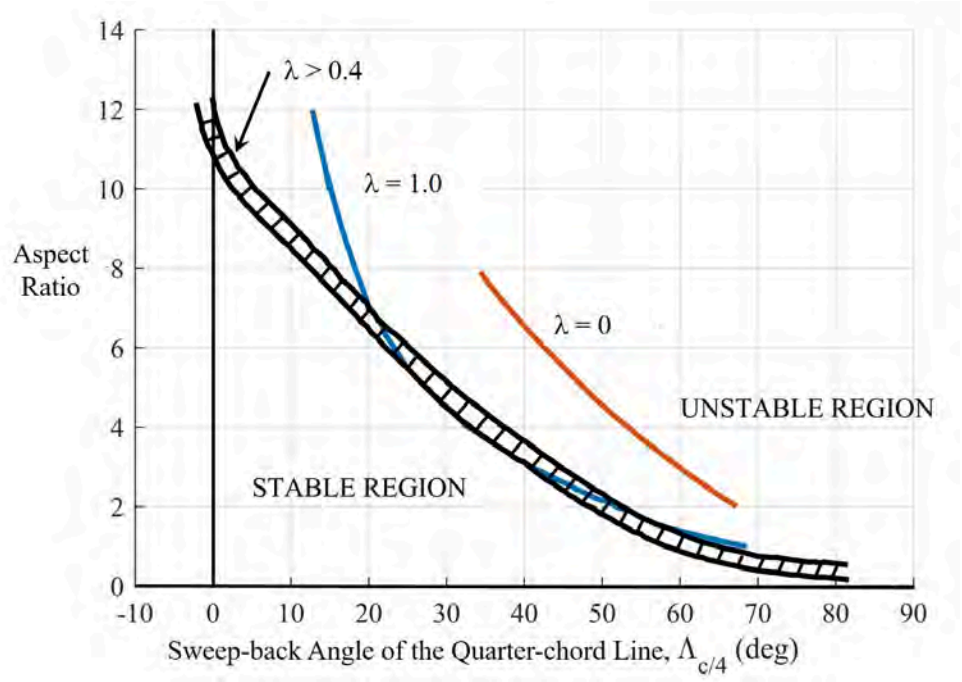


Figure 4-9: The pitchup boundary for various wing planforms. *From S. Madden from US Air Force data.*

Lateral control is normally achieved using ailerons. However, spoilers can also be used. Waaland[40] makes the case for spoilers in his Wright Brothers Lecture. Directional stability and control is achieved using a conventional vertical tail and rudder when stealth considerations allow their use. Otherwise, nonconventional directional control must be used, with the drag rudders used on many flying airplanes being an example.

4.3 Configuration Sizing: Aerodynamic Considerations

Some of the key design characteristics can be defined with relatively little detailed information. One design consideration is wing loading (*W*/*S*), used to size the wing. The problem is multidisciplinary, and wing weight is also important in selecting the wing size. However, we can define the problem reasonably well.

The aerodynamic requirements are driven by two opposing conditions. To find the wing loading, we first consider how the wing characteristics affect the value of the specific range, *sr*, of the airplane (typically given in units of nautical miles of range per pound of fuel used). Equation (4-1) can be obtained (ignoring drag rise), showing how the various design characteristics affect the maximum *sr*, or sr_{max}.[41]

$$sr_{\max} = \frac{1.07}{sfc}\left\{\frac{(W/S)}{\rho}\right\}^{1/2}\frac{\{AR\cdot E\}^{1/4}}{\{C_{D_0}\}^{3/4}}\frac{1}{W} \qquad (4\text{-}1)$$

Here we see that a high value of *W*/*S*, high-altitude flight (low air density, ρ), high aspect ratio, *AR*, and planform efficiency, *E*, are desired. Similarly, specific range increases with low specific fuel consumption, *sfc*, drag coefficient at zero lift, C_{D0}, and aircraft weight, *W*.

If we consider maneuvering flight as well as takeoff and landing requirements, the demands on *W/S* are reversed. Consider the requirement for obtaining a sustained maneuver load factor:

$$n_{\text{sustained}} = \frac{q}{(W/S)}\sqrt{\pi ARE\left(\frac{1}{q}\left(\frac{T}{W}\right)\left(\frac{W}{S}\right) - C_{D_0}\right)} \qquad (4\text{-}2)$$

Clearly a low *W/S* is a key requirement for achieving a high value of $n_{\text{sustained}}$. Similarly, the takeoff distance is related to the so-called takeoff parameter, *TOP*, which also includes $C_{L\max}$, which is another key aerodynamic parameter:

$$TOP = \frac{(W/S)}{C_{L_{\max}}(T/W)}. \qquad (4\text{-}3)$$

The landing distance can be related to the approach speed:

$$V_{APP} = 17.15\sqrt{\frac{W/S}{\sigma \cdot C_{L_{APP}}}} \quad (\text{knots}) \qquad (4\text{-}4)$$

In each of these cases, a low *W/S* is desired (σ is the ratio of air density at a specific altitude to the density at sea level). For the takeoff and landing cases, the need for a low *W/S* and high lift coefficient must be considered in a trade study.

So how is the selection of wing loading made? A constraint diagram is used to help the design team understand the requirements. Figure 4-10 is a notional constraint diagram adapted by McDonald[42] from Loftin,[43] which illustrates the situation. Typical constraints for a transport aircraft are:

- Cruise
- Takeoff field length
- Landing field length
- Second segment climb gradient
- Missed approach
- Top of climb rate of climb

See appendix C for the relevant specifications of each of these requirements. They are defined very precisely by FAA and military specifications.

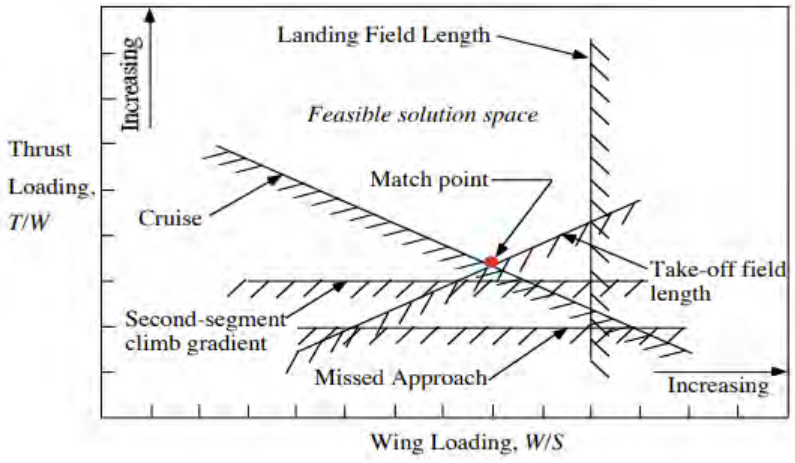


Figure 4-10: Conceptual illustration of a T/W–W/S constraint diagram. *From R. A. McDonald. Adapted from Loftin. Fair use.*

For some cases involving point performance (local quantities), the trade between aerodynamics and structures can be found analytically. As an example, consider the transonic maneuver–dominated fighter. Minimizing the sum of the wing and engine weight, the maneuver lift coefficient can be found to be

$$C_{L_{MDP_{opt}}} = \sqrt{\pi ARE\left(C_{D_{0_W}} + \frac{1}{q}\frac{dW_{WNG}/dS_W}{dW_{ENG}/dT_{REQ'D}}\right)} \qquad (4\text{-}5)$$

We see the connection between the aerodynamic, structural, and propulsion characteristics. For the derivation of this equation and example applications, see the paper by Mason.[44]

4.4 Overview of the Specific Aerodynamic Design Tasks

Initially, the aerodynamicist works with the design team to establish the appropriate concept(s) for meeting the design requirements. The wing planform as well as the control approach should be chosen, and the wing loading and thrust-to-weight should be estimated, as described in the preceding sections above. Targets are set for the design lift coefficients at key points in the mission, such as cruise, takeoff, landing, and any sustained and instantaneous maneuver requirements. The wing sweep and maximum *t/c* are naturally part of a design tradeoff between the structural and aerodynamic requirements. Another consideration may also be the wing volume available for fuel. Once the wing sweep and thickness distribution are selected, it will be very difficult to change them because of their pervasive impact on many other parameters.

The baseline configuration geometry is obtained from the configuration designer. The aerodynamic design job starts with an analysis of the baseline geometry to establish the performance relative to the requirements. Then the aerodynamic designer modifies the geometry to improve the aerodynamic performance. Remember that one definition of aerodynamics is "50% flow field and 50% geometry" (though actually, geometry is much more than 50% of the day-to-day work of the aerodynamics designer). The aerodynamicist controls the flow field by manipulating the geometry. Thus geometric modeling is a key aspect of an aerodynamicists' job. Appendix A provides the geometry definitions of commonly used airfoils and bodies of revolution.

The next item of business is to obtain the neutral point* of the configuration and work with the configuration designer to ensure that the wing is placed longitudinally on the fuselage to obtain the desired stability level. To do this, you may need to do a minimum trimmed drag analysis to establish the desired stability level. The weights engineer (historically referred as the weights "guy") defines the center of gravity. If the airplane is to fly at supersonic speeds, the volumetric wave drag analysis should begin immediately and the cross-sectional area distribution should be developed to minimize the wave drag. An important aspect of this work is to ensure that the maximum cross-sectional area is minimized. The other initial aerodynamic task is to estimate the parasite drag. This requires the wetted area of the configuration at a component-by-component level.

> *The neutral point is the longitudinal location on the airplane where the center of gravity can be placed and where the pitching moment will not change with angle of attack.

Once this work is done, the detailed aerodynamic design can begin. The nominal *t/c* distribution is typically defined during the initial studies, and once specified, an appropriate airfoil can be either picked or designed. Given the wing planform and thickness, the wing camber and twist are found. This is a major part of the detailed design effort. In addition, at this time, the high lift system requirements are defined and a high lift system design is selected to meet the requirements. Although the performance can be predicted with some certainty at key

design conditions, issues with the airplane's handling qualities are associated with the boundaries of the flight envelope, where significant separated flow exists; they are also associated with flight with unusual combinations of controls, engine thrust, etc. As such, once the basic aerodynamic design is done, much of the remaining effort, involving wind tunnel and flight testing, will be devoted to "fine tuning" the shape to obtain the desired handling qualities.

Another consideration in defining the aerodynamic shape is the difficulty of manufacturing complicated shapes. Ultimately, the master dimensions, created by the lofting group, controls the contour, and this group may change the shape specified by the aerodynamicist. If the aerodynamicist specifies the shape at only a few span stations (e.g., the root and tip airfoils and wing root incidence and wingtip washout), the contours between these control stations may not be the contours expected by the aerodynamicist. Work the exercises at the end of this chapter to derive the details substantiating this statement.

4.5 Use of Computational Aerodynamics in Aerodynamic Design

Today, computational aerodynamics plays a key role in aerodynamic design, and we start with some sage words from one of the most inventive aerodynamicists in US history, R. T. Jones, whose book highlights his concerns about the use of computational aerodynamics.

> Aeronautical calculations today rely on the awesome power of the computer. However, as has been observed, power can corrupt. Equipped with an appropriate address book, giving the location and availability of various programs, the aeronautical engineer can now command the solution of a great variety of aerodynamics problems. Moreover, the capacity of the computer has made possible the inclusion of many small physical influences that until now had to be neglected but sometimes create a false impression of high accuracy. However, the basic physical assumptions of calculations, if they are discussed at all, are often not given adequate treatment. If 'computer aerodynamics' is to realize its full potential, then more attention must be devoted to these underlying principles.[45]

Although the powerful software described by Jones can, in many cases, be used on a standard laptop computer, the user must acquire experience with it before using it to make design decisions. In fact, experts are continually evaluating the accuracy of their methods. A set of test cases was developed by the Fluid Dynamics Panel Working Group, and selected test results and detailed geometric descriptions were published in advisory reports by AGARD.[46,47]

A series of CFD Drag Prediction Workshops (DPWs) has been held in the US since 2001 to help the developers and users of computational aerodynamics to better understand the accuracy of the computational methods. For additional information, see the references cited in section 3.6.1. In 2003, the prediction of stability and control characteristics using CFD was the topic of a symposium sponsored by NASA.[48] In the following sections, we list a few steps that should be taken when using computational aerodynamics programs.

4.5.1 Steps to Take When Using a Program for the First Time and on a New Configuration

The checklist that we provide is perhaps obvious. In fact, it is sometimes apparently so trivial, we are tempted to skip some of the steps. Speaking from personal experience, skipping steps is always a *big* mistake.

4.5.1.1 Initial Validation

1. *Demand that you be provided a sample input and output.*
   It is impossible to use a code obtained from any source without checking that you have a version that actually works properly. Together with the user's manual, you must also obtain a sample input and corresponding output. Without these files, the code is unlikely to be worth your time to try and use.
2. *Run the code yourself using the provided sample input.*
   The next step is to run the code on the platform you intend to use with the input sample dataset you were provided. Often, the code won't run on a system even slightly different than the one on which it was developed. At this point, some interaction with the provider of the code is typically required. This should be done the same day you obtain the code!*
3. *Carefully study the output ,and compare with the sample output provided.*
   You need to examine the input and the output obtained on your system with the sample output provided. There are two reasons for this. First, you need to make sure you get the same answers. Often you won't. When this happens, you need to try to understand why the answers are different. Often, the sample input you were provided doesn't correspond exactly to the one used to create the sample output. I've been guilty of doing this. The second reason to study the sample input and output in detail is to learn the details of the code and its capabilities. At this point, make sure you understand factors such as the nondimensionalizations, the detailed definition of the reference area, and the exact coordinate system used, among others. Collect your questions, and contact the person that sent you the code. However, don't call too quickly. Review your issues, making sure you really need to ask the question. You need to establish that you are a serious and informed user if you expect to get support. This is especially true if you are not paying for support.
4. *Investigate sensitivity to various parameters.*
   Today's aerodynamics codes come with numerous options. You will never be able to test every combination. However, establish which ones are key for your problem, and investigate their effects. The options typically come in two classes. One class will be associated with obtaining the numerical solution. This includes convergence criteria, numerical step sizes, the number of panels, and the number of grid points, among other options. Make sure you understand how to exercise the code to obtain a solution that is converged with respect to these factors. The other class of options is associated with the flow physics. This group includes the options for turbulence models, boundary condition treatment, and possibly differences in behavior, depending on Mach and Reynolds numbers. This type of study is another important step in developing experience using a particular code.

*Once, I waited a few months before I tried to use a code I got from NASA because the code arrived too late to be used on the immediate problem for which I had requested it. When I did start to use the code, I found that the developer had passed away.

4.5.1.2 Configuration Buildup Approach

Once you have performed the steps outlined above, you are ready to start using the code for your own work.

1. *Make up your own test case.*
   Pick a case “close” to the one you are trying to solve and for which there is an analytic solution available, whether it's in the form of a published numerical solution or experimental data. Run the code to compare to the other results. See how closely you match this

result, and try to understand the reason for any differences.

2. Finally, start to use the code for the configuration you are interested in investigating.
    a. Start with the simplest possible model. This is probably an isolated airfoil or wing. Investigate the solution and its convergence process. Study the physics.
    b. Add the tail and/or canard to the isolated wing case. Does the code still work? What is the effect of the added component?
    c. Add the fuselage to the isolated wing case. What are the fuselage effects on the results?
    d. Finally, run configuration with the full level of geometric complexity. Following this procedure, you will gain confidence in the results and will be able to identify the contributions of the components to the complete results.

4.6 A Review of Detailed Computational Aerodynamic Design Approaches

This section originated in a three-volume report written a few decades ago.[49] Revisions have been made to the software program to reflect current practices. Surveys of the use of computational aerodynamics have appeared regularly since the beginning of computational aerodynamics' extensive use in aerodynamic design. Among the many reviews, we cite two surveys. Jameson[50] discusses the role of CFD in the design of aircraft, providing an overview of the design process in a multidisciplinary environment. Johnson, Tinoco, and Yu[51] provide specific examples of CFD application to Boeing designs in their Seattle facility.

4.6.1 Introduction: Analysis Versus Design

Although the use of the computer to simulate the flow field about a vehicle with a specific geometric configuration is an extremely useful and important capability, it is an indirect response to the aerodynamic design question. The aerodynamic design question is typically posed at several levels, starting with some vague and general question about the "best" shape of the airplane for a particular mission, before proceeding to more specific and detailed questions concerning the actual wing (and fuselage) lines, which are subject to a large variety of constraints. In the old paradigm, the aerodynamicist designs a wing using the methods of computational aerodynamics, the lines are given to the contour development group, and a wind tunnel model is built and tested. In the analysis mode, aerodynamic computer programs are used to simulate a wind tunnel. Of course, the computer simulation can be used much sooner in the design cycle than a wind tunnel test, and this strategy should produce an improved final design at a reduced cost in a shorter time period. This was the proper initial introduction of computer simulations into the wing design process. Indeed, this technique was used for subsonic and supersonic wing design since the 1960s, employing linear aerodynamics methods. Subsequently, transonic wing design using fully transonic three-dimensional wing-body computer methods was done in a similar manner.

Once the computer is introduced into the design cycle, it becomes evident that it can be used in a fundamentally different mode than to simply supplement wind tunnel testing. The use of flow field simulation in this manner is naturally referred to as the "design mode," as opposed to the "analysis mode" of operation. A design mode has been available for linearized subsonic and supersonic flow fields since shortly after the analysis codes became available. The most extensive use of a design mode appears to have been the elaborate system of linear aerodynamics supersonic wing design codes that evolved from the work of Carlson and Middleton,[52] developed for the US SST program.

After a brief review of the design problem and some of the methods used over the years, we describe the current approach to aerodynamic design. We include a few illustrations of very simple problems to provide some insight. Specific codes will be discussed in more detail in subsequent chapters.

4.6.2 Review of the Computational Design Process

A variety of possibilities emerge when the problem formulation for a design mode of operation is explored. The reason for this range of possibilities can be attributed to the manner in which the design problem is posed, as noted above. Ideally, the aircraft designer would specify the aircraft mission (or missions) and a computer program would provide the detailed lines of the optimum aircraft, but such a smart computer program will not exist for some time. However, most aircraft companies and governmental agencies routinely employ programs that predict the gross features of an optimum aircraft for a particular mission with some assumption regarding the rate of development of various technologies. These programs use low-fidelity models of the various disciplines, as well as databases developed from previous aircraft designs. Typical aerodynamic outputs from the programs are takeoff gross weight, wing area, wing loading, and planform details such as aspect ratio (AR), taper ratio (λ), sweep (Λ), and thickness ratio (t/c). Usually, a target/assumed drag level for the configuration is also specified. Examples of this type of program are the NASA ACSYNT program[53] and the NASA FLOPS program.[54]

Hence, the computer is used to determine the overall features of the required airplane. The typical aerodynamic design problem thus becomes less vague and more manageable, with the statement being reduced to something along the following process.

Given:

- AR, λ, Λ, t/c (basic geometric parameters)
- M, Re (flight conditions)
- $C_{L\text{cruise}}$ or $C_{D\text{max allowable}}$ (design goals)

Find:

- $C_{D\text{min}}$ for $C_{L\text{cruise}}$ or $C_{L\text{max}}$ for $C_{D\text{max allowable}}$
- Detailed geometry (i.e., detailed aerodynamic aircraft design definition), subject to geometric constraints on twist, camber, root bending moment, etc., and subject to aerodynamic requirements on performance at other flight conditions.

At this point, we could begin to consider the direct use of a computer code to help determine the optimum aerodynamic shape and performance that can be obtained for the specified problem. More typically, the aerodynamic designer employs his experience and judgment to specify a desired pressure distribution (unfortunately, it appears that designers with this ability are becoming increasingly rare). This type of program is usually described as an "inverse method," while a program that attempts to address the problem more directly is usually termed an "optimization method." The "classical optimization" approach uses well established numerical optimization methods to find the aerodynamic shape. Each of these approaches has its own strengths and weaknesses. A contrast between optimization and inverse methods is summarized below.

Classical Optimization

- Requires many analysis submissions for a single design case
- Solution depends critically on the user-assumed form of the answer.
- Can handle a variety of geometric and off-design constraints
- If performed through a large optimization code, solution is not obtained from "aerodynamic thinking."

Inverse

- Generally almost as fast as a single analysis
- The geometry may not always exist for a given pressure distribution.
- Difficult to treat off-design and geometric constraints
- Solution is a direct result of best current "aerodynamic thinking."

Another drawback of the optimization approach is that the path taken to the final result is often rather obscure, ensuring that the relative importance of the various aspects of the final design produced in this manner are not readily apparent.

The original numerical optimization techniques employed in the design methods were of the search type and did not employ any of the elements of calculus of variations to obtain the maxima. More importantly, in fluid mechanics, it was not clear how to find the aerodynamic gradients of design variables without using simple finite-difference approaches. This meant that many additional calculations had to be made at each optimization iteration. Although an entire book by Angelo Miele[55] had been devoted to aerodynamic optimization using calculus of variations, these concepts were not used until Antony Jameson introduced the current modern methods for aerodynamic design. His adjoint methods are closely connected to classical calculus of variations and control theory.[56] Jameson's 1997 paper contains numerous references to his design research. The advantage of current modern methods is that the gradients of the solutions can be obtained very efficiently.

4.6.3 Examples of Design Methods and Issues Drawn From Two-Dimensional Studies

A variety of numerical approaches have been used to design transonic airfoils. The book edited by Thwaites[57] discusses the classical approaches to the incompressible inverse methods and points out that some judgment must be used by the designer in specifying the desired pressure distribution. A solution does not necessarily exist. You cannot specify any arbitrary pressure distribution and obtain a real geometry. Inverse methods for transonic speed airfoil design have to contend with this same problem. However, in practice, aerodynamicists have been able to use inverse methods without any undue hardship. A review of inverse methods is available in the AIAA book edited by Henne,[58] in articles by Drela,[59] and in Volpe's writing on transonic flow.[60] The computer programs have proven to be very useful.

Another approach to transonic airfoil design must be mentioned in any review, although it isn't used today. Hodograph methods were used to design some very good airfoil sections. The method worked well in the hands of the skilled users at the Courant Institute.[61] One of the main problems with the method was extending it to three dimensions.

The numerical optimization approach to airfoil design is more recent, unlike the inverse methods, which were available in the 1940s for subsonic flows. However, like many of the currently used aerodynamics methods, inverse methods for detailed aircraft work were not routine engineering tools until the widespread availability of computers. An initial study of numerical optimization applied to aerodynamic design was presented in 1974 by Hicks, Murman, and Vanderplaats.[62] The underlying idea in this approach is to couple a modern numerical optimization code with an aerodynamic analysis code. The airfoil design problem is then cast as an optimization problem, and the entire apparatus associated with optimization methods is brought to bear on the problem. The most attractive aspect of the optimization method is its ability to handle design constraints. These constraints include both off-design performance requirements and design-point geometry restrictions. The report by Vanderplaats and Hicks[63] provides a detailed description of the techniques used to formulate the design problem as an optimization problem.

The optimization method has become the standard approach to aerodynamic computational design. However, there are some drawbacks that need to be addressed. These drawbacks are in part related to computer run times. In optimization methods jargon, optimization

methods minimize an "objective function," which is a function of a set of design variables subject to a set of constraints. The objective function could be drag, for example, while the design variables are typically the variables used to specify the shape of the airfoil. The constraints could be a minimum lift coefficient, a prescribed pitching moment, airfoil thickness, off-design drag values, or virtually any other requirement that might arise in practice. The selection of the appropriate objective function and design variables is *crucial* to the success of optimization methods.

The design variable specification is perhaps the biggest challenge in the application of optimization methods. In principle, the number of airfoil ordinates used to specify the shape could each be used as design variables, however, if sixty upper-surface and forty lower-surface points (a typical number of ordinates) are used, then there are 100 design variables. In practice, no more than about ten independent design variables can be treated reliably. Thus the airfoil shape must be constructed from shape functions that describe more than a single ordinate (i.e., coefficients of polynomials used to approximate airfoil shapes).

Experience led to the realization that polynomials were not appropriate shape functions, and schemes that use linear combinations of present supercritical shapes and local geometric perturbations to these shapes appear to be the most practical method to obtain useful results with a small number of design variables. Thus the linear combination of known airfoil shapes, as used by Vanderplaats and Hicks,[64] and the use of shape functions obtained using inverse methods proved very effective.[65] This approach also proved effective in three dimensions, although it requires some modifications. It is important to realize that the optimization method will only identify the best of a particular set of possible airfoil shapes arising from the shape functions. If the actual optimum airfoil is not among this set of shapes, the method cannot find this shape. Hence, the optimization methods also require the user to apply insight into the problem.

Three key issues are worth mentioning. Jameson and his coworkers have addressed the issue of low-cost gradient calculations.[66] They combined the efficient calculation of gradients with a numerical optimization procedure to obtain an aerodynamic design procedure. Their work has been demonstrated in numerous applications.[67] Another issue is the need to avoid designs that are too narrowly optimized. Any practical design must be efficient over a range of flight conditions and in the presence of possible uncertainty in the shape specification. The work of Huyse and his collaborators[68,69,70] provides practical methods of addressing these issues. The third key area of concern is reflected in the work carried out at Virginia Tech[71] addressing the issue of using high-fidelity aerodynamics in the early stages of design by exploiting parallel computing to precompute aerodynamic results for the specific design space and using statistical methods to interpolate this "data base" during optimization studies. This approach is tailored to multidisciplinary design since other disciplines are also involved in optimizing an entire system.

The comments concerning inverse and optimization methods in 2D in the previous section carry over to the 3D design case. One curious aspect of the 3D inverse and optimization methods is that the solution may be non-unique near the wing root, a result that was reported by Sloof.[72] This occurs because the same pressure distribution can be obtained by shaping the surface on either side of the junction. Although complicating the design method, the result is more freedom available to the designer.

In the next section, we illustrate the possible use of the three-dimensional transonic methodology in a design environment by applying it to two model problems.

4.6.4 Application of the 3D Transonic Program to Wing Design Problems

The feasibility of using the present computer program in transonic wing design as more than a straightforward analysis tool was investigated through two model problems. The first model problem was conducted making use of the NASA optimization program CONMIN.[73] The main purpose of the exercise was to gain familiarity with the use of optimization codes in aerodynamic applications. The second model problem was undertaken to assess the effort required to introduce an automatic geometry alteration loop driven by the results of a previous iteration into the code. The stability of this type of iterative procedure is also of interest.

4.6.4.1 First Model Problem

The first model problem provided an opportunity to obtain experience using CONMIN. The problem was specified simply as follows: *Using lifting-line theory for the aerodynamic representation of the finite wing, have CONMIN determine the twist distribution required to minimize the induced drag*. In this case, the exact solution can be found for straight tapered wings to be

$$\alpha_g(\eta) = \frac{C_L}{\pi AR}\left\{1 + \frac{AR(1+\lambda)}{\pi} \cdot \frac{\left(1-\eta^2\right)^{1/2}}{[1-(1-\lambda)\eta]}\right\}. \qquad (4\text{-}6)$$

For an untapered wing, equation (4-6) for α_g shows that the basic incidence variation along the span is elliptic. Observing the functional form of the exact solution, we note that this particular ratio of the root of a second-order polynomial to a first-order polynomial would have been an unlikely selection for the assumed variation of spanwise twist. To repeat, unless equation (4-6) was contained as a subset of the functional forms selected for the optimization study, the true optimum twist distribution would not have been found. This fact serves to demonstrate the importance of using the insight gained from analytical theories to maximize the benefits of numerical solutions.

Indeed, initial efforts to obtain the minimum solution using a cubic polynomial for the span variation of twist were not particularly satisfying. The results never approached the true minimum, and apparently there were several combinations of coefficient values that were equally close to true minimum, such that several substantially different answers for the twist variation could be obtained depending on the initial guess supplied to the program. These calculations typically took on the order of ten iterations, each of which required a number of function evaluations to obtain the local gradient of the objective function. In aerodynamic terms, this means that there were ten main executions of the aerodynamic program and a number of "small" executions that were required to be run long enough to provide the local gradient of the solution with respect to each design variable. It is clear that this can quickly lead to an immense amount of computational effort.

Finally, the optimization scheme was run with the design variables consisting of a coefficient to equation (4-6) and the coefficient of an additional term added to equation (4-6). Figure 4-11[74] shows the path through design space for this two-parameter optimization run. Note that the minimum occurs when $\beta_2 = 0$, and $\beta_1 \approx 1$ (β_1 is not exactly because a lift-curve slope slightly different than 2π was employed). The run terminated after eight iterations, with the numerical solution predicting that the optimum had been achieved.

Figure 4-12 shows a close-up view of the last iterations of the path through the design space. The result demonstrated that the program could in fact select the true optimum if it was embedded in the design variable space. This effort demonstrated both the difficulties and possibilities associated with the use of optimization methods.

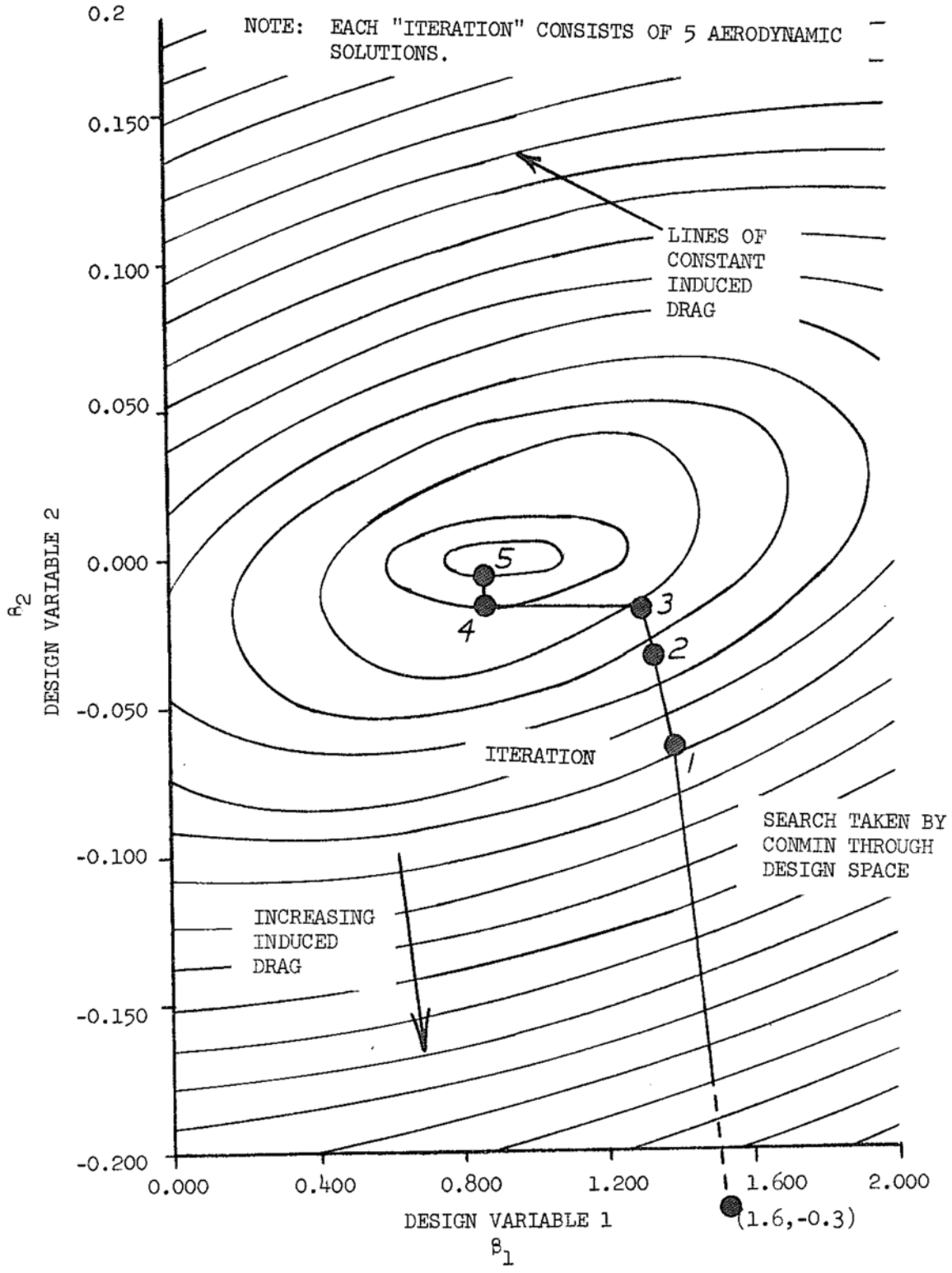


Figure 4-11: Twist optimization using numerical optimization and lifting-line theory. *From W. H. Mason. US Air Force. Public domain.*

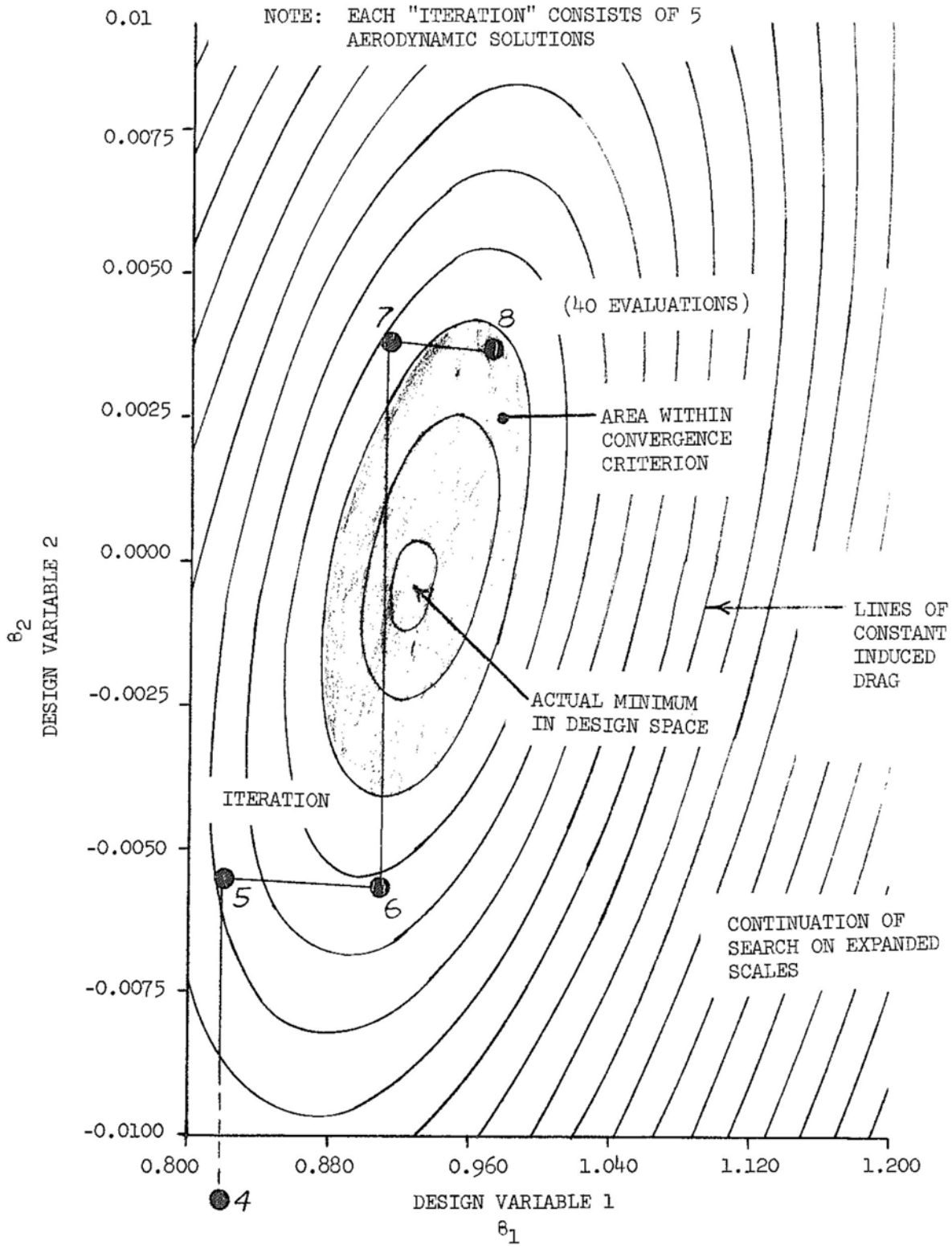


Figure 4-12: Close-up of the final iterations through the design space. *From W. H. Mason. US Air Force. Public domain.*

4.6.4.2 Second Model Problem

The second model problem is considerably different in concept. For this problem, the question posed was simple: *For a given planform and spanload, determine the twist required to produce the spanload.* Initially, lifting-line theory was employed to verify that the basic iteration scheme adopted would converge for a simple aerodynamics model before attempting to incorporate the iteration into a transonic computational method. The twist was determined by adjusting the section incidence at the finite set of span stations at which the computation provided results, without making any assumption concerning the functional relationship between the incidence at adjacent span stations. The basic iteration tested was

$$\alpha_{D_j} = \alpha_j^K + \left(\frac{C_{l_{D_j}} - C_{l_j^K}}{C_{l_{\alpha_j}}} \right) \qquad (4\text{-}7)$$

where *j* denotes the particular span station, *D* denotes the design condition, and *K* indicates the iteration number. $C_{l\alpha}$ is approximated by

$$C_{l\alpha}^k = \frac{C_l^k - C_l^{k-1}}{\alpha^k - \alpha^{k-1}}. \qquad (4\text{-}8)$$

For the lifting-line simulation, this iteration procedure converged to the exact solution given by equation (4-6) in about four or five iterations. This result was obtained without difficulty even though the approximation given in equation (4-8) is poor for numerical computation due to the progressively smaller differences between the values as the iteration converges.

Equation (4-7) is equivalent to a more general form,

$$\{\alpha_D\} = \{\alpha^K\} + \left[\tilde{A}^{K-1}\right]^{-1} \{C_{l_D} - C_l^K\} \qquad (4\text{-}9)$$

where [A] with a tilde on top in equation (4-9) is an approximation to the actual influence coefficient matrix [A], which relates C_l and α:

$$\{C_l\} = [A]\{\alpha\}. \qquad (4\text{-}10)$$

In the present method, [A] with a tilde on top in equation (4-9) has been given by the extremely simplified relationship in equation (4-8) for the diagonal terms, with the off-diagonal terms assumed to be zero. This result shows that [A] in equation (4-10) can be crudely approximated if an iteration is allowed to determine the final result. Naturally, as the approximation to the matrix [A] improves, the number of iterations required is reduced.

The basic inviscid program was modified to incorporate this type of iteration scheme without difficulty. It was found that a relatively fine grid was required to obtain the straight-wing result computed previously using the lifting-line aerodynamic model. Refinements to the iteration included the use of underrelaxation of the twist increment and the use of the initial $C_{l\alpha}$ value for all iterations. These refinements led to a smoothly converging solution that took about 50% longer than the basic solution. The method was then applied to a 45° swept untapered wing. The refined procedure led to a solution with the results obtained shown in figure 4-13, which also contains the straight-wing results for comparison. In this case, attempts to compute the result with $C_{l\alpha}$ changing from iteration to iteration led to a diverging result at the point where no shift in angle was required (about 45% semispan), and this experience showed that, in an actual production program, an improved approximation to [A] should be used. However, this improved approximation can be constructed without difficulty so that a design option of the type described above could be included in the basic analysis program.

In this section, we have demonstrated the variety of possibilities that arise when incorporation of design options is suggested. One of the options would provide immediate benefits to the designer, allowing analysis codes to be easily modified to provide design options.

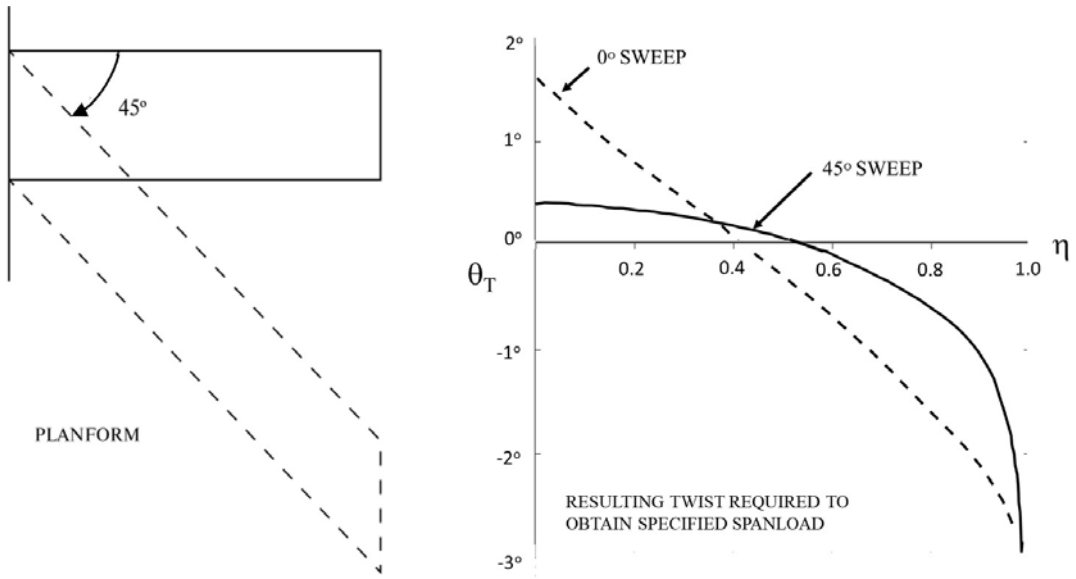


Figure 4-13(a): Wing-twist design results using simple modifications to an analysis code. US Air Force. Adapted by S. Madden. Public domain.

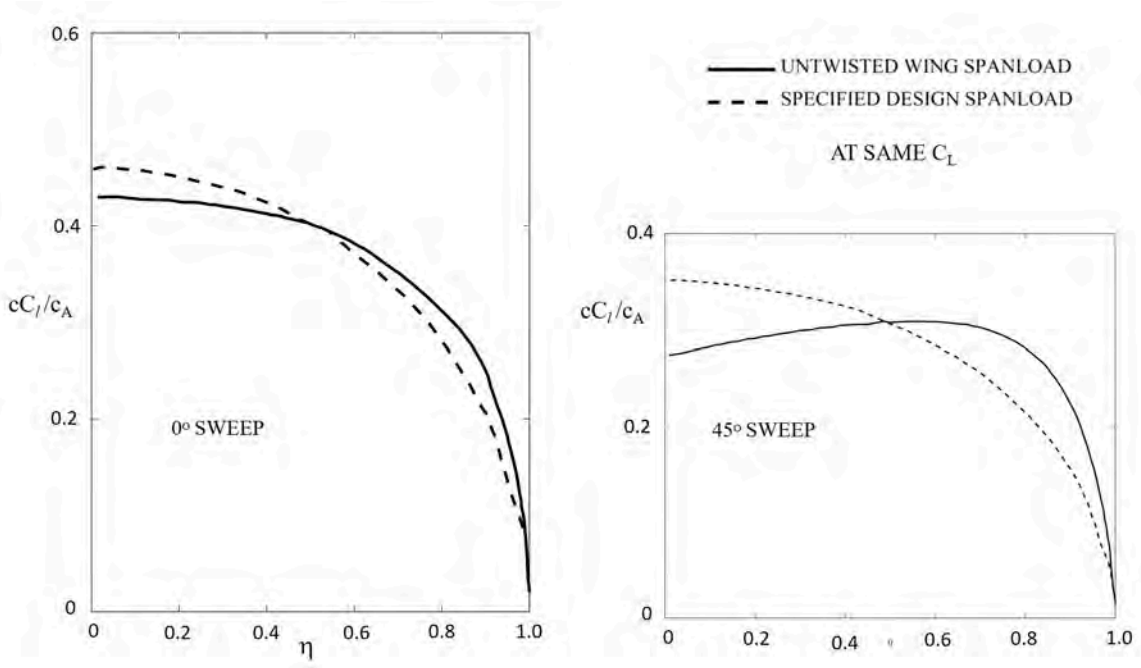


Figure 4-13(b): Wing-twist design results using simple modifications to an analysis code. U.S. Air Force. Adapted by S. Madden. Public domain.

4.6.5 Design Within the Context of Multidisciplinary Design Optimization

Broader issues related to aerodynamic design within the MDO context, which considers other disciplines simultaneously, have been the subject of extensive research at Virginia Tech since the 1990s. An overview of our thinking is given in a paper by Giunta, et al.[75] Another source is the MAD Center Report 96-06-01 (Virginia Tech, AOE Dept., Blacksburg, VA, June 1996). The ability to combine high-fidelity results from numerous disciplines in early design is an important area of research for configuration aerodynamics.

4.7 Summary of the Status of Aerodynamic Design

Aerodynamic optimization has become practical using CFD. The ability to use it in conjuncture with other disciplines simultaneously is currently being addressed. We conclude with a quote from a 2004 paper by Jameson:

> The accumulated experience in the last decade suggests that most existing aircraft which cruise at transonic speeds are amenable to a drag reduction of the order of 3 to 5 percent, or an increase in the drag rise Mach number of at least 0.02. These improvements can be achieved by very small shape modifications, which are too subtle to allow their determination by trial and error methods. When larger scale modifications such as planform variations or new wing sections are allowed, larger gains in the range of 5-10 percent are attainable.[76]

Chapter 4 Exercises

4.1 Estimate W/S for a variety of aircraft types. What conclusions can you make?

4.2 Estimate cruise C_L for a variety of aircraft types. What conclusions can you make?

4.3 Straight line wrap: t/c – considering a simple trapezoidal planform, derive an expression for the maximum thickness distribution between the root and tip stations when different maximum t/c's are specified at the root and tip station. Illustrate your result by plotting the maximum thickness-to-chord distribution across the span for a wing with an aspect ratio of 7 and a taper ratio of 0.3. The root t/c is 12%, and the tip t/c is 6%.

4.4 Straight line wrap: *twist* – considering a simple trapezoidal planform, derive an expression for the twist distribution between the root and tip stations given the root and tip twist. Illustrate your result by plotting the spanwise twist distribution between the root and tip for a wing with an aspect ratio of 4 and a taper ratio of 0.2. The root twist is +2°, and the tip twist is –4°.

4.5 Derive the formula for the twist distribution required to achieve an elliptic spanload distribution using lifting-line theory (hint: use the monoplane equation). For the wing in exercise 4.4, plot the required spanwise twist distribution required for a lift coefficient of one. Compare your results with the results from 4.4.

4.6 Use LAMDES (see appendix E) to obtain the required twist distribution for the wing in problem 4.5 above, assuming the wing has a leading-edge sweep of 45°.

Figure References

Figure 4-1: Kaboldy. Boeing 747-400. CC BY-SA 4.0. Dimensions added. https://en.m.wikipedia.org/wiki/File:Boeing_747-400_3view.svg

Figure 4-2: NASA. X-29 #82-003. 2014. Public domain. https://www.nasa.gov/image-article/where-are-they-now-x-29-82-003

Figure 4-3: Northrop Grumman. Copyright undetermined. Fair use.

Figure 4-4: US Department of Defense. Northrop B-2 Spirit flying wing aircraft. Public domain. https://media.defense.gov/2009/Jun/01/2000562028/1200/1200/0/090512-F-2482B-218.JPG

Figure 4-5: Tibboh. Piaggio P-180 Avanti in in-flight demonstration at Rennes AirShow 2010. CC BY-SA 3.0 Unported. https://commons.wikimedia.org/wiki/File:Piaggio_P-180_Avanti_Rennes_2010_(cropped).jpg

Figure 4-6: NASA. F-16XL CAWAP Flight (ship #1). 1996. Public domain. https://www.nasa.gov/image-article/f-16xl-1-cawap-flight-4

Figure 4-7: NASA. F-14 VSTFE. 1986. Public domain. https://web.archive.org/web/20250428180901/https://www.dfrc.nasa.gov/Gallery/Photo/F-14/HTML/ECN-33403-2.html

Figure 4-8: W. H. Mason. Winglet on a Canadair Regional Jet at Roanoke, Virginia, Airport.

Figure 4-9: S. Madden, from data in Hoak, D. E., et al., "USAF Stability and Control DATCOM," Flight Control Division, Air Force Flight Dynamics Laboratory, WPAFB, Ohio, 45433-0000, 1978. https://apps.dtic.mil/sti/tr/pdf/ADA086557.pdf

Figure 4-10: Figure 11 from McDonald, R. A., et al., "Future aircraft concepts and design methods," The Aeronautical Journal, Vol. 126, No. 1295, pp. 92–124, 2022. DOI: https://doi.org/10.1017/aer.2021.110; adapted from figure 3.19 in Loftin, L. K., "Subsonic Aircraft: Evolution and the Matching of Size to Performance," NASA RP-1060, Aug. 1980. Fair use. https://ntrs.nasa.gov/citations/19800020744

Figure 4-11: From figure 64(a) in Mason, W. H., MacKenzie, D., Stern, M., Ballhaus, W. F., and Frick, J., "An Automated Procedure for Computing the Three Dimensional Transonic Flow Over Wing-Body Combinations, Including Viscous Effects," US Air Force. AFFDL TR-77-122, Feb. 1978, p. 194. https://archive.aoe.vt.edu/mason/Mason_f/AFFDL-TR-77-122GACAmes.pdf

Figure 4-12: From figure 64(b) in Mason, W. H., MacKenzie, D., Stern, M., Ballhaus, W. F., and Frick, J., "An Automated Procedure for Computing the Three Dimensional Transonic Flow Over Wing-Body Combinations, Including Viscous Effects," US Air Force. AFFDL TR-77-122, Feb. 1978, p. 195. https://archive.aoe.vt.edu/mason/Mason_f/AFFDL-TR-77-122GACAmes.pdf

Figure 4-13(a): From figure 65 in Mason, W. H., MacKenzie, D., Stern, M., Ballhaus, W. F., and Frick, J., "An Automated Procedure for Computing the Three Dimensional Transonic Flow Over Wing-Body Combinations, Including Viscous Effects," US Air Force. AFFDL TR-77-122, Feb. 1978, p. 196. https://archive.aoe.vt.edu/mason/Mason_f/AFFDL-TR-77-122GACAmes.pdf

Figure 4-13(b): From figure 65 in Mason, W. H., MacKenzie, D., Stern, M., Ballhaus, W. F., and Frick, J., "An Automated Procedure for Computing the Three Dimensional Transonic Flow Over Wing-Body Combinations, Including Viscous Effects," US Air Force. AFFDL TR-77-122, Feb. 1978, p. 196. https://archive.aoe.vt.edu/mason/Mason_f/AFFDL-TR-77-122GACAmes.pdf

Notes

1. Küchemann, D., *The Aerodynamic Design of Aircraft*, Pergamon Press, Oxford, 1978.
2. Waaland, I. T., "Technology in the Lives of an Aircraft Designer," AIAA 1991 Wright Brothers Lecture, Baltimore, MD., Sept. 1991.
3. Whitford, R. *Design for Air Combat*, Jane's Information Group, Jan. 1987.
4. Abzug, M. J., and Larrabee, E. E., *Airplane Stability and Control: A History of the Technologies that Made Aviation Possible*, Cambridge University Press, 1997.
5. Raymer, D. P., *Aircraft Design: A Conceptual Approach*, 3rd ed., AIAA, Reston, 1999, pp. 617–680.
6. Roskam, J., *Airplane Design: Part II. Preliminary Configuration Design and Integration of the Propulsion System*, DARCorp., Lawrence, KS, 1986.
7. Olason, M. L., and Norton, D. A., "Aerodynamic Design Philosophy of the Boeing 737," *Journal of Aircraft*, Vol. 3, No. 6, Nov.-Dec. 1966, pp. 524–528. (*Note:* This is also found in AIAA Paper 65-739.)
8. Jones, R. T., *Wing Theory*, Princeton University Press, Princeton, 1990.
9. Schairer, G. S., "Evolution of Modern Air Transport Wings," AIAA Paper 80-3037, in "Evolution of Aircraft Wing Design: Proceedings of the Symposium," Dayton, Ohio, March 18-19, 1980, pp. 61-65. https://doi.org/10.2514/6.1980-3037
10. Shevell, R. S., and Schaufele, R. D., "Aerodynamic Design Features of the DC-9," Journal of Aircraft, Vol. 3, No. 6, Nov.-Dec. 1966, pp. 515–523.
11. Spacht, G., "The Forward Swept Wing: A Unique Design Challenge," AIAA Paper 80-1885, Aircraft Systems Meeting, Anaheim, CA, Aug. 4-6, 1980.
12. Moore, M., and Frei, D., "X-29 Forward Swept Wing Aerodynamic Overview," AIAA Paper 83-1834, Applied Aerodynamics Conference, Danvers, MA, Jul. 13-15, 1983.
13. Pace, S., *The Grumman X-29*, TAB Books, Blue Ridge Summit, 1991.
14. Meyer, R. C., and Fields, W. D., "Configuration Development of a Supersonic Cruise Strike-Fighter," AIAA Paper 78-148, AIAA 16th Aerospace Sciences Meeting, Huntsville, AL, Jan. 16-18, 1978.
15. Hendrickson, R., Grossman, R., and Sclafani, G., "Design Evolution of a Supersonic Cruise Strike Fighter," AIAA Paper 78-1452, AIAA Aircraft Systems and Technology Conference, Los Angeles, CA, August 21-23, 1978.
16. Modin, K. E., and Claréus, U., "Aerodynamic Design Evolution of the SAAB JAS 39 Gripen Aircraft," AIAA Paper 91-3195, AIAA/AHS/ASEE Aircraft Design Systems and Operations Meeting, Baltimore, MD, September 23-25, 1991.

17. Garrison, P., "Go South, Young Duck," FLYING Magazine, Vol. 127, No. 2, Feb. 2000, pp 100–101. ISSN: 0015-4806.
18. Northrop, J. K., "The Development of the All-Wing Aircraft," The Journal of the Royal Aeronautical Society, Vol. 51, No. 438, Jun. 1947, pp. 481–510. https://doi.org/10.1017/S0368393100123624
19. Sears, W. R., "Flying-Wing Airplanes: The XB-35/YB-49 Program," AIAA Paper 80-3036, in "Evolution of Aircraft Wing Design; Proceedings of the Symposium," Dayton, Ohio, Mar. 18-19, 1980, pp. 61–65. https://doi.org/10.2514/6.1980-3036
20. Abzug, M. J., and Larrabee, E. E., *Airplane Stability and Control: A History of the Technologies that Made Aviation Possible*, Cambridge University Press, 1997.
21. Waaland, I. T., "Technology in the Lives of an Aircraft Designer," AIAA Wright Brothers Lecture, Aircraft Design and Operations Meeting, Baltimore, MD, Sept. 23-25, 1991. https://doi.org/10.2514/6.1991-3069
22. Mason, W. H., "Flying Wings including the B-2." http://archive.aoe.vt.edu/mason/Mason/ACiFlyWngs.html
23. Liebeck, R. H., "Design of the Blended Wing Body Subsonic Transport," *Journal of Aircraft*, Vol. 41, No. 1, Jan.-Feb. 2004, pp. 10–25.
24. Agnew, J. W., and Hess, J. R., Jr., "Benefits of Aerodynamic Interaction to the Three-Surface Configuration," AIAA Journal of Aircraft, Vol. 17, No. 11, Nov. 1980; based on AIAA Paper 79-1830, AIAA Aircraft Systems and Technology Conference, New York, NY, Aug. 20-22, 1979.
25. Agnew, J. W., Lyerla, G. W., and Grafton, S. B., "The Linear and Non-linear Aerodynamics of Three-Surface Aircraft Concepts," AIAA Paper 80-1581, AIAA Atmospheric Flight Mechanics Conference, Danvers, MA, August 11-13, 1980.
26. "Piaggio Avanti, Beech Starship Offer Differing Performance Characteristics," Aviation Week & Space Technology, Oct. 2, 1989, pp. 75–78.
27. Loftin, L. K., Jr., "Subsonic Aircraft: Evolution and the Matching of Size to Performance," NASA RP-1060, Aug. 1980.
28. Roskam, J., *Roskam's Airplane War Stories*, DARcorp., Lawrence, KS, 2002, pp. 194–198.
29. Polhamus, E. C., "Applying Slender Wing Benefits to Military Aircraft," AIAA Wright Brothers Lecture, Journal of Aircraft, Vol. 21, No. 6, Aug. 1984, pp. 545–559.
30. Poisson-Quinton, P., "Slender Wings for Civil and Military Aircraft," Eighth Theodore von Kármán Memorial Lecture, Israel Journal of Technology, Vol. 16, No. 3, 1978, pp. 97–131.
31. Kress, R. W., "Variable Sweep Wing Design," AIAA Paper 80-3043, in "Evolution of Aircraft Wing Design; Proceedings of the Symposium," Dayton, OH, March 18-19, 1980.
32. Poisson-Quinton, P., "Aerodynamics of Variable Sweep," in "Assessment of Lift Augmentation Devices," AGARD-LS-43-71, Aug. 1970 (71N20054).
33. Marchman, J. F., III, Faery, H. F., Jr., and Manor, D., "Whitcomb Winglet Applications to General Aviation Aircraft," AIAA Paper 78-1478, Aircraft Systems and Technology Conference Los Angeles, CA, August 21-23, 1978.
34. Kroo, I., "Drag Due to Lift: Concepts for Prediction and Reduction," Annual Review of Fluid Mechanics, Vol. 33, 2001, pp. 587–617.
35. Mason, W. H., "Winglet Aerodynamics (including tip sails)." http://archive.aoe.vt.edu/mason/Mason/AeroWinglets.html
36. Swan, W. C., and Sigalla, A., "The Problem of Installing a Modern High Bypass Engine on a Twin Jet Transonic Transport," in "Aerodynamic Drag," AGARD CP-124, Apr. 1973.
37. Shevell, R. S., and Schaufele, R. D., "Aerodynamic Design Features of the DC-9," Journal of Aircraft, Vol. 3, No. 6, Nov.-Dec. 1966, pp. 515–523.
38. Furlong, G. C., and McHugh, J. G., "A Summary and Analysis of the Low-Speed Longitudinal Characteristics of Swept Wings at High Reynolds Number," NACA TR-1339, 1957.
39. Finck, R. D., "USAF Stability and Control DATCOM," AFWAL-TR-83-3048, Air Force Flight Dynamics Laboratory, Air Force Wright Aeronautical Laboratories, Wright-Patterson Air Force Base, OH, Apr. 1978, p. 2074. https://apps.dtic.mil/sti/pdfs/ADB072483.pdf
40. Waaland, I. T., "Technology in the Lives of an Aircraft Designer," AIAA Wright Brothers Lecture, Aircraft Design and Operations Meeting, Baltimore, MD, September 23-25, 1991. https://doi.org/10.2514/6.1991-3069
41. Hale, F. J., *Introduction to Aircraft Performance, Selection, and Design*, John Wiley & Sons, New York, 1984.
42. McDonald, R. A., German, B. J., Takahashi, T., Bil, C., Anemaat, W., Chaput, A., Vos, R., and Harrison, N., "Future aircraft concepts and design methods," The Aeronautical Journal, Vol. 126, No. 1295, pp. 92–124, 2022. https://doi.org/10.1017/aer.2021.110
43. Loftin, L. K., Jr., "Subsonic Aircraft: Evolution and the Matching of Size to Performance," NASA RP-1060, Aug. 1980. https://ntrs.nasa.gov/citations/19800020744
44. Mason, W. H., "Analytic Models for Technology Integration in Aircraft Design," AIAA Paper 90-3262, AIAA/AHS/ASEE Aircraft Design, Systems, and Operations Conference, Dayton, OH, September 17-19, 1990.
45. Jones, R. T., *Wing Theory*, Princeton University Press, 1990.
46. "Experimental Data Base for Computer Program Assessment," AGARD AR-138, May, 1979; AR-138-Addendem, Jul. 1984.
47. "Test Cases for Inviscid FlowField Methods," AGARD AR-211, May 1985.
48. COMSAC: Computational Methods for Stability and Control, NASA/CP-2004-213028/PT1 and NASA/CP-2004-213028/PT2, Proceedings of a Symposium compiled by Fremaux, C. M., and Hall, R. M., Apr. 2004. https://ntrs.nasa.gov/api/citations/20040086515/downloads/20040086515.pdf
49. Mason, W. H., MacKenzie, D., Stern, M., Ballhaus, W. F., and Frick, J., "An Automated Procedure for Computing the Three Dimensional Transonic Flow Over Wing-Body Combinations, Including Viscous Effects," AFFDL TR-77-122, Vols. 1, 2, and 3, Air Force Flight Dynamics Laboratory, Wright-Patterson Air Force Base, OH, Feb. 1978.
50. Jameson, A., "The Role of CFD in Preliminary Aerospace Design," FEDSM2003-45812, Proceedings of FEDSM'03, 4th ASME_JSME Joint Fluids Engineering Conference, Honolulu, HI, Jul. 6-11, 2003. (*Note*: Available from Jameson's website at Stanford University, http://aero-comlab.stanford.edu/Papers/jame-

son.fedsm.03-45812.pdf)

51. Johnson, F. T., Tinoco, E., and Yu, N. J., "Thirty Years of Development and Application of CFD at Boeing Commercial Airplanes, Seattle," AIAA Paper 2003-3439, 16th AIAA Computational Fluid Dynamics Conference, Orlando, FL, Jun. 2003.
52. Carlson, H. W., and Middleton, W. H., "A Numerical Method for the Design of Camber Surfaces of Supersonic Wings with Arbitrary Planforms," NASA TN-D-2341, 1964.
53. Vanderplaats, G. N., "Automated Optimization Techniques for Aircraft Synthesis," AIAA Paper No. 76-909, AIAA Aircraft Systems and Technology Meeting, Dallas, TX, Sept. 27-29, 1976.
54. McCullers, L. A., "Aircraft Configuration Optimization Including Optimized Profiles," in "Proceedings of Symposium on Recent Experiences in Multidisciplinary Analysis and Optimization" (Sobieski, J., ed.) NASA CP-2327, pp. 396–412, Apr. 1984.
55. Miele, A. (ed.), *Theory of Optimum Aerodynamic Shapes*, Academic Press, New York, 1965.
56. Jameson, A., "Re-Engineering the Design Process Through Computation," AIAA Paper 97-0641, 35th Aerospace Sciences Meeting & Exhibit, Reno, NV, January 6-9, 1997.
57. Thwaites, B. (ed.), *Incompressible Aerodynamics*, Oxford University Press, Oxford, 1960.
58. Henne, P. (ed.), *Applied Computational Aerodynamics*, AIAA Progress in Astronautics and Aeronautics Series, Vol. 125, Washington, 1990.
59. Drela, M., "Elements of Airfoil Design Methodology," *Applied Computational Aerodynamics*, edited by P. Henne, Vol. 125, Progress in Astronautics and Aeronautics Series, AIAA, 1990, pp. 167–189.
60. Volpe, G., "Inverse Airfoil Design: A Classical Approach Updated for Transonic Applications," *Applied Computational Aerodynamics*, edited by P. Henne, Vol. 125, Progress in Astronautics and Aeronautics Series, AIAA, 1990, pp. 191–220.
61. Bauer, F., Garabedian, P., and Korn, D., *Supercritical Wing Sections*, Springer Verlag, Berlin, 1972.
62. Hicks, R. M., Murman, E. M., and Vanderplaats, G. N., "An Assessment of Airfoil Design by Numerical Optimization," NASA TM X-3092, Jul. 1974.
63. Vanderplaats, G. N., and Hicks, R. M., "Numerical Airfoil Optimization Using a Reduced Number of Design Coordinates," NASA TM X-73151, Jul. 1976.
64. Vanderplaats, G. N., and Hicks, R. M., "Numerical Airfoil Optimization Using a Reduced Number of Design Coordinates," NASA TM X-73151, Jul. 1976.
65. Aidala, P. V., Davis, W. H., Jr., and Mason, W. H., "Smart Aerodynamic Optimization," AIAA Paper No. 83-1863, AIAA Applied Aerodynamics Conference, Danvers, MA, Jul. 13-15, 1983.
66. Jameson, A., "Efficient Aerodynamic Shape Optimization," AIAA Paper 2004-4369, 10th AIAA/ISSMO Multidisciplinary Analysis and Optimization Conference, Albany, NY, Aug. 30-Sept. 1, 2004.
67. Davis, W. H., Jr., Aidala, P. V., and Mason, W. H., "A Study to Develop Improved Methods for the Design of Transonic Fighter Wings by the Use of Numerical Optimization," NASA CR-3995, Aug. 1986.
68. Huyse, L., and Lewis, R. M., "Aerodynamic Shape Optimization of Two-Dimensional Airfoils Under Uncertain Conditions," NASA/CR-2001-210648, ICASE Report No. 2001-1, Jan. 2001.
69. Li, W., Huyse, L., and Padulla, S., "Robust Airfoil Optimization to Achieve Consistent Drag Reduction Over a Mach Range," NASA/CR-2001-211042, ICASE Report No. 2001-22, Aug. 2002.
70. Huyse, L., Padula, S., and Li, W., "Probabilistic Approach to Free-Form Airfoil Shape Optimization Under Uncertainty," *AIAA Journal*, Vol. 40, No. 9, Sept. 2002, pp. 1764–1772.
71. Mason, W. H., Knill, D. L., Giunta, A. A., Grossman, B., Haftka, R. T. and Watson, L. T., "Getting the Full Benefits of CFD in Conceptual Design," AIAA Paper 98-2513, AIAA 16th Applied Aerodynamics Conference, Albuquerque, NM, Jun. 1998.
72. Sloof, J. W., "Computational Methods for Subsonic and Transonic Aerodynamic Design," in "Special Course on Subsonic/Transonic Aerodynamic Interference for Aircraft," AGARD-R-712, 1983.
73. Vanderplaats, G. N., "CONMIN: A FORTRAN program for constrained function minimization: User's Manual," NASA TM-X-62282, 1973.
74. Mason, W. H., Mackenzie, D., Stern, M., Ballhaus, W. F., and Frick, Juanita. "An Automated Procedure for Computing the Three Dimensional Transonic Flow Over Wing-Body Combinations, Including Viscous Effects," AFFDL TR-77-122, Vol. 1, Air Force Flight Dynamics Laboratory, Wright-Patterson Air Force Base, Feb. 1978.
75. Giunta, A. A., Golovidov, O., Knill, D. L., Grossman, B., Mason, W. H., Watson, L. T., and Haftka, R. T., "Multidisciplinary Design Optimization of Advanced Aircraft Configurations," Fifteenth International Conference on Numerical Methods in Fluid Dynamics, in *Lecture Notes in Physics*, Vol. 490, edited by P. Kutler, J. Flores, and J.-J. Chattot, Springer-Verlag, Berlin, 1997, pp. 14-34.
76. Jameson, A., "Efficient Aerodynamic Shape Optimization," AIAA Paper 2004-4369, 10th AIAA/ISSMO Multidisciplinary Analysis and Optimization Conference, Albany, NY, Aug. 30-Sept. 1, 2004.

5. Subsonic Aerodynamics: Airfoils and Wings

In this chapter, we discuss subsonic aerodynamics, mainly in relation to airfoils and wings. We look at the basic aerodynamics mainly from an inviscid point of view. Generally, this is a reasonable starting point for thinking about aerodynamics in attached flows. Traditionally, the methods used to make these calculations are known as surface panel methods (or simply panel methods) and vortex lattice methods. The theory is described in Chapters 4 and 5 of the *Applied Computational Aerodynamics* book.[1] Although we are primarily addressing the aerodynamic features, we provide brief overviews of the methods used to compute the results shown.

One of the key features of subsonic flow is the use of Laplace's equation as the basis for the inviscid solution. Solutions of this linear equation can be obtained using superposition of "singularities" of unknown strength distributed over discretized portions of the surface (i.e., panels).* Hence the flow field solution is found by representing the surface by a number of panels and solving a linear set of algebraic equations to determine the unknown strengths of the singularities. An excellent entry into the panel method literature is available through two reviews by Hess.[2,3] Two other good sources are the survey by Erickson[4] and the book by Katz and Plotkin.[5]

A more approximate—yet physically appealing—approach is often used to compute wing aerodynamics. In this approach, the wing is represented by a system of horseshoe vortices placed on the mean surface. These methods are known as vortex lattice methods (VLMs). Generally, they ignore the thickness effects. This is possible because, for relatively thin surfaces, the effects of thickness cancel between the upper and lower surfaces, meaning that the lift is not influenced by the thickness to first order. We will illustrate wing aerodynamics using vortex lattice methods. A key reference for these methods is a workshop devoted to them at NASA in the mid-seventies.[6] A nearly universal standard for vortex lattice predictions had been established by then in the form of a code developed at NASA Langley by Rich Margason, John Lamar, and their collaborators.[7,8,9,10] See section E.6.1 for more.

Chapter 5 of *Applied Computational Aerodynamics*[11] provides complete details on the VLM method, together with references to other implementations of the method. Some of the most noteworthy variations on the basic method have been developed by Lan[12] (developer of the quasi-vortex lattice method), Hough,[13] DeJarnette,[14] and Frink.[15] Mook et al.[16] at Virginia Tech have developed vortex lattice class methods that treat flow fields containing leading-edge vortex type separation and also handle general unsteady motions and deforming wakes. The book by Katz and Plotkin[17] contains another variation. At Virginia Tech, Jacob Kay wrote a code using the method of Katz and Plotkin to estimate stability derivatives; see section E.9.1.[18] Three other vortex lattice methods are worthy of note:

1. Tornado, a MATLAB code developed in Sweden[19] (see section E.6.3)
2. AVL by Prof. Drela and Harold Youngren[20] (see section E.6.4)
3. VSPAero by NASA (see section E.6.5)

*The singularities are distributed across the panel. They are not specified at a point. However, the boundary conditions usually are satisfied at specific locations.

5.1 Airfoils

In this section, we highlight basic ideas of airfoil subsonic aerodynamics. We discuss the accuracy and validation aspects of flow simulation computer programs in section 5.1.1. This is followed by a discussion of airfoil aerodynamics characteristics in section 5.1.2. We conclude by discussing issues related to airfoil selection in section 5.1.3.

The computed results presented in this section mainly use Jack Moran's program PANEL.[21] The flow is assumed to be inviscid and irrotational, governed by the Laplace's equation or the potential flow equation. As the name of the program suggests, the body surface is approximated by a collection of panels, each with a distribution of singularities. It is important to emphasize that our choice of program PANEL should not be construed as an indication of any preference; it was more a matter of convenience. Once you understand the basic ideas of airfoil subsonic aerodynamics that we illustrate using PANEL, you will be well prepared to effectively use any other code of your choice. As a matter of fact, the current standard program for subsonic airfoil analysis and design is due to Mark Drela of MIT and is known as XFOIL.[22] It includes viscous effects and is in the public domain for academic use; see section E.7.1 for the software website for accessing this code and more details.

5.1.1 PANEL and Other Flow Simulation Methods: Accuracy and Validation

PANEL was essentially created by Moran.[23] PANEL's node points are distributed employing the widely used cosine spacing function. This approach is used to provide a smoothly varying distribution of panel node points that concentrate points around the leading and trailing edges. An example of the accuracy of the program is given in figure 5-1, where the results from PANEL for the NACA 4412 airfoil are compared with results obtained from an exact conformal mapping of the airfoil (which can be considered to be an exact solution). The agreement is nearly perfect.

Most codes require that you select the number of panels to represent the surface. How many should you use? One of the first things the user should do is evaluate how many panels are needed to obtain the desired level of accuracy. As a matter of fact, this is the best practice for using any computer program. For a panel method, the user must determine the number of panels required to generate accurate results. It is best to examine forces, moments, and pressure distributions.

To check the sensitivity of the solution to the number of panels, compare force and moment results as well as pressure distributions as the number of panels increase. To estimate the limit for a large number of panels, the results can be plotted as a function of the reciprocal of the number of panels. Thus the limit result occurs as $1/n$ reaches zero. Figures 5-2 through 5-4 present the results in this manner for the case given above, including the pitching moment for examination in the analysis. We see in figure 5-2 that the drag is approaching zero, which is the correct result for a two-dimensional inviscid incompressible solution.

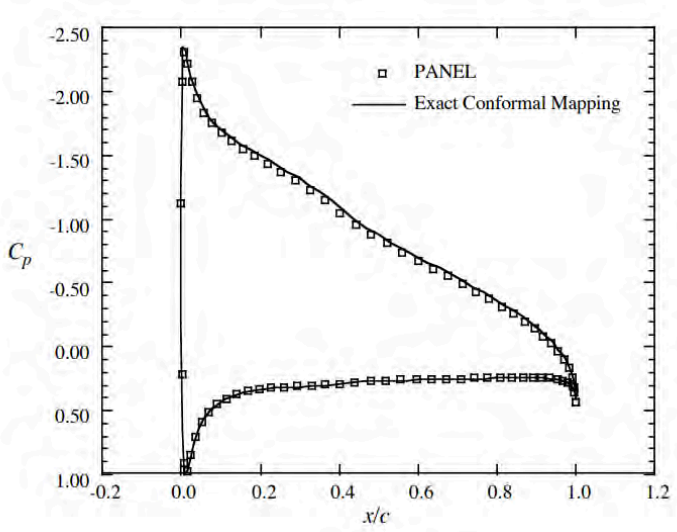


Figure 5-1: Comparison of results from program PANEL with an essentially exact mapping solution for the NACA 4412 airfoil at 6° angle of attack.

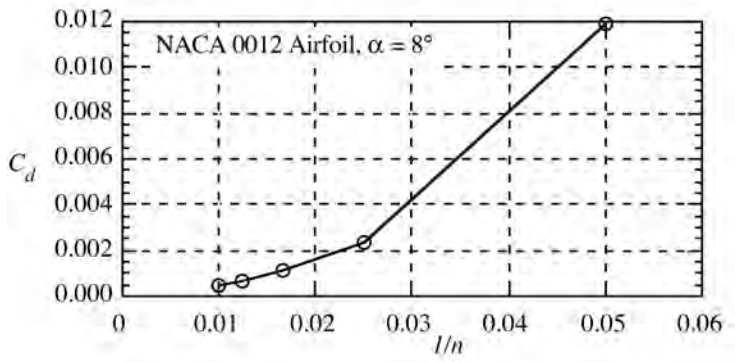


Figure 5-2: Change in computed drag coefficient with the inverse of the number of panels.

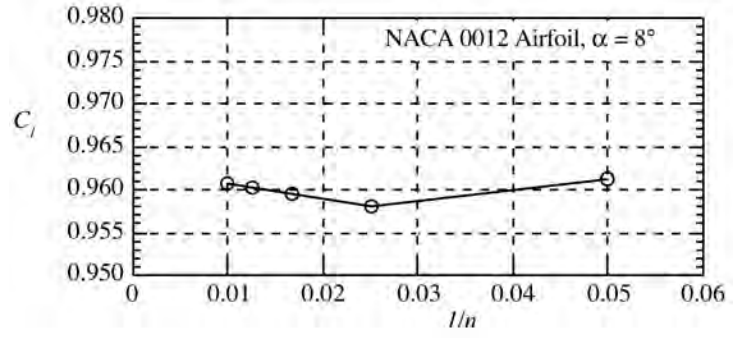


Figure 5-3: Change in computed lift coefficient with the inverse of the number of panels.

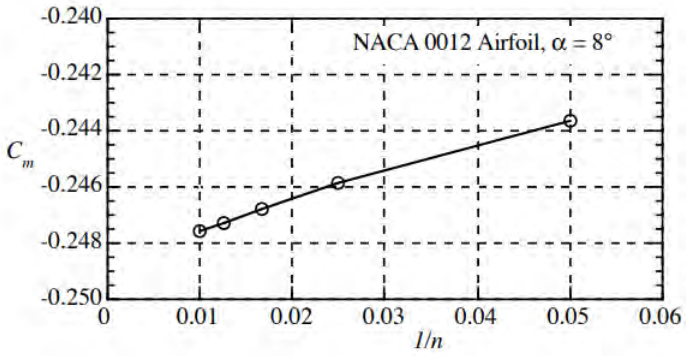


Figure 5-4: Change of pitching moment with the inverse of the number of panels.

Figures 5-2 through 5-4 show that PANEL produces results that are relatively insensitive to the number of panels once fifty or sixty panels are used. By extrapolating to $1/n = 0$, an estimate of the limiting value can be obtained.

In addition to forces and moments, the sensitivity of the pressure distributions to changes in panel density should also be investigated. Pressure distributions are shown in figures 5-5 and 5-6. Figure 5-5 contains a comparison between the cases of twenty panels and sixty panels. It appears that the pressure distribution is well defined with sixty panels. This is confirmed in figure 5-6, which demonstrates that it is almost impossible to identify the differences between the sixty and 100 panel cases. This type of study should (in fact, *must*) be conducted when using computational aerodynamics methods.

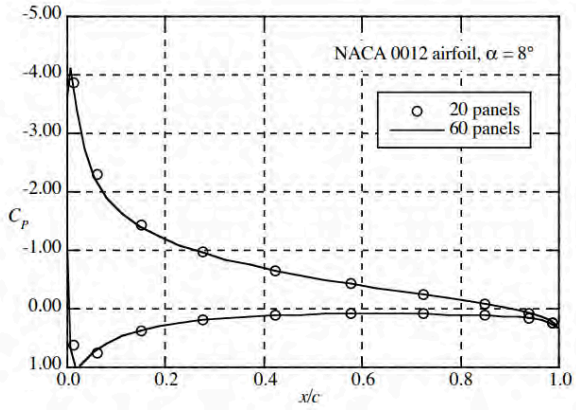


Figure 5-5: Pressure distribution from the program PANEL, comparing results using twenty and sixty panels.

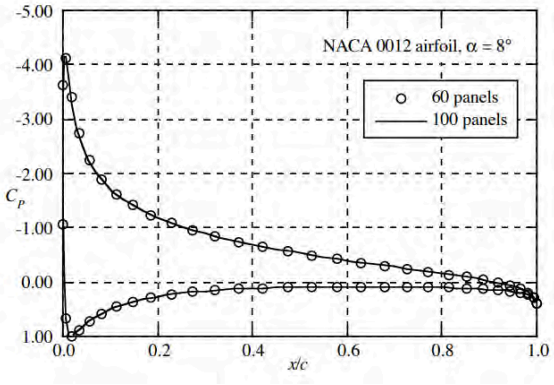


Figure 5-6: Pressure distribution from the program PANEL, comparing results using sixty and 100 panels.

Having examined the convergence of the mathematical solution, we investigate the agreement with experimental data in a process called validation of the code. Figure 5-7 compares the lift coefficients from the inviscid solutions obtained from PANEL with experimental data from Abbott and von Doenhoff.[24] Agreement is good at low angles of attack, where the flow is fully attached. The agreement deteriorates as the angle of attack increases. Viscous effects start to show up as a reduction in lift as angle of attack increases until, finally, the airfoil stalls. The inviscid solutions from PANEL cannot capture this part of the physics. There are significant differences in the airfoil behavior at stall between the cambered and uncambered airfoil. Essentially, the differences arise due to different flow separation locations on the different airfoils. The cambered airfoil separates at the trailing edge first. Stall occurs gradually as the separation point moves forward on the airfoil with increasing incidence. The uncambered airfoil stalls due to a sudden separation at the leading edge. Differences in pressure distributions can be studied next to see why this might be the case.

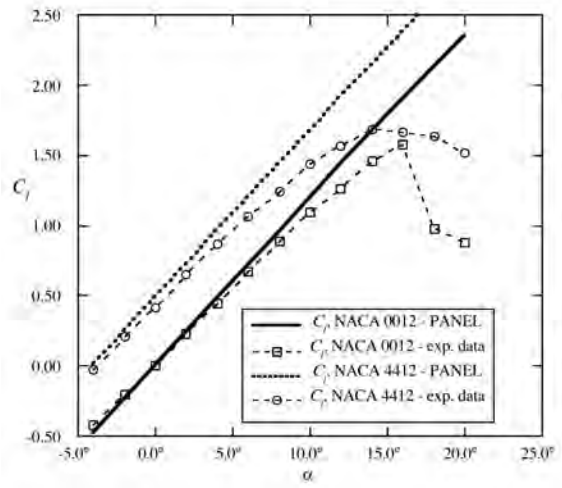


Figure 5-7: Comparison of PANEL code lift coefficient predictions with the available experimental data. From I. H. Abbott and A. E. von Doenhoff. "Theory of Wing Sections." Adapted. Fair use.

The pitching moment characteristics are also very important. Figure 5-8 provides a comparison of the PANEL pitching moment predictions (about the quarter chord point) with experimental data. In this case, the calculations indicate that the computed location of the aerodynamic center, $dC_m / dC_l = 0$, is not exactly at the quarter chord, although the experimental data is very close to this value. The uncambered NACA 0012 data shows nearly zero pitching moment until flow separation starts to occur. The cambered airfoil shows a significant pitching moment and a trend due to viscous effects that is exactly opposite the computed prediction.

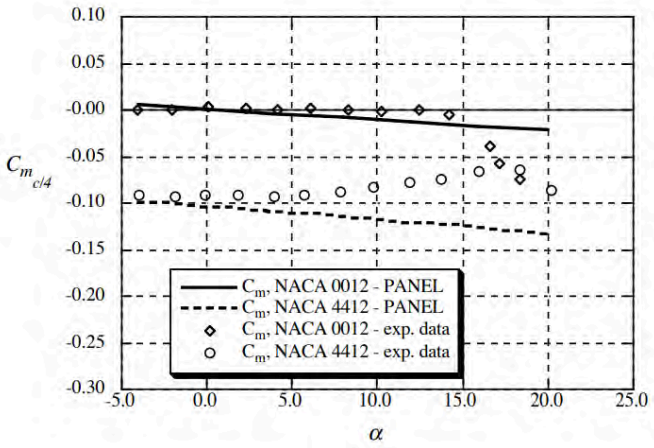


Figure 5-8: Comparison of PANEL moment predictions with experimental data. From I. H. Abbott and A. E. von Doenhoff. "Theory of Wing Sections." Adapted. Fair use.

We do not compare the drag prediction from PANEL with experimental data. In two-dimensional incompressible inviscid flow, the drag is supposed to be zero. In the actual case, drag arises from skin friction effects, additional form drag from the small change of pressure on the body due to the boundary layer (which primarily prevents full pressure recovery* at the trailing edge), and drag due to increasing viscous effects with increasing angle of attack. A well designed airfoil will have a drag value very nearly equal to the skin friction and nearly invariant with incidence until the maximum lift coefficient is approached.

*Pressure recovery is the term we use to describe the increase in static pressure on the rear portion of an airfoil where the flow slows down in subsonic flows. Most airfoils in subsonic flow exhibit a gradual increase in pressure from a minimum value somewhere on the airfoil to the trailing edge. We reserve the use of the term recompression for transonic flows in which flow expands to supersonic speeds on a portion of the airfoil surface and then recompresses to subsonic speeds across a shock.

Even though we don't include predictions, we include the experimental drag polars corresponding to the lift and moment cases given above. Figure 5-9 contains the experimental data showing the effect of camber on the drag polar based on the 0012 and 4412 test cases. Note that the cambered airfoil has a higher drag than the uncambered airfoil at low lift coefficients but starts to show an advantage at a C_l above about 0.3 and is clearly superior at a C_l of around 0.6 to 0.9. The minimum drag is always higher for the cambered airfoil. The aerodynamicist has to decide on the appropriate amount of camber for each application. Keep in mind that the results given here are for old airfoils. The opportunity exists to design modern airfoils that operate over a wide range of lift coefficients without incurring drag penalties. The appeal of variable camber, either through leading-edge and trailing-edge device deflection schedules or smart structure "morphing," is also evident.

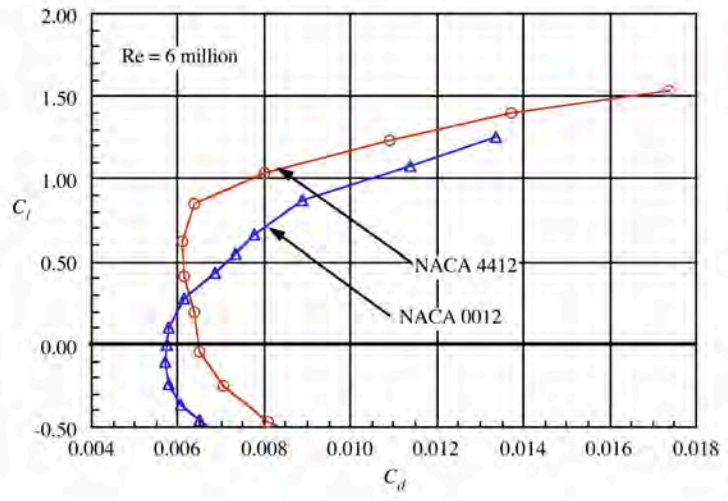


Figure 5-9: Experimental drag polars for the NACA 0012 and NACA 4412 airfoils. *From I. H. Abbott and A. E. von Doenhoff. "Theory of Wing Sections." Adapted. Fair use.*

In addition to force and moment comparisons, we need to compare the pressure distributions predicted with PANEL to experimental data. Figure 5-10 provides one example, comparing the NACA 4412 experimental pressure distribution to PANEL predictions. The agreement is generally very good. The primary disagreement is at the trailing edge. Here, viscous effects act to prevent the recovery of the experimental pressure to the levels predicted by the inviscid solution.

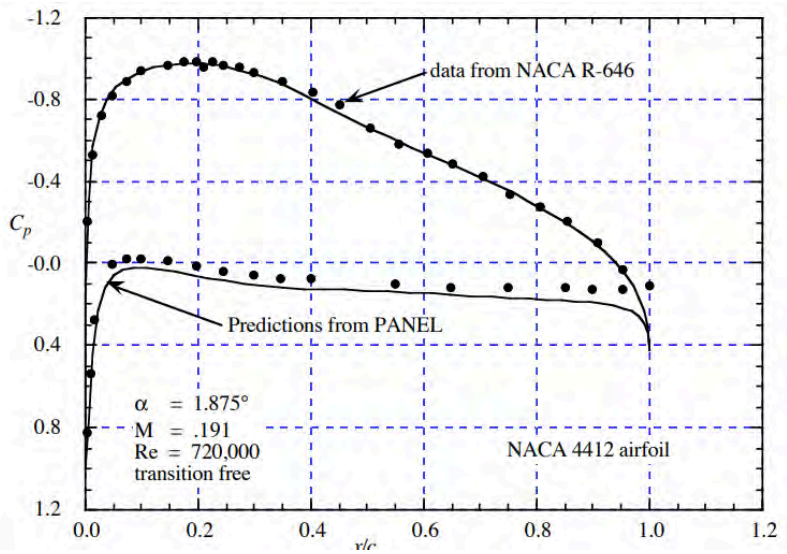


Figure 5-10: Comparison of pressure distribution from PANEL with experimental data. *From W. H. Mason. Adapted by S. Madden.*

Finally, panel methods often have trouble in accurately simulating the flow at the trailing edge of thin airfoils with cusped trailing edges, where the included angle at the trailing edge is zero. The 6-series airfoils are an example. In those cases, PANEL may give poor results locally near the trailing edge. This problem is demonstrated in figure 5.21 in Chapter 5 of *Applied Computational Aerodynamics*.[25]

While the 6-series airfoils were very difficult to use on operational aircraft because of their thin, cusped trailing edges, the subsequent 6A-series airfoils were introduced to remedy the problem. These airfoils have larger trailing-edge angles (approximately the same as the 4-digit series) and were made of nearly straight (or flat) surfaces over the last 20% of the airfoil. Most applications of 6-series airfoils today actually use the modified 6A-series thickness distribution.

5.1.2 Subsonic Airfoil Aerodynamics

> "[M]ankind can be divided into two great classes: those who take airfoil selection seriously and those who don't."
>
> —Peter Garrison, *Flying Magazine*, September 2002

In this section, we attempt to demonstrate how airfoil selection is related to subsonic aerodynamics. Using PANEL, we have a means of easily examining pressure distributions as well as forces and moments for different airfoil shapes. We present a discussion of airfoil characteristics using an inviscid analysis. In figure 5-11, we illustrate key areas to examine when studying airfoil pressure distributions using the NACA 0012 airfoil at 4° angle of attack as a typical example.

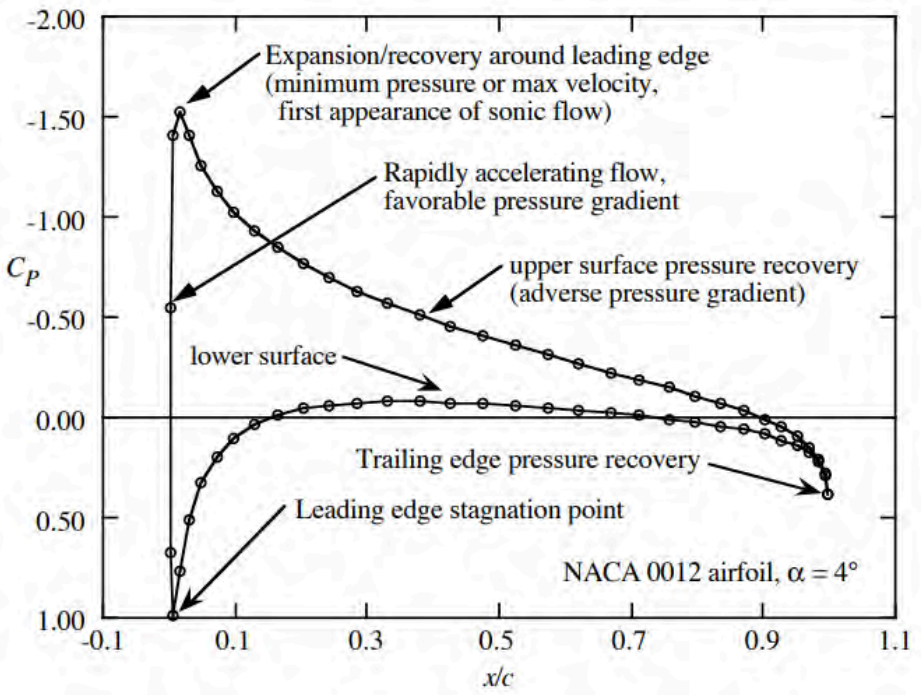


Figure 5-11: Key areas of interest when examining airfoil pressure distributions illustrated for the NACA 0012 airfoil surface pressure distribution at 4° angle of attack. From W. H. Mason. Adapted by S. Madden. CC BY-NC-SA 4.0.

Several aspects of the pressure distribution shown in figure 5-11 should be discussed. First, for subsonic 2D flow, the stagnation pressure coefficient should be one. As the Mach number increases, the value will increase slightly. For swept wings, the stagnation point pressure coefficient will be less than one. The rapid flow acceleration near the leading edge and the subsequent recompression can suggest the possibility of flow separation. The abruptness depends on the airfoil shape close to the leading edge. Bigger leading edge radii soften this flow feature, as well as reducing sensitivity to angle of attack. Another relevant aspect of pressure distribution concerns the value of the pressure coefficient at the trailing edge. If the C_p seen in data or a viscous calculation is greater than about 0.20, the flow can be assumed to be attached, a desirable feature.

Remember that we are making an incompressible, inviscid analysis when we use the program PANEL. Thus, in this section, we examine the basic characteristics of airfoils from that point of view. We will examine viscous and compressibility effects later. However, the best way to understand airfoil characteristics from an engineering standpoint is to examine the inviscid properties and then consider changes in properties due to the effects of viscosity. The aerodynamicist controls the pressure distribution through selection of the geometry, controlling, or suppressing, adverse viscous effects. The mental concept of the flow best starts as a flow field driven by the pressure distribution that would exist if there were no viscous effects. The airfoil characteristics then change through the "relieving" effects of viscosity, where flow separation or boundary layer thickening reduces the degree of pressure recovery that would occur otherwise. For efficient airfoils, the viscous effects should be small at normal operating conditions.

5.1.2.1 Overview of Airfoil Characteristics: Good and Bad

We next illustrate the connection between the airfoil geometry and the airfoil pressure distribution, including ways to control the inviscid pressure distribution by changing the airfoil geometry. An aerodynamicist controls viscous effects by controlling the pressure distribution. Further discussion and examples providing insight into aerodynamic design are available in the excellent book by Jones.[26] A book that captures much of the experience of the original designers of the NACA airfoils was written by aeronautical pioneer E. P. Warner.[27]

Drag. We discussed the requirement that drag should be zero for this two-dimensional* inviscid incompressible irrotational prediction method when we studied the accuracy of the method in the previous section (section 5.1.1). At this point, we infer possible drag and adverse viscous effects by examining the effects of airfoil geometry and angle of attack on the pressure distribution.

Lift. Thin-airfoil theory predicts that the lift-curve slope should be 2π, and thick-airfoil theory says that it should be slightly greater than 2π, with 2π being the limit for zero thickness. You can easily determine how close PANEL comes to this value. These tests should give you confidence that the code is operating correctly. The other key parameter is α_{ZL}, the angle at which the airfoil produces zero lift; a related value is C_{l_0}, the value of C_l at $\alpha = 0°$.

Moment. Thin-airfoil theory predicts that subsonic airfoils have their aerodynamic centers at the quarter chord for attached flow. The value of C_{m_0} depends on the camber. We have seen in figure 5-8 that the computed aerodynamic center is not precisely located at the quarter chord. However, the slope of the moment curve in figure 5-8 corresponds to an aerodynamic center location of $x/c = 0.2597$, which is reasonably close to 0.2500.

Multi-element airfoils are also an important class of airfoils. However, their performance is so closely connected to the effects of viscosity that we must defer discussion of those airfoils until we address viscous effects at the first order in Chapter 7, "High-Lift Aerodynamics."

*Three-dimensional panel methods can estimate the induced drag.

Angle-of-attack effect

The starting place for understanding airfoil characteristics is an examination of the angle-of-attack effect on an uncambered airfoil. Figure 5-12 presents this effect for the NACA 0012 airfoil. Here, we see the progression from the symmetric zero angle-of-attack result. The $\alpha = 0°$ case produces a mild expansion around the leading edge followed by a monotonic recovery to the trailing-edge pressure. As the angle of attack increases, the pressure begins to expand rapidly around the leading edge, reaching a very low pressure and resulting in an increasingly steep pressure recovery at the leading edge.

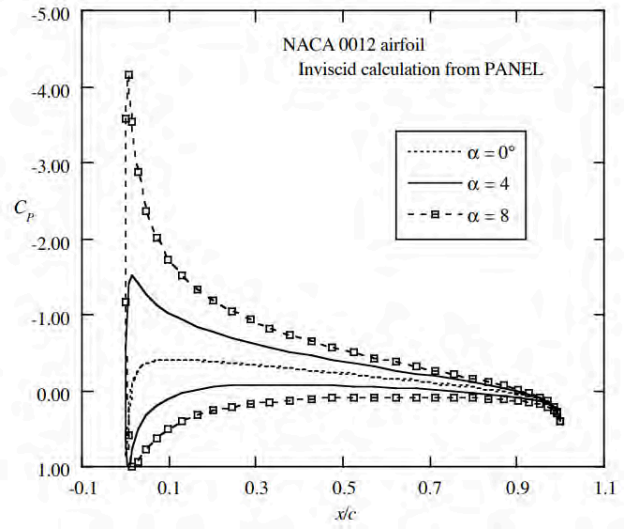


Figure 5-12: Effect of angle of attack on the pressure distribution. From W. H. Mason. Adapted by S. Madden. CC BY-NC-SA 4.0.

Thickness effect

The next effect of interest is thickness. Figure 5-13 presents airfoil shapes for NACA 4-digit sections of 6%, 12%, and 18% thickness-to-chord ratio, *t/c*. The associated basic pressure distributions at zero angle of attack are shown in figure 5-14. Clearly, the thicker airfoil produces a larger disturbance and thus a lower minimum pressure. However, the 18-percent-thick airfoil produces a slightly milder expansion around the leading edge. The recompression near the trailing edge is also milder, and it extends further upstream than the thinner airfoils.

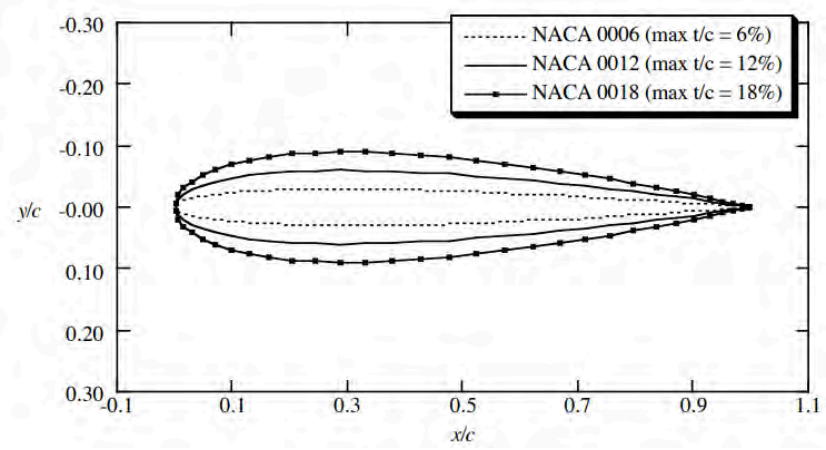


Figure 5-13: Comparison of NACA 4-digit airfoils of 6%, 12%, and 18% thicknesses. From W. H. Mason. Adapted by S. Madden. CC BY-NC-SA 4.0.

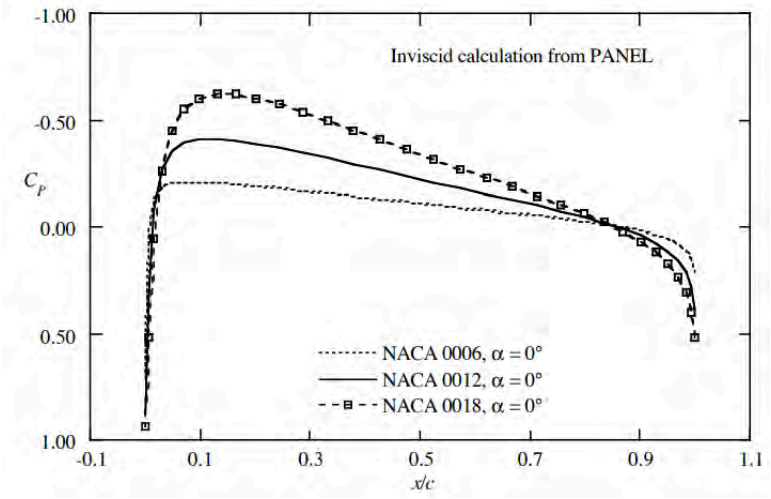


Figure 5-14: Effect of airfoil thickness on the pressure distribution at zero lift. From W. H. Mason. Adapted by S. Madden. CC BY-NC-SA 4.0.

The effect of thickness in softening the expansion and recompression around the leading edge is even more evident at an angle of attack. Figure 5-15 shows this effect at a lift coefficient of 0.48. The thinnest airfoil shows a dramatic expansion/recompression due to the location of the stagnation point below the leading-edge point, requiring a rapid flow expansion around the leading edge that has a very small radius of curvature. The thicker airfoil results in a significantly milder expansion and subsequent recompression due to the large radius of its leading edge. It is important to note that the pressure distributions shift "upward" as the thickness increases. However, the ΔC_p is nearly the same for each thickness, as predicted using the superposition of thickness effects and angle-of-attack effects arising in thin-airfoil theory.

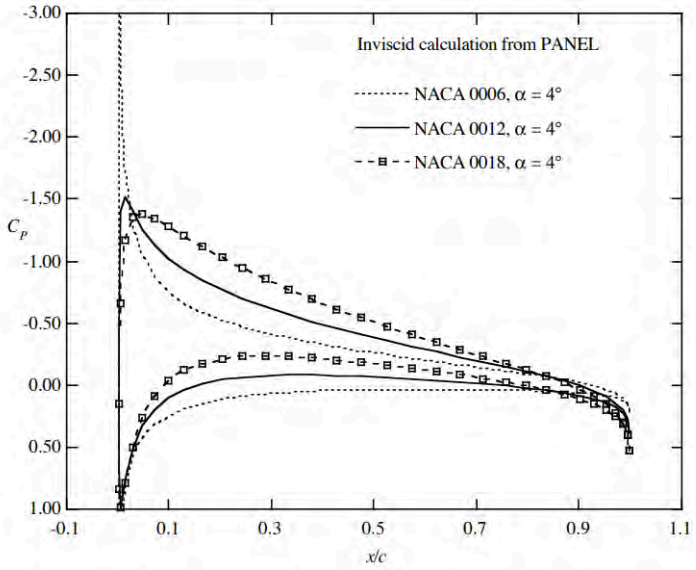


Figure 5-15: Effect of airfoil thickness on the pressure distribution at $C_l = 0.48$. From W. H. Mason. Adapted by S. Madden. CC BY-NC-SA 4.0.

Camber effect

The next effect to examine in understanding airfoil characteristics is camber. Figure 5-16 compares the shapes of the NACA 0012 and 4412 airfoils. The pressure distributions on the cambered airfoil for two different angles of attack are shown in figure 5-17. Note the role of camber in obtaining lift without producing the rapid leading-edge expansion and subsequent recompression that we've seen before. This reduces the possibility of leading-edge separation. Instead, the lift is distributed along the airfoil.

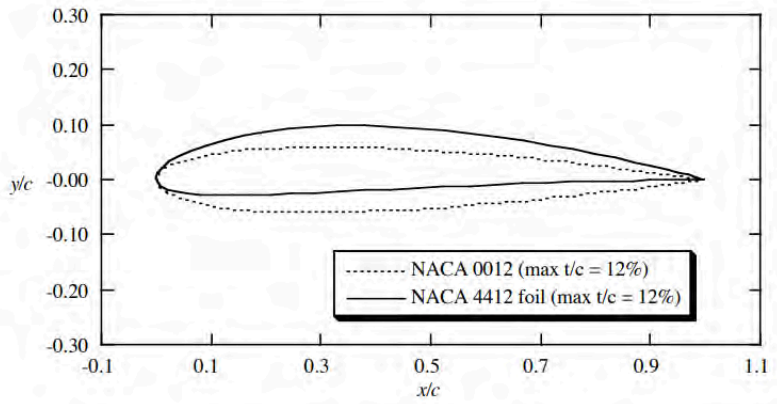


Figure 5-16: Comparison of uncambered and cambered NACA 4-digit airfoils. From W. H. Mason. Adapted by S. Madden. CC BY-NC-SA 4.0.

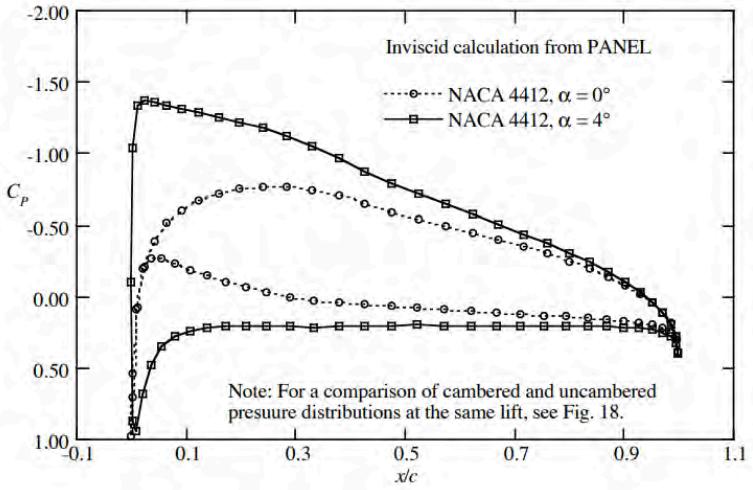


Figure 5-17: Effect of angle of attack on cambered airfoil pressure distributions at low lift. From W. H. Mason. Adapted by S. Madden. CC BY-NC-SA 4.0.

A comparison of the NACA 0012 and NACA 4412 airfoil pressure distributions at the same lift coefficient is presented for several values of lift in figures 5-18, 5-19, and 5-20. As the lift increases, the camber effects start to be overcome by the angle-of-attack effects, and the dramatic effects of camber are diminished until, at a lift coefficient of 1.43, the pressure distributions start to appear to be very similar.

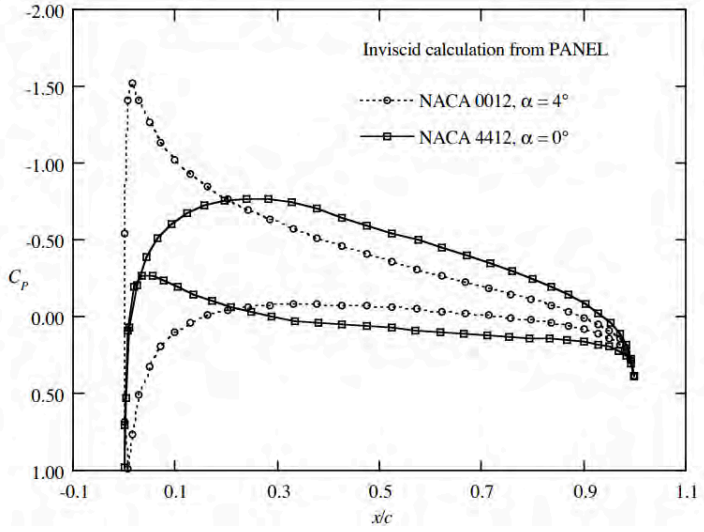


Figure 5-18: Camber effects on airfoil pressure distributions at $C_l = 0.48$. From W. H. Mason. Adapted by S. Madden. CC BY-NC-SA 4.0.

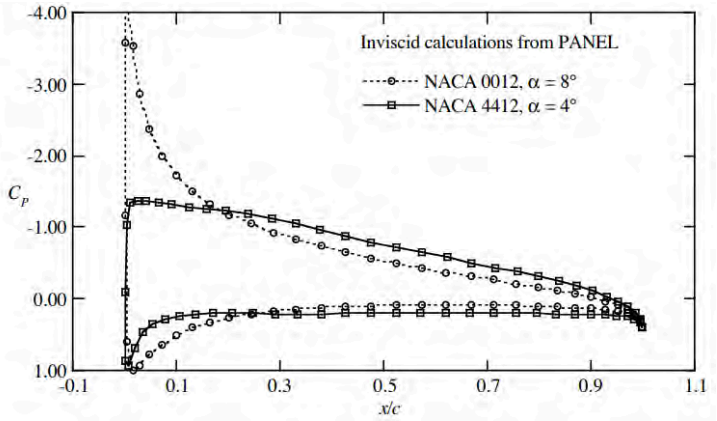


Figure 5-19: Camber effects on airfoil pressure distributions at $C_l = 0.96$. From W. H. Mason. Adapted by S. Madden. CC BY-NC-SA 4.0.

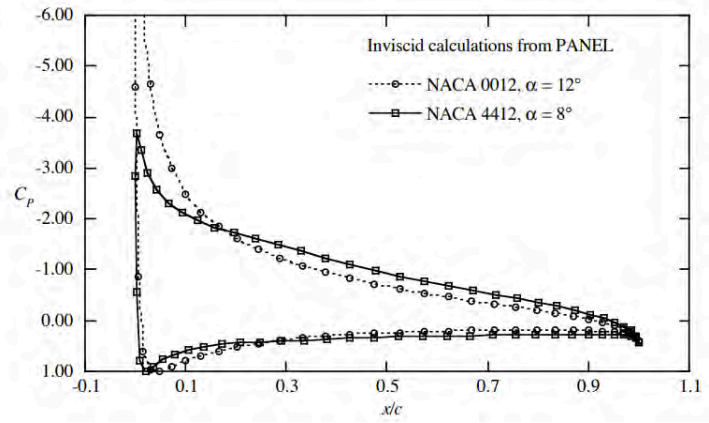


Figure 5-20: Camber effects on airfoil pressure distributions at $C_l = 1.43$

Finally, we examine the effect of extreme aft camber, which was part of the design strategy of Richard Whitcomb when the NASA supercritical airfoils were developed. This effect can be simulated using the NACA 6712 airfoil shown in figure 5-21. The computed pressure distribution, given in figure 5-22, shows that the aft camber "opens up" the pressure distribution near the trailing edge. Two adverse properties of this type of pressure distribution are the large zero-lift pitching moment and the delayed-then-rapid pressure recovery on the upper surface. This type of pressure recovery is a very poor way to try to achieve a significant pressure recovery because the boundary layer will separate early. Whitcomb's design work primarily improved the pressure recovery curve.

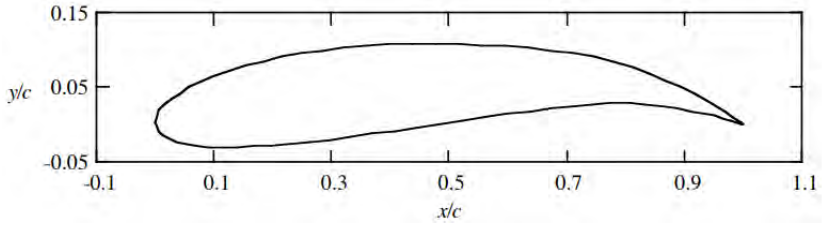


Figure 5-21: Highly aft-cambered NACA airfoil, an NACA 6712. From W. H. Mason. Adapted by S. Madden. CC BY-NC-SA 4.0.

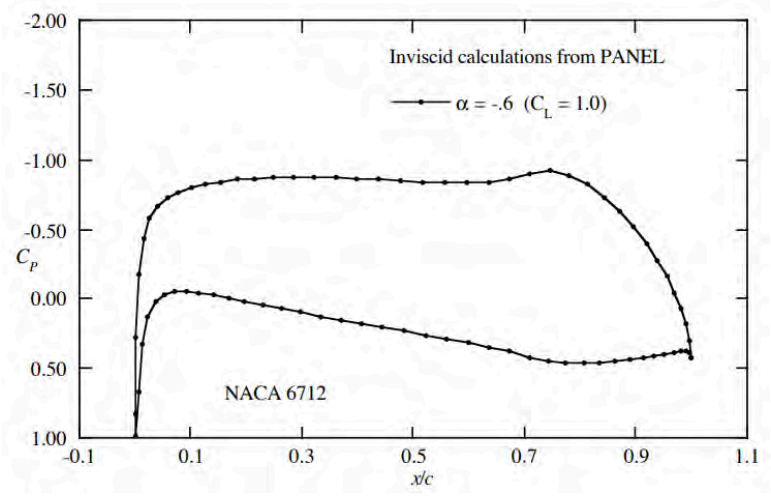


Figure 5-22: Example of the use of aft camber to "open up" the pressure distribution near the trailing edge. From W. H. Mason. Adapted by S. Madden. CC BY-NC-SA 4.0.

The airfoils used above to demonstrate geometry effects on pressure distributions use parametric geometry definition formulas developed in the 1930s. More modern airfoils are available to today's aerodynamicist. Unfortunately, to obtain improved performance, the designs were developed without the use of simple geometric definitions and are available only as tables of coordinates. One modern airfoil that extends some of the previous shapes to obtain a high-performance airfoil is the GA(W)-1 airfoil.[28] This 17-percent-thick airfoil designed by NASA's Richard Whitcomb provides improved maximum lift and stall characteristics compared to previous NACA airfoils. Figure 5-23 shows the airfoil shape, and figure 5-24 shows the pressure distribution.

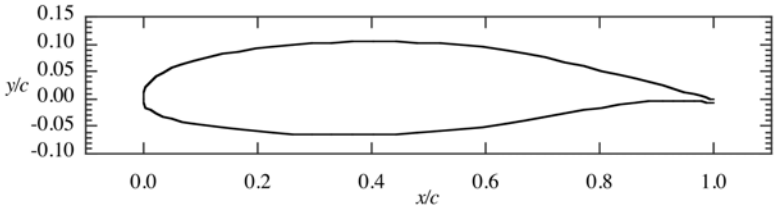


Figure 5-23: GA(W)-1 airfoil, also known as NASA LS(1)-0417. From W. H. Mason. Adapted by S. Madden. CC BY-NC-SA 4.0.

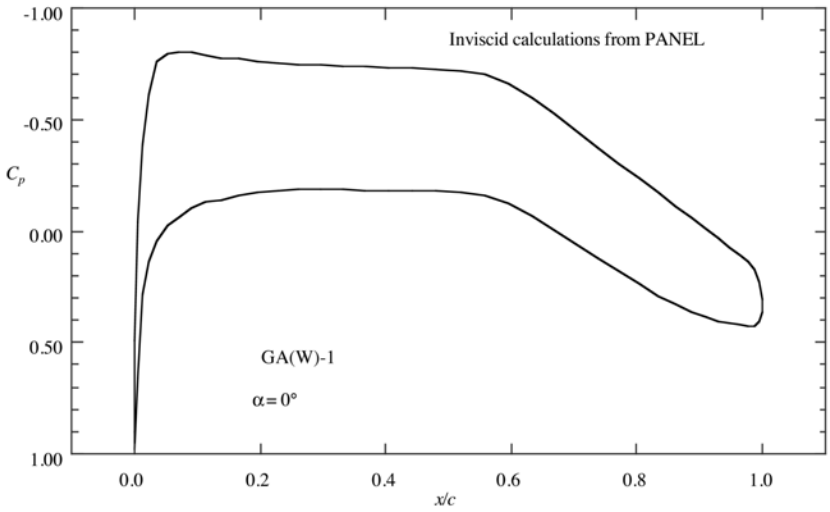


Figure 5-24: Pressure distribution at zero angle of attack of the GA(W)-1. From W. H. Mason. Adapted by S. Madden. CC BY-NC-SA 4.0.

In this case, the upper-surface pressure distribution reaches a constant pressure plateau and then has a moderate pressure recovery. Aft camber is used to obtain lift on the lower surface and open up the airfoil pressure distribution near the trailing edge in a manner suggested previously in figure 5-22. The area of aft camber on the lower surface is known as the "cove" region. If the camber is too extreme here, the adverse pressure gradient will be too steep and the flow will separate on the lower surface before it separates on the upper surface. This type of pressure distribution has a significantly more negative C_{m_0} than conventional airfoil sections.

5.1.2.2 Comments on airfoil design

Having surveyed the broad effects of various shape changes on the airfoil pressure distribution, we now make a few comments on airfoil design. At subsonic speeds, the key considerations are low parasite (skin friction) drag at low lift coefficients, basic airfoil pitching moment, and maximum lift values. To get low skin friction drag, a significant portion of the boundary layer should be laminar. This is possible for relatively small airplanes (up to around regional jet size) and surfaces with small sweep angles. Modern composite manufacturing techniques, which can produce extremely smooth surfaces, are an enabling technology. Generally, this smoothness is achieved passively by delaying the onset of any adverse pressure gradients until aft on the airfoil. There are various possible combinations of active laminar flow control (boundary layer suction) and passive laminar flow control. A nice survey of laminar flow technology is available in an article by Joslin,[29] as well as a chapter in a 1990 AIAA Progress in Astronautics and Aeronautics book.[30]

The aft camber illustrated above provides extra lift, but with a possible penalty of a large C_{m_0}. Finally, high maximum lift coefficients are desirable; ways of obtaining high lift are discussed in Chapter 7, "High-Lift Aerodynamics." Essentially, achieving high lift depends on using a pressure distribution that maximizes the load-carrying capacity of the boundary layer. Note that most current airfoil design also actively addresses transonic flow effects, where the shock strength for a specified lift coefficient should be minimized.

Effects of shape changes on pressure distributions: So far, the examples have demonstrated global effects of camber and thickness. To develop an understanding of the typical effects of adding local modifications to the airfoil surface, one must carry out an investigation into the effects of local shaping on the airfoil characteristics. I have had good luck using a smooth "cubic bump" to modify surfaces. The key with those types of airfoil shape modifications is to distribute the bump over a large portion of the airfoil, say one half to nearly the entire chord, with relatively low amplitude changes. Short bumps lead to poor off-design performance. It is also worthwhile to investigate the very powerful effects that small deflections of the trailing edge can produce. This reveals the power of the Kutta condition and alerts the aerodynamicist to the importance of the viscous effects at the trailing edge.

Computational experimentation is extremely educational when implemented in an interactive computer program, where the aerodynamicist can make shape changes with a mouse and immediately see the effects on pressure distribution. Ilan Kroo created an outstanding code that does just this, called PANDA.[31]

Shape for a specified pressure distribution: There is another way that aerodynamicists view the design problem. The local modification approach described above is useful to make minor changes in airfoil pressure distributions. Often, the aerodynamic designer wants to find the geometric shape corresponding to a prescribed pressure distribution. This problem is known as the inverse problem. It is more difficult than the analysis problem. In fact, it is possible to prescribe a pressure distribution for which no geometry exists! Even if the geometry exists, it may not be acceptable from a structural standpoint. For two-dimensional incompressible flow, it is possible to obtain conditions on the surface velocity distribution that ensure that a closed airfoil shape exists. Excellent discussions of this problem have been given by Volpe[32] and Sloof.[33] A two-dimensional panel method for airfoil analysis and design has been developed by Bristow.[34] Numerical optimization can also be used to find the shape corresponding to a prescribed pressure distribution.[35]

Camber line design and DesCam: Most of the discussion above corresponds to the analysis problem, and we've given only a very brief summary of the inverse problem for subsonic flows. However, the airfoil camber line for a prescribed loading, ΔC_p, can be found easily with

vortex lattice methods, which are used often in three-dimensional flows (see section 5.2). Here, the chord load is specified and the camber shape required to produce the prescribed load is found. In this section, we provide an example. The program DesCam is used to make the calculation using a slight variation of the VLM method known as the quasi-vortex lattice method and developed by Prof. Edward Lan of the University of Kansas.[36] His method involves mathematically selecting vortex and control point placements instead of the 1/4 – 3/4 rule typically used in VLM methods. One interesting aspect of the inverse problem is that it is a direct solution and does not require the solution of a system of equations. Instead, the shape is computed from a straightforward algebraic calculation to find camber line slopes. Once the slopes are known, they are integrated to obtain the camber line.

Figure 5-25 provides an example. We compare the results from DesCam with the analytic formula given in appendix A, "Geometry for Aerodynamicists," for the NACA 6-series mean line with $a = 0.4$. The camber scale is greatly enlarged to demonstrate the excellent comparison. Even though the chord load is constructed by prescribing two straight-line segments, the resulting required camber line is highly curved over the forward portion of the airfoil. Additionally, thin-airfoil theory allows only two possible values for the pressure differential at the leading edge: zero or infinity. A finite load at the leading edge is not possible. A close examination of the camber line shape required to produce a finite load reveals a singularity. The camber slope is infinite at the leading edge. This feature is much easier to study using the analytic solution given in appendix A. This type of approach to obtaining the desired pressure loading can easily be extended to three dimensions.

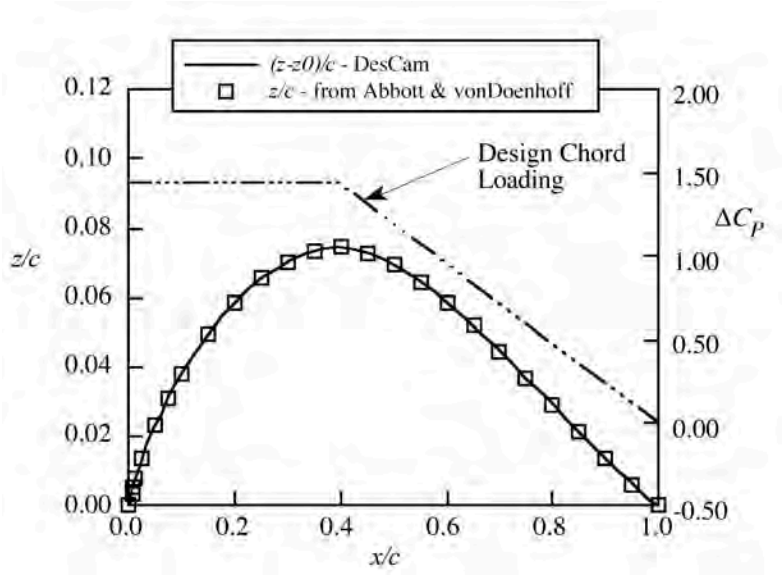


Figure 5-25: Example and verification of camber design using DesCam. *From W. H. Mason. Adapted by P. Raj.*

Finally, to learn more about subsonic airfoil design, read the papers by Liebeck[37] and Drela[38] in the *Applied Computational Aerodynamics* volume of the AIAA Progress in Aeronautics and Astronautics series.

5.1.3 Airfoil Selection

Having covered some of the basic ideas of airfoil aerodynamics, we conclude our airfoil discussion by summarizing the issues associated with choosing an airfoil for a particular application. Even though we've discussed airfoils before planforms, the logical progression in airplane design is to start with the mission of the airplane (requirements), then select the appropriate planform(s) and finally the airfoil(s) that best match the wing planform to deliver the desired aerodynamic performance. The basic considerations are the cruise performance

(cruise C_L) and the field performance (C_{Lmax}). When considering trade studies for various planform and airfoil combinations, recall that the objective is to minimize drag, not drag coefficient. So the aerodynamicist should be evaluating $D/q = S_{wng}C_D$.

5.1.3.1 Cruise Performance

In cruise, the C_L for L/D_{max} should be found from the planform selection and the estimated C_{D0}. In general, the higher the aspect ratio, the higher the C_L for L/D_{max}. The choice of a predominantly laminar flow or turbulent flow airfoil should be addressed at this point. In particular, the laminar flow airfoils tend to operate in a narrowly defined range of lift coefficients to achieve the design performance (drag). Note that the wing C_L and airfoil section C_l's may be different. The airfoil C_l requirement should be used to select the camber required. In addition, transonic cruise speeds require special consideration (see the next chapter), and the 2D airfoil problem for an airfoil on a swept wing differs from just defining a streamwise cut for an airfoil on the wing. The relation between the airfoil problem and the swept-wing planform is given later in this chapter. In general, the thickness-to-chord ratio (t/c) should be as large as possible to allow the wing structural weight to be low and to provide internal volume.

5.1.3.2 Field performance

We start with the requirement for the airplane to meet a specified stall or approach speed. This translates to a required C_{Lmax}. The conflict in requirements between efficient cruise (small wing) and low landing speed (big wing) means that most airplanes will have some type of high-lift system, ranging from a simple flap to triple-slotted flap systems described in Chapter 7. Either a large leading-edge radius is selected or a separate leading-edge device is used to assist in obtaining the required lift. The high-lift system should be as simple as possible to reduce manufacturing and maintenance cost.

5.1.3.3 Tail sections

For a vertical tail, the section should be symmetric. For a horizontal tail, the section is often symmetric. Low-drag 6A-series airfoils are often selected for tail surfaces, but they have poor values for C_{Lmax}. The NACA 4-digit sections have higher values of C_{Lmax} but more zero-lift drag. If the horizontal tail may be required to generate large downloads, a cambered airfoil may be used. This is more likely to occur when the airplane has a very powerful high-lift system. B-52s have vortex generators on the bottom surface of the horizontal tail to allow the tail to achieve the downforce required to trim the plane in takeoff and landing.

Finally, some help is available in choosing an airfoil. Gil Crouse has developed a software package called Airfoil Optimizer.[39] This program allows the user to specify design requirements, and the program will suggest an airfoil based on a large library of airfoils. This type of procedure falls under the category of an "expert system." Peter Garrison devoted a column to this package along with an excellent discussion of airfoil selection issues in his *Flying* magazine column Technicalities in 2002.

5.2 Wings

In this section, we highlight basic ideas of the subsonic aerodynamics of 3D wings. Before discussing the aerodynamics of wings, we first provide examples of the typical use and accuracy of vortex lattice methods (VLMs) that are widely used for simulating wing aerodynamics in the early stages of conceptual design. Complete details of the VLMs (as well as surface panel methods) are available in Chapter 5 of the *Applied Computational Aerodynamics* book.[40] The vortex lattice layout is clear for most wings and wing-tail or wing-canard configurations. The method can be used for wing-body cases by simply specifying the projected planform of the entire configuration as a flat lifting surface made up of a number of straight line segments. The exact origin of this somewhat surprising approach is unknown. Examples in the following sections will help illustrate the success of this approach.

5.2.1 Use and Accuracy of the VLM Method

To get good, consistent, reliable results, some simple rules for panel layout should be followed. This requires that a few common rules of thumb be used in selecting the planform break points: (i) the number of line segments should be minimized; (ii) breakpoints should line up streamwise* on front and rear portions of each planform and should line up between planforms; (iii) streamwise tips should be used; (iv) small spanwise distances should be avoided by making edges streamwise if they are actually very highly swept; and (v) trailing vortices from forward surfaces cannot hit the control point of an aft surface. Figure 5-26 illustrates these common best practices.

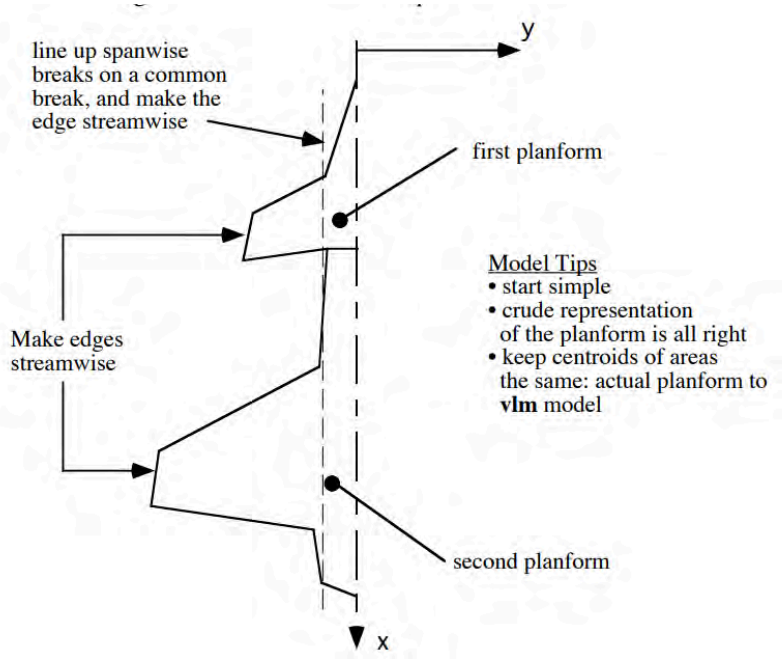


Figure 5-26: Example of a VLM model of an aircraft configuration. Note that one side of a symmetrical planform is shown.

*"Streamwise" means parallel to the freestream. In this coordinate system, it means that *y* is a constant.

To illustrate typical results that can be expected from vortex lattice methods, we provide some examples from a study by John Koegler[41] that illustrates the range of uses for the VLM method. This study provides specific applications of several methods for fighter airplanes. In addition to the vortex lattice method, he also used the PAN AIR and Woodward II panel methods (see Chapter 5 of *Applied Computational Aerodynamics*[42] for a description of panel methods). Koegler compared his computed predictions with available data for the three-surface F-15, which became known as the STOL/Maneuver Demonstrator, and the F/A-18. These configurations are illustrated in figure 5-27.

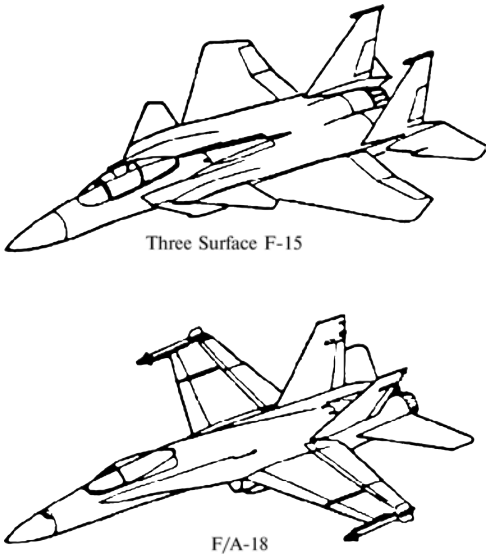


Figure 5-27: Configurations used by McDonnell Aircraft to study VLM method accuracy. From J. Koegler. US Air Force. Public domain.

As with panel method calculations for airfoils, there must be a study of the number of horseshoe vortices required to obtain good results before the actual calculations are made. The effects of the number of panels and the way they are distributed is presented in figure 5-28 for the F/A-18 configuration (see figure 5-27 for the geometry). In this case, the VLM method is seen to take between 130 to 220 panels to produce converged results. The change in neutral point is used because this is perhaps one of the most important uses of these methods in early aircraft design. For the vortex lattice method, it appears important to use a large number of spanwise rows and a relatively small number of chordwise panels (five or six appear to be enough).

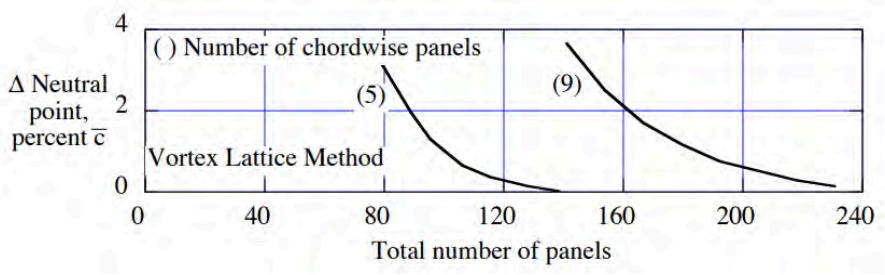


Figure 5-28: F/A-18 panel convergence study for a vortex lattice method. From J. Koegler. US Air Force. Public domain.

The basic panel layout of the F-15 STOL/Maneuver Demonstrator is given in figure 5-29. Several computational models were studied. This shows how the aircraft was modeled as a flat planform, and the corner points of the projected configuration were used to represent the shape in the vortex lattice method. In this case, the rake of the wingtip was included in the computational model. In the vortex lattice model, the configuration was divided into three separate planforms, with divisions at the wing root leading and trailing edges. On this configuration, each surface was at a different height, and after some experimentation, the vertical distribution of surfaces shown in figure 5-30 was found to provide the best agreement with wind tunnel data.

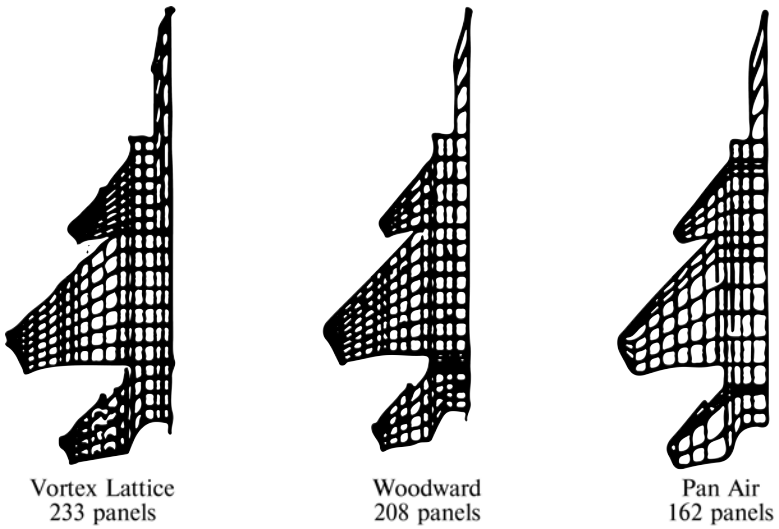


Figure 5-29: Panel models used for the F-15 STOL/Maneuver Demonstrator. *From J. Koegler. US Air Force. Public domain.*

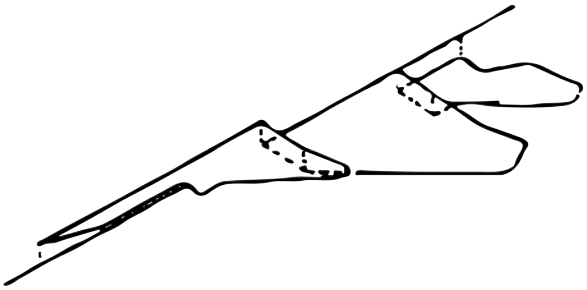


Figure 5-30: Canard and horizontal tail height representation. *From J. Koegler. US Air Force. Public domain.*

The results from these models are compared with wind tunnel data in table 5-1.[43] The vortex lattice method is seen to produce excellent agreement with the data for the neutral point location and for lift and moment curve slopes at Mach 0.2.

Data source		Neutral point (% mac)	$C_{m\alpha}$ (per deg.)	$C_{L\alpha}$ (per deg.)
M = 0.2	Wind tunnel	15.70	0.00623	0.0670
	Vortex lattice	15.42	0.00638	0.0666
	Woodward	14.18	0.00722	0.0667
	Pan air	15.50	0.00627	0.0660
M = 0.8	Wind tunnel	17.70	0.00584	0.0800
	Vortex lattice	16.76	0.00618	0.0750
	Pan air	15.30	0.00684	0.0705
M = 1.6	Wind tunnel	40.80	-0.01040	0.0660
	Woodward	48.39	-0.01636	0.0700

Table 5-1: Three-surface F-15 longitudinal derivatives

Subsonic Mach number effects are simulated in VLM methods by transforming the Prandtl–Glauert equation, which describes the linearized subsonic flow to Laplace's equation using the Göthert transformation. However, this is only approximately correct, and the agreement with wind tunnel data is not as good at the transonic Mach number of 0.8. Nevertheless, when the VLM method is used in this manner, it is as good as PAN AIR, which is a high-order panel method. Note that the VLM method used in the three-surface F-15 study is not applicable at supersonic speeds. The wind tunnel data shows the shift in the neutral point between subsonic and supersonic flow. The Woodward method, as applied here, overpredicted the shift with Mach number. We can conclude that the three-surface F-15 configuration is neutral to slightly unstable subsonically, becoming stable at supersonic speeds.

Figure 5-31 provides an example of the use of the VLM method to study the effects of moving the canard with respect to the plane of the wing. Here, the wind tunnel test result is used to validate the method and to provide an "anchor" for the numerical study. (It would have been useful to have an experimental point at -15 inches.) This is typical of the use of the VLM method in aircraft design. When the canard is above the wing (positive values of canard height; see figure 5-31), the neutral point is essentially independent of the canard height. However, when the canard is below the wing (negative values of canard height), the neutral point varies rapidly with canard height.

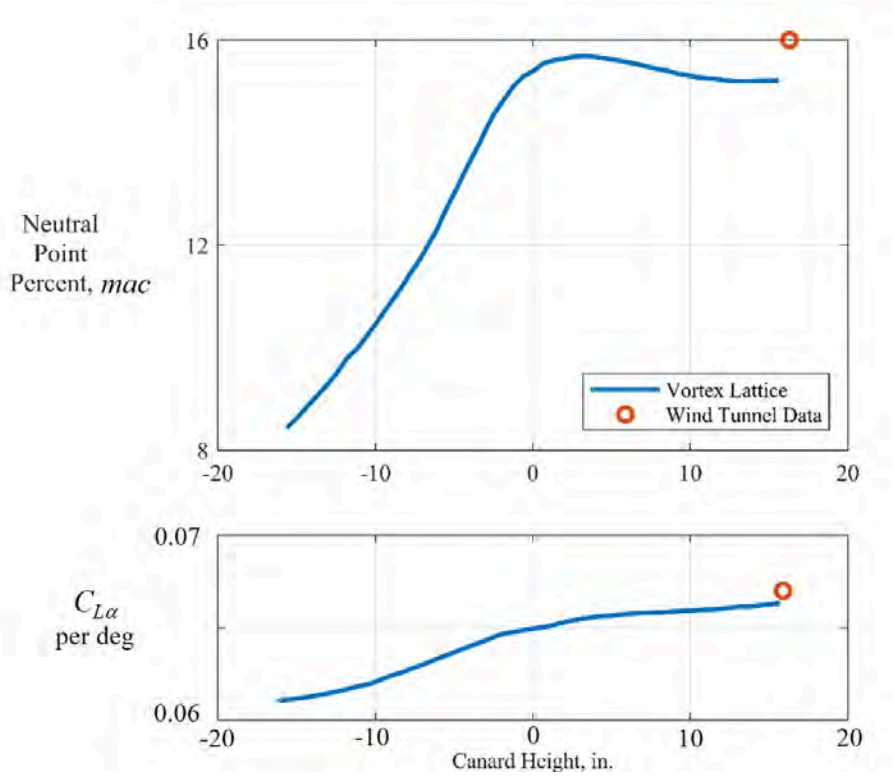


Figure 5-31: Effect of canard height variation with respect to the plane of the wing on three-surface F-15 characteristics. From J. Koegler. US Air Force. Public domain. Adapted.

Control effectiveness is also of interest in conceptual and preliminary design, and the VLM method can be used to provide estimates. Figure 5-32 provides an apparently accurate example of this capability for F-15 horizontal tail effectiveness. Change in lift coefficient and pitching moment coefficient with respect to horizontal tail deflection, $C_{L\delta h}$ and $C_{m\delta h}$, respectively, are presented. The VLM estimate is within 10% accuracy at both Mach 0.2 and 0.8. However, the F-15 has an all-moving horizontal tail to provide sufficient control power under both maneuvering and supersonic flight conditions. Thus, the tail effectiveness presented here is effectively a measure of the accuracy of the prediction of wing lift and moment change with angle of attack in a nonuniform flow field, rather than the effectiveness of a flap-type control surface. A flapped device such as a horizontal stabilizer and elevator combination will have significantly larger viscous effects, and the inviscid estimate from a vortex lattice or panel method (or any inviscid method) will overpredict the control effectiveness. This is shown next for an aileron.

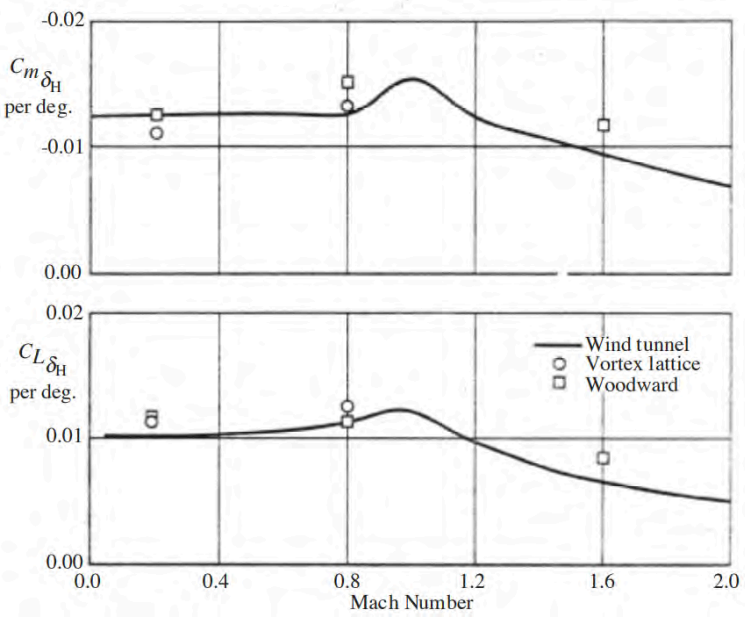


Figure 5-32: F-15 horizontal tail effectiveness–comparison of computed and measured values of moment and lift coefficients per degree of horizontal tail deflection. *From J. Koegler. US Air Force. Public domain.*

The aileron effectiveness for the F-15 is presented in figure 5-33. It is more representative of classical elevator or flap effectiveness correlation between VLM estimates and experimental data. This figure presents the change in the airplane's rolling moment coefficient due to aileron deflection. In this case, the device deflection is subject to significant viscous effects, and the figure shows that only a portion of the effectiveness predicted by the VLM method is realized in the actual data. The VLM method, or *any* method, should always be calibrated with experimental data close to the cases of interest to provide an indication of the agreement between theory and experiment. In this case, the actual results are found to be about 60% of the inviscid prediction at low speed.

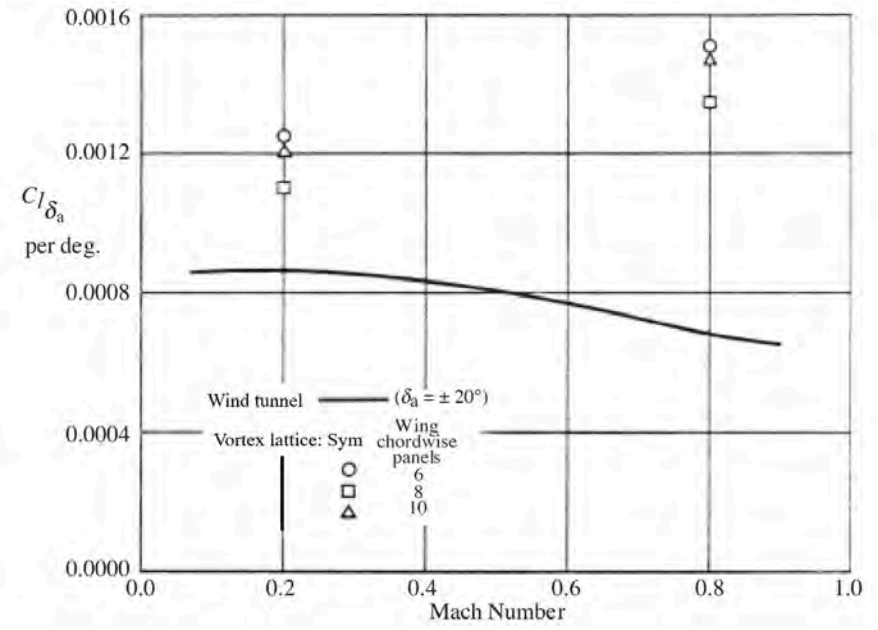


Figure 5-33: F-15 aileron effectiveness comparison of computed and measured values. *From J. Koegler. US Air Force. Public domain.*

5.2.2 VLMpc and the Warren-12 Test Case

The VLMpc vortex lattice method can be used on personal computers. The version of the Lamar program described in NASA TN D-7921[44] works easily with personal computers and is available for student use as VLMpc (in fact, students typed this code in from the listing in the TN). See section E.6.1 for links to the code and input instructions. This code is still used in advanced design work and can be used to investigate many ideas in wing aerodynamics. As shown above, results can be obtained and used before the large time-consuming methods of CFD are used to examine a particular idea in detail.

Next, we define one reference wing case that is typically used to check the accuracy of vortex lattice codes. It provides a good test case for the evaluation of any new or modified code, as well as a check on the panel scheme layout. It is known as the Warren-12 planform and is defined, together with the "official" characteristics from previous calculations, in figure 5-34. For the results given in the figure, the reference chord used in the moment calculation is the average chord (which is slightly nonstandard, as the mean aerodynamic chord is normally used as the reference chord), and the moment reference point is located at the wing apex (which is also nonstandard). Any calculations made in checking your proficiency in making a VLM calculation should include this case.

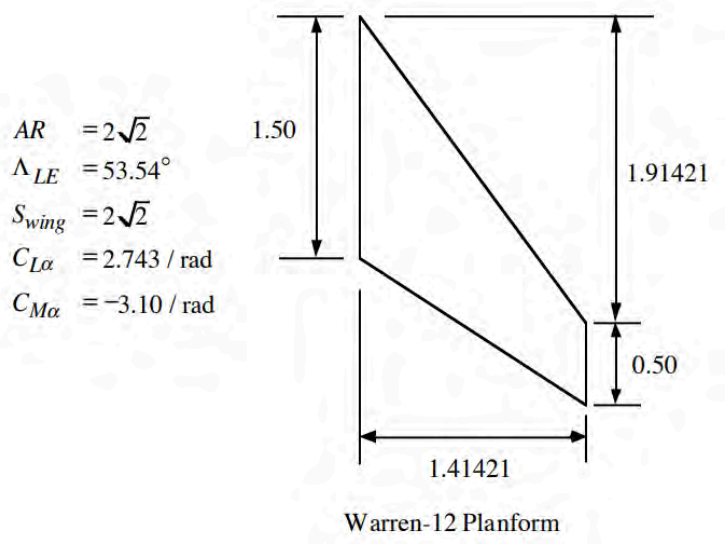


Figure 5-34: Definition and reference results for the Warren-12 wing test case (all dimensions in meters). From W. H. Mason. Adapted.

5.2.3 Other VLM Programs

In addition to VLMpc, the MATLAB program Tornado is capable of handling very general geometries and flow conditions. The program, written by Tomas Melin at KTH in Stockholm,[45] has been used by many students and may be replacing VLMpc. It is also worth noting that the AVL code, developed some years ago by Mark Drela and Harold Youngren at MIT, has been placed in the public domain. It is quite effective for the aerodynamic and flight-dynamic analysis of rigid aircraft of arbitrary configuration. It employs an extended vortex lattice model for the lifting surfaces, together with a slender-body model for fuselages and nacelles.

The NASA-developed VSPAERO is another popular VLM code which also has an option for using surface panels for computational simulations using linearized potential flow equations. VSPAERO is one of the many analysis tools bundled in OpenVSP (Open Vehicle Sketch Pad). OpenVSP[46] is an open source parametric geometry tool for creating three-dimensional models that are well suited for conceptual design studies. VSPAERO is an easy-to-use, robust, and cost-effective tool with fast turnaround time.

5.2.4 Aerodynamics of High Aspect Ratio Wings

With cost-effective flow simulation methods available for three-dimensional geometries, we can examine the aerodynamics of wings. Most of the results presented in this section were computed using VLMpc. One key advantage of the vortex lattice method compared to lifting-line theory is the ability to treat swept wings. Classical Prandtl lifting-line theory is essentially correct for unswept wings, but it is completely erroneous for swept wings. Aerodynamics of unswept wings are closely related to the airfoil characteristics of the airfoil used in the wing. This relationship is less direct for swept wings. Many of the most important wing planform–oriented characteristics of wings arise when the planforms are swept. Even though sweep is used primarily to reduce compressibility effects, the important aerodynamic features of swept wings can be illustrated at subsonic speeds using the VLM method.

5.2.4.1 Basic requirements

Wings are designed to satisfy requirements related to stability and handling characteristics while achieving low drag at the design conditions (usually cruise and sustained maneuver). They must also attain high maximum lift coefficients to meet field performance and maneuver requirements. Although these requirements might at first appear overwhelming, a small number of key characteristics (e.g., aerodynamic center, spanload, taper, and sweep) can provide a basic physical understanding of the aerodynamics of wings. Table 5-2 provides some key characteristics of well known major transport aircraft with wings designed to emphasize efficient cruise while meeting takeoff and landing requirements.

1st flight	Aircraft	W/S	AR	$\Lambda_{c/4}$°	λ
1957	B707-120	105.6	7.04	35.0	0.293
1958	DC-8-10	111.9	7.32	30.0	0.230
1963	B707-320C	110.0	7.06	35.0	0.250
1970	B747-200B	149.1	6.96	37.5	0.254
1970	L-1011	124.4	8.16	35.0	0.200
1972	LC-10-30	153.7	7.57	35.0	0.230
1972	A300 B2	107.9	7.78	28.0	0.230
1982	A310-100	132.8	8.80	28.0	0.260
1986	B767-300	115.1	7.99	31.5	0.182
1988	B747-400	149.9	7.61	37.5	0.240
1990	MD-11	166.9	7.57	35.0	0.230
1992	A330	119.0	9.30	29.7	0.192
1994	B777-200	118.3	8.68	31.6	0.172

Table 5-2: Typical planform characteristics of major transport aircraft (data courtesy of Nathan Kirschbaum)*

*Nathan Kirschbaum served as an adjunct professor of Aeronautical Engineering at Virginia Tech in Blacksburg, VA, from 1990 until fully retiring in 2001. He joined VT after retiring from Grumman Aerospace Corporation, Bethpage, NY, in 1989 as Chief Configuration Designer, Aircraft. He was mainly motivated by a strong desire to share his practical experience with the VT Aircraft Design students. He graduated from Massachusetts Institute of Technology in 1951. https://www.legacy.com/us/obituaries/pressofatlanticcity/name/nathan-kirschbaum-obituary?id=28313925

5.2.4.2 Key Characteristics

Aerodynamic center

The first key characteristic is the aerodynamic center of the wing, defined as the location at which $dC_m/dC_L = 0$. The neutral point of the configuration is the aerodynamic center for the entire configuration. The VLM method was shown to provide accurate predictions of the neutral point for many configurations in the previous sections. The location of the neutral point is important in initial configuration layout to position the wing and any longitudinal stability and control surfaces at the proper location on the aircraft. Subsequently, this information is fundamental in developing the control system. Wing planform shaping, as well as positioning, is used to control the location of the configuration's neutral point.

Spanload

The next key consideration is the spanload distribution, cC_l/c_a, where c is the local chord, c_a is the average chord of the wing, and C_l is the local section lift coefficient. The spanload controls the location of the maximum section lift coefficient, the induced drag of the wing, and the magnitude of the wing's root bending moment. The location and value of the maximum section lift coefficient provides a good initial estimate of where the wing will stall first.* If the wing stalls in front of a control surface, control will be poor at flight conditions just when control becomes very important. The shape of the spanload, together with the actual value of the wingspan, determines the value of the induced drag. For a specified span, the performance of the wing is evaluated by finding the value of the span efficiency factor, e, as described in Chapter 3. Finally, the wing root bending moment provides an indication of the structural loading requirements that the wing structure must be designed to accommodate. When considering the total system, the basic aerodynamic efficiency may be compromised to reduce structural wing weight. The shape of the spanload can be controlled through a combination of planform selection and wing twist. Typical twist distributions required to produce good wing characteristics are presented below.

*For a trapezoidal wing with an elliptic spanload, the maximum value of the local lift coefficient occurs at $\eta = 1 - \lambda$, where η is the nondimensional spanwise location of a section from the plane of symmetry and is denoted by $2y/b$ for wing of span b.

The simplest example of planform shaping is the selection of wing aspect ratio (AR), wing taper (λ), and wing sweep (Λ), usually of the quarter-chord line or the wing leading edge. While the aerodynamicist would like to see high values for the aspect ratio, several considerations limit this factor. Perhaps the most important limitation is the increase of wing structural weight with increasing aspect ratio. In addition, the lift coefficient required to maximize the benefits of high-aspect-ratio wings increases with the square root of the aspect ratio. Hence, airfoil performance limits can restrict the usefulness of high aspect ratios, especially for highly swept wings based on airfoil concepts. In recent years, advances in both aerodynamics and structures have allowed aircraft to be designed with higher aspect ratios and reduced sweep.

Taper

Several considerations are used in selecting the wing taper. For a straight untwisted, unswept wing, the minimum induced drag corresponds to a taper ratio of about 0.4. However, a tapered wing is more difficult and therefore expensive to build than an untapered wing. Many general aviation aircraft wings are built with no taper; in this case, all ribs are the same, reducing fabrication cost, and the maximum section C_l occurs at the root, well away from the control surface, providing positive roll control at stall (a very good feature). To reduce structural weight, the wing should be highly tapered, with $\lambda < 0.4$. Although highly tapered wings are desirable structurally, the section lift coefficient near the tip may become quite high, which limits the amount of taper employed. Current jet transports use taper ratios in the range of 0.2 to 0.3, as well as progressively increasing twist upward from the tip. In one other example, the Aero Commander 500 has an aspect ratio of 9.5 and a taper ratio of 0.5; it also has -6.5° of twist and the quarter chord of the wing was swept forward 4°.

Sweep

Sweep is used primarily to delay the effects of compressibility and increase the drag divergence Mach number. The Mach number controlling these effects is approximately equal to the Mach number normal to the leading edge of the wing, $M_{eff} = M_\infty \cos\Lambda$. The treatise on swept planforms by Küchemann is very helpful in understanding swept-wing aerodynamics.[47] Aerodynamic performance is based on the wingspan, b. For a fixed span, the structural span increases with sweep, $b_s = b/\cos\Lambda$, resulting in a higher wing weight. Wing sweep also leads to aeroelastic problems. For aft-swept wings, flutter becomes an important consideration. If the wing is swept forward, divergence is a problem. Small changes in sweep can be used to control the aerodynamic center when it is not practical to adjust the wing position on the fuselage (the DC-3 is the most famous example of this approach).

To understand the effects of sweep, the Warren-12 wing is compared with wings of the same span and aspect ratio, but unswept and swept forward. The planforms are shown in figure 5-35. The wing leading-edge sweep of the aft-swept wing becomes the trailing-edge sweep of the forward-swept wing.

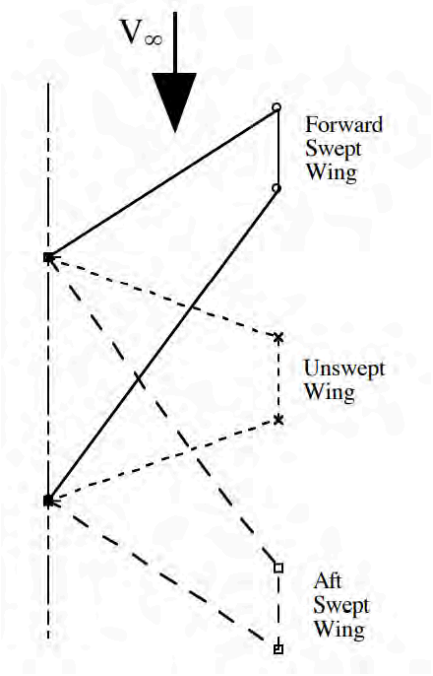


Figure 5-35: Comparison of forward-swept, aft-swept, and unswept wing planforms, AR = 2.8.

Figure 5-36(a) provides the spanload, cC_l/c_a, for the three wings in figure 5-35 from VLMpc. Here, c is the local chord, C_l is the local lift coefficient based on the local chord, and c_a is the average chord, S/b. Using this nomenclature, the area under the curve is the total wing lift coefficient. Sweeping the wing aft increases the spanload outboard, while sweeping the wing forward reduces the spanload outboard. This follows directly from a consideration of the vortex lattice model of the wing. In both cases, the portion of the wing aft on the planform is operating in the induced upwash flow field of the wing ahead of it, resulting in an increased spanload.

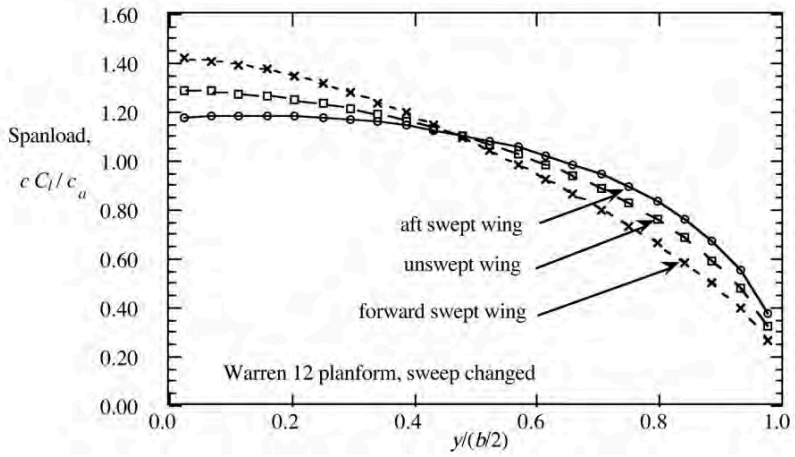


Figure 5-36(a): Effect of sweep on planform spanload distribution for aft-swept, unswept, and forward-swept Warren-12 planform, AR = 2.8.

Figure 5-36(b) shows the corresponding value of the local lift coefficient for the three wings shown in figure 5-35. Here, the effect of sweep is more apparent. The forward-swept wing naturally results in a spanload with a nearly constant lift coefficient. This means that a comparatively higher wing lift coefficient can be achieved before the wing begins to stall. The program LIDRAG can be used to compare the span e's associated with these spanloads.

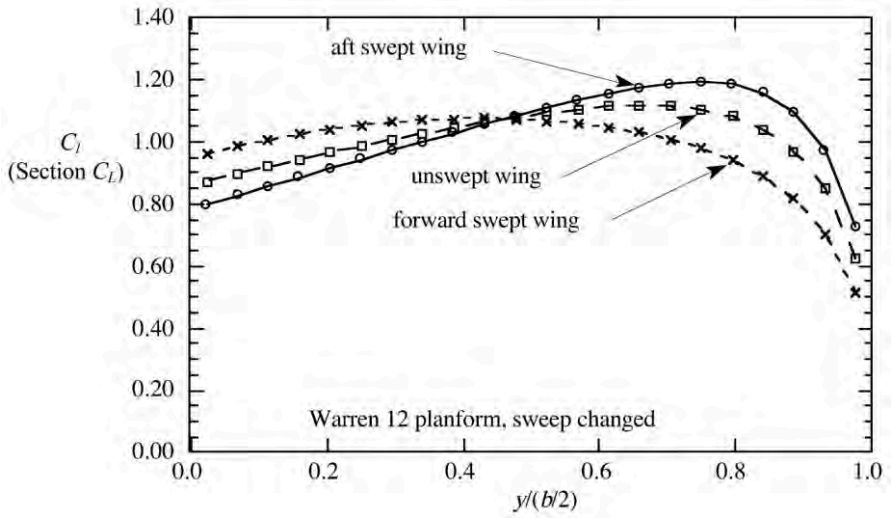


Figure 5-36(b): Effect of sweep on spanwise lift distribution for aft-swept, unswept, and forward-swept Warren-12 planforms, AR = 2.8.

Similar results are now presented for a series of wings with larger aspect ratios ($AR = 8$) than the wings used in the study given above. Figure 5-37 shows the three wing planforms. These results are similar to the previous results. However, the trends observed above are in fact exaggerated at the higher aspect ratio.

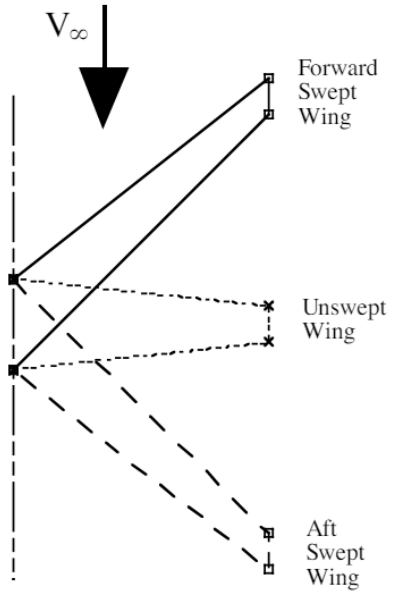


Figure 5-37: Comparison of forward-swept, aft-swept, and unswept wing planforms, AR = 8.

Figure 5-38(a) presents VLMpc-computed results for the spanwise distribution of spanload, cC_l/c_a, where c is the local chord, C_l is the local lift coefficient based on the local chord, and c_a is the average chord, S/b. Using this nomenclature, the area under the curve is the total wing lift coefficient. Sweeping the wing aft increases the spanload outboard, while sweeping the wing forward reduces the spanload outboard. This follows directly from a consideration of the vortex lattice model of the wing. In both cases, the portion of the wing aft on the planform is operating in the induced upwash flow field of the wing ahead of it, resulting in an increased spanload.

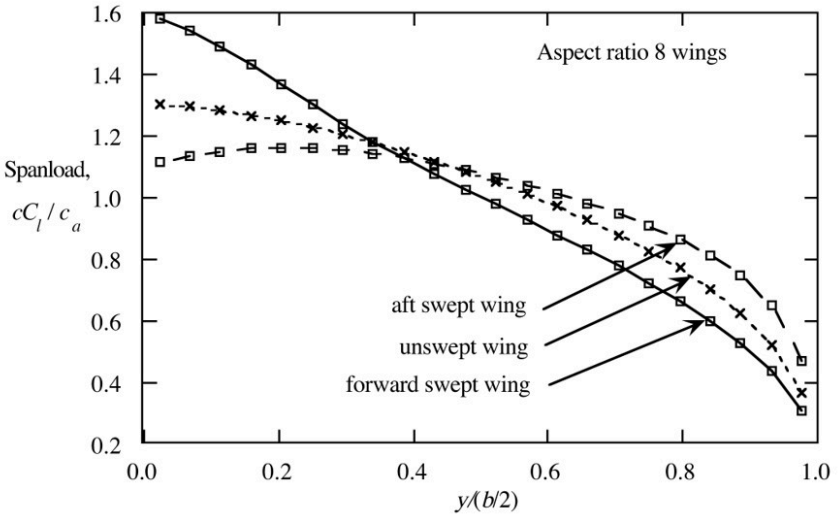


Figure 5-38(a): Effect of sweep on planform spanload distribution for aft-swept, unswept, and forward-swept planform, AR = 8.

Figure 5-38(b) shows the corresponding value of the local lift coefficient for the three wings shown in figure 5-37. Here, the effect of sweep is more apparent. The forward-swept wing naturally results in a spanload with a nearly constant lift coefficient. This means that a comparatively higher wing lift coefficient can be achieved before the wing begins to stall. The program LIDRAG can be used to compare the span *e*'s associated with these spanloads.

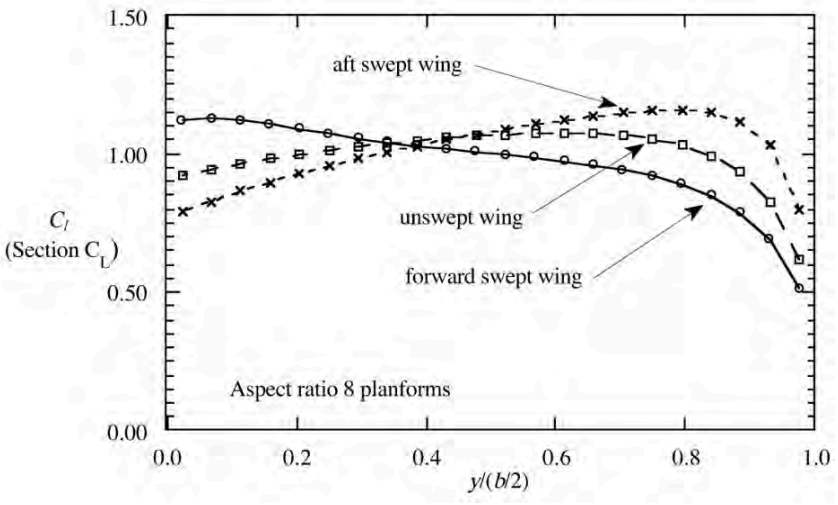


Figure 5-38(b): Effect of sweep on spanwise lift distribution for aft-swept, unswept, and forward-swept planforms, AR = 8.

Aerodynamic problems as well as structural penalties arise when using a swept wing. Because of the high section lift coefficient near the tip, aft-swept wings tend to stall near the tip first. Since the lift at the tip is generated well aft, the pitching moment characteristics change when the stall occurs. With the inboard wing continuing to lift, a large positive increase in pitching moment occurs when the wingtip stalls. This is known as pitchup and can be difficult to control, resulting in unsafe flight conditions. Frequently, the swept-wing pitching moment characteristics are compounded by the effects of flow separation on the outboard control surface. Figure 5-39 provides an example of the pitching moment characteristics of an isolated wing with an aspect ratio of 10 using experimental data.[48] The figure also includes the predictions from VLMpc. The agreement is reasonably good at low angle of attack but deteriorates at high angle of attack as viscous effects become important. This is another reason that sweep is minimized.

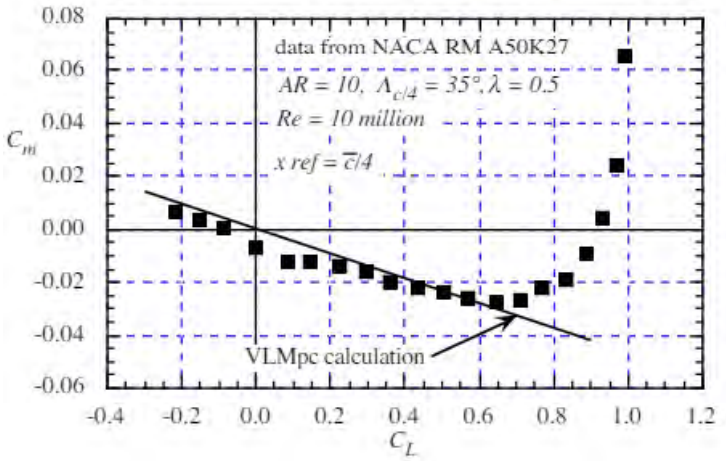


Figure 5-39: Example of isolated wing pitchup: NACA data compared with VLMpc computations. From W. H. Mason. Data from B. E. Tinling and W. R. Kolk, NACA.

Twist

To control the spanload, the wing can be twisted. Figure 5-40 shows typical twist distributions for aft-swept and forward-swept wings, obtained from John Lamar's program LAMDES[49] (see Chapter 3 for a description of this code). In each case, the twist is used to reduce the highly loaded areas and increase the loading on the lightly loaded portions of the wing, bringing the spanload to an elliptical shape. For an aft-swept wing, this means the geometric incidence is increased at the wing root, known as washin, and reduced at the wingtip, known as washout. Just the reverse is true for the forward-swept wing. The sudden drop in required twist at the tip for the forward-swept wing case is frequently seen in typical design methods; it is attributed to a weakness in the method and is accounted for by the aerodynamicist in giving the design to the lofting group.

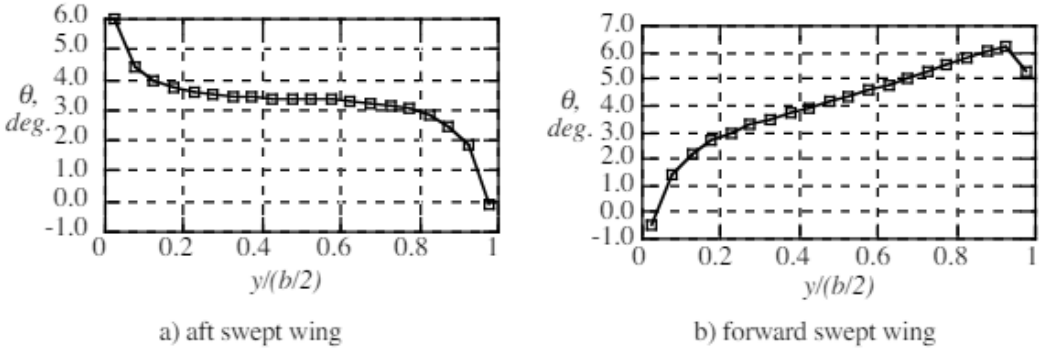


Figure 5-40(a) and (b): Typical twist distribution required to improve spanload on swept wings. From W. H. Mason, LAMDES.

Although geometric sweep is used to reduce the effective Mach number of the airfoil, the geometric sweep is not completely effective. The flow field resists the sweep. In particular, the wing root and tip regions tend to effectively unsweep the wing. Aerodynamicists study lines of constant pressure on the wing planform known as isobars to investigate this phenomenon. Figure 5-41 presents the computed isobars for a typical swept wing,[50] using a transonic small-disturbance method.[51] The effect is dramatic. The effective sweep may actually correspond to the isobar line from the wing root trailing edge to the leading edge at the wingtip. To increase the isobar sweep, in addition to geometric sweep and twist, the camber surface and thickness are typically adjusted to move the isobars forward at the wing root and aft at the wingtip. This is a key part of the aerodynamic wing design job, regardless of the computational methodology used to obtain the predicted isobar pattern.

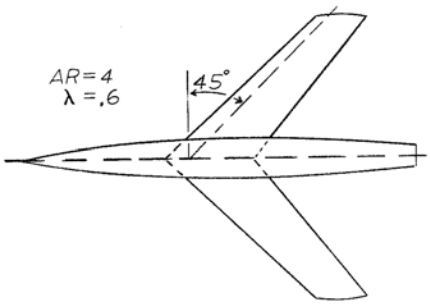


Figure 5-41(a): L51F07 configuration with an untwisted swept wing. From W. H. Mason, D. A. MacKenzie, M. A. Stern, W. F. Ballhaus Jr., and J. Frick. US Air Force. Public domain.

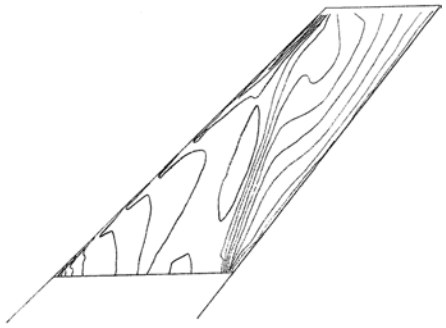


Figure 5-41(b): Upper surface isobars on L51F07 configuration at $M = 0.93$, $\alpha = 2°$. From W. H. Mason, D. A. MacKenzie, M. A. Stern, W. F. Ballhaus Jr., and J. Frick. US Air Force. Public domain.

Using the wing planform and twist, together with a constant chord loading, figure 5-42 provides the camber lines required to support the load near the root, the midspan, and the wingtip. These results were also computed using LAMDES.[52] At each station, a similar chord load is specified. We can easily see the differences in the camber required. This is an explicit illustration of the modification to an airfoil camber line required to maintain two-dimensional airfoil-type performance when the airfoil is placed in a swept wing. These modifications represent the explicit effects of the three dimensionality of the flow field.

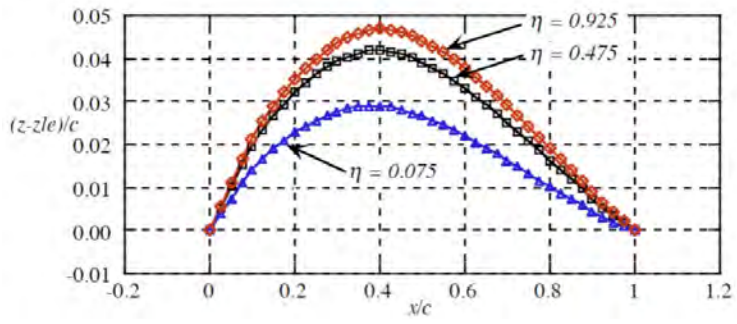


Figure 5-42: Comparison of camber lines required to develop the same chord load shape at the root ($\eta = 0.075$), midspan ($\eta = 0.475$), and tip region ($\eta = 0.925$) of an aft-swept wing. From W. H. Mason. Data generated using LAMDES. Code by J. E. Lamar. NASA. Public domain.

Many other refinements are available to the aerodynamic designer. Insight into both the human and technical aspects of wing design prior to the introduction of computational aerodynamics is available in two recent books describing the evolution of the Boeing series of jet transports.[53,54]

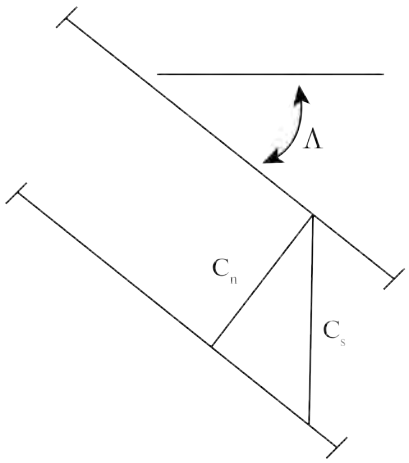
Yehudi flap

One interesting refinement of swept wings has been the addition of trailing-edge area at the wing root. Generally known as a Yehudi flap, this additional area arises for at least two reasons. The reason cited most frequently is the need to provide structure to attach the landing gear at the proper location. However, the additional chord lowers the section lift coefficient at the root, where wing-fuselage interference can be a problem, and the lower required section lift makes the design job easier.

Douglas introduced this planform modification for swept wings on the DC-8, while Boeing did not incorporate it until the 320 model of the 707. However, as retired Boeing engineer William Cook writes on page 83 of his book,[55] it was first introduced on the B-29 to solve an interference problem between the inboard nacelle and the fuselage. The aerodynamic benefit to the B-29 can be found in the paper by Snyder.[56] In a letter to me, Cook wrote that the device got its name because each wind tunnel part needed a name and there was a popular radio show at the time that featured the continuing punchline "Who's Yehudi?" (*Note*: This was the Bob Hope Radio show featuring Jerry Colonna, who had the line.) Thus, a Boeing engineer decided to call it a Yehudi flap. This slight extra chord is readily apparent when examining the B-29, though it is very difficult to photograph.

5.2.5 The Relation Between Airfoils and Swept Wings

In section 5.1, we examined the basic aerodynamics of airfoils using panel methods. So far in section 5.2, we have emphasized the planform shape and its analysis using vortex lattice methods. The connection between the airfoil and planform is important. In most cases, the integration of the airfoil concept and the wing planform concept is crucial to the development of a successful configuration. Simple sweep theory can be used to provide, at least approximately, the connection between the airfoil and the planform for swept wings. The typical aerodynamic design problem for an airfoil in a wing is defined by specifying the streamwise thickness-to-chord ratio, t/c, the local section lift coefficient, $C_{l_{des}}$, at design conditions, and the Mach number. This three-dimensional problem is then converted to a corresponding two-dimensional problem. The desired two-dimensional airfoils are then designed and transformed back to the streamwise section to be used as the wing airfoil section. Examples of the validity of this technique, together with details on other properties (including the "cosine cubed" law for profile drag due to lift) are available in the NACA report by Hunton.[57] Figure 5-43 shows the relationships between the streamwise airfoil properties and the chordwise properties (values normal to the leading edge).



$$C_n = C_s \cos\Lambda$$
$$M_n = M_\infty \cos\Lambda$$
$$t/c_n = t/c_s \cos\Lambda$$
and
$$C_{Ls} = C_{Ln} \cos^2\Lambda$$

Figure 5-43: Definitions connecting the airfoil and wing design problems. From W. H. Mason. Adapted by P. Raj.

These relations demonstrate that the equivalent two-dimensional airfoil is thicker and operates at a lower Mach number and at a higher lift coefficient than the related three-dimensional wing airfoil section. Taper effects on real wings require the selection of an effective sweep angle. Numerous approaches have been used to determine the effective angle, where guidance has been obtained by examining experimental data. The quarter-chord sweep or shock sweep are typical choices.

One good example of airfoil/planform matching is the Grumman X-29. In that case, wind tunnel testing of advanced transonic maneuver airfoil sections on aft-swept wing configurations led the aerodynamicists (Glenn Spacht in particular) to conclude that the proper planform to take advantage of the advanced airfoil section performance should be swept forward.

5.2.6 Wing-Tail and Canard-Wing Aerodynamics

Additional lifting surfaces are used to provide control of aircraft configurations over a wide range of flight conditions. If modern advanced control systems are not used, the extra surface is also designed, together with the rest of the configuration, to produce a stable design. In considering aft-tail configurations, the problem of pitchup described above for isolated wings must be reconsidered. In particular, T-tail aircraft can encounter problems when the horizontal tail interacts with the wake of the wing at stall. The pitching moment characteristics of the DC-9[58] show that an initial abrupt nose-down characteristic is the result of careful design, occurring before a large pitchup develops. Even though pitchup is a viscous effect, inviscid calculations clearly show why it happens and can provide valuable information. On the DC-9, a stable trim condition occurs at an angle of attack of 43°. This is an undesirable equilibrium condition, which could result in the vehicle actually trying to fly at this angle of attack. If adequate control power is not available, it may even be difficult to dislodge the vehicle from this condition, which is commonly known as a deep or hung stall. This will result in a rapid loss of altitude due to the very high drag. For this configuration, full down elevator eliminates the possibility of getting trapped in a trimmed flight condition at this angle of attack, but the amount of pitching moment available may not be sufficient to affect a rapid recovery from this condition. Examples of pitchup characteristics are not readily available. Aerodynamic designers do not like to admit that their configurations might have this characteristic. This aspect of swept-wing and wing-tail aerodynamics is an important part of aerodynamic configuration development.

Even low tail placement cannot guarantee that there will not be a problem. The pitching moment characteristics for an F-16 wind tunnel model[59] showed a deep stall. In fact, the allowable angle of attack on the F-16 is limited by the control system to prevent the airplane from encountering this problem. In this case, the pitchup arises because of powerful vortices generated by the strakes, which continue to provide lift as the wing stalls.

Canard configurations provide another interesting example of multiple lifting surface interaction. The downwash from the canard wake as it streams over the wing reduces the effective angle of attack on the wing locally and the local lift on the wing behind the canard. Wing twist is used to counteract this effect. Figure 5-44 illustrates how this interaction occurs. The relative loading of the surfaces (how much lift is carried by the canard and how much is carried by the wing) is an important consideration in configuration aerodynamics. The induced drag is highly dependent on the relative wing loading, which is determined by the selection of the configuration stability level and the requirement to trim about the center of gravity.

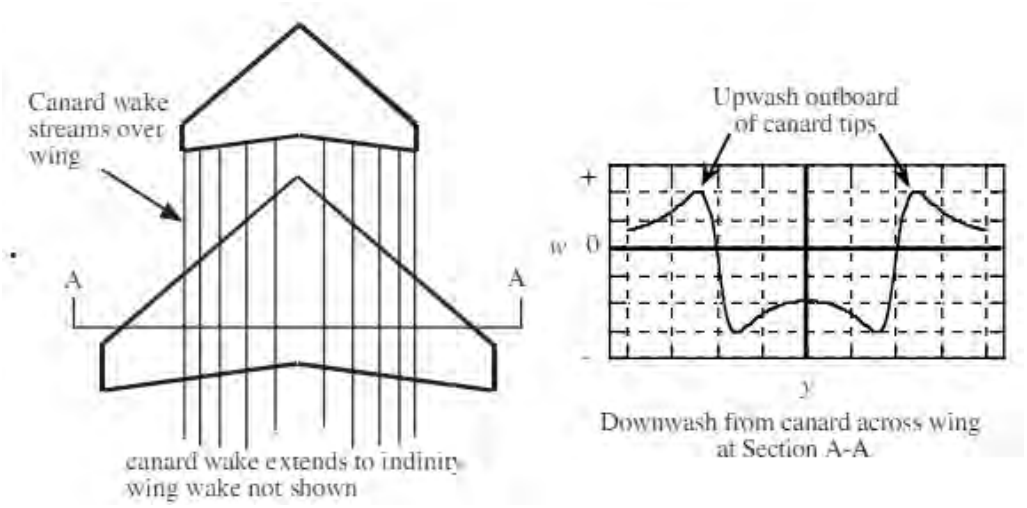


Figure 5-44: Illustration of wing-canard interaction.

Figure 5-45 shows a wing-canard combination that can be used to illustrate the strong effect of CG position on induced drag. This figure shows the plan view of the configuration (bottom) and notional chordwise loadings at a spanwise station on the canard and the wing (top).

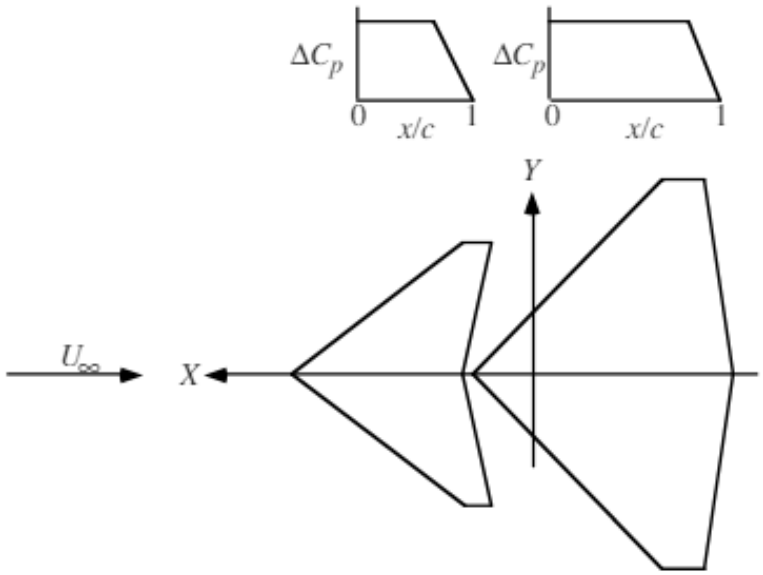


Figure 5-45: Canard-wing planform (bottom) and notional chordwise loadings on a spanwise station of the canard and of the wing (top) used for induced drag calculation.

Figure 5-46 presents the induced drag computed using LAMDES[60] and shows the variation of trimmed drag changes with CG position. Anything above the minimum drag value should be considered the trimmed drag penalty. Three different canard heights are shown for a range of CG positions, which is equivalent to varying the stability level.

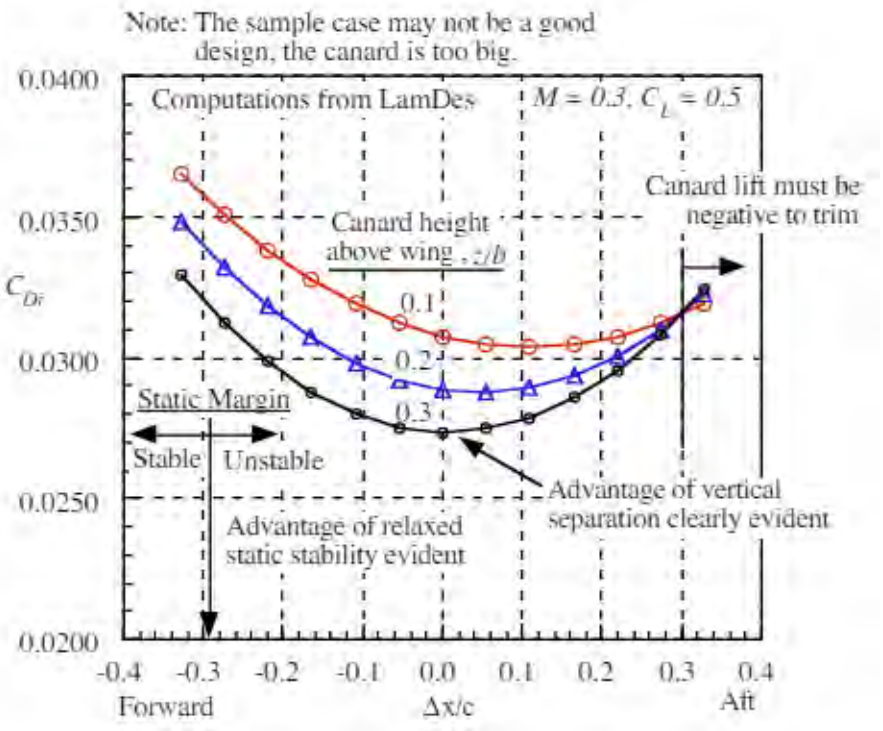


Figure 5-46: Minimum trimmed drag variation with trim position and canard-wing separation, an example of the relation of minimum trimmed drag to balance (stability). *From W. H. Mason. Data generated using LAMDES. Code by J. E. Lamar. NASA. Public domain.*

Figure 5-47 provides an example of the wing twist required to account for the effect of the canard downwash. Results depend on configuration details, balance, and the numerics that lead to sudden drop in incidence at the wingtip of the forward-swept wing, all of which may or may not be accurate. Due to the canard, the forward-swept wing twist increment acts to reduce the twist required, which is exactly opposite of the canard effect for the aft-swept wing.

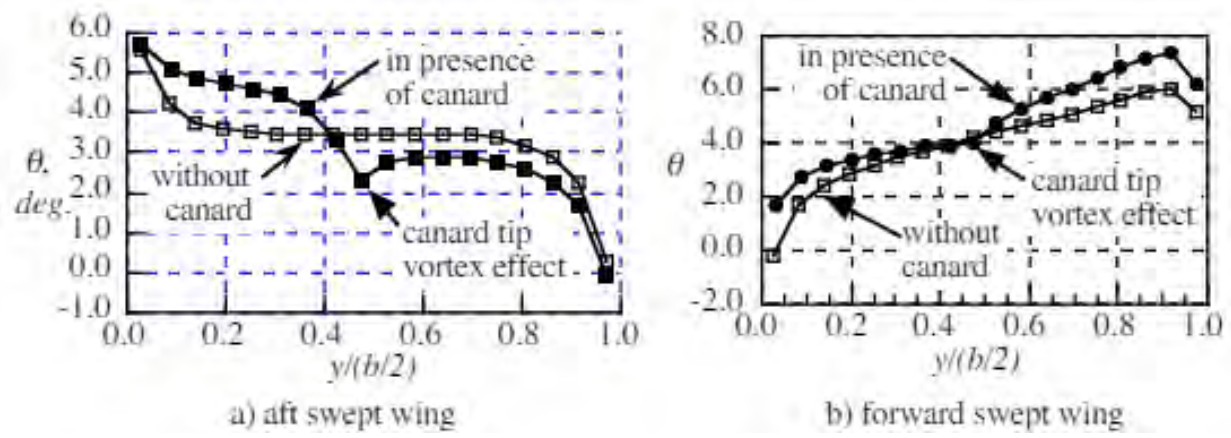


Figure 5-47: Effects of canard wake on wing twist requirements. Twist required for minimum drag. *From W. H. Mason. Data generated using LAMDES. Code by J. E. Lamar. NASA. Public domain.*

5.2.7 Ground Effects Using a VLM Code

We complete our discussion of wings at subsonic speeds with an example of ground effects, computed using VLM codes. Figure 5-48 shows the effects of the presence of the ground on the aerodynamics of simple unswept rectangular wings. The lift and pitching moment slopes are presented for calculations made using JKayVLM[61] and compared with the results published by Kalman et al.[62] and with experimental data. The agreement between the data and calculations is excellent for the lift-curve slope. The *AR* = 1 wing shows the least effects of ground proximity because of the three-dimensional relief provided around the wingtips. As the aspect ratio increases, the magnitude of the ground effects increases. The lift-curve slope starts to increase rapidly as the ground is approached.

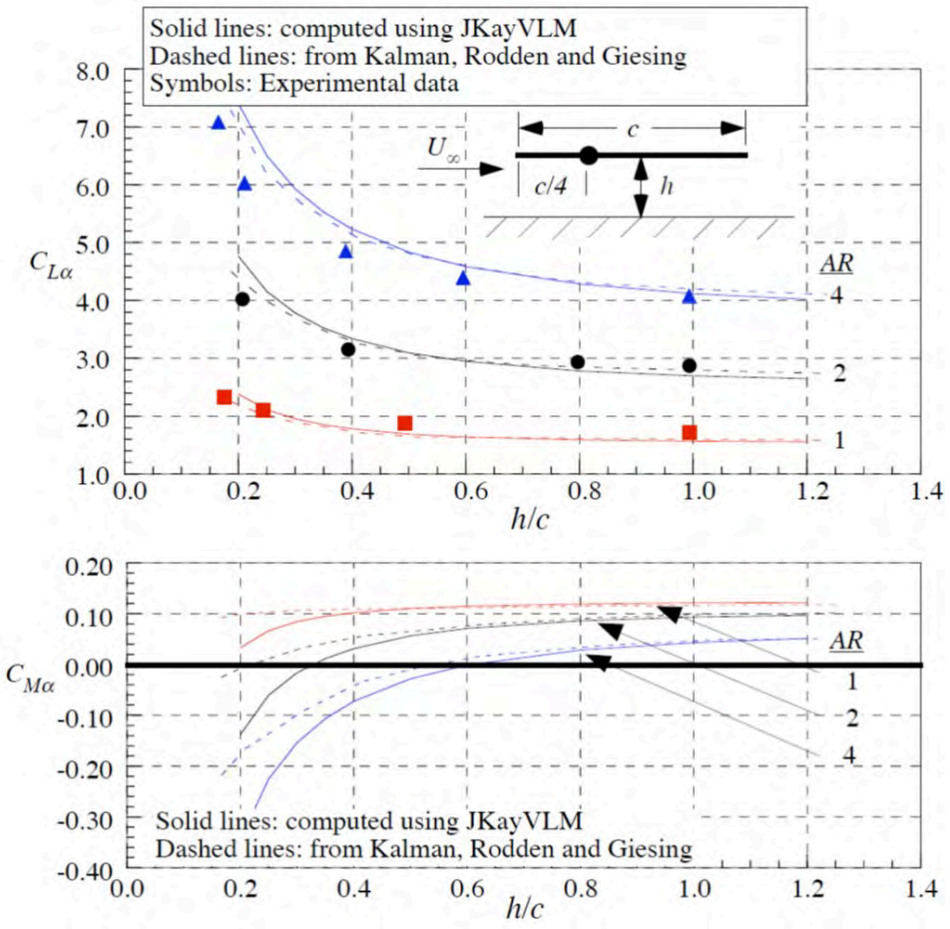


Figure 5-48: Example of ground effects on lift-curve slope (top) and pitching-moment curve slope (bottom) for three simple rectangular wings with aspect ratio (AR) of 1, 2, and 4. From W. H. Mason. Computed results from JKayVLM and experimental data and computational results from "Application of the Doublet-Lattice Method to Nonplanar Configurations in Subsonic Flow" by Kalman et al. Adapted by P. Raj.

As shown in the image, the wings also experience a significant change in the pitching moment slope (aerodynamic center shift). Note that the predictions start to differ as the ground is approached. JKayVLM actually rotates the entire surface to obtain another solution to use in estimating the lift-curve slope. The standard procedure used by most methods is to simply change the slope condition at the mean line location. Because of the proximity to the ground, this approach might be a case where the application of the boundary condition on the mean line may not be accurate.

Figure 5-49 presents similar information for the effect of dihedral angle, Γ, on a wing with an aspect ratio of 4. In this case, the effects of anhedral changes (negative Γ), where the wingtip approaches the ground, are extremely great. The results of dihedral changes for a wing out of ground effect ($h/c = \infty$) are shown for comparison. The figure compares computed results from JKayVLM[63] and published results

of Kalman et al.[64] Both methods agree well with each other, with differences appearing only as the wingtips approach the ground. Here again, JKayVLM actually rotates the entire geometry, apparently resulting in an increase in the effects as the tips nearly contact the ground. It also prevents calculations from being obtained as close to the ground as the published results. In making these calculations, it was discovered that the wing panel was rotated and not sheared, so that the projected span decreases as the dihedral increases, and this produces much more pronounced changes in the lift-curve slope due to the reduction in projected span. Most of the decrease in lift-curve slope values for the wing out of ground effect is due to the reduced span as the wing rotates from the zero-dihedral condition.

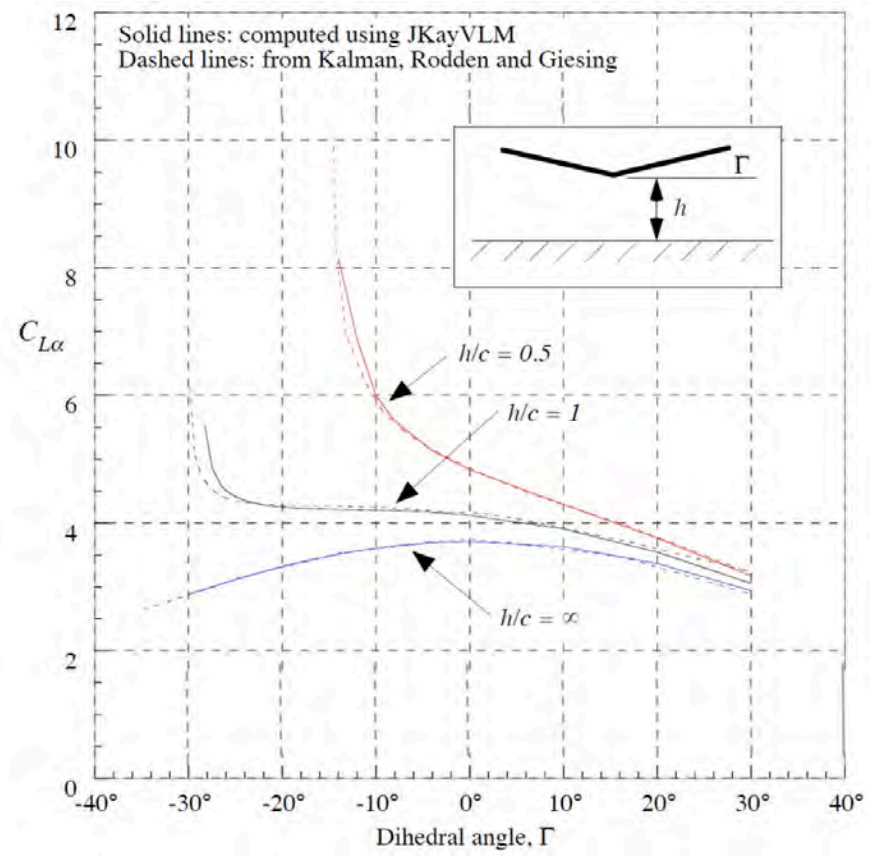


Figure 5-49: Example of the effect of dihedral angle on the lift-curve slope for a wing with AR = 4 in ground effect. From W. H. Mason. Computed results from JKayVLM and experimental data and computational results from "Application of the Doublet-Lattice Method to Nonplanar Configurations in Subsonic Flow" by Kalman et al. Adapted by P. Raj.

Ground effects shown here arise because of the nonpenetration condition at the ground, resulting in generally higher lift slopes. The effect is associated with three-dimensional flow. However, ground effects are considerably more complicated than suggested here. See Torenbeek[65] for a more complete discussion.

5.2.8 Low Aspect Ratio "Slender Wings"

Vortex flow effects: For highly swept wings at even moderate angles of attack, the classical attached flow/trailing-edge Kutta condition flow model we've adopted is wrong. Instead of the flow remaining attached on the wing and leaving the trailing edge smoothly, the flow separates at the leading edge, forming a well defined vortex. This vortex plays an important role in the design of highly swept, or "slender wing," aircraft. The most notable example of this type of configuration is the Concorde. Sharp leading edges promote this flow phenomena. The basic idea is illustrated in the sketch from Payne and Nelson[66] given here in figure 5-50.

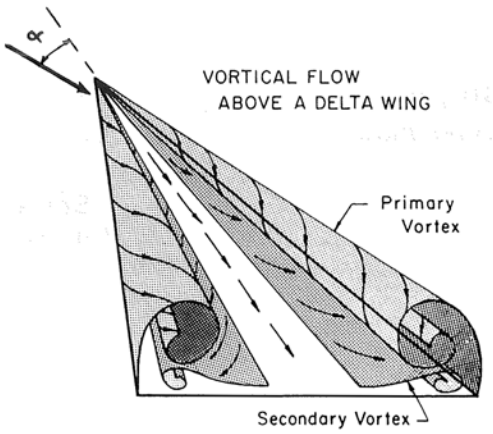


Figure 5-50: Vortex flow development over a delta wing with sharp edges. From F. W. Payne and R. C. Nelson. NASA. Public domain.

An important consequence of this phenomena is the change in the characteristics of the lift generation as the wing angle of attack increases. The vortex that forms above the wing provides an additional low pressure force due to the strongly spiraling vortex flow. The low pressure associated with the centrifugal force due to the vortex leads to lower pressure on the wing. As the wing increases its angle of attack, the vortex gets stronger, further reducing the pressure on the wing. The resulting increase in lift due to the vortex can be large, as Polhamus[67] shows in figure 5-51.

This is an important flow feature. Slender wings have very low attached-flow lift-curve slopes, and without the additional vortex lift, it would be impractical to build configurations with low aspect ratio wings. The low attached-flow lift-curve slope would prevent them from being able to land at acceptable speeds or angle of attack. Vortex lift made the Concorde possible. Another feature of the flow is the high angle of attack at which maximum lift occurs; it also typically suffers only a very mild lift loss past maximum lift. These features are a direct result of the leading-edge vortex flow structure that occurs on slender wings.

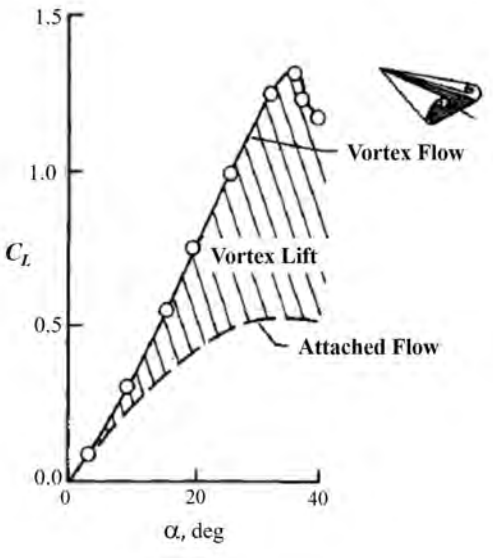


Figure 5-51: Vortex lift significantly changes the characteristic of lift development with angle of attack as shown for a slender delta wing with a leading-edge sweep of 75° in subsonic flow. From E. C. Polhamus. "Application of Slender Wing Benefits to Military Aircraft." AIAA. Fair use. Adapted.

Leading-edge suction analogy: Although the vortex lattice method formulation presented above does not include this leading-edge vortex effect, VLMs are often used as the basis for extensions that *do* include the leading-edge vortex effects. A remarkable, reasonably accurate flow model for leading-edge vortex flows was introduced by Polhamus[68,69] at NASA Langley in 1966 after examining lots of data. This flow model is known as the leading-edge suction analogy. The concept is quite simple and was invented for sharp-edged wings. The leading-edge suction that should exist according to attached flow theory is assumed to rotate 90° and generate a vortex-induced force instead of a suction when leading-edge vortex flow exists. Thus, the vortex flow force is assumed to be equal to the leading-edge suction force. However, the force now acts in the direction normal to the wing surface in the direction of lift rather than in the plane of the wing's leading edge. The concept is shown in figure 5-52 from the original Polhamus NASA report.[70] Further details on the effects of vortex flow effects are also available in reports by Kulfan.[71,72]

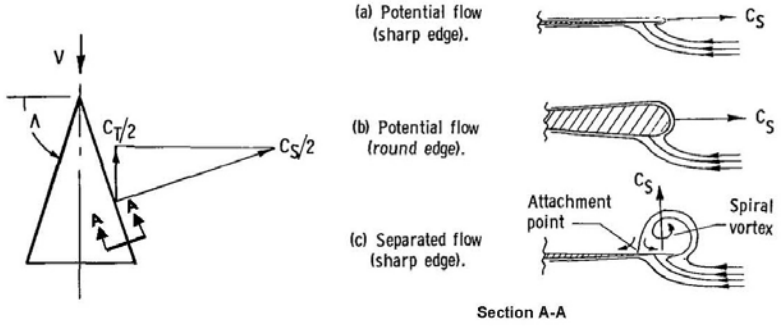


Figure 5-52: The Polhamus leading-edge suction analogy. From E. C. Polhamus. "A Concept of the Vortex Lift of Sharp-Edge Delta Wings Based on A Leading-Edge-Suction Analogy." NASA. Public domain.

Polhamus developed charts to compute the suction force for simple wing shapes. For a delta wing with a sharp leading edge, the prediction using the suction analogy is compared with the experimental data of Bartlett and Vidal[73] in figure 5-53. The agreement is quite good. Though my reconstruction doesn't show agreement as good as that presented by Polhamus,[74] it is still impressive. The figure also shows the large amount of the vortex lift and the nonlinear shape of the lift curve when large angles are considered. This characteristic was exploited in the design of the Concorde.

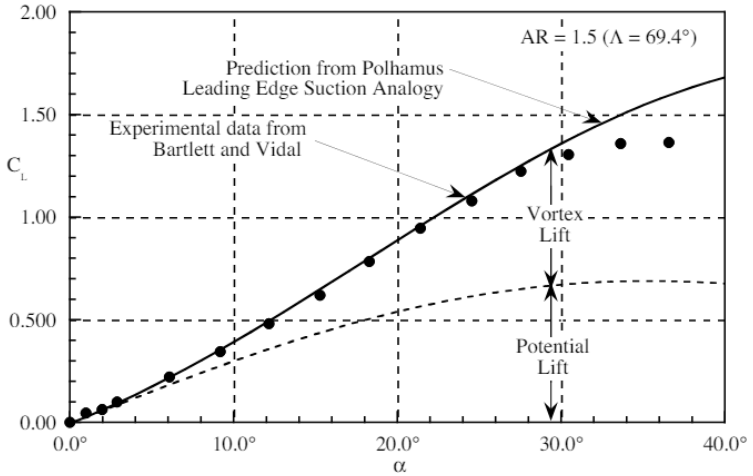


Figure 5-53: Comparison of the leading edge suction analogy. From W. H. Mason. Data from Polhamus ("A Concept of the Vortex Lift of Sharp-Edge Delta Wings Based on A Leading-Edge-Suction Analogy") and from Bartlett and Vidal ("Experimental Investigation of Influence of Edge Shape on the Aerodynamic Characteristics of Low Aspect Ratio Wings at Low Speeds")

To find the vortex lift using the leading-edge suction analogy, an estimate of the leading-edge suction distribution is required. However, the suction analogy does not result in an actual flow field analysis that includes leading-edge vortices. The VLMpc computer program optionally includes a fully developed suction analogy based on Polhamus' ideas, with extensions to treat side-edge suction that can be found in a NASA report by Lamar.[75]

Other approaches have been developed to compute leading-edge vortex flows in more detail. Many of these methods allow vortex filaments, simulating the leading-edge vortices, to leave the leading edge. The location of these vortices are explicitly computed, as are their effect on the wing aerodynamics as they roll up. Mook et al.[76] are leaders in this methodology.

The area of vortex flows in configuration aerodynamics is so fascinating that, in 1985, an entire conference at NASA Langley[77] was devoted to this topic. The references cited above were selected to provide an entry to the literature on these flows. Interest in the area remains strong. The effects of round leading edges have been investigated by Ericsson and Reding[78] and by Kulfan.[79] The relationship between sweep, vortex lift, and vortex strength has been explored by Hemsch and Luckring.[80]

Chapter 5 Exercises

5.1 PANEL

a. Obtain a copy of the program PANEL and the sample case.
b. Convert PANEL to run on your PC.
c. Run the sample case: NACA 4412, 20 pts. upper, 20 pts. lower, and $\alpha = 4°$. Verify against sample case.
d. Document:
    - Compile time required on your PC (cite computer and compiler used)
    - The execution time for the sample case
    - The accuracy relative to the sample case
    - The exact modifications required to make the code work on your computer

5.2 Start work on PANEL.

a. Save a reference copy of the working code!
b. Check convergence with panels (NLOWER+NUPPER must be less than 100 currently). How many panels do you need to get results independent of the number of panels? What happens to the computer time as the number of panels increases?
c. Check the coordinates generated by the airfoil routine compared to exact. (*Note*: Consider using NACA 0012; see appendix A for the geometry definitions.) Examine the coordinates at the trailing edge. This is best done by making a table of exact and computed values at selected values of x/c. What did you find?
d. Locate the source strengths, multiply the source strength on each panel by the length of the panel, and add all of the resulting values to get the total source strength. Does it sum to zero? Should it?
e. Where is the moment reference center in this code?
f. Submit an assessment of your findings.

5.3 Modify PANEL.

You need a version of PANEL that will allow you to compute the pressure distribution on arbitrary airfoils. This exercise will give you this capability. Modify the code to interpolate input airfoil points to the program-defined surface points, x/c. The resulting code should meet the following criteria:

- Accept arbitrary airfoil input data
- Echo all the input data on the output
- Generate an output file for post-processing (both for plotting and as the input to a boundary layer code)

Output *Cm* about the airfoil quarter-chord point.

Hint: Don't alter the panel distribution. The paneling scheme should be independent of the input distribution of airfoil coordinates. This produces a much more general and accurate program. This problem is usually solved by finding both the *x/c* and *y/c* values as functions of the airfoil arc length, starting at the lower surface trailing edge. A spline fit is usually used to interpolate the values along the arc length.

Check your modified code. Run the airfoil you ran previously with internal coordinate generation. This time, use an input file with the same coordinates as external inputs. Submit a description of your work, and assess your results.

5.4 Assess the accuracy of incompressible potential flow theory.

Run your modified PANEL code using the airfoil you selected in the exercise in Chapter 1. (What happens if your airfoil has a trailing edge with finite thickness? What do you do now?)

a. Compare the computed pressure distribution with the experimental data.
b. Compare the computed force and moment results with the data (over a range of angles of attack).

Turn in a *concise* report describing the results of your work. Include a plot showing the pressure distribution comparison and a plot(s) showing comparison with forces and moments. What do you conclude about the accuracy of this method?

5.5 Airfoil design using PANEL
Take your reference airfoil:

a. Add thickness on the bottom (mid chord). What happens?
b. Shave some thickness off the bottom (mid chord). What happens?
c. Add thickness on the top (mid chord). What happens?
d. Deflect the trailing edge down a couple of degrees. How sensitive is the airfoil to changes at the TE?

Hint: Use smooth δ's to the reference foil employing analytic formulas.

Turn in a *concise* report comparing the effects on the pressure distribution due to the above modifications.

5.6 How good is thin-airfoil theory? Compare the thin airfoil ΔCp for a flat plate with PANEL.

Recall thin-airfoil theory for an uncambered flat plate: $\Delta C_p = 4\alpha\,(1 - x/c)$

a. Pick an NACA 0012 airfoil at $\alpha = 2°$ and 12°, and run PANEL.
b. Plot $\Delta Cp/\alpha$ as a function of *x/c*.
c. How many panels do you need to get a converged solution from PANEL?
d. What conclusions do you reach?

5.7 Get a copy of VLMpc from the website. The detailed instructions for this program are included on the software's website. Install the program on your personal computer and repeat the sample case, checking that your output is the same as the sample output files on the web. Study the output to familiarize yourself with the variety of information generated. Turn in a report describing your efforts (not the output), including any mods required to make the code run on your computer.

5.8 How good is thin-airfoil theory? Compare the thin-airfoil theory ΔCp for a 2D flat plate airfoil with program VLMpc.
Flat plate thin airfoil theory: $\Delta C_p = 4\alpha$

a. Pick an unswept wing with an aspect ratio of 10 at $\alpha = 3°$ and 12°, and run VLMpc.

b. Plot $(\Delta Cp)/\alpha$ as a function of x/c at the wing root.
c. How many panels do you need to get a converged solution from VLM?
d. What conclusions do you reach?

5.9 Compare the validity of an aerodynamic strip theory using VLMpc. Consider an uncambered, untwisted wing ($AR = 4$; $\lambda = 0.4$; $\Lambda_{le} = 50°$) at a lift coefficient of 1.0. Plot the spanload, the ΔC_p distribution at approximately the center section, the midspan station, and the 85% semispan station. Compare your results with a spanload constructed assuming that the wing flow is approximated as 2D at the angle of attack required to obtain the specified lift. Next, compare the chordloads, ΔC_p, at the three span stations. How many panels do you need to obtain converged results? Document your results. Do you consider this aerodynamic strip theory valid based on this investigation? Comment.

5.10 Compare the wing aerodynamic center location relative to the quarter chord of the wing's mean aerodynamic chord in exercise 9. Consider one wing with zero sweep on the quarter chord and a forward-swept wing with a leading edge sweep of -50°. Compare the spanloads. Document and analyze these results. What did you learn from this comparison?

5.11 For the wings in exercise 10, compare the section lift coefficients. Where would each one stall first? Which wing appears to be able to reach the highest lift coefficient before the section stalls?

5.12 For the problem in exercise 11, add twist to each wing to obtain near elliptic spanloads. Compare the twist distributions required in each case.

5.13 Pick a NASA or NACA report describing wind tunnel results for a simple one- or two-lifting-surface configuration at subsonic speeds. Compare the lift-curve slope and stability level predicted by VLMpc with wind tunnel data. Submit a report describing your work and assessing the results.

5.14 Add a canard to the aft- and forward-swept wings analyzed in exercise 10. Plot the sum of the spanloads. How does the canard effect the wing spanload?

5.15 Consider the wings in exercise 14. How does lift change with canard deflection? Add an equivalent tail. Compare the effect of tail or canard deflection on total lift and moment. What did you learn?

5.16 Construct a design code using the 1/4 – 3/4 rule, and compare with DESCAM.

5.17 Construct a little 2D code to study ground effects.

5.18 Compare wing and wing-tail(canard) results for $C_{L\alpha}$ with standard analytic formulas.

Figure References

Figure 5-7: Adapted from Abbott, I. H., and von Doenhoff, A. E., *Theory of Wing Sections*, Dover, New York, 1959.

Figure 5-8: Adapted from Abbott, I. H., and von Doenhoff, A. E., *Theory of Wing Sections*, Dover, New York, 1959.

Figure 5-9: Adapted from Abbott, I. H., and von Doenhoff, A. E., *Theory of Wing Sections*, Dover, New York, 1959.

Figure 5-10: W. H. Mason. Adapted by S. Madden.

Figure 5-11: W. H. Mason. Adapted by S. Madden.

Figure 5-12: W. H. Mason. Adapted by S. Madden.

Figure 5-13: W. H. Mason. Adapted by S. Madden.

Figure 5-14: W. H. Mason. Adapted by S. Madden.

Figure 5-15: W. H. Mason. Adapted by S. Madden.

Figure 5-16: W. H. Mason. Adapted by S. Madden.

Figure 5-17: W. H. Mason. Adapted by S. Madden.

Figure 5-18: W. H. Mason. Adapted by S. Madden.

Figure 5-19: W. H. Mason. Adapted by S. Madden.

Figure 5-20: W. H. Mason. Adapted by S. Madden.

Figure 5-21: W. H. Mason. Adapted by S. Madden.

Figure 5-22: W. H. Mason. Adapted by S. Madden.

Figure 5-23: W. H. Mason. Adapted by S. Madden.

Figure 5-24: W. H. Mason. Adapted by S. Madden.

Figure 5-25: W. H. Mason. Adapted by P. Raj.

Figure 5-27: Koegler, J., "Appendix B: Evaluation of Aerodynamic Panel Methods" in Thomas, R. W., "Analysis of Aircraft Stability and Control Design Methods," AFWAL-TR-84- 3038, Vol. II, May, 1984. Public domain.

Figure 5-28: Koegler, J., "Appendix B: Evaluation of Aerodynamic Panel Methods" in Thomas, R. W., "Analysis of Aircraft Stability and Control Design Methods," AFWAL-TR-84- 3038, Vol. II, May, 1984. Public domain.

Figure 5-29: Koegler, J., "Appendix B: Evaluation of Aerodynamic Panel Methods" in Thomas, R. W., "Analysis of Aircraft Stability and Control Design Methods," AFWAL-TR-84- 3038, Vol. II, May, 1984. Public domain.

Figure 5-30: Koegler, J., "Appendix B: Evaluation of Aerodynamic Panel Methods" in Thomas, R. W., "Analysis of Aircraft Stability and Control Design Methods," AFWAL-TR-84- 3038, Vol. II, May, 1984. Public domain.

Table 5-1: Data from Koegler, John, App. B., "Evaluation of Aerodynamic Panel Methods" in Thomas, R. W., "Analysis of Aircraft Stability and Control Design Methods," AFWAL-TR-84- 3038, Vol. II, May, 1984. Public domain.

Figure 5-31: Koegler, J., "Appendix B: Evaluation of Aerodynamic Panel Methods" in Thomas, R. W., "Analysis of Aircraft Stability and Control Design Methods," AFWAL-TR-84- 3038, Vol. II, May, 1984. Public domain.

Figure 5-32: Koegler, J., "Appendix B: Evaluation of Aerodynamic Panel Methods" in Thomas, R. W., "Analysis of Aircraft Stability and Control Design Methods," AFWAL-TR-84- 3038, Vol. II, May, 1984. Public domain.

Figure 5-33: Koegler, J., "Appendix B: Evaluation of Aerodynamic Panel Methods" in Thomas, R. W., "Analysis of Aircraft Stability and Control Design Methods," AFWAL-TR-84- 3038, Vol. II, May, 1984. Public domain.

Table 5-2: Data courtesy of N. Kirshbaum.

Figure 5-39: W. H. Mason. Data from Tinling, B. E., and Kolk, W. R., "The Effects of Mach Number and Reynolds Number on the Aerodynamic Characteristics of Several 12-Percent-Thick Wings Having 35° of Sweepback and Various Amounts of Camber," NACA RM-A50K27, Feb. 1951. https://ntrs.nasa.gov/citations/19930086568

Figure 5-41(a): Figure (a) in Mason, W. H., MacKenzie, D. A., Stern, M. A., Ballhaus, W. F, Jr., and Frick, J., "Automated Procedure for Computing the Three-Dimensional Transonic Flow Over Wing-Body Combinations, including Viscous Effects," Vol. I, Description of Methods and Applications, AFFDL-TR-77-122, Feb. 1978, p. 121. https://archive.aoe.vt.edu/mason/Mason_f/AFFDL-TR-77-122GACAmes.pdf

Figure 5-41(b): Figure (a) in Mason, W. H., MacKenzie, D. A., Stern, M. A., Ballhaus, W. F, Jr., and Frick, J., "Automated Procedure for Computing the Three-Dimensional Transonic Flow Over Wing-Body Combinations, including Viscous Effects," Vol. I, Description of Methods and Applications, AFFDL-TR-77-122, Feb. 1978, p. 121. https://archive.aoe.vt.edu/mason/Mason_f/AFFDL-TR-77-122GACAmes.pdf

Figure 5-42: W. H. Mason. Data generated using Lamar's LAMDES code from Lamar, J. E., "A Vortex Lattice Method for the Mean Camber Shapes of Trimmed Non-Coplanar Planforms with Minimum Vortex Drag," NASA TN D-8090, June 1976. https://ntrs.nasa.gov/citations/19760019073

Figure 5-43: W. H. Mason. Definitions connecting the airfoil and wing design problems. Adapted by P. Raj.

Figure 5-46: W. H. Mason. Data generated using Lamar's LAMDES code from Lamar, J. E., "A Vortex Lattice Method for the Mean Camber Shapes of Trimmed Non-Coplanar Planforms with Minimum Vortex Drag," NASA TN D-8090, June 1976. https://ntrs.nasa.gov/citations/19760019073

Figure 5-47: W. H. Mason. Data generated using Lamar's LAMDES code from Lamar, J. E., "A Vortex Lattice Method for the Mean Camber Shapes of Trimmed Non-Coplanar Planforms with Minimum Vortex Drag," NASA TN D-8090, June 1976. https://ntrs.nasa.gov/citations/19760019073

Figure 5-48: W. H. Mason and P. Raj. Adapted from figures 14 and 16 in Kalman, T. P., Rodden, W. P., and Giesing, J., "Application of the Doublet-Lattice Method to Nonplanar Configurations in Subsonic Flow," Journal of Aircraft, Vol. 8, No. 6, June 1971, p. 411. Fair use. https://doi.org/10.2514/3.59117. Adapted.

Figure 5-49: P. Raj. Added JKayVLM lines to rerendered figure 17 in Kalman, T. P., Rodden, W. P., and Giesing, J., "Application of the Doublet-Lattice Method to Nonplanar Configurations in Subsonic Flow," Journal of Aircraft, Vol. 8, No. 6, June 1971, p. 412. Fair use. https://doi.org/10.2514/3.59117.

Figure 5-50: Payne, F. W., and Nelson, R. C., "An Experimental Investigation of Vortex Breakdown on a Delta Wing," in "Vortex Flow Aerodynamics," NASA CP-2416, 1986, p. 143. https://ntrs.nasa.gov/citations/19860017724

Figure 5-51: Polhamus, E. C. "Application of Slender Wing Benefits to Military Aircraft," AIAA Wright Brothers Lecture, AIAA-83-2566, 1983. Adapted under fair use. https://doi.org/10.2514/6.1983-2566

Figure 5-52: Polhamus, E. C. "A Concept of the Vortex Lift of Sharp-Edge Delta Wings Based on A Leading-Edge-Suction Analogy," NASA TN D-3767, 1966. https://ntrs.nasa.gov/api/citations/19670003842/downloads/19670003842.pdf

Figure 5-53: W. H. Mason. Data from Bartlett, G. E., and Vidal, R. J., "Experimental Investigation of Influence of Edge Shape on the Aerodynamic Characteristics of Low Aspect Ratio Wings at Low Speeds," Journal of the Aeronautical Sciences, Vol. 22, No. 8, Aug. 1955, pp. 513–533, 588. https://arc.aiaa.org/doi/10.2514/8.3391

Notes

1. Cummings, R. M., Mason, W. H., Morton, S., A., and McDaniel, D. R., *Applied Computational Aerodynamics: A Modern Engineering Approach*, Cambridge University Press, New York, NY, 2015.
2. Hess, J. L., "Panel Methods in Computational Fluid Dynamics," Annual Review of Fluid Mechanics, Vol. 22, 1990, pp. 255–274.
3. Hess, J. L., "Linear Potential Schemes," *Applied Computational Aerodynamics*, edited by P. A. Henne, AIAA, Washington, 1990. pp. 21–36.
4. Erickson, L. L., "Panel Methods—An Introduction," NASA TP-2995, Dec. 1990.
5. Katz, J., and Plotkin, A., *Low-Speed Aerodynamics From Wing Theory to Panel Methods*, 2nd ed., Cambridge University Press, 2001.
6. "Vortex Lattice Utilization Workshop," NASA SP-405, May, 1976.
7. Margason, R. J., and Lamar, J. E., "Vortex-Lattice FORTRAN Program for Estimating Subsonic Aerodynamic Characteristics of Complex Planforms," NASA TN D-6142, 1971.
8. Lamar, J. E., and Gloss, B. B., "Subsonic Aerodynamic Characteristics of Interacting Lifting Surfaces With Separated Flow Around Sharp Edges Predicted by a Vortex-Lattice Method," NASA TN D-7921, 1975. https://archive.aoe.vt.edu/mason/Mason_f/MRsoft.html#VLMpc
9. Lamar, J. E., and Herbert, H. E., "Production Version of the Extended NASA-Langley Vortex Lattice FORTRAN Computer Program," Vol. I, User's Guide, NASA TM-83303, 1982. (*Note*: Requires update packet, Jul. 1984.)
10. Herbert, H. E, and Lamar, J. E., "Production Version of the Extended NASA-Langley Vortex Lattice FORTRAN Computer Program," Vol. II, Source Code, NASA TM-83304, 1982.
11. Cummings, R. M., Mason, W. H., Morton, S., A., and McDaniel, D. R., *Applied Computational Aerodynamics: A Modern Engineering Approach*, Cambridge University Press, New York, NY, 2015.
12. Lan, C. E., "A Quasi-Vortex-Lattice Method in Thin Wing Theory," Journal of Aircraft, Vol. 11, No. 9, Sept. 1974, pp. 518–527.
13. Hough, G. R., "Remarks on Vortex-Lattice Methods," Journal of Aircraft, Vol. 10, No. 5, May 1973, pp. 314–317.
14. DeJarnette, F. R., "Arrangement of Vortex Lattices on Subsonic Wings," in "Vortex Lattice Utilization Workshop," NASA SP-405, May, 1976, pp. 301–319.
15. Frink, N. T., "Lifting-Surface Theory for Skewed and Swept Subsonic Wings," Journal of Aircraft, Vol. 19, No. 7, Jul., 1982, pp. 519–524.
16. Mook, D. T., and Nayfeh, A. H., "Application of the Vortex-Lattice Method to High-Angle-of-Attack Subsonic Aerodynamics," SAE Paper No. 851817, Oct. 1985.
17. Katz, J., and Plotkin, A., *Low-Speed Aerodynamics From Wing Theory to Panel Methods*, 2nd ed., Cambridge University Press, 2001.
18. Kay, J., Mason, W. H., Durham, W., Lutze, F., and Benoliel, A., "Control Power Issues in Conceptual Design: Critical Conditions, Estimation Methodology, Spreadsheet Assessment, Trim and Bibliography," VPI-Aero-200, Nov. 1993.
19. Tomas Melin, "Tornado", KTH, Stockholm, Sweden, Master's Thesis. (*Note*: Includes continued developments.)
20. Drela, M., and Youngren, H., "AVL Overview." http://web.mit.edu/drela/Public/web/avl
21. Moran, J., *An Introduction to Theoretical and Computational Aerodynamics*, John Wiley & Sons, New York, 1984, pp. 103–112, 118–123, 260–287. (*Note*: Now reprinted by Dover.)
22. Drela, M. "XFOIL: An Analysis and Design System for Low Reynolds Number Airfoils," in *Low Reynolds Number Aerodynamics*, edited by T. J. Mueller, Lecture Notes in Engineering #54, Springer-Verlag, 1989.
23. Moran, J. *An Introduction to Theoretical and Computational Aerodynamics*, John Wiley & Sons, New York, 1984. pp. 103–112, 118–123, 260–287.
24. Abbott, I. H., and Von Doenhoff, A. E., *Theory of Wing Sections*, Dover, New York, 1959.
25. Cummings, R. M., Mason, W. H., Morton, S. A., and McDaniel, D. R., *Applied Computational Aerodynamics: A Modern Engineering Approach*, Cambridge University Press, New York, NY, 2015.
26. Jones, R. T., *Wing Theory*, Princeton University Press, Princeton, New Jersey, 1990.
27. Warner, E. P., *Airplane Design: Performance*, McGraw-Hill, New York, 1936.
28. McGhee, R. J., and Beasley, W. D., "Low Speed Aerodynamic Characteristics of a 17-Percent-Thick Airfoil Section Designed for General Aviation Applications," NASA TN D-7428, 1973.
29. Joslin, R. D., "Aircraft Laminar Flow Control," Annual Review of Fluid Mechanics, Vol. 30, pp. 1–29. 1998.
30. Braslow, A. L., Maddalon, D. V., Bartlett, D. W., and Wagner, R. D., "Applied Aspects of Laminar Flow Technology," *Viscous Drag Reduction in Boundary Layers*, edited by D. M. Bushnell, and J. N. Hefner, Progress in Astronautics and Aeronautics, Vol. 123, AIAA, Washington, 1990, pp. 47–78.
31. Kroo, I., "Aerodynamic Analyses for Design and Education," AIAA Paper 92-2664, 10th Applied Aerodynamics Conference, Palo Alto, CA, Jun. 22-24, 1992.
32. Volpe, G., "Inverse Airfoil Design: A Classical Approach Updated for Transonic Applications," in *Applied Computational Aerodynamics*, edited by P. A. Henne, AIAA Progress in Astronautics and Aeronautics, Vol. 125, AIAA, New York, 1990, pp. 191–220.
33. Labrujere, T. E., and Sloof, J. W., "Computational Methods for the Aerodynamic Design of Aircraft Components," Annual Review of Fluid Mechanics, Vol. 25, 1993, pp.183–214.
34. Bristow, D. R., "A New Surface Singularity Method for Multi-Element Airfoil Analysis and Design," AIAA Paper 76-20, Jan. 1976.

35. Aidala, P. V., Davis, W. H., Jr., and Mason, W. H., "Smart Aerodynamic Optimization," AIAA Paper 83-1863, Applied Aerodynamics Conference, Danvers, MA, Jul. 13-15, 1983.
36. Lan, C. E., "A Quasi-Vortex-Lattice Method in Thin Wing Theory," Journal of Aircraft, Vol. 11, No. 9, Sept. 1974, pp. 518–527.
37. Liebeck, R. H., "Subsonic Airfoil Design," in *Applied Computational Aerodynamics*, edited by P. A. Henne, AIAA Progress in Astronautics and Aeronautics, Vol. 125, AIAA, New York, 1990, pp. 133–165.
38. Drela, M., "Elements of Airfoil Design Methodology," in *Applied Computational Aerodynamics*, edited by P. A. Henne, AIAA Progress in Astronautics and Aeronautics, Vol. 125, AIAA, New York, 1990, pp. 191–220.
39. Crouse, G., "Airfoil Optimizer," DaVinci Technologies.
40. Cummings, R. M., Mason, W. H., Morton, S. A., and McDaniel, D. R., *Applied Computational Aerodynamics: A Modern Engineering Approach*, Cambridge University Press, New York, NY, 2015.
41. Thomas, R. W., "Analysis of Aircraft Stability and Control Design Methods," AFWAL-TR-84- 3038, Vol. II, App. B., "Evaluation of Aerodynamic Panel Methods," by J. Koegler, May, 1984.
42. Cummings, R. M., Mason, W. H., Morton, S. A., and McDaniel, D. R., *Applied Computational Aerodynamics: A Modern Engineering Approach*, Cambridge University Press, New York, NY, 2015.
43. Thomas, R. W., "Analysis of Aircraft Stability and Control Design Methods," AFWAL-TR-84- 3038, Vol. II, App. B., "Evaluation of Aerodynamic Panel Methods," by John Koegler, May, 1984.
44. Lamar, J. E., and Gloss, B. B., "Subsonic Aerodynamic Characteristics of Interacting Lifting Surfaces With Separated Flow Around Sharp Edges Predicted by a Vortex-Lattice Method," NASA TN D-7921, 1975.
45. Melin, T., "Tornado", KTH, Stockholm, Sweden, Master's Thesis.
46. McDonald R. A., and Gloudemans, J. R., "Open Vehicle Sketch Pad: An Open Source Parametric Geometry and Analysis Tool for Conceptual Aircraft Design," AIAA 2022-0004, SciTech Forum, Jan. 3-7, 2022.
47. Küchemann, D., *The Aerodynamic Design of Aircraft*, Pergamon Press, Oxford, 1978.
48. Tinling, B. E., and Kolk, W. R., "The Effects of Mach Number and Reynolds Number on the Aerodynamic Characteristics of Several 12-Percent-Thick Wings Having 35° of Sweepback and Various Amounts of Camber," NACA RM A50K27, Feb. 1951. https://ntrs.nasa.gov/citations/19930086568
49. Lamar, J. E., "A Vortex Lattice Method for the Mean Camber Shapes of Trimmed Non-Coplanar Planforms with Minimum Vortex Drag," NASA TN D-8090, Jun. 1976.
50. Loving, D. L., and Estabrooks, B. B., "Transonic Wing Investigation in the Langley Eight Foot High Speed Tunnel at High Subsonic Mach Numbers and at Mach Number of 1.2," NACA RM L51F07, 1951.
51. Mason, W. H., MacKenzie, D. A., Stern, M. A., Ballhaus, W. F, Jr., and Frick, J., "Automated Procedure for Computing the Three-Dimensional Transonic Flow Over Wing-Body Combinations, including Viscous Effects," Vol. I, Description of Methods and Applications, AFFDL-TR-77-122, Feb. 1978.
52. Lamar, J. E., "A Vortex Lattice Method for the Mean Camber Shapes of Trimmed Non-Coplanar Planforms with Minimum Vortex Drag," NASA TN D-8090, Jun. 1976.
53. Cook, W. C., *The Road to the 707*, TYC Publishing, Bellevue, 1991.
54. Irving, C., *Wide-Body: The Triumph of the 747*, William Morrow, New York, 1993.
55. Cook, W. C., *The Road to the 707*, TYC Publishing, Bellevue, 1991.
56. Snyder, G., "Structural Design Problems in the B-29 Airplane," Aeronautical Engineering Review, Feb. 1946, pp. 9–12.
57. Hunton, L. W., "A Study of the Application of Airfoil Section Data to the Estimation of the High-Subsonic-Speed Characteristics of Swept Wings," NACA RM-A55C23, Jun. 1955.
58. Shevell, R. S., and Schaufele, R. D., "Aerodynamic Design Features of the DC-9," Journal of Aircraft, Vol. 3, No. 6, Nov.-Dec. 1966, pp. 515–523.
59. Nguyen, L. T., Ogburn, M. E., Gilbert, W. P., Kibler, K. S., Brown, P. W., and Deal, P. L., "Simulator Study of Stall/Post-Stall Characteristics of a Fighter Airplane With Relaxed Longitudinal Static Stability," NASA TP-1538, Dec. 1979.
60. Lamar, J. E., "A Vortex Lattice Method for the Mean Camber Shapes of Trimmed Non-Coplanar Planforms with Minimum Vortex Drag," NASA TN D-8090, Jun. 1976.
61. Kay, J., Mason, W. H., Durham, W., Lutze, F., and Benoliel, A., "Control Power Issues in Conceptual Design: Critical Conditions, Estimation Methodology, Spreadsheet Assessment, Trim and Bibliography," VPI-Aero-200, Nov. 1993. https://archive.aoe.vt.edu/mason/Mason_f/VPI-Aero-200.pdf
62. Kalman, T. P., Rodden, W. P., and Giesing, J., "Application of the Doublet-Lattice Method to Nonplanar Configurations in Subsonic Flow," Journal of Aircraft, Vol. 8, No. 6, Jun. 1971, pp. 406–415.
63. Kay, J., Mason, W. H., Durham, W., Lutze, F., and Benoliel, A., "Control Power Issues in Conceptual Design: Critical Conditions, Estimation Methodology, Spreadsheet Assessment, Trim and Bibliography," VPI-Aero-200, Nov. 1993. https://archive.aoe.vt.edu/mason/Mason_f/VPI-Aero-200.pdf
64. Kalman, T. P., Rodden, W. P., and Giesing, J., "Application of the Doublet-Lattice Method to Nonplanar Configurations in Subsonic Flow," Journal of Aircraft, Vol. 8, No. 6, Jun. 1971, pp. 406–415.
65. Torenbeek, E., *Synthesis of Subsonic Airplane Design*, Delft University Press, 1981, pp. 551–554.
66. Payne, F. W., and Nelson, R. C., "An Experimental Investigation of Vortex Breakdown on a Delta Wing," in "Vortex Flow Aerodynamics," NASA CP-2416, 1985.
67. Polhamus, E. C., "Application of Slender Wing Benefits to Military Aircraft," AIAA Wright Brothers Lecture, AIAA-83-2566, Aircraft Design, Systems and

Technology Meeting, Fort Worth, TX, Oct. 17-19, 1983.

68. Polhamus, E. C., "A Concept of the Vortex Lift on Sharp Edge Delta Wings Based on a Leading-Edge Suction Analogy," NASA TN-3767, 1966.
69. Polhamus, E. C., "Prediction of Vortex Lift Characteristics by a Leading-edge Suction Analogy," Journal of Aircraft, Vol. 8, No. 4, 1971, pp. 193–199.
70. Polhamus, E. C., "A Concept of the Vortex Lift on Sharp Edge Delta Wings Based on a Leading-Edge Suction Analogy," NASA TN-3767, 1966.
71. Kulfan, R. M., "Wing Airfoil Shape Effects on the Development of Leading-Edge Vortices," AIAA Paper 79-1675, 5th Atmospheric Flight Mechanics Conference for Future Space Systems, Boulder, CO, Aug. 6-8, 1979.
72. Kulfan, R. M., "Wing Geometry Effects on Leading Edge Vortices," AIAA Paper 79-1872, Aircraft Systems and Technology Meeting, New York, NY, Aug. 20-22, 1979.
73. Bartlett, G. E., and Vidal, R. J., "Experimental Investigation of Influence of Edge Shape on the Aerodynamic Characteristics of Low Aspect Ratio Wings at Low Speeds," Journal of the Aeronautical Sciences, Vol. 22, No. 8, Aug., 1955, pp. 517–533, 588.
74. Polhamus, E. C., "A Concept of the Vortex Lift on Sharp Edge Delta Wings Based on a Leading-Edge Suction Analogy," NASA TN-3767, 1966.
75. Lamar, J. E., and Gloss, B. B., "Subsonic Aerodynamic Characteristics of Interacting Lifting Surfaces With Separated Flow Around Sharp Edges Predicted by a Vortex-Lattice Method," NASA TN D-7921, 1975.
76. Mook, D. T., and Nayfeh, A. H., "Application of the Vortex-Lattice Method to High-Angle-of-Attack Subsonic Aerodynamics," SAE Technical Paper No. 851817, Aerospace Technology Conference and Exposition, Oct. 1985.
77. Vortex Flow Aerodynamics, NASA SP-2416 (Vol. I) and NASA SP-2417 (Vol. II), Oct. 1985.
78. Ericsson, L. E., and Reding, J. P., "Nonlinear Slender Wing Aerodynamics," AIAA Paper No. 76-19, Aerospace Sciences Meeting, Washington, DC, January 26-28, 1976.
79. Kulfan, R. M., "Wing Airfoil Shape Effects on the Development of Leading-Edge Vortices," AIAA 79-1675, 1979.
80. Hemsch, M. J., and Luckring, J. M., "Connection Between Leading-Edge Sweep, Vortex Lift, and Vortex Strength for Delta Wings," Journal of Aircraft, Vol. 27, No. 5, May 1990, pp. 473–475.

6. Transonic Aerodynamics: Airfoils and Wings

Transonic flow occurs when there is mixed subsonic and supersonic local flow in the same flow field (typically with freestream Mach numbers from $M = 0.6$ or 0.7 to 1.2). Usually the supersonic region of the flow is terminated by a shock wave, allowing the flow to slow down to subsonic speeds. This complicates both computations and wind tunnel testing. There is also very little analytic theory available for guidance in designing for transonic flow conditions. Importantly, not only is the outer inviscid portion of the flow governed by nonlinear flow equations, but the nonlinear flow features typically require that viscous effects be included in the flow field analysis for accurate design and analysis work. Hypersonic vehicles with bow shocks necessarily have a region of subsonic flow behind the shock, so there is an element of transonic flow on those vehicles too.

In the days of propeller airplanes, the transonic flow limitations on the propeller mostly kept airplanes from flying fast enough to encounter transonic flow over the rest of the airplane. Since the propeller was moving much faster than the airplane, adverse transonic aerodynamic problems appeared on the propeller first, limiting the speed and thus transonic flow problems over the rest of the aircraft. However, WWII fighters could reach transonic speeds during dives, and major problems often arose. One notable example was the Lockheed P-38 Lightning. Transonic effects prevented the airplane from readily recovering from dives, and during one flight test, Lockheed test pilot Ralph Virden had a fatal accident. The pitching moment changing with the Mach number (Mach tuck) and Mach-induced changes in control effectiveness were major culprits identified in a paper by Foss.[1] This paper also contains the estimated drag rise characteristics of the P-38.

The invention of the jet engine allowed aircraft to fly at much higher speeds. Recall that the Germans used the Me 262 at the end of WWII in 1944, and the Gloster Meteor was apparently the first operational jet fighter. Since the advent of the jet engine, virtually all commercial transports now cruise in the transonic speed range. However, as the Mach number increases, shock waves appear in the flow field, getting stronger as the speed increases. The shock waves lead to a rapid increase in drag, both due to the emergence of wave drag and also because the pressure rise from a shock wave thickens the boundary layer, leading to increased viscous drag. Thus cruise speed is limited by the rapid drag rise. To pick the value of the Mach number associated with the rapid increase in drag, we need to define the drag divergence Mach number, M_{DD}. Several definitions are available. The one used here is the Mach number at which $dC_D/dM = 0.10$. Review section 3.5.4 for more.

After WWII, it was found that the Germans were studying swept wings to delay the drag rise Mach number. Allied examination of German research led to both the North American F-86 and the Boeing B-47 designs being changed to swept-wing configurations. The idea of swept wings can be traced to Busemann's paper at the fifth Volta Congress held in Rome, Italy, in 1935 on the topic of high velocities in aviation and to the wartime ideas of R. T. Jones at NACA. Ironically, the airplane used for the first manned supersonic flight (the X-1, in 1947) did not use a jet engine or wing sweep. It was a rocket-powered straight-wing airplane. However, shortly thereafter, the F-86, a swept-wing jet-powered fighter, went supersonic in a shallow dive.

Thus, advances in one technology, propulsion, had a major impact on another, aerodynamics, illustrating the need to carefully integrate various technologies to achieve the best total system performance. The formal process of performing this integration has become known as multidisciplinary design optimization (MDO).

6.1 Physical Aspects of Flowfield Development With Mach Number

Figure 6-1, taken from the classic training manual, *Aerodynamics for Naval Aviators*,[2] shows how the flow develops with increasing Mach number, starting from subsonic speeds. At some freestream Mach number, the local flow becomes sonic at a single point on the upper sur-

face where the flow reaches its highest local speed; this is known as the critical Mach number. As the freestream Mach number increases further, a region of supersonic flow develops. Normally the flow is brought back to subsonic speed by the occurrence of a shock wave in the flow. Although it is possible to design an airfoil to have a shock-free recompression, this situation is usually possible for only a single combination of Mach number and lift coefficient, with shock waves appearing if one deviates from this shock-free design condition. As the Mach number increases, the shock moves aft and becomes stronger. As the Mach number continues to increase, a supersonic region and shock wave also develop on the lower surface. As the Mach number approaches one, the shocks move all the way to the trailing edge. Finally, when the Mach number becomes slightly greater than one, a bow wave appears just ahead of the airfoil and the shocks at the trailing edge become oblique. These shock waves are the basis for the sonic boom. Many variations in the specific details of the flow field development are possible, depending on the specific geometry of the airfoil.

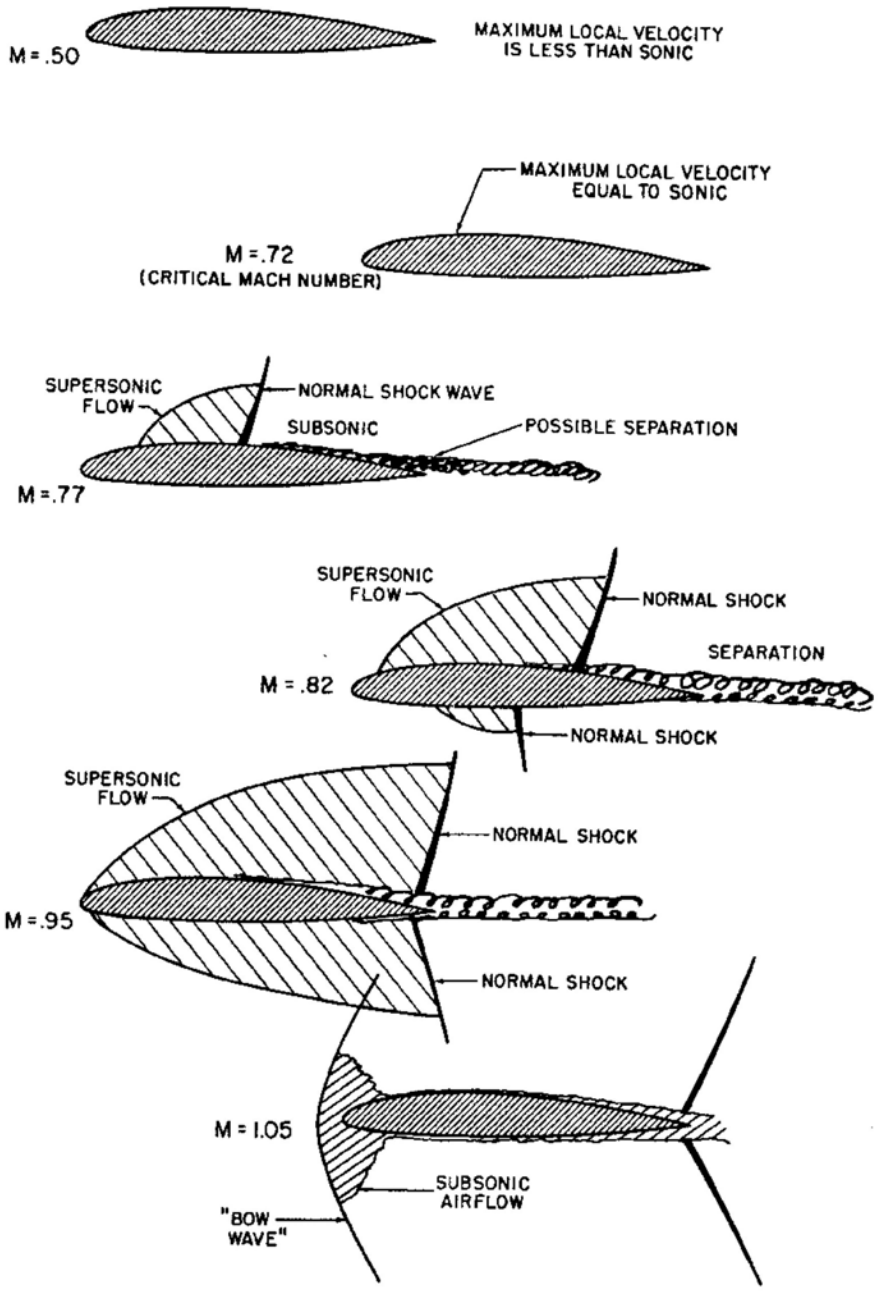


Figure 6-1: Progression of shock waves with increasing Mach number. *From H. H. Hurt, Jr. US Navy. Public domain.*

This typical progression of the flow pattern with increasing Mach number, shown in figure 6-1, leads to rapid variations in drag, lift, and pitching moment with change in Mach number. Today we can predict these variations computationally. However, when these changes were initially found in flight, they were dangerous and appeared mysterious to designers because there was little to no understanding of the fluid mechanics of the phenomena.

Note that problems with pitching moment variation with Mach number and the flow field over a control surface using a hinged deflection led to the introduction of the all-flying tail in the X-1 and later models of the F-86. Subsequently, all-flying tails became standard on most supersonic tactical aircraft. This was considered an important military advantage, and was classified for several years. Based on military experience, Lockheed used an all-flying tail on the L-1011, while the other transport manufacturers continued to use a horizontal tail and elevator.

6.2 Technology Issues and Developments

6.2.1 The Slotted-Wall Wind Tunnel

Several advances in technology were key to our ability to design efficient transonic aircraft. Wind tunnel testing posed several problems, including the reflection of shocks from the tunnel walls and the tendency of the flow to choke as it passed the model. As a result, wind tunnel results were completely wrong. The invention of the slotted-wall wind tunnel at NACA Langley in the late 1940s allowed the tunnel interference effects to be significantly reduced, leading to practical wind tunnel testing methods. A chapter in Becker's book[3] describes how this capability was achieved. It's a must read to get insight into the aerodynamic research and development process, as well as to get a physical understanding of how airfoils work and how the slotted-wall tunnel evolved. The slots are clearly shown in figure 6-2.

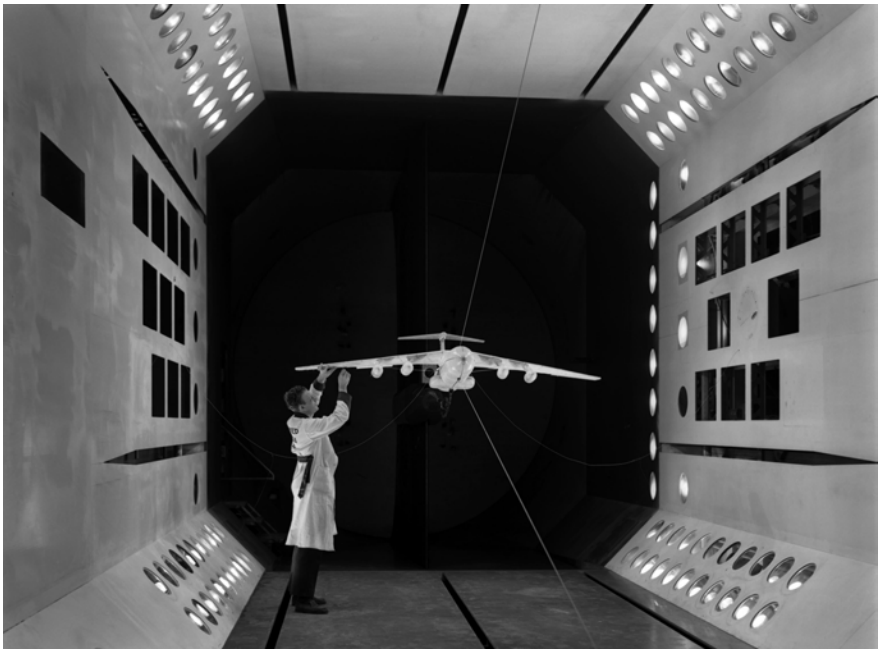


Figure 6-2: NASA Langley Research Center 16-foot Transonic Dynamics Tunnel (TDT) with slotted walls. From NASA. Wikimedia. Public domain.

Using the eight-foot slotted-wall wind tunnel at NASA Langley, Whitcomb, who had earlier developed the area rule, made a breakthrough in airfoil design. His supercritical airfoil designs spurred renewed interest in airfoil design for increased efficiency at transonic speeds.[4] His group also had to figure out how to simulate the full-scale Reynolds number at sub-scale conditions, as discussed by Blackwell,[5] who worked for Whitcomb at NASA before going to work for Lockheed. Finally, in the early 1970s, breakthroughs in computational methods produced the first transonic airfoil analysis codes, which are described briefly in the next section.

6.2.2 Computational Challenges and Methods

The theoretical/computational transonic flow problem was very hard. Initially, very few analytic or numerical methods were available. By 1970, it seemed like everybody was trying to come up with a method to compute the transonic flow over an airfoil. What was known as the "blunt-body problem" had just been conquered (see Chapter 10), which was important in predicting the flow field at the nose of reentering ballistic missiles and the manned space program. The transonic problem is difficult because it is inherently nonlinear, and the steady flow assumption changes the mathematical type of the equation, being elliptic in the subsonic portion of the flow and hyperbolic in the supersonic part of the flow. Earll Murman and Julian Cole made the major breakthrough.[6] Using transonic small-disturbance theory, they came up with a scheme that could be used to develop a practical computational method. Equation 6-1 illustrates how the nonlinear term in the equation allows for the equation to change type and indeed provides a way for the type to be found locally in a computational scheme.

$$\underbrace{\left[1 - M_\infty^2 - (\gamma + 1) M_\infty^2 \phi_x\right]}_{\substack{>0 \text{ elliptic PDE} \\ <0 \text{ hyperbolic PDE}}} \phi_{xx} + \phi_{yy} = 0 \qquad (6\text{-}1)$$

In Murman and Cole's scheme, shocks emerged naturally during the numerical solution of the equation. Essentially, they used finite-difference approximations for the partial derivatives in the transonic small-disturbance equation. The key to making the scheme work was to test the flow at each point to see if the flow was subsonic or supersonic. If it was subsonic, a central difference was used for the second derivative in the *x*-direction. If the flow was supersonic, they used an upwind difference to approximate this derivative. This allowed the numerical method to mimic the physical behavior of the flow field. The nonlinear coefficient of the ϕ_{xx} term in equation (6-1) includes a first derivative of potential, ϕ_x. A central difference approximation can be used for this term. Since the solution is found by iteration, old values can be used for ϕ_x. Their approach became known as "mixed differencing," and it was a simple way to capture the physics of the mixed elliptic-hyperbolic type of the partial differential equation. Because shocks emerge during the solution process, the method is referred to as a "shock-capturing" method. It was much simpler for a general 3D method than competing methods at the time, in which shocks were located and the Rankine–Hugoniot conditions were satisfied analytically (called a "shock-fitting" method). Although several theoretical refinements were required, Murman and Cole's scheme paved the way for today's computational methods. Hall[7] has described the circumstances under which this breakthrough took place. The code known as TSFOIL was the final development of small-disturbance theory methods for 2D.[8] See section E.7.5 for pertinent software for such methods.

After hearing Earll Murman describe his new method at the AIAA Aerospace Sciences Meeting in New York City in January 1970, Antony Jameson, at the time working for Grumman, returned to Bethpage on Long Island, coded up the method himself, and then went on to extend the approach to solve the full-potential equation in body-fitted coordinates. This required several additional major contributions to the theory.[9] The code he developed was known as FLO 6 and, after several more major methodology developments, resulted in the extremely efficient 2D full-potential flow code known as FLO 36.[10] These were the first truly accurate and useful transonic airfoil analysis codes. Holst has published a survey of full-potential methods.[11]

The next logical development was to add viscous effects to the inviscid calculations and then to switch to the Euler equations for the outer inviscid flow. By that point, many researchers were working on computational flow methodology, which had become an entire field known as CFD. An entrance to the literature on computational methodology is available in the survey article by Jameson.[12] The Euler solution method used here is from a code known as MSES by Prof. Mark Drela of MIT.[13]

Figure 6-3 provides a comparison of the predictions for the transonic flow over an NACA 0012 airfoil at $M = 0.75$ and 2° angle of attack for three inviscid flow models (TSFOIL2, FLO 36, and MSES). In general, the results are in good agreement. However, the full-potential solution (FLO 36) predicts a shock that is too strong and too far aft. The solution based on small-disturbance theory (TSFOIL2) is in close agreement with the full-potential solution, while the Euler equation model (MSES), which is the most accurate of these flow models, has a weaker shock located further forward on the airfoil compared to the other two methods. This occurs for two reasons. First, the potential

flow model does not contain the correct shock jump. Second, there is no loss in stagnation pressure across the shock in the potential flow models, making them insensitive to the "back pressure" downstream, to borrow terminology from nozzle flows.

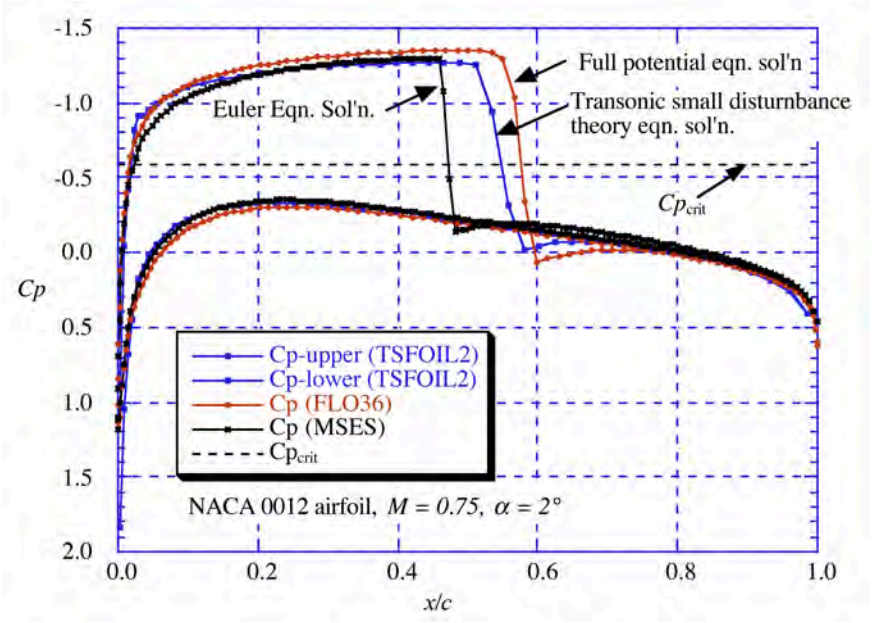


Figure 6-3: Comparison of pressure distributions on an NACA 0012 airfoil at M = 0.75 and α = 2° using three different computational methods, small-disturbance theory (TSFOIL2), full-potential equation (FLO36), and Euler equations (MSES)

Several key points need to be made while examining figure 6-3. First, the solutions for transonic flow are found from iterative solutions of a system of nonlinear algebraic equations. This is much more difficult than the subsonic case, where the equations for panel methods are linear. The codes require much more care in their operation to obtain good results. Students often ask for solutions for flow cases that are too difficult to solve. You can't ask for a solution at $M = 0.95$ and 10° angle of attack and expect to get a result from most codes. Students should start with known cases that work and try to progress slowly to the more difficult cases. Another key point to consider is that the shock is typically smeared over several grid points in the numerical solution. The actual solution point symbols have been included in the plots in figure 6-3 to illustrate this. Finally, the region where the flow is locally supersonic can be observed by comparing the local value of the pressure coefficient to the critical value, shown on the figure as a dashed line labeled $C_{p\text{crit}}$. If the pressure coefficient at a point on the airfoil is lower (more negative) than the critical value at that point, the flow is supersonic at that point. The critical value is the point on the airfoil where, assuming isentropic flow, the value of the pressure corresponds to a local Mach number of one. The derivation of $C_{p\text{crit}}$ is given in any good basic compressible flow textbook, and the formula is

$$C_{p_{\text{crit}}} = -\frac{2}{\gamma M_\infty^2}\left[1 - \left(\frac{2}{\gamma+1} + \frac{\gamma-1}{\gamma+1}M_\infty^2\right)^{\frac{\gamma}{\gamma-1}}\right]. \qquad (6\text{-}2)$$

Dedicated airfoil pressure distribution plotting packages usually include a tick mark on the C_p scale to indicate the critical value.

Next, we show the full-potential equation solutions using FLO 36 to illustrate the development of the flow with increasing Mach number for the same NACA 0012 airfoil used in figure 6-3. Figure 6-4 shows how the pressure distribution changes from subcritical to supercritical as Mach number increases from 0.5 to 0.75. At $M = 0.50$, the flow expands around the leading edge and then starts to slow down. This is the typical subsonic flow behavior. At $M = 0.70$, the flow continues to expand after going around the leading edge, and it returns to subsonic speed through a shock wave, which is fairly weak. As the freestream Mach number increases further, the shock moves aft rapidly, becoming much stronger. In this case, we are looking at inviscid solutions, and this strong shock would likely separate the boundary layer, requiring the inclusion of viscous effects to get a solution that accurately models the real flow.

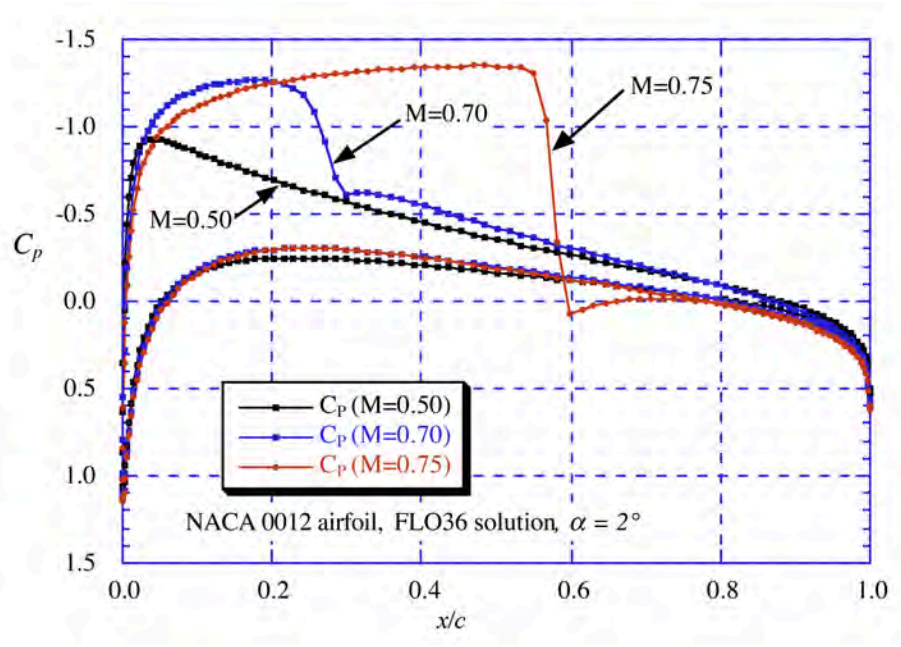


Figure 6-4: Pressure distribution change with increasing Mach number for NACA 0012 airfoil, $\alpha = 2°$.

Figure 6-5 shows the effect of changing angle of attack from 0° to 2° on the pressure distribution using the NACA 0012 airfoil, the same one used in figures 6-3 and 6-4. The results are similar to what occurs when the Mach number increases. The solution changes rapidly with relatively small changes in angle of attack. The shock wave develops fast, with the strength increasing and the position moving aft rapidly.

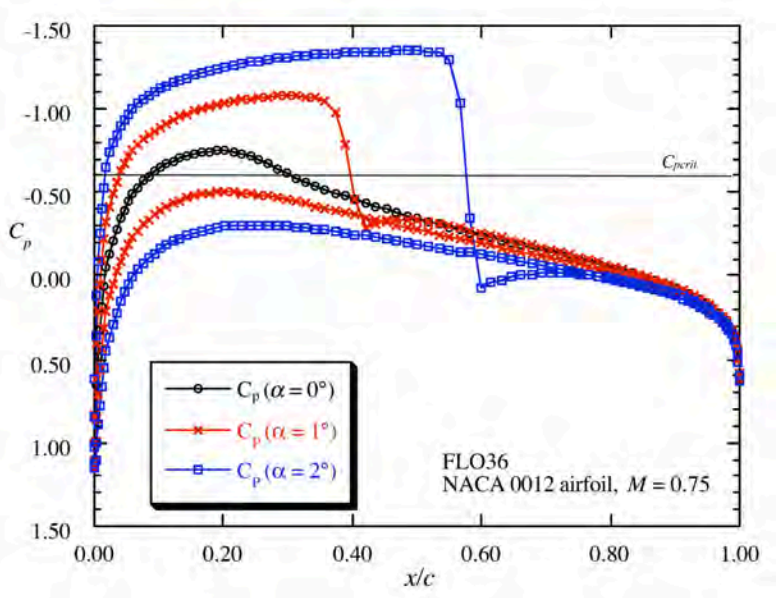


Figure 6-5: Change in pressure distribution with change in angle of attack, NACA 0012 airfoil, M = 0.75.

6.3 Airfoils

6.3.1 NASA Supercritical Airfoils

As mentioned in section 6.2.1, in the late 1960s, Richard Whitcomb developed airfoils at NASA Langley that had significantly better transonic performance than previous airfoils. It was found that airfoils could be designed to have a drag rise Mach number much higher than previously obtained. To illustrate how this occurs, we will compare the typical transonic airfoils in use at the time, the NACA 6A-series foils, with one of the NASA supercritical airfoils. The differences in the solutions clearly illustrate the merits and drawbacks of the modern approach to transonic airfoil design.

Figure 6-6 contains a plot of the NACA 64A410 airfoil and its transonic pressure distribution at a Mach number of 0.72 and an angle of attack of 0°. The computed lift coefficient is 0.665.

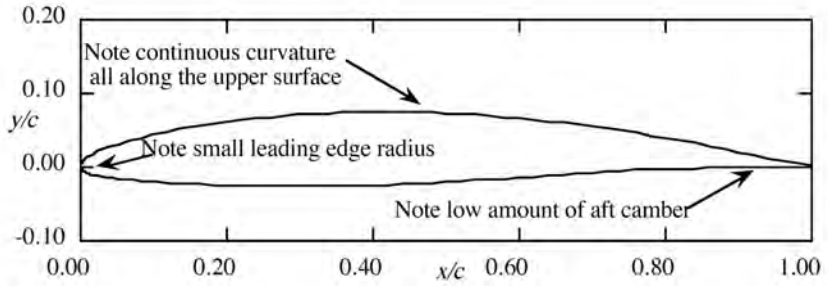


Figure 6-6(a): NACA 64A410 airfoil shape.

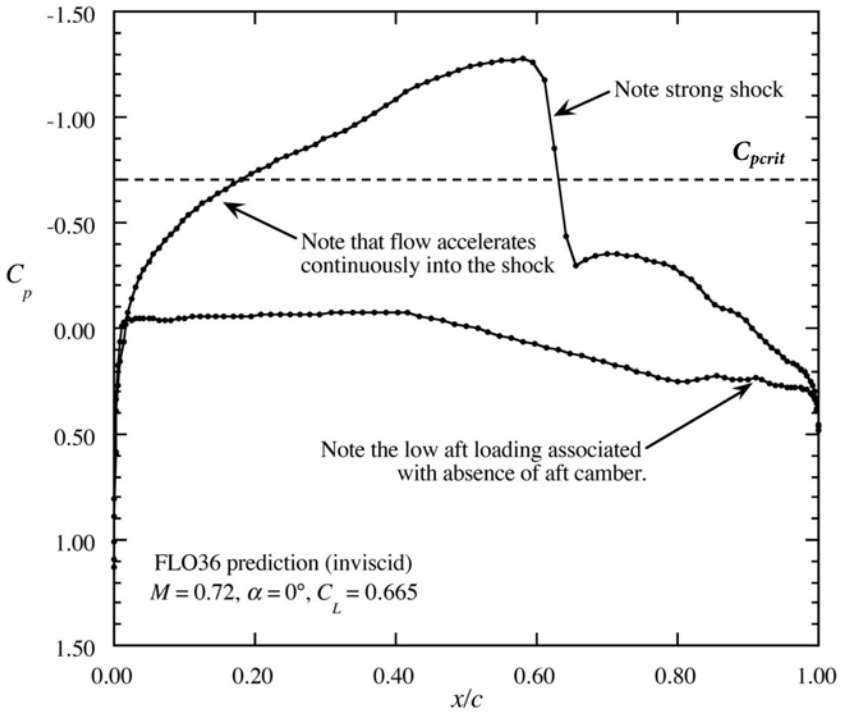


Figure 6-6(b): NACA 64A410 surface pressure distribution at transonic speed.

Figure 6-7 contains similar data for a NASA supercritical airfoil, Foil 31, at a Mach number of 0.73 and an angle of attack of 0°. The computed lift coefficient is 1.04. The "jagged" pressure distribution in figure 6-7(b) is the result of the airfoil being defined by a set of discrete points which do not produce a smooth surface rather than the result of an analytical function which produces smooth surface.

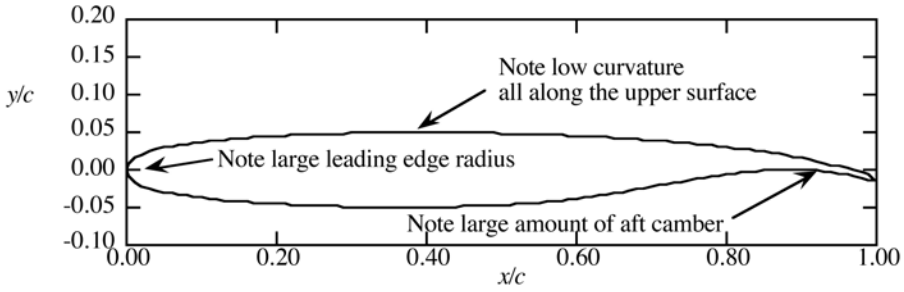


Figure 6-7(a): FOIL 31 supercritical airfoil shape.

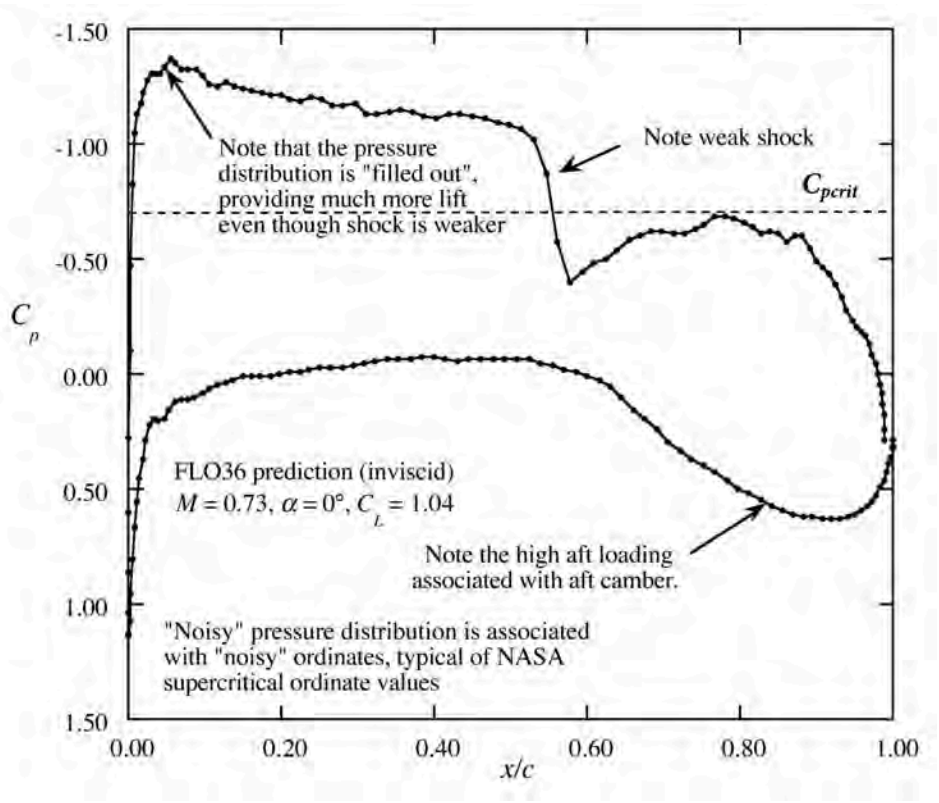


Figure 6-7(b): FOIL 31 supercritical airfoil surface pressure distribution at transonic speed.

It can be seen that the shock wave on the supercritical airfoil is much weaker than the shock on the 64A410, even though the lift is significantly higher. This illustrates the advances made in airfoil design. Although the 6A-series airfoils were widely used in transonic and supersonic applications, they were actually designed during and just after WWII to attain laminar boundary layer flow over a portion of the airfoil. They were not designed for good transonic performance (no one knew how to do this at that time). The history and development of supercritical airfoils has been described by Harris[14] using the written version of a talk given by Whitcomb and Harris at the NASA Langley Advanced Technology Airfoil Research Conference in March 1978. Most of the conference papers appeared in NASA CP-2046 in January 1979. However, publication of the Harris paper was delayed until 1990! The NASA TP-2969 by Harris explains the reasoning behind the concept development and the refinement in design. This is a must-read paper which also contains the coordinates for the entire family of airfoils and updates the research to 1990. In addition to this paper, we recommend two papers for readers to get the authentic description

of the development of supercritical airfoils. The first is by Becker,[15] and the other, by Whitcomb, is his first unclassified public release paper on the new airfoil concept presented in 1974.[16] We give a very brief overview of the transonic supercritical airfoils here next.

Essentially, the key to transonic airfoil design is to control the expansion of the flow to supersonic speed and its subsequent recompression. It was remarkable that Whitcomb was able to do this using an experimental approach. Because his test-based approach was so difficult, he was a major proponent of developing computational methods for transonic airfoil design.

The following are four key elements of supercritical airfoils:

i. A relatively large leading-edge radius is used to expand the flow at the upper surface leading edge, thus obtaining more lift than obtained on airfoils like the 64A410 shown in figure 6-6.
ii. To maintain the supersonic flow along a constant pressure plateau or to even have it slow down slightly approaching the shock, the upper surface is much flatter than previous airfoils. By slowing the flow going into the shock, a relatively weak shock (compared to the amount of lift generated) is used to bring the flow down to subsonic speed.
iii. Another means of obtaining lift without strong shocks at transonic speed is to use aft camber. Note the amount of lift generated on the lower surface aft portion of the supercritical airfoil in figure 6-7(b) compared to the conventional airfoil in figure 6-6(b). One potential drawback to the use of aft camber is the large zero-lift pitching moment.
iv. Finally, to avoid flow separation, the upper and lower surfaces at the trailing edge are nearly parallel, resulting in a finite-thickness trailing edge. The base drag is small at transonic speeds compared to the reduction in profile drag.

These are the essential ingredients in supercritical airfoil design, and modern aerodynamic designers pick the best aspect of these elements to fit their particular applications.

Whitcomb cited four design guidelines for airfoil development:

1. An off-design criterion is to have a well behaved sonic plateau at a Mach number that is 0.025 below the design Mach number.
2. The gradient of the aft pressure recovery should be gradual enough to avoid separation. This may mean a thick trailing-edge airfoil, typically 0.7% thick on a 10-percent- or 11-percent-thick airfoil.
3. The aft camber should ensure that, with $\alpha_{des} \cong 0$, the upper surface is not sloped aft.
4. Gradually decreasing supercritical velocity will result in a weak shock.

Aerodynamicists in the industry have also made significant contributions to transonic aerodynamic design. The best summary of transonic design for transport aircraft is by Lynch.[17] Figure 6-8 contains a summary chart developed by Lynch to identify the issues associated with leading-edge radius and aft camber.

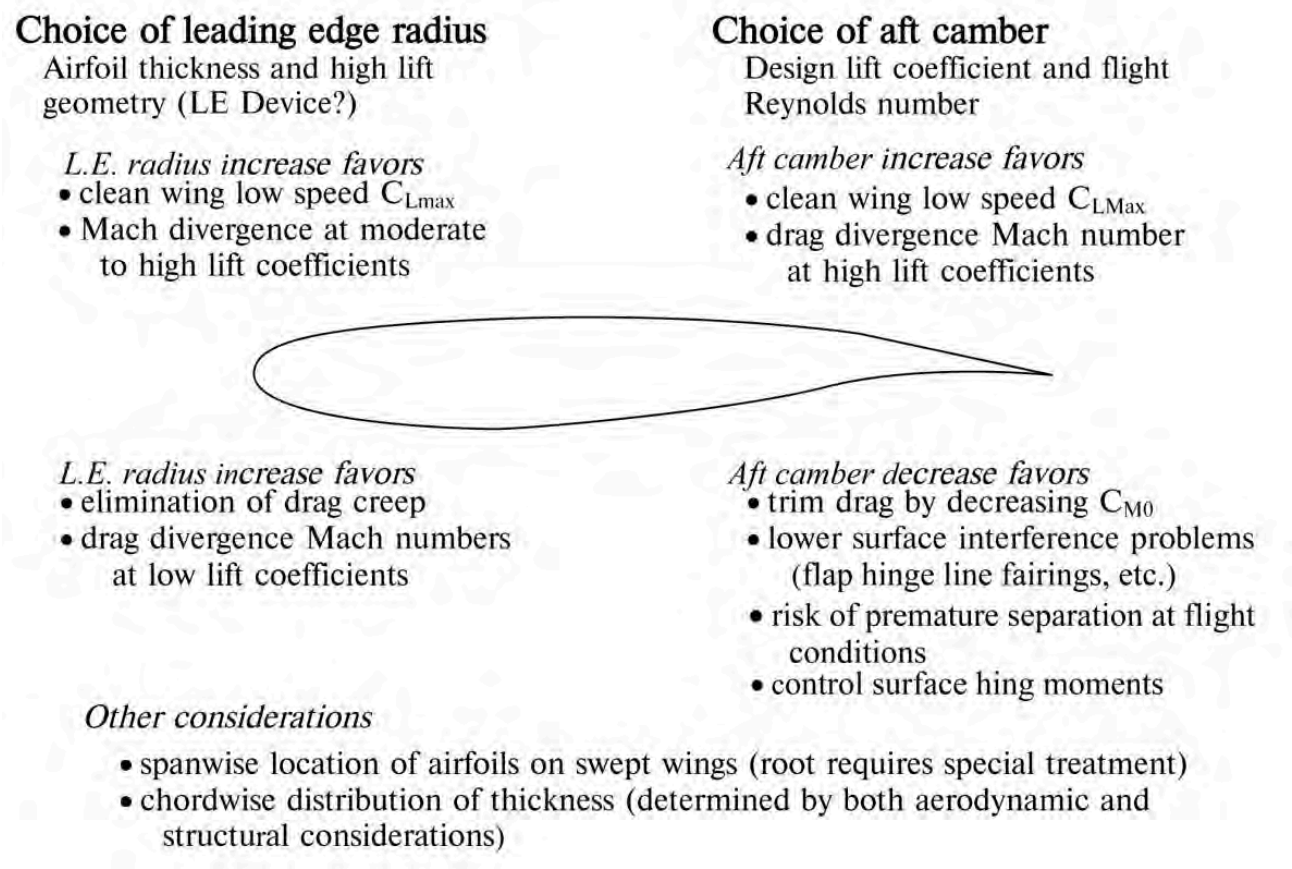


Figure 6-8: Some supercritical airfoil design considerations for leading-edge radius and aft camber. *From F. Lynch. "Commercial Transports—Aerodynamic Design for Cruise Efficiency." Adapted. Fair use.*

6.3.2 The Divergent Trailing-Edge Airfoil

Just when supercritical airfoil development appeared to be completed, a further development in airfoil design was made: the divergent trailing-edge (DTE) airfoil. Henne and Gregg [18] at McDonnell Douglas made further improvements in airfoil performance by using a trailing edge where the upper and lower surfaces are not just parallel to each other but diverging. Their paper takes airfoil design concepts one step further, describing the development and benefits of the DTE airfoil, which was discovered by the use of then-current computational aerodynamics methods.* Although the DTE concept is related to a simple triangular wedge that was added to the MD-11 outboard wing trailing edge for improved performance, the DTE airfoil is much more effective.

*Although I was told this concept was used on the C-17, a close examination of the trailing-edge flaps manufactured at Marion Composites during an Aerospace Manufacturing Class tour showed that this airfoil isn't on the plane. Email from Preston Henne confirmed this when he read an earlier version of these notes. According to Robb Gregg, the co-inventor of the DTE airfoil concept, the C-17 wing design was already completed before DTE concept was validated.

6.3.3 Transonic Airfoil Performance: The Korn Equation

Note: The material in this section has a lot of commonality with that in section 3.5.4. However, it is included here for the sake of completeness. Furthermore, the focus here is on the application of airfoil performance information for aircraft design.

Attempts have been made to estimate the capability of transonic airfoils for the purposes of design studies without performing wind tunnel tests or detailed computational design work. This is important in the initial stages of aircraft design, where airfoil performance needs to be estimated before the actual airfoil design has been done. Here we provide an approximate method for estimating the transonic performance of airfoils. It is based on the Korn equation, which was an empirical relation developed by Dave Korn at the NYU Courant Institute in the early 1970s and that was in use at Grumman when I arrived in 1974. Based on his experience, it appeared that airfoils could be designed for a variety of Mach numbers, thickness-to-chord ratios, and design lift coefficients, but in all cases, there seemed to be a limit to the combination of three parameters: drag divergence Mach number (M_{dd}), thickness-to-chord ratio (t/c), and lift coefficient (C_l). The limit is an airfoil technology factor, κ_A, and the Korn equation defines the relationship between the combination of these three parameters and the airfoil technology factor as follows:

$$M_{\mathrm{dd}} + \frac{C_l}{10} + \left(\frac{t}{c}\right) = \kappa_A \qquad (6\text{-}3)$$

The airfoil technology factor on the right-hand side has a value of 0.87 for an NACA 6-series airfoil section and a value of 0.95 for a supercritical section. This relation provides a simple means of estimating the possible combination of Mach number, lift coefficient, and thickness ratio that can be obtained using modern airfoil design, and variations of it have been shown graphically by many authors, where the scales are often left off when presented for the public by aircraft companies. Note that the Korn equation is sensitive to the value of the technology factor.

Figure 6-9, from Mason,[19] compares the prediction from the Korn equation with other estimates. In figure 6-9(a), the estimates of older airfoils and Shevell's estimates of modern supercritical airfoil performance[20] are compared, and the agreement is good, with the exception of being overly pessimistic regarding older conventional airfoils at lower thickness ratios. Figure 6-9(b) compares the Korn equation with NASA projections[21] for supercritical airfoils based on a wealth of data and experience. In this case, the Korn equation is extremely good at lift coefficients of 0.4 and 0.7 but overly optimistic at higher lift coefficients. This type of technology representation is important in developing integrated designs. Developing each point on this type of charge requires a large effort on the part of the designer (in this case, the aerodynamicist).

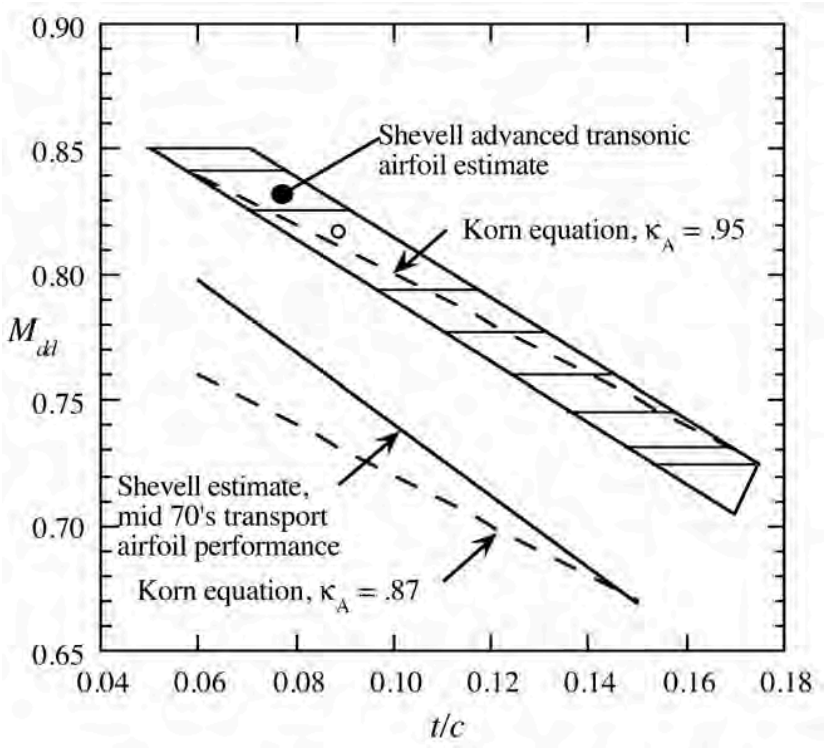


Figure 6-9(a): Comparison of the Korn equation with Shevell's estimates. *From W. H. Mason. "Analytic Models for Technology Integration in Aircraft Design." Reprinted by permission of the American Institute of Aeronautics and Astronautics, Inc.*

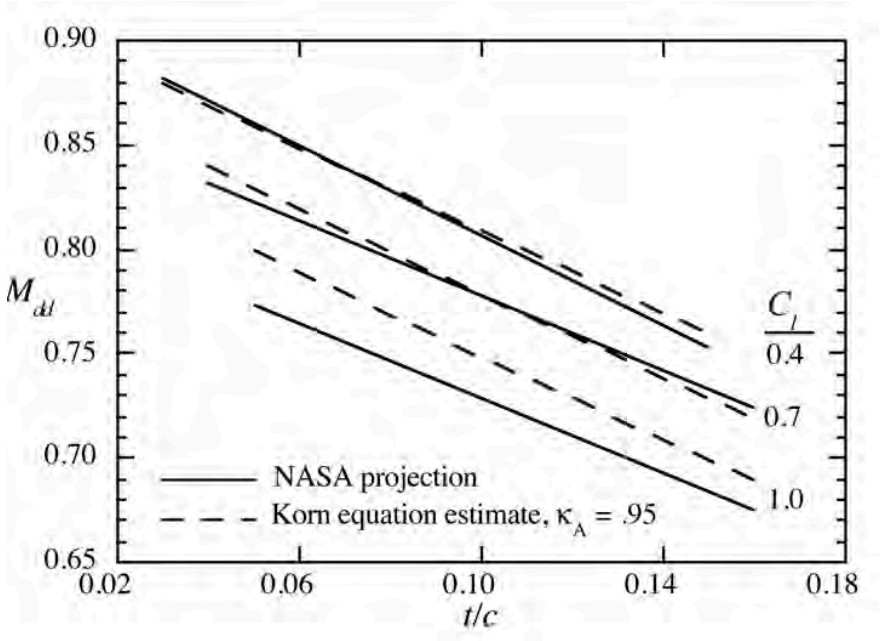


Figure 6-9(b): Comparison of the Korn equation with NASA projections. *From W. H. Mason, "Analytic Models for Technology Integration in Aircraft Design." Reprinted by permission of the American Institute of Aeronautics and Astronautics, Inc.*

The extension of this method to swept wings using simple sweep theory and an approximate drag rise curve shape will be given in the section on wings below.

6.3.4 Design Methods

We gave some general approaches and guidelines for airfoil design for transonic flow above when describing Whitcomb's supercritical airfoils. Although there are details beyond the scope (as they say!) of this chapter, we should point out that there are two distinct approaches available for airfoil design. Aerodynamicists frequently use inverse methods, where a target pressure distribution is specified and the required shape (which might not exist for an arbitrary pressure distribution prescription) is found. Alternatively, optimization methods may be used, where the shape is described by a set of design variables that are then used in an optimization routine, which can be computationally expensive. In addition, many optimization methods require gradients of the solution with respect to the design variables, and modern computational fluid dynamics methods have been developed to obtain the design's sensitivity to geometric and flow perturbations as part of the solution. Finally, at transonic speed, we need to avoid undo sensitivity to the specified design conditions. This requires a statistical design approach. An important advance in this area has been made by Huyse.[22]

6.4 Wings

We now turn our attention to wings. Today, at transonic speeds, wings are swept to delay drag rise. However, even though the Boeing B-47 had a swept wing, they weren't adopted across the board immediately, even at Boeing. Initially, jet engines had poor fuel efficiency and weren't considered appropriate for very long-range aircraft. In one famous instance, Boeing was working on a long-range turboprop bomber for the Air Force. When the Boeing team started to present their design to the Air Force at Wright-Patterson Air Force Base (WPAFB) in Dayton, Ohio, they were immediately told to switch to a swept-wing pure jet design. The team didn't have time to return to Seattle, so they recruited other Boeing engineers already in Dayton and did the work there (with the help of phone calls back to Seattle). To show the Air Force the design, they made a model. Figure 6-10 shows the actual model on display at the Museum of Flight in Seattle. This design became the B-52. It is famous for having been designed in a Dayton, Ohio, hotel room!



Figure 6-10(a): Model of the B-52, as carved by George Schairer, Boeing aerodynamicist, in the Van Cleve Hotel in Dayton in October 1948. *From K. Bean. The Museum of Flight. CC BY-NC-SA 4.0. Model courtesy of the Boeing Historical Archives.*



Figure 6-10(b): Model of the B-52, as carved by George Schairer, Boeing aerodynamicist, in the Van Cleve Hotel in Dayton in October 1948. *From K. Bean. The Museum of Flight. CC BY-NC-SA 4.0. Model courtesy of the Boeing Historical Archives.*

Although swept wings delay drag rise, they are still associated with some problems, so that the aerodynamicist will want to use as little sweep as possible. Even at subsonic speed, as shown in the previous chapter, wing sweep will tend to shift the load outboard, leading to high section lift coefficients and the possibility of outboard stall, accompanied by pitchup. The wing is twisted (washed out) to unload the tip. The lift-curve slope also decreases. In addition, for a given span, the actual wing length is longer and therefore heavier. Another problem is that high-lift devices aren't as effective if the trailing edge is swept. Finally, swept wings are prone to flutter. Thus, the total system design must be considered when selecting the wing sweep. One of the benefits of advanced airfoils is that they can achieve the same performance as a wing with a less-capable airfoil using less sweep. This explains the general trend to modern transports having less sweep than earlier transports.

6.4.1 Transonic Transport Wing Concepts

The transonic transport wings are generally high aspect ratio, swept, tapered wings that clearly have an airfoil embedded in them. Generally we consider aft-swept wings.

Cruise design. Normally, the aerodynamic designer is given the planform and maximum thickness and told to design the twist and camber, as well as shifting the thickness envelope slightly. He or she then tries to obtain "good" isobars on the wing. Since the natural tendency is for the flow to unsweep at the root and tip, the designer tries to reduce this tendency to obtain an effective aerodynamic sweep as large as the geometric sweep. If possible, they would actually like to make the effective aerodynamic sweep greater than the geometric sweep. This is unlikely to happen. Generally, the wing has a weak shock wave. Possibly the best tutorial paper on the problem of isobar unsweep is by Haines,[23] who actually considers the thickness effects at zero lift. This is an old but important paper that explains how root and tip modifications are made to make the isobars swept on a swept wing.

We illustrate the problem of isobar unsweep with an example taken from work at Grumman to design the initial G-III wing (though the G-III doesn't actually have this wing, as it was considered too expensive; the actual G-III has a highly modified version of the G-II wing). Figure 6-11 from a paper by Mason et al.[24] illustrates the situation.

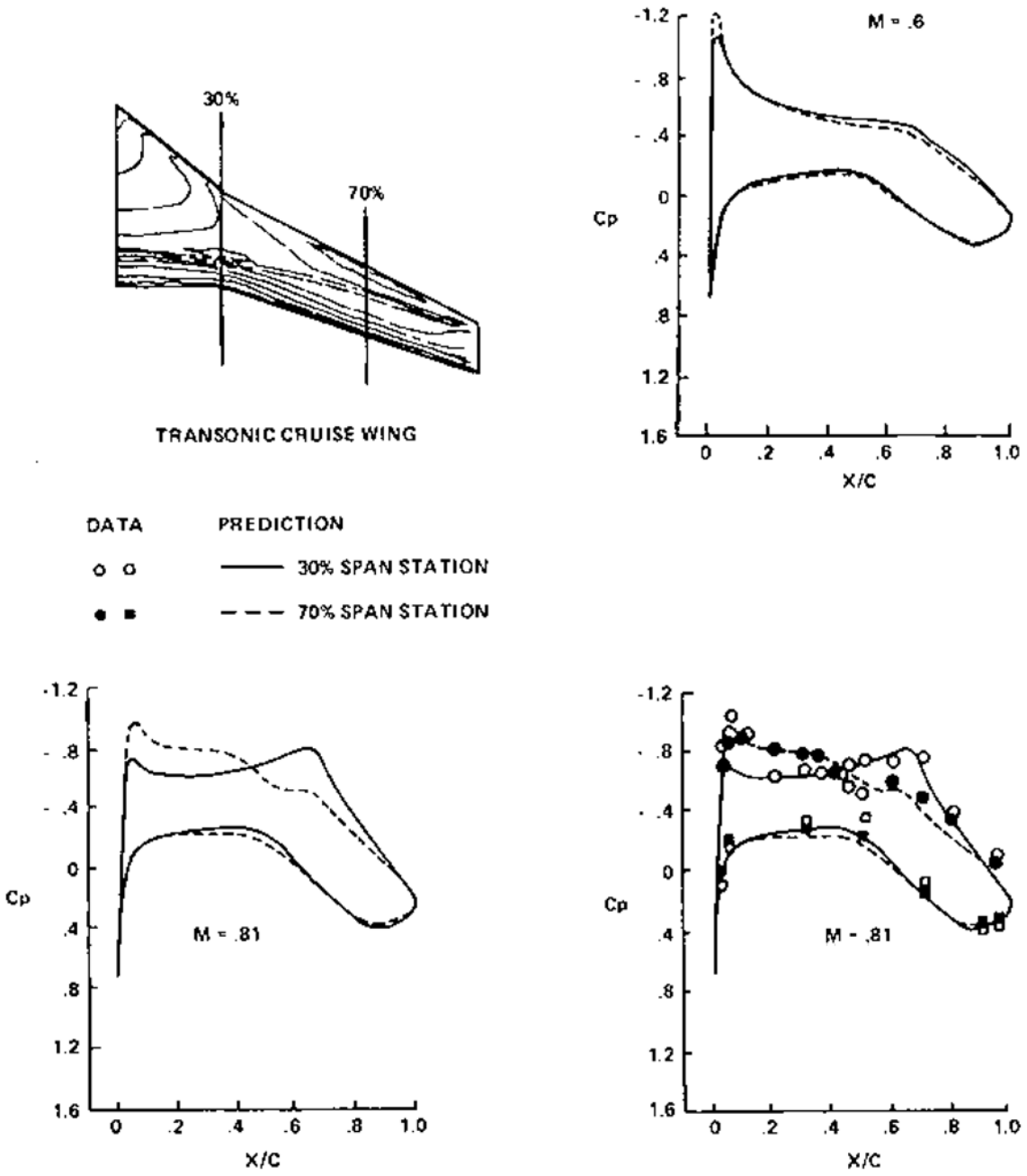


Figure 6-11: Explicit transonic three-dimensional effects. *From W. H., MacKenzie, D. A., Stern, M. A., and Johnson, J. K. "A Numerical Three Dimensional Viscous Transonic Wing-Body Analysis and Design Tool." Copyright undetermined by AIAA. Fair use. (Note: Best-available image quality.)*

In figure 6-11, we see the isobar pattern at transonic speed on the planform in the upper left-hand side of the figure. This wing was designed with subsonic methods, which were essentially all that was available at the time. Note that the isobars are tending to unsweep. On the upper right-hand side of the figure, we see that at subsonic speed the pressure distributions at the 30% and 70% span stations lie on top of each other, the isobars are good. The lower left-hand side of the figure shows the predicted pressure distributions at these same two stations when the Mach number is increased to the transonic cruise Mach. There has been a large change in the distributions at the two stations, with the outboard shock ahead of the inboard shock. Finally, on the lower right-hand side, we see the same predictions but with wind tunnel data included. Clearly, the prediction and the test results agree well and show that extra effort is required to design the wing when the flow is transonic.

Although the aerodynamicist generally prefers an elliptic spanload for a given span, it might be better for the design if the load is shifted inboard slightly, reducing the root bending moment and therefore wing structural weight.[25] The optimum spanload with a winglet present is not elliptic either.

Essentially, the twist distribution is found to generate the design spanload. Spanloads are predicted fairly well using linear theory codes; it is primarily the chord load that reflects the nonlinearity of transonic flow. Once the basic twist is found, root and tip mods are developed to maintain the isobar pattern. Without special effort, the chord load is drawn aft at the root and shifts forward at the tip. Changes in camber and thickness are introduced to counter these effects. The planform may deviate from pure trapezoidal. In all likelihood, there will be a Yehudi (see Chapter 5) at the inboard trailing edge to house the landing gear. The planform in figure 6-11 also has a leading-edge glove inboard. This allows the t/c to be lower for the same t, and increasing the chord lowers the section C_l required to obtain the spanload required, as well as helping maintain isobar sweep. Breaks in the planform chord distribution produce rapid variations in the section lift distribution because the spanload will tend to remain smooth. The section lift distribution may be smoothed out by using several smaller spanwise breaks. This has been used in modern Boeing and Airbus designs.

The designer also has to consider buffet margins. This means the wing C_L has to be capable of a 1.3 g turn at the highest cruise Mach number without predicting any significant flow separation. The relevant considerations are presented in section 6.4.4.

Other important details include nacelle/pylon interference and the resulting detailed shaping, as well as manufacturing constraints. This means considering the limits to curvature and the manufacturing department's desire for straight-line wrap or ruled surfaces.

Once the design starts to get close to the desired properties, local inverse methods can be applied to achieve the target pressure distributions.

Transonic configuration design. Finally, a review of the design process by Jameson is worth reading to get some idea of the design process and possibilities of improving it through the use of computations.[26] This paper contains a good description of the transport wing design problem. Jameson clearly articulates the process for the nonexpert wing designer, something the company experts haven't done often (possibly because they consider the process to be competition sensitive).

6.4.2 The Korn Equation Applied to Drag Prediction on Swept Wings

Note: The material in this section has a lot of commonality with that in section 3.5.4. However, it is included here for the sake of completeness. Also, the focus here is on the application of transonic drag prediction methodology to aircraft design.

As described in section 3.5.4, the Korn equation has been extended to estimate the drag divergence Mach number for a 3D swept wing by including sweep using simple sweep theory.[27,28] The result for a 3D wing is given by

$$M_{DD} = \frac{\kappa_A}{\cos\Lambda} - \frac{(t/c)}{\cos^2\Lambda} - \frac{C_L}{10\cos^3\Lambda}. \qquad (6\text{-}4)$$

This model estimates the drag divergence Mach number, M_{DD}, as a function of an airfoil technology factor (κ_A), the thickness-to-chord ratio (t/c), the lift coefficient (C_L), and the sweep angle (Λ). Recall that the airfoil technology factor has a value of 0.87 for a NACA 6-series airfoil section and a value of 0.95 for a supercritical section.

With this approximation for the drag divergence Mach number, we can now calculate the critical Mach number. The definition of the drag divergence Mach number is given in equation (6-5).

$$\frac{\partial C_D}{\partial M} = 0.1 \qquad (6\text{-}5)$$

Next, we make use of Lock's proposed empirically-derived shape of the drag rise.[29]

$$C_D = 20(M - M_{crit})^4 \qquad (6\text{-}6)$$

The definition of the drag divergence Mach number is equated to the derivative of the drag rise formula given above to produce the following equation:

$$\frac{\partial C_D}{\partial M} = 0.1 = 80(M - M_{crit})^3 \qquad (6\text{-}7)$$

We can then solve this equation for the critical Mach number:

$$M_{crit} = M_{DD} - \left(\frac{0.1}{80}\right)^{1/3} \qquad (6\text{-}8)$$

where the drag divergence Mach number is given by the extended Korn equation.

Joel Grasmeyer et al.[30] then developed a method to compute the wave drag coefficient for use in MDO studies of a transonic strut-braced wing concept using the following relation:

$$C_{d_{\text{wave}}} = 20(M - M_{crit})^4 \frac{S_{\text{strip}}}{S_{\text{ref}}} \quad \text{for} M > M_{crit}, \qquad (6\text{-}9)$$

where the local t/c, C_l, and half-chord sweep angle are specified for a number of spanwise strips along the wing and the drag of each strip is combined to form the total wave drag. In the equation above, the wave drag for each strip is multiplied by the ratio of the strip area (S_{strip}) to the reference area (S_{ref}).

This method has been validated with the Boeing 747-100 using eight spanwise strips. The results are shown in figure 6-12. The curved lines represent the current model predictions, and the discrete data points represent the Boeing 747 flight test data from Mair and Birdsall.[31] The predictions show good agreement with the data over a wide range of Mach numbers and lift coefficients. We reemphasize that the results are sensitive to the value of the airfoil technology factor. A value of 0.89 was used for the Boeing 747 results in figure 6-12. Based on an analysis of the Boeing 777, a value of 0.955 was used to simulate that aircraft's wave drag characteristics.

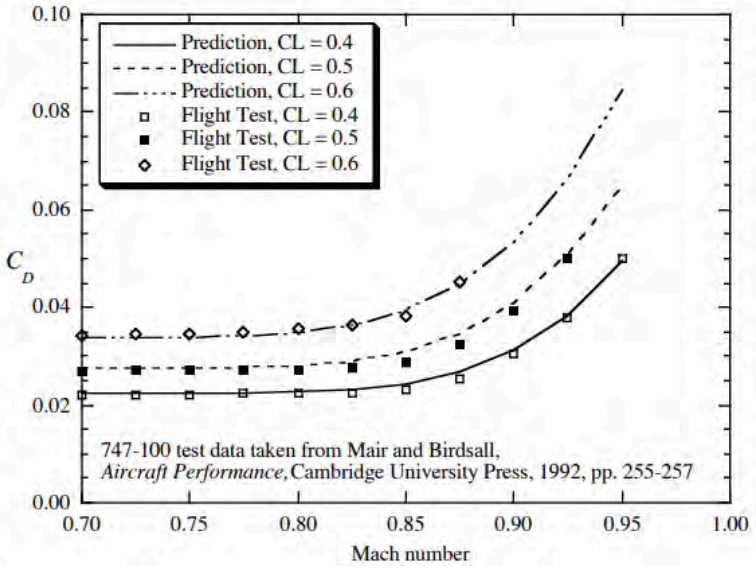


Figure 6-12: Comparison of approximate drag rise methodology with Boeing 747-100 flight test data. From W. H. Mason. Data from Mair and Birdsall.

6.4.3 Fighter Wing Concepts and Issues

In this section, we provide a few comments on fighter wing concepts and issues in transonic flight. A good survey of the issues for transonic aerodynamic design of fighters has been given by Bradley.[32]

Attached flow maneuver wing design. To push performance past the cruise lift condition, the situation changes. If the goal is to obtain efficient lift at high lift coefficients using attached flow design, the emphasis switches from an elliptic loading to a span loading that pushes each section lift coefficient to its limit. Thus, if the planform is a simple trapezoidal planform with a single airfoil section, the goal is to attain a constant section C_l across the wing.[33] The penalty for a nonelliptic spanload is small compared to the additional profile drag for airfoils operating past their attached flow condition on portions of the wing. This is essentially what was done on the X-29. The so-called Grumman K airfoil was used on the X-29.

Two other considerations need to be addressed. Wings designed to operate over a wide range of conditions can use the leading- and trailing-edge devices to approximate the optimum wing shape by using a deflection schedule to automatically deflect to the best shape. Although research has been done on smooth surfaces to do this, in most cases, the devices are simply flap deflections. In the case of the X-29, the airfoil was shaped for the maneuver design point, and the devices were used to reduce the trailing-edge camber at lower lift coefficients.

The second consideration is airfoil-planform integration. If the airfoil is designed to be heavily loaded, there is likely to be a fairly strong shock well aft on the wing. To obtain low drag, this shock should be highly swept. This means that the trailing edge of the wing should be highly swept. This can be done using a wing with inverse taper or a forward-swept wing. This is one reason to consider a forward-swept wing concept. However, a forward-swept wing with a canard must be balanced with a large negative static margin to gain the full benefit of the concept. The X-29 is about 32% to 35% unstable for this reason.

Finally, when the airfoils are being pushed to their limits, planform kinks are a very poor idea. The tendency of the spanload to remain smooth means that the local lift coefficients change rapidly in the kink region, and local lift coefficients often become excessively large.

Another alternative is to include a canard in the configuration. A canard can be used to carry additional load at extreme maneuver conditions.

Vortex flow/strake maneuver wing design. Another method of obtaining high-maneuver lift has proven effective on the F-16 and F-18 aircraft. In this case, inboard strakes are used (Northrop called theirs a LEX, leading-edge extension, dating back to the F-5 days). The strakes produce a strong vortex at high angles of attack. The vortices flow over the aircraft surfaces and, as a result of the low-pressure field, create additional lift. Careful shaping of the strake is required, but good performance can be obtained. Note that these airplanes also use leading- and trailing-edge wing device scheduling to achieve optimum performance.

Figure 6-13 shows, in a rough sense, how the two concepts compare. Here, E is the efficiency factor in the drag due to lift term of the classic drag polar:

$$C_{D_L} = \frac{C_L^2}{\pi ARE} \qquad (6\text{-}10)$$

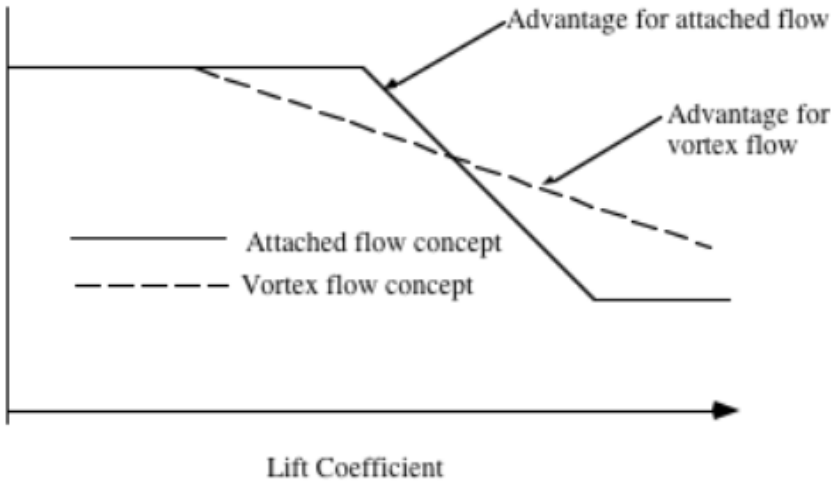


Figure 6-13: Effectiveness of various wing concepts in terms of efficiency, E.

6.4.4 Buffeting Considerations

Buffeting* is defined as a response of the structural modes to the aerodynamic excitation imposed as pressure fluctuations produced by separated flow.[34,35] The pressure fluctuations excite the flexible modes, resulting in structural vibrations that can have a strong influence on aircraft aerodynamic performance and, when left unchecked, can lead to structural damage or even catastrophic failure.[36] The fluctuations may excite rigid body modes, such as "wing rocking," "wing dropping," or "nose slicing," at much lower frequencies, but these modes can be regarded as aircraft handling problems.

*The term buffeting was first introduced in the 1931 final report published by the Aeronautical Research Committee in the UK that attributed the "failure of the tailplane under severe buffeting" for the apparent disintegration and crash of an all-metal Junkers F.13ge on 21 July 1930, killing four passengers and two pilots. The report concluded the cause of the buffeting to be "air eddies produced by the centre section of certain low-wing monoplanes when the aircraft approaches the stalling attitude."

The flow separation over the wing is usually the primary cause of buffet, and three factors that strongly influence flow separation are (i) Mach number, (ii) angle of attack, and (iii) wing geometry. (Although localized flow separation may occur on other parts of the aircraft, such as fuselage, it rarely causes the buffet phenomenon.) For a given wing geometry, the 1.0 g buffet onset boundary is typically represented by a C_{LB}-vs-M curve shown in figure 6-14, which implicitly accounts for the relative influence of the angle of attack.[37] At subsonic speeds, buffet is commonly caused by vortex shedding or turbulent wake regions behind the wing at angles of attack near stall. A well known example is twin-tail buffet of the F/A-18 aircraft caused by bursting of vortices emanating from the leading-edge extensions (LEX) under high-angle-of-attack maneuvering conditions. At transonic speeds, buffet is caused by self-sustained, low-frequency oscillations of the shock on the upper surface of the wing due to shock-induced boundary layer separation, which imposes unsteady loading on the aircraft wings.

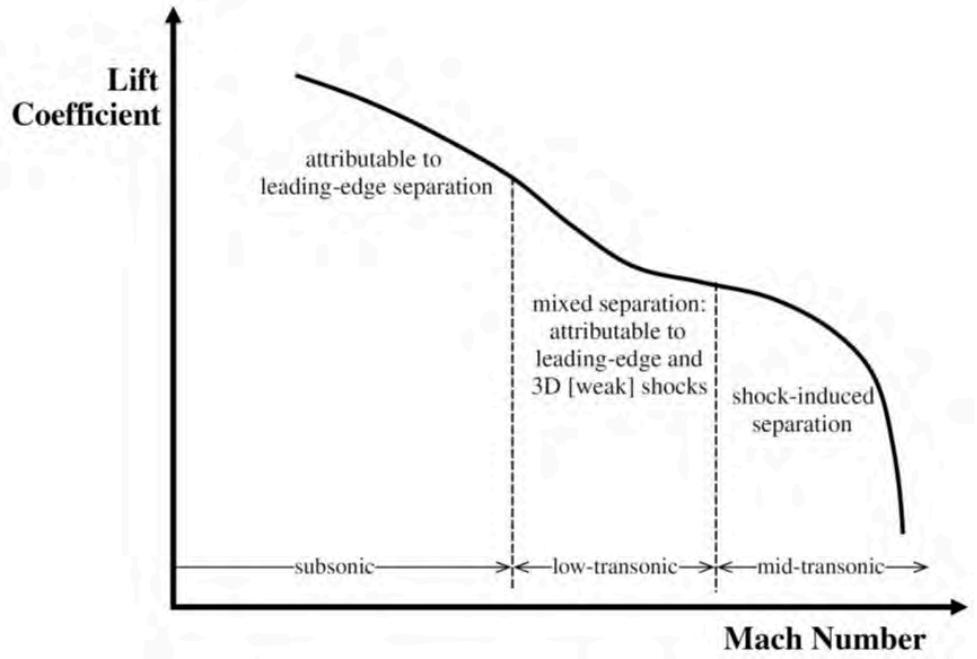


Figure 6-14: Typical buffet boundary and flow separation mechanisms in subsonic-to-transonic flight regimes. *From A. Berard and A. T. Isikveren. "Conceptual Design Prediction of the Buffet Envelope of the Transport Aircraft." Reprinted with permission of the American Institute of Aeronautics and Astronautics, Inc.*

For a given aircraft, a $C_L M^2$ is a constant curve, representing flying at a certain pressure altitude. The point where such a curve becomes tangent to the buffet boundary represents the highest achievable altitude regardless of the available thrust. This altitude is called the aerodynamic ceiling. Flying at this altitude is problematic because any change in M will lead to buffeting and/or stalling. Pilots call it the coffin corner.

Airplanes are typically constrained to fly in the region to the left of the buffet onset boundary shown in figure 6-14 to avoid potentially damaging effects of buffet. Regulatory agencies require that C_L in operational conditions be limited to ensure that the airplane can fly at a load factor ($n = L/W$) of 1.3 without encountering buffet. This load factor is equivalent to a 40° bank angle while maintaining level flight. For aircraft that cruise at transonic Mach numbers, a strong gust can increase the incidence to a level where flow separation occurs. To meet the regulatory requirements, operational aircraft buffet envelope is defined by flight test. The 1.0 g onset is typically identified as the speed at which the vibration reaches ±0.050 g at the pilot's seat position while the pilot executes windup turns at a constant Mach number. This means that the certified operational constraint of the 1.0 g buffet onset is not to be taken as a strict physical limit to the actual flight envelope of the aircraft; it basically sets a boundary between a safe flight domain and a flight domain in which the flight crew may encounter serious control problems and/or the aircraft is prone to severe instantaneous or fatigue loads.[38] Additional operator specific requirements would also include maneuver capability through moderate turbulence (e.g., penetration with 0.50 g margin).

Clearly, the buffet boundary has a strong influence on the choice of the design lift coefficient, C_L, at the design Mach number, M. Since M and C_L are chosen during the early conceptual design phase, it is imperative to consider the influence of buffet boundary. Otherwise, designers run the risk of having the design C_L limited by buffet in later stages of design. This may adversely impact flight performance by limiting the maximum lift-to-drag ratio and operational ceiling.[39] However, the overarching challenge for the designers during the conceptual design phase is to accurately estimate the buffet boundary when the wing geometry is not fully defined. As a matter of fact, one of the key outputs of the early design efforts is an efficient wing geometry and associated parameters such as planform area, aspect ratio, sweep, taper, camber, and thickness. Of course, once the wing geometry is specified, we can use buffet prediction methods based on data from wind tunnel tests[40,41] or computational fluid dynamics (CFD) simulations.[42,43]

6.4.4.1 Buffet Boundary Prediction Methods

Berard and Isikveren[44] and Eijndhoven[45] present a relatively simple, economical, flexible, and robust semi-empirical method that is well suited for conceptual design of new transport aircraft. Berard and Isikveren identify six wing geometry parameters that have functional sensitivity with the maximum attainable lift coefficient for buffet onset, and they provide mathematical models of C_L as a function of wing geometric parameters for a given M. Figure 6-15 illustrates the effect of wing geometric parameters—namely, leading edge sweep (Λ), thickness-to-chord ratio (t/c), and camber—in a mutually exclusive sense. Two variants of the method are discussed in their paper. The first uses a generic reference curve for a generic reference wing to evaluate the buffet envelope of the target aircraft. The second variant starts from the buffet onset of a known seed aircraft and uses fractional change theory to predict buffet onset boundary of the new wing geometry.

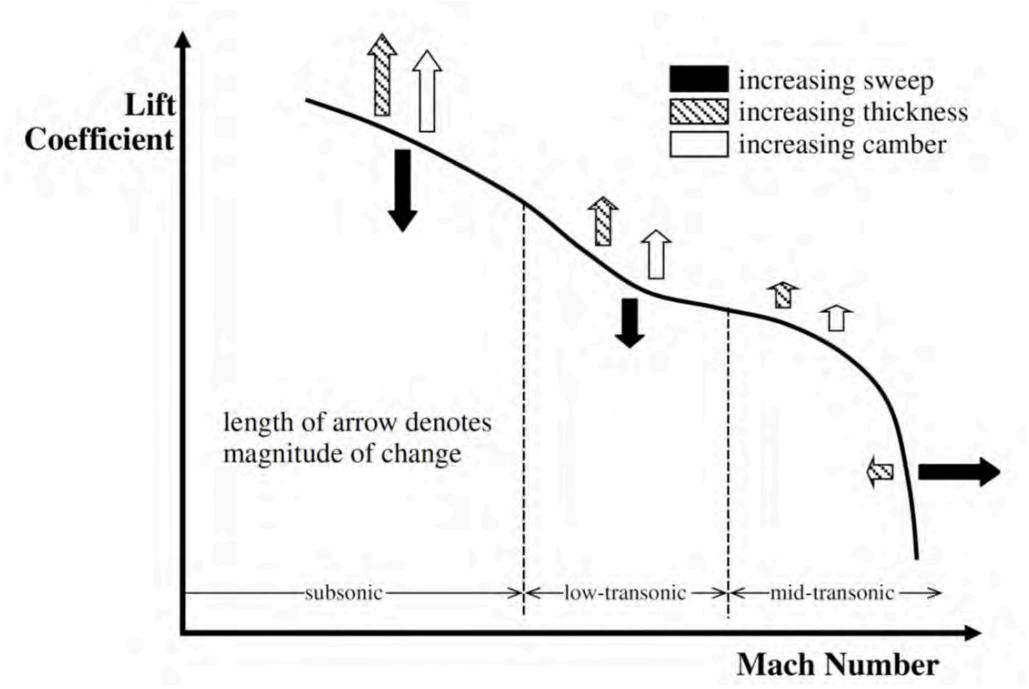


Figure 6-15: Effect of change in wing geometric parameters on the buffet onset boundary. From A. Berard and A. T. Isikveren. "Conceptual Design Prediction of the Buffet Envelope of the Transport Aircraft." Reprinted with permission of the American Institute of Aeronautics and Astronautics, Inc.

Segee et al.[46] developed a surrogate model of the maximum allowable lift coefficient before buffet offset for multidisciplinary design optimization (MDO) applications for transonic transport aircraft studies. The authors generated aerodynamic data for the BACJ airfoil using steady RANS (Reynolds-averaged Navier–Stokes) CFD for a series of thickness ratios, and they developed C_{LB}-vs-M models for different thickness ratios using correlation of "shock position" and "local Mach number ahead of shock." When performing MDO studies, this model was applied in a stripwise manner. That is, the 2D lift coefficient for each wing strip was kept below 0.8. Kenway and Martins[47] present a new formulation of 3D wing buffet-onset prediction that is well suited for MDO studies. Their method is based on the integration of a flow separation sensor along with a cutoff value. It can determine buffet onset using data from one steady RANS CFD simulation.

Chapter 6 Exercises

6.1 Read the following paper and write a one-page summary in preparation for a class discussion on the paper: Lynch, F., "Commercial Transports—Aerodynamic Design for Cruise Efficiency," in *Transonic Aerodynamics*, edited by D. Nixon, AIAA Progress in Astronautics and Aeronautics, Vol. 81, AIAA, Washington, 1982, pp. 81-144.

Figure References

Figure 6-1: H. H. Hurt, Jr. (1965). Aerodynamics for Naval Aviators, Revised edition. US Navy. NAVAIR 00-80T-80 https://www.faa.gov/sites/faa.gov/files/regulations_policies/handbooks_manuals/aviation/00-80T-80.pdf

Figure 6-2: NASA. Lockheed C-141 model in the Transonic Dynamics Tunnel (TDT). Public domain. https://commons.wikimedia.org/wiki/File:Lockheed_C-141_Model_in_TDT_-_GPN-2000-001741.jpg

Figure 6-8: Lynch, F., "Commercial Transports—Aerodynamic Design for Cruise Efficiency," in *Transonic Aerodynamics*, edited by D. Nixon, AIAA Progress in Astronautics and Aeronautics, Vol. 81, AIAA, Washington, 1982, pp. 81–144. Adapted. Fair use.

Figure 6-9(a): W. H. Mason. Figure 1(a) in "Analytic Models for Technology Integration in Aircraft Design," AIAA Paper 90-3262, AIAA-AHS-ASEE Aircraft Design, Systems and Operations Conference, Dayton, OH, Sept. 17-19, 1990. https://arc.aiaa.org/doi/10.2514/6.1990-3262

Figure 6-9(b): W. H. Mason. Figure 1(a) in "Analytic Models for Technology Integration in Aircraft Design," AIAA Paper 90-3262, AIAA-AHS-ASEE Aircraft Design, Systems and Operations Conference, Dayton, OH, Sept. 17-19, 1990. https://arc.aiaa.org/doi/10.2514/6.1990-3262

Figure 6-10(a): K. Bean. The Museum of Flight. CC BY-NC-SA 4.0. Model courtesy of Boeing Historical Archives.

Figure 6-10(b): K. Bean. The Museum of Flight. CC BY-NC-SA 4.0. Model courtesy of Boeing Historical Archives.

Figure 6-11: Mason, W. H., MacKenzie, D. A., Stern, M. A., and Johnson, J. K., "A Numerical Three Dimensional Viscous Transonic Wing-Body Analysis and Design Tool," AIAA Paper 78-101, Jan. 1978. Copyright undetermined by AIAA. Fair use.

Figure 6-12: W. H. Mason, from data in Mair, W. A., and Birdsall, D. L., *Aircraft Performance*, Cambridge University Press, 1992, pp. 255–257.

Notes

1. Foss, R. L., "From Propellers to Jets in Fighter Aircraft Design," AIAA Paper 78-3005, in *Diamond Jubilee of Powered Flight, The Evolution of Aircraft Design*, edited by J. D. Pinson, Dayton-Cincinnati Section, Dec. 14-15, 1978, pp. 51–64.
2. Hurt, H. H., Jr., *Aerodynamics for Naval Aviators, Revised Edition*, 1965, published by Direction of the Commander, Naval Air Systems Command, United States Navy, reprinted by Aviation Supplies and Academics, Inc., Renton, WA.
3. Becker, J. V., "Chapter III: Transonic Wind Tunnel Development (1940-1950)," in *The High-Speed Frontier*, NASA SP-445, 1980.
4. Becker, J. V., "Chapter II: The High-Speed Airfoil Program," in *The High-Speed Frontier,* NASA SP-445, pp. 55–60.
5. Blackwell, J. A., Jr., "Experimental Testing at Transonic Speeds," in *Transonic Aerodynamics*, edited by D. Nixon, Progress in Astronautics and Aeronautics, Vol. 81, AIAA, Washington, 1982. pp. 189–238.
6. Murman, E. M., and Cole, J. D., "Calculation of Plane Steady Transonic Flows," AIAA Journal, Vol. 9, No. 1, 1971, pp. 114–121. (*Note*: Presented at the 8th Aerospace Sciences Meeting, New York, NY, Jan. 19-21, 1970.)
7. Hall, M. G., "On innovation in aerodynamics," The Aeronautical Journal, Vol. 100, No. 1000, Dec. 1996, pp. 462–470. https://doi.org/10.1017/S0001924000067506
8. Murman, E. M., Bailey, F. R., and Johnson, M. L., "TSFOIL — A Computer Code for Two- Dimensional Transonic Calculations, Including Wind-Tunnel Wall Effects and Wave Drag Evaluation," NASA SP-347, Mar. 1975.
9. Jameson, A., "Iterative Solution of Transonic Flows Over Airfoils and Wings, Including Flows at Mach 1," Communication on Pure and Applied Mathematics, Vol. 27, 1974, pp. 283–309.
10. Jameson, A., "Acceleration of Transonic Potential Flow Calculations on Arbitrary Meshes by the Multiple Grid Method," AIAA Paper 79-1458, AIAA 4th Computational Fluid Dynamics Conference, Williamsburg, VA, Jul. 1979, pp. 122–146.
11. Holst, T. L., "Transonic flow computations using nonlinear potential methods," Progress in Aerospace Sciences, Vol. 36, No. 1, 2000, pp. 1–61. https://doi.org/10.1016/S0376-0421(99)00010-X
12. Jameson, A., "Full-Potential, Euler, and Navier-Stokes Schemes," in *Applied Computational Aerodynamics*, edited by P. Henne, AIAA Progress in Astronautics and Aeronautics, Vol. 125, AIAA, Washington, 1990, pp. 39–88.

13. Drela, M., "Newton Solution of Coupled Viscous/Inviscid Multielement Airfoil Flows," AIAA Paper 1990-1470, 21st Fluid Dynamics, Plasma Dynamics, and Lasers Conference, Seattle, WA, Jun. 18-20, 1990.
14. Harris, C. D., "NASA Supercritical Airfoils," NASA TP-2969, Mar. 1990.
15. Becker, J. V., "Chapter II: The High-Speed Airfoil Program," in *The High-Speed Frontier*, NASA SP-445, pp. 55–60.
16. Whitcomb, R., "Review of NASA Supercritical Airfoils," ICAS Paper 74-10, Proceeding of the 9th Congress of the International Council of Aeronautical Science, Haifa, Israel, Aug. 25-30, 1974, pp 8-18.
17. Lynch, F., "Commercial Transports—Aerodynamic Design for Cruise Efficiency," in *Transonic Aerodynamics*, edited by D. Nixon, AIAA Progress in Astronautics and Aeronautics, Vol. 81, AIAA, Washington, 1982, pp. 81–144.
18. Henne, P., "Innovation with Computational Aerodynamics: The Divergent Trailing edge Airfoil," in *Applied Computational Aerodynamics*, edited by P. Henne, AIAA Progress in Astronautics and Aeronautics, Vol. 125, American Institute of Aeronautics and Astronautics, Washington, DC, 1990, pp. 221–261.
19. Mason, W. H., "Analytic Models for Technology Integration in Aircraft Design," AIAA Paper 90-3262, AIAA/AHS/ASEE Aircraft Design, Systems, and Operations Conference, Dayton, OH, Sept. 17-19, 1990.
20. Shevell, R. S., *Fundamentals of Flight*, 2nd ed., Prentice-Hall, Englewood-Cliffs, 1989, p. 223.
21. Harris, C. D., "NASA Supercritical Airfoils," NASA TP-2969, Mar. 1990.
22. Huyse, L., "Free-form Airfoil Shape Optimization Under Uncertainty Using Maximum Expected Value and Second-order second-moment Strategies," NASA/CR-2001-211020, ICASE Report No. 2001-18, Jun. 2001.
23. Haines, A. B., "Wing Section Design for Swept-Back Wings at Transonic Speed," Journal of the Royal Aeronautical Society, Vol. 61, Apr. 1957, pp. 238–244.
24. Mason, W. H., MacKenzie, D. A., Stern, M. A., and Johnson, J. K., "A Numerical Three Dimensional Viscous Transonic Wing-Body Analysis and Design Tool," AIAA Paper 78-101, 16th Aerospace Sciences Meeting, Huntsville, AL, Jan. 16-18, 1978.
25. Iglesias, S., and Mason, W. H., "Optimum Spanloads Including Wing Structural Weight," AIAA Paper 2001-5234, 1st AIAA Aircraft Technology, Integration, and Operations Forum, Los Angeles, CA, Oct. 16-17, 2001.
26. Jameson, A., "Re-Engineering the Design Process through Computation," AIAA Paper 97-0641, 35th Aerospace Sciences Meeting and Exhibit, Reno, NV, Jan. 6-9, 1997.
27. Mason, W. H., "Analytic Models for Technology Integration in Aircraft Design," AIAA Paper 90-3262, AIAA/AHS/ASEE Aircraft Design, Systems, and Operations Conference, Dayton, OH, Sept. 17-19, 1990.
28. Malone, B. and Mason, W. H., "Multidisciplinary Optimization in Aircraft Design Using Analytic Technology Models," Journal of Aircraft, Vol. 32, No. 2, Mar.-Apr. 1995, pp. 431–438.
29. Hilton, W. F., *High Speed Aerodynamics*, Longmans, Green, & Co., London, 1952, pp. 47–49.
30. Grasmeyer, J. M., Naghshineh, A., Tetrault, P.-A., Grossman, B., Haftka, R. T., Kapania, R. K., Mason, W. H., Schetz, J. A., "Multidisciplinary Design Optimization of a Strut-Braced Wing Aircraft with Tip-Mounted Engines," MAD Center Report MAD 98-01-01, Jan. 1998.
31. Mair, W. A., and Birdsall, D. L., *Aircraft Performance*, Cambridge University Press, 1992, pp. 255–257.
32. Bradley, R., "Practical Aerodynamic Problems—Military Aircraft," in *Transonic Aerodynamics*, edited by D. Nixon, AIAA Progress in Astronautics and Aeronautics, Vol. 81, AIAA, Washington, 1982, pp. 149–187.
33. Mason, W. H., "Wing-Canard Aerodynamics at Transonic Speeds - Fundamental Considerations on Minimum Drag Spanloads," AIAA Paper 82-0097, 20th Aerospace Sciences Meeting, Orlando, FL, Jan. 11-14, 1982.
34. Mabey, D. G., "Beyond the Buffet Boundary," Aeronautical Journal, Vol. 77, No. 748, 1973, pp. 201–215.
35. Mabey, D. G., "Some Remarks on Buffeting," Technical Memorandum Structures 980, Royal Aircraft Establishment, 1981.
36. Berard, A., and Isikveren, A. T., "Conceptual Design Prediction of the Buffet Envelope of the Transport Aircraft," Journal of Aircraft, Vol. 46, No. 5, Sept.-Oct. 2009.
37. Berard, A., and Isikveren, A. T., "Conceptual Design Prediction of the Buffet Envelope of the Transport Aircraft," Journal of Aircraft, Vol. 46, No. 5, Sept.-Oct. 2009.
38. Berard, A., and Isikveren, A. T., "Conceptual Design Prediction of the Buffet Envelope of the Transport Aircraft," Journal of Aircraft, Vol. 46, No. 5, Sept.-Oct. 2009.
39. Van Eijndhoven, J. N. A., "Buffet Envelope Prediction of Transport Aircraft During the Conceptual Design Phase," Master of Science Thesis, Delft University of Technology, Jan. 2012.
40. Benoit, B., and Legrain, I., "Buffeting Prediction for Transport Aircraft Applications Based on Unsteady Pressure Measurements," AIAA Paper 87-2356, 5th Applied Aerodynamics Conference, Monterey, CA, 17-19 Aug. 1987.
41. Sousa, R. S., Girardi, R. D., and Annes da Silva, R. G., "A New Criterion for Transonic Buffeting Onset Estimation," AIAA 2017-4231, 35th Applied Aerodynamics Conference, Denver, CO, 5-9 Jun. 2017.
42. Sartor, F., Martin, M., Moreno, C. R., and Dandois, J., "Numerical Simulations of Transonic Buffet on a Half Wing-Body Configuration," ICAS 2021, 32nd Congress of the International Council of the Aeronautical Sciences, Shanghai, China, 6-10 Sept. 2021.
43. Browne, O. M. F., Maldonado, D., Housman, J. A., Duensing, J. C., and Milholen, W. E., "Predicting Transonic Buffet Onset for the Boeing Transonic Truss-Braced Wing Aircraft." Journal of Aircraft, Sept. 2024, pp. 1–19.
44. Berard, A., and Isikveren, A. T., "Conceptual Design Prediction of the Buffet Envelope of the Transport Aircraft," Journal of Aircraft, Vol. 46, No. 5, Sept.-Oct. 2009.

45. Van Eijndhoven, J. N. A., "Buffet Envelope Prediction of Transport Aircraft During the Conceptual Design Phase," Master of Science Thesis, Delft University of Technology, Jan. 2012.

46. Segee, M., Schetz, J. A., and Kapania, R. K., "Transonic Aerodynamic Analysis for Multidisciplinary Design Optimization Applications," AIAA 2016-4039, 34th Applied Aerodynamics Conference, Washington, D.C., 13-17 Jun. 2016.

47. Kenway, G. K. W., and Martins, J. R. R. A., "Buffet-Onset Constraint Formulation for Aerodynamic Shape Optimization," AIAA Journal, Vol. 55, No. 6, Jun. 2017, pp. 1930–1947.

7. High-Lift Aerodynamics

For transonic transports, the high-lift system is a critical part of the configuration design. To achieve "reasonable" field performance while also obtaining efficient transonic cruise, the design will require a fairly sophisticated high-lift system. Its critical importance is substantiated by the following excerpts (presumably referring to the B-777)from a paper by Boeing aerodynamicists:[1]

- "A 0.10 increase in lift coefficient at constant angle of attack is equivalent to reducing the approach attitude by one degree. For a given aft body-to-ground clearance angle, the landing gear may be shortened for a savings of airplane empty weight of 1400 lb."
- "A 1.5% increase in maximum lift coefficient, $C_{L\max}$, is equivalent to a 6600 lb increase in payload at a fixed approach speed"
- "A 1% increase in take-off L/D is equivalent to a 2800 lb increase in payload or a 150 NM increase in range."

For fighters, high-lift devices are also scheduled for efficient maneuver.

High-lift systems are critical for STOVL (short takeoff and vertical landing) and V/STOL (vertical and short takeoff and landing) aircraft. They also use the propulsion system to help generate the lift. It has always seemed peculiar to design fighter aircraft, or virtually any military aircraft, to operate from traditional runways; the one thing the adversary is going to know is the exact location of your runways. So a STOVL capability seems to be critical in a serious confrontation.

7.1 Characteristics of High-Lift Systems

High-lift systems employ various means of flow manipulation around a wing to increase its lift, enabling the airplane to perform specified missions. The systems exploit one or more of the following basic aerodynamic concepts: (i) increase effective camber of the airfoil, which increases C_l; (ii) increase wing area to increase lift; and (iii) boundary layer control (BLC) on the surface through active or passive means to delay or prevent flow separation.

Boundary layer control through active means requires additional energy to either remove low-momentum fluid from the boundary layer by suction or inject air into the boundary layer to increase momentum; both delay onset of separation and could increase $C_{L\max}$. Although highly promising, practical implementation requires additional equipment to manage the distribution of energy.

Passive means of flow manipulation, on the other hand, are the well known leading-edge (LE) and trailing-edge (TE) devices that are found on most of the aircraft in service. For operating these devices, we only need a drive system for retracting and extending the flaps. Our primary focus in this chapter is on passive LE and TE high-lift devices as described in sections 7.2 and 7.3.

Table 1 shows typical values of $C_{L\max}$. They come from papers by Brune and McMasters,[2] Roskam and Lan,[3] and Sanders.[4] Clearly the 727 emphasized short fields and thus required a higher $C_{L\max}$. Anyone who ever looked out the window while landing in a 727 noticed the elaborate high-lift system employed.

Model	$C_L$max
B-47/B-52	1.8
367-80/KC-135	1.78
707-320/E-3A	2.2

Model	C_{L}max
727	2.79
DC-9	3.0
737-200	3.2
747/E-4A	2.45
767	2.45
777	2.5

Table 7-1: Values of C_{Lmax} for some airplanes. (Note: There is a significant variation of values from different sources.)

Some key aspects:

- Compressibility can be important early.
- Reynolds number scaling from wind-tunnel to flight may be problematic.
- Today, *simple* high-lift systems are critical, and the high manufacturing cost for high-lift systems is important.

Classes of systems:

- High lift for a single element airfoil
- Multi-element airfoils
- Use of "blowing" in some form (powered lift)

Computational simulation:

- Computational simulation requires consideration of viscous effects immediately (unlike typical cruise airfoil analysis and design, where some insight can usually be gained using inviscid simulations that ignore viscous effects).
- Predicting high lift is done almost entirely with Reynolds-averaged Navier–Stokes (RANS) codes (one important exception is Mark Drela's MSES [5] code). A summary of the computational capability is given by Rumsey and Ying.[6]

Single element airfoils:

- Central to the story of how to obtain high lift on a single element airfoil is Liebeck's high-lift airfoil[7] and the Stratford "pressure recovery" shape of the pressure distribution. This introduces the classic paper by A. M. O. Smith.[8] See section 7.4 below for some insights from this paper.

Multi-element airfoils:

- *Understanding the physics:* Section 6.3 of Smith's paper[9] is critical to understanding the physics. Review the paper to make sure you understand (i) the slat effect, (ii) the circulation effect, (iii) the dumping effect, (iv) off-the-surface pressure recovery, and (v) the fresh boundary layer effect. (*Note*: some people combine the circulation and dumping effects and call it the "vane effect"; see section 7.4 below for details.)
- *Design:* See a comprehensive survey by C. P. van Dam.[10]
- *Existing systems on commercial transports:* Peter Rudolph has surveyed the high-lift systems on several subsonic transport aircraft.[11]

7.2 Examples of High-Lift Devices

In this section, we include examples of high-lift devices based on the original hand-drawn sketches of Grumman's Dick Kita.[12] These are fairly realistic drawings, as opposed to many of the drawings in textbooks, which may at times be somewhat cartoonish. Kita worked in the high-lift aerodynamics area for many years. I am aware of his work on the Gulfstream II and F-14, but he worked on many other Grumman aircraft high-lift systems as well. Examples of trailing-edge devices are presented in section 7.2.1 and of leading-edge devices in section 7.2.2. Deployment of these devices changes the airfoil shape. Due to notable change in airfoil camber shape, the airfoil aerodynamic characteristics show substantial changes, as illustrated in section 7.3.

Of the large number of papers addressing high lift, several deserve mention. Van Dam, et al.[13] provides a good summary of high-lift methodology. A summary of the Boeing 777 high-lift system development, as well as the overall design process, is available in the paper by Nield.[14] A valuable description of high lift on transports in contained in Gratzer.[15] The use of powered lift is covered in the survey by Korbacher.[16] Somewhat dated but valuable resources include the book by Hoerner and Borst[17] and the book by McCormick[18] (recently reissued unchanged from the 1967 edition as a Dover paperback). Perhaps the best chapter on high lift in a basic textbook is in Shevell.[19]

7.2.1 Types of Trailing-Edge Devices

Figure 7-1 shows examples of typical trailing-edge (TE) devices such as plain flap, slotted flap, and Fowler flap. In this figure, the flap deflection angle is denoted by δ_f. Note also that the standard convention for flap deflection angle is flap-down positive and flap-up negative. Deploying nonextending flaps, such as plain flap, split flap, or slotted flap, increases the camber of the airfoil. When an extending flap like the Fowler flap is deployed, it increases the planform area in addition to changing the camber.

More complicated TE devices, such as double-slotted flap or double slotted extensible flap, have been developed, as shown in figure 7-2. Their use results in greater increase in lift than one can obtain from the basic devices.

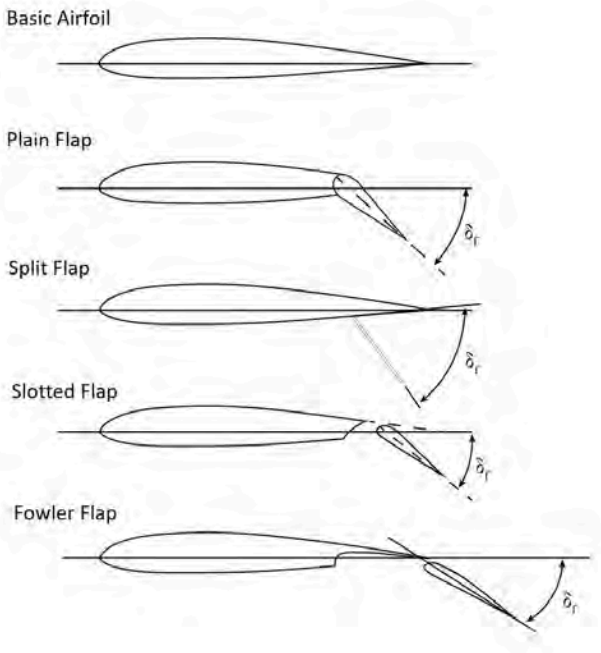


Figure 7-1: Examples of typical basic trailing-edge devices. *From D. Kita. Adapted by S. Madden. Fair use.*

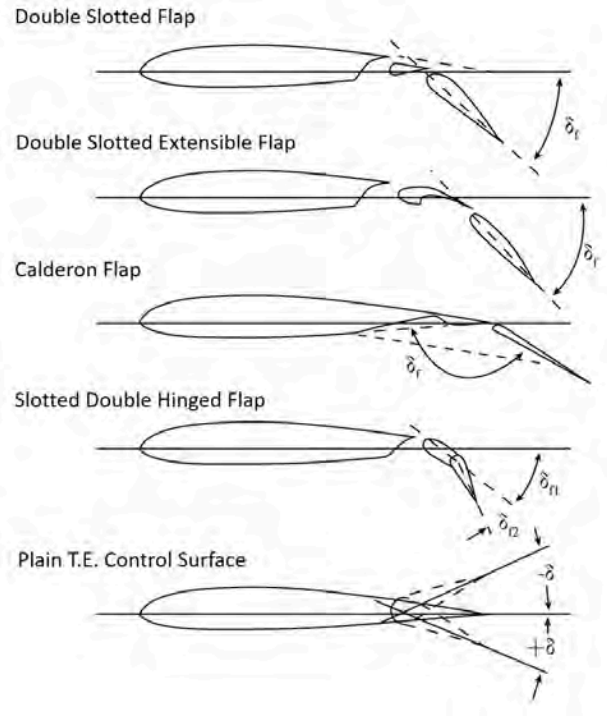


Figure 7-2: Examples of more complicated trailing-edge devices. *From D. Kita. Adapted by S. Madden. Fair use.*

7.2.2 Types of Leading-Edge Devices

Figure 7-3 shows examples of typical leading-edge (LE) devices such as nose flap, Krueger flap, or slat.

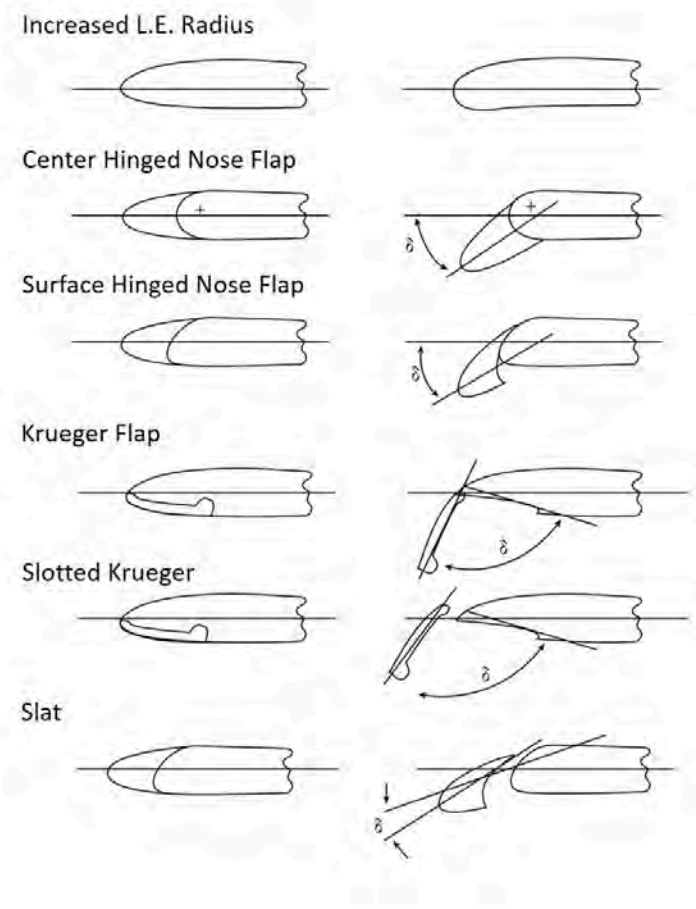


Figure 7-3: Typical leading edge device concepts. From Dick Kita. Adapted by S. Madden. Fair use.

7.2.3 Integration of Devices on the F-14 Wing

Figure 7-4 illustrates integration of LE and TE high-lift devices and control surfaces on the wing of the F-14 in their stowed and deployed positions. For low-speed combat maneuvering with the wing unswept, the outer two sections of trailing-edge flaps can be deployed at 10° and the nearly full-span leading-edge slats are drooped to 8.5°. This airplane has a fairly elaborate scheme, where the cove region is smoothed with a moving flap and the upper surface of the slat also has a movable piece to fair the flap. Many fighter airplanes use spoilers instead of ailerons for roll control, although their use varies from company to company.

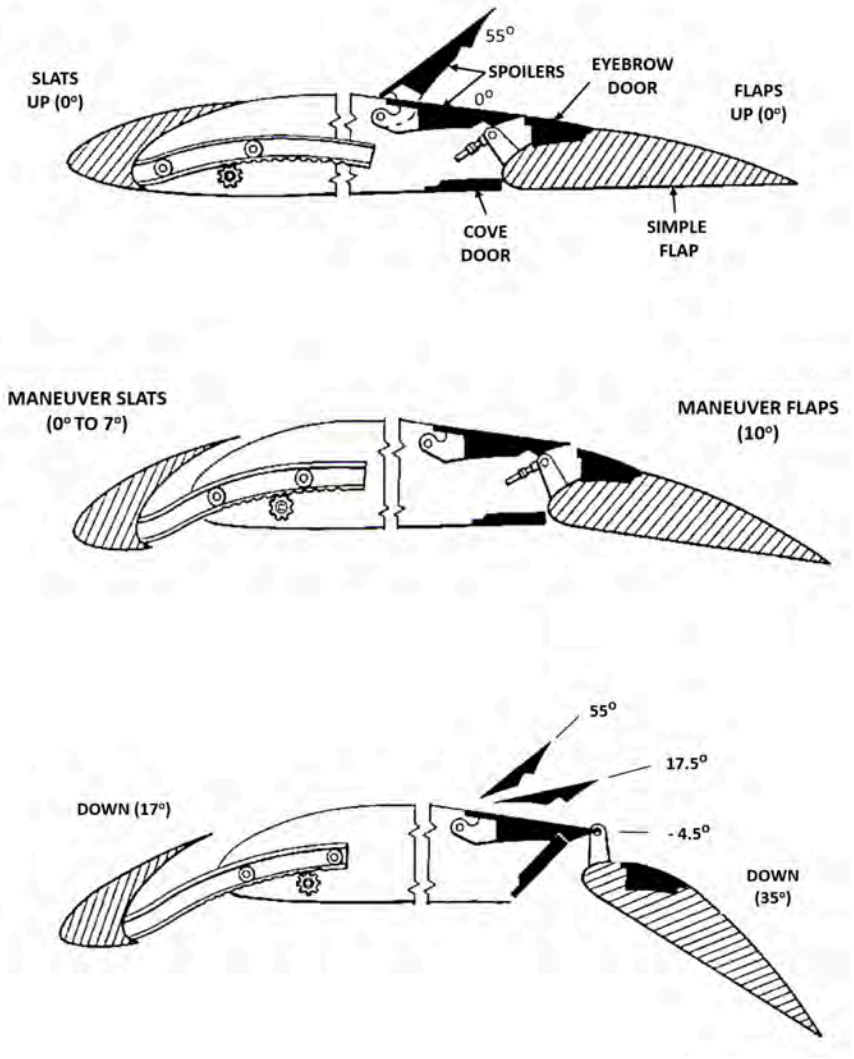


Figure 7-4: Illustrations of actual high-lift system deployment on the F-14 Tomcat. *From US Navy. NATOPS Flight Manual. Public domain.*

7.3 Aerodynamics of Leading- and Trailing-Edge Devices

7.3.1 Trailing-Edge Devices

The typical effects of the trailing edge flap deflection on the lift of a cambered airfoil are illustrated in figure 7-5. For a given angle of attack, α, deflecting flaps down increases the lift coefficient due to the increased effective camber. With increasing flap deflection angle, δ_f, the zero-lift angle of attack becomes more negative and $C_{l\max}$ increases, but the lift-curve slope does not change. However, the stall angle of attack for $C_{l\max}$ actually decreases slightly with increasing flap-deflection angle. The lift characteristics in this figure represent deployment of trailing-edge devices only without deploying any leading-edge devices.

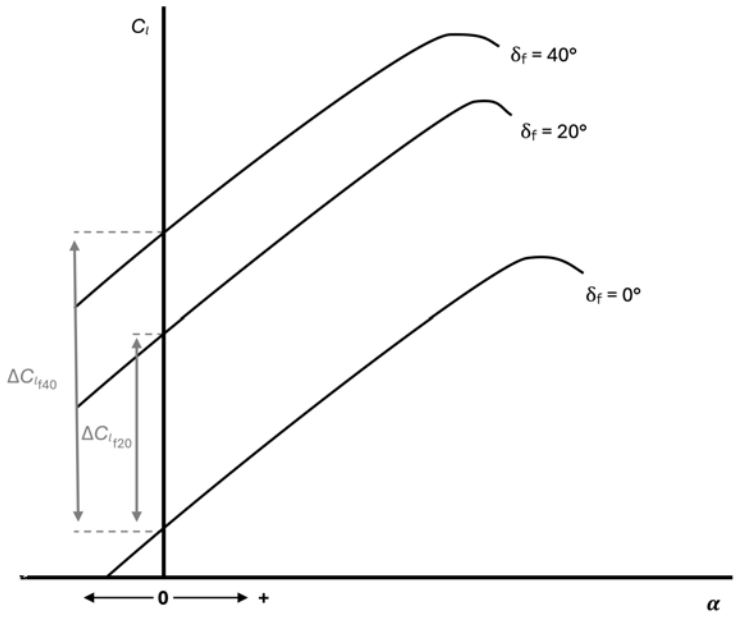


Figure 7-5: Typical effect of flap deflection on airfoil lift coefficient. From D. Kita. Adapted by K. Grey. Fair use.

Flaps that extend in a Fowler motion increase the wing planform area, which is shown in figure 7-6(a) by the hatched region in the planview of the wing. Therefore, the wing with extension generates more lift at any angle of attack. However, the original wing reference area, $S_{REF.}$—not the extended wing area, ($S_{REF.} + \Delta S_{EXT.}$)—is used in computing the C_L for wing flaps down (with extension). This has the effect of increasing the effective lift-curve slope by approximately the ratio of the total extended wing area to the original wing reference area—i.e., ($S_{REF.} + \Delta S_{EXT.}$)/ $S_{REF.}$, as shown in the figure.

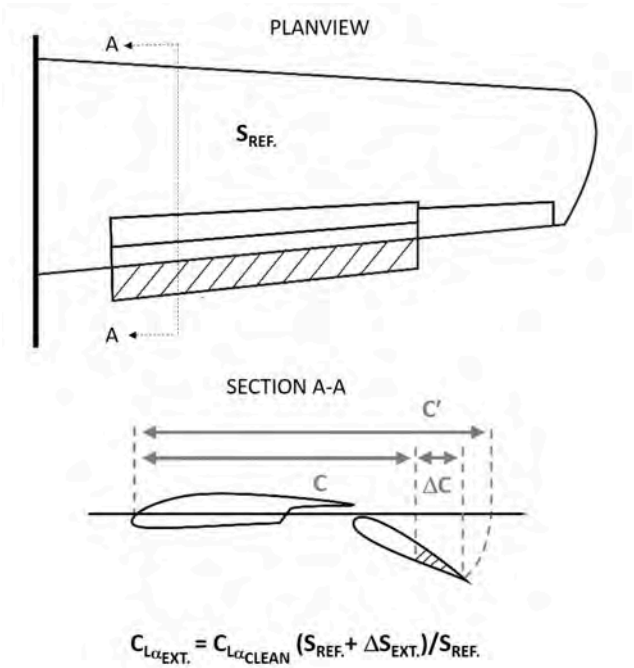


Figure 7-6(a): Effect of deploying flaps that extend in a Fowler motion on the wing lift-curve slope. From D. Kita. Adapted by K. Grey. Fair use.

The lift curves, C_L versus α, for the clean wing (flaps up) and for the wing with its extending flaps down are illustrated in figure 7-6(b). Much like with other types of flaps, the flap's downward curves show that the zero-lift angle of attack becomes more negative, $C_{L\max}$ increases, and stall angle is slightly reduced. The figure also shows that, when flaps with no extension are deployed, they do not change the lift-curve slope of the wing. However, the lift-curve slope for flaps with extension changes by the ratio of the total extended wing area to the original wing reference area.

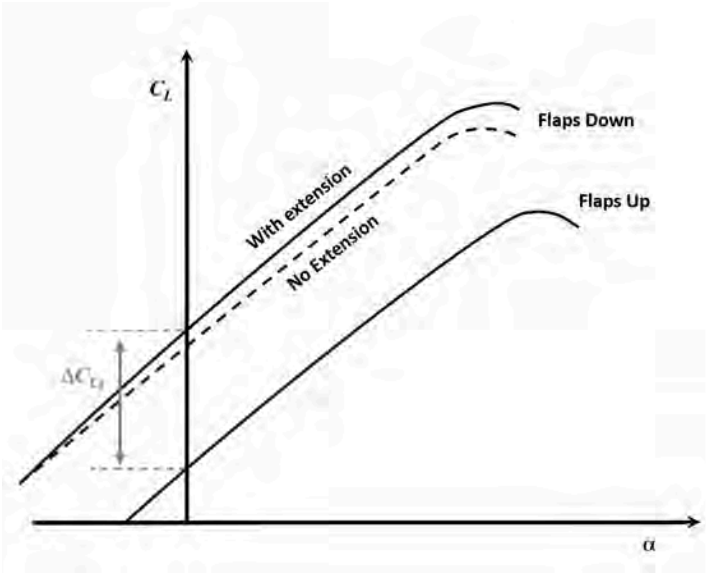


Figure 7-6(b): Effect of deploying flaps that extend in a Fowler motion on the variation of wing lift coefficient with angle of attack. From Dick Kita. Adapted by K. Grey. Fair use.

In general, we expect $C_{l\max}$ to increase with Reynolds number for a clean airfoil as shown in the top part of figure 7-7. However, sometimes the projection is not so straightforward, and $C_{l\max}$ may even decrease.[20] Considering the adverse effect of Mach number on $C_{l\max}$ in the bottom part of figure 7-7, the low Mach numbers at which the effects take place is worth noticing. This result is rather surprising to the uninitiated.

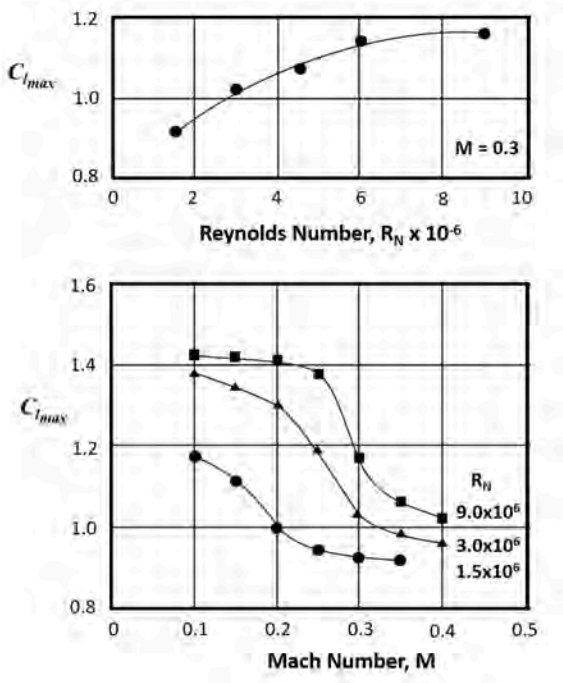


Figure 7-7: Typical variation of $C_{l\max}$ with Reynolds number, R_N, for a Mach number, M, of 0.3 (top) and variation of $C_{l\max}$ with M for three different R_N (bottom) for the NACA 64-210 airfoil with smooth surface. From D. Kita. Adapted by K. Grey. Fair use.

7.3.2 Leading-Edge Devices

Leading-edge devices, such as a slotted flap or slat, work to delay flow separation near the leading edge. Therefore, they don't really do anything until you reach the angle of attack where the leading-edge flow would "let go" if it didn't have the slats for protection. Thus the slats allow the lift to continue to rise to higher angles of attack before $C_{l\max}$ is reached, as illustrated in figure 7-8. The figure also shows that slats mitigate the effect of TE flaps on stall angle, which is somewhat reduced as flap deflection increases. Slats permit high-pressure air from the lower surface to blow over the top of the wing and delay separation by energizing the boundary layer.

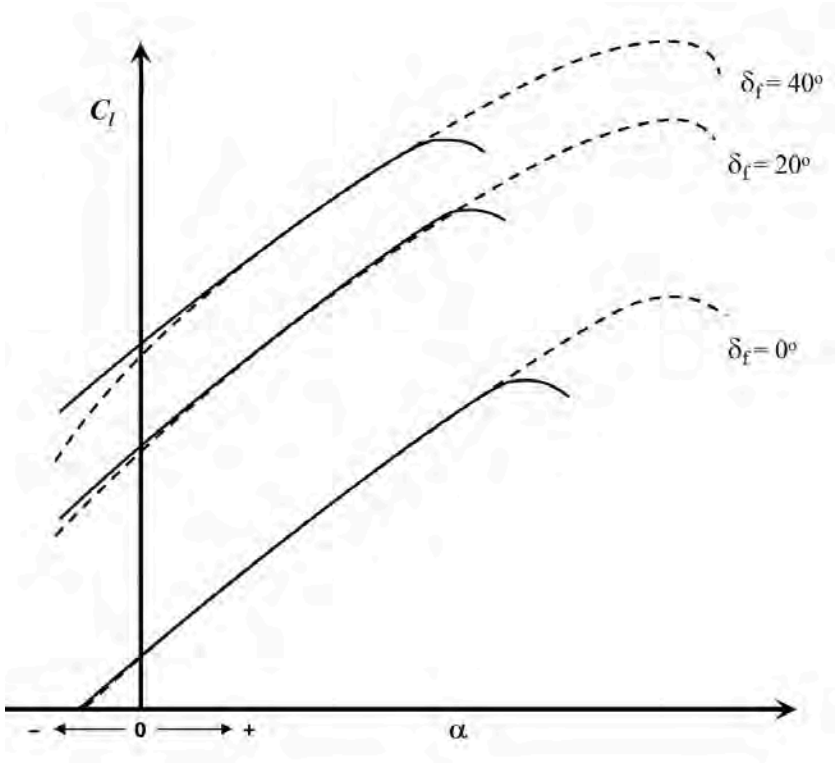


Figure 7-8: Effect of leading-edge slats on $C_{l_{max}}$. From D. Kita. Adapted by K. Grey. Fair use.

Different types of leading-edge devices differ in their effectiveness. Figure 7-9 is Kita's estimate of how each type of device increases the angle of attack and level of maximum lift. Due to the higher effectiveness of slats, they are more widely used.

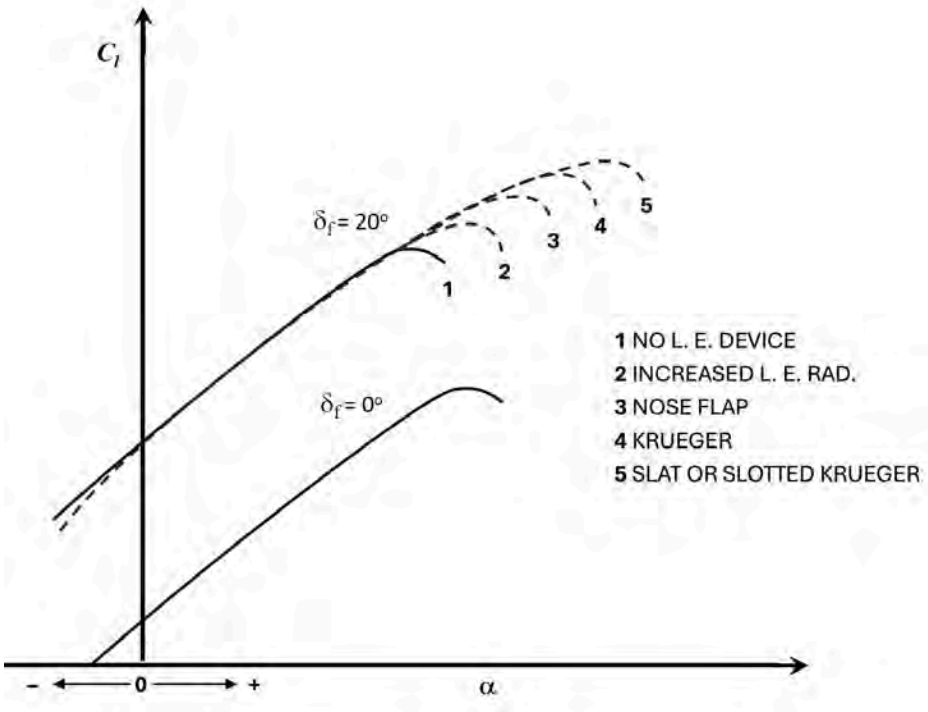


Figure 7-9: Effects of various types of leading-edge devices on $C_{l_{max}}$. From D. Kita. Adapted by K. Grey. Fair use.

Figure 7-10 shows Kita's estimate of the typical "best" performance in terms of C_{Lmax} you can get from various types of high-lift systems. You can see that sweeping the trailing edge reduces the effectiveness of all high-lift systems. The curve labeled "advanced" is typical of projections made in advanced design or aerodynamics departments, where the assumption is that an advanced technology development effort can improve the performance of any system. This may or may not be true.

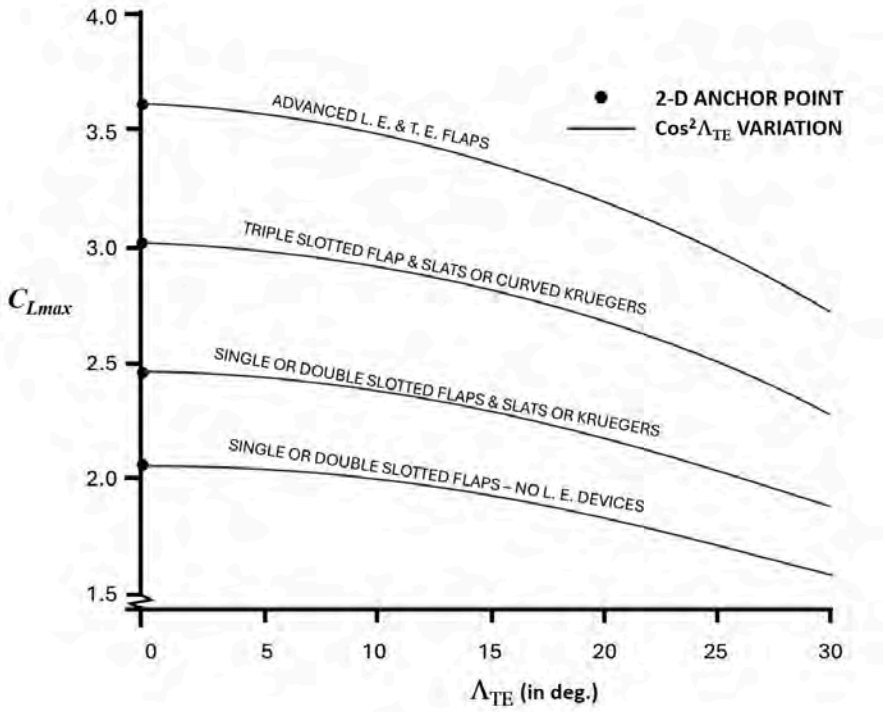


Figure 7-10: Estimated performance of various types of high-lift systems in terms of variation of C_{Lmax} with trailing-edge sweep. From D. Kita. Adapted by K. Grey. Fair use.

In addition to changing lift, flaps also cause a large change in drag, as shown in figure 7-11. Clearly, you don't want the flaps deployed at low lift. This is why flaps aren't deflected in cruise. As lift increases, there may be an optimum flap-deflection schedule; for example, the F-18's flaps are scheduled with angle of attack and Mach number. This was also done on the Grumman X-29.

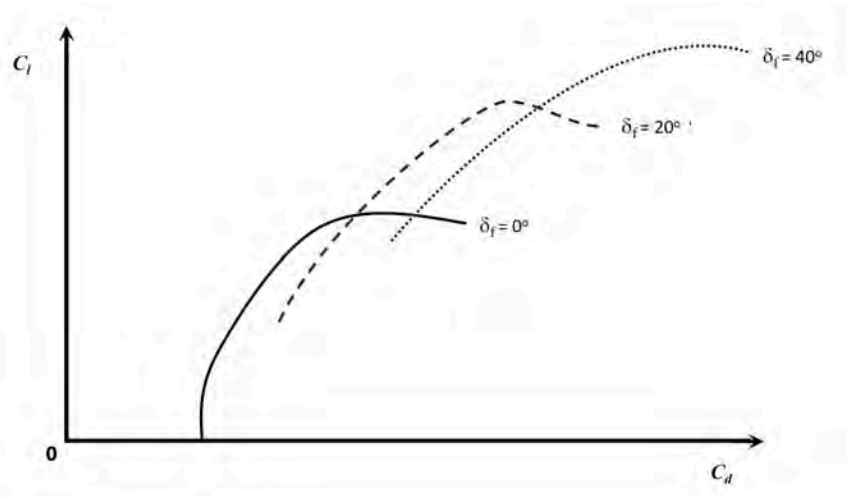


Figure 7-11: Typical drag polars illustrating the effects of flap deflections. From D. Kita. Adapted by K. Grey. Fair use.

Flap deflection also produces a large change in pitching moment, as illustrated in figure 7-12. This is an important consideration, since you need to be able to trim this pitching moment. In the case of the Beechcraft Starship, the canards actually changed sweep to be able to generate the required force. So this effect cannot be ignored in developing high-lift systems.

In developing the high-lift system, two key parameters are the selection of the gap between the flap and main element and the selection of the overlap. Figure 7-13 provides Kita's definition of these parameters. In trying to identify the values of these parameters that produce the highest lift, aerodynamicists require a lot of time for wind tunnel testing and considerable computer resources for simulations. At higher flap deflections, say 25° to 40°, flap tangency to the tangency line is secondary to gap and overlap criteria. Flap type and shape may preclude this occurrence.

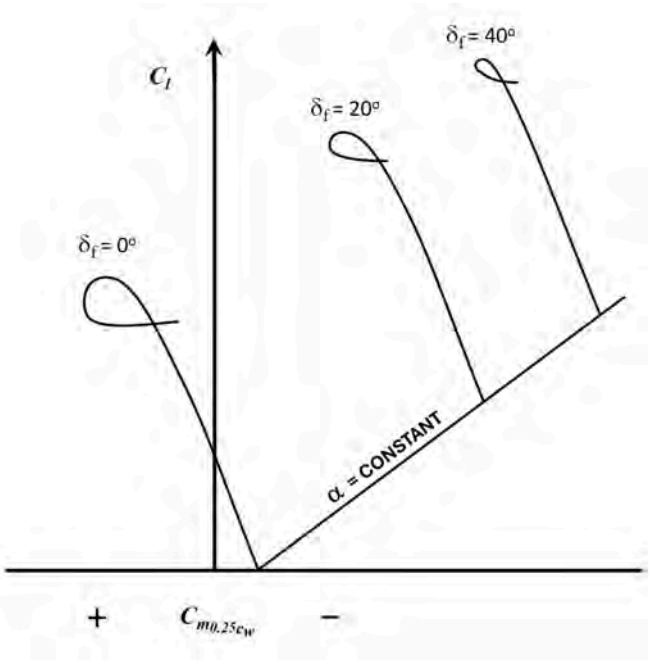


Figure 7-12: Typical effect of flap deflection on pitching moment. *From D. Kita. Adapted by K. Grey. Fair use.*

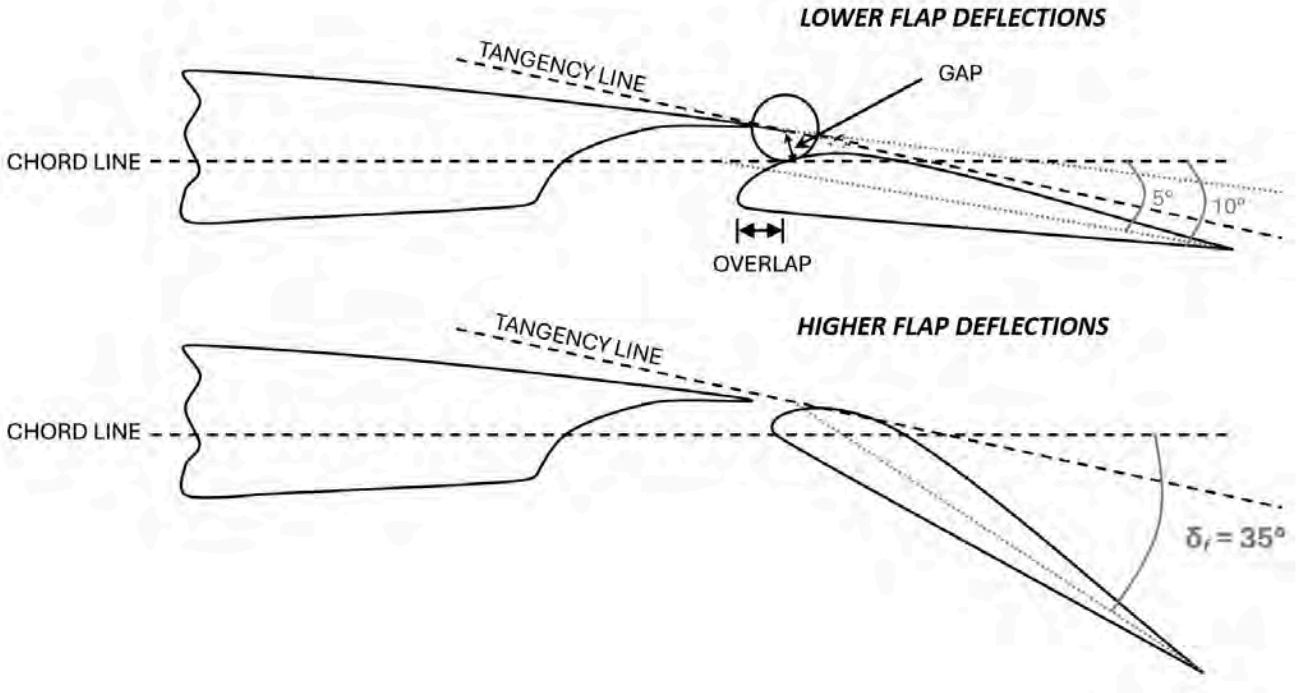


Figure 7-13: Definition of gap and overlap in Fowler-type flap layout. *From D. Kita. Adapted by K. Grey. Fair use.*

7.4 Physics of High Lift: A. M. O. Smith's Analysis of the High-Lift Aerodynamics

Now that we've surveyed the characteristics of high-lift systems, we need to examine the physical basis for the operation and limits of high-lift systems. A. M. O. Smith "wrote the book" on the physics of high-lift systems with his 1975 lecture "High-Lift Aerodynamics,"[21] which is required reading. His message? You need to carry as much lift (load) as you can on the airfoil's upper surface without separating the boundary layer. His classic paper describes the physics associated with the high-lift characteristics we described above and details how to achieve the available high-lift performance. We summarize his description here.

To obtain insight into the characteristics of pressure distributions that affect boundary layer separation, Smith introduced the use of a canonical pressure distribution. He felt strongly that this was necessary to understand and compare possible separation on different airfoils. It is essentially another type of dimensionless, or "scaled," pressure distribution. For boundary layer investigations, it is found that the best scaling factor is the velocity u_0 just before the flow deceleration begins due to rising pressure. Smith defines the canonical pressure distribution as

$$\bar{C}_p = 1 - \left(\frac{u_e}{u_0} \right)^2. \qquad (7\text{-}1)$$

Here, u_e is the velocity at the edge of the boundary layer. In this canonical system, the canonical C_p value of zero represents the start of the pressure rise and +1 is the maximum possible value, $u_e = 0$. The next step is to examine the best way to specify the pressure distribution to allow the pressure to recover to as close as possible to the canonical C_p of +1. Smith made a parametric study of various possibilities to gain insight into the best way to prescribe a pressure distribution to delay separation. However, our focus here is on his limiting case. It makes use of an analysis by Stratford [22] that was done to estimate separation before the days when boundary layer computer programs were available. Using Stratford's analysis, it is possible to define a pressure distribution where the boundary layer is just on the verge of separation everywhere. To do this, we manipulate the Stratford criteria, as seen in equation (7-2).

$$\frac{\bar{C}_p \left[x \left(d\bar{C}_p / dx \right) \right]^{1/2}}{\left(10^{-6} R \right)^{1/10}} = S \qquad (7\text{-}2)$$

Here, R is the unit Reynolds number (per unit length), defined as u_0/ν. Note that originally, Stratford used this relation to say that separation occurred when the quantity on the left-hand side of the equation reached the value of S (typically 0.35). However, we can define a canonical C_p distribution using this relation that is equal to S everywhere, just on the verge of separation, and this pressure distribution is the best way to achieve a very large pressure recovery without separation.

Figure 7-14 shows the resulting pressure distribution. Examining this pressure distribution, several key observations can be made. The initial slope is infinite and then decreases. Thus, when the boundary layer is thin, it can withstand a very large pressure gradient. As the boundary layer thickens (either when it starts to recover or as it recovers), it cannot sustain the large pressure gradient, and the pressure gradient to maintain attached flow decreases. This illustrates the idea that thick boundary layers are more likely to separate than thin boundary layers. Note also that the Reynolds number effect is relatively weak. Finally, the boundary layer could recover all the way to a canonical C_p of +1, but to attain this, x would need to go to infinity. These shapes are the best possible pressure distributions to use to recover the pressure without separating the boundary layer. As A. M. O. Smith notes, the only way to do better is to use some sort of active boundary layer control (suction or blowing).

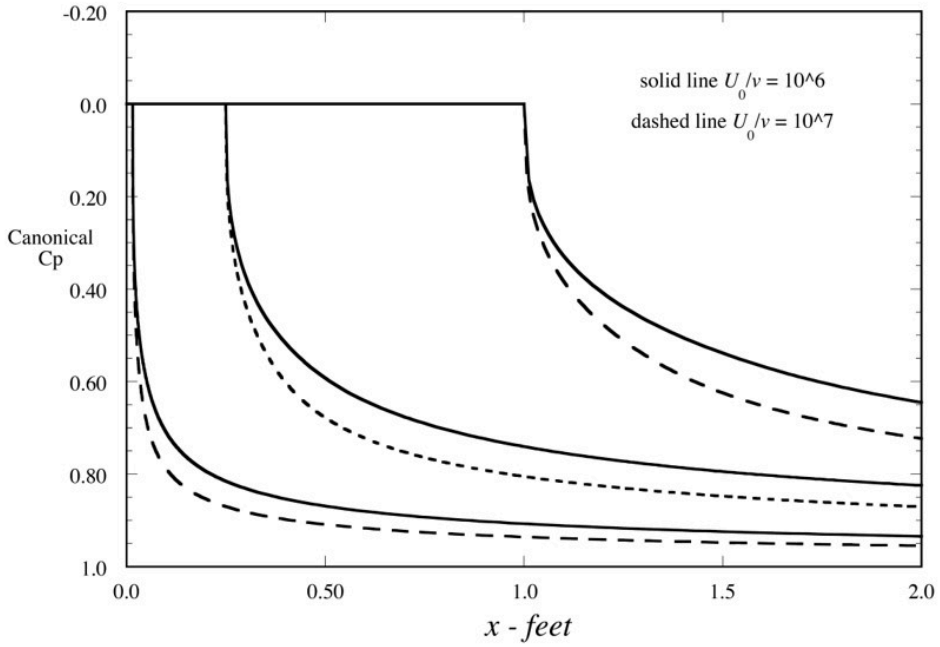


Figure 7-14: Stratford limiting flows for two different Reynolds numbers.

7.4.1 Single-Element Airfoils

The key to obtaining high lift on a single-element airfoil is essentially the inspiration for Liebeck's high-lift airfoil[23] and the Stratford "pressure recovery" shape of the pressure distribution described above, as told by Smith.[24] The question of how much lift you can obtain on a single-element airfoil involves how low the pressure can be on the upper surface and how the pressure can recover to a positive pressure coefficient at the trailing edge and keep the boundary layer attached. Smith describes two aspects of the problem. In the first case, he explains the limit of the pressure coefficient in terms of the vacuum C_p when a zero pressure is specified on the airfoil's upper surface. Thus, using the definition of C_p,

$$C_p = \frac{p - p_\infty}{\frac{1}{2}\rho_\infty U_\infty^2} \quad , \qquad (7\text{-}3)$$

we can obtain an alternate form using $q = 0.5\rho_\infty U_\infty^2 = 0.5\gamma P_\infty M_\infty^2$, giving us equation (7-4).

$$C_p = \frac{p - p_\infty}{\frac{\gamma}{2} p_\infty M_\infty^2} \qquad (7\text{-}4)$$

Vacuum C_p occurs when the pressure is zero:

$$C_{P_{\text{vac}}} = \frac{-2}{\gamma M_\infty^2} \qquad (7\text{-}5)$$

Smith points out that, at this point, only 70% of the vacuum C_p has been achieved in practice. This results in a C_p limit of $M^2 C_p = -1$ for γ of 1.4.

Next, Liebeck and Smith used the analytical analysis by Stratford illustrated above to specify a pressure distribution that allows the most lift to be obtained. Given this pressure distribution, an inverse method is used to obtain the associated airfoil shape. The result is the Liebeck family of high-lift airfoils.

7.4.2 Multi-Element Airfoils

Section 6.3 of A. M. O. Smith's conference lecture (AIAA Paper No. 74-939, 6th Aircraft Design, Flight Test and Operations Meeting, Los Angeles, California, August 12-14, 1974) is an excellent source for anyone interested in understanding the flow physics of multi-element airfoils. The foundational paper discusses five main ideas underlying flow physics:

1. **The slat effect.** The slat protects the leading edge of the main element. That's why its effect is only observed near $C_{l\max}$ of the single element. Considered a point vortex, the slat velocity acts to reduce the velocity around the leading edge of the main element.
2. **The circulation effect.** The downstream element causes the upstream element to be in a high-velocity region, inclined to its mean line. To meet the Kutta condition, the circulation has to be increased. Instead of the airfoil deflecting as a plain flap, the trailing edge is placed in an inclined flow and something else (the downstream element) turns the flow.
3. **The dumping effect.** The trailing edge of the forward element is in a region of velocity appreciably higher than the freestream velocity. Thus, the boundary layer can come off the forward element at a higher velocity. You don't have to recover back to $C_p = +0.2$ for attached flow, relieving the pressure rise on the boundary layer, alleviating separation problems, and permitting increased lift. The suction lift can be increased in proportion to U_{TE}^2 for the same margin against separation.
4. **Off-the-surface pressure recovery.** The boundary layer leaves the trailing edge faster than the freestream and now becomes a wake (a viscous phenomena). The recovery back to freestream velocity happens in an efficient manner since the deceleration of the wake occurs out of contact with the wall. Wakes withstand pressure rises that boundary layers cannot. The wake can actually "separate" out in the flow field. (*Note*: For a well designed high-lift system, the local boundary layers and wakes remain separate. If they merge, everything is more complicated.)
5. **The fresh boundary layer effect.** Thin boundary layers can sustain a greater pressure gradient than a thick boundary layer. Thus, three thin boundary layers (on three airfoil elements) are more effective than one thick boundary layer (on a single element). (*Note*: Some people combine the circulation and dumping effects and call it the "vane effect".)

7.5 Computational Methods for High Lift

Significant effort has been devoted to improving prediction capabilities for high-lift systems. As stated in the introduction, one of the best surveys is by Rumsey and Ying.[25] XFOIL[26] can be used for low-speed predictions of the maximum lift for a single-element airfoil. Experience shows that the program's predictions are slightly higher than experimental results. Figure 7-15 shows typical agreement between XFOIL and wind tunnel data for the NACA 0012 and 4412 airfoils. Although the prediction is not perfect at maximum lift, this is a remarkable capability of a code that can be run on a laptop PC.

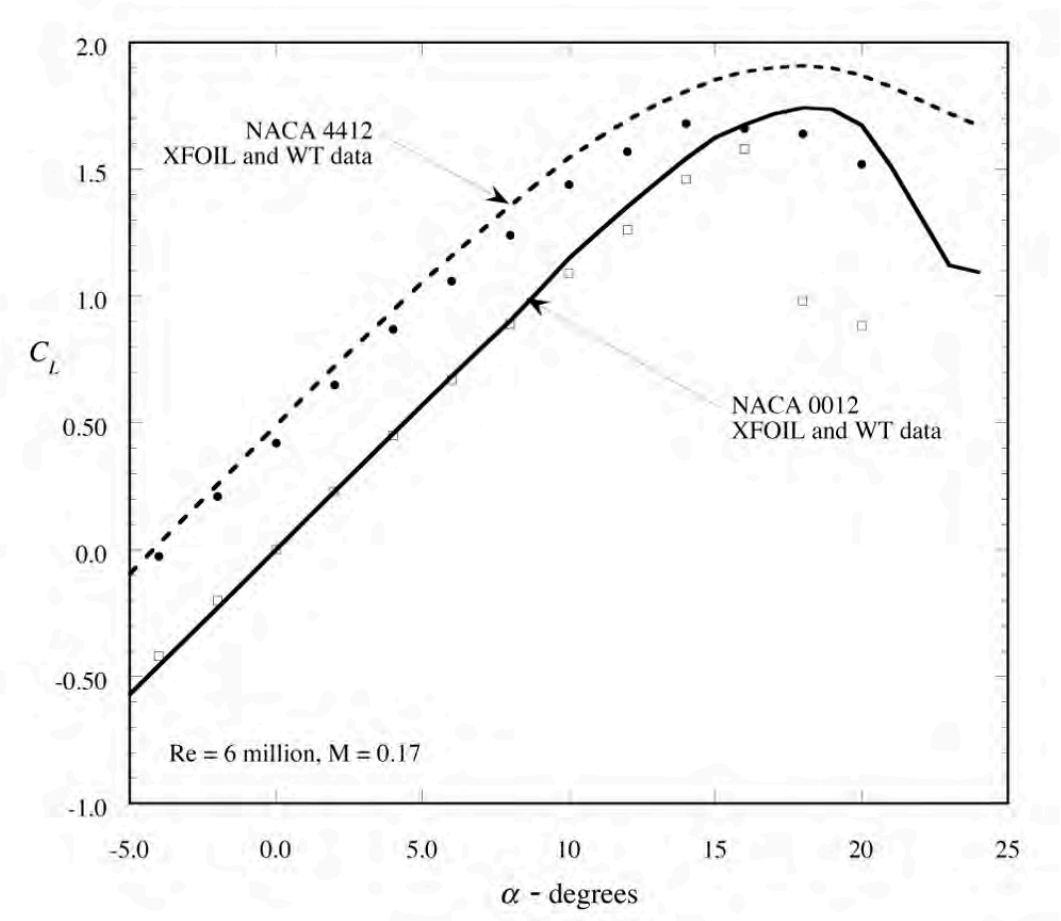


Figure 7-15: Typical agreement between XFOIL and wind tunnel data. From W. H. Mason. Calculations courtesy of D. Lurie.

7.6 Passive and Active Boundary Layer Control

7.6.1 Passive Boundary Layer Control

The boundary layer can be prevented from separating by the use of vortex generators, "snags," and fences.[27] Vortex generators (VGs) are small vanes mounted on the wing surface to produce mini-vortices that energize the boundary layer and delay separation. "Snag" is a discontinuity in the leading edge of a swept wing where an outer wing panel has an increased chord compared to the inner panel which creates a discontinuity at the junction of the inner and outer panels. A vortex is produced at the junction which delays flow separation. Fences are flat strips mounted to the surface of a swept wing at selected span stations, typically wrapping around the leading edge. The fences obstruct the spanwise airflow and thereby prevent boundary layer growth and flow separation.

7.6.2 Active Boundary Layer Control

If suction or blowing is used to suppress boundary layer separation, the blowing (which is generally preferred to suction) is known as boundary layer control (BLC); if the amount of blowing exceeds the value required for BLC, then the blowing is know as powered lift. The key parameter used to describe the amount of blowing is the blowing coefficient, which is defined as follows for 2D airfoils:

$$C_\mu = \frac{m_j V_j}{qc} \qquad (7\text{-}6)$$

where the subscript *j* refers to the jet, *m* is mass flow rate of the blowing device, *V* is the velocity of the blowing jet, *q* is the dynamic pressure, and *c* is the reference chord. Blowing-based BLC was used often in early fighters but is not used nearly as much today. The F-4 Phantom originally had blowing on both the leading edges and over the trailing-edge flap. However, to improve transonic maneuver characteristics and to improve resistance to departure, the leading-edge blowing was replaced by leading-edge slats.[28]

7.7 Powered Lift

A large variety of concepts have been tried to increase maximum lift using high-pressure air from the engine. Some examples of powered lift concepts are:

- Propeller slipstream deflection (Brequet 941/McDonnell Model 188)
- Externally blown flaps (McDonnell DouglasYC-15/C-17)
- Internally blown flaps (Lockheed F-104, Blackburn Buccaneer)
- Upper-surface blowing (Boeing YC-14, NASA QSRA, Ball-Bartoe JetWing)
- Vectored thrust (AV-8 Harrier)
- Jet flaps (Hunting H.126)
- Jet augmentor wings (NASA-deHavilland Augmentor Wing Aircraft)
- Circulation control (advocated by Hokie Bob Englar,[29] A-6 CCW)

7.8 Configuration Integration Issues

There are a few key considerations for integrating high-lift devices into your aircraft configuration:

- The best airplane $C_{L\text{max}}$ you can achieve with a mechanical high-lift system is about 3 to 3.5.
- The military and civil air regulations require a margin between $C_{L\text{max}}$ and the operating C_L of the airplane. This must be accounted for during design. For example, the approach speed must be 1.3 times the stall speed. This would suggest that the maximum approach C_L is only 59% of the $C_{L\text{max}}$. However, some relief is available because the measured stall speed, $V_{s\text{min}}$, is usually about 0.94 times the stall speed in 1 *g* steady flight (the wind tunnel case). This means that you can use a C_L of about 67% of the $C_{L\text{max}}$.[30,31]
- Increased span can be used to reduce the induced drag, so a bigger flap angle can be used before a climb limit is encountered (though this solution will increase the airplane weight).
- Sweep decreases max lift.
- In converting 2D to 3D, there are lots of losses. Don't be mislead by 2D $C_{l\text{max}}$ values, as the actual 3D value will be much less.

- The maximum C_L available for takeoff and landing for many swept-wing airplanes is actually the limit on angle of attack to avoid tailscrape.
- Engine out is much more critical with V/STOL airplanes, typically leading to a complicated engine cross-shafting arrangement to ensure uniform thrust on each side of the plane if an engine fails. The ability to do this dictates whether the concept is practical.
- The best high-lift configuration integration description also involves powered lift. The YC-14 AIAA Case Study[32] is highly recommended.

Finally, it is worth mentioning a couple more relevant issues, like the concept of the Gurney flap[33] and the need for accuracy around the leading edge. Maintaining an accurate leading edge contour is critical at high-lift conditions. Once, after a Navy depot had repainted an F-14 wing, a small ridge was left on the leading edge where the upper and lower surface paint overlapped. This was enough to cause early stall. Ed Heinemann reported a similar experience on a Douglas airplane during World War II in his autobiography.

Chapter 7 Exercises

7.1 Examine the predictive capability of XFOIL for $C_{L\max}$. Use the data from Abbott and von Doenhoff supplied previously for the NACA 0012 and 4412 airfoils at a Reynolds number of 6 million and free transition. Comment on your results.

7.2 Read A. M. O. Smith's paper on high lift. Summarize what you learned in one page. Pay special attention to the details of single- and multi-element airfoils described in sections 3 to 6.

Figure References

Figure 7-1: Adapted from D. Kita. Grumman Lecture. Feb. 1985.

Figure 7-2: Adapted from D. Kita. Grumman Lecture. Feb. 1985.

Figure 7-3: Adapted from D. Kita. Grumman Lecture. Feb. 1985.

Figure 7-4: Figure 2-47 in US Navy, "NATOPS Flight Manual Navy Model F-14B. NAVAIR 01-F14AAP-1," Aug. 2001, pp. 2–92.

Figure 7-5: D. Kita. Adapted by S. Madden. Fair use.

Figure 7-6: D. Kita. Adapted by K. Grey. Fair use.

Figure 7-7: D. Kita. Adapted by K. Grey. Fair use.

Figure 7-8: D. Kita. Adapted by K. Grey. Fair use.

Figure 7-9: D. Kita. Adapted by K. Grey. Fair use.

Figure 7-10: D. Kita. Adapted by K. Grey. Fair use.

Figure 7-11: D. Kita. Adapted by K. Grey. Fair use.

Figure 7-12: D. Kita. Adapted by K. Grey. Fair use.

Figure 7-13: D. Kita. Adapted by K. Grey. Fair use.

Figure 7.15: W. H. Mason. Calculations courtesy of David Lurie.

Notes

1. Garner, P. L., Meredith, P. T., and Stoner, R. C., "Areas for Future CFD Development as Illustrated by Transport Aircraft Applications," AIAA Paper 91-1527, 1991.
2. Brune, G. W., and McMasters, J. H., "Chapter 10: Computational Aerodynamics Applied to High Lift Systems," in *Applied Computational Aerodynamics*, edited by P. Henne, Progress in Astronautics and Aeronautics, Vol. 125, AIAA, Washington, 1990.
3. Roskam, J., and Lan, C.-T. E., *Airplane Aerodynamics and Performance*, DARcorporation, Kansas, 1997, p. 343.
4. Sanders, K. L., "High-Lift Devices, A Weight and Performance Trade-Off Methodology," Society of Allied Weight Engineers (SAWE) TP-761, May 1969.
5. Drela, M., "Design and Optimization Method for Multi-Element Airfoils," AIAA Paper 93-0969, Aerospace Design Conference, Irvine, CA, Feb. 16-19, 1993.
6. Rumsey, C. L., and Ying, S. X., "Prediction of high lift: review of present CFD capability," Progress in Aerospace Sciences, Vol. 38, pp. 145–180, 2002. (*Note*:

Articles in Progress in Aerospace Sciences are available for download through the Virginia Tech University Library if you search "Addison" and have a vt.edu address.)

7. Liebeck, R. H., "Design of Subsonic Airfoils for High Lift," Journal of Aircraft, Vol. 15, No. 9, Sept. 1978, pp. 547–561.
8. Smith, A. M. O., "High-Lift Aerodynamics," 37th Wright Brothers Lecture, Journal of Aircraft, Vol. 12, No. 6, Jun. 1975. https://doi.org/10.2514/3.59830
9. Smith, A. M. O., "High-Lift Aerodynamics," 37th Wright Brothers Lecture, Journal of Aircraft, Vol. 12, No. 6, Jun. 1975. https://doi.org/10.2514/3.59830
10. Van Dam, C. P ., "The aerodynamic design of multi-element high-lift systems for transport airplanes," Progress in Aerospace Sciences, Vol. 38, pp. 101–144, 2002.
11. Rudolph, P. K. C., "High-Lift Systems on Commercial Subsonic Airliners," NASA CR-4746, Sept. 1996.
12. Kita, D., "Mechanical High Lift Systems," Grumman Aerodynamics Lecture Series, Grumman Aerospace Corporation, Feb. 1985.
13. Van Dam, C. P., Vander Kam, J. C., and Paris, J. K., "Design-Oriented High-Lift Methodology for General Aviation and Civil Transport Aircraft," Journal of Aircraft, Vol. 38, No. 6, Nov.-Dec. 2001, pp. 1076–1084.
14. Nield, B. N., "An overview of the Boeing 777 high lift aerodynamic design," The Aeronautical Journal, Vol. 99, No. 989 (Special issue on high lift and separation control), Nov. 1995, pp. 361–371.
15. Gratzer, L. B., "Analysis of Transport Applications for High Lift Schemes," AGARD Lecture Series: Assessment of Lift Augmentation Devices, AGARD LS-43, 1971.
16. Korbacher, G. K., "Aerodynamics of Powered High-Lift Systems," Annual Review of Fluid Mechanics, Vol. 6, 1974. pp. 319–358.
17. Hoerner, S. F., and Borst, H. V., *Fluid Dynamic Lift*, 2nd ed., Jun. 1992. (*Note*: Available from Hoerner Fluid Dynamics, PO Box 21992, Bakersfield, CA 93390.)
18. McCormick, B. W., Jr., *Aerodynamics of V/STOL Flight*, Dover, 1999.
19. Shevell, R. S., *Fundamentals of Flight*, 2nd ed., Prentice-Hall, 1989.
20. McMasters, J. H., and Mack, M. D., "High Reynolds Number Testing in Support of Transonic Airplane Development (Invited Paper)," AIAA Paper 92-3982, 17th Aerospace Ground Testing Conference, Nashville, TN, Jul. 6-8, 1992.
21. Smith, A. M. O., "High-Lift Aerodynamics," 37th Wright Brothers Lecture, Journal of Aircraft, Vol. 12, No. 6, Jun. 1975. https://doi.org/10.2514/3.59830
22. Stratford, B., "The prediction of separation of the turbulent boundary layer," Journal of Fluid Mechanics, Vol. 5, No. 1, 1959, pp. 1–16.
23. Liebeck, R. H., "Design of Subsonic Airfoils for High Lift," Journal of Aircraft, Vol. 15, No. 9, Sept. 1978, pp. 547–561.
24. Smith, A. M. O., "High-Lift Aerodynamics," 37th Wright Brothers Lecture, Journal of Aircraft, Vol. 12, No. 6, Jun. 1975. https://doi.org/10.2514/3.59830
25. Rumsey, C. L., and Ying, S. X., "Prediction of high lift: Review of present CFD capability," Progress in Aerospace Sciences, Vol. 38, pp. 145–180, 2002.
26. Drela, M. "XFOIL: An Analysis and Design System for Low Reynolds Number Airfoils," in *Low Reynolds Number Aerodynamics*, edited by T. J. Mueller, Lecture Notes in Physics, #54, Springer-Verlag, 1989.
27. Mabry, D. G., "Design features which influence flow separations on aircraft," The Aeronautical Journal. Vol. 92, No. 920, Dec. 1988, pp. 409–415.
28. Bennett, D. H., and Rousseau, W. A., "Seven Wings the F-4 Has Flown," AIAA Paper 80-3042, Evolution of Aircraft Wing Design Symposium, Dayton, OH, Mar. 1980.
29. Englar, R. J., Smith, M. J., Kelley, S. M., and Rover, R. C., III, "Development of circulation control technology for application to advanced subsonic transport aircraft," AIAA Paper 93-0644, 31st Aerospace Sciences Meeting, Reno, NV, Jan. 11-14, 1993.
30. Van Dam, C. P., "The aerodynamic design of multi-element high-lift systems for transport airplanes," Progress in Aerospace Sciences, Vol. 38, pp. 101–144, 2002.
31. Flaig, A., and Hilbig, B., "High-lift design for large civil aircraft," in "AGARD High-Lift System Aerodynamics," AGARD CP-515, Sept. 1993.
32. Wimpress, J. K., and Newberry, C. F., "The YC-14 STOL Prototype: Its Design, Development, and Flight Test," AIAA Case Study, AIAA, Reston, 1998.
33. Liebeck, R. H., "Design of Subsonic Airfoils for High Lift," Journal of Aircraft, Vol. 15, No. 9, Sept. 1978, pp. 547–561.

8. High-Angle-of-Attack (High-α) Aerodynamics

High-angle-of-attack (high-α) aerodynamics is inherently associated with:

- Separated flows (and thus nonlinear aerodynamics)
    - One of the key aspects is the interaction of components—vortex flows in particular (since vortex bursting is also an important effect).
- Heavy dependence on wind tunnel testing
- Flight simulation to ensure good handling qualities
    - This means that large amounts of data have to be acquired to construct the mathematical models of aerodynamics.

The key tutorials and surveys on high-angle-of-attack aerodynamics were written by Chambers and Grafton[1] and later by Chambers on his own.[2] Typical high-α issues and concerns for three classes of aircraft are highlighted below. Addressing them requires a good understanding of the high-α aerodynamic characteristics of the aircraft.

General aviation aircraft

- *Prevention/recovery from spins.* To improve spin resistance, consider the drooped outer panel (NASA LaRC) or the interrupted leading edge (NASA Ames). Do consider placing the vertical tail where it can get "good" flow during a spin, including inclining the rudder hinge line forward rather than aft. It will make it more effective. Also, placing a ventral strake ahead of the rudder, as seen on many general aviation (GA) airplanes, not only adds side area but also produces a vortex at sideslip that helps maintain the entire surface effectiveness. Finally, *do not* use the tail-damping power factor (TDPF) available in the old NACA literature. It is known not to work. Folklore has it that T-tail configurations may have a benefit; the vertical tail and rudder may not be blocked by the wake of the horizontal tail. This may or may not be true.

Fighters

- Resistance to departure from controlled flight
- Ability to control aircraft at high-α air combat maneuvering[3]
- Allowance for unlimited α range (the F-16 requires an angle of attack limiter)
- Requirement to be able to perform velocity vector rolls[4] (through inertial coupling, this adds additional nose-down pitching moment requirement)
- Perform the Herbst maneuver (causing a rapid change of heading but also losing a lot of energy, so in a multiple engagement, you may become a sitting duck for someone else)
- Fuselage pointing to allow missile lock-on and fire
- Use of the control system to enhance maneuver capability
- Controls enhanced using thrust vectoring (possibly especially important for stealth a/c).
    - Well known high-angle-of-attack research aircraft: F-18 HARV (thrust vectoring with vanes), X-31 (thrust vectoring with vanes), X-29 (no. 2 had nose blowing)
- Supermaneuverability and aircraft agility are of major interest for advanced fighter design. This requires the use of dynamic measures to assess performance. Supermaneuverability seeks to exploit an unsteady flow effect—the fact that you can get higher C_{Lmax}'s by so-called dynamic overshoot.

Transports

- As discussed previously in terms of basic transport configuration aerodynamics, the primary high-α problem is the suppression and control of pitchup and avoidance of deep stall. The case study of the DC-9's development provides an excellent overview of the issues with the T-tail configuration and the stall issues in general.

8.1 Basic Aerodynamics of High-α

8.1.1 Longitudinal

The basic aerodynamic characteristics are illustrated in figure 8-1. This is a notional pitching moment curve. For modern airplanes, the stability may not be a major issue (within reason), but the envelope defining the maximum nose-up and nose-down moments that can be generated is critical, and the minimum value of nose-down pitching moment is a critical condition.

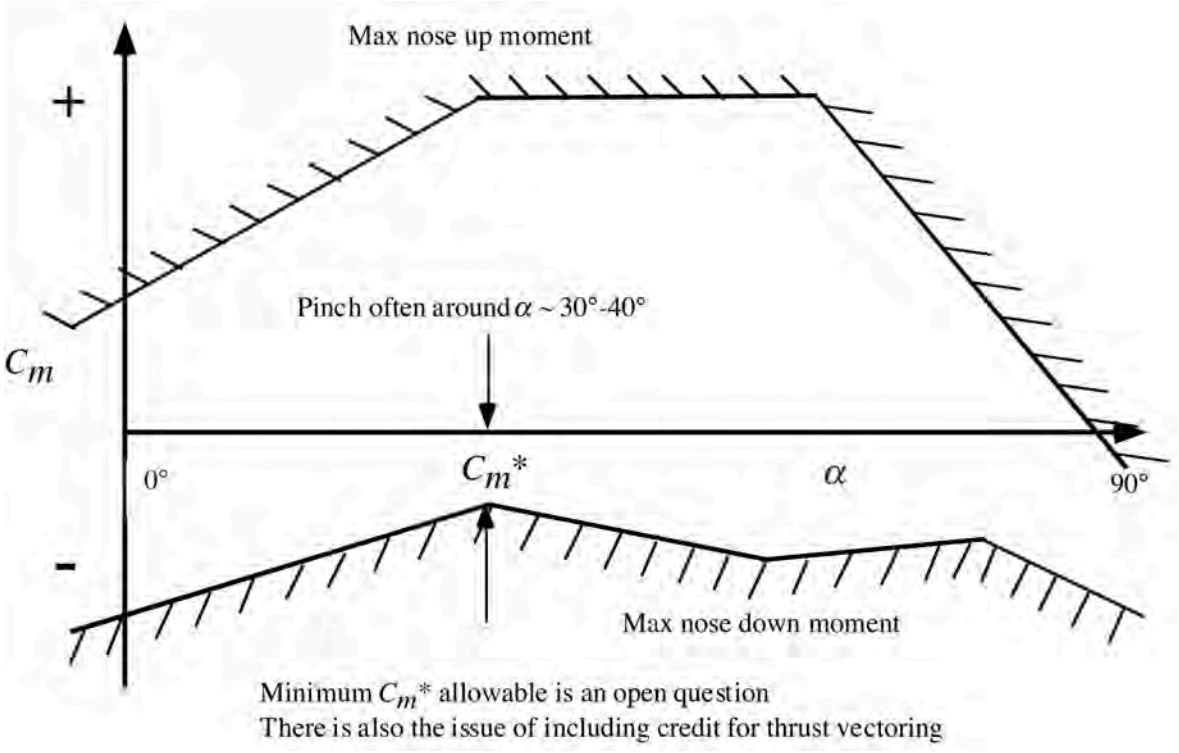


Figure 8-1: Typical example of pitching moment assessment chart (notional). *From W. H. Mason. Adapted by P. Raj.*

Wind tunnel data[5] for the F-16 contained in figure 8-2 shows that, for this CG location, the F-16 is limited in angle of attack (AOA) at which it can be trimmed to obtain $C_m = 0$. Thus the control system is designed to limit the angle of attack that the F-16 can reach to prevent the airplane from encountering a problem. This reference is a classic study and includes detailed aerodynamic math model data.

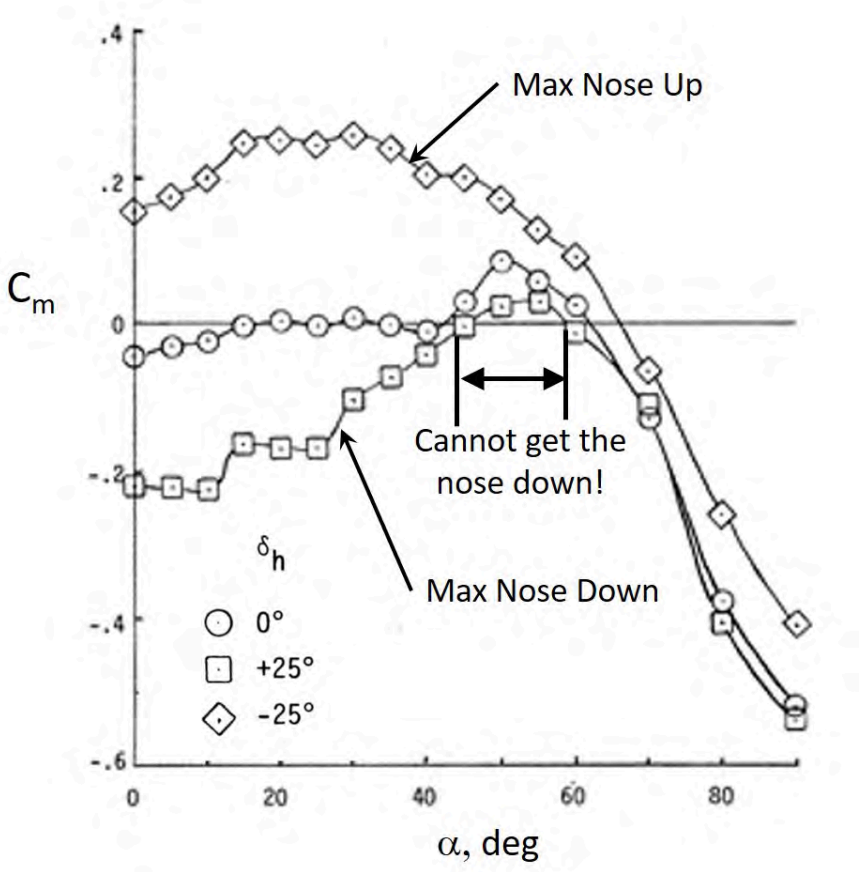


Figure 8-2: Pitching moment wind-tunnel data for the F-16. From L. T. Nguyen, M. E. Ogburn, W. P. Gilbert, K. S. Kibler, P. W. Brown, and P. L. Deal. "Simulator Study of Stall/Post-Stall Characteristics of a Fighter Airplane With Relaxed Static Stability." NASA. Public domain. Adapted.

The following values of suggested design criteria for nose-down pitching moment were developed by Marilyn Ogburn and John Foster at NASA Langley, supported by the Navy.[6] These are design goals for modern maneuvering aircraft.

	Pitch accel in 1st second (rad/sec^2)	Minimum pitch rate at 2 sec & after command input (deg/sec)
Desirable	-0.25	-24.0
Safety	-0.07	-5.0

Table 8-1: Suggested design criteria for nose-down pitching moment

8.1.2 Lateral/Directional

The typical directional characteristics are assessed in terms of the directional stability, $C_{n\beta}$. Figure 8-3 provides the generic expectation, while figure 8-4 contains wind tunnel results for an F-5.[7] Initially the vertical tail provides the stability. However, at angles of attack where the wake from the wing prevents the tail from operating in clean flow, the vertical becomes ineffective. At higher angles of attack, the long forebody on modern fighters can be designed to provide direction stability.

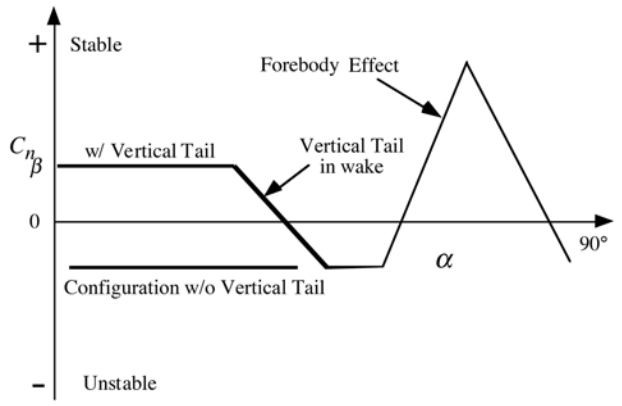


Figure 8-3: Generic directional aerodynamic characteristics. *From W. H. Mason. Adapted by P. Raj.*

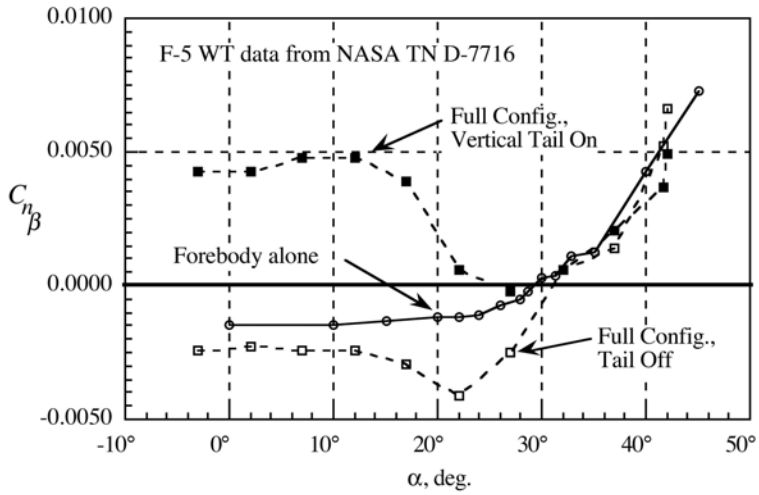


Figure 8-4: Directional characteristics of the F-5. *From S. Grafton, J. Chambers, and P. Coe, Jr. "Wind-Tunnel Free-Flight Investigation of a Model of a Spin-Resistant Fighter Configuration." NASA. Public domain.*

Figure 8-5 shows the generic characteristics for lateral characteristics, which is examined in terms of C_{l_β}. Initially, wing dihedral or sweep will cause the stability derivative to decrease with angle of attack. However, in a swept-wing situation, asymmetric flow separation characteristics cause the curve to "break" and abruptly become positive.

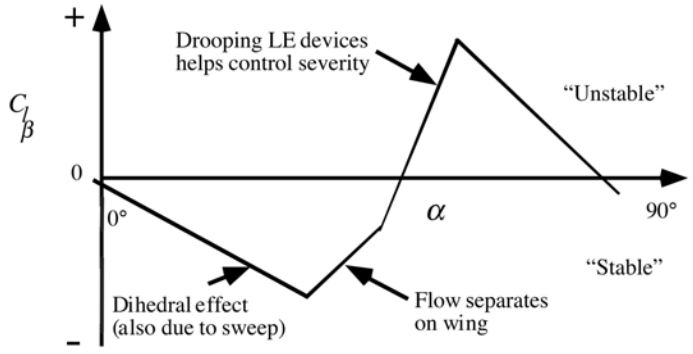


Figure 8-5: Generic lateral aerodynamic characteristics. *From W. H. Mason. Adapted by P. Raj.*

Figure 8-6 contains actual characteristics of an F-4, with the effects of the maneuvering slats, which are seen to be extremely beneficial.[8]

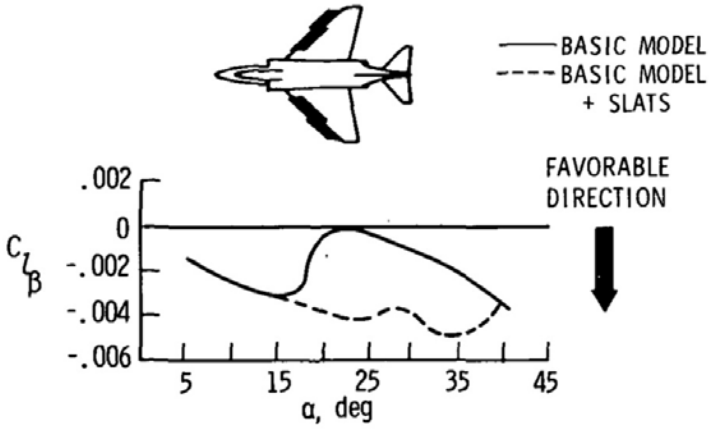


Figure 8-6: Lateral characteristics of the F-4, including the effects of the maneuver slats.
From E. Ray, L. W. McKinney, and J. G. Carmichael. "Maneuver and Buffet Characteristics of Fighter Aircraft." NASA. Public domain.

These characteristics are used to establish the basic lateral-directional static stability. One of the complications associated with canard aircraft is the wide variation in these characteristics based on canard setting. The trailing vortex system from the canard interacts with the leading-edge vortices of the main wing, forebody vortices, and also the vertical tail. Thus the lateral-directional characteristics of canard configurations play a large role in deciding if a canard configuration is practical. Recall that for classical static stability:

- Directional stability (must be in the stability axis): $C_{n\beta} > 0.0$
- Dihedral effect (also promoted by wing sweep): $C_{l\beta} < 0.0$

8.2 Flight Mechanics of High-α

Controllability of flight at high angle of attack can encounter several different types of problems.[9] Here are some brief descriptions of terms you are likely to encounter.

- *Departure:* This occurs when the airplane departs controlled flight. It may develop into a spin.
- *Wing drop:* A roll-type problem caused by asymmetric wing stall (or unstall).
- *Wing rock:* The aerodynamic rate-damping moments become negative, and the wing starts to oscillate in roll. This is associated with an interaction of the separated flow above the wing, typically the leading-edge vortices that are above the wing.
- *Nose slice:* When the aerodynamic yaw moments exceed the control authority of the rudder, the airplane will tend to exceed the acceptable sideslip angle and depart through a yawing motion (making this a yaw-type problem).

The basic aerodynamic characteristics described above are often used to try to assess, at least approximately, how susceptible the aircraft is to departure. In reality, you also need dynamic aerodynamic characteristics, but these are usually not available early in the design process. Some static derivative-based dynamic criteria are available to provide guidance. Greer[10] provided a summary of directional data for numerous aircraft, as well as a very easy-to-read description of the departure problem as it changed from piston fighters to high-speed swept-wing jet fighters. Greer's report contains nominal characteristics of the following aircraft: XP-92, YF-102, XF4D-1, F-8, F-86D, Mig 15, Bell D-188A, X-15, A-7, F-4E, F-111, F-5, XB-58, Winged Missile, Lockheed SST, the initial Boeing SST B2707, and NASA Generic SST.

In his 1972 paper, Greer wrote:

> In the late 1940s low-aspect-ratio swept-wing fighter configurations began to emerge, and it soon became apparent that they would behave very differently at the stall than their predecessor straight-wing configurations. Whereas straight-wing configurations generally experienced a roll-off type of divergence at the stall because of one wing dropping before the other and unstable damping in roll immediately after stall, the swept-wing configurations began to show a directional divergence at high angles of attack.

Thus, it appeared that both $C_{n\beta}$ and $C_{l\beta}$ were important. Greer went on to explain:

> A theoretical analysis group headed by Leonard Sternfield, then of Langley, studied the problem and concluded that the divergences occurred when the C-term of the stability quartic became negative and they developed a simplified form of the C-term and called it $C_{n\beta_{dyn}}$, or the directional stability parameter. The derivation of this parameter is given in the appendix.

Greer's report shows the correlation of various aircraft data with the directional stability parameter. The reasonable correlation showed that this parameter could be used to estimate when aircraft departure would become likely. Note that Lutze et al.[11] show how this parameter can be derived in very general terms. The discussion of $C_{n\beta_{dyn}}$ by Calico[12] is also useful.

8.2.1 Directional Stability Parameter, $C_{n\beta_{dyn}}$

According to Johnston and Heffley,[13] $C_{n\beta_{dyn}}$ may not be a highly precise predictor of aircraft departure, only approximate. Its target value should be positive, as shown in equation (8-1).

$$C_{n_{\beta_{dyn}}} > 0 \qquad (8\text{-}1)$$

where

$$C_{n_{\beta dyn}} = C_{n_\beta} \cos\alpha - \left(\frac{I_z}{I_x}\right) C_{l_\beta} \sin\alpha. \qquad (8\text{-}2)$$

This is an open-loop parameter. To improve resistance to directional divergence, Greer suggested increasing the vertical tail size ($C_{n\beta}$) and using leading edge slats ($C_{l\beta}$). The vertical tail size was increased in the case of the F-100 aircraft. Just looking at pictures of the original design give the impression that the tail was too small. However, since the vertical tail loses effectiveness at high angle of attack, this by itself is not sufficient.

8.2.2 The Lateral Control Divergence Parameter (LCDP)

LCDP is a "good predictor" according to Johnston and Heffley[14] and shown in equation (8-3).

$$LCDP = C_{n\beta} - C_{l_\beta}\left(\frac{C_{n_{\delta a}}}{C_{l_{\delta a}}}\right) > 0 \qquad (8\text{-}3)$$

Negative values imply roll reversal, where the pilot commands roll in one direction, and the plane rolls the other way!

This is a closed-loop parameter. To improve this value, the control system can be used to include the use of the rudder at high angle of attack. This approach, known as an aileron-rudder interconnect (ARI), can dramatically improve the value of LCDP at high angle of attack.

Figures 8-7 and 8-8 show the lateral-directional characteristics of the F-16 aircraft, together with $C_{n\beta dyn}$ and LCDP.[15] Figure 8-8 shows the significant effect the ARI has on LCDP.

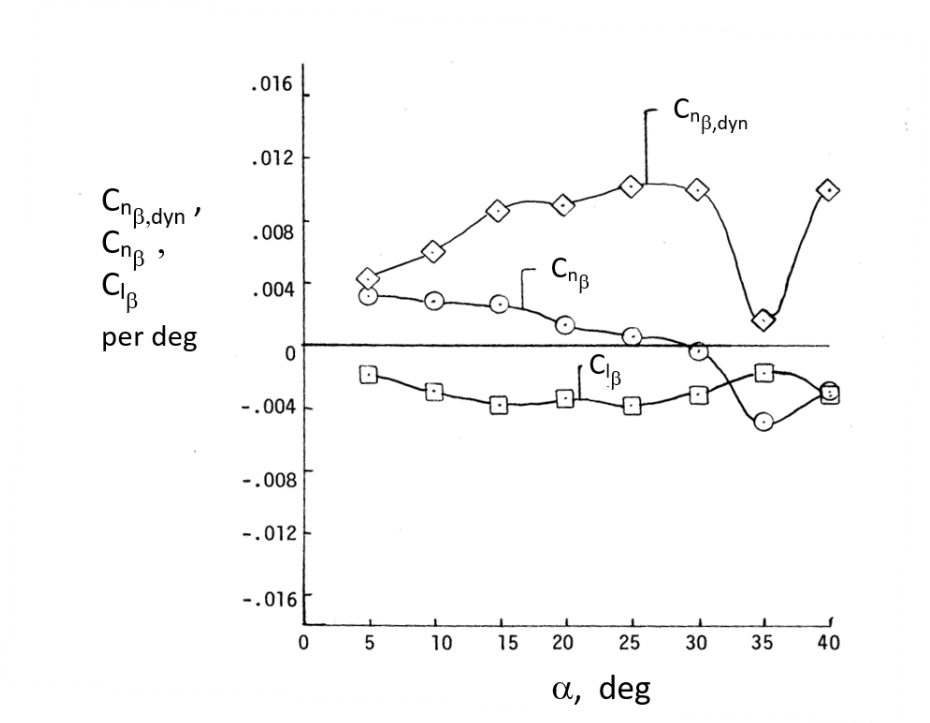


Figure 8-7: Variation of lateral-directional stability characteristics of the basic F-16 configuration with angle of attack for scheduled leading-edge flap deflection of 0°. From L. T. Nguyen, M. E. Ogburn, W. P. Gilbert, K. S. Kibler, P. W. Brown, and P. L. Deal. "Simulator Study of Stall/Post-Stall Characteristics of a Fighter Airplane With Relaxed Static Stability." NASA. Public domain. Labels adapted.

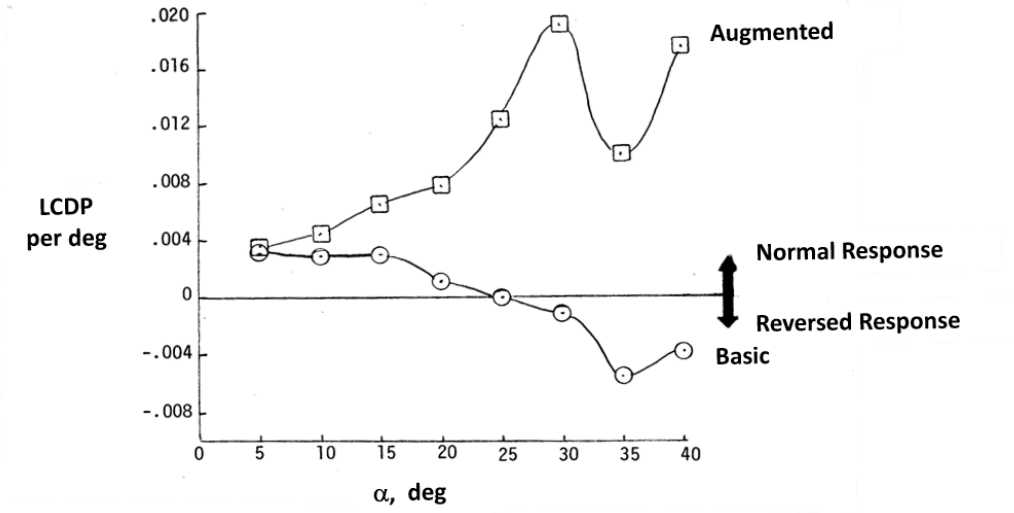


Figure 8-8: Variation of lateral control divergence parameter (LCDP) with angle of attack from the F-16 wind-tunnel test data. From L. T. Nguyen, M. E. Ogburn, W. P. Gilbert, K. S. Kibler, P. W. Brown, and P. L. Deal. "Simulator Study of Stall/Post-Stall Characteristics of a Fighter Airplane With Relaxed Static Stability." NASA. Public domain. Labels adapted.

Some effort has been made to correlate the values of these parameters to define regions in which something can be said about departure characteristics. These parameters have been combined to suggest the best region to operate in the design space. The original chart is derived from Weissman,[16] but Bill Bihrle added some more details,[17] leading to the chart shown in figure 8-9.

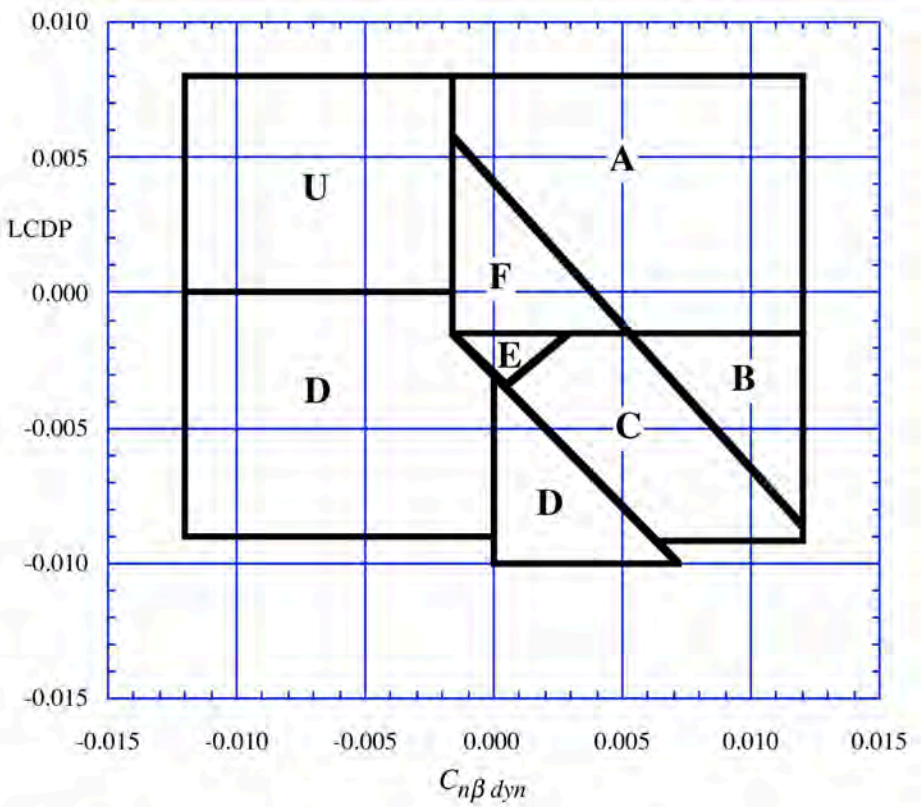


Figure 8-9: The Integrated Bihrle–Weissman chart. From W. Bihrle, Jr. and B. Barnhart. "Design Charts and Boundaries for Identifying Departure Resistant Fighter Configurations." NADC. Public domain.

Other requirements:

- Dynamic derivatives (generally from forced oscillation testing):
  - C_{nr} < 0.0 (yaw damping) not too pro spin
  - C_{lp} < 0.0 (roll damping) < 0 to prevent wing rock

8.2.3 The Spin

If the departure develops into a spin, there are a few things that are known.

First, the mechanics depend on the sign of the term ($Ix - Iy$).

- If ($Ix - Iy$) > 0, the plane is said to be wing heavy (typically GA airplanes).
- If ($Ix - Iy$) < 0, the plane is said to be fuselage heavy (typically modern supersonic fighters).

There are also some rough guidelines to recover from a spin:

- If ($Ix - Iy$) > 0, ailerons are applied *against* the spin, elevator down.
- If ($Ix - Iy$) < 0, ailerons are applied *with* the spin.

A key survey on spins is again by Chambers[18] and should be studied for further insight.

8.3 Control Effectiveness With Angle of Attack

Control effectiveness tends to diminish as the angle of attack increases. This is especially true for the ability to generate yawing moment. Figure 8-10 shows the reduction in control forces with angle of attack for the same F-16 wind tunnel test illustrated previously.[19] Note that this reference is a classic study that includes detailed aerodynamic math model data.

Figure 8-11 shows a somewhat novel way of generating yawing moment for a supersonic tactical aircraft configuration (STAC) using differential canard deflections to make up for the loss of rudder effectiveness.[20] Here, differential tail is also used to make up for the rudder.

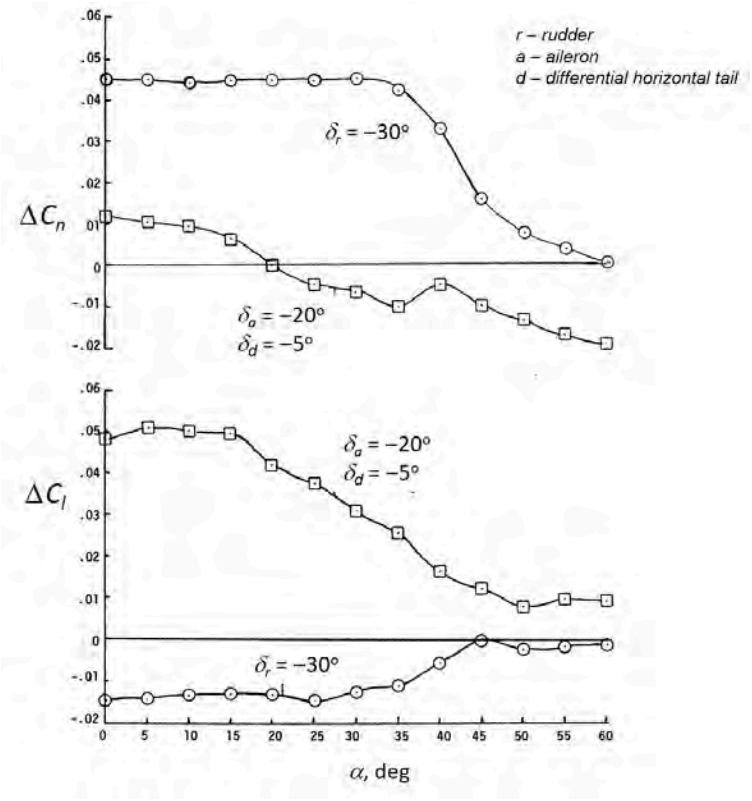


Figure 8-10: Control effectiveness loss as angle of attack increases for the F-16. From L. T. Nguyen, M. E. Ogburn, W. P. Gilbert, K. S. Kibler, P. W. Brown, and P. L. Deal. "Simulator Study of Stall/Post-Stall Characteristics of a Fighter Airplane With Relaxed Static Stability." NASA. Public domain. Labels adapted.

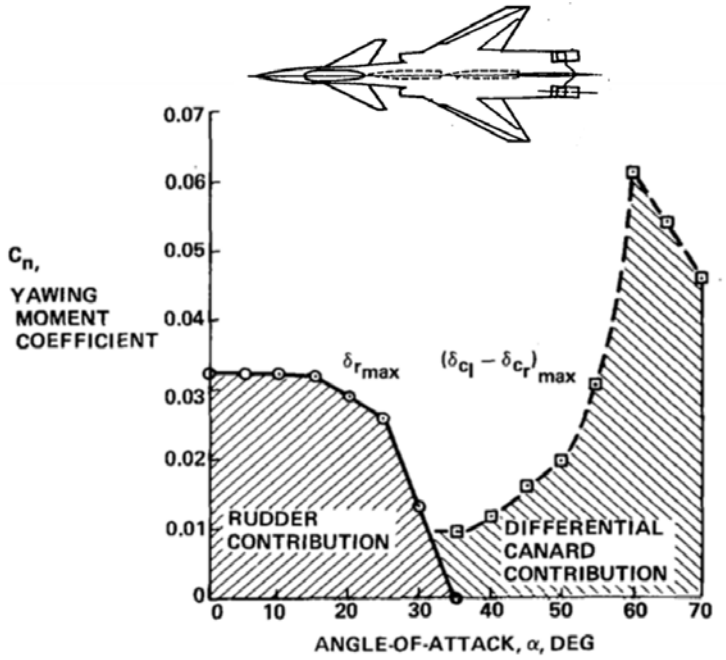


Figure 8-11: Yawing moment from rudder and differential canard on the supersonic tactical aircraft configuration (STAC). From M. Lapins, P. Martorella, R. W. Klein, R. C. Meyer and M. J. Sturm. "Control Definition Study for Advanced Vehicles." NASA. Public domain.

Thrust vectoring can also play an important role in providing control power at high angles of attack. This also means that the thrust must be provided so as to create a moment arm. Sometimes this is a problem, preventing the use of deflected thrust to be used for trimmed lift.

8.4 The F-22: Putting It All Together (An Example)

The F-22 is one of the more recent airplanes to require high-angle-of-attack capability. Charles M. Wilson from Lockheed Martin gave a talk at Virginia Tech in November 1996 called "High Angle of Attack Design Considerations." The main purpose was to give the attendees an appreciation for integrating high-angle-of-attack (high-α) flight into the F-22 external configuration (or the outer mold line). Charlie left a copy of the charts he used in his discussion of the high-α development effort. He used examples of wind tunnel data for YF-22 (the prototype configuration) to present design considerations for forebodies and vertical tails of the F-22. He showed the effect of the leading-edge flap (LEF) schedule on the lateral-directional characteristics and the nose-down pitching moment across the angle-of-attack range, including the effect of thrust vectoring. Finally, he presented the maximum roll rate as a function of angle of attack, also showing the significant benefit of thrust vectoring using comparisons with the F-15. Images and narratives from selected slides from his presentation are shown in figures 8-12 through 8-15. A related paper on the YF-22 is by Clark and Bernens.[21]

Figure 8-12 shows a perspective view of the F-22 configuration that illustrates blended-wing body shaping for stealth with integrated propulsion for supercruise capability. The figure shows flight control surfaces, their no-load rates, and deflection limits. For example, the ailerons have a no-load rate of 70° per second and a deflection limit of ±25°. Horizontal tails are primarily for longitudinal control with considerable assistance from thrust vectoring at lower speeds. Leading-edge flap, flaperon, and ailerons are scheduled with angle of attack and Mach number to improve performance, stability, and control. Flaperon, aileron, and differential horizontal tail combine for roll control with leading-edge flap added at moderate angles of attack. Rudder power is augmented at high angles of attack by differential horizontal tail and nonsymmetric aileron/flaperon. Instead of a dedicated speed brake, the aircraft combines up-deflected aileron, down-deflected flaperon, and outboard rudder to increase drag, using horizontal tails to trim.

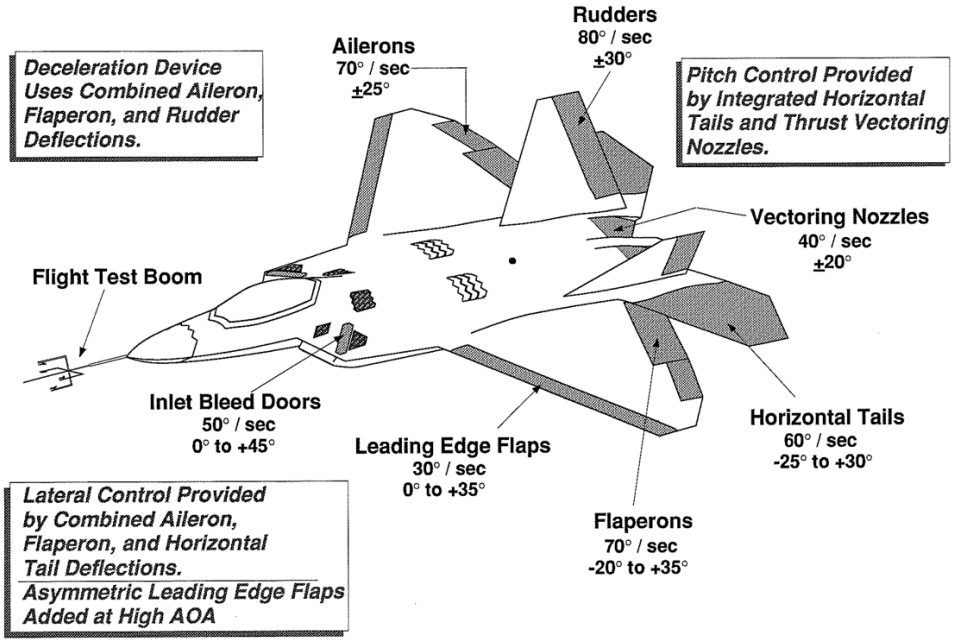


Figure 8-12: F-22 flight control surfaces. *From C. M. Wilson, LMAS. "High Angle of Attack Design Considerations" seminar. Reprinted with permission under CC BY-NC-SA 4.0.*

Figure 8-13 illustrates enhancement of YF-22 maneuvering capability by thrust vectoring. The longitudinal benefits of thrust vectoring are substantial at high angles of attack, where control power can be maintained equivalent to that achieved at low angles of attack. As AOA increases, aerodynamic controls such as the horizontal tail lose effectiveness. Jet-induced effects contribute a significant portion of the pitching moment due to vectoring. Since the YF-22 propulsion system does not have afterburning (A/B) capability, thrust vectoring supports pitch rates of at least 20° per second to be generated even when initiated from 120 KEAS and 24° per second, whereas an F-16 can only generate 4° per second nose-up pitch rate. Typical pitch characteristics break stable at some AOAs. The nose can no longer be held above the AOA where full nose-up control crosses the pitch axis to the nose-down side. Without A/B, thrust vectoring extends the controllable AOA range by about 20°. However, if you rely on thrust vectoring, remember that the engines may be at idle thrust and you need confidence that the engine will keep running, which isn't always a sure thing at high-α.

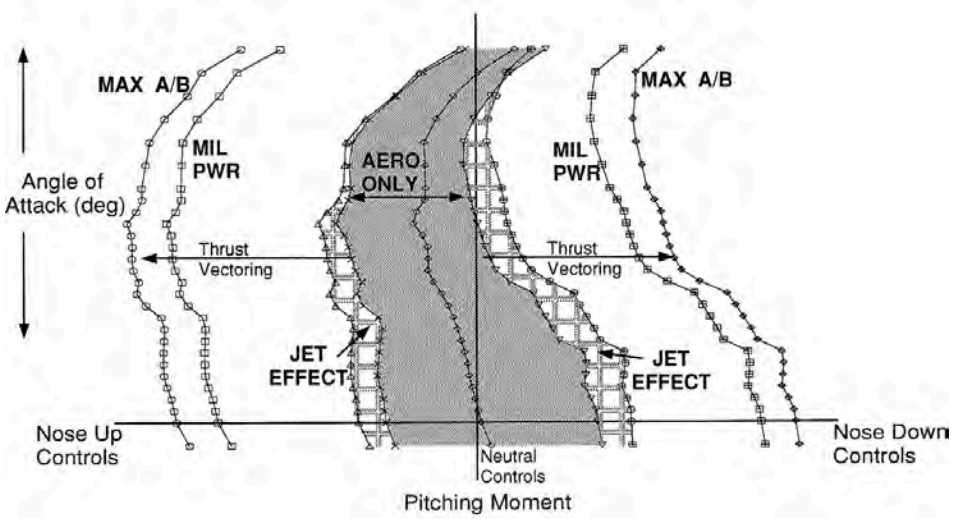


Figure 8-13: YF-22 high-angle-of-attack maneuverability enhanced by thrust vectoring as shown by increased range of nose-up and nose-down pitching moments at a given angle of attack as compared to aerodynamic controls alone. *From C. M. Wilson, LMAS. "High Angle of Attack Design Considerations" seminar. Reprinted with permission under CC BY-NC-SA 4.0. Adapted.*

Figure 8-14 provides strong evidence that leading-edge flaps (LEFs) are indispensable for high-α flights. With proper scheduling, they smooth out nonlinearities in pitch characteristics, as shown in figure 8-14(a). This helps decrease gains in longitudinal control laws. LEFs can be scheduled to improve lateral-directional stability, as shown in figures 8-14(b) and (c). They provide additional roll and anti-spin control power at moderate-to-high angles of attack. In addition, LEFs allow the wing camber to be tailored to maximize performance and improve control effectiveness of trailing-edge devices. They can also be a resource at higher speeds to control wing loads in order to change pressure distributions or to decrease buffet energy. During the F-22 configuration development, leading-edge flaps improved stability and control characteristics more than any of the vertical tail locations.

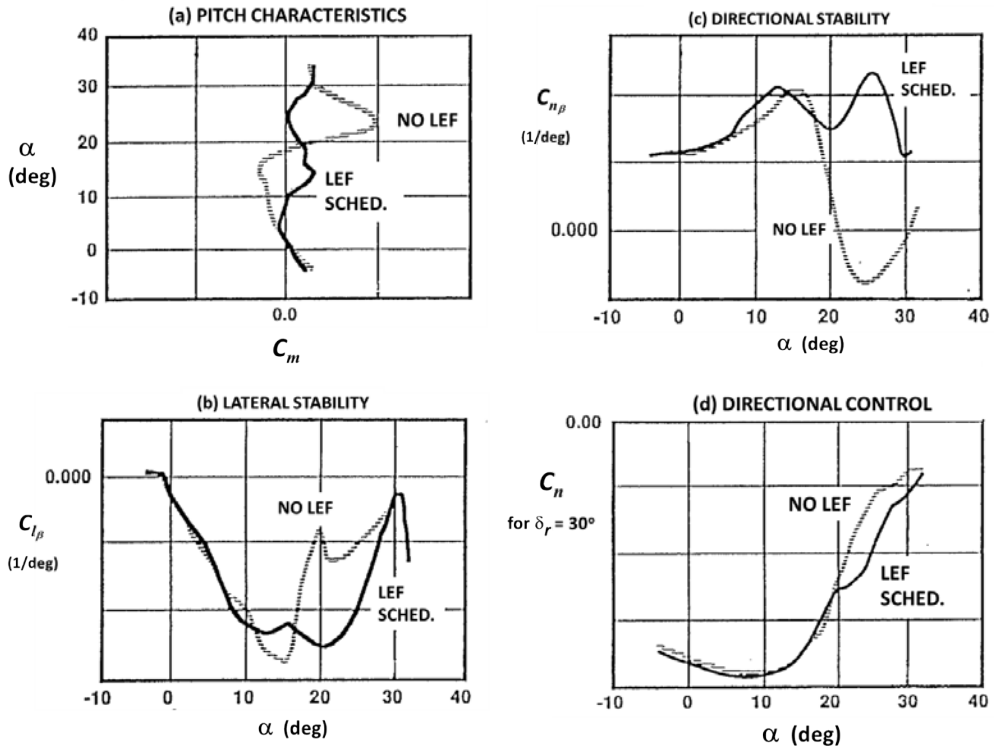


Figure 8-14: YF-22 leading-edge flaps are powerful devices for improvements to stability and control characteristics as shown by (a) pitching moment characteristics; (b) lateral stability; (c) directional stability; and (d) directional control. From C. M. Wilson, LMAS. "High Angle of Attack Design Considerations" seminar. Reprinted with permission under CC BY-NC-SA 4.0. Adapted.

The impact of thrust vectoring on the F-22 roll rate can be illustrated by data from the YF-22 configuration shown in figure 8-15. For fighter aircraft at high angles of attack, stability axis roll rates are limited by the available yaw control power. That is why augmented aerodynamic rudder power and yaw thrust vectoring was used on the following demonstrators:

1. The Rockwell-Messerschmitt-Bölkow-Blohm experimental jet aircraft X-31 was designed to test fighter thrust vectoring technology, demonstrating significantly more maneuverability than most conventional fighters.
2. The General Dynamics (now Lockheed Martin) F-16 MATV (multi-axis thrust vectoring) demonstrated effective maneuvering beyond its 25° angle of attack limit to almost 100° AOA.
3. The McDonnell Douglas F-18 HARV (High Alpha Research Vehicle) demonstrated stable flight at approximately 70° angle of attack and rolling at high rates at 65° angle of attack, which would have been nearly impossible above 35° without thrust vectoring.

The F-22 blends use of differential horizontal tail from primarily rolling moment below 20° AOA to primarily yawing moment at high AOA. Pitch thrust vectoring relieves some of the demand for longitudinal control from the symmetric horizontal tail position, which allows it to be positioned for more effective yaw command. Figure 8-15 shows that the F-15 runs out of roll capability around 30° AOA, but the innovative use of the YF-22 horizontal tail provides the pilot with the ability to continue controlling the plane of the lift vector and to out-maneu-

ver the adversary to higher AOAs. Thrust vectoring allows the F-22 to counter higher levels of inertial pitch coupling due to roll rate. This is evidenced near 20° AOA, where roll rates for the YF-22 are comparable to the smaller F-16 and more than twice that of the F-15.

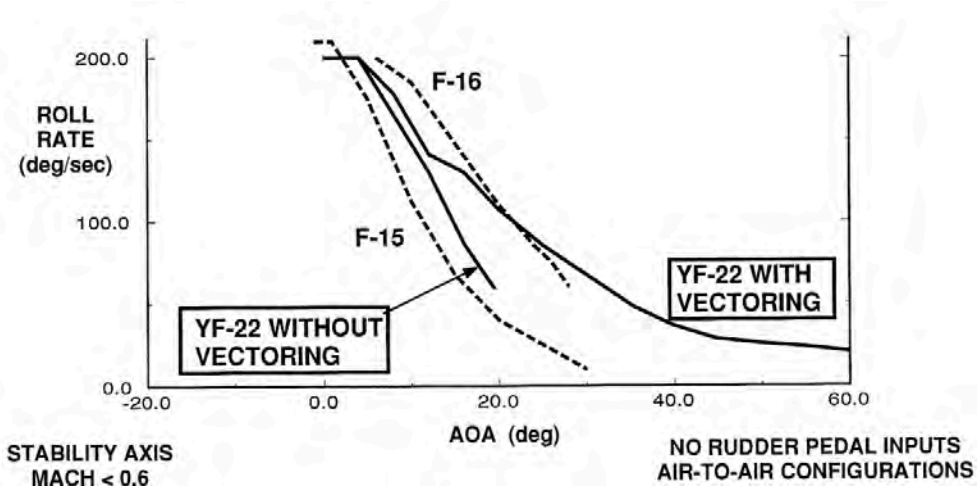


Figure 8-15: F-22 thrust vectoring provides roll rate advantage, especially at high AOAs. From C. M. Wilson, LMAS. "High Angle of Attack Design Considerations" seminar. Reprinted with permission under CC BY-NC-SA 4.0. Adapted.

8.5 Some Configuration Issues: Amazing Stories

8.5.1 Story No. 1: Flow Asymmetries at High Angle of Attack

In many cases, as the angle of attack increases, the flow develops asymmetrically even though the body is as nearly symmetric as possible, and the body is not yawed! The effect is to produce a side force over the nose of the body and therefore a yawing moment for the vehicle. This is particularly important for fighter aircraft with long forebodies.

In fluid mechanics terms, an axisymmetric body can produce an asymmetric flow at certain angles of attack. This is not too surprising, as the flow is simply unstable (recall the Kármán vortex street). Perhaps the key study relevant to fluid mechanics of aircraft at high-α was a fundamental study by Lamont[22] in the NASA Ames Research Center low-turbulence 12-foot pressure wind tunnel. An ogive cylinder was studied over a range of angles of attack (20° to 90°) and Reynolds numbers (0.2×10^6 to 4.0×10^6). More importantly, the model was tested at numerous different roll angles, which should not have resulted in any changes in the results. However, the results showed large variations in the side force with roll angle at angles of attack starting at about 30° or 35°. Reynolds number effects were also identified. For our purposes, it turns out that the low and high Reynolds number results were similar, but there was a large Reynolds number range, which unfortunately includes most of the wind tunnels, which saw significant variation in the Reynolds number effect. This could explain something I used to hear from engineers at the Full-Scale Tunnel at NASA Langley, who would claim, "We get the right answer, the one found in flight." Turns out they were operating at a very low Reynolds number, and it was lucky they got the right answer! The problem of Reynolds number scaling effects applied to high-angle-of-attack flow has received continuing attention.[23]

To address flow asymmetry, small nose chines were added to fix the separation location at the nose in the X-29 aircraft. The F-22 and F-35 also have chined forebodies.

8.5.2 Story No. 2: The Role of the Forebody on Stability at High-α—The F-5 Nose Story

At low angle of attack, the vertical tail provides directional stability. However, as the angle of attack increases, its effectiveness decreases. Typically this occurs because it's operating in the wake of the wing flow field. However, some aircraft start to exhibit increasing stability at higher angles of attack. In particular, the F-5 was tested at NASA's Langley Research Center, and a novel investigation was made.[24] Directional stability was found for the entire configuration. Then the vertical tail was removed. Finally, the forebody alone was tested. As expected, at low angle of attack, the tail provided directional stability. The contribution of the tail started to disappear at about 17° or 18° α. The vertical tail-on and -off data were essentially the same starting at 30° α. However, at this angle of attack, directional stability was becoming positive and increasing rapidly. When the forebody was tested alone, the results agreed with the other configurations beginning at about 30° α. Thus, the conclusion was that the forebody was responsible for creating a stable configuration even though it had significant side area ahead of the center of gravity.

The reason for this phenomena? The vortices shed from the nose developed asymmetrically with sideslip. The vortex on the lee side left the surface, while the vortex on the windward side remained close to the surface (in effect, it was blown onto the surface). The low pressure under the windward vortex in effect "sucked" the forebody back toward the zero-sideslip condition, the condition for stability. The forebody result was simulated computationally by Mason and Ravi.[25]

As a result of the favorable forebody characteristics found in the wind tunnel data, many investigations have been made to find good forebody shapes.[26] Chines have also been of interest due to their good stealth characteristics. However, there is a problem, as forebodies with too much directional stability tend to lack yaw damping and want to "swing past" the unyawed position. Hence, a combination of directional stability and yaw damping must be found. The F-22 forebody reflects this trade. The forebody was set to have minimum basic flow asymmetry while maintaining reasonable yaw damping and directional stability.

8.5.3 Story No. 3: The Complexity of Component Interaction at High Angle of Attack

The Research Fighter Configuration (RFC) was a joint project between Grumman and NASA's Langley Research Center to understand high-angle-of-attack aerodynamic design within the context of a supersonic cruise-maneuver and transonic-maneuver airplane. Anticipating success based on a previous program with a smaller canard,[27] the configuration was designed and several wind tunnel models were built. The design was tested at NASA Langley and at Grumman. Essentially, the results for the different models and different facilities agreed.

It was found that the directional stability of the model was extremely sensitive to the canard setting and that the twin vertical tail version of the airplane had a significantly lower maximum lift because of an adverse interaction with the vortices from the wing. This configuration showed complicated interactions between the forebody vortices, the canard trailing vortex system, the wing leading-edge vortices, and the vertical tail. No open literature report was ever published on this work.

Chapter 8 Exercises

8.1 Read the high-angle-of-attack aerodynamics paper by Joseph R. Chambers: "High-angle-of-attack Aerodynamics: Lessons Learned," AIAA Paper 86-1774, 4th Applied Aerodynamics Conference, San Diego, CA, June 9-11, 1986. Come prepared to participate in a class discussion on the impact of the lessons learned in the paper on modern fighter aircraft development.

Figure References

Figure 8-1: W. H. Mason. Adapted by P. Raj.

Figure 8-2: Nguyen, L. T., Ogburn, M. E., Gilbert, W. P., Kibler, K. S., Brown, P. W., and Deal, P. L., "Simulator Study of Stall/Post-Stall Characteristics of a Fighter Airplane With Relaxed Static Stability," NASA TP-1538, Dec. 1979. Adapted. https://ntrs.nasa.gov/citations/19800005879

Figure 8-3: W. H. Mason. Adapted by P. Raj.

Figure 8-5: W. H. Mason. Adapted by P. Raj.

Figure 8-6: Ray, E. J., McKinney, L. W., and Carmichael, J. G., "Maneuver and Buffett Characteristics of Fighter Aircraft," NASA TN D-7131. https://ntrs.nasa.gov/citations/19730017272

Figure 8-7: Figure 12 from Nguyen, L. T., Ogburn, M. E., Gilbert, W. P., Kibler, K. S., Brown, P. W., and Deal, P. L., "Simulator Study of Stall/Post-Stall Characteristics of a Fighter Airplane With Relaxed Static Stability," NASA TP-1538, Dec. 1979. https://ntrs.nasa.gov/citations/19800005879

Figure 8-8: Figure 14 from Nguyen, L. T., Ogburn, M. E., Gilbert, W. P., Kibler, K. S., Brown, P. W., and Deal, P. L., "Simulator Study of Stall/Post-Stall Characteristics of a Fighter Airplane With Relaxed Static Stability," NASA TP-1538, Dec. 1979. https://ntrs.nasa.gov/citations/19800005879

Figure 8-9: Bihrle, William, Jr., and Billy Barnhart, "Design Charts and Boundaries for Identifying Departure Resistant Fighter Configurations," NADC-76154-30. Jul. 1978. https://apps.dtic.mil/sti/tr/pdf/ADA058043.pdf

Figure 8-10: Figure 13 from Nguyen, L. T., Ogburn, M. E., Gilbert, W. P., Kibler, K. S., Brown, P. W., and Deal, P. L., "Simulator Study of Stall/Post-Stall Characteristics of a Fighter Airplane With Relaxed Static Stability," NASA TP-1538, Dec. 1979. Adapted. https://ntrs.nasa.gov/citations/19800005879

Figure 8-11: Lapins, M., Martorella, P., Klein, R. W., Meyer, R. C., and Sturm, M. J., "Control Definition Study for Advanced Vehicles," NASA CR-3738, Nov. 1983.

Figures 8-12: Wilson, C. M., "High Angle of Attack Design Considerations," Seminar at Virginia Tech, Nov. 1996, via LMAS.

Figures 8-13: Wilson, C. M., "High Angle of Attack Design Considerations," Seminar at Virginia Tech, Nov. 1996, via LMAS.

Figures 8-14: Wilson, C. M., "High Angle of Attack Design Considerations," Seminar at Virginia Tech, Nov. 1996, via LMAS.

Figures 8-15: Wilson, C. M., "High Angle of Attack Design Considerations," Seminar at Virginia Tech, Nov. 1996, via LMAS.

Notes

1. Chambers, J. R., and Grafton, S. B., "Aerodynamics of Airplanes at High Angles of Attack," NASA TM-74097, Dec. 1977. (*Note*: Developed for an AGARD-VKI Lecture Series given in April of 1977.)
2. Chambers, J. R., "High-Angle-of-Attack Aerodynamics: Lessons Learned," AIAA Paper 86-1774, 4th Applied Aerodynamic Conference, San Diego, CA, Jun. 9-11, 1986.
3. Nguyen, L. T., "Control System Techniques for Improved Departure/Spin Resistance for Fighter Aircraft," SAE Paper 791083, Aerospace Meeting, Dec. 1, 1979.
4. Durham, W., Lutze, F., and Mason, W. H., "Kinematics and Aerodynamics of the Velocity Vector Roll," Journal of Guidance, Control, and Dynamics, Vol. 17, No. 6, Nov.-Dec. 1994, pp. 1228–1233.
5. Nguyen, L. T., Ogburn, M. E., Gilbert, W. P., Kibler, K. S., Brown, P. W., and Deal, P. L., "Simulator Study of Stall/Post-Stall Characteristics of a Fighter Airplane With Relaxed Static Stability," NASA TP-1538, Dec. 1979.
6. Ogburn, M. E., Foster, J. V., Pahle, J. W., Wilson, R. J., and Lackey, J. B., "Status of the Validation of High-Angle-of-Attack Nose-Down Pitch Control Margin Design Guidelines," AIAA Paper 93-3623, Atmospheric Flight Mechanics Conference, Monterey, CA, Aug. 9-11, 1993.
7. Grafton, S., Chambers, J., and Coe, P., Jr., "Wind-Tunnel Free-Flight Investigation of a Model of a Spin Resistant Fighter Configuration," NASA TN D-7716, Jun. 1974.
8. Ray, E. J., McKinney, L. W., and Carmichael, J. G., "Maneuver and Buffet Characteristics of Fighter Aircraft," NASA TN D-7131, Jul. 1973.
9. Hamilton, W. T., Andrews, H., Chambers, J. R., Czinczenheim, J., Ettinger, R. C., Jeffries, R., Marconi, G. P., Foroni, C. P., Rabion, C., Ross, A. J., and Wunnenberg, H., "Manoeuver Limitations of Combat Aircraft," AGARD AR-155A, Aug. 1979.

10. Greer, H. D., "Summary of Directional Divergence Characteristics of Several High-Performance Aircraft Configurations," NASA TN D-6993, Nov. 1972.
11. Lutze, F. H., Durham, W. C., and Mason, W. H., "Unified Development of Lateral-Directional Departure Criteria," Journal of Guidance, Control, and Dynamics, Vol. 19, No. 2, Mar.-Apr. 1996, pp. 489–493.
12. Calico, R. A., Jr., "A New Look at C_{n_β}, dyn.," Journal of Aircraft, Vol. 16, No. 12, Dec. 1979, pp. 895–896.
13. Johnston, D. E. and Heffley, R. K., "Investigation of High AOA Flying Qualities Criteria and Design Guidelines," AFWAL TR-81-3108, Dec., 1981.
14. Johnston, D. E. and Heffley, R. K., "Investigation of High AOA Flying Qualities Criteria and Design Guidelines," AFWAL TR-81-3108, Dec., 1981.
15. Nguyen, L. T., Ogburn, M. E., Gilbert, W. P., Kibler, K. S., Brown, P. W., and Deal, P. L., "Simulator Study of Stall/Post-Stall Characteristics of a Fighter Airplane With Relaxed Static Stability," NASA TP-1538, Dec. 1979.
16. Weissman, R., "Development of Design Criteria for Predicting Departure Characteristics and Spin Susceptibility of Fighter Type Aircraft," AIAA Paper 72-984, 2nd Atmospheric Flight Mechanics Conference, Palo Alto, CA, Sept. 11-13, 1972.
17. Bihrle, W., Jr., and Barnhart, B., "Design Charts and Boundaries for Identifying Departure Resistant Fighter Configurations," NADC-76154-30, Jul. 1978.
18. Chambers, J. R., "Overview of Stall/Spin Technology," AIAA Paper 80-1580, Atmospheric Flight Mechanics Conference, Danvers, MA, Aug. 11-13, 1980.
19. Nguyen, L. T., Ogburn, M. E., Gilbert, W. P., Kibler, K. S., Brown, P. W., and Deal, P. L., "Simulator Study of Stall/Post-Stall Characteristics of a Fighter Airplane With Relaxed Static Stability," NASA TP-1538, Dec. 1979.
20. Lapins, M., Martorella, P., Klein, R. W., Meyer, R. C., and Sturm, M. J., "Control Definition Study for Advanced Vehicles," NASA CR-3738, Nov. 1983.
21. Clark, C., and Bernens, M., "High Angle-of-Attack Flight Characteristics of the YF-22," AIAA Paper 91-3194, Aircraft Design Systems and Operations Meeting, Baltimore, MD, Sept. 23-25, 1991.
22. Lamont, P. J., "Pressures Around an Inclined Ogive Cylinder with Laminar, Transitional, or Turbulent Separation." AIAA Journal, Vol. 20, No. 11, Nov. 1982, pp. 1492–1499.
23. Fisher, D. F., Cobleigh, B. R., Brooks, D., Hall, R. M., and Wahls, R., "Reynolds Number Effects at High Angles of Attack," NASA TP-1998-206553, Jun. 1998.
24. Grafton, S., Chambers, J. and Coe, P., Jr., "Wind-Tunnel Free-Flight Investigation of a Model of a Spin Resistant Fighter Configuration," NASA TN D-7716, Jun. 1974.
25. Mason, W. H., and Ravi, R., "Computational Study of the F-5A Forebody Emphasizing Directional Stability," Journal of Aircraft, Vol. 31, No. 3, May-Jun. 1994, pp. 488–494.
26. Ravi, R., and Mason, W. H., "Chine-Shaped Forebody Effects on Directional Stability at High-α," Journal of Aircraft, Vol. 31, No. 3, May-Jun. 1994, pp. 480–487.
27. Lapins, M., Martorella, P., Klein, R. W., Meyer, R. C., and Sturm, M. J., "Control Definition Study for Advanced Vehicles," NASA CR-3738, Nov. 1983.

9. Supersonic Aerodynamics

There have actually only been a few airplanes that are truly supersonic (able to cruise at supersonic speeds). Before the F-22, classic "supersonic" fighters used brute force (afterburners) and had extremely limited duration. As an example, consider the two defined supersonic missions for the F-14A:

F-14A Supersonic Missions

- CAP (combat air patrol)
  - 150 miles subsonic cruise to station
  - Loiter
  - Accel, M = 0.7 to 1.35, then dash 25 nautical miles (NM)—4 1/2 minutes and 50 NM total
  - Then, must head home or to a tanker!

- DLI (deck launch intercept)
  - Energy climb to 35K ft, M = 1.5 (4 minutes)
  - 6 minutes at M = 1.5 (out 125-130 NM)
  - 2 minutes combat (slows down fast)
  - After 12 minutes, must head home or to a tanker!

In this chapter, we explain the key supersonic aerodynamics issues facing the configuration aerodynamicist. We start by reviewing the most significant airplanes that had substantial sustained supersonic capability in section 9.1. We examine the key physical underpinnings of supersonic gas dynamics and their implications for configuration design in section 9.2. We present an overview of wave drag in section 9.3 (primarily looking at bodies of revolution), and then we examine supersonic aerodynamics of wings in section 9.4 and aerodynamic center shift in section 9.5. In section 9.6, we discuss the novel oblique-wing concept and aeropropulsion integration issues in section 9.7. We show applications of modern CFD and the application of MDO in section 9.8. This is followed by examples of supersonic airplane design in section 9.9. We will see that developing a practical supersonic airplane is extremely demanding and requires careful integration of the various contributing technologies. We also discuss some examples of efforts to develop new supersonic airplanes.

9.1 Supersonic "Cruise" Airplanes

The supersonic capability is typical of most of the so-called supersonic fighters, but obviously the supersonic performance is limited, as illustrated by the F-14 example above. The following list represents my selection of the previous manned supersonic aircraft. It is a very short list. It is important for aerodynamic designers to be familiar with these airplanes. We cite maximum lift-to-drag (L/D_{max}) ratio for each design (unless not publicly available) for supersonic flight.

- 1956: The B-58 ($L/D_{max} = 4.5$), Convair, 1st flight Nov. 1956
  - In 1962: Mach 2 for 30 minutes
- 1962: The A-12 (SR-71 in '64) ($L/D_{max} = 6.6$), Lockheed, 1st flight April 1962
  - 1st flight as SR-71, Dec. 1964
  - 1st supersonic flight, May 4, 1962

- 1st flight to exceed Mach 3, July 20, 1963
- 1964: The XB-70 (L/D_{max} = 7.2). North American Aviation, 1st flight Sept. 1964
  - 1st Mach 3 flight Oct. 1965
  - In 1966: Mach 3 for 33 minutes
- 1968: The TU-144, Tupolev
  - 1st flight: Dec. 31, 1968
- 1969: The Concorde (L/D_{max} = 7.4), Aérospatiale/BAC design
  - 1st flight, March 2, 1969
  - 1st Mach 2 flt., Nov. 4, 1970)*
- 1990: The YF-22 and YF-23 (supercruisers)
  - YF-23: Northrop-led team, 1st flight: Aug. 27, 1990
  - YF-22: Lockheed-led team, 1st flight: Sept. 29, 1990**
- 1997: The F-22 (supercruiser, supermaneuverable, superstealth)
  - F-22: Lockheed Martin–led team, 1st flight: Sept. 7, 1997

Note the low *L/D* values associated with supersonic flight. Nevertheless, these airplanes were all remarkable.

*The last flights of the Concorde occurred on October 24, 2003.

**The prototype that won the Advanced Tactical Fighter competition.

9.1.1 The B-58

The B-58 is shown in figure 9-1. It is a strikingly attractive design. It followed the Convair approach of using a conically cambered delta wing in the tradition of the F-102 (first flight: 1953) and F-106 (first flight: 1956) airplanes from the same company. Today, B-58s can be seen at numerous museums, notably the Museum of the Air Force in Dayton, Ohio, and the Pima Air & Space Museum outside of Tucson, Arizona.



Figure 9-1: The B-58 in flight. *From US Air Force. Wikimedia. Public domain.*

The B-58 had a three-man crew and weighed around 160,000 pounds, of which over 100,000 pounds was fuel! The structural-weight fraction was an amazingly low 14%. To achieve the required aerodynamic performance, the wings were thin—4.08% at the tip and 3.46% at the root. In 1962, the B-58 flew 1,300 mph for 30 minutes and 43 seconds, thus being the first airplane to fly over 2,000 km/h for 30 minutes, enabling its creators to claim the Bleriot prize. It also set a record by flying from Los Angeles to New

York in 2 hours and 57 seconds (for comparison, the SR-71 later made the trip in 68 minutes). The required static margin for longitudinal stability was 3%, but greater than 3% was required for directional stability to handle the engine-out case. An aileron-rudder interconnect (ARI) was used to cancel the yawing moment due to aileron deflection. The plane was powered by four pylon-mounted GE J-79 engines, making it an extremely loud airplane.

One of the curious features was the use of a "double bubble" attached pod below the fuselage. The outer pod carried fuel and was jettisoned when empty. The inner pod was in fact the nuclear bomb.

The best paper to read on the B-58 is by Erickson.[1] The airplane had a poor safety record. In part, this was because the tires were very small to allow the gear to fit in the fuselage. The takeoff and landing speeds were high, and the tires sometimes blew up. It was also very difficult to maintain.

9.1.2 The SR-71 Family

This section covers what is probably the most amazing design achievement ever made in aeronautics. Figure 9-2 shows this familiar airplane, the SR-71. Its predecessor, the A-12, first flew in 1962, while the SR-71's first flight occurred in 1964. It served for many years after having been developed in complete secrecy. Aerodynamic heating was an important consideration on the design. The airplane was powered by two Pratt J-58 turboramjet engines. The SR-71 had a crew of two. Its wing area was 1,800 square feet, the span was 55 feet 7 inches, and the MTOGW was 172,000 pounds. Its last military flight was in 1990. NASA operated SR-71s sporadically until 1999.

The definitive paper on the aerodynamics of the SR-71 (on "the edge" between supersonic and hypersonic flight) was written by Ben Rich,[2] who later went on to be a key member of the team that developed the F-117 stealth "fighter." It is impossible to provide a better description of the plane than the one given by Rich.

A good description of the airplane is available in the AIAA book by Peter Merlin.[3] This book comes with a DVD that has a wealth of information, including flight manuals, photos, and videos.



Figure 9-2: The SR-71. From Jim Ross. NASA. Public domain.

9.1.3 The XB-70

The XB-70[4] is shown in figure 9-3. The airplane was intended to be a Mach 3 intercontinental bomber. However, the successful development of ICBMs meant there was no longer a need for the plane, so instead it became a research airplane. Two were built. It was a large airplane with a wing area of 6,297 square feet, a span of 105 feet, and a MTOGW of 542,000 pounds. In May 1966, the XB-70 flew at Mach 3 for 33 minutes. It had six GE YJ93 engines.



Figure 9-3: The XB-70 on takeoff. Note the large delta wing. The canard is essentially a trimmer. From NASA. Public domain.

It only reached Mach 3 a few times. This was in part because the second airplane was destroyed in a midair collision with an F-104 in June 1966 during a publicity photo flight for General Electric. Joe Walker, the pilot of the F-104, was killed; Carl Cross, the XB-70 pilot, also died, though his co-pilot Al White survived. To increase directional stability and minimize the aerodynamic center shift, the XB-70 deflected its wingtips down in supersonic flight. This is shown in figure 9-4. Only the second airplane had full wingtip-deflection capability.



Figure 9-4: This figure shows the XB-70 flying with its wingtips deflected down. From NASA. Public domain.

Although it was also said to have increased aerodynamic efficiency through the use of compression lift on the lower surface, this could have been achieved by mild wing camber. Note that the canard was essentially a foreplane, acting as a trimmer. It also had a very high base drag associated with the propulsion installation in the transonic flight regime.

The remaining XB-70 is on display at the National Museum of the Air Force in Dayton, Ohio. It was flown to Dayton in February 1969.

9.1.4 The TU-144

The Tupolev TU-144 was a Soviet Union contemporary of the Concorde. It flew before the Concorde, on December 31, 1968. Fifteen were built. It was similar in configuration to the Concorde with the notable exception that it had a retractable "mustache" canard (as well as the drooping nose used by the Concorde). It also had a braking parachute, very unusual for a commercial airplane. The program suffered when a TU-144 crashed during a demonstration flight at the Paris Airshow in June 1973. Although it made a number of operational flights, it wasn't practical and the program ended. It was resurrected during the US High-Speed Civil Transport (HSCT) program in the 1990s when it was used by NASA as a testbed for supersonic flight research. The TU-144 is cited as having a wing area of 5,450 square feet, a span of 94.4 feet, and a MTOGW of 455,950 pounds.

9.1.5 The Concorde

The development of the Concorde, together with a discussion of the Russian SST effort and the aborted attempt by the US, is described in a wonderful paper by Poisson-Quinton.[5] His paper includes data showing how the TU-144 used its mustache canard. The AIAA published a case study on the Concorde[6] that provided a description of its aerodynamic design. Figure 9-5 is a photo from the National Archives website that shows the Concorde planform. The Concorde has a wing area of 3,856 square feet, a span of 84 feet, and a MTOGW of 412,000 pounds. The aerodynamic design of the wing is described in a paper by Wilde and Cormery.[7] To allow the slender wing configuration to land and takeoff at an acceptable angle of attack, the Concorde took advantage of vortex lift as well as ground effects.



Figure 9-5: The Concorde. From the National Archives. Public domain.

During the years that the Concorde was in service, I saw it frequently, flying over Long Island on its way to Kennedy Airport, taxiing around Kennedy, and also at London Heathrow. Compared to the other planes, it was small, and the wing was extremely thin. One of the most notable aspects of its flight was how loud it was. If it had flown over my house more than once a day, it would have been very annoying, even to me (and I lived about 35 miles from the airport).

9.1.6 The F-22

During the late 1970s and the 1980s, the US Air Force studied the requirements for a new fighter. A key requirement was identified as the ability to "supercruise," wherein the airplane could fly supersonically without the use of the afterburner. This decreased fuel burn and allowed for significantly longer supersonic range than previous fighter aircraft. Stealth was also important, though not publicly discussed. The fighter requirement became official as the Advanced Tactical Fighter (ATF) in 1981. In 1986, teams led by Northrop (YF-23) and Lockheed (YF-22) won awards to build demonstrators. In 1991, after the flight demonstrations were completed, Lockheed was awarded the contract for the F-22. This process is described in detail in the AIAA book by Aronstein, Hirschberg, and Piccirillo.[8] A description of the F-22 aircraft was given in the 1992 Wright Brothers Lecture by Sherman Mullin.[9] A photo of the F-22 is shown in figure 9-6.



Figure 9-6: The Lockheed F-22. *From Rob Shenk. Wikipedia. CC BY-SA 2.0.*

9.2 The Challenge for Supersonic Airplane Design

From this small number of actual supersonic cruising airplanes, we see that supersonic flight is a challenge. We can get some insight from the range equation:

$$R = \frac{V\left(\frac{L}{D}\right)}{sfc}\ln\left(\frac{W_{\text{initial}}}{W_{\text{final}}}\right) \qquad (9\text{-}1)$$

Here we have to counterbalance the reduction in *L/D* as shown above for these airplanes with an increase in *V* (recall that subsonic transport *L/D* values should be between 18 and 20). However, we always incur the extra cost of supersonic wave drag, which reduces the *L/D*. We also need to be able to fly without afterburner to keep the *sfc* low. This is difficult because modern transonic transports use high-bypass-ratio engines. The large engine/nacelle diameters are not possible at supersonic speeds; the drag would be unacceptable. Thus we have numerous challenges for economical supersonic flight.

The basic physics of the flow field change between subsonic and supersonic flow is illustrated in figure 9-7. It was originally presented by Von Kármán.[10]

Poisson-Quinton[11] has shown how the wave drag leads to a reduction in *L/D* at supersonic Mach numbers. This is illustrated in figure 9-8. The chief culprit is the C_{D_0} increase with Mach number due to the volumetric wave drag.

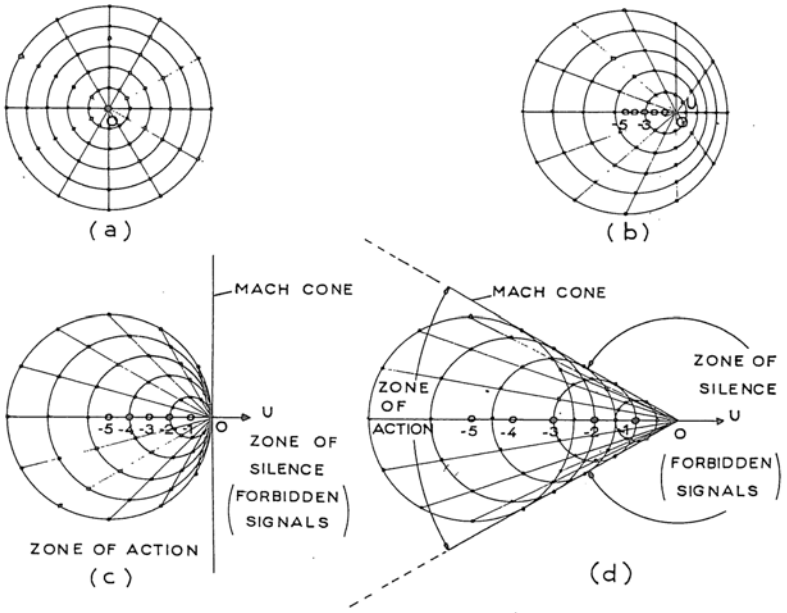


Figure 9-7: The change in flowfield physics from subsonic to supersonic speeds: (a) stationary source, (b) source moving at half the speed of sound, (c) source moving at the speed of sound, (d) source moving at twice the speed of sounds. *From T. von Kármán. "Supersonic Aerodynamics—Principles and Applications." Copyright undetermined by AIAA. Fair use.*

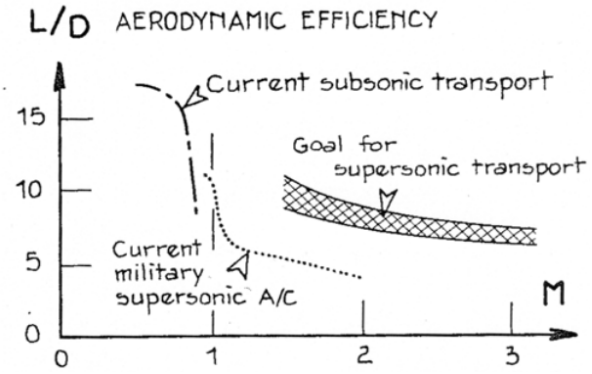


Figure 9-8: The L/D problem for supersonic flow. *From P. Poisson-Quinton. "First Generation Supersonic Transport." No known copyright.*

Nicolai and Carichner [12] have collected the minimum drag values for a number of supersonic fighters, as shown in figure 9-9. Clearly, the wave drag is large. For modern supersonic designs, the drag increase would be much less. However this figure provides insight into the challenge.

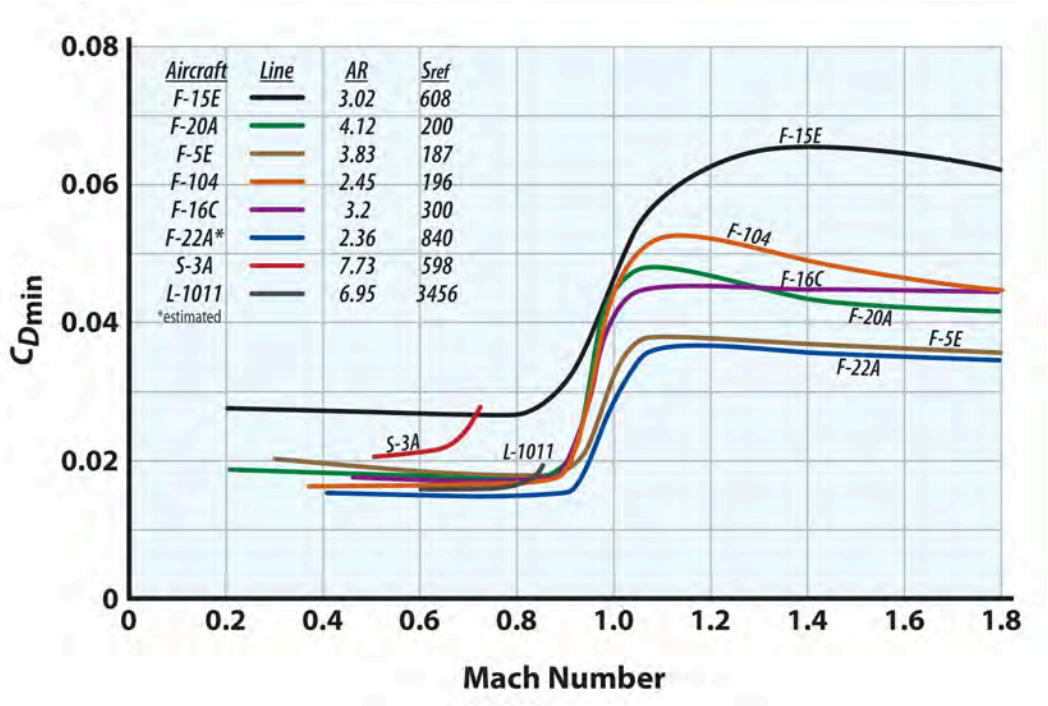


Figure 9-9: C_{Dmin} increase with Mach number for several supersonic fighters. *From L. M. Nicolai and G. Carichner. "Fundamentals of Aircraft and Airship Design." AIAA Education Series. Fair use.*

A key overview of the supersonic aerodynamic design issues has been written by Baals et al.[13] This paper provides a basis for thinking about supersonic airplane design and should be studied for the details of the aerodynamic design thinking used in the US SST program to be described later.

In addition to the pure aerodynamic performance challenge, supersonic airplanes must address the noise problem, both around the airport ("community noise") and the sonic boom. This proved to be a significant issue during the studies of a possible new supersonic transport in the 1990s, the HSCT.[14] That airplane was intended to operate at Pacific-Rim ranges with 250 to 300 passengers. This was followed by investigations of the possibility of designing small supersonic business jets with an acceptable level of boom noise.[15,16] It is likely that these airplanes will be the next generation of supersonic airplanes, and we will discuss the boom issues below in section 9.9.4.

Next, to understand some of the key aerodynamic ideas, we will be break our discussion into two parts. First, we will present an overview of zero-lift drag in section 9.3 (primarily looking at bodies of revolution), and then we will discuss drag due to lift in section 9.4. By splitting the discussion into two parts, we are implicitly using linear theory to help us understand the main contributors to supersonic aerodynamics.

Before proceeding, we note that the increase in zero-lift drag means that the drag due to lift will also be higher at L/D_{max} since the drag due to lift should approach the zero-lift drag to maximize L/D. Thus, every effort must be made to reduce the volumetric wave drag. It is unlikely there will ever be enough thrust to cruise at L/D_{max}.

9.3 Wave Drag

The key idea underlying wave drag is the area rule. We already discussed this in Chapter 3. Basically we want a smooth area distribution. In addition, there are specific shapes that produce the minimum drag. They have been worked out analytically for axisymmetric bodies. The derivation of the wave drag integral is given in Chapter 6 of Ashley and Landahl.[17] We cite it here because they also provide the derivation of minimum drag bodies of revolution. Equation 9-2 is the slender body wave drag formula:

$$D_{\text{wave}} = -\frac{\rho_\infty U_\infty^2}{4\pi} \int_0^l \int_0^l S''(x_1) S''(x_2) \ln|x_1 - x_2| dx_1 dx_2 \qquad (9\text{-}2)$$

where $S(x)$ is the cross-sectional area along the body. The integral in equation 9-2 requires that the ends of the body be closed, $S = 0$, or that $S'(l)$ be zero. This equation is used to analyze different cross-sectional area distributions and also to find shapes with minimum drag. Since the equation is from slender-body theory, the Mach number does not appear (see the derivation in section 9.3 of Ashley and Landahl's work).

The integral shows that it is actually the second derivative of the area distribution that is required for the computation. Clearly we want to make $S''(x)$ small. Unless care is taken, the numerical method may result in values that are too high because of artificial noise in the interpolation procedures and the quality of the input data for the area distribution, S. This difficulty was substantially reduced with a rather ingenious scheme due to Evelyn Eminton in Great Britain[18] and adopted for use in the now-standard Harris wave drag program written by Roy Harris for Boeing at NASA Langley.[19] Eminton's approach to finding the value of the integral was to find the interpolating curve passing through the specified input points that minimized the value of the wave drag. Thus she solved an optimization problem to eliminate problems arising artificially from the interpolation procedure. The code that makes this calculation is generally known as the Harris wave drag program and is available from Ralph Carmichael's PDAS website.[20]

Minimum wave drag shapes subject to a variety of constraints have been found using the wave drag formual. For an open base (ignoring base pressure), the minimum wave drag is the Von Kármán ogive. Given the base area and length, the minimum wave drag is

$$D_{\text{wave}} = \frac{2\rho_\infty U_\infty^2}{\pi} \frac{[S(l)]^2}{l^2}. \qquad (9\text{-}3)$$

Or, if S_{ref} is the base area, the coefficient of wave drag is given by

$$C_{D_{\text{wave}}} = \frac{4}{\pi} \frac{[S(l)]}{l^2}. \qquad (9\text{-}4)$$

See appendix A, "Geometry for Aerodynamicists," for the equation of the shape of the Von Kármán ogive. The corresponding radius and area distributions are shown in figures 9-10 and 9-11.

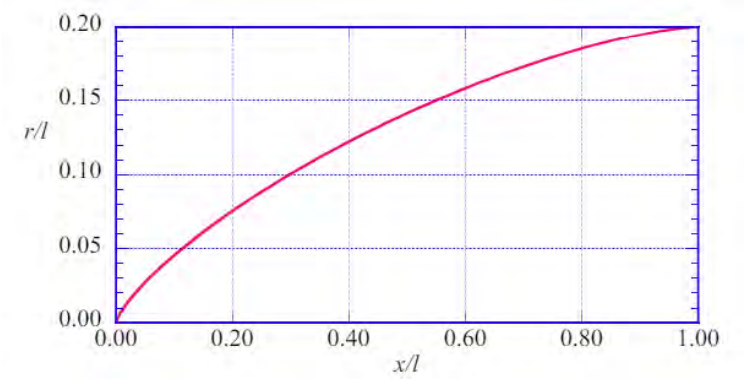


Figure 9-10: Radius distribution of a Von Kármán ogive.

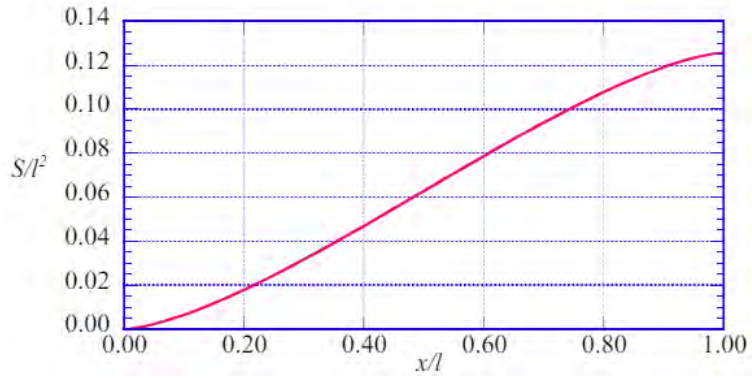


Figure 9-11: Cross-sectional area distribution of a Von Kármán ogive.

Instead of having an open base, if the body is closed at both ends, then for a given length, l, and volume, V, the wave drag is

$$D_{\text{wave}} = \frac{64V^2}{\pi l^4}\rho_\infty U_\infty^2. \qquad (9\text{-}5)$$

Or, based on the maximum cross-sectional area, the wave drag coefficient is given by

$$C_{D_{\text{wave}}} = \frac{24\text{V}}{l^3}. \qquad (9\text{-}6)$$

This is known as the Sears–Haack body. See appendix A for the equation of the shape. Figures 9-12 and 9-13 show the radius and cross-sectional area distribution for this body.

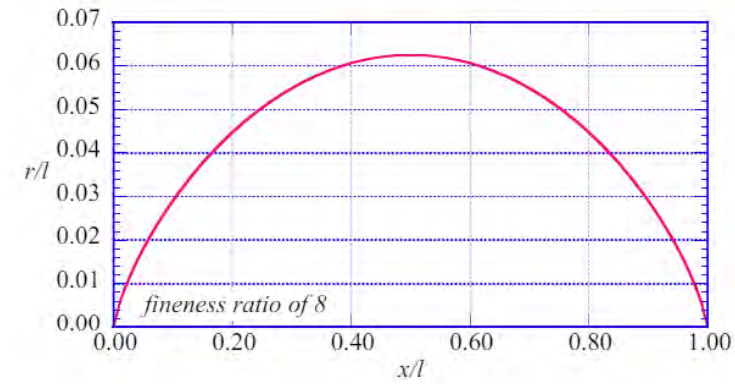


Figure 9-12: Radius distribution of the Sears–Haack body.

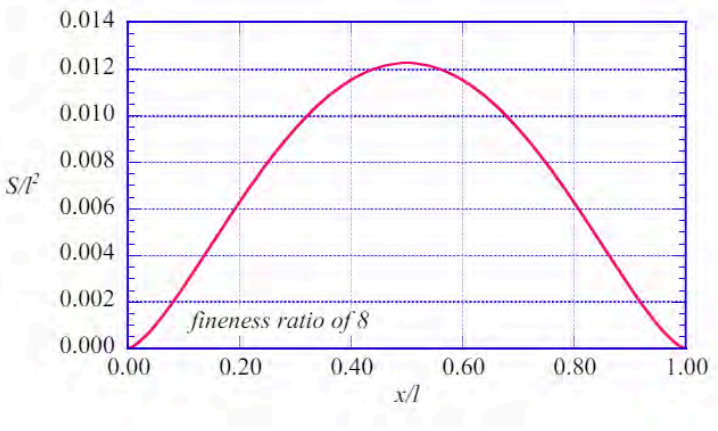


Figure 9-13: Cross-sectional area distribution of the Sears–Haack body.

Adams[21] provides derivations of minimum wave drag axisymmetric body shapes for other constraints (i.e., other than the ones for the Von Kármán ogive and Sears–Haack body).

The Sears–Haack body is *not* the minimum wave drag body for a given max cross-sectional area, which may often be the more relevant constraint. However, using the connection between volume and maximum body radius,

$$V = \pi r_{\max}^2 \frac{3\pi d}{16}. \qquad (9\text{-}7)$$

we get a form that shows the connection between the drag coefficient and fineness ratio, *l*/*d*:

$$C_{D_{\text{wave}}} = \frac{9\pi^2}{8} \frac{1}{\left(l/d_{\max}\right)^2}. \qquad (9\text{-}8)$$

Figure 9-14 shows how important the use of a high fineness ratio is to reduce the wave drag. To make the drag nondimensional, we divide by the dynamic pressure and by the volume raised to the 2/3rd power. Care must always be taken when looking at drag values to make sure you understand the reference area used to define the nondimensional drag coefficient. It is not unheard of that incorrect drag coefficient values were used!

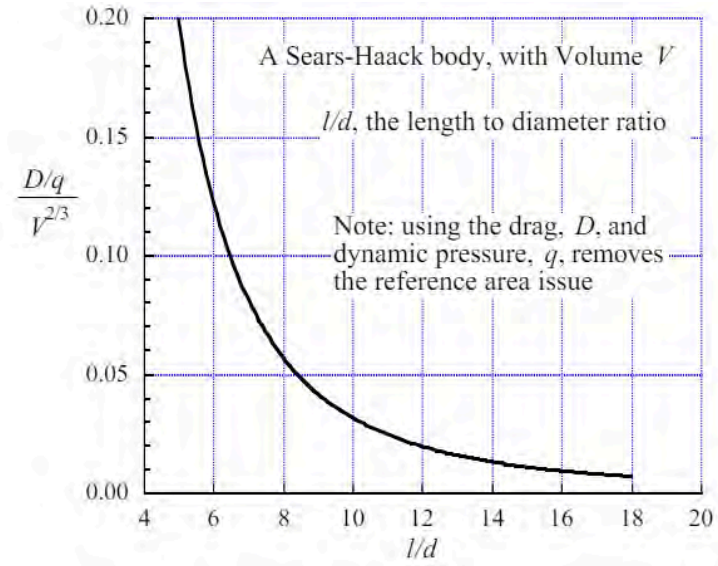


Figure 9-14: Wave drag reduction as fineness ratio increases.

It is worth investigating the minimum wave drag shapes in a little more detail. Since we've seen the key role that the fineness ratio plays in the drag, we can write the wave drag coefficient for three different cases: (i) the Sears–Haack minimum wave drag for a given volume and length, equation 9-9; (ii) the minimum wave drag for a specified maximum cross-sectional area, equation 9-10; and (iii) the minimum wave drag for the Von Kármán ogive, equation 9-11

$$C_{D_{S-H}}\left(\frac{l}{d}\right)^2 = \frac{9\pi^2}{8} = 11.1 \qquad (9\text{-}9)$$

$$C_{D_{S-H}}\left(\frac{l}{d}\right)^2 = \pi^2 = 9.87 \qquad (9\text{-}10)$$

$$C_{D_{S-H}}\left(\frac{l}{d}\right)^2 = 1 \qquad (9\text{-}11)$$

Thus the minimum wave drag body for a given max cross-sectional area is 11% less than the minimum wave drag body of a given volume with the same max cross-sectional area. This also shows that ignoring base drag (reasonable if the base is filled with a jet exhaust), the drag is much lower when the base is open. In fact, the wave drag is very nearly a linear function of the ratio of the base area to the max cross-sectional area (see figure 3 in NACA TN-2550 by Adams):

$$C_{D_w}\left(\frac{l}{d}\right)^2 = \pi^2 - \left(\pi^2 - 1\right)\frac{S_n}{S_{\max}} \qquad (9\text{-}12)$$

The minimum drag for a body of revolution with a constant cross section placed between the front and back of a body (with a fairing to close the shape in the front and back) has been given by Heaslet and Lomax.[22] To be a little more complete, we note that Harder and Rennemann[23] found minimum drag shapes that have slightly less drag than Adams found. Their work presents results for the case of a given volume.

For comparison, Krasnov[24] points out that using a simple cone forebody has a drag of about twice the value of the optimum forebody value for a fineness ratio of 3. However, a tangent ogive only has a drag about 7% higher than the optimum value.

A general minimum wave drag axisymmetric shape can also be found using the analysis by Lord and Eminton.[25] I have implemented this analysis in the interactive program MinDrag. It computes the minimum value of the supersonic wave drag for an axisymmetric body as well as the area distribution required to attain this value for a given length, volume, nose area, base area, and another area specified at a given location along the body. A screenshot of the program is shown in figure 9-15, and the program can be interactively executed by selecting Mindrag.exe in section E.5.2.4.

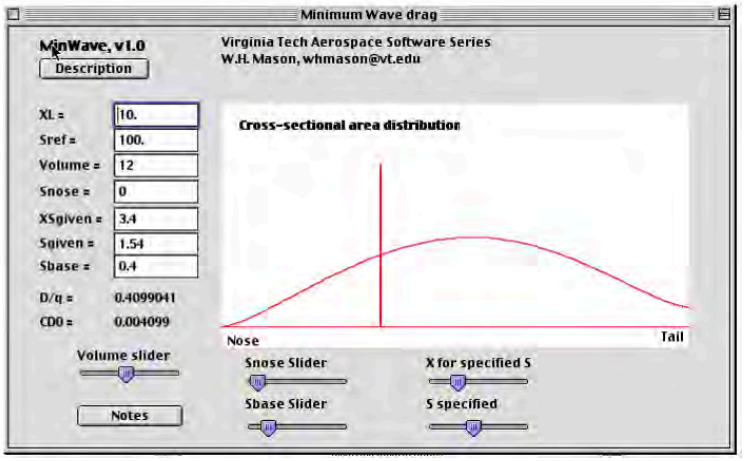


Figure 9-15: MinDrag, the minimum wave drag body shape interactive code subject to a variety of constraints.

Often, the wave drag of supersonic airplanes is given in terms of a multiple of the wave drag of a minimum drag body of revolution. Typically the Sears–Haack body is chosen because of its well known drag expression. In the early stages of design, it's worth collecting data from previous designs. One rule of thumb was to use $19/(l/d)^2$ as opposed to the Sears–Haack value of 11.1. Jobe has collected data in an AIAA book[26] based on his Air Force Report.[27] It is also worth investigating examples of cross-sectional area distributions for the B-58 and XB-70 given by Tinetti, Maglieri, and Bobbitt.[28]

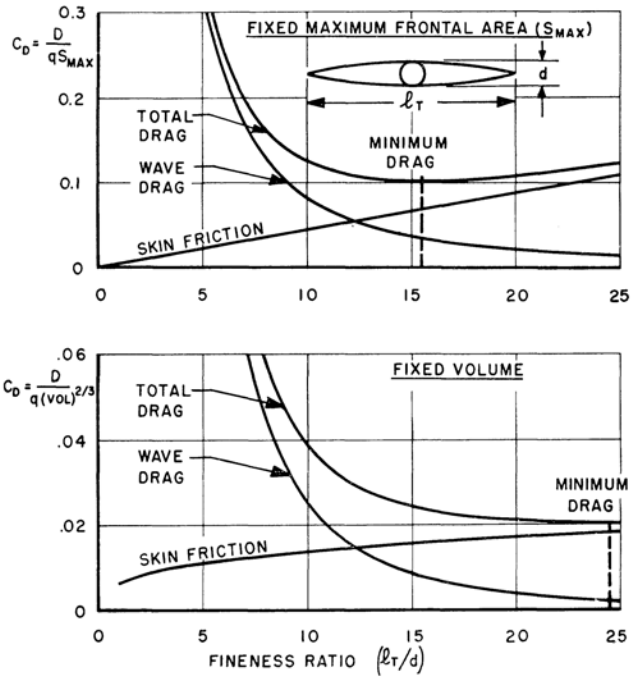


Figure 9-16: Drag coefficient variation with fineness ratio for bodies of revolution at M = 2.5 and an assumed skin friction coefficient of 0.0018. *From W. B. Oswald. "Applied Aerodynamics and Flight Mechanics." Copyright undetermined by AIAA. Fair use.*

Because the surface area can change as the fineness ratio changes, it would be interesting to find the minimum of the sum of the friction and wave drag. Although I worked this out many years ago, I discovered that it had already been done by W. Bailey Oswald.[29] Figure 9-16 shows his result for two cases. The first is the minimum drag fineness ratio when the maximum frontal cross sectional area is specified, and the second case is the result when the volume is specified. For the first case, the minimum fineness ratio occurs for a value slightly above 15 (this would be the usual case). When the volume is specified, the minimum drag fineness ratio is a little less than 25 (this is much too high for a practical manned airplane). In both cases, the minimum is fairly shallow, so you can select values that are significantly lower than the minimum shown in his results without incurring a large penalty.

Once we get past the "smooth area," the next step is to make the area distribution for the entire airplane close to the axisymmetric minimum wave drag shapes described above. We will see examples below.

9.3.1 A Curious Story

Both the Von Kármán ogive and Sears–Haack bodies have a curious feature. They are slightly blunted. Intuitively we expect them to have sharp noses. Yet, the slope at the nose is 90°, and the leading-edge radius is zero, which is hard to visualize. The explanation is that it's better to have a high slope, and thus high pressure, at the nose, where dS is small, rather than further aft, where r is larger and dS is much larger ($dS = 2\pi r dr$). These shapes are geometrically blunt while being aerodynamically sharp. More details associated with this feature of the geometry are available.[30]

In addition, our analysis revealed that the nose shape of the Von Kármán ogive and Sears–Haack bodies are essentially equivalent to a power law body with an exponent of 0.75. This means that the minimum drag supersonic and hypersonic bodies are related. Figure 9-17 shows an extreme "blow-up" of the power law body at the nose.

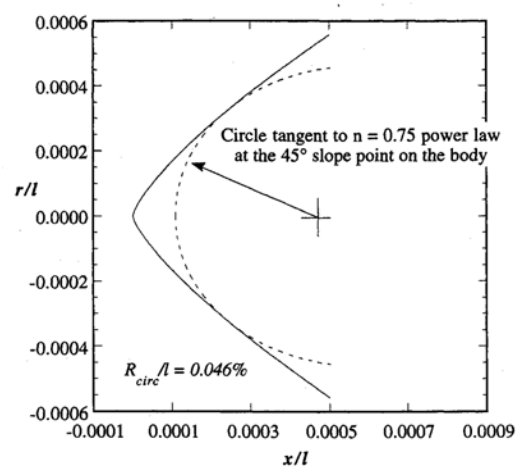


Figure 9-17: The nose region of a power law or Sears-Haack body. From W. H. Mason and J. Lee. "Aerodynamically Blunt and Sharp Bodies." Reprinted by permission of the American Institute of Aeronautics and Astronautics, Inc.

9.3.2 Multiple Bodies to Reduce Wave Drag and Favorable Interference

Another possibility for reducing wave drag occurs when multiple bodies of revolution are arranged for that purpose. There can be both a favorable and an unfavorable interaction between bodies that are located in close proximity. The idea of favorable interaction is the reason for concepts like the Grumman Tribody of 1978. Unfortunately, the interaction can be sensitive to the Mach number. One of the ideas has been to stagger stores based on flight Mach number to reduce drag, which was the basis for the work of Jack Nielsen.[31] Previously, Friedman [32] had also done an analysis that showed the possibility of favorable interaction. Nielsen says that, compared to the sum of the drag of the individual bodies, "the drag of a pair of bodies can be either double or nearly halved, depending upon the lateral and longitudinal spacings of the bodies." According to Friedman, a "three-body configuration is found for which the total wave drag is about 35 percent less than the sum of the individual wave drags of the three bodies." Figure 9-18 from Nielsen[33] shows the sensitivity of the interference drag for one Mach number. The potential advantage is available, but it must be used very carefully.

Multiple axisymmetric bodies are just one possibility for favorable interference. A number of other possibilities exist. Kulfan has examined many of them for applications in supersonic airplanes.[34] That paper includes the pertinent ideas and an extensive reference list.

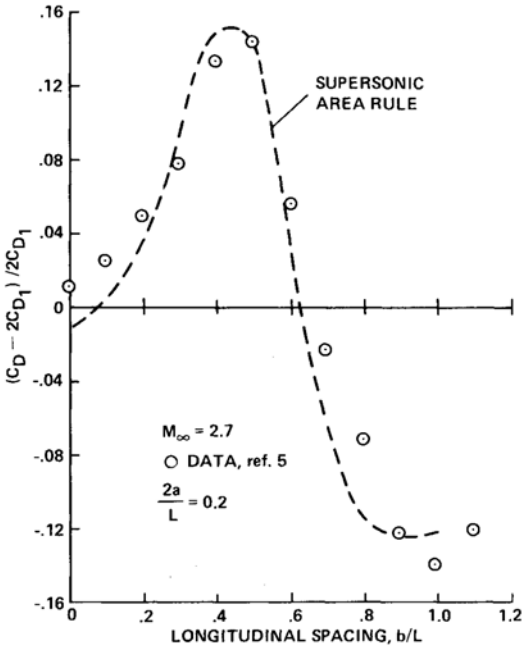


Figure 9-18: Effect of longitudinal spacing on the interference wave drag of a pair of Sears–Haack bodies at M = 2.7. Negative values denote favorable interference. From J. N. Nielsen. "Arrays of Bodies of Revolution for Minimum Wave Drag." Public domain. (Note: "DATA, ref. 5" in the figure refers to Bantle, J. W., "Analysis of the Interference Effects Between Two Sears-Haack Bodies at Mach 2.7," Engineering and Applied Sciences Thesis, George Washington University, Washington, DC, 1982.)

9.3.3 Planar Wing Wave Drag

We generally think of axisymmetric bodies as the shapes that minimize wave drag. However, this isn't the case. An example of a potential reduction has been shown in Küchemann's book.[35] Planar wings with the same volume as a Sears–Haack body can actually have less drag than the axisymmetric body. The data is plotted as a fraction of the Sears–Haack drag values in figure 9-19. A significant reduction in wave drag can be obtained with these flattened-out volumes.

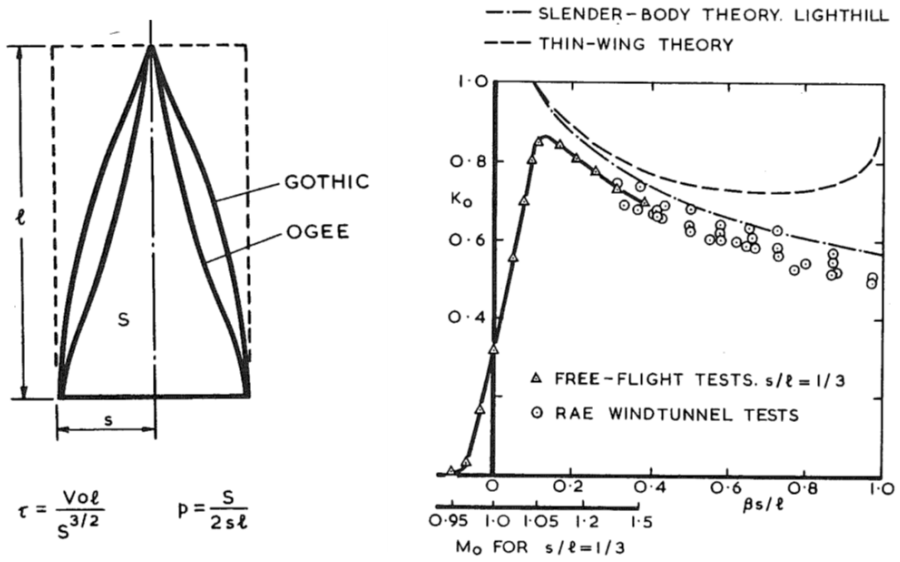


Figure 9-19(a) and (b): Wave drag reduction available for planar-type volumetric bodies; planform shapes and nomenclature (left) and wave drag for seven slender wings with the same area distribution (right). *From D. Küchemann. "The Aerodynamic Design of Aircraft." Reprinted by permission of the American Institute of Aeronautics and Astronautics, Inc. (Note: $K_o = 1$ for the Sears–Haack body.)*

9.4 Wings: Lift and Drag Due to Lift

Now we consider the lift and drag for traditional supersonic wing planforms. One of the fundamental notions in supersonic aerodynamics is the distinction between a subsonic edge and a supersonic edge. The concept is illustrated in figure 9-20.

Essentially all trailing edges are supersonic. This disconnects the upper- and lower-surface pressure distributions at the trailing edge, so there is no need for Kutta condition. The issue then becomes whether the leading edge is subsonic or supersonic. If the leading edge is subsonic, the flow about the leading edge is similar to the subsonic case in two dimensions. If the leading edge is supersonic, the flow at the leading edge behaves as if it were in a locally two-dimensional supersonic flow. This leads to a significant difference in the physics of the flow on the wing.

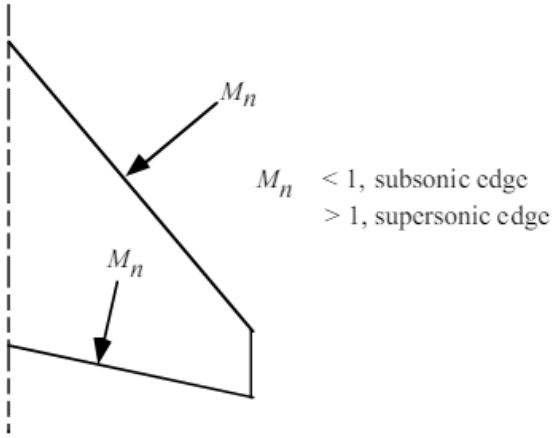


Figure 9-20: Definition of subsonic and supersonic edges in supersonic flow.

We will use a delta wing planform as an example. Figure 9-21 shows the difference in the planform and shock wave locations. It also introduces the concept of conical flows as important in thinking about supersonic wing performance. In a conical flow, both the geometry and the flow properties are constant along rays through the apex.

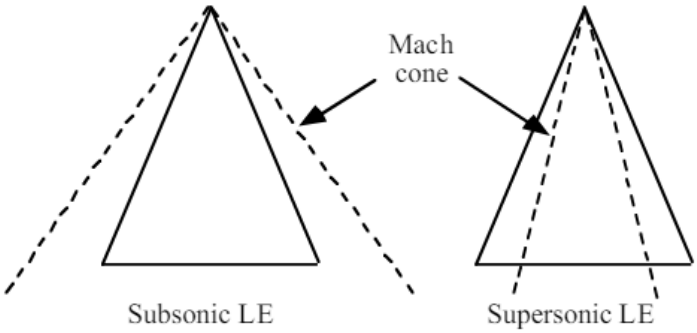


Figure 9-21: Examples of delta wings with subsonic and supersonic leading edges.

For the subsonic leading edge case, the upper and lower surfaces can still communicate with each other, as shown in the figure 9-22. Here, a point on the lower surface can create a disturbance that propagates in front of the wing, where a point on the upper surface aft of the lower surface disturbance point can be influenced.

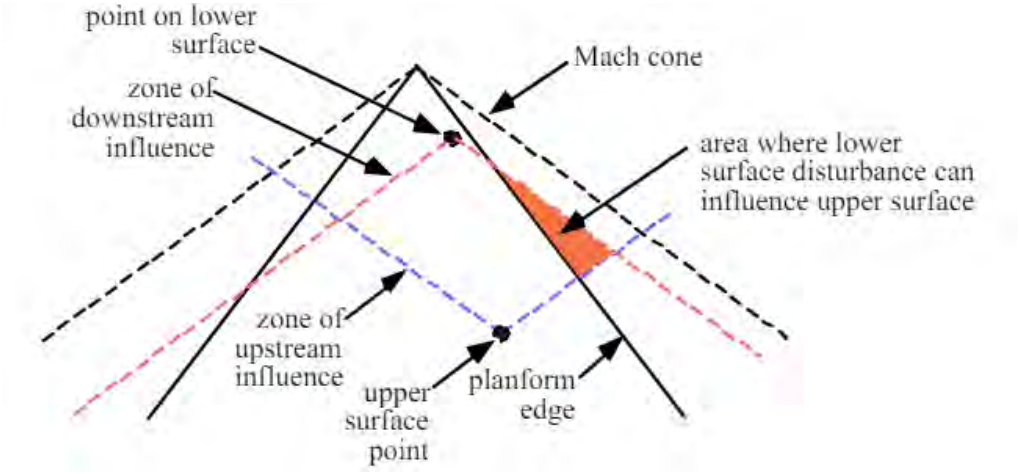


Figure 9-22: Example of how a disturbance on the lower surface of a wing in a supersonic flow with a subsonic leading edge can influence the flow on the upper surface.

Let's examine the linear theory spanwise pressure distributions for the two different cases, with the first case being subsonic leading edge and the second being supersonic. Figure 9-23 is for the case of a subsonic leading edge, showing the singularity at the leading edge, just as we expect in subsonic flow. The equation for the loading is given by

$$\frac{\Delta C_p}{C_L} = \frac{2}{\pi} \frac{1}{\sqrt{1 - \left(\frac{\tau}{m}\right)^2}} \qquad (9\text{-}13)$$

where $m = \beta\cot\Lambda$, and $\tau = (\beta y/x)$.

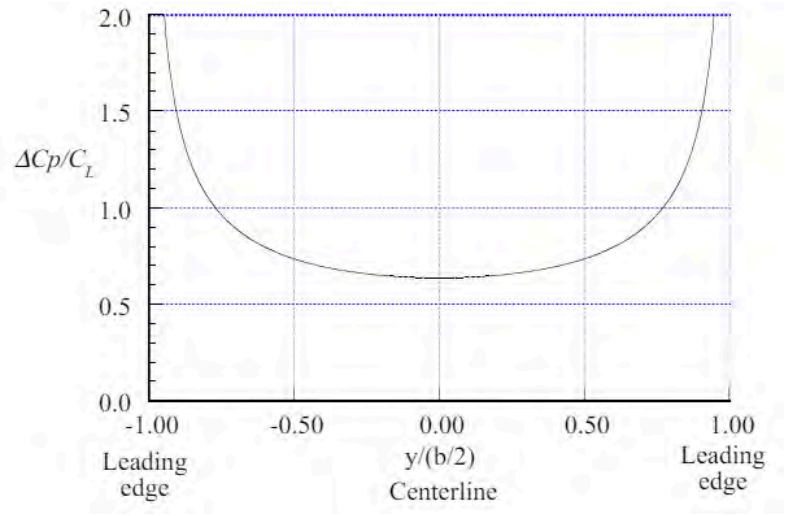


Figure 9-23: Spanwise pressure distribution (actually loading) for a subsonic edge case from linear theory.

Figure 9-24 is based on a supersonic leading edge, and here we see that the pressures outside of the Mach cone are constant. Thus, outside the Mach cone, the constant value of the loading is given by

$$\frac{\Delta C_p}{C_L} = \frac{1}{\sqrt{1-n^2}} \qquad (9\text{-}14)$$

where $n = \tan\Lambda/\beta = 1/(\beta\cot\Lambda) = 1/m$, $m>1$. Inside the Mach cone,

$$\frac{\Delta C_\rho}{C_L} = \frac{1}{\sqrt{1-n^2}}\left(1 - \frac{2}{\pi}\sin^{-1}\sqrt{\frac{n^2-\sigma^2}{1-\sigma^2}}\right) \qquad (9\text{-}15)$$

where $\sigma = y\tan\Lambda/x$, $0<\sigma<1$.

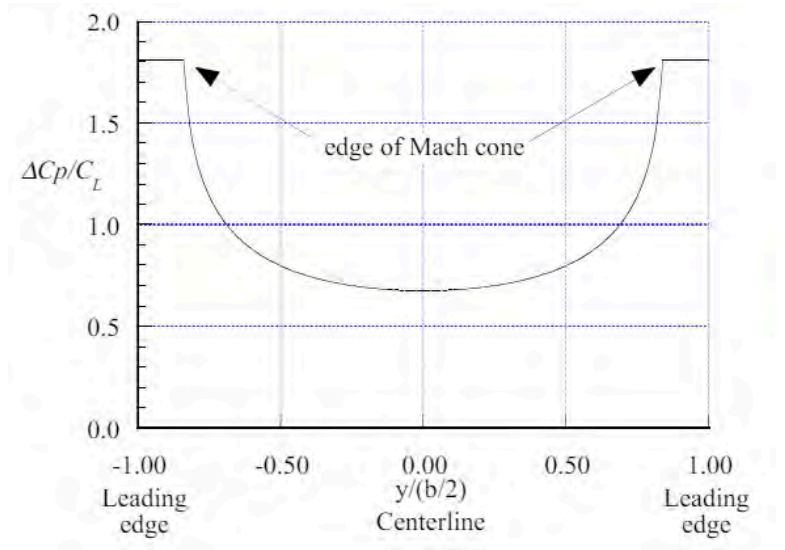


Figure 9-24: Spanwise pressure distribution (actually loading) for a supersonic edge case from linear theory ($m = 1.2$).

The solutions reflect the significant difference in the physics of the two cases.

9.4.1 Arrow Wings and Conical Camber

To think about the supersonic aerodynamics of wings, it is useful to consider a class of planforms for which exact linear theory solutions are available, namely the arrow wing. The flow is still conical and departs from a delta wing by adding a trailing-edge cutout, usually described as the notch ratio. Figure 9-25 provides the nomenclature.

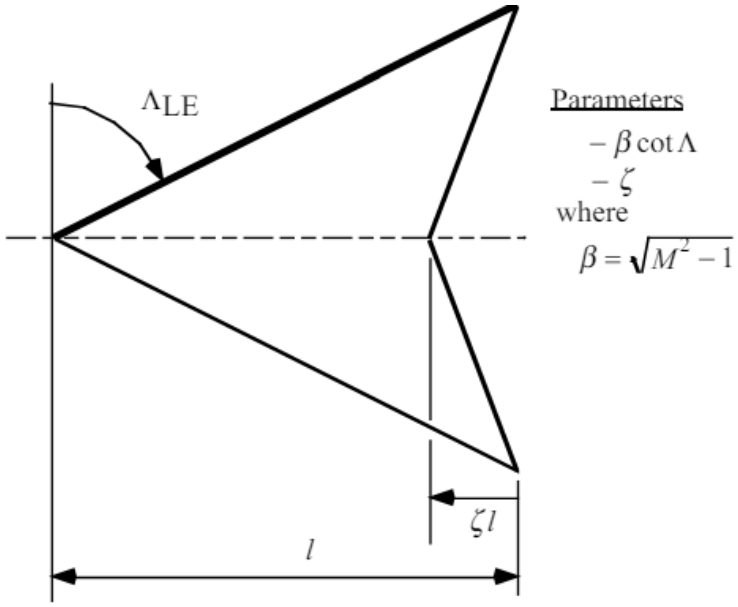


Figure 9-25: The classic arrow wing and the describing terminology.

The linear theory lift is given in figure 9-26 for two different notch ratios, ζ. The calculations were made using program *arrow.f* (see section E.8.3). Note the change in character when passing from the subsonic-edge case to the supersonic-edge case. The parameters are presented in the figure to "scale out" the Mach number, so the results are applicable for all Mach numbers.

Using conical flow theory, the analytic solution programmed in *arrow.f* for a subsonic leading edge is

$$\beta C_{L_0} = \frac{4m}{E'(m)}\left[\frac{\zeta}{1+\zeta} + \frac{1-\zeta}{(1-\zeta^2)^{3/2}}\cos^{-1}(-\zeta)\right], \quad m \le 1 \qquad (9\text{-}16)$$

where $m = \beta\cot\Lambda_{LE}$ and $E'(m) = E(k)$, where $k = \sqrt{(1-m^2)}$ and $E(k)$ is the complete elliptic integral of the second kind.[36]

In the case of the supersonic leading edge[37]

$$\beta C_{L_0} = \frac{8m}{\pi(1+\zeta)}\left[\frac{1}{\sqrt{m^2-\zeta^2}}\cos^{-1}\left(-\frac{\zeta}{m}\right) + \frac{\zeta}{\sqrt{m^2-1}}\cos^{-1}\left(\frac{1}{m}\right)\right], \quad m \ge 1. \qquad (9\text{-}17)$$

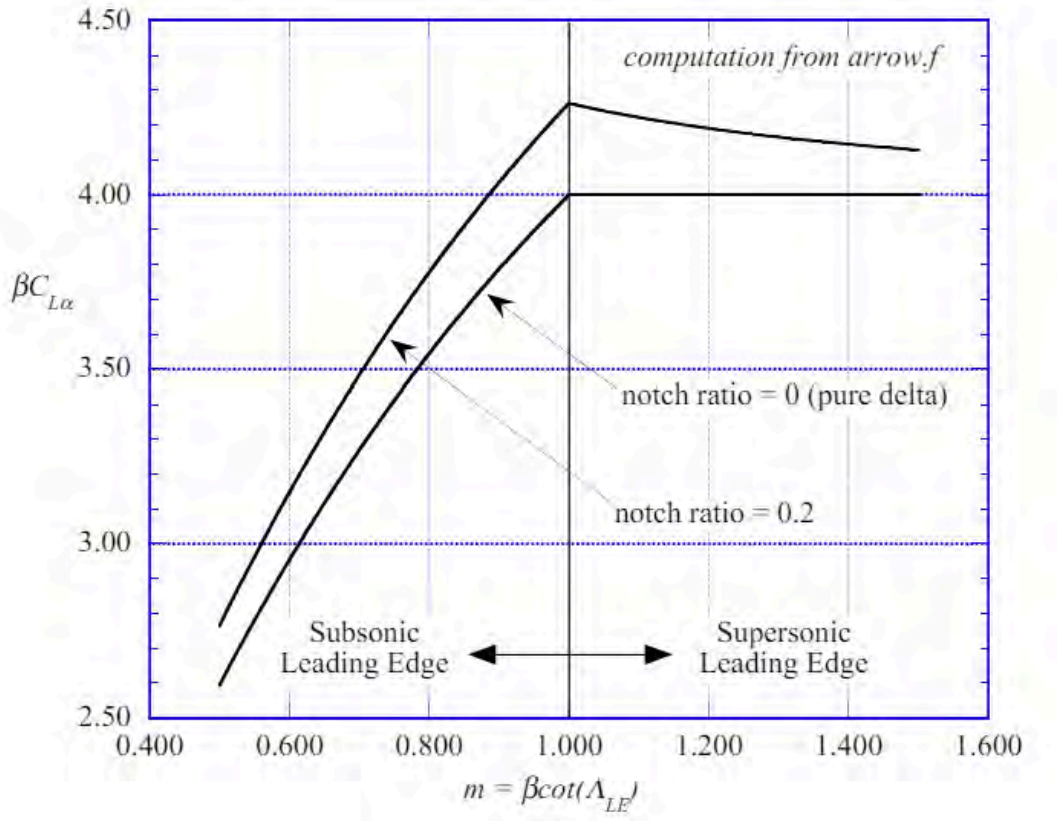


Figure 9-26: Arrow wing lift-curve slope.

The drag due to lift is also available from the theory. It is computed based on the 0% leading-edge suction drag, and then it is reduced if the leading edge is subsonic by the leading-edge suction; the component of the suction parallel to the velocity vector is called the leading-edge thrust, *T*. Thus the drag due to lift is

$$D = \alpha L - T \qquad (9\text{-}18)$$

where *T* is zero if the leading edge is supersonic. This can be put in terms of the force coefficients and written in a form that eliminates both Mach number and C_L dependence using the equation given above. The second term inside the bracket is zero for the supersonic leading-edge case:

$$\frac{\Delta C_D}{\beta C_L^2} = \frac{1}{\beta C_{L_0}}\left[1 - \frac{\pi m}{\beta C_{L_0}}\frac{1}{(1-\zeta)}\frac{\sqrt{1-m^2}}{E^2}\right] \qquad (9\text{-}19)$$

The results are shown in figure 9-27. This time, the figure is more complicated. For subsonic edges, two branches of the drag are shown. One assumes that the full leading-edge suction can be realized, while the other assumes that no leading-edge suction is achieved. If full leading-edge suction can be obtained, subsonic edges are desirable to reduce the drag. However, if no suction can be obtained, then the drag is reduced when the edges are supersonic. Although we have presented results for planar wings, the effect of leading suction is attained in practice by cambering the wing. Essentially, the linear theory says that by cambering the wing, a benefit equivalent to the full leading-edge suction can be realized. Experience shows that only a portion of the leading-edge suction predicted by linear theory can be achieved, possibly explaining why many of the supersonic airplanes listed above have had supersonic leading edges at the design Mach number. Many NASA designs were more aggressive, and selected an *m* of about 0.75. They were expected to attain the full value of leading-edge suction. In general, the calculation of the leading-edge suction is difficult. However, progress has been made.[38]

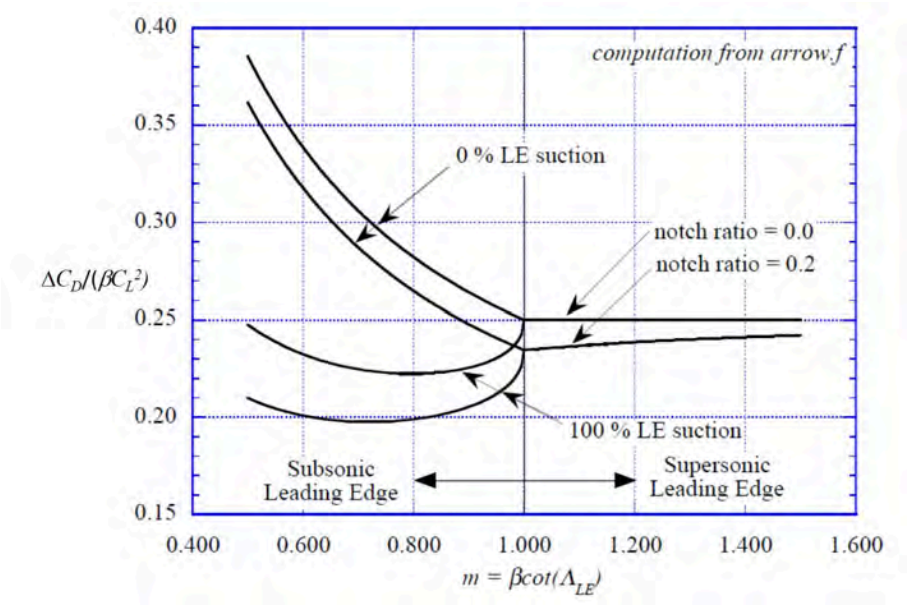


Figure 9-27: Arrow wing drag due to lift.

The conical flow theory used to obtain the solutions presented here was also the basis for a special type of camber that was widely applied to many delta-wing supersonic aircraft to reduce the drag due to lift. Known as conical camber, the surface was cambered so that the geometry was straight along rays through the apex of the wing.[39] Conical camber was used on the F-102, F-106, and B-58. It was also used on the F-15.

Figure 9-28 shows the conical camber on an F-102. The photo was taken by W. H. Mason at the Pima Air & Space Museum outside of Tucson, Arizona. It is taken from behind the airplane looking forward along the leading edge, showing the large amount of camber. The camber is pronounced on this plane because it was added after the plane was built and was limited to the wing outboard of the 85% spanwise cuts to maintain the basic structure. The F-15 has conical camber, but it is distributed across the span and difficult to see.



Figure 9-28: The F-102, showing the leading-edge spanwise camber. *From W. H. Mason. At Pima Air & Space Museum near Tucson, AZ.*

Figure 9-29 shows one of the inventors of conical camber, NACA/NASA research scientist Charles F. Hall, looking at a model in a wind tunnel at the Ames Research Center.



Figure 9-29: Conically cambered model in the NACA Ames Wind Tunnel. *From NASA. Wikimedia. Public domain.*

Figure 9-30, from a survey paper by Von Kármán,[40] shows how the concept works. With a small leading-edge radius required for supersonic flight, the effect of leading edge suction can be achieved by providing a forward-facing surface with a low pressure. The resulting drag polar is shifted upward, approaching the value of a flat surface with 100% leading suction.

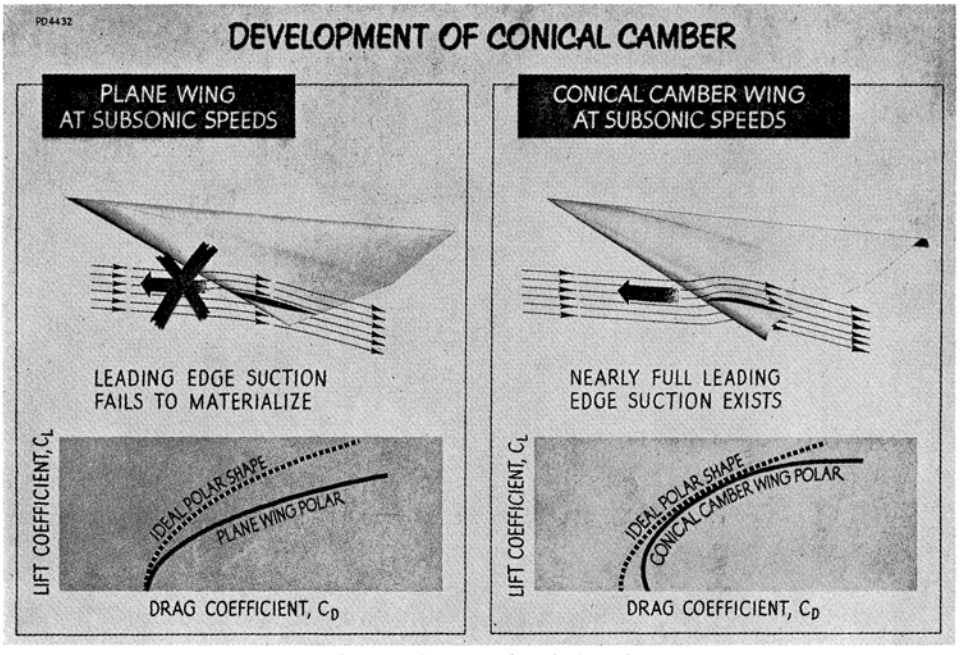


Figure 9-30: Conical camber produces leading-edge suction and thus reduces drag; notice the shift in the drag polar. *From T. von Kármán. "Some Significant Developments in Aerodynamics Since 1946." Copyright undetermined by AIAA. Fair use.*

9.4.2 Modified Arrow Wings

Once the arrow wing is used to establish a basis for thinking about the aerodynamics of supersonic wings, one proceeds to think in terms of modifying it for practical application. The literature frequently refers to a "modified arrow wing" configuration that to me never appeared at all like the planform shown above.[41]

Figure 9-31 traces the evolution of the arrow wing to a configuration applicable to actual aircraft design.[42] The sequence of modifications shown in the figure can be described as follows. For the basic arrow planform, the tip is "clipped." The structural span is decreased, and a portion of the wing that doesn't actually contribute aerodynamically is eliminated. Next, for planform A, the outboard portion of the wing is unswept slightly. This improves the subsonic efficiency with little penalty for supersonic efficiency. It also reduces the aerodynamic center (*ac*) shift. Finally, for planform B, the trailing edge is filled in. This helps the subsonic pitchup, makes trailing-edge flaps more effective, and also further reduces the *ac* shift. For a specified thickness, the extra chord means that the root *t/c* is reduced. This explains why a planform that doesn't look anything like an arrow wing becomes a "modified" arrow wing.

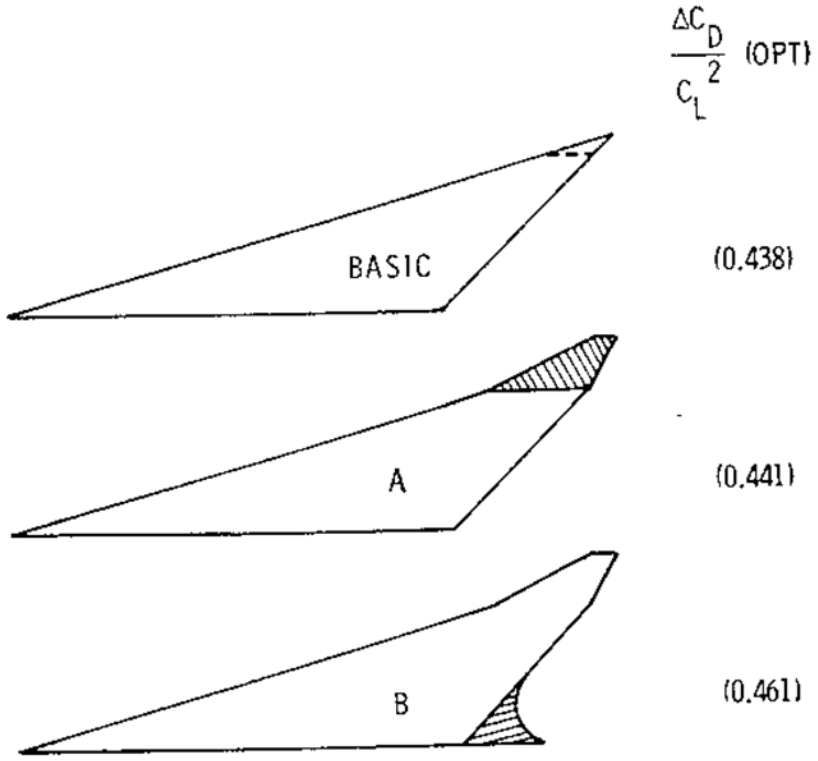


Figure 9-31: Classic modified arrow wing progression. From D. D. Baals, A. W. Robins, and R. V. Haris, Jr. "Aerodynamic Design Integration of Supersonic Aircraft." Copyright undetermined by AIAA. Fair use.

A related issue for modified arrow wings with the outboard portion unswept is the potential for pitchup at subsonic speeds and high angle of attack (described previously in Chapter 5). A review of this effect and an approximate method for estimating for pitchup for these types of planforms is available in a paper by Benoliel and Mason.[43]

9.5 The Aerodynamic Center Shift

Another important consideration in supersonic configuration design is the shift of the aerodynamic center (AC). In the classical 2D case illustrated in figure 9-32, the aerodynamic center shifts from the 25% chord to the 50% chord. The *arrow.f* program also provides the aerodynamic center location as well as the lift and drag (but only at supersonic conditions). We need to see how modifications to the classic delta wing shape can be used to reduce the AC shift.

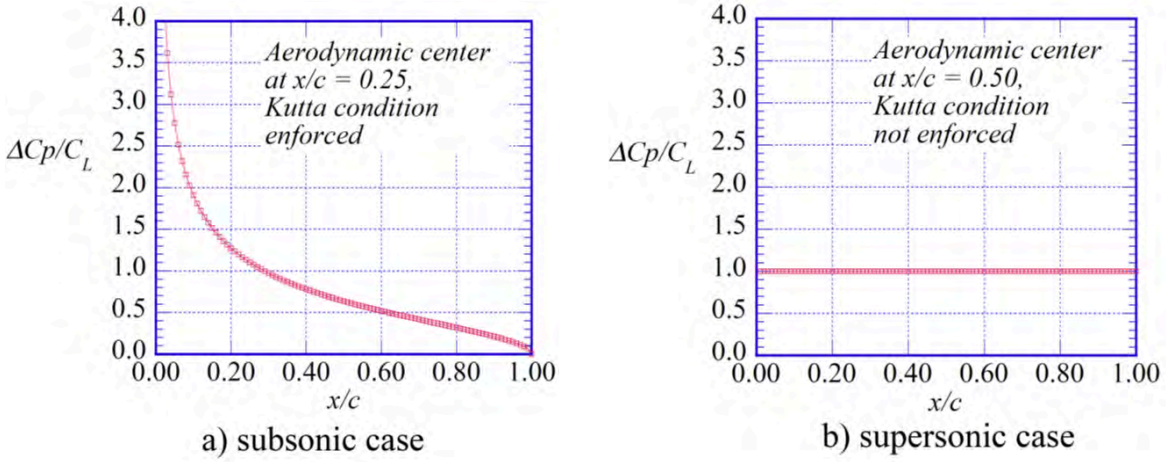


Figure 9-32: Comparison of load distributions for 2D subsonic and supersonic flat plates. From W. H. Mason. Adapted.

Figure 9-33 is taken from the Concorde case study,[44] and it shows that the Concorde planform shaping is critical in reducing the shift. However, the shift is still significant and fuel transfer must be used to maintain an acceptable relation between the center of gravity and aerodynamic center.

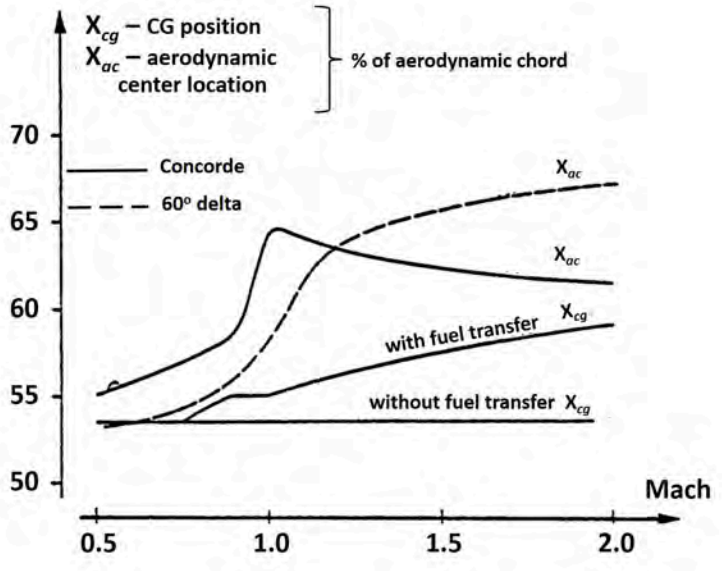


Figure 9-33: Concorde example showing planform shaping to control the AC shift. From J. Rech and C. S. Leyman. "A Case Study by Aerospatiale and British Aerospace on the Concorde." Reprinted by permission of the American Institute of Aeronautics and Astronautics, Inc. Adapted by P. Raj.

The allowable CG range shown in figure 9-34 for the Concorde shows how important the CG control was.[45] The Concorde used a root chord of 90.75 feet as the reference chord. At takeoff and landing, the CG was required to be between 52.5% and 53.5% of the root chord. At supersonic cruise, the AC shifts about 5.5%, or 5 feet. The allowable CG limits are between 58% and 59% of the root chord. Thus for an airplane of slightly over 101 feet in length, the CG must be maintained within about 11 inches. This is why configuration designers consider airplane balance immediately upon examining any design drawing.

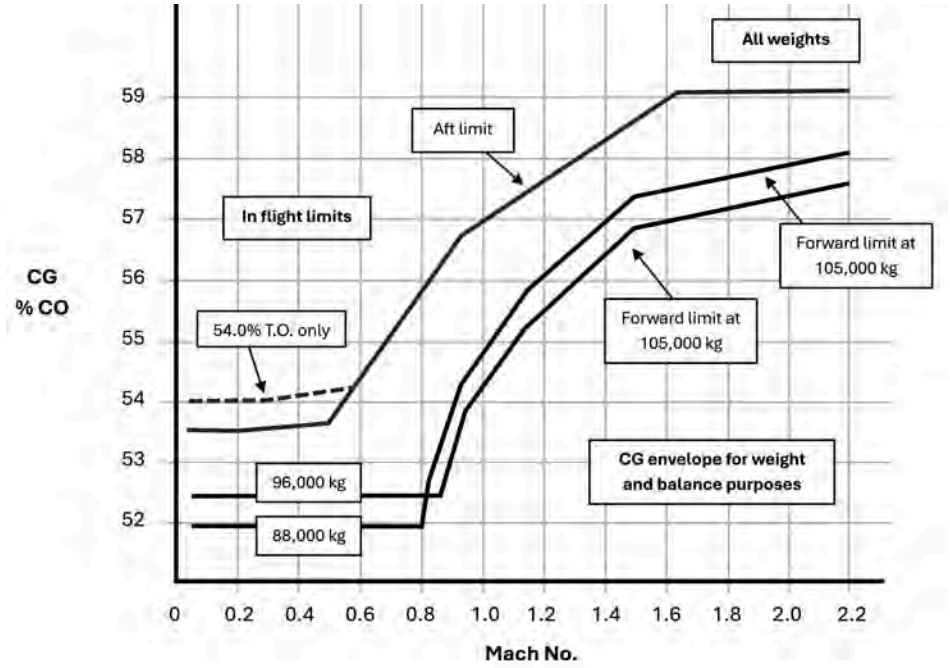


Figure 9-34: Concorde CG limit changes with Mach number, given as a fraction of the root chord. *From British Aerospace Corporation. Copyright undetermined. Fair use. Adapted by K. Grey.*

All supersonic airplanes use fuel transfer to control the CG location and maintain a relation between the CG and AC that allows the airplane to be adequately controlled and also fly with minimum control surface deflections to minimize trim drag. The XB-70 was unusual in that the wingtips folded down in supersonic flight. Although usually described as providing extra aerodynamic efficiency and additional directional stability, perhaps the most important consequence of folding the tips was to control the AC shift.

Additional examples of planform shaping to reduce the AC shift were presented by Lamar and Alford.[46] They used a slightly different parameter to correlate AC shift, showing the benefit of using a double-delta planform, which would be a rough approximation of the Concorde planform. Figure 9-35 shows the result of their parametric study of the aerodynamic center shift. They show that a pure delta wing has a much larger AC shift then a double delta. They found that the inboard delta meeting the aft delta at about 45% of the semispan produces the smallest AC shift. When it comes to the extent of the more highly swept inboard delta, the larger the better.

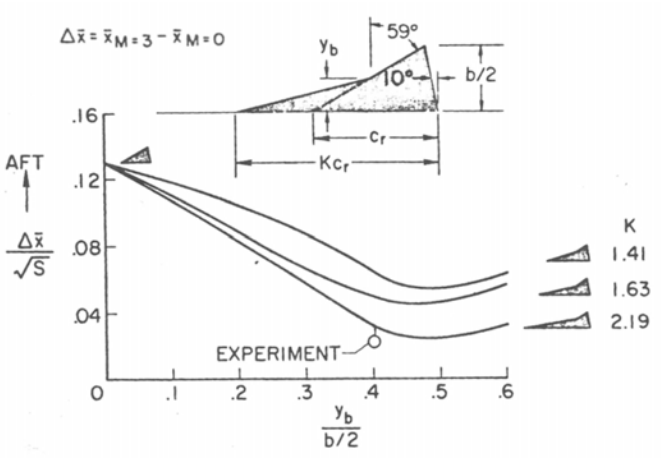


Figure 9-35: Effect of planform on the aerodynamic center shift, subsonic to supersonic. *From J. E. Lamar and W. J. Alford, Jr. "Aerodynamic-Center Considerations of Wings and Wing-Body Combinations." NASA. Public domain.*

Why does this work? The idea is that the inboard wing, being more highly swept and having a lower aspect ratio, has a lower $C_{L\alpha}$, that is insensitive to Mach number. The outboard section, with less sweep, has a higher aspect ratio and a $C_{L\alpha}$ that decreases with

Mach number. Thus the composite planform has a smaller AC shift. How this was discovered is a little mysterious. The NASA paper has a date of 1966. Ben Rich provided a similar explanation is his paper on the SR-71.[47] The first version of the SR-71, the A-12, was flown in 1962. The Lockheed's proposed commercial supersonic transport (SST) design used a double delta, and the configuration was apparently chosen in 1963.*

*Directly from page 829 of Raymer's cited book:footnote]Raymer, D. P., *Aircraft Design: A Conceptual Approach*, 4th ed., AIAA, Reston, 2006, p. 667.[/footnote] *The Lockheed SR-71 has such extensive fuselage chines that it is technically a double-delta, and when the engineers in the "nonblack" side of Lockheed were developing their supersonic transport design, their counterparts from the Skunkworks gave them a sketch of the double-delta arrangement and said "use it—it works but don't ask how we know!"*

A final example requiring attention to aerodynamic center shift arises for airplanes with variable-swept wings. Although no longer fashionable, variable-sweep wings have the attraction of performing well at both subsonic and supersonic speeds. When the wings are swept back, the low aspect ratio also reduces the gust-load response for high subsonic-speed on-the-deck penetration missions. The problem of the airplane becoming too stable when the AC shifts aft is aggravated when the variable-sweep wing is swept back at supersonic speeds. This adds more (stabilizing) planform area aft of the CG. Figure 9-36(a) from a paper by Kress[48] illustrates the problem by comparing the static margin shift with Mach number for F-111 and F-14. Clearly the F-111 supersonic static margin is excessive. The F-14 has a lower static margin, and it has another feature that decreases the static margin even more: the glove vane.

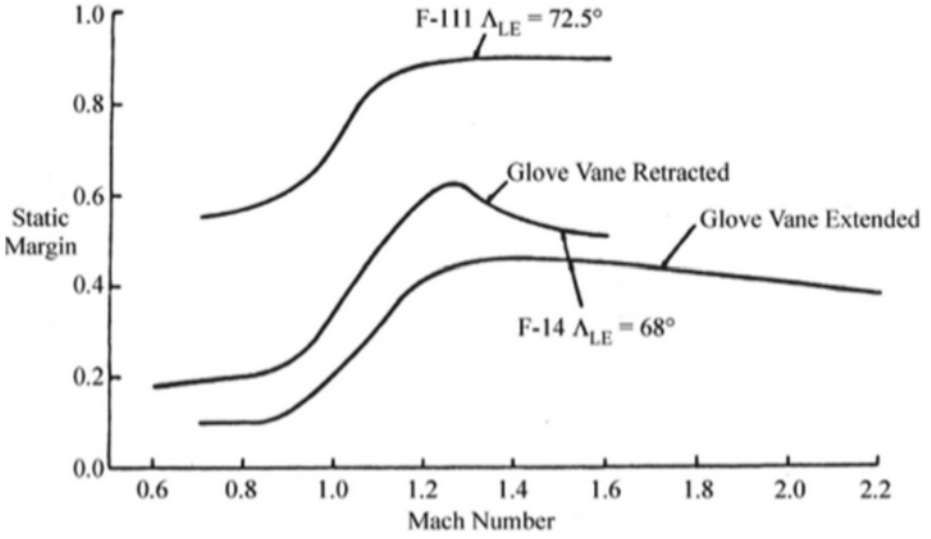


Figure 9-36(a): Static margin change with Mach number for variable-sweep wings. From R. W. Kress. "Variable Sweep Wing Design." Copyright undetermined by AIAA. Fair use.

Kress invented the glove-vane for the F-14, as shown in figure 9-36(b), to further reduce the static margin. When the wings were swept back, the glove vane came out, adding planform area forward of the center of gravity. This resulted in a reduction in AC shift.

The main reason that the F-14 had a reduced static margin shift was the use of an outboard pivot location, which differed in comparison to the F-111, as shown in figure 9-36(c). The use of the outboard pivot reduced the AC shift. The effect of pivot location had been the subject of numerous wind tunnel tests at NASA Langley. Good background information on variable-sweep aircraft development can be found in the report by Polhamus and Toll.[49] Their paper also discusses the skewed-wing concept that became known as an oblique wing, as detailed in the next section.

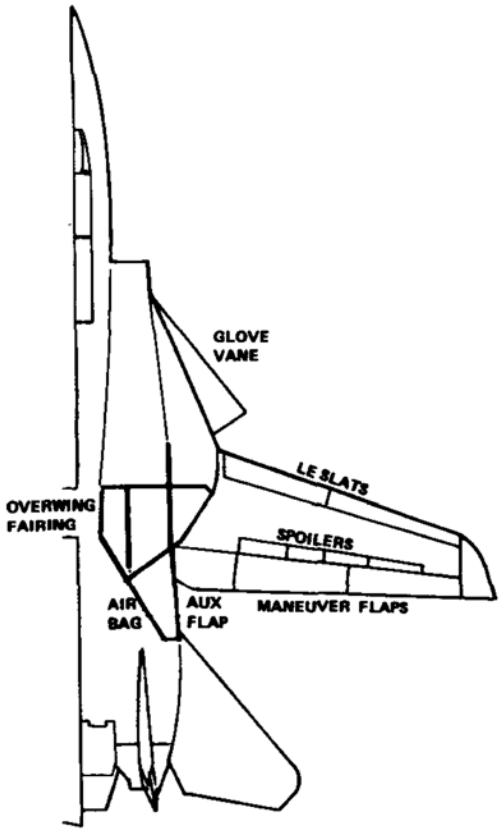


Figure 9-36(b): Glove vane on a F-14 wing. *From R. W. Kress. "Variable Sweep Wing Design." Copyright undetermined by AIAA. Fair use.*

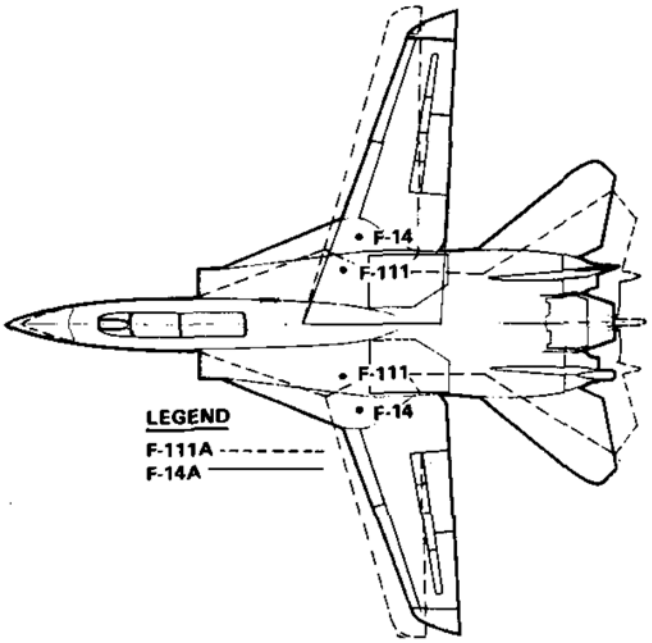


Figure 9-36(c): F-14 and F-111 pivot point locations. *From R. W. Kress. "Variable Sweep Wing Design." Copyright undetermined by AIAA. Fair use.*

9.6 The Oblique-Wing Concept

This section describes the supersonic airplane concept based on the oblique wing. When considering both lift and volumetric drag, a somewhat radical wing concept with good potential for a supersonic transport application is the oblique-wing idea advocated by R. T. Jones for many years.[50,51] The idea is that both the longitudinal as well as spanwise distribution of lift should be elliptical. The natural way to do this is with an oblique wing planform. Jones made the argument that there is no reason that an airplane has to be symmetrical.

Originated for its good drag-due-to-lift characteristics, this shape is also good for volumetric wave drag because the area diagram can be very good, especially for a flying wing configuration. Figure 9-37 from the *Wing Theory* book by Jones[52] illustrates the advantage. It compares the wave drag for an oblique elliptic wing to a swept wing having the same aspect ratio and thickness-to-chord ratio. There is a clear advantage for the oblique wing. Note that the advantage occurs for Mach numbers around 1.4 to 1.5. Earlier in this chapter, we saw how important length was in reducing the drag of axisymmetric bodies, and that is important here too. Admittedly, the speed range where the concept shows most benefit is less than the usual notion of a Mach 2 airplane attributed to the Concorde. However, the large decrease in drag makes this concept compelling for a supersonic configuration. Because Jones worked at NACA/NASA and had made many contributions, he was able to convince NASA to conduct numerous wind tunnel tests. Many of the wind tunnel tests were nominally "transonic" tests, but they actually emphasized the upper-transonic speed regime, which might actually be called lower supersonic.

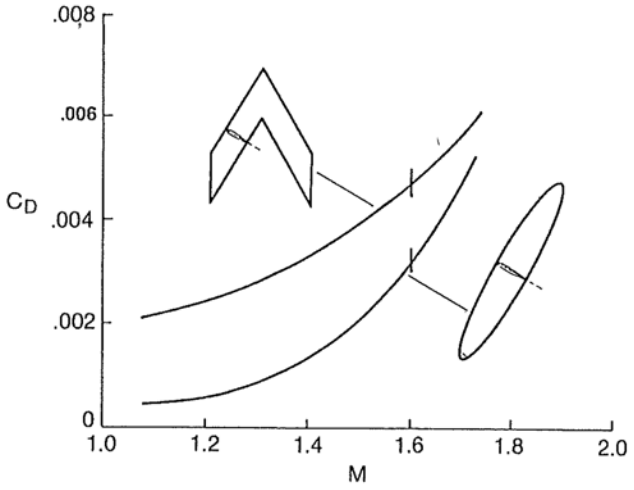


Figure 9-37: A comparison of the variation in drag coefficient with Mach number for an oblique and a swept wing with the same aspect ratio and t/c. *From R. T. Jones. Wing Theory. Fair use.*

Many other aerodynamicists have examined the concept. It has always been found to be attractive. We only cite one among many, the paper by Li, Seebass, and Sobieczky.[53] They include a good reference list to other work and advocated the design of an oblique flying wing at a Mach number of 1.4. Aeroelasticity was also an issue, and Weisshaar and his colleagues have presented results of their work in this area in numerous papers; we reference only one here.[54] Although aeroealsticity needs to be addressed, today's modern design and active control technology should be capable of handling any serious issues.

As an unconventional configuration, an oblique wing was built and flown by NASA. The AD-1 (Ames-Dryden-1) oblique-wing research aircraft was successful; figure 9-38 shows it in flight. It was strictly a subsonic airplane, intended to investigate the flying qualities of an oblique wing. The wing could sweep from 0 to 60 degrees in flight. Its first flight was in December 1979, and it finished the flight test program in August 1982. The demonstrator was very basic; there was no automatic flight control system. The plane suffered from some issues with handling qualities, as well as adverse aeroelastic effects. With the use of a modern flight control system, however, it seems that the oblique wing would be a viable concept. A description of the program and outcomes are documented in two AIAA Papers.[55,56]

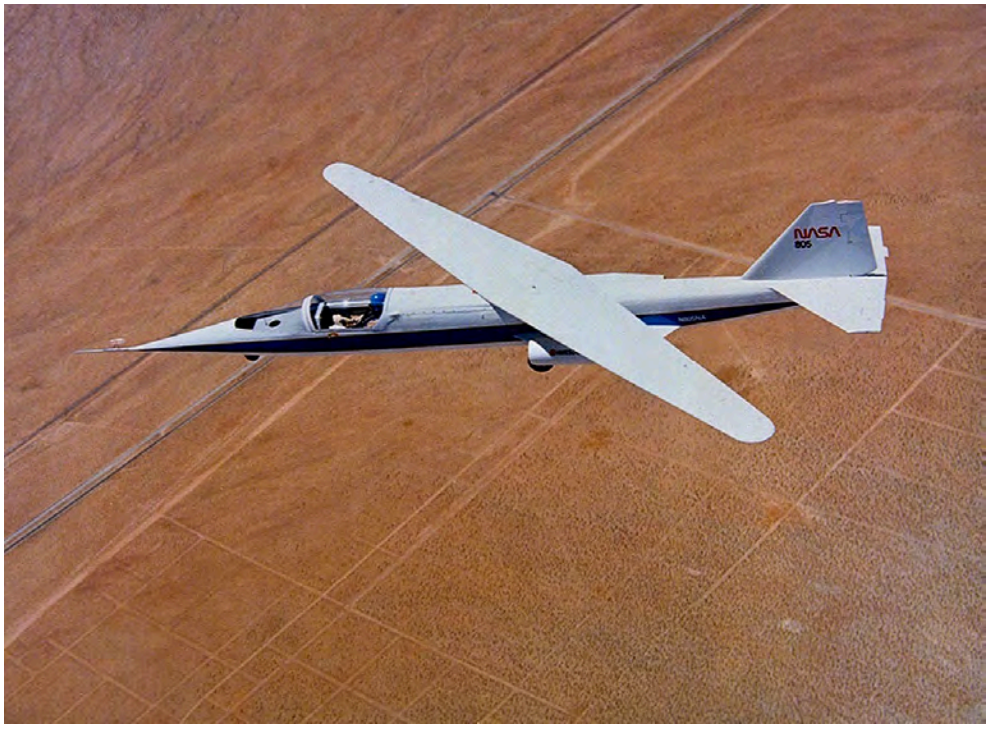


Figure 9-38: Oblique wing flight demonstration by the AD-1. From NASA. Public domain.

After it finished its demonstration, it was displayed at the visitor's center at NASA Ames Research Center, located at Moffett Field in California, as shown in figure 9-39. It was so small that we include a photo with the pilot standing in front of it (figure 9-40) to appreciate its size. Today, it's on display indoors at Hiller Aviation Museum in San Carlos, California.



Figure 9-39: The AD-1 outside the NASA Ames Visitor Center. From W. H. Mason, many years ago.



Figure 9-40: The AD-1 shown with pilot to emphasize its small size. From NASA. Public domain.

Numerous studies of the oblique wing as a new supersonic transport have been made,[57,58] but it was not considered in the HSCT studies conducted by NASA with the industry in the 1990s.

A comprehensive survey of oblique-wing work has been compiled by Hirschberg, Hart, and Beutner.[59] Subsequent to this paper, a major optimization study was carried out at NASA Ames showing that advanced computational methods could further improve oblique-wing aerodynamic designs.[60] The case in favor of the oblique-wing concept for modest supersonic speeds remains compelling.

9.7 Aeropropulsion Integration

Efficiently integrating the propulsion system with the airframe requires much more effort for supersonic airplane design than for subsonic airplanes. Covering the entire subject here is beyond the scope of this course, but we point out a few of the issues and provide an example showing how to include the propulsion system efficiently. The design of the inlet and exhaust nozzle often requires as much computational and testing effort as the rest of the airframe.

The inlet has to be carefully designed to handle the required mass flow at supersonic cruise while also operating efficiently at low speed. A variable geometry inlet is often required if the cruise Mach number is more than 1.6. A stable shock system providing the air to the engines is hard to maintain. The XB-70 and SR-71 had notorious problems with unstarts (breakdowns of the supersonic airflow). Eventually the

SR-71 had an automated system to recover from an unstart. Many fighters that have inlets close to the side of the fuselage are offset and use boundary layer diverters to ensure a uniform flow into the inlet. The F-35 uses a diverterless inlet, which features a "bump" on the fuselage side in front of the inlet to force most of the boundary layer to flow around the inlet. This became possible when CFD could be used to design the fuselage/inlet.

Figure 9-41 from Don Baals et al.[61] shows how integrating a podded-engine installation under the wing can lead to favorable interference. The wing is reflexed around the nacelle. The drag of the aircraft is very sensitive to the location of the pod.[62]

The exhaust nozzle also requires careful design. Because of the afterburner, the nozzle has to have a variable geometry. Thrust vectoring may also be used. Each of these features will require careful attention. The external contour typically has what is known as a boattail shape, which has to be carefully shaped to avoid extra drag. Boattail analysis was one of the first intense CFD efforts.

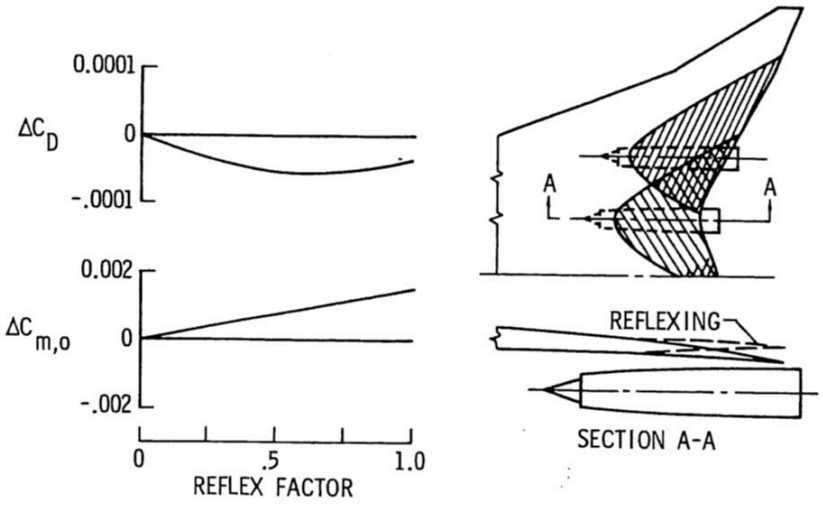


Figure 9-41: Possible favorable aeropropulsion interference when the engines are located in the right position. From D. D. Baals, A. W. Robins, and R. V. Haris, Jr. "Aerodynamic Design Integration of Supersonic Aircraft." Copyright undetermined by AIAA. Fair use.

The best place to learn about propulsion system installation in supersonic aircraft configuration work is in the book by Nicolai and Carichner,[63] which describes inlet design in Chapter 15 and nozzles in Chapter 16. Studies continue to be carried out for the aeropropulsion integration of proposed supersonic business jets.[64]

9.8 Computational Methods and Supersonic Aerodynamic Design

Although powerful CFD methods are available today, we need to provide a context for their use. We've described the fundamental aerodynamic ideas that can be used to develop a supersonic configuration. These came from slender-body and linear-theory analysis. For most supersonic flight, the flow is necessarily attached to keep drag low, ensuring that the inviscid flow field combined with skin friction estimated from boundary layer theory can provide good estimates for drag. However, supersonic flight is demanding and very sensitive to the accuracy of the estimates. We will describe methods to use as a starting point, but complete CFD will have to be used for accurate drag values.

The drawbacks to using CFD during the initial stages of design are threefold. First, CFD requires a high-quality grid to be generated on a detailed geometry. We need the grid to perform computational aerodynamic simulations. The process is time consuming, and it is highly desirable to have a good starting point for the design when starting the work of creating a detailed geometry. The second issue is the need to represent the geometry with a flexible parametric representation that is capable of being readily changed to improve the design. The third issue is that, to obtain the design shape using CFD, some sort of formal optimization method is needed because the "cut-and-try" approach is inefficient. Formulating the optimization problem to achieve a good design requires skill and experience. The optimizer is excellent at finding any weaknesses in the problem formulation or the analysis! It's harder than it appears in typical student textbooks. Nevertheless numerical optimization methods are very powerful and will be increasingly used to develop future configurations. More

importantly, serious aerodynamic design is only of interest when the entire system is included. This means using the techniques that fall under the umbrella of multidisciplinary design optimization (MDO) to do the aerodynamic design together with the other key disciplines.

With all this in mind, we'll lay out a way to get to a good supersonic design. Details on CFD can be found in the companion volume to this work.[65]

9.8.1 The Linear Theory Starting Point

Linear theory was used to investigate many configurations at NASA and in the aviation industry during the 1960s, used in conjunction with an active aerodynamic testing program. This was done in anticipation of the development of the US SST (supersonic transport). The program produced many insights into supersonic aerodynamics for application to aircraft configurations. The basic tools are the Harris wave drag code,[66] a supersonic panel method[67] with corrections for attainable leading-edge thrust,[68] and formulas for estimating skin friction drag using the Van Driest method.[69] We will review how well these methods work.

Let us look at the wave drag estimation first. Figure 9-42 is one of the famous figures from the NASA wave drag report by Harris.[70] The Harris wave drag code uses the input geometry to find the cross-sectional areas to compute the wave drag integral; see equation 9-2 and Chapter 3. Like most NASA codes of that era, it used the Craidon input, as described in NASA TM X-2074.[71] It was much more efficient to use essentially the same input geometry in numerous codes.

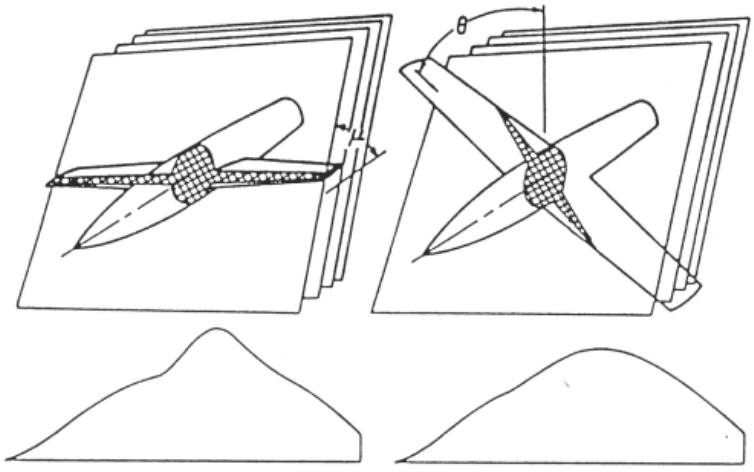


Figure 9-42: Illustration of cross-sectional area cuts used in the wave drag code. *From Haris, R. V., Jr. "An Analysis and Correlation of Aircraft Wave Drag." NASA. Public domain.*

9.8.1.1 Body of Revolution

Examples of the accuracy of the Harris code for a Haack–Adams body of revolution of fineness ratio (l/d) of 10 are shown in figure 9-43. The geometry is shown in figure 9-43(a) in terms of normalized radius distribution along the length of the body, and the computed zero-lift wave drag coefficients at different Mach numbers are shown in figure 9-43(b). Wind tunnel data is from a NASA Langley Research Center Test.[72] The solution labeled *GASP: Space Marched* is an inviscid Euler solution from the GASP CFD code.[73,74] At moderate Mach numbers, the Harris code is reasonably good. These results are from work at Virginia Tech.[75] If you are interested in more details of the analysis performed to generate the results presented here, you should read the cited MAD Center report.

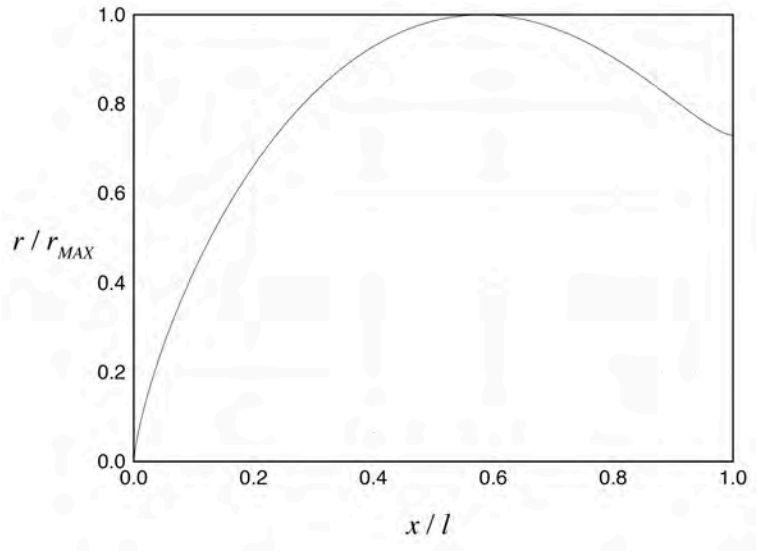


Figure 9-43(a) The Haack–Adams body of revolution, l/d = 10. From D. L. Knill, L., V. Balabanov, O. Golovidov, B. Grossman, W. H. Mason, R. T. Haftka, and L. T. Watson. "Accuracy of Aerodynamic Predictions and Its Effects on Supersonic Transport Design." Used with permission of Virginia Tech.

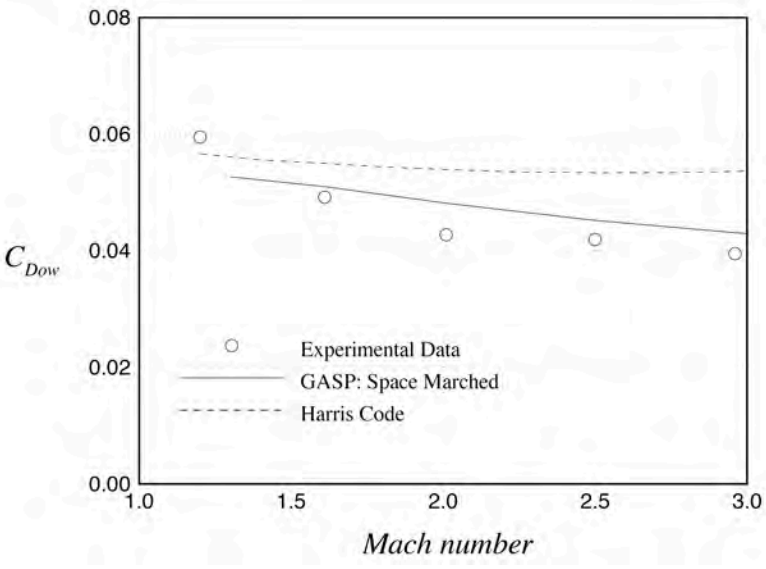


Figure 9-43(b): Comparison of computed and measured wave drag results for the Haack–Adams body of revolution, l/d = 10. From D L. Knill, V. Balabanov, O. Golovidov, B. Grossman, W. H. Mason, R. T. Haftka, and L. T. Watson. "Accuracy of Aerodynamic Predictions and Its Effects on Supersonic Transport Design." Used with permission of Virginia Tech.

9.8.1.2 Wing

We next consider the zero-lift wave drag prediction for a wing shape. The geometry of the so-called Squire wing[76] is shown in figure 9-44(a). The wing has a 9-percent-thick biconvex airfoil section on the centerline, and it features elliptic spanwise sections that are picked to match the centerline airfoil. The wing may be a little thick for wave drag application but has wind tunnel data available for comparison in the same report (ARC R&M 3818).

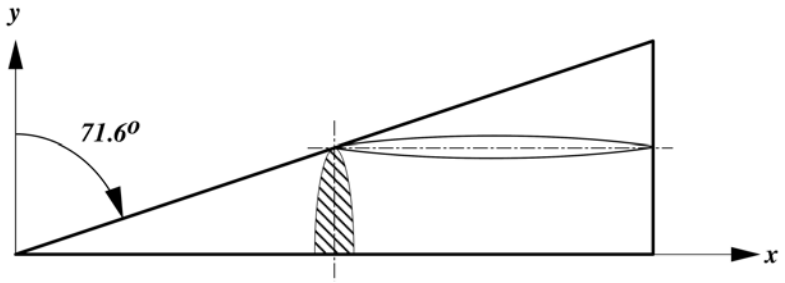


Figure 9-44(a): The Squire-wing geometry. *From D. L. Knill, V. Balabanov, O. Golovidov, B. Grossman, W. H. Mason, R. T. Haftka, and L. T. Watson. "Accuracy of Aerodynamic Predictions and Its Effects on Supersonic Transport Design." Used with permission of Virginia Tech.*

As shown in figure 9-44(b), for Mach numbers less than 2.2, the Harris code correctly predicts the trend of the zero-lift wave drag coefficient with increasing Mach number. However, the Harris code overpredicts the drag, as in the body of revolution case examined above.

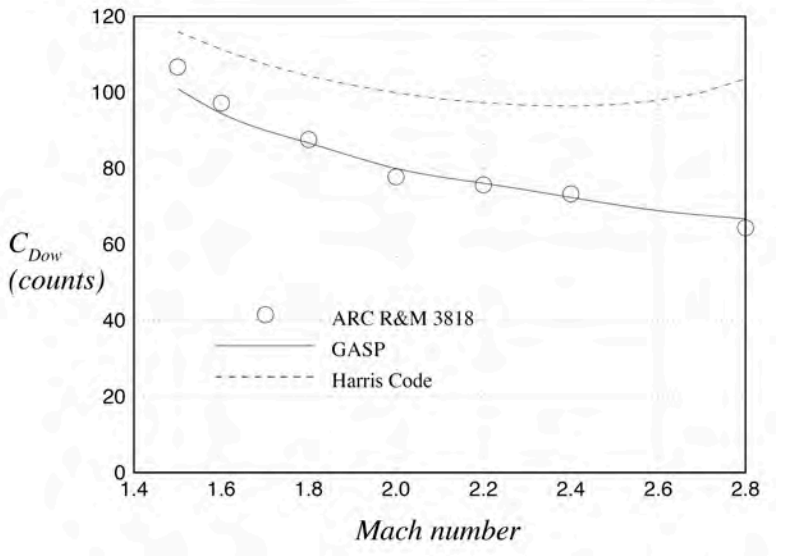


Figure 9-44(b): Comparison of computed and measured zero-lift wave drag results for the Squire-wing geometry. *From D. L. Knill, V. Balabanov, O. Golovidov, B. Grossman, W. H. Mason, R. T. Haftka, and L. T. Watson. "Accuracy of Aerodynamic Predictions and Its Effects on Supersonic Transport Design." Used with permission of Virginia Tech.*

9.8.1.3 HSCT Configuration

We complete our examples of what to expect from the Harris code and a linear theory panel code by comparing results for a hypothetical high-speed civil transport (HSCT) study from the same MAD Center report (MAD 96-12-01, Dec. 1996) that we used to compare wave drag above. Figure 9-45 shows the configuration geometry and the grid for GASP code analysis. In much of our work, we used the space marching option in GASP to reduce computer time. As long as the flow is supersonic, we can replace iterations in time with iterations in space, starting at the nose and marching downstream. This scheme was key to our optimization work that required thousands of analysis runs. We were fortunate to be able to use an automatic grid-generation code written by Ray Barger at NASA Langley.[77,78]

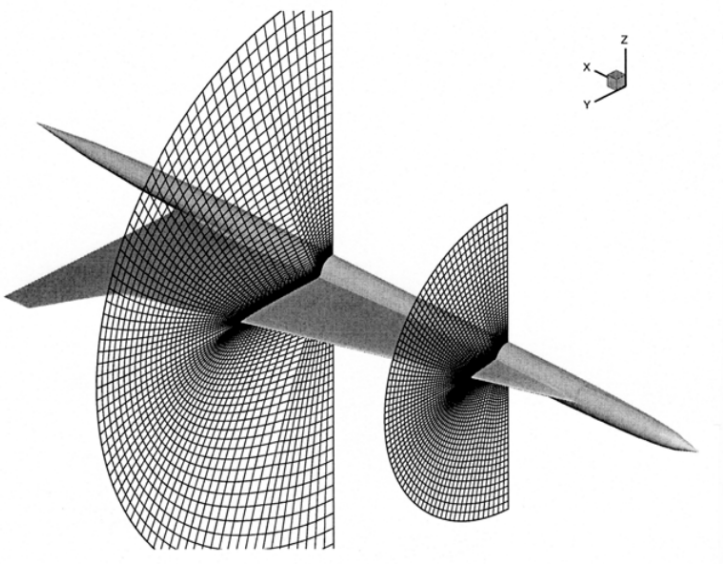


Figure 9-45: HSCT configuration and the associated grid. *From D. L. Knill, V. Balabanov, O. Golovidov, B. Grossman, W. H. Mason, R. T. Haftka, and L. T. Watson. "Accuracy of Aerodynamic Predictions and Its Effects on Supersonic Transport Design." Used with permission of Virginia Tech.*

Figure 9-46 compares the computed lift and pitching moment coefficients from CFD methods and linear theory at $M = 2.4$ for the HSCT configuration. Both the linear theory and Euler results include skin friction (SF) estimates, although they don't influence the lift and moment estimates. The figure also contains the predictions from GASP using the parabolized Navier–Stokes (PNS) option in GASP using the Baldwin–Lomax turbulence model, which can be expected to be accurate for attached flow. The linear theory overpredicts the lift slightly, as well as being slightly different for the pitching moment. In general, however, it appears that the simpler methods can provide valuable information.

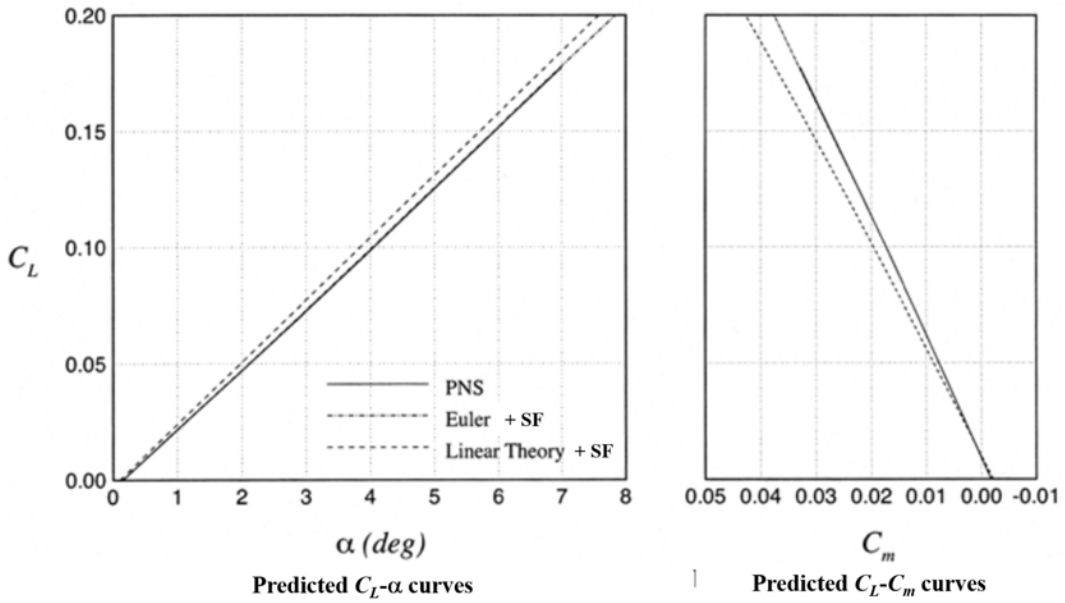


Figure 9-46: Comparison of predicted lift and moment coefficients on HSCT configuration at M = 2.4. *From D. L. Knill, V. Balabanov, O. Golovidov, B. Grossman, W. H. Mason, R. T. Haftka, and L. T. Watson. "Accuracy of Aerodynamic Predictions and Its Effects on Supersonic Transport Design." Used with permission of Virginia Tech.*

The drag polar comparison is presented in figure 9-47. This is the most important comparison for design. Let us look at the values at the design C_L of 0.082. The value of the drag coefficient, C_D, is 79.2 counts for PNS analysis, 78.9 counts for Euler plus skin friction (SF), and 77.1 counts for linear theory plus skin friction. We see that the linear theory predicts a drag that is consistently low. The Harris wave drag estimates are within two counts of the Euler CFD values. The skin friction estimate is about one count higher than that of the PNS prediction. So at first glance, it appears that combining data from the Harris code, linear theory, and skin friction code provides an excellent estimate. The drawback for this case is that a two-count drag underprediction results in a 120-NM overestimation of the range. This illustrates how sensitive the HSCT design was to drag. Eventually the HSCT program was cancelled, and presumably it was in part because of the extreme requirements, as reflected in the sensitivity to drag.

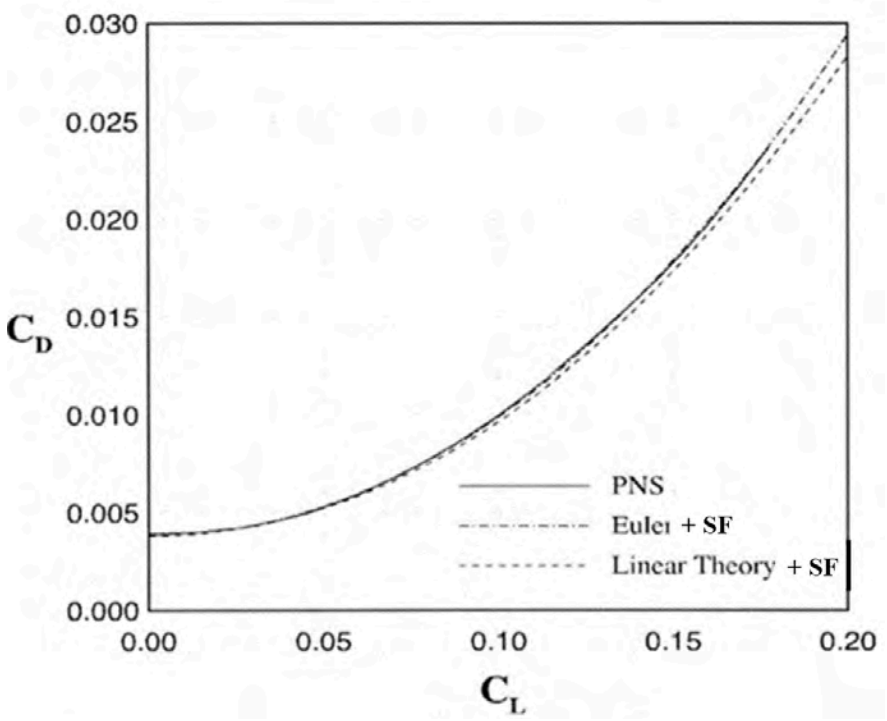


Figure 9-47: Comparison of predicted drag polars for HSCT configuration at M = 2.4. From D. L. Knill, V. Balabanov, O. Golovidov, B. Grossman, W. H. Mason, R. T. Haftka, and L. T. Watson. "Accuracy of Aerodynamic Predictions and Its Effects on Supersonic Transport Design." Used with permission of Virginia Tech.

9.8.1.4 Wing-Body Configuration

Figure 9-48 is the final example of basic linear theory. The model, shown in the top-left corner of the figure, is a mid-mounted 45° swept wing on an ogive cylinder body. The wing has an NACA 64A005 airfoil section. The correlation between wing pressures from a wind tunnel test[79] and predictions from the panel method code Woodward II[80] is shown at three stations on the wing and the agreement is reasonably good. But the main reason I'm including this figure is to reiterate that, for a supersonic trailing edge, there is no Kutta condition and the upper- and lower-surface pressures don't come together. For highly swept wings, we often look at spanwise pressure distributions and this feature of the trailing-edge behavior isn't readily apparent. Students should be aware of this difference between subsonic and supersonic flow.

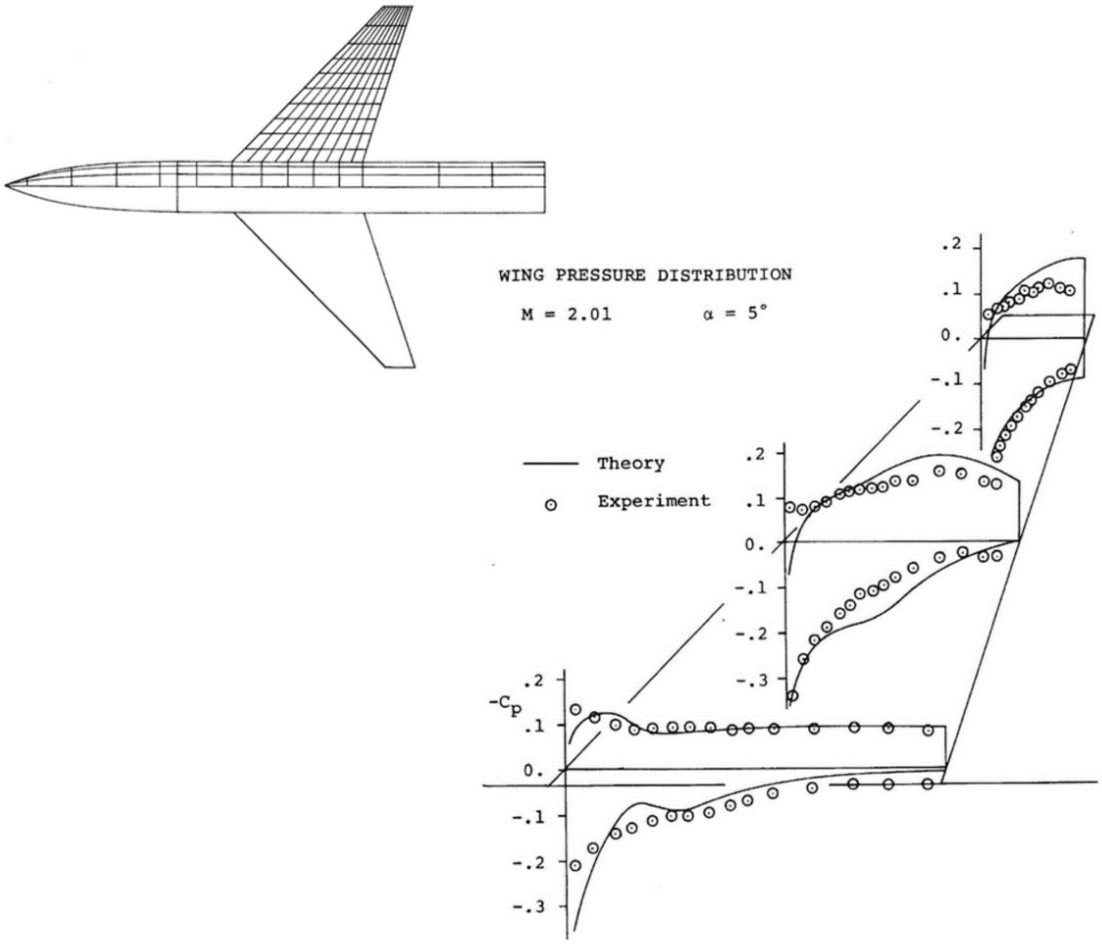


Figure 9-48: Comparison of surface pressure distributions computed using the Woodward II code based on linear theory with those from a wind tunnel test at three stations on the wing; M = 2.01 and ∝ = 5°. From (1) J. P. Gapcynski and E. J. Landrumb. "Tabulated Data from a Pressure Distribution Investigation at Mach Number 2.01 of a 45 Deg Sweptback Wing Airplane Model at Combined Angles of Attack and Sideslip." NASA. Public domain. (2) F. A. Woodward. "An Improved Method for the Aerodynamic Analysis of Wing-BodyTail Configurations in Subsonic and Supersonic Flow," Part I — Theory and Application. NASA. Public domain.

The linear theory tools available can be used very effectively to understand supersonic configurations. Before undertaking your own studies, there are a few aspects of supersonic aerodynamics that are worth understanding.

9.8.1.5 Wave Drag

It is important to remember to subtract the capture area from the cross-sectional area values. Although the wave drag code does this automatically, students should be aware that this is how it's done. In addition, although we often talk about the Sears–Haack body as a minimum wave drag value, opening up the base results in an even lower value of drag. I suggest "playing" with the simple interactive MinDrag code on the software site. Of course, base drag would have to be added to the wave drag. Often we assume that the base is the exhaust nozzle from the propulsion system, meaning there is no base drag. The Harris code is available from the PDAS site.[81]

9.8.1.6 Wing Camber to Reduce Drag Due to Lift

At supersonic speeds, the minimum drag design for a typical cruise lift coefficient (often 0.1 or less) has very little camber and twist compared to the camber and twist used in subsonic and transonic wings. The camber and twist tend to achieve a drag level essentially the same as a flat surface achieving 100% suction (of course this is zero for supersonic leading edges). This was surprising to me when I observed this.

Linear theory methods normally provide optimization options that allow the drag due to lift to be minimized due to constraints on the specified lift coefficient and trim. This is an important advantage for these methods. For a supersonic planform, we often think of the wing camber and twist as being combined, designating the combination "warp."

Three panel method codes are available at PDAS:[82] (1) TEA201, the Boeing wing design methods originating from their US SST work,[83] (2) the original Carmichael–Woodward code,[84] and (3) the combination of Woodward versions with other capabilities, W12SC3.[85]

Several survey papers should be read or reread to review key aspects of supersonic configuration design before designing a new configuration.[86,87,88]

9.8.2 Modifications to Linear Theory: Attainable Thrust

"Normal" linear theory supersonic methods are weak with respect to the amount of leading-edge suction predicted. Over many years, Harry Carlson at NASA Langley developed a modified linear theory to address the problem. After studying massive amounts of experimental results, he developed the concept of attainable thrust, which supplements linear theory with an empirically based expression for the degree of leading-edge suction that should be expected in practice. Work was summarized together with a discussion of wing design in NASA TP-3202.[89] A final version of the attainable thrust formulation was published in NASA TP-3557.[90] This led to development of a design method to determine the wing camber and twist required to get the best possible wing.[91] The code is known as WNGDES; we will describe an application below.

9.8.3 Nonlinear Aerodynamics of Supersonic Wings

To do wing design in conditions where linear theory may no longer be applicable, we need to use higher fidelity methods. One way to include better physics involves using the nonlinear full-potential flow theory (see section 2.5) and the conical-flow theory, not the linear theory approximation. It provides an excellent framework for thinking about wing design at supersonic speeds.

For highly swept wings used at supersonic speeds, the equivalent of an airfoil on a moderately-swept high-aspect-ratio transonic transport wing is the spanwise section. To analyze spanwise sections on supersonic wings, the first modern computational method used the full-potential equation. The method solved the flow in the crossplane between the bow shock and the spanwise geometry on the wing (actually a spherical cut).[92] In this plane, the crossflow can become "supercritical," and the result is that a crossflow shock wave may arise for high lift coefficients, just as the shock wave occurs in transonic flow over a two-dimensional airfoil. The full potential flow model is a good approximation under conditions where the shocks are not too stong. Extensive comparison with theory was done to validate the method for these applications.

The code developed to make this calculation is known as COREL (for COnical RELaxation), and several supersonic maneuver wings were designed and tested at supersonic speed. The idea was to shape the spanwise section to control the crossflow such that the crossflow shock was weak. This concept was known as SC3, or supercritical conical camber. Wings tested in the NASA Langley Unitary Plan Wind Tunnel demonstrated that the full-potential method could be used to design wings with superior performance.[93] SC3 will be discussed in more detail in section 9.9.2. The conical-flow code was extended to handle nonconical flows and was known as NCOREL.[94]

Today, a Euler code would be used based on solving the Euler equations given by equation (2-65) without the visous terms. The advantage of the approach used in COREL and NCOREL was that the grid generation was done as part of the calculation, removing that often time-consuming step from the computational process.

9.9 Supersonic Airplane Configuration Design Examples

We conclude this chapter with examples of supersonic airplane and wing design experiences.

9.9.1 The US Supersonic Transport (SST) Story

In the 1950s and 1960s, the public assumed that rapid advances in aircraft performance would continue and that the next step would be supersonic commercial passenger travel. The experts recognized that a supersonic transport would be difficult to achieve. Essentially no aircraft company could do this alone. By 1962, the British and French had merged their individual work into a single program and had agreed to build Concorde.

In response to the Anglo-French program, and also because the Soviet Union was developing a supersonic transport, President Kennedy made a national program for the development of US SST in 1963. This was very much in the spirit of the notion that "the US has to be the leader." The following timeline recounts what turned out to be a poor decision. Since the program was too big for one company, a national program was established, funded in large part by the government and administered mainly by the FAA (did they have experience with aircraft design?). What follows is a very brief description of events.

- Aug. 15, 1963: FAA issued an RFP.
- May 15, 1964: The FAA selected Boeing and Lockheed to propose the airframes, and General Electric and Pratt & Whitney to propose the engines.
    - Lockheed proposed a double delta.
    - Boeing proposed a variable-sweep wing.
- Dec. 31, 1966: Boeing and General Electric were selected to build the SST.
- Oct. 21, 1968: Boeing abandoned the variable-sweep concept.
- Mar. 24, 1971: The program was cancelled by congress.*

*As a student during this period, I was very disappointed, although in hindsight the program cancellation was the right decision.

A little more information may be helpful. The US SST was to be much bigger than the Concorde and would fly faster. This necessitated using titanium instead of aluminum, a very difficult and expensive difference between the airplanes. During the time the design was being developed, the government ruled that there would be no supersonic flight over the US (a restriction imposed by many governments). This is due, in part, to the fact that the much-heavier US SST would have generated a stronger sonic boom than the Concorde. All the while, Boeing was discovering a multitude of problems with their variable-sweep concept, as we'll see below. The US design was becoming much more expensive. The US Congress was asking why the government should be expected to support this program. To add to the confusion, the noise, both around the airport and from the sonic boom, was not the only issue. Environmental concerns had emerged everywhere, and the SST was predicted to destroy the ozone layer. The result of all these issues was that the program was cancelled.

Despite controversy over noise and environmental pollution, the Concorde entered service in 1976 and flew its last flights in 2003.

Figure 9-49 compares the different planform for SSTs. The figure is taken from a 1969 paper by Swan.[95] The Boeing 2707-300—the final proposed design—is clearly much larger than the others.

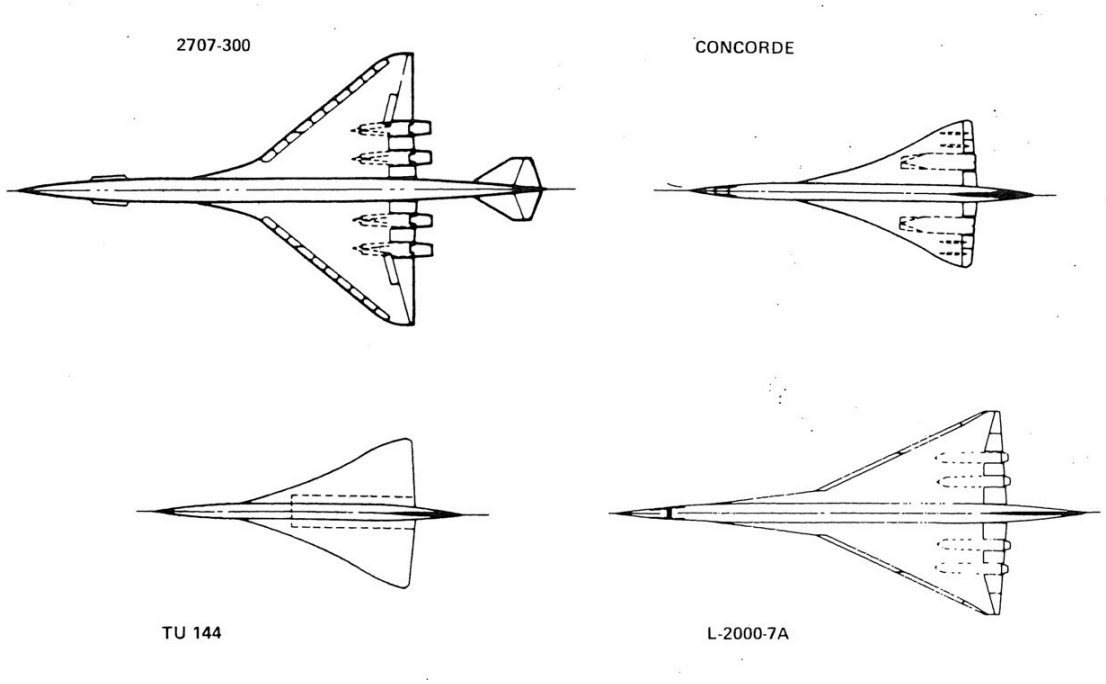


Figure 9-49: Comparison of supersonic transport concepts in the 1960s. From W. C. Swan. "A Review of the Configuration Development of the U.S. Supersonic Transport." Public domain.

The cited paper by Swan is well worth reading for any supersonic airplane designer. He describes the evolution of the configuration and includes a description of design criteria used in developing the final configuration. The issues he describes are just as valid today as they were back then. Swan explains why the Boeing 2707-300 had a horizontal tail, while the other designs were tailless. Although the horizontal tail contributed little to the stability at low alpha (recall that $1 - d\varepsilon/d\alpha$ can be very small or negative for a tail behind a huge wing), it helped prevent the configuration from pitching up at high alpha.

It is worth taking a look at the initial design. The original variable-sweep wing had become what can only be described as a monstrosity. Figure 9-50 shows the Boeing 2707-200 design. The figure is from a review by Leroy Spearman.[96] Since Spearman worked at NASA Langley, his review also covers the Langley work. The Boeing 2707-200 had engines that were mounted on the horizontal tail. The inboard engines were mounted behind the landing gear (not shown in Spearman's figure). To avoid ingesting the landing gear wake and any spray from a wet runway, a ramp was used to provide air for the inboard engines from the wing upper surface. Clearly the design was out of control! The features evident in figure 9-50 do not address the problems faced by the designers.

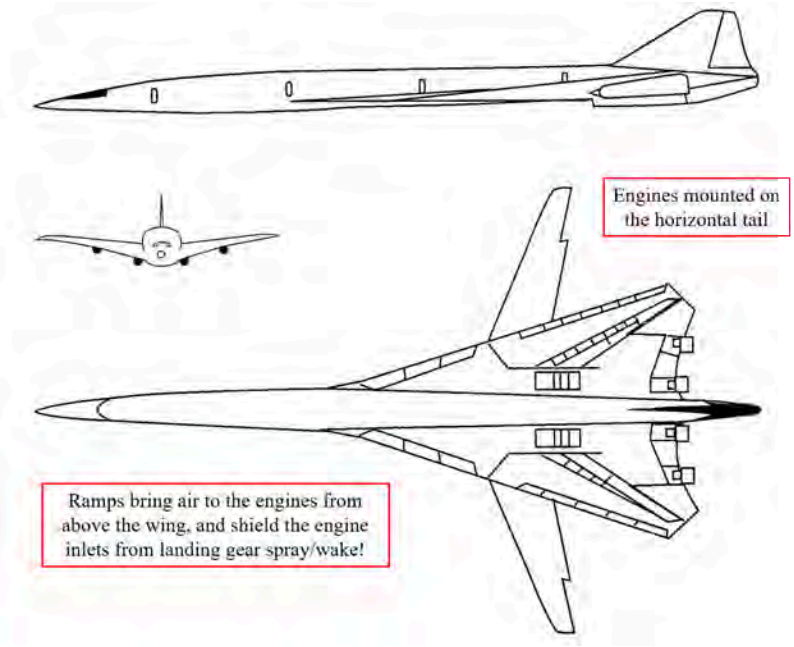


Figure 9-50: Boeing SST 2702-200 design from 1966. From M. L. Spearman. "The Evolution of the High-Speed Civil Transport." NASA. Public domain.

Figure 9-51 shows a plastic model that was sold at the time. Figure 9-51 shows the upper and lower surfaces for both the cruise and low-speed configurations (the landing gear have been broken off for many years). The cruise configuration does indeed look terrific. However, look at the landing configuration. Instead of the single drooped nose on the Concorde, the plane has a double-droop design. Additionally, its high-lift system and airflow ramps are much more complicated than the impression given in figure 9-50. Taken all together, it's easy to see why the design was abandoned. I can't imagine the internal chaos surrounding the project.

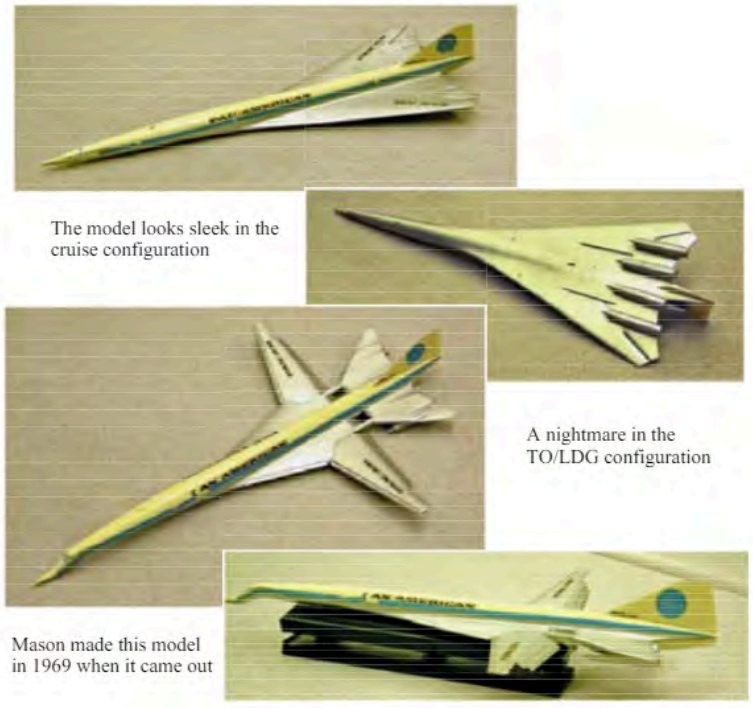


Figure 9-51: W. H. Mason's photos of the plastic models of the Boeing 2707-200.

There's another key issue. We have neglected aeroelasticity in most of our discussions, but this was also a major problem. Figure 9-52 is from a paper by Kumar Bhatia,[97] written when the government resurrected SST design, this time calling it High-Speed Civil Transport (HSCT). Clearly aeroelasticity needs to be considered early on in the design process.

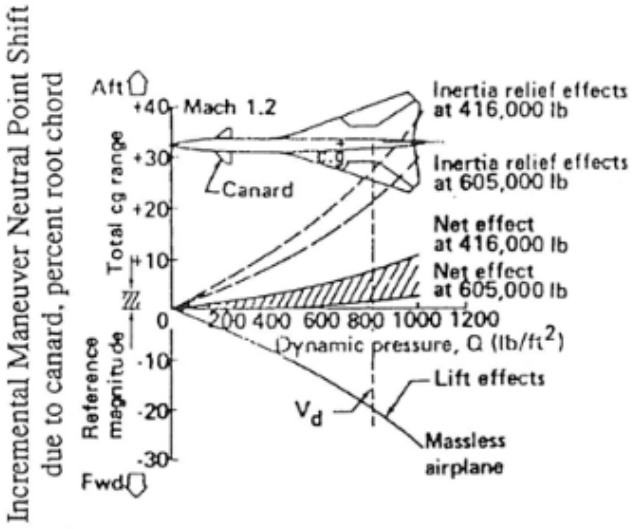


Fig 5. EFFECT OF AEROELASTICITY ON CANARD CONTRIBUTION TO LONGITUDINAL STABILITY IN MANEUVERING FLIGHT

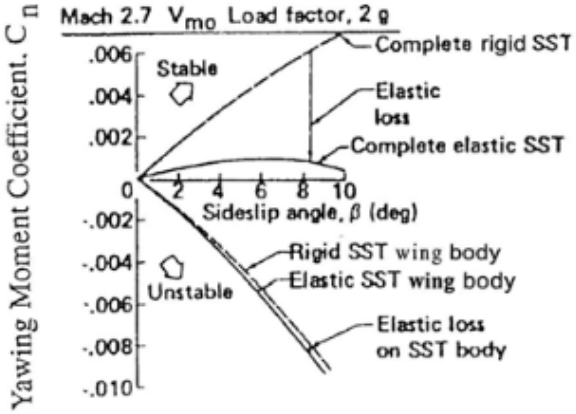


FIG 6. EFFECT OF AEROELASTICITY ON DIRECTIONAL STABILITY

Figure 9-52: Aeroelastic effects were important. *From (1) W. T. Kehrer. "Design Evolution of the Boeing 2707-300 Supersonic Transport, Part II, Design Impact of Handling Qualities Criteria, Flight Control System Concepts, and Aeroelastic Effects on Stability and Control." (2) K. G. Bhatia and J. Wetheimer, "Design Evolution of the Boeing 2707-300 Supersonic Transport, Part II, Design Impact of Handling Qualities Criteria, Flight Control System Concepts, and Aeroelastic Effects on Stability and Control." Reproduced with permission of the Boeing Corporation.*

Once the Boeing engineers realized that the variable-sweep wing concept had to be abandoned, they selected a fixed delta wing with a horizontal tail and a slight inboard glove. Many of the Lockheed engineers are of the opinion that Boeing decided to build the Lockheed design! Looking at the designs, that position seems to be a little bit of a stretch. At the time, there was a discussion of recompeting, but it was decided to continue with Boeing as the airframer. The resulting redesign was known as the Boeing 2707-300, shown in figure 9-53. It was obviously much simpler. Although the plane was still supposed to fly at Mach 2.7, most of the wing was swept at 50° and thus had a supersonic leading edge. This must have been hard for the NASA Langley engineers to accept. It points to the importance of making the design with all the considerations, not just aerodynamics. We'll see this below when we discuss the HSCT and MDO. Erik Conway's book* is highly recommended for anyone interested in the history and technical issues of supersonic transport designs.

*Erik Conway has written a book that I perceive to be an accurate description of the US SST program.[98] I got interested in the book because it also describes the HSCT program of the 1990s. Often and naturally, authors describe programs from a personal viewpoint that may not be entirely objective. Conway's book strikes me as being a candid description of all the complicating events. He is an historian who combines both the technical issues and the political environment that is ever-present in large government programs. This is another book well worth reading.

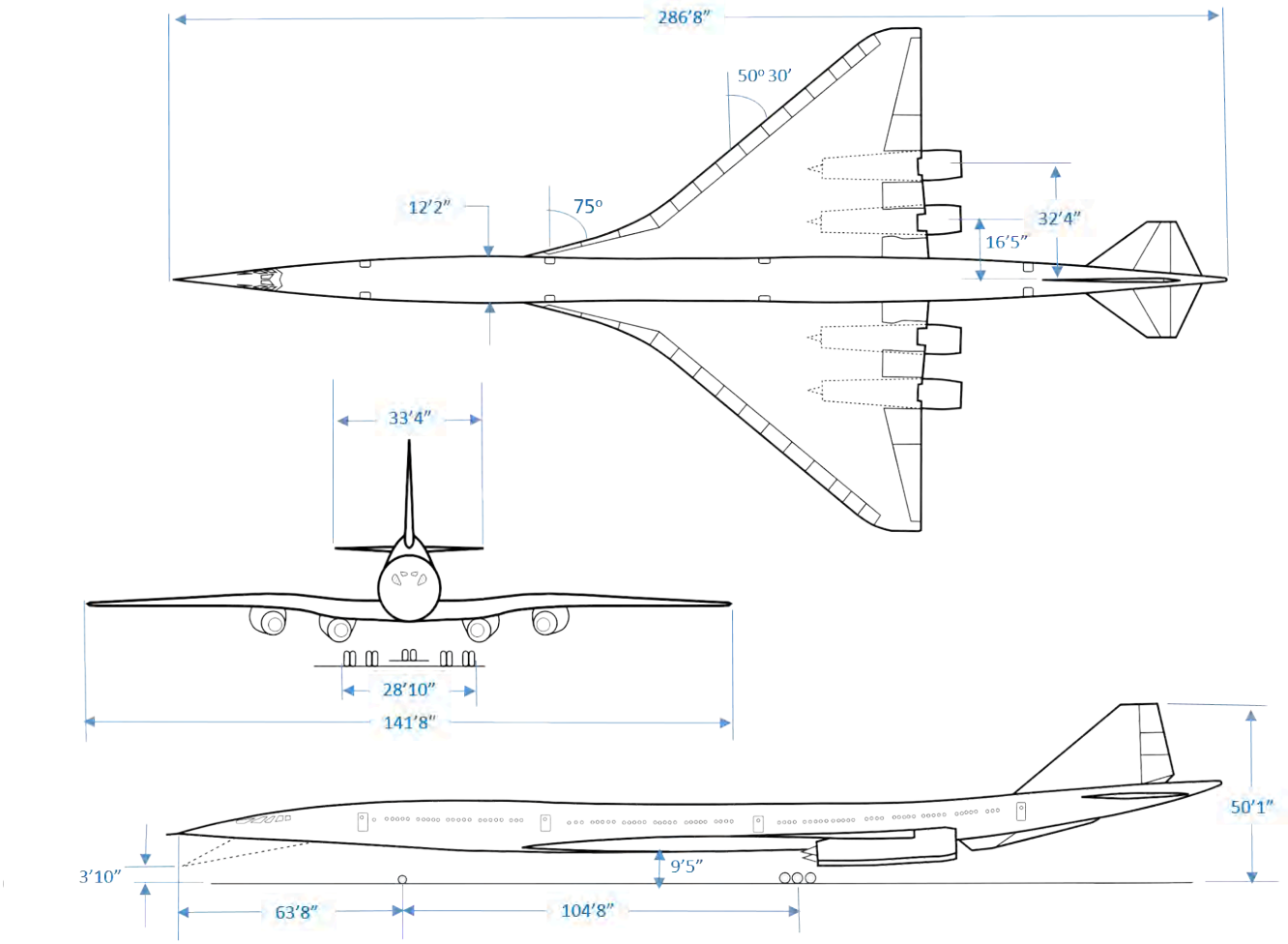


Figure 9-53: Final proposed design of Boeing 2707-300. From Nubifer. Wikimedia. CC BY-SA 3.0. Dimensions added by P. Raj.

9.9.2 Supersonic Maneuver Wing—Transonic Aerodynamics at Supersonic Speed

During the early stages of the advanced tactical fighter (ATF) program in the late 1970s, there was interest in the design of a wing capable of maneuvering efficiently at supersonic speeds. As the supercruise requirement emerged, it was clear that efficient supersonic maneuvering could be a requirement also. As previously discussed, linear theory was adequate for cruise design. However, it was not adequate for maneuvering C_L's. This deficiency was shown in work from NASA Langley, as illustrated in figure 9-54.[99] Although linear theory predicted good performance, wings designed and tested at higher C_L's fell short of the predictions. The requirement for supersonic maneuvering meant that C_L's well above the linear theory limit would be required. The figure also shows the expected maneuver C_L's. A detailed discussion of the relationship between linear theory breakdown and supercrtical crossflow is given in a paper by Mason and Miller.[100]

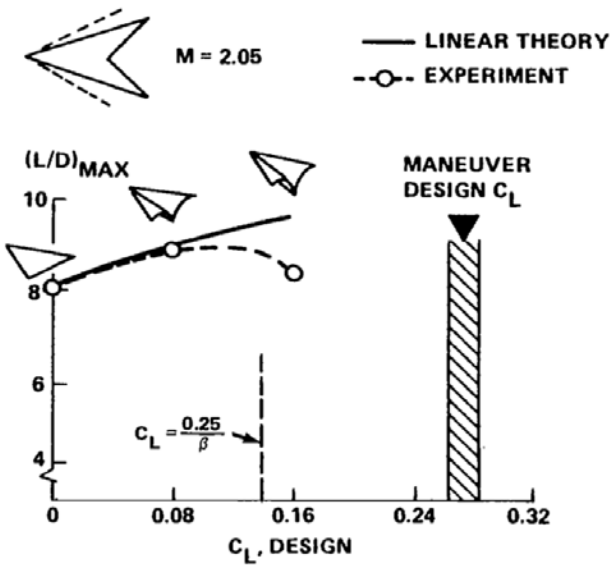


Figure 9-54: Wings designed using linear theory fail to achieve the predicted drag due to lift in practice as shown by the mismatch between theory and experiments. From W. H. Mason and S. Miller. "A Wing Concept for Supersonic Maneuvering." NASA. Public domain.

We have included this discussion on supersonic maneuver wing design because it shows how an understanding of flow physics can be used to develop an aerodynamic concept. Rudy Meyer at Grumman realized that there was a close correspondence between the 2D full-potential equation that was then being solved numerically at transonic speeds and the full-potential conical flow equations for supersonic flow.[101]* He knew that the same techniques could be used for supersonic conical flow. He had also read a paper by Clint Brown that attributed the performance shortfall of wings designed by linear theory to the presence of crossflow shocks on the wing.[102] Rudy was sure that a numerical method that included crossflow shocks could be used to shape the spanwise wing section to reduce the strength of the crossflow shock. The resulting concept was called supercritical conical camber, SC3.

*Recall from Chapter 2 that the classic version of the full-potential flow model used for early two-dimensional transonic flow calculations has coefficients that cause the type of the equation to change between elliptic and hyperbolic. Rudy knew that, at supersonic speeds, the potential flow model for conical flow had a very similar structure, meaning the numerical methods used for 2D transonic flow would be directly applicable for supersonic conical flow.

Figure 9-55 from the final report on this work[103] shows an illustration of the flow field physics and the associated spanwise pressure distribution. Part A (on the left side of the figure) is a schematic that shows a conical geometry and the spanwise section pressure distribution that will be used to do the design. Part B shows the predicted spanwise pressure distribution for an uncambered conical wing computed using the full-potential flow model that can include the supercritical crossflow shock and the prediction from linear theory (which obviously can't include the key physics of the flow field). Clearly the nonlinear effect has to be included on the calculation.

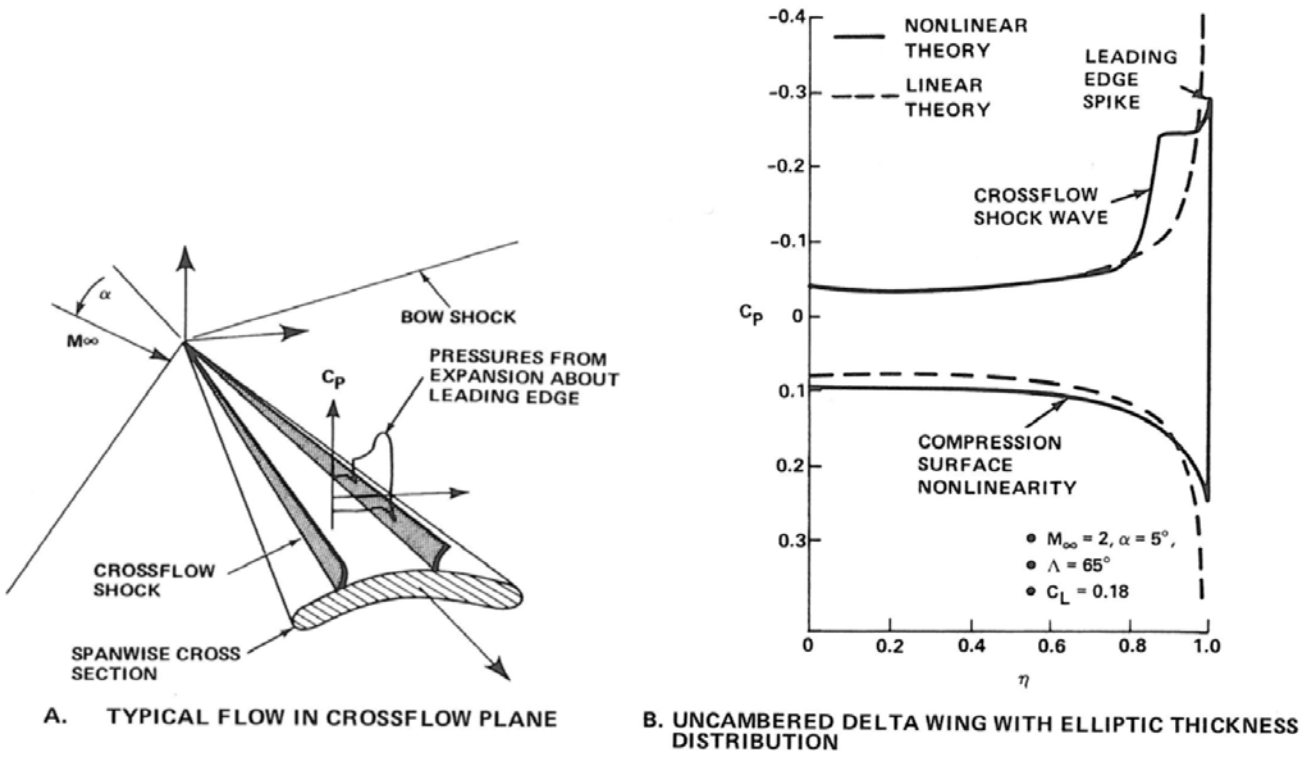


Figure 9-55: Conical flow and related spanwise pressure distribution. *From W. H. Mason and S. Miller. "A Wing Concept for Supersonic Maneuvering." NASA. Public domain.*

The program to design a wing demonstrating controlled supercritical crossflow was carried out in a series of steps. The following history illustrates a physics-based approach to aerodynamic development:

- SC3 was conceived by Rudy Meyer in 1977.
- The program concept was developed by Gianky DaForno in 1977 and funded by NASA.
- The computational method COREL was developed by Bernie Grossman in 1978.
- Aerodynamic design was done by W. H. Mason from 1978 to 1982 in cooperation with NASA Langley, primarily Dave Miller.

The SC3 program included three different prototypes in the NASA Langley Unitary Wind Tunnel. To start, two purely conical wings were designed, built, and tested. One was flat, and the other was cambered based on the computational design work. This wing was termed the "conceptual wing" and was designed using iterative analysis with COREL. Initially, the wing used a simple cambered spanwise shape. The thickness distribution used a superellipse with the leading edge slightly "rounder" than a typical parabolic nose shape. The crossflow shock was considerably weaker than the flat wing. Next, local shaping was used in the vicinity of the crossflow shock to completely eliminate the crossflow shock. This was done by reducing the spanwise curvature around the crossflow shock in the same way that Whitcomb had reduced the shock strength for transonic supercritical airfoils. Figure 9-56 shows both the initial spanwise camber design and the final shockless supercritical crossflow design.[104]

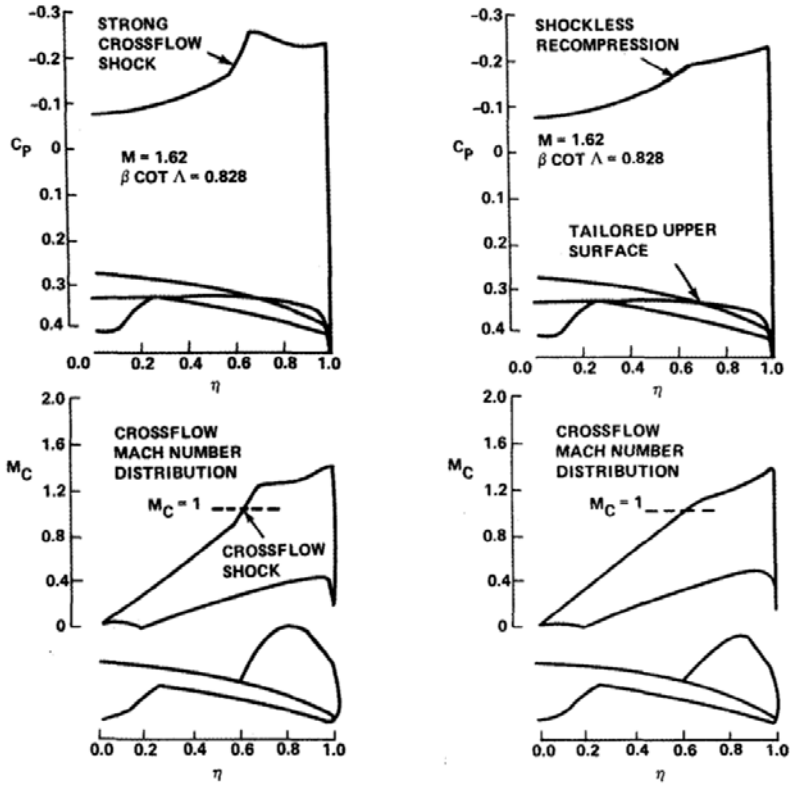


Figure 9-56: Example of conical-flow design, showing the crossflow Mach number distribution. *From W. H. Mason and D. S. Miller. "Controlled Supercritical Cross-Flow on Supersonic Wings-An Experimental Validation." AIAA. Public domain.*

The dimensioned planform of the wind tunnel test model is shown in figure 9-57(a), which also shows the location of pressure taps. In figure 9-57(b), the final conical cambered wing cross section with shockless supercritical flow is compared to that of a flat uncambered wing model. A photo of the model installed in the wind tunnel is shown in figure 9-57(c).

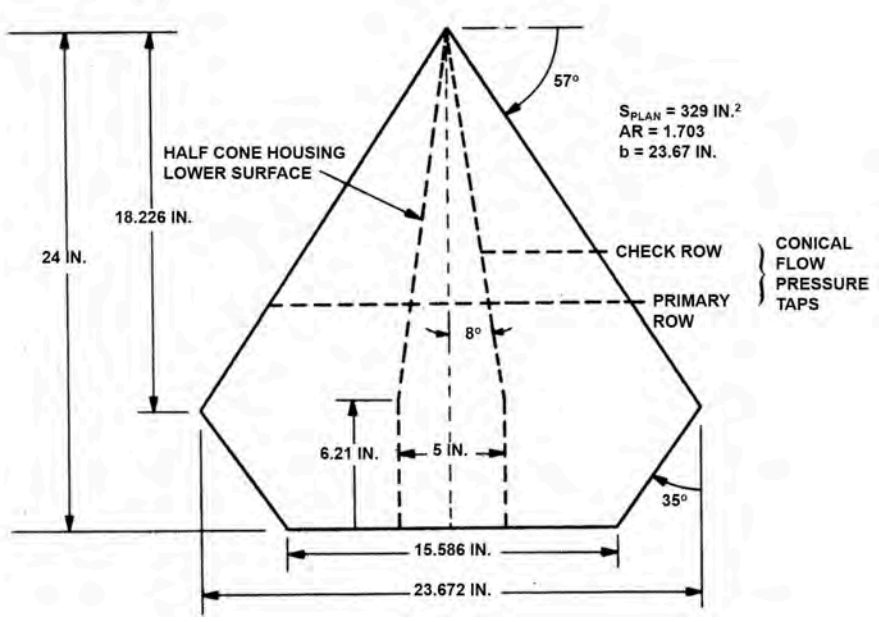


Figure 9-57(a): Dimensioned planform of the wind tunnel test model to validate the conical cambered wing design for shockless supercritical flow.

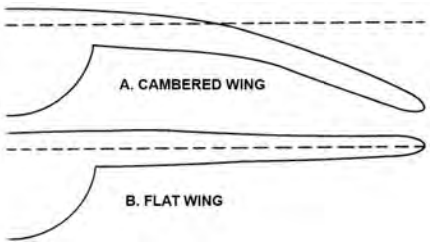


Figure 9-57(b): The conical cambered cross section (top) is compared to a flat uncambered cross section (bottom) for the wing model in figure 9-57(a). *From W. H. Mason and D. S. Miller. "Controlled Supercritical Cross-Flow on Supersonic Wings-An Experimental Validation." AIAA. Public domain.*

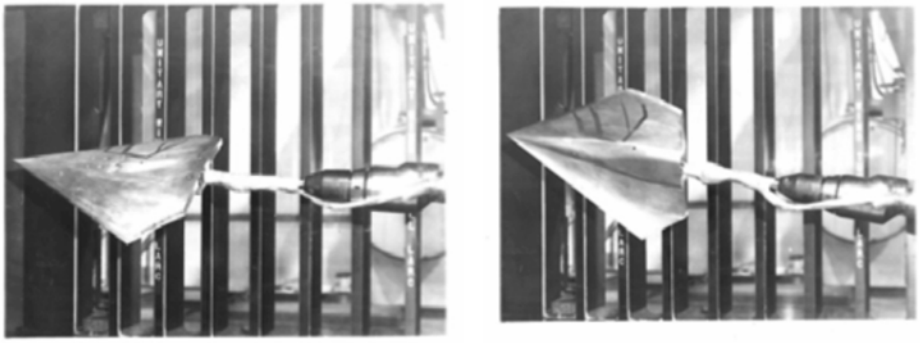


Figure 9-57(c): The conical cambered wing model in the wind tunnel with its upper surface shown on the left and the lower surface on the right. *From W. H. Mason and D. S. Miller. "Controlled Supercritical Cross-Flow on Supersonic Wings-An Experimental Validation." AIAA. Public domain.*

Figure 9-58 shows the resulting pressure distribution at several angles of attack. The results were considered highly successful.[105]

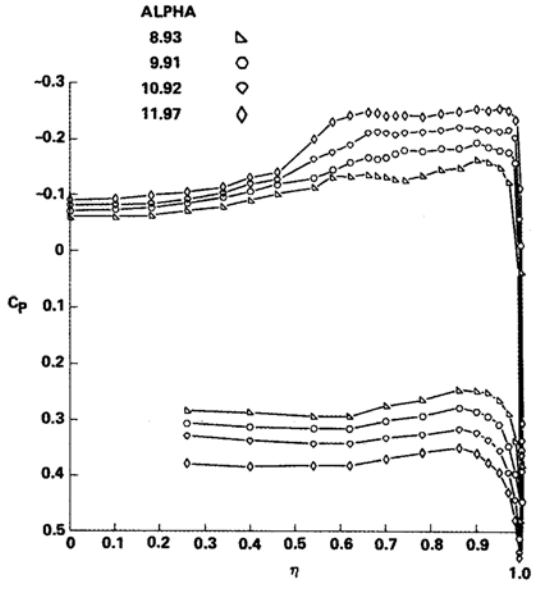


Figure 9-58: Spanwise surface pressure distributions at M = 1.62 at several angles of attack (denoted by ALPHA) from the wind tunnel test, showing the shockfree recompression of the supercritical crossflow. *From W. H. Mason. "A Wing Concept for Supersonic Maneuvering." NASA. Public domain.*

The next step was to design and test a three-dimensional wing using the SC3 concept to create what was called the "demonstration wing." Figure 9-59 shows the demonstration wing installed in the wind tunnel.

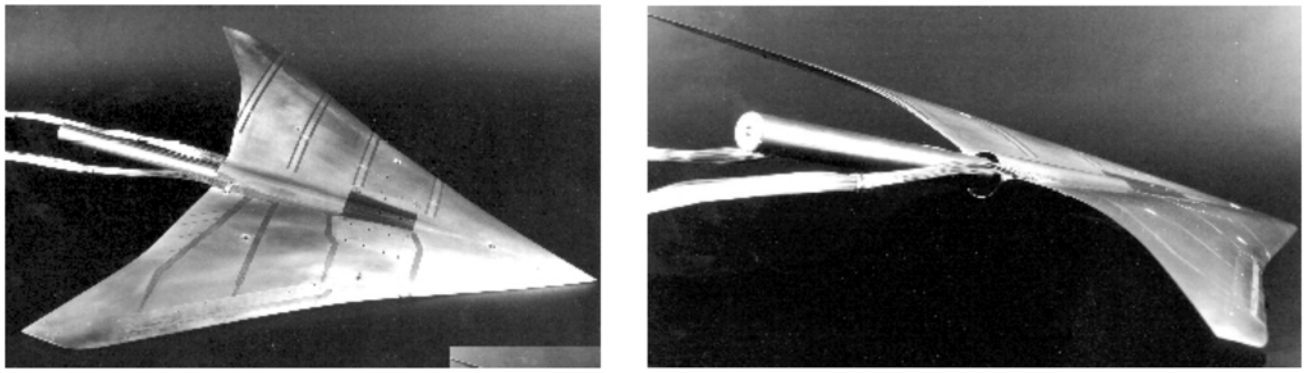


Figure 9-59: SC3 demonstration wing in the wind tunnel. The upper surface view on the left shows rows of spanwise pressure taps covered by tape, and the after-quarter view on the right shows spanwise camber. *From W. H. Mason. "A Wing Concept for Supersonic Maneuvering." NASA. Public domain.*

The drag polar from the wind tunnel test is shown in figure 9-60. At the design lift coefficient of 0.4, a 21% reduction in drag due to lift was achieved compared to the 0% and 100% leading-edge suction envelopes. The work is described in the paper by Mason et al.[106]

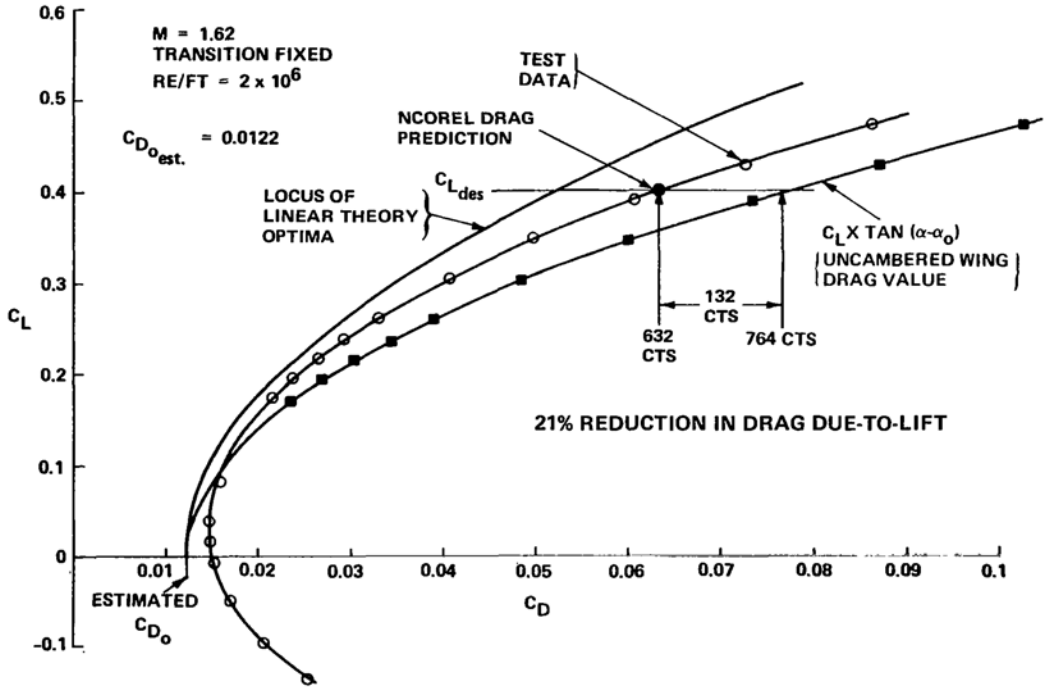


Figure 9-60: The demonstration wing drag polar at 1.62 Mach number. *From W. H. Mason. "A Wing Concept for Supersonic Maneuvering." NASA. Public domain.*

The work produced a number of papers, including AIAA papers and NASA reports. The following NASA reports are available online at no charge and contain details of the work and wind tunnel results with tabulated data: NASA TP-1759, April 1981; NASA TP-2249, February 1984; and NASA TP-2336, August 1984.

9.9.3 HSCT and MDO

Supersonic research continued as a low-level effort ever since the US SST was cancelled. In the 1980s, NASA began to revisit the possibility of a supersonic commercial transport. The initial NASA study was for a tailless Mach 3 design exploiting the ideas of attainable leading-edge thrust.[107] This design was wind tunnel tested.[108] Both McDonnell Douglas and Boeing were involved in the program,[109,110] though Boeing had not bought McDonnell Douglas yet. After these studies, a Mach number of 2.4 was chosen as the HSCT design Mach number. The companies also investigated control issues for an HSCT.[111,112] Although the program was not classified as such, access was restricted. Eventually the results of the work were made available, and many papers were given at AIAA Meetings. See the book by Conway for details of the evolution of the program.[113] The public planform was known as Reference H and is shown in figure 9-61.[114] The design Mach number was 2.4, and it was required to have a range of 5,000 to 6,000 NM. It was intended to carry 250 to 300 passengers. The notional TOGW was 700,000 lbs.

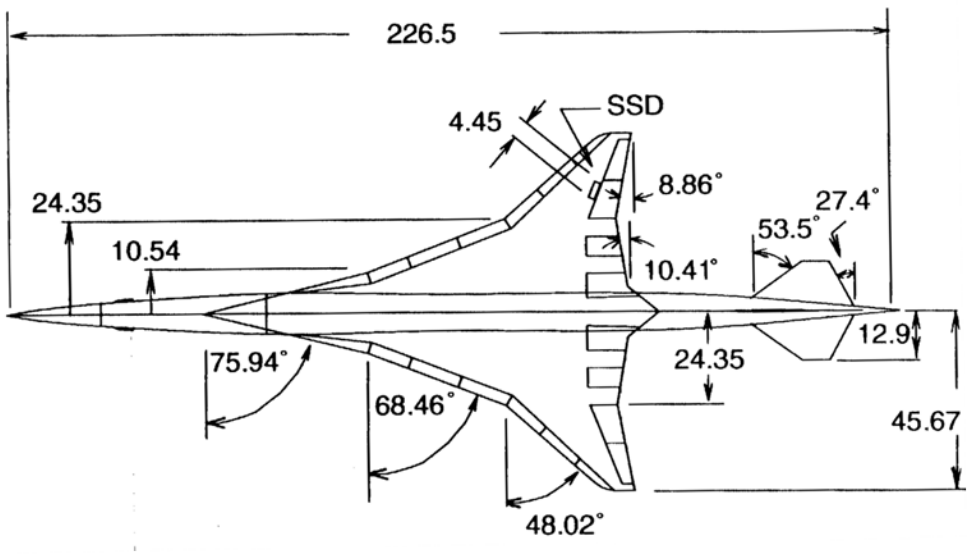


Figure 9-61: The public Reference H HSCT model (all dimensions are in inches). *From G. T. Kemmerly, B. A. Campbell, D. W. Banks, and S. F. Yaros, "Low-Speed Stability-and-Control and Ground-Effects Measurements on the Industry Reference High Speed Civil Transport," NASA. Public domain.*

At the cruise Mach number, the major portion of the leading edge of the Reference H configuration is subsonic. The planform is much closer to the ideas we described in section 9.4.2 for the modified arrow wing. This design was pushing technology to the limit, with the sensitivity of the takeoff gross weight to drag quoted at 10,400 pounds per count! From work we will describe below, we found a value of 14,000 pounds per count. From a commercial point of view, this was too sensitive to be practical. Some of my peers at NASA turned this around to say that the design would be a success if the drag could only be reduced by a few more counts. Nevertheless, concerns over the environment—in the form of noise (community and sonic boom) and emissions (concerns about high-altitude atmospheric chemistry)—remained formidable challenges. These concerns, together with the uncertainty about economic viability, resulted in the program being cancelled. The story is well told by Conway.[115]

9.9.3.1 Multidisciplinary Design Optimization (MDO)

As part of the HSCT program, various universities, including Virginia Tech, conducted a nearly decade-long program developing MDO methods for HSCT design. The work explored a number of approaches to MDO. The key objective was to find ways to include high-fidelity

disciplinary analysis methods in conceptual design, where the high-fidelity methods could have the most impact. The primary disciplines included aerodynamics and structures. Numerous constraints were specified. Some of these were practical geometric constraints, but many also addressed trim and static stability and control requirements. Figure 9-62 shows a nominal statement of the optimization problem. One of the key issues was the development of a general parametric geometry model, where the parameters could be used as design variable in the optimization, as described in the figure. Numerous variations of this problem were investigated.

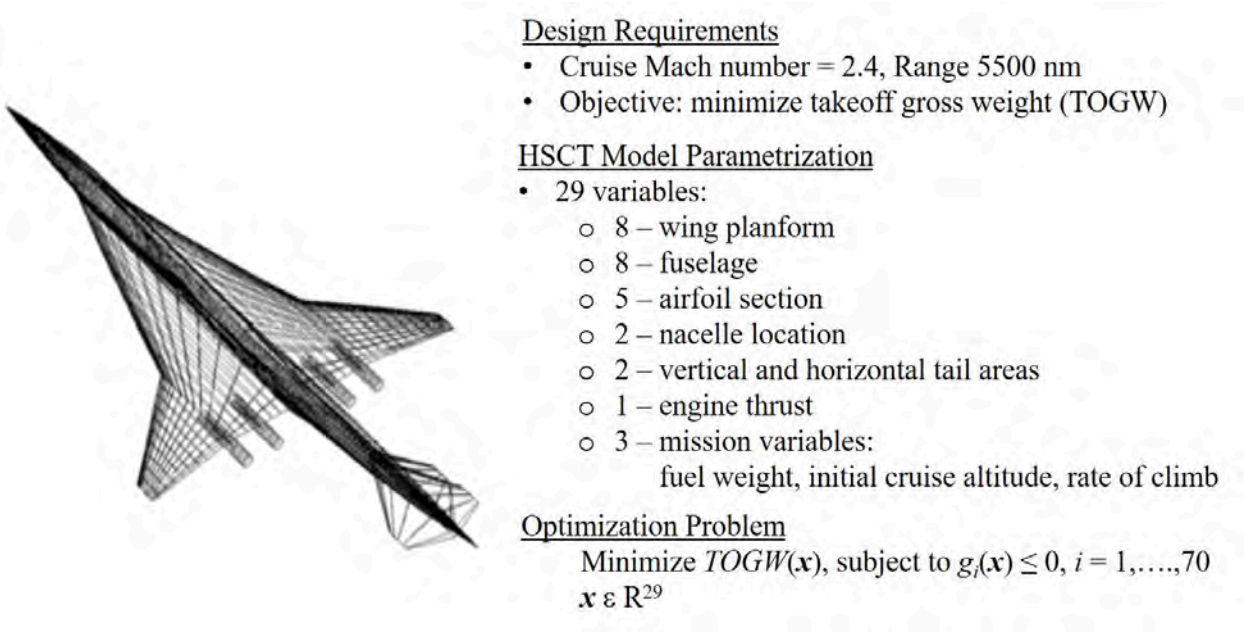


Figure 9-62: Nominal statement of the Virginia Tech HSCT optimization problem.

There were a variety of outcomes from this work. Perhaps the key understanding was that it was impractical to include high-fidelity analysis methods into a "giant" program, which we called disaggregation.[116] Instead, it was necessary to represent the disciplines through models that could be used during the optimization. These models are called response surface models (RSMs) by the statisticians. We used these RSMs for several reasons. First, we were interested primarily in using gradient-based optimization. Just about any analysis method will produce slightly "noisy" results as geometry changes are made (shocks bouncing between grid lines, etc.). Gradient-based optimizers are extremely sensitive to this artificial noise. In addition, the experts can use the latest versions of their software to provide data for the RSMs to be built for the optimization. Finally, in this approach, the many analysis runs needed from an analysis code can be carried out simultaneously rather than sequentially. This allows the use of coarse-grained parallel computing to reduce the time required to do a design. The RSMs representing the disciplines can be used with a variety of optimization schemes. Because we found local minima in the design space, the models could be employed with global optimization schemes. The models also allowed parameter studies to be made very easily. We've repeated some of the discussion given previously in Chapter 4 because this was the work that led to our preferred aerodynamic design and optimization process.

An example result from the HSCT optimization work described above is shown in figure 9-63.[117] The figure contains the results from two different approaches. The first is labeled *VCM Optimum*, in which VCM stands for "variable complexity model." In this approach, low-fidelity models for the aerodynamics are used together with a few high-fidelity aerodynamic models. The other approach is labeled *Drag RS Optimum*, and it uses response surface models. Both produce similar results.

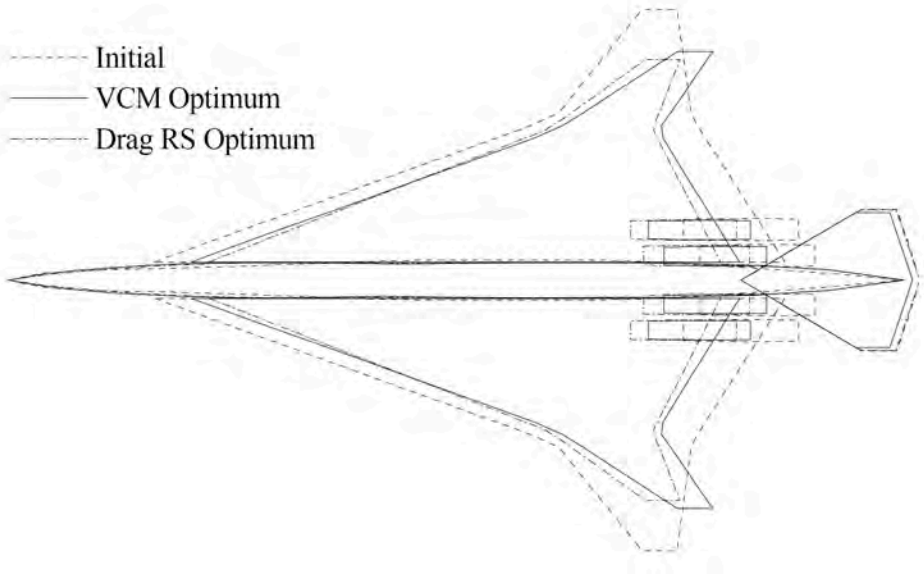


Figure 9-63: Planform shapes of two different optimization approaches for a HSCT configuration. *From C. A. Baker, B. Grossman, R. T. Haftka, W. H. Mason, and L. T. Watson. "High-Speed Civil Transport Design Space Exploration Using Aerodynamic Response Surface Approximation." Reprinted by permission of the American Institute of Aeronautics and Astronautics, Inc.*

In the optimization process, we used numerous different starting designs or starting points. With the high-dimensional design space used here, there are many local minima in which a gradient-based optimization can get "stuck." Figure 9-64 shows the convergence history of the optimization. An example of design space visualization illustrating the local minima issue is discussed in the paper by Knill et al.[118]

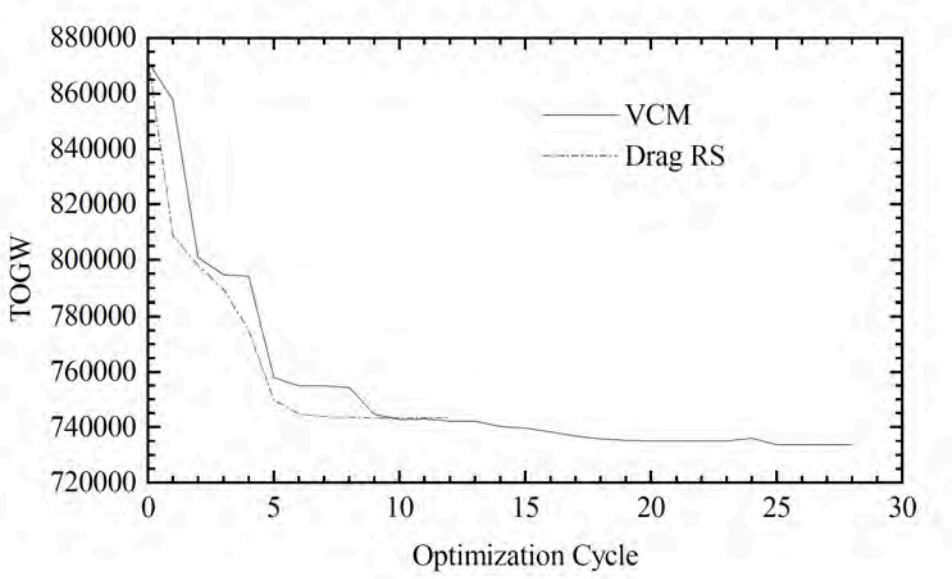


Figure 9-64: Takeoff gross weight reduction convergence history from two different optimization approaches. *From C. A. Baker, B. Grossman, R. T. Haftka, W. H. Mason, and L. T. Watson. "High-Speed Civil Transport Design Space Exploration Using Aerodynamic Response Surface Approximation." Reprinted by permission of the American Institute of Aeronautics and Astronautics, Inc.*

A great deal of work on this problem has been carried out by other researchers, and we cite two that are of interest.[119,120]

9.9.4 Design to Reduce the Strength of the Sonic Boom

As stated earlier in this chapter, government regulations do not allow supersonic flight over the United States as well as most other countries. This is a major limiting factor preventing the development of a commercial supersonic airplane. Thus, attention in the research community turned to an effort to reduce the strength of the sonic boom enough that a new noise criteria could be established allowing low-strength/no-boom supersonic flight over land. On August 27, 2003, a modified F-5 flown at Edwards AFB demonstrated sonic boom shaping, proving that the strength of the sonic boom hitting the ground could be reduced. The modified F-5 used for the demonstration is shown in figure 9-65.



Figure 9-65: Northrop-Grumman's modified US Navy F-5E Shaped Sonic Boom Demonstrator (SSBD) aircraft. From Carla Thomas, NASA. Public domain.

Quieting the Boom: The Shaped Sonic Boom Demonstrator and the Quest for Quiet Supersonic Flight, by Lawrence R. Benson, part of the NASA Aeronautics Book Series, is an excellent source of complete story.[121] Examples of the theory that can be used to design low-boom concepts have been published by Li and Rallabhandi[122] and Rallabhandi et al.[123] This remains an area of active research.

The goal behind research into shaped booms is to change the shape of the classic N-wave associated with the sonic boom. Figure 9-66 shows the N-wave and a design from a paper by Aronstein and Schueler[124] that reduces the sudden pressure jump.

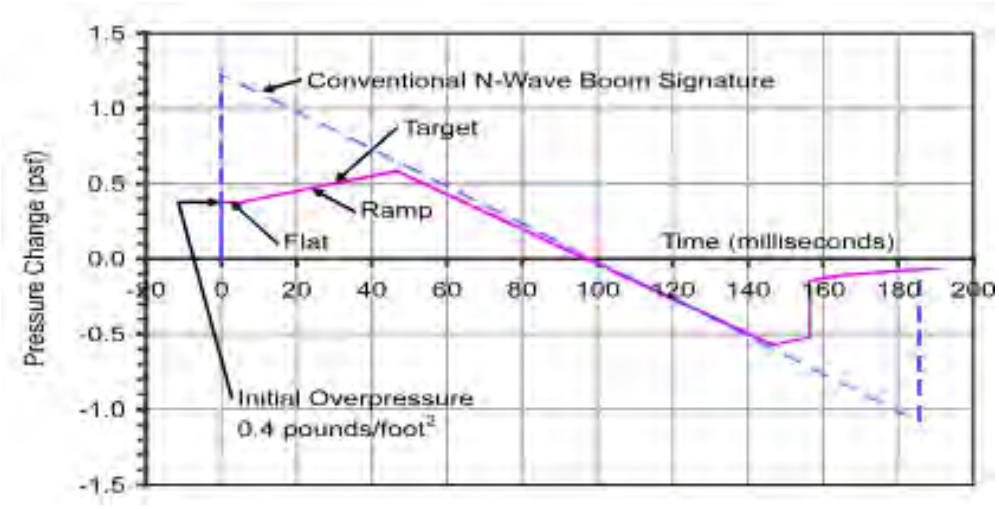


Figure 9-66: Example of the sonic boom N-wave and design to reduce the overpressure. From D. C. Kronstein and K. L. Schueler. "Conceptual Design of a Sonic Boom Constrained Supersonic Business Aircraft." Reprinted by permission of the American Institute of Aeronautics and Astronautics, Inc.

Another idea is to use an extensible nose spike to make the length of an airplane longer. Figure 9-67 shows an F-15 modified with what they call a Quiet Spike to extend a nose boom in flight. This was a program conducted by Gulfstream and NASA from 2004 to 2007.[125]



Figure 9-67: Gulfstream's Quiet Spike concept to reduce the strength of the sonic boom. From Jim Ross, NASA. Public domain.

9.9.5 Additional Efforts

In this section, we describe two projects that may lead to new supersonic airplanes. After having tried to pursue a large commercial transport without success, the future appears to be in more modest designs for executive jets. One has been underway for a number of years, and the other is a new NASA effort. Both are much smaller than the HSCT program discussed above. The NASA design has the purpose of demonstrating a supersonic airplane with a low sonic boom strength. Hopefully the NASA work will establish the basis for relaxing the restriction on supersonic flight over land in the US.

9.9.5.1 Aerion

The Aerion Corporation* has been working on a small supersonic airplane design since 2003. Figure 9-68 shows one of the preferred concepts, which is a three-engine design. Nominally they expect to be able to have a boomless cruise at Mach 1.1 to 1.2, with a long-range cruise Mach number of 1.4. The AS2 is designed to carry 8 to 11 passengers and is expected to operate at runways from 6,000 to 7,500 feet depending on the airplane weight. The range is expected to be 7,500 NM.

*Aerion Corporation, an American aircraft manufacturer based in Reno, Nevada, was founded in 2003 by Robert Bass of Fort Worth, Texas. From 2004 until 2021, the company was developing a ten-passenger supersonic jet to cut transatlantic flights by three hours, using "boomless cruise" technology to negate the sonic boom. It was expected to be the first supersonic aircraft without an afterburner to lower emissions and the first to run on biofuels. Aerion abruptly announced on May 21, 2021, that the company would be shutting down due to inability to raise needed capital to proceed.



Figure 9-68: The Aerion AS2. From Aerion website. Copyright undetermined. Fair use.

The Aerion concept depends on a fundamental property of fluid mechanics. Note the essentially unswept wing. The concept arose from the idea that, for an unswept wing at supersonic speed, the pressure decreases on the wing falls continuously from the leading edge to the trailing edge. This means that the pressure gradient is favorable over the entire wing and for a modest Reynolds number the flow should be laminar. The resulting low skin friction drag is an enabling technology. Here we have an example where two-dimensional supersonic airfoil theory is useful.[126] We discuss the relevant aspects of the supersonic airfoil theory in the next section below.

2D: The supersonic airfoil story

Supersonic airfoil theory has not been particularly useful in the swept-wing concepts discussed above. Now we have a case where supersonic airfoil characteristics can be exploited, as seen in the example provided below. Generally the textbooks have students work the diamond airfoil problem. In this section, we'll look at a biconvex airfoil. Let's examine the pressure distribution on the 5-percent-thick biconvex airfoil shown in figure 9-69.

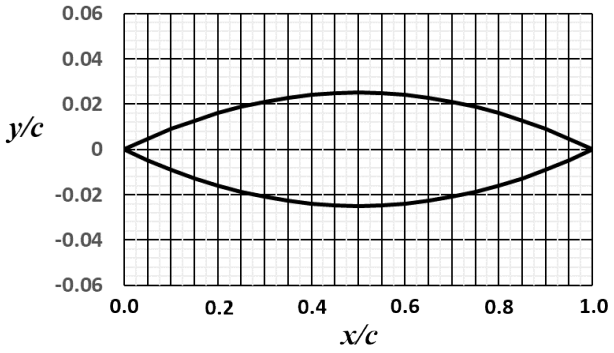


Figure 9-69: A 5-percent-thick biconvex airfoil. From W. H. Mason. Adapted by P. Raj.

The linear theory pressure distribution on the 5-percent-thick biconvex airfoil is given in figure 9-70 for a Mach 2 case at 5° angle of attack. Note that the pressures vary linearly so that there is a constant favorable pressure gradient all the way from the leading edge to the trailing edge. And of course since the trailing edge is supersonic, the pressures don't need to come together at the trailing edge as they would for a subsonic case.

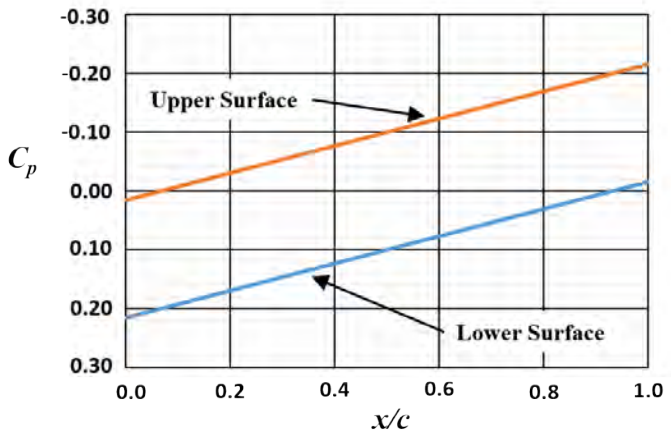


Figure 9-70: Surface pressure distributions on the upper and lower surfaces of a 5-percent-thick biconvex airfoil (see figure 9-69) at a Mach number of 2 and an angle of attack of 5° as computed using 2D supersonic thin airfoil linear theory. From W. H Mason. Adapted by P. Raj.

This is the idea behind using the unswept wing on the Aerion. The hope is that, without an adverse pressure gradient, the wing will achieve a significant amount of natural laminar flow. Once we've started this discussion, we use the opportunity to make a few other points.

Although figure 9-70 shows the idea for the Aerion concept, we are left to wonder how well linear theory agrees with data. Looking at the literature, almost all data used for comparison with airfoils comes from the wind tunnel tests conducted by Antonio Ferri at Guidonia in Italy.[127] Figure 9-71 shows a comparison of the predictions from linear theory, Ferri's wind tunnel data, and predictions from second-order supersonic airfoil theory. The model was a 10-percent-thick biconvex airfoil at 10° angle of attack and Mach 2.13. This is a fairly thick airfoil at a fairly high angle of attack, so we may be asking too much from linear theory. The second-order airfoil theory formulas are available in NACA TN-1428.[128] The figure shows that the second-order theory is in generally good agreement with the wind tunnel data, and the idea of a favorable pressure gradient is still essentially valid. Because first- and second-order supersonic airfoil theories are relatively simple analytically, numerous studies have been conducted seeking optimum aerodynamic characteristics. We will not repeat them here, instead referring to an entire book that covers the subject.[129]

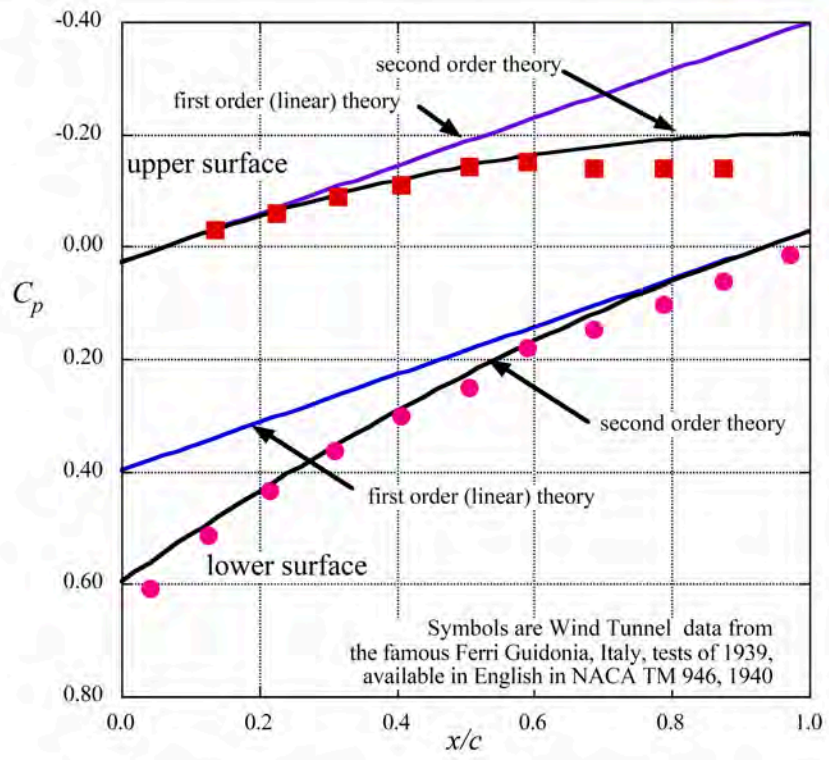


Figure 9-71: Comparison of theoretical airfoil pressure predictions and wind tunnel data for a 10-percent-thick biconvex airfoil at 2.13 Mach number and 10° angle of attack. From W. H. Mason, adapted. Data from A. Ferri. "Experimental Results with Airfoils Tested in the High-Speed Tunnel at Guidonia." NACA.

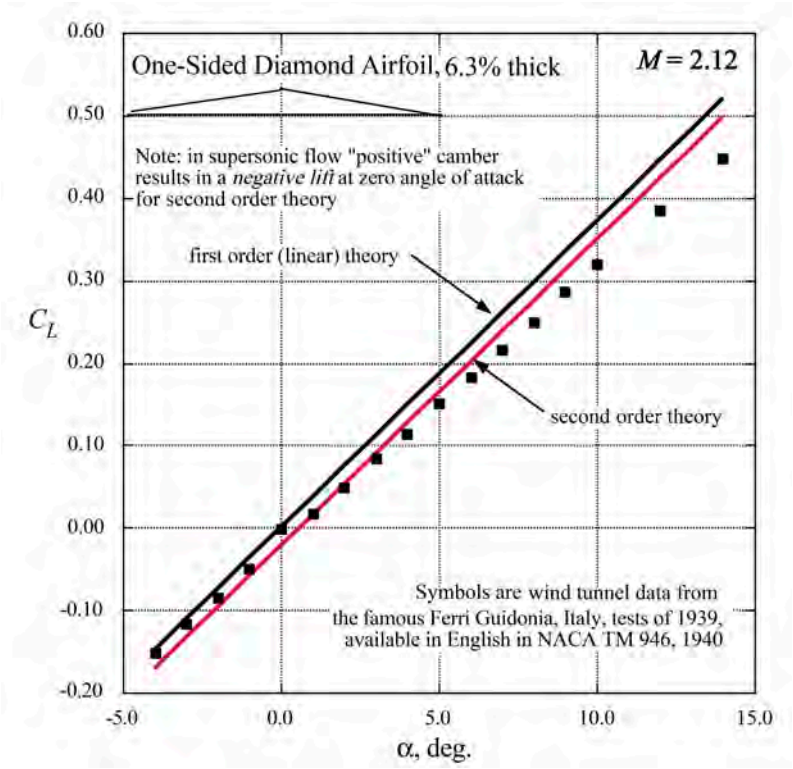


Figure 9-72: Although not large, the effect of camber is clear when considering the results of the second-order supersonic airfoil theory applied to a one-sided diamond airfoil (having a positive camber) at 2.12 Mach number. *From W. H. Mason, adapted. Data from A. Ferri. "Experimental Results with Airfoils Tested in the High-speed Tunnel at Guidonia." NACA.*

The other interesting feature of supersonic airfoil theory is the effect of camber. Linear theory only considers the leading- and trailing-edge values; camber and thickness don't affect lift. This is not true for second-order supersonic airfoil theory. For a flat lower surface and a curved upper surface, generally considered positive camber, the lift at zero angle of attack is negative. Figure 9-72 shows this effect for one of the airfoils tested by Ferri—a one-sided wedge 6.3% thick. Although the camber effect is not huge, it is noticeable. This is particularly interesting in that it explains the F-16 device deflection schedule. At supersonic speed, the F-16 automatic device schedule includes leading and trailing edges with a negative deflection, as shown in figure 9-73. The F-16 has a NACA 64A204 airfoil, and the leading and trailing edges use an automatic -2° deflection at supersonic speeds.[130]

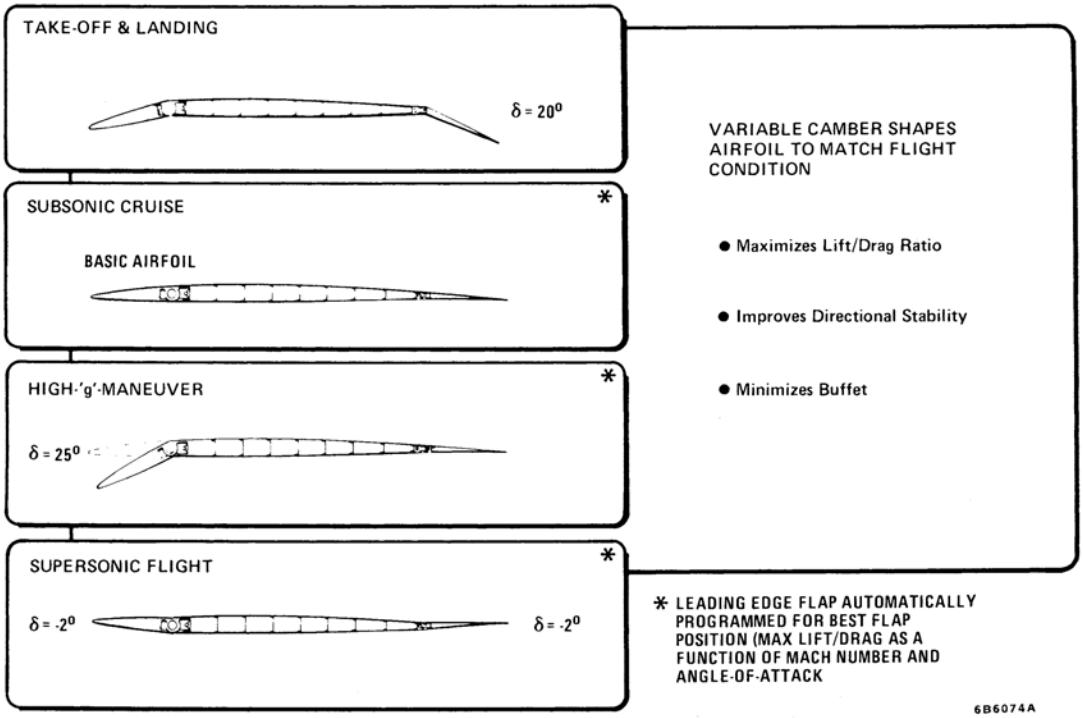


Figure 9-73: The F-16 device schedule to automatically vary the camber to match flight conditions. *From C. S. Droste and J. E. Walker, "The General Dynamics Case Study on the F-16 Fly-by-Wire Flight Control System." Reprinted by permission of the American Institute of Aeronautics and Astronautics, Inc.*

9.9.5.2 Sonic QueSST

In 2016, NASA started work on a low-boom flight demonstrator. The Lockheed Martin's Skunk Works is responsible for designing and building the vehicle. The project is known as the QueSST, and the US Air Force assigned it the X-59 designation in 2018. Figure 9-74 shows the final configuration.[131] It is a very long (nearly 100 feet), lightweight design. The design Mach number is 1.42.

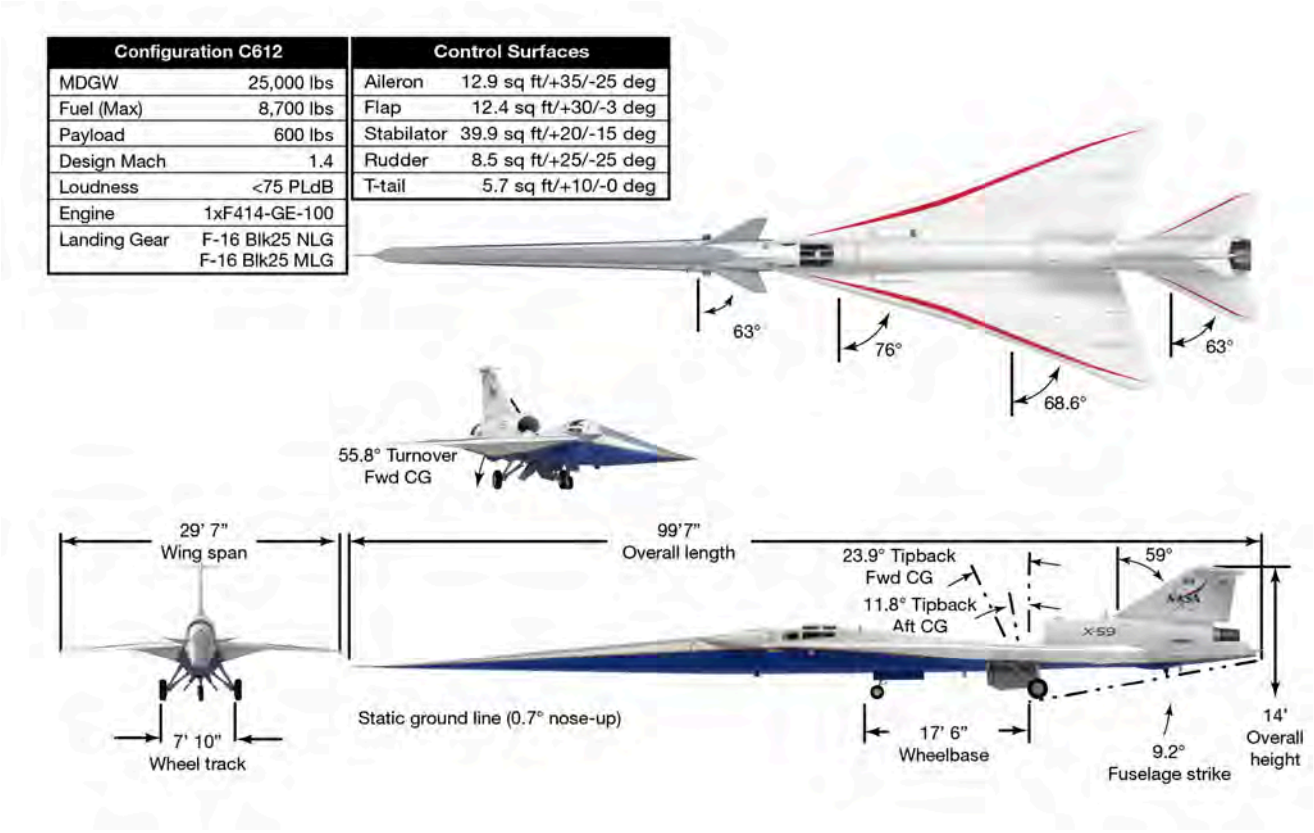


Figure 9-74: The X-59 QueSST configuration C612. *From NASA. Public domain.*

Chapter 9 Exercises

9.1 Subsonic and supersonic leading edges

Consider the following airplanes:

a. The F-22
b. The B-58
c. The XB-70

For each airplane at its supersonic cruise Mach number, determine if the leading edge is subsonic or supersonic. Is the trailing edge subsonic or supersonic? Comment on your findings.

9.2 Build and fly an oblique-wing glider.

You may want to use the plans shown in the figure on page 9 of the May 1991 issue of *Popular Science* magazine.[132] Submit a photo and hopefully a video of your glider in flight.

Figure References

Figure 9-1: US Air Force. Convair B-58A Hustler. Public domain. https://commons.wikimedia.org/wiki/File:B-58_Hustler.jpg

Figure 9-2: J. Ross. NASA. SR-71B in flight. Public domain. https://web.archive.org/web/20250508092919/https://www.dfrc.nasa.gov/Gallery/Photo/SR-71/HTML/EC97-43902-1.html

Figure 9-3: NASA. Take-off of #1 XB-70A (62-0001). 1965. Public domain. https://www.nasa.gov/image-article/xb-70-climbs-out-after-takeoff

Figure 9-4: NASA. Cruising #1 XB-70A (62-0001). 1968. Public domain. https://www.nasa.gov/image-article/xb-70-cruise-configuration

Figure 9-5: National Archives. Concorde. Public domain. https://catalog.archives.gov/id/17448564

Figure 9-6: R. Shenk. F-22 Raptor. CC BY-SA 2.0. https://en.wikipedia.org/wiki/File:Lockheed_Martin_F-22A_Raptor_JSOH.jpg

Figure 9-7: Von Karman, T., "Supersonic Aerodynamics – Principles and Applications," Journal of the Aeronautical Sciences, Vol. 14, No. 7, Jul. 1947, pp. 373–402. Copyright undetermined by AIAA. Fair use. https://doi.org/10.2514/8.1394

Figure 9-8: Poisson-Quinton, P., "First Generation Supersonic Transport," Princeton University Conference Meeting on the Future of Aeronautical Transportation, Nov. 10-11, 1975. Copyright undetermined.

Figure 9-9: Nicolai, L. M., and Carichner, G., *Fundamentals of Aircraft Design*, AIAA Education Series, 2010. Fair use.

Figure 9-16: Oswald, W. B., "Applied Aerodynamics and Flight Mechanics," Journal of the Aeronautical Sciences, Vol. 23, No. 5, May 1956, pp. 469–484. Copyright undetermined by AIAA. Fair use. https://doi.org/10.2514/8.3586

Figure 9-17: Figure 1 in Mason, W. H., and Lee, J., "Aerodynamically Blunt and Sharp Bodies," Journal of Spacecraft and Rockets, Vol. 31, No. 3, May-June 1994, pp. 406–413. https://arc.aiaa.org/doi/10.2514/3.26449

Figure 9-18: Nielsen, J. N., "Arrays of Bodies of Revolution for Minimum Wave Drag," Journal of Aircraft, Vol. 22, No. 10, Oct. 1985, pp. 901–909. Public domain. https://doi.org/10.2514/3.45222. *Note*: The "DATA, ref. 5" in the figure refers to Bantle, J. W., "Analysis of the Interference Effects Between Two Sears-Haack Bodies at Mach 2.7," Engineering and Applied Sciences Thesis, George Washington University, Washington, DC, 1982.

Figure 9-19: Figures 6.9 and 6.64 from Küchemann, D., *The Aerodynamic Design of Aircraft*, Pergamon Press, Oxford, 1978, pp. 352 and 420. (*Note*: Now reissued from the AIAA.) https://arc.aiaa.org/doi/book/10.2514/4.869228

Figure 9-29: NASA. Tunnel model AR-2. Public domain. https://commons.m.wikimedia.org/wiki/File:ARC-1957-A-22437.jpg

Figure 9-30: Von Kármán, T., "Some Significant Developments in Aerodynamics Since 1946," Journal of the Aero/Space Sciences, Vol. 26, No. 3, Mar. 1959, pp. 129–144, 154. Copyright undetermined by AIAA. https://doi.org/10.2514/8.7977

Figure 9-31: Baals, D. D., Robins, A. Warner and Haris, Roy V. Jr., "Aerodynamic Design Integration of Supersonic Aircraft," Journal of Aircraft, Vol. 7, No. 5, Nov-Dec. 1970. pp. 385-394 Copyright undetermined by AIAA.

Figure 9-33: P. Raj. Adapted from Rech, J., and Leyman, C. S., "A Case Study by Aerospatiale and British Aerospace on the Concorde," AIAA Professional Study Series. https://arc.aiaa.org/doi/book/10.2514/4.868122

Figure 9-34: Adapted by K. Grey from British Aerospace Corporation. Copyright undetermined. Fair use.

Figure 9-35: Adapted from Lamar, J. E., and Alford, W. J., Jr., "Aerodynamic-Center Considerations of Wings and Wing-Body Combinations," Conference on Aircraft Aerodynamics, NASA SP-124, May 1966. https://ntrs.nasa.gov/citations/19750065512

Figure 9-36: Kress, R. W., "Variable Sweep Wing Design," AIAA Paper 80-3043, 1980. Copyright undetermined by AIAA. Fair use.

Figure 9-37: Jones, R. T., *Wing Theory*, Princeton University Press, 1990. Fair use.

Figure 9-38: NASA, Oblique wing flight demonstration by the AD-1, ECN-133028, Jul. 1980. Public domain. https://web.archive.org/web/20240725113929/https://www.dfrc.nasa.gov/Gallery/Photo/AD-1/HTML/ECN-13302B.html

Figure 9-40: NASA, AD-1 with research pilot, Jan. 1982. Public domain. https://web.archive.org/web/20250309005840/https://www.dfrc.nasa.gov/Gallery/Photo/AD-1/HTML/ECN-17954.html

Figure 9-41: Baals, D. D., Robins, A. W., and Haris, R. V., Jr., "Aerodynamic Design Integration of Supersonic Aircraft," Journal of Aircraft, Vol. 7, No. 5, Nov.-Dec. 1970, pp. 385–394. Copyright undetermined by AIAA. Fair use.

Figure 9-42: Haris, R. V., Jr., "An Analysis and Correlation of Aircraft Wave Drag," NASA TM X-947, 1964. https://catalog.hathitrust.org/Record/011430825

Figure 9-43(a): Knill, D. L., Balabanov, V., Golovidov, O., Grossman, B., Mason, W. H., Haftka, R. T., and Watson, L. T., "Accuracy of Aerodynamic Predictions and Its Effects on Supersonic Transport Design," MAD Center Report 96-12-01, Dec. 1996. https://archive.aoe.vt.edu/mason/Mason_f/MAD961201.pdf

Figure 9-43(b): Knill, D. L., Balabanov, V., Golovidov, O., Grossman, B., Mason, W. H., Haftka, R. T., and Watson, L. T., "Accuracy of Aerodynamic Predictions and Its Effects on Supersonic Transport Design," MAD Center Report 96-12-01, Dec. 1996. https://archive.aoe.vt.edu/mason/Mason_f/MAD961201.pdf

Figure 9-44(a): Knill, D. L., Balabanov, V., Golovidov, O., Grossman, B., Mason, W. H., Haftka, R. T., and Watson, L. T., "Accuracy of Aerodynamic Predictions and Its Effects on Supersonic Transport Design," MAD Center Report 96-12-01, Dec. 1996. https://archive.aoe.vt.edu/mason/Mason_f/MAD961201.pdf

Figure 9-44(b): Knill, D. L., Balabanov, V., Golovidov, O., Grossman, B., Mason, W. H., Haftka, R. T., and Watson, L. T., "Accuracy of Aerodynamic Predictions and Its Effects on Supersonic Transport Design," MAD Center Report 96-12-01, Dec. 1996. https://archive.aoe.vt.edu/mason/Mason_f/MAD961201.pdf

Figure 9-45: Knill, D. L., Balabanov, V., Golovidov, O., Grossman, B., Mason, W. H., Haftka, R. T., and Watson, L. T., "Accuracy of Aerodynamic Predictions and Its Effects on Supersonic Transport Design," MAD Center Report 96-12-01, Dec. 1996. https://archive.aoe.vt.edu/mason/Mason_f/MAD961201.pdf

Figure 9-46: Knill, D. L., Balabanov, V., Golovidov, O., Grossman, B., Mason, W. H., Haftka, R. T., and Watson, L. T., "Accuracy of Aerodynamic Predictions and Its Effects on Supersonic Transport Design," MAD Center Report 96-12-01, Dec. 1996. https://archive.aoe.vt.edu/mason/Mason_f/MAD961201.pdf

Figure 9-47: Knill, D. L., Balabanov, V., Golovidov, O., Grossman, B., Mason, W. H., Haftka, R. T., and Watson, L. T., "Accuracy of Aerodynamic Predictions and Its Effects on Supersonic Transport Design," MAD Center Report 96-12-01, Dec. 1996. https://archive.aoe.vt.edu/mason/Mason_f/MAD961201.pdf

Figure 9-48: (1) Gapcynski, J. P., and Landrum, E. J., "Tabulated Data from a Pressure Distribution Investigation at Mach Number 2.01 of a 45 Deg Swept-back Wing Airplane Model at Combined Angles of Attack and Sideslip," NASA-MEMO-10-15-58L, Nov. 1958. https://ntrs.nasa.gov/citations/19630002621; (2) Woodward, F. A., "An Improved Method for the Aerodynamic Analysis of Wing-Body-Tail Configurations in Subsonic and Supersonic Flow," Part I—Theory and Application, NASA CR-2228, May 1973. https://ntrs.nasa.gov/citations/19730016318

Figure 9-49: Figure 2 in Swan, W. C., "A Review of the Configuration Development of the U.S. Supersonic Transport," Aircraft Engineering and Aerospace Technology, Vol. 41, No. 10, pp. 10–16. Public domain. https://doi.org/10.1108/eb034563.

Figure 9-50: Spearman, M. L., "The Evolution of the High-Speed Civil Transport," NASA TM-109089, Feb. 1994. https://ntrs.nasa.gov/citations/19940021652

Figure 9-52(a): Figures 10 and 11 in Kehrer, W. T., "Design Evolution of the Boeing 2707-300 Supersonic Transport, Part II, Design Impact of Handling Qualities Criteria, Flight Control System Concepts, and Aeroelastic Effects on Stability and Control," AGARD Conference Proceedings, No. 147, 1974, p. 10-6 (p. 232 of PDF available at: https://apps.dtic.mil/sti/tr/pdf/AD0783307.pdf). Reproduced with permission of Boeing Corporation.

Figure 9-52(b): Figures 5 and 6 in Bhatia, K. G., and Wertheimer, J., "Aeroelastic Challenges for a High Speed Civil Transport," 34th Structures, Structural Dynamics, and Materials Conference, AIAA Paper 1993-1478, 1993, p. 3672. https://doi.org/10.2514/6.1993-1478

Figure 9-53: Nubifer, Boeing 2707-300 3-view. CC BY-SA 3.0 Unported. Dimensions added by P. Raj. https://commons.wikimedia.org/wiki/File:Boeing_2707-300_3-view.svg

Figure 9-54: Figure 3 in Mason, W. H., "A Wing Concept for Supersonic Maneuvering," NASA Contractor Report 3763. 1983. Public domain. https://ntrs.nasa.gov/api/citations/19840007047/downloads/19840007047.pdf

Figure 9-55: (1) Figure 4a in Mason, W. H., "A Wing Concept for Supersonic Maneuvering," NASA Contractor Report 3763, 1983. Public domain. https://ntrs.nasa.gov/api/citations/19840007047/downloads/19840007047.pdf; (2) Figure 4b in Mason, W. H., "A Wing Concept for Supersonic Maneuvering," NASA Contractor Report 3763, 1983. Public domain. https://ntrs.nasa.gov/api/citations/19840007047/downloads/19840007047.pdf

Figure 9-56: W. H. Mason and David S. Miller, "Controlled Supercritical Cross-Flow on Supersonic Wings-An Experimental Validation," AIAA Paper 1980-1421, Jul. 1980. Public domain. https://arc.aiaa.org/doi/pdf/10.2514/6.1980-1421

Figure 9-57: Mason, W. H., and Miller, D. S., "Controlled Supercritical Cross-Flow on Supersonic Wings-An Experimental Validation," AIAA Paper 1980-1421, Jul. 1980. Public domain. https://arc.aiaa.org/doi/pdf/10.2514/6.1980-1421

Figure 9-58: Figure 21 in Mason, W. H., "A Wing Concept for Supersonic Maneuvering," NASA Contractor Report 3763, 1983. Public domain. https://ntrs.nasa.gov/citations/19840007047

Figure 9-59: Figure 30 in Mason, W. H., "A Wing Concept for Supersonic Maneuvering," NASA Contractor Report 3763, 1983. Public domain. https://ntrs.nasa.gov/citations/19840007047

Figure 9-60: Figure 40 in Mason, W. H., "A Wing Concept for Supersonic Maneuvering," NASA Contractor Report 3763, 1983. Public domain. https://ntrs.nasa.gov/citations/19840007047

Figure 9-61: Figure 2 in Kemmerly, G. T., Campbell, B. A., Banks, D. W., and Yaros, S. F., "Low-Speed Stability-and-Control and Ground-Effects Measurements on the Industry Reference High Speed Civil Transport," NASA TM-1999-209702, 1994. https://ntrs.nasa.gov/citations/20000025329

Figure 9-63: Baker, C. A., Grossman, B., Haftka, R. T., Mason, W. H., and Watson, L. T., "High-Speed Civil Transport Design Space Exploration Using Aerodynamic Response Surface Approximation," Journal of Aircraft, Vol. 39, No. 2, Mar.-Apr. 2002, pp. 215–220. https://doi.org/10.2514/2.2941

Figure 9-64: Baker, C. A., Grossman, B., Haftka, R. T., Mason, W. H., and Watson, L. T., "High-Speed Civil Transport Design Space Exploration Using Aerodynamic Response Surface Approximation," Journal of Aircraft, Vol. 39, No. 2, Mar.-Apr. 2002, pp. 215–220. https://doi.org/10.2514/2.2941

Figure 9-65: C. Thomas/NASA. Northrop-Grumman Corporation's modified U.S. Navy F-5E Shaped Sonic Boom Demonstration (SSBD) aircraft. Sept. 2009. Public domain. https://www.nasa.gov/centers/dryden/multimedia/imagegallery/SSBD/EC03-0210-1.html

Figure 9-66: Figure 1 in Aronstein, D. C., and Schueler, K. L., "Conceptual Design of a Sonic Boom Constrained Supersonic Business Aircraft," AIAA Paper 2004-0697. https://arc.aiaa.org/doi/pdf/10.2514/6.2004-697

Figure 9-67: J. Ross/NASA. Quiet Spike. Public domain. https://www.nasa.gov/image-article/sonic-boom-mitigator-f-15b-836

Figure 9-68: Aerion. Copyright undetermined. Fair use.

Figure 9-69: W. H. Mason. Adapted by P. Raj.

Figure 9-70: W. H. Mason. Adapted by P. Raj.

Figure 9-71: W. H. Mason. Data from Ferri, A., "Experimental Results with Airfoils Tested in the High-speed Tunnel at Guidonia," NACA TM-946, 1940. https://ntrs.nasa.gov/citations/19930094471

Figure 9-72: W. H. Mason. Data from Ferri, A., "Experimental Results with Airfoils Tested in the High-speed Tunnel at Guidonia," NACA TM-946, 1940. https://ntrs.nasa.gov/citations/19930094471

Figure 9-73: Figure 7 in Droste, C. S., and Walker, J. E., "The General Dynamics Case Study on the F-16 Fly-by-Wire Flight Control System." AIAA Professional Study Series. Jan. 2010. https://doi.org/10.2514/4.867873

Figure 9-74: NASA. Four-view of the X-59 QueSST Configuration C612 research aircraft. Public domain. https://www.nasa.gov/quesst-the-aircraft

Notes

1. Erickson, B. A., "Flight Characteristics of the B58 Mach 2 Bomber," Journal of the Royal Aeronautical Society, Vol. 66, No. 623, Nov. 1962, pp. 665–671.
2. Rich, B. R., "F-12 Series Aircraft Aerodynamic and Thermodynamic Design in Retrospect," AIAA Journal of Aircraft, Vol. 11, No. 7, Jul. 1974, pp. 401–406.
3. Merlin, P. W., From Archangel to Senior Crown: Design and Development of the Blackbird, AIAA Legacy of Flight Series, 2008.
4. Pike, I., "B-70: The State of the Art Improver," Flight International, Jun. 1964 (Part I), Jul. 1964 (Part II).
5. Poisson-Quinton, P. "First Generation Supersonic Transport," Proceedings of the Princeton University Conference, Princeton, NJ, Nov. 10-11, 1975.
6. Rech, J., and Leyman, C. S., "A Case Study by Aerospatiale and British Aerospace on the Concorde," AIAA Professional Study Series, 2003.
7. Wilde, M. G., and Cormery, G., "The Aerodynamic Derivation of the Concorde Wing," Canadian Aeronautics and Space Journal, May 1970, pp. 175–184.
8. Aronstein, D. C., Hirschberg, M. J., and Piccirillo, A. C., *Advanced Tactical Fighter to F-22 Raptor: Origins of the 21st Century Air Dominance Fighter,* AIAA, Reston, 1998.
9. Mullin, S. N., "The Evolution of the F-22 Advanced Tactical Fighter," AIAA Paper 1992-4188, Flight Simulation Technologies Conference, Hilton Head Island, SC, Aug. 24-26 1992. https://doi.org/10.2514/6.1992-4188
10. Von Karman, T., "Supersonic Aerodynamics – Principles and Applications," Journal of the Aeronautical Sciences, Vol. 14, No. 7, Jul. 1947, pp. 373–402.
11. Poisson-Quinton, P., "First Generation Supersonic Transport," Proceedings of the Princeton University Conference, Princeton, NJ, Nov. 10-11, 1975.
12. Nicolai, L. M., and Carichner, G. E., *Fundamentals of Aircraft and Airship Design, Volume I: Aircraft Design*, AIAA Education Series, 2010.
13. Baals, D. D., Robins, A. W., and Harris, R. V., Jr., "Aerodynamic Design Integration of Supersonic Aircraft," Journal of Aircraft, Vol. 7, No. 5, Nov.–Dec. 1970. pp. 385–394.
14. Coen, P. G., Sobieszczanski-Sobieski, J., and Dollyhigh, S. M., "Preliminary Results from the High-Speed Airframe Integration Research Project," AIAA Paper 1992-1004, Aerospace Design Conference, Irvine, CA, Feb. 3-6, 1992. https://doi.org/10.2514/6.1992-1004
15. Wilson, J. R., "The New Shape of Supersonics," AIAA Aerospace America, Jun. 2002, pp. 26–33.
16. Aronstein, D. C., and Schuler, K. L., "Conceptual Design of a Sonic Boom Constrained Supersonic Business Jet," AIAA Paper 2004-0697, 42nd Aerospace Science Meeting and Exhibit, Reno, NV, Jan. 5-8, 2004.
17. Ashley, H., and Landahl, M., *Aerodynamics of Wings and Bodies*, Addison-Wesley, Reading, MA, 1965. (*Note*: Now published by Dover.)
18. Eminton, E., and Lord, W. T., "Note on the Numerical Evaluation of the Wave Drag of Smooth Bodies Using Optimum Area Distributions for Minimum Wave Drag," Journal of the Royal Aeronautical Society, Vol. 60, Jan. 1956, pp. 61–63.
19. Harris, R. V., Jr., "An Analysis and Correlation of Aircraft Wave Drag," NASA TM X-947, 1964.
20. Carmichael, R., Public Domain Aeronautical Software. http://www.pdas.com
21. Adams, M. C., "Determination of Shapes of Boattail Bodies of Revolution for Minimum Wave Drag," NACA TN-2550, Nov. 1951.
22. Heaslet, M. A., and Lomax, H., "Supersonic and Transonic Small Perturbation Theory," in *General Theory of High Speed Aerodynamics*, edited by W. R. Sears, Princeton University Press, Princeton, 1954, pp. 240–249.
23. Harder, K. C., and Rennemann, C., Jr., "On Boattail Bodies of Revolution Having Minimum Wave Drag," NACA R-1271, 1956.
24. Krasnov, N. F., *Aerodynamics of Bodies of Revolution*, American Elsevier Publishing, New York, 1970, pp. 376–378.
25. Lord, W. T., and Eminton, E., "Slender Bodies of Minimum Wave Drag," Journal of the Aeronautical Sciences, Vol. 21, No. 8, Aug., 1954, pp. 569–570.
26. Jobe, C. E., "Prediction and Verification of Aerodynamic Drag, Part 1: Prediction" in *Thrust and Drag: Its Prediction and Verification*, edited by E. E. Covert, AIAA Progress in Astronautics and Aeronautics, Vol. 98, AIAA, New York, 1985, p. 152.
27. Jobe, C. E., "Prediction of Aerodynamic Drag," AFWAL TM-84-203, Jul. 1984, Fig. 23. https://apps.dtic.mil/sti/tr/pdf/ADA326842.pdf
28. Tinetti, A. F., Maglieri, D. J., and Bobbitt, P. J., "Equivalent Longitudinal Area Distributions of the B-58 and XB-70-1 Airplanes for Use in Wave Drag and Sonic Boom Calculations," NASA/CR-2011-217078, Mar. 2011.
29. Oswald, W. B., "Applied Aerodynamics and Flight Mechanics," Journal of the Aeronautical Sciences, Vol. 23, No. 5, May 1956. pp. 469–484.
30. Mason, W. H., and Lee, J., "Aerodynamically Blunt and Sharp Bodies," Journal of Spacecraft and Rockets, Vol. 31, No. 3, May-Jun. 1994, pp. 406–413.
31. Nielsen, J. N., "Arrays of Bodies of Revolution for Minimum Wave Drag," AIAA Journal of Aircraft, Vol. 22, No. 10, Oct. 1985, pp. 901–909.
32. Friedman, M. D., "Arrangement of Bodies of Revolution in Supersonic Flow to Reduce Wave Drag," NACA RM-A51I20, 1961.
33. Nielsen, J. N., "Arrays of Bodies of Revolution for Minimum Wave Drag," AIAA Journal of Aircraft, Vol. 22, No. 10, Oct. 1985, pp. 901–909.
34. Kulfan, R. M., "Application of Hypersonic Favorable Interference Concepts to Supersonic Aircraft," AIAA Paper 1978-1458, Aircraft Systems and Technology Conference, Los Angeles, CA, Aug. 21-23, 1978.
35. Küchemann, D., *The Aerodynamic Design of Aircraft*, Pergamon Press, Oxford, 1978, pp. 352, 420. (*Note*: Now reissued from the AIAA.)
36. Jones, R. T., and Cohen, D., *High Speed Wing Theory*, Princeton Aeronautical Paperbacks, Princeton, 1960.
37. Jones, R. T., and Cohen, D., *High Speed Wing Theory*, Princeton Aeronautical Paperbacks, Princeton, 1960.
38. Li, W.-L., and Livne, E., "Design-Oriented Leading-Edge Thrust Force Prediction for Supersonic Lifting Surfaces," Journal of Aircraft, Vol. 34, No. 4, Jul.-

Aug. 1997, pp. 457–464.

39. Boyd, J. W., Migotsky, E., and Wetzel, B. E., "A Study of Conical Camber for Triangular and Sweptback Wings," NACA A55G19, Nov. 1955.
40. Von Kármán, T., "Some Significant Developments in Aerodynamics Since 1946," Journal of the Aero/Space Sciences, Vol. 26, No. 3, Mar., 1959, pp. 129–144, 154.
41. Wright, B. R., Bruckman, F., and Radovcich, N. A., "Arrow Wings for Supersonic Cruise Aircraft," Journal of Aircraft, Vol. 15, No. 12, Dec. 1978. pp. 829–836.
42. Baals, D. D., Robins, A. W., and Harris, R. V., Jr., "Aerodynamic Design Integration of Supersonic Aircraft," Journal of Aircraft, Vol. 7, No. 5, Nov.–Dec. 1970. pp. 385-394.
43. Benoliel, A., and Mason, W. H., "Pitch-Up Characteristics for HSCT Class Planforms: Survey and Estimation," AIAA Paper 94-1819, 12th Applied Aerodynamics Conference, Colorado Springs, CO, Jun. 20-23, 1994.
44. Rech, J., and Leyman, C. S., A Case Study by Aerospatiale and British Aerospace on the Concorde, AIAA Professional Study Series, 2003.
45. Courtesy of British Aerospace Corporation.
46. Lamar, J. E., and Alford, W. J., Jr., "Aerodynamic-Center Considerations of Wings and Wing-Body Combinations," Conference on Aircraft Aerodynamics, NASA SP-124, May 1966.
47. Rich, B. R., "F-12 Series Aircraft Aerodynamic and Thermodynamic Design in Retrospect," Journal of Aircraft, Vol. 11, No. 7, Jul. 1974, pp. 401–406.
48. Kress, R. W., "Variable Sweep Wing Design," AIAA Paper 80-3043.
49. Polhamus, E. C., and Toll, T. A., "Research Related to Variable Sweep Aircraft Development," NASA TM-83121, 1981.
50. Jones, R. T., "New Design Goals and a New Shape for the SST," Astronautics & Aeronautics, Vol. 10, Dec. 1972, pp. 66–70.
51. Jones, R. T., and Nisbet, J. W., "Transonic Transport Wings-Oblique or Swept?" Astronautics and Aeronautics, Jan. 1974, pp. 40–47.
52. Jones, R. T., *Wing Theory*, Princeton University Press, Princeton, 1990.
53. Li, P., Seebass, R., and Sobieczky, H., "Oblique flying wing aerodynamics," AIAA Paper 1996-2120, Jun. 1996.
54. Crittenden, J. B., Weisshaar, T. A., Johnson, E. H., and Rutkowski, M. J., "Aeroelastic Stability Characteristics of an Oblique-Wing Aircraft," Journal of Aircraft, Vol. 15, No. 7, Jul. 1978, pp. 429–434.
55. McMurtry, T. C., Sim, A. G., and Andrews, W. H., "AD-1 oblique wing research program," AIAA Paper 1981-2354, 1st Flight Test Conference, Las Vegas, NV, Nov. 11-13, 1981.
56. Curry, R. E., and Sim, A. G., "Unique flight characteristics of the AD-1 oblique-wing research airplane," Journal of Aircraft, Vol. 20. No. 6, Jun. 1983, pp. 564–568.
57. Van der Velden, A. J. M., "The Conceptual Design of a Mach 2 Oblique Flying Wing Supersonic Transport," NASA CR-177529, May 1989.
58. Galloway, T., Gelhausen, P., and Moore, M. "Oblique Wing Supersonic Transport Concepts," AIAA Paper 92-4230, Guidance, Navigation, and Control Conference, Hilton Head Island, SC, Aug. 10-12, 1992.
59. Herschberg, M. J., Hart, D. M., and Beutner, T. J. "A Summary of a Half-Century of Oblique Wing Research," AIAA Paper 2007-0150, 45th AIAA Aerospace Sciences Meeting and Exhibit, Reno, NV, Jan. 8-11, 2007.
60. Cliff, S. E., Thomas, S. D., and Hawke, V. M., "Swing-Wing Inline-Fuselage Transport Design Studies at Supersonic Flight Conditions," AIAA Paper 2009-7073, 9th AIAA Aviation Technology, Integration, and Operations Conference, Hilton Head, SC, Sept. 21-23, 2009.
61. Baals, D. D., Robins, A. W., and Harris, R. V., Jr., "Aerodynamic Design Integration of Supersonic Aircraft," Journal of Aircraft, Vol. 7, No. 5, Nov.-Dec. 1970, pp. 385–394.
62. Sigalla, A., and Hallstaff, T. H., "Aerodynamics of Powerplant Installation on Supersonic Aircraft," Journal of Aircraft, Vol. 4, No. 4, Jul.-Aug. 1967, pp. 273–277.
63. Nicolai, L. M., and Carichner, G. E., *Fundamentals of Aircraft and Airship Design, Volume I: Aircraft Design*, AIAA Education Series, 2010.
64. Rodriguez, D. L., "Propulsion/Airframe Integration and Optimization on a Supersonic Business Jet," AIAA Paper 2007-1048, Jan. 2007.
65. Cummings, R. M., Mason, W. H., Morton, S. A., and McDaniel, D. R., *Applied Computational Aerodynamics: A Modern Engineering Approach*, Cambridge University Press, 2015.
66. Harris, R. V., Jr., "An Analysis and Correlation of Aircraft Wave Drag," NASA TM X-947, 1964.
67. Carlson, H. W., and Miller, D. S., "Numerical Methods for the Design and Analysis of Wings at Supersonic Speeds," NASA TN D–7713, 1974.
68. Carlson, H. W., and Mack, R. J., "Estimation of Leading-Edge Thrust for Supersonic Wings of Arbitrary Planforms," NASA TP-1270, 1978.
69. Hopkins, E. J., and Inouye, M., "An Evaluation of Theories Predicting Turbulent Skin Friction and Heat Transfer on Flat Plates at Supersonic and Hypersonic Mach Numbers," AIAA Journal, Vol. 9, No. 6, Jun. 1971, pp. 993–1003.
70. Harris, R. V., Jr., "An Analysis and Correlation of Aircraft Wave Drag," NASA TM X-947, 1964.
71. Craidon, C. B., "Description of a Digital Computer Program for Airplane Configuration Plots," NASA TM X-2074, Sept. 1970.
72. Harris, R. V., Jr., and Landrum, E. J., "Drag Characteristics of a Series of Low-Drag Bodies of Revolution at Mach Numbers from 0.6 to 4.0," NASA TN D-3163, Dec. 1965.
73. McGrory, W. D., Slack, D. C., Applebaum, M. P., and Walters, R. W., "GASP Version 2.2 Users Manual," Aerosoft, Inc., 1993.
74. AeroSoft, Inc. "GASP: Features." https://www.aerosoftinc.com/gasp/features_main.php
75. Knill, D. L., Balabanov, V., Golovidov, O., Grossman, B., Mason, W. H., Haftka, R. T., and Watson, L. T., "Accuracy of Aerodynamic Predictions and Its Effects

on Supersonic Transport Design," MAD Center Report 96-12-01, Dec. 1996.

76. Weber, J., and King, C., "Analysis of the Zero-Lift Wave Drag Measured on Delta Wings," Aeronautical Research Council Reports and Memoranda No. 3818, 1978. https://reports.aerade.cranfield.ac.uk/handle/1826.2/3100
77. Barger, R. L., Adams, M. S., and Krishnan, R. R., "Automatic Computation of Euler-Marching and Subsonic Grids for a Wing-Fuselage Configuration," NASA TM-4573, Jul. 1994.
78. Barger, R. L., and Adams, M. S., "Automatic Computation of Wing-Fuselage Intersection Lines and Fillet Inserts with Fixed-Area Constraints," NASA TM-4406, Mar. 1993.
79. Gapcynski, J. P., and Landrum, E. J., "Tabulated Data from a Pressure Distribution Investigation at Mach Number 2.01 of a 45 Deg Sweptback-Wing Airplane Model at Combined Angles of Attack and Sideslip," NASA MEMO-10-15-58L, Nov. 1958.
80. Woodward, F. A., "An Improved Method for the Aerodynamic Analysis of Wing-Body-Tail Configurations in Subsonic and Supersonic Flow," Part I – Theory and Application, NASA CR-2228 Part I, May 1973.
81. Carmichael, R., Public Domain Aeronautical Software. http://www.pdas.com
82. Carmichael, R., Public Domain Aeronautical Software. http://www.pdas.com
83. Middleton, W. D., and Lundry, J. L., "A System for Aerodynamic Design and Analysis of Supersonic Aircraft," Part 1 – General Description and Theoretical Development, NASA CR-3351; Part 2 – User's Manual, NASA CR-3352; Part 3 – Computer Program Description, NASA CR-3353; Part 4 – Test Cases, NASA CR-3354, Dec. 1980.
84. Carmichael, R. L., and Woodward, F. A., "An Integrated Approach to the Analysis and Design of Wings and Wing-Body Combinations in Supersonic Flow," NASA TN D-3685, Oct. 1966.
85. Mason, W. H., and Rosen, B. S., "The COREL and W12SC3 Computer Programs for Supersonic Wing Design and Analysis," NASA CR-3676, Dec. 1983.
86. Robins, W., Morris, O. A., and Harris, R. V., Jr., "Recent Research Results in the Aerodynamics of Supersonic Vehicles," Journal of Aircraft, Vol. 3, No. 6, Nov.-Dec. 1966, pp. 573–577.
87. Baals, D. D., Robins, A. W., and Harris, R. V., Jr., "Aerodynamic Design Integration of Supersonic Aircraft," Journal of Aircraft, Vol. 7, No. 5, Nov.-Dec. 1970, pp. 385–394.
88. Kulfan, R. M., and Sigalla, A., "Real Flow Limitations in Supersonic Wing Design," Journal of Aircraft, Vol. 16, No. 10, Oct. 1979, pp. 645–658.
89. Carlson, H. W., and Mann, M. J., "Survey and Analysis of Research on Supersonic Drag-Due-to-Lift Minimization With Recommendations for Wing Design," NASA TP-3202, Sept. 1992.
90. Carlson, H. W., McElroy, M. O., Lessard, W. B., and McCullers, L. A., "Improved Method for Prediction of Attainable Wing Leading-Edge Thrust," NASA TP-3557, Apr. 1996.
91. Carlson, H. W., Chu, J., Ozoroski, L., and McCullers, L. A., "Guide to AERO2S and WINGDES Computer Codes for Prediction and Minimization of Drag," NASA TP-3637, Nov. 1997.
92. Grossman, B., "Numerical Procedure for the Computation of Irrotational Conical Flows," AIAA Journal, Vol. 17, No. 9, Aug. 1979, pp. 828–837.
93. Mason, W. H., "SC3 — A Wing Concept for Supersonic Maneuvering," AIAA Paper 83-1858, Applied Aerodynamics Conference, Danvers, MA, Jul. 13-15, 1983. (*Note*: See also NASA CR-3763, Dec. 1983.)
94. Siclari, M. J., "The NCOREL Computer Program for 3D Nonlinear Supersonic Potential Flow Computations," NASA CR-3694, Aug. 1983.
95. Swan, W. C., "A Review of the Configuration Development of the U.S. Supersonic Transport," 11th Anglo-American Aeronautical Conference, London, Sept. 1969. (*Note:* Included in the AIAA Selected Reprint Series, Vol. VIII, Jet Transport Design, edited by J. M. Swihart, 1969.)
96. Spearman, M. L., "The Evolution of the High-Speed Civil Transport," NASA TM-109089, Feb. 1994.
97. Bhatia, K. G., and Wertheimer, J., "Aeroelastic Challenges for a High Speed Civil Transport," AIAA Paper 1993-1478. https://doi.org/10.2514/6.1993-1478
98. Conway, E. M., "NASA and the Technopolitics of Supersonic Transportation, 1945-1999," in *High-Speed Dreams*, The Johns Hopkins University Press, Baltimore, 2005.
99. Mason, W. H., "A Wing Concept for Supersonic Maneuvering," NASA CR-3763, 1983.
100. Mason, W. H., and Miller, D. S., "Controlled Supercritical Cross-Flow on Supersonic Wings-An Experimental Validation," AIAA Paper 1980-1421, 13th Fluid and PlasmaDynamics Conference, Snowmass, CO, Jul. 14-16, 1980.
101. Ferri, A., *Elements of Aerodynamics of Supersonic Flow*, The Macmillan Company, New York, 1949, p. 237, eqn. 446.
102. Brown, C. E., McLean, F. E., and Klunker, E. B., "Theoretical and Experimental Studies of Cambered and Twisted Wings Optimized for Flight at Supersonic Speeds," Proceedings of the Second International Congress of the Aeronautical Sciences, Zurich, Sept. 12-16, 1960.
103. Mason, W. H., "SC3 — A Wing Concept for Supersonic Maneuvering," AIAA Paper 83-1858, Applied Aerodynamics Conference, Danvers, MA, Jul. 13-15, 1983. (*Note*: See also NASA CR-3763, Dec. 1983.)
104. Mason, W. H., and Miller, D. S., "Controlled Supercritical Cross-Flow on Supersonic Wings-An Experimental Validation," AIAA Paper 1980-1421, 13th Fluid and PlasmaDynamics Conference, Snowmass, CO, Jul. 14-16, 1980.
105. Mason, W. H., and Miller, D. S., "Controlled Supercritical Cross-Flow on Supersonic Wings-An Experimental Validation," AIAA Paper 1980-1421, 13th Fluid and PlasmaDynamics Conference, Snowmass, CO, Jul. 14-16, 1980.
106. Mason, W. H., Siclari, M. J., Miller, D. S., and Pittman, J. L., "A Supersonic Maneuver Wing Designed for Nonlinear attached Flow," AIAA Paper 1983-0425, Aerospace Sciences Meeting, Reno, NV, Jan. 10-13, 1983.
107. Robins, A. W., Dollyhigh, S. M., Beissner, F. L., Jr., Geiselhart, K., Martin, G. L., Shields, E. W., Swanson, E. E., Coen, P. G., and Morris, S. J., Jr., "Concept

Development of a Mach 3.0 High-Speed Civil Transport," NASA TM-4058, Sept. 1988.

108. Hernandez, G., Covell, P. F., and McGraw, M. E., Jr., "An Experimental Investigation of a Mach 3.0 High-Speed Civil Transport at Supersonic Speeds," NASA TP-3365, Nov. 1993.
109. Boeing Commercial Airplanes, "High-Speed Civil Transport Study," NASA CR-4233, 1989.
110. Douglas Aircraft Company, "Study of High-Speed Civil Transports," NASA CR-4235, Dec. 1989.
111. Ray, J. K., Carlin, C. M., and Lambregts, A. A., "High-Speed Civil Transport Flight- and Propulsion Control Technological Issues," NASA CR-186015, Mar. 1992.
112. McCarty, C. A., Feather, J. B., Dykman, J. R., Page, M. A., and Hodgkinson, J., "Design and Analysis Issues of Integrated Control Systems for High-Speed Civil Transports," NASA CR-186022, May 1992.
113. Conway, E. M., "NASA and the Technopolitics of Supersonic Transportation, 1945-1999," in *High-Speed Dreams*, The Johns Hopkins University Press, Baltimore, 2005.
114. Kemmerly, G. T., Campbell, B. A., Banks, D. W., and Yaros, S. F., "Low-Speed Stability-and-Control and Ground-Effects Measurements on the Industry Reference High Speed Civil Transport," NASA TM-1999-209702, Dec. 1999.
115. Conway, E. M., "NASA and the Technopolitics of Supersonic Transportation, 1945-1999," in *High-Speed Dreams*, The Johns Hopkins University Press, Baltimore, 2005.
116. Haftka, R., Grossman, B., and Mason, W., "Multidisciplinary Optimization via Intelligent Response Surface Methodology," MAD Center White Paper No. 1, Sept. 1995. https://archive.aoe.vt.edu/mason/Mason_f/MADCtrWhitePaper1.pdf
117. Baker, C. A., Grossman, B., Haftka, R. T., Mason, W. H., and Watson, L. T., "High-Speed Civil Transport Design Space Exploration Using Aerodynamic Response Surface Approximation," Journal of Aircraft, Vol. 39, No. 2, Mar.-Apr. 2002, pp. 215–220.
118. Knill, D. L., Giunta, A. A., Baker, C. A., Grossman, B., Mason, W. H., Haftka, R. T. and Watson, L. T., "Response Surface Models Combining Linear and Euler Aerodynamics for Supersonic Transport Design," Journal of Aircraft, Vol. 36, No. 1, Jan.-Feb. 1999, pp. 75–86.
119. Cliff, S. E., Reuther, J. J., Saunders, D. A., and Hicks, R. M., "Single-Point and Multipoint Aerodynamic Shape Optimization of High Speed Civil Transport," Journal of Aircraft, Vol. 38, No. 6, Nov.-Dec. 2001, pp. 997–1005.
120. Choi, S., Alonso, J. J., and Kroo, I. M., "Two-Level Multifidelity Design Optimization Studies for Supersonic Jets," Journal of Aircraft, Vol. 46, No. 3, May-Jun. 2009, pp. 776–790.
121. Gipson, L., "Quieting the Boom: The Shaped Sonic Boom Demonstrator and the Quest for Quiet Supersonic Flight," NASA, 2013. https://www.nasa.gov/aeronautics/quieting-the-boom-the-shaped-sonic-boom-demonstrator-and-the-quest-for-quiet-supersonic-flight
122. Li, W., and Rallabhandi, S., "Inverse Design of Low-Boom Supersonic Concepts Using Reversed Equivalent-Area Targets," Journal of Aircraft, Vol. 51, No. 1, Jan.-Feb. 2014, pp. 29–36.
123. Rallabhandi, S. K., Nielsen, E. J., and Diskin, B., "Sonic-Boom Mitigation Through Aircraft Design and Adjoint Technology," Journal of Aircraft, Vol. 51, No. 2, Mar.-Apr. 2014, pp. 502–510.
124. Aronstein, D. C., and Schueler, K. L., "Conceptual Design of a Sonic Boom Constrained Supersonic Business Aircraft," AIAA 2004-0697, 42nd AIAA Aerospace Sciences Meeting and Exhibit, Reno, NV, Jan. 5-8, 2004.
125. Cowart, R., and Grindle, T., "An Overview of the Gulfstream/NASA Quiet SpikeTM Flight Test Program," AIAA Paper 2008-0123, 46th AIAA Aerospace Sciences Meeting and Exhibit, Reno, NV, Jan. 7-10, 2008.
126. Sturdza, P., "Extensive Supersonic Natural Laminar Flow on the Aerion Business Jet," AIAA Paper 2007-0685, 45th AIAA Aerospace Sciences Meeting and Exhibit, Reno, NV, Jan. 8-11, 2007.
127. Ferri, A., "Experimental Results with Airfoils Tested in the High-Speed Tunnel at Guidonia," NACA TM-946, Jul. 1940.
128. The Staff of the Ames 1- by 3-foot Supersonic Wind-Tunnel Section, "Notes and Tables for Use in the Analysis of Supersonic Flow," NACA TN-1428, Dec. 1947.
129. Miele, A. (ed.), *Theory of Optimum Aerodynamic Shapes*, Academic Press, New York, 1965.
130. Droste, C. S., and Walker, J. E., "The General Dynamics Case Study on the F-16 Fly-by-Wire Flight Control System," AIAA Professional Study Series. https://doi.org/10.2514/4.867873
131. NASA, "Quesst: The Aircraft." https://www.nasa.gov/quesst-the-vehicle
132. Popular Science, Vol 238, No. 5, page 9; https://books.google.com/books?id=qR8DAAAAMBAJ

10. Hypersonic Aerodynamics

Hypersonic vehicles are commonplace. There are many more of them than the supersonic aircraft discussed in the last chapter. Applications include missiles, launch vehicles, and entry bodies. A huge effort has been made in developing hypersonic aerodynamic methods and configurations. This began with missiles, including the intercontinental ballistic missile (ICBM) effort of the 1950s, followed by development work for the Mercury, Gemini, and Apollo manned space flight programs. The next major effort was devoted to the Space Shuttle. There is continued work on hypersonics for future entry vehicles and vehicles that can land on other planets. Finally, there is a perennial effort to develop atmospheric hypersonic vehicles. These efforts have resulted in a massive amount of literature, and we will provide references for further study. In this chapter, we limit our discussion to the key things to know from a configuration aerodynamics viewpoint.

Despite the effort to develop hypersonic configurations, there is no exact consensus on what defines the start of the hypersonic flow regime. Possibilities include:

1. Mach numbers at which supersonic linear theory fails
2. Where the ratio of the constant-pressure and constant-volume specific heats, γ, is no longer constant, and we must consider temperature effects on fluid properties
3. Mach numbers from 3 to 5, where Mach 3 might be required for blunt bodies that cause large disturbances to the flow and Mach 5 might be the starting point for more highly streamlined bodies.

In this section, we will provide a brief outline of the key distinguishing concepts. The books by Bertin and Cummings[1] and Anderson[2] provide a starting point for further study.

Essentially, there are five key points to remember:

1. In many cases, surface pressure can be estimated fairly easily.
2. Control and stability issues lead to different shapes.
3. Temperature and aerodynamic heating become critically important.
4. Blunt shapes are commonplace.
5. Engine-airframe integration is critical.

Our discussion will conclude with a summary of the flight vehicles that have been studied extensively and sometimes even flown. Our interest is in the lessons learned from these configurations.



Figure 10-1: The X-15. From NASA. Public domain.

The X-15, shown in figure 10-1, is the only true manned hypersonic airplane flown to date. It was rocket powered and started flight by being dropped from a B-52, so it was purely a research airplane. The first flight was by Scott Crossfield in June of 1959. The X-15 reached 314,750 feet in July 1962, piloted by Joe Walker. An improved version reached a Mach number of 6.7 at an altitude of 102,100 feet in October 1967 with Pete Knight at the controls. The X-15 program flew 199 flights, with the last one being in October 1968. Milt Thompson's book[3] describes the X-15 program, including the crackling sounds the airframe made as it heated up!

10.1 Surface Pressure Estimation

In many cases, surface pressures are relatively easy to estimate at hypersonic speeds. At supersonic speed, we have a local relation for two-dimensional flows relating surface slope and pressure, where θ is the surface inclination relative to the freestream:

$$C_p = \frac{2\theta}{\sqrt{M^2 - 1}} \qquad (10\text{-}1)$$

However, this relation is not particularly useful for most cases in actual aircraft configurations. In comparison, hypersonic rules *are* useful. The most famous relation is based on Newton's concepts. Although Newton was incorrect about low-speed flow, his ideas happens to apply at hypersonic speeds. The oncoming flow can be thought of as a stream of particles that lose all their momentum normal to a surface when they "hit" the surface. This leads to the relation

$$C_p = 2\sin^2\theta, \qquad (10\text{-}2)$$

where θ is the angle between the flow vector and the surface. Thus you only need to know the geometry of the body locally to estimate the local surface pressure. Particles only impact the portion of the body facing the flow, as shown in figure 10-2. The rest of the body is in a "shadow," and the C_p is assumed to be zero.* See Bertin and Cummings[4] or Anderson[5] for the derivation of this and other pressure-slope rules.

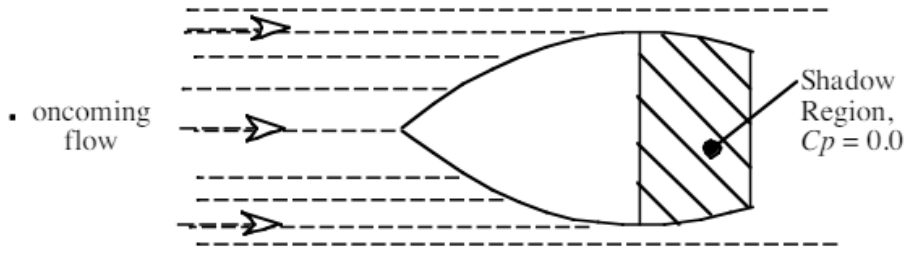


Figure 10-2: Shadow sketch, showing region where C_p is zero.

*Recall that $Cp_{vac} = -2/(\gamma M^2)$ and that it quickly approaches zero as the Mach number increases.

Two key observations come from the Newtonian pressure rule. First, the Mach number does not appear! Second, the pressure is related to the square of the inclination angle in hypersonic flows and not related linearly as in the supersonic formula. This illustrates how the situation in hypersonic flow is significantly different than the linear flow models at lower speeds.

The Newtonian flow model can be refined to improve agreement with data. This form is known as the modified Newtonian flow formula,

$$C_p = C_{p_{\max}} \sin^2\theta, \qquad (10\text{-}3)$$

where the stagnation $C_{p\max}$ is a function of Mach and γ,

$$C_{p_{\max}} = \frac{p_{0_2} - p_\infty}{(1/2)\rho_\infty V_\infty^2} \qquad (10\text{-}4)$$

and P_{02} is the stagnation or total pressure behind a normal shock. This expression brings both the Mach number and the ratio of specific heats back into the problem. (Derivation of an expression in terms of Mach number, M, and ratio of specific heats, γ, is left as an exercise

for the reader; see exercise 10.2.) The classical Newtonian theory is actually the limit as $M \to \infty$ and $\gamma \to 1$. These formulas are only valid when θ is positive. There are lots of other local rules (known as surface inclination rules), and Anderson's book[6] should be consulted for a more complete discussion. The methods normally heard in hypersonic discussions include the tangent cone, tangent wedge, and shock expansion methods. There is also a modification to the Newtonian pressure rule to include surface curvature effects. This is known as the Newtonian-Busemann rule.

How well do these methods work? We look at two cases. First we look at a blunt-body case, and then we will compare results with the pressure on a circular cone at zero angle of attack.

10.1.1 Blunt-Body Case

Figure 10-3 shows the agreement with wind tunnel data for a blunted cone.[7] This report includes results from a wind tunnel test and has the tabulated data. In this case, the agreement is remarkably good for a Mach number of 1.9. There are two things to note. First, for many hypersonic cases, we plot with a different axis direction than classic subsonic or supersonic aerodynamics; second, it is important to observe the change in slope at s/r of about 0.9. The geometry is not a pure hemisphere cone but has a transition arc. If we had used the standard Newtonian formula, the pressure at the nose would have been 2.0. Clearly the modified formula does an excellent job.

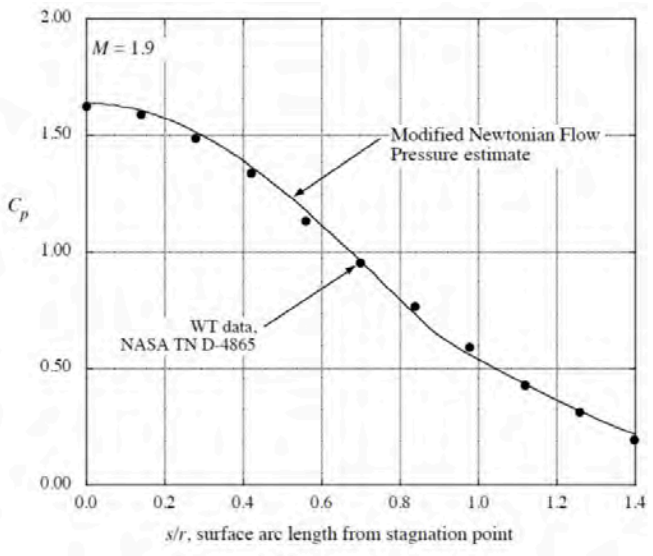


Figure 10-3: Comparison of the modified Newtonian estimate over the nose of a blunted cone with wind tunnel data. From W. H. Mason. Data from NASA.

10.1.2 Cones

Next we examine the results of Newtonian and modified Newtonian theory for two cones at zero angle of attack together with predictions from a theory given by DeJarnette et al.[8] and the exact results from the NASA cone tables.[9] Figure 10-4 shows the surface pressure results over a Mach number range from 4 to 10 and cone angles of 15° and 25°. The cone table results can be considered to be the exact inviscid values. Again, the cone produces a conical flow field, and the surface pressure variation is constant along the surface for an attached shock. In this case, the Newtonian approximations are not nearly as good.

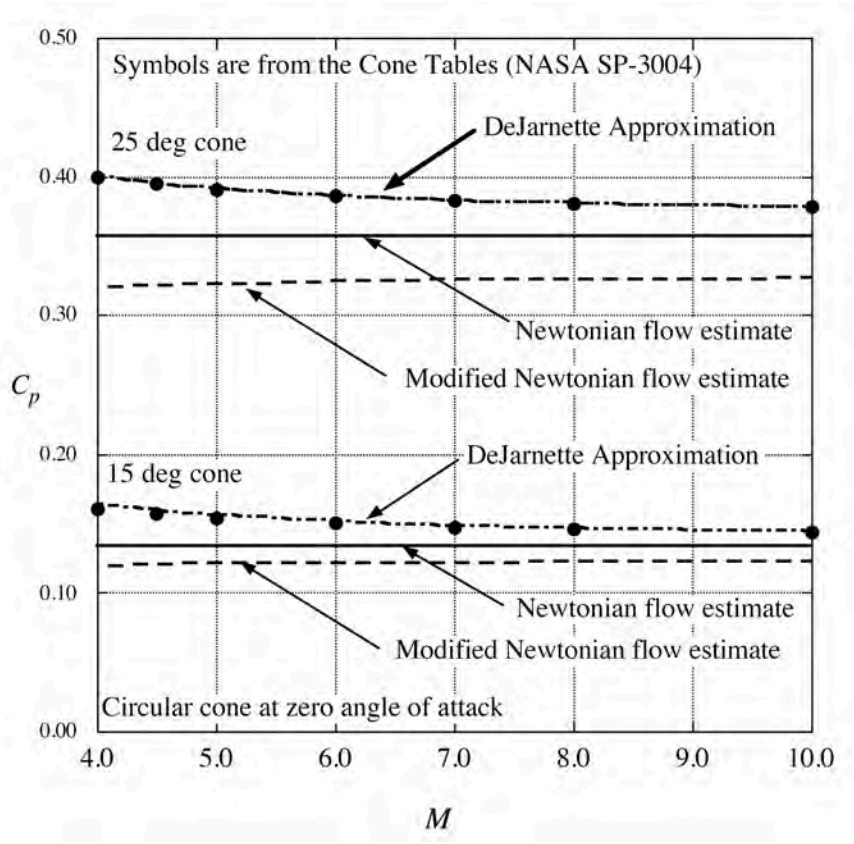


Figure 10-4: Comparison of surface pressures for a circular cone at zero angle of attack. From W. H. Mason. Data from NASA.

Since the Newtonian estimates are not particularly good, we will provide the simple approximation from DeJarnette[10] et al. that works well:

$$C_{p_{\alpha=0}} = \sin^2 \delta_v \left[1 + \frac{(\gamma+1)K^2+2}{(\gamma-1)K^2+2} \ln\left(\frac{\gamma+1}{2} + \frac{1}{K^2} \right) \right] \qquad (10\text{-}5)$$

where

$$K^2 = \left(M^2 - 1\right) \sin^2 \delta.$$

The advantage of the surface inclination rules is that they only need the local geometry. These methods were combined into a program known as the Hypersonic Arbitrary Body Program (HABP), originally developed at Douglas Aircraft and also known as the Gentry code. The program is available for free download from the Carmichael's Public Domain Aeronautical Software site.[11] Unfortunately, the user has to be wise enough to choose which rule should be used over various parts of the body. Of course, once you proceed beyond the early stages of configuration design, it is appropriate to use CFD. You essentially trade one set of choices (selecting the right rule) for another (CFD grid and parameters)!

While we are looking at surface pressures, we should look at the change in physics from subsonic to hypersonic flow. This is a key concept in configuration development. What is the maximum (fictitious) lift on a flat plate? I call this the "ultimate" lift. The values are plotted in figure 10-5. To estimate the ultimate lift at a given Mach number, the lower-surface pressure is taken equal to be the stagnation value and the upper-surface pressure is set equal to the vacuum value. We can see that, at low speeds, the lift is generated on the upper surface, while at high speed, the lift is almost completely generated on the lower surface. This is an important consideration when designing hypersonic vehicles.

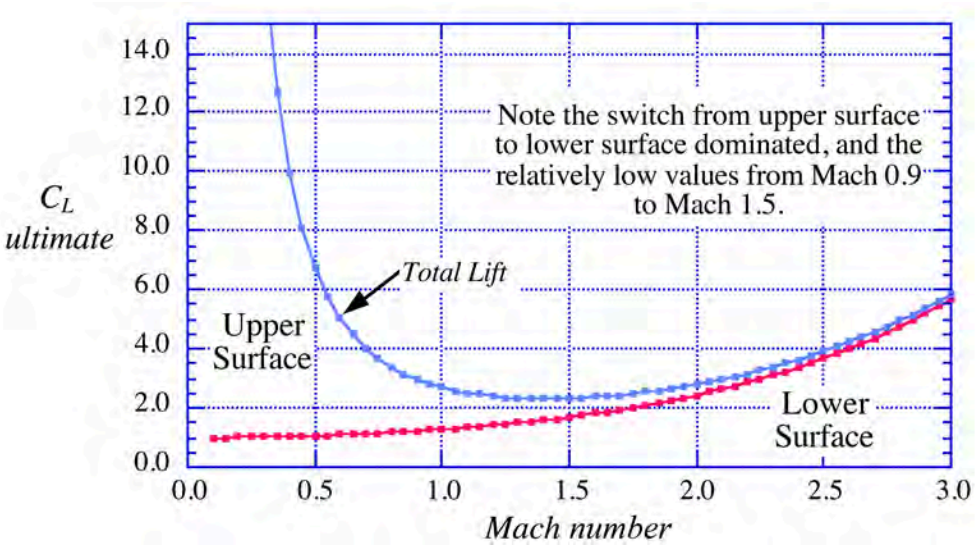


Figure 10-5: The "ultimate C_L" plot (showing the dominance of the lower surface at hypersonic speeds)

10.2 Aerodynamic Stability and Control

For stability, many hypersonic vehicles display an unusual geometric feature—thick bases. In this section, we illustrate why they are desirable. Our example relates to the thick trailing edge on the vertical tail of the X-15 shown above in figure 10-1.

The example of the difference in the flow characteristics at hypersonic speed will be used in the hypersonic directional stability problem. To start, we consider the yawing moment contribution from the vertical tail:

$$N_{VT} = q_{VT} S_{VT} l_{VT} C_{Y_{VT}} \qquad (10\text{-}6)$$

where q_{VT} is the dynamic pressure at the vertical tail, S_{VT} is the vertical tail area, l_{VT} is the moment arm, and C_{YVT} is the side force coefficient. The standard definition of the yawing moment coefficient, C_n, is

$$C_n = \frac{N}{q_{ref} S_{ref} b_{ref}} \qquad (10\text{-}7)$$

where b_{ref} is the reference span. We can write the yawing moment due to the vertical tail as

$$C_{n_{VT}} = \underbrace{\frac{l_{VT} S_{VT}}{b_{ref} S_{ref}}}_{\substack{\text{vertical} \\ \text{tail volume} \\ \text{coefficient}, V_{VT}}} \cdot \underbrace{\frac{q_{VT}}{q_{ref}}}_{\substack{\text{ratio of} \\ \text{dynamic pressures,} \\ \text{assume}=1}} \cdot C_{Y_{VT}}. \qquad (10\text{-}8)$$

The nomenclature associated with the problem and the equations is illustrated in figure 10-6.

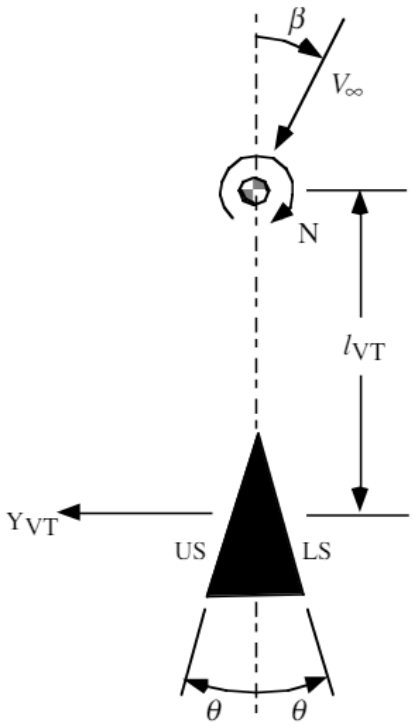


Figure 10-6: Sketch defining the hypersonic directional stability problem.

For a high-speed flow, we will assume that the vertical tail is a two-dimensional surface with a constant pressure on each side, so that $C_{YVT} = Cp_{LS} - Cp_{US}$. We will consider two cases, one supersonic and the other hypersonic. We compare the results for directional stability at high Mach number using the two-dimensional rule for linearized supersonic flow and Newtonian theory for hypersonic flow, as shown below.

$$\begin{array}{ll} \text{Linear theory} & \text{Newtonian theory} \\ C_p = \frac{2\theta}{\sqrt{M^2-1}} & C_p = 2\sin^2\theta \end{array} \qquad (10\text{-}9)$$

10.2.1 Case 1: Linearized Supersonic Theory

$$C_{Y_{VT}} = \Delta C_p = \frac{2(\theta+\beta)}{\sqrt{M^2-1}} - \frac{2(\theta-\beta)}{\sqrt{M^2-1}} = \frac{4\beta}{\sqrt{M^2-1}} \qquad (10\text{-}10)$$

Equation (10-10) above shows that the θs cancel. We use this expression to get $C_{n\beta}$:

$$C_{n_{\beta_{VT}}} = V_{VT}\frac{\partial C_{Y_{VT}}}{\partial \beta} = V_{VT}\frac{4}{\sqrt{M^2-1}} \qquad (10\text{-}11)$$

Note that V_{VT} is defined in equation (10-8). This expression shows that $C_{n\beta}$ is positive but vanishes for hypersonic Mach numbers.

10.2.2 Case 2: Newtonian Hypersonic Flow Theory

This time, the expression for the side force is

$$C_{Y_{VT}} = \Delta C_p = 2\sin^2(\theta+\beta) - 2\sin^2(\theta-\beta). \qquad (10\text{-}12)$$

Using trig functions, we arrive at

$$C_{Y_{\beta_{VT}}} = 2\begin{bmatrix}\sin^2\theta\cos^2\beta + 2\cos\theta\sin\beta\sin\theta\cos\beta + \cos^2\theta\sin^2\beta \\ -\sin^2\theta\cos^2\beta + 2\cos\theta\sin\beta\sin\theta\cos\beta - \cos^2\theta\sin^2\beta\end{bmatrix}, \qquad (10\text{-}13)$$

which reduces to

$$\begin{aligned} C_{Y_{\beta_{VT}}} &= 8\underbrace{\cos\theta}_{=1}\underbrace{\sin\beta}_{=\beta}\underbrace{\sin\theta}_{=\theta}\underbrace{\cos\beta}_{=1}, \qquad (10\text{-}14) \\ &\cong 8\theta\beta \end{aligned}$$

and at $\beta = 0$,

$$C_{n_{\beta_{VT}}} = 8V_{VT}\theta. \qquad (10\text{-}15)$$

If θ is zero, so is $C_{n\beta}$! But opening up the angle rapidly increases $C_{n\beta}$. In addition, there is no Mach number dependence. The Case 2 results were verified experimentally, and the wedge vertical tail concept literally saved the X-15 program.[12] This effect is also the reason for flared "skirts" seen on some launch vehicles. Figure 10-7 shows the X-15 airplane at the Smithsonian Air and Space Museum on the Mall in Washington, DC. This is a photo I took to highlight the wedge vertical tail with the large base area. This airfoil results in significant base pressure drag. However, the airplane was rocket propelled and had enough thrust to ensure the base drag wasn't critical.



Figure 10-7: X-15 on display at the National Air and Space Museum. From W. H. Mason.

This analysis brings out another key issue. For a flat plate at hypersonic speeds, the use of the classic stability derivative concept is problematic. $C_{L\alpha}$ is no longer a constant with angle of attack. This means that the stability and control analysis has to be generalized.

There is, however, more to the story. Let's take another look at the X-15.

Observe the top and side view of the airplane in figure 10-8.[13] Though the wedge vertical tail can be seen in the top view, we are really interested in the side view's depiction of the ventral fin portion of the vertical tail. The lower dashed portion of the ventral tail was designed to be dropped before landing. This turned out to be a fortuitous design feature.

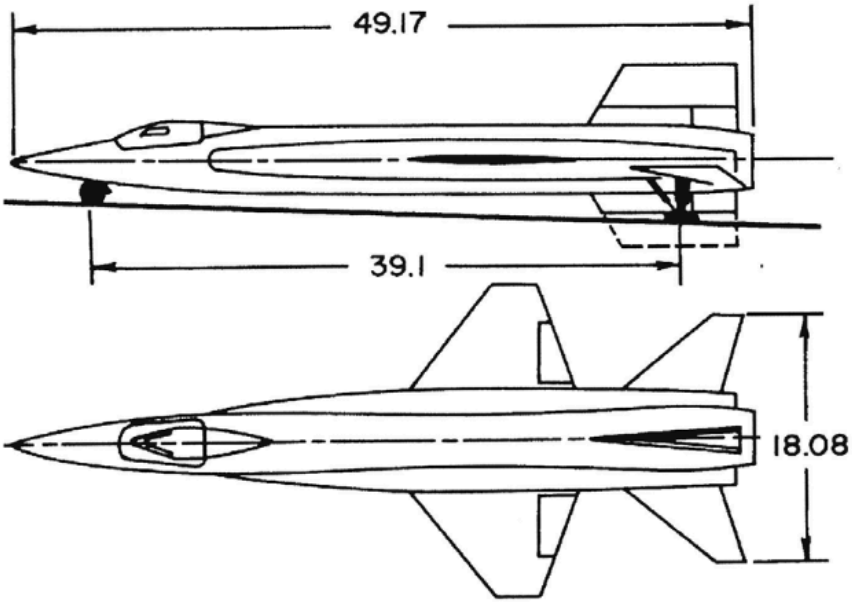


Figure 10-8: Side- and top-view drawings of the X-15. Note the dashed lines outlining a portion of the ventral tail. From R. B. Yancy. "Flight Measurements of Stability and Control Derivatives of the X-15 Research Airplane to a Mach Number of 6.02 and an Angle of Attack of 25°." NASA. Public domain.

To reenter the atmosphere, a high-α recovery was desired. Initial lateral-directional data for the simulator was for the horizontal stabilizer at zero deflection. Once the math model was updated, there was a pilot-induced oscillation (PIO) if the stability augmentation system (SAS) was inoperative above 15° angle of attack. After the aerodynamic characteristics were updated, the roll damper was flight critical. Loss of the SAS at an altitude above 200,000 feet would result in loss of the aircraft. It turns out that although $C_{n\beta}$ was good, the $C_{l\beta}$ was poor. Bob Hoey,[14] who was one of the flight test engineers, described this story. The problem was the adverse rolling moment created by the large ventral fin. Although the airplane had plenty of directional stability, the dihedral effect was strongly negative at high alpha (with the left sideslip producing left roll). Famous flight test pilot Joe Walker said it was "like a marble rolling on the outside of a barrel."

The fix proposed by the flight test engineers was to simply leave the detachable portion of the ventral fin off. $C_{n\beta}$ was reduced, but $C_{l\beta}$ was now acceptable at high alpha and Dutch roll was "about the same." This was counterintuitive since vertical tail size was typically being increased after flight testing at that time (recall the F-100 story in Chapter 8).

It is worthwhile to look at the stability derivatives as presented by Roxanah Yancy.[15] Figure 10-9 contains the directional data, and figure 10-10 presents the lateral data.

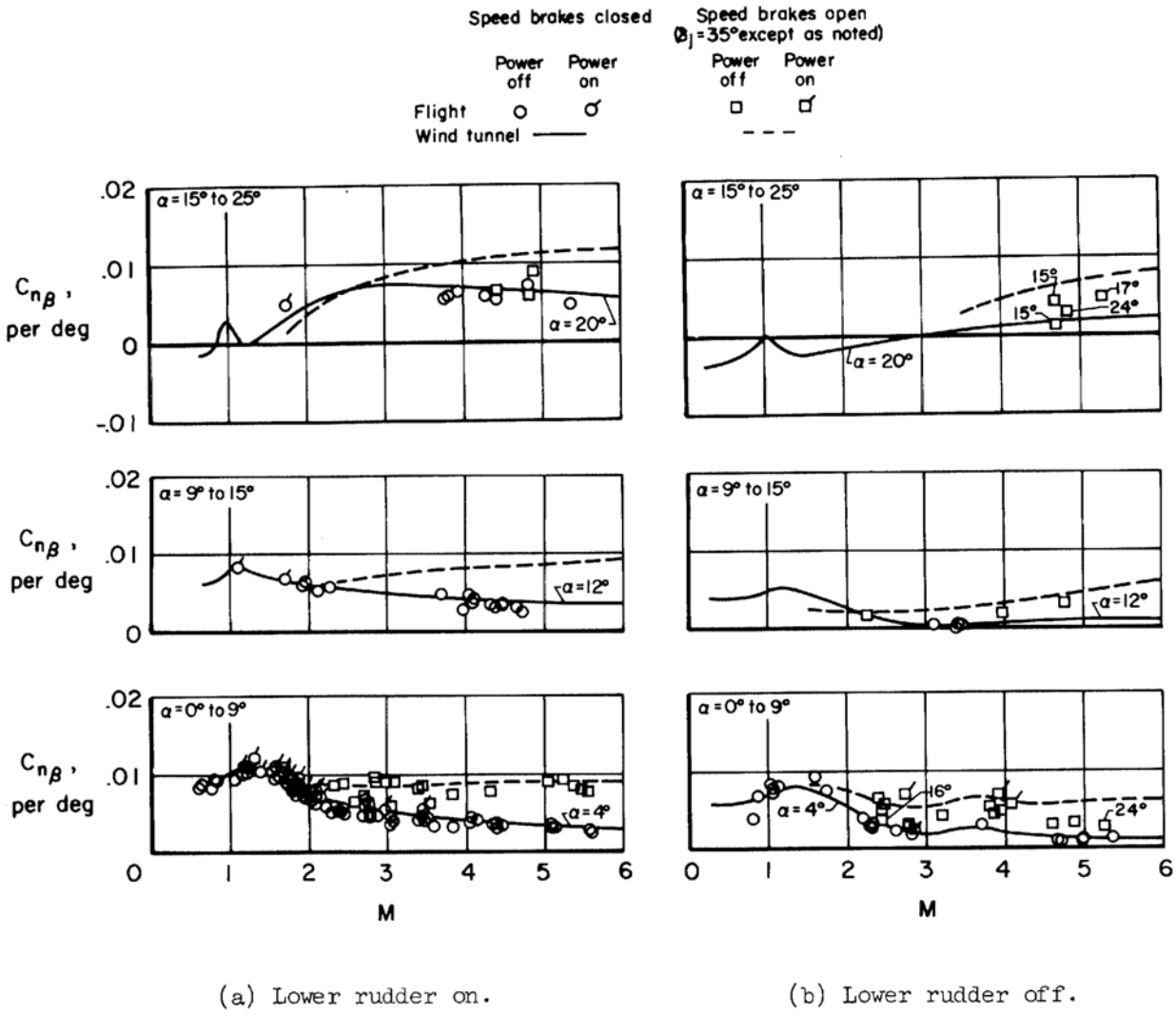


Figure 10-9: Variation of directional stability derivative with Mach number. *From R. B. Yancy. "Flight Measurements of Stability and Control Derivatives of the X-15 Research Airplane to a Mach Number of 6.02 and an Angle of Attack of 25°." NASA. Public domain.*

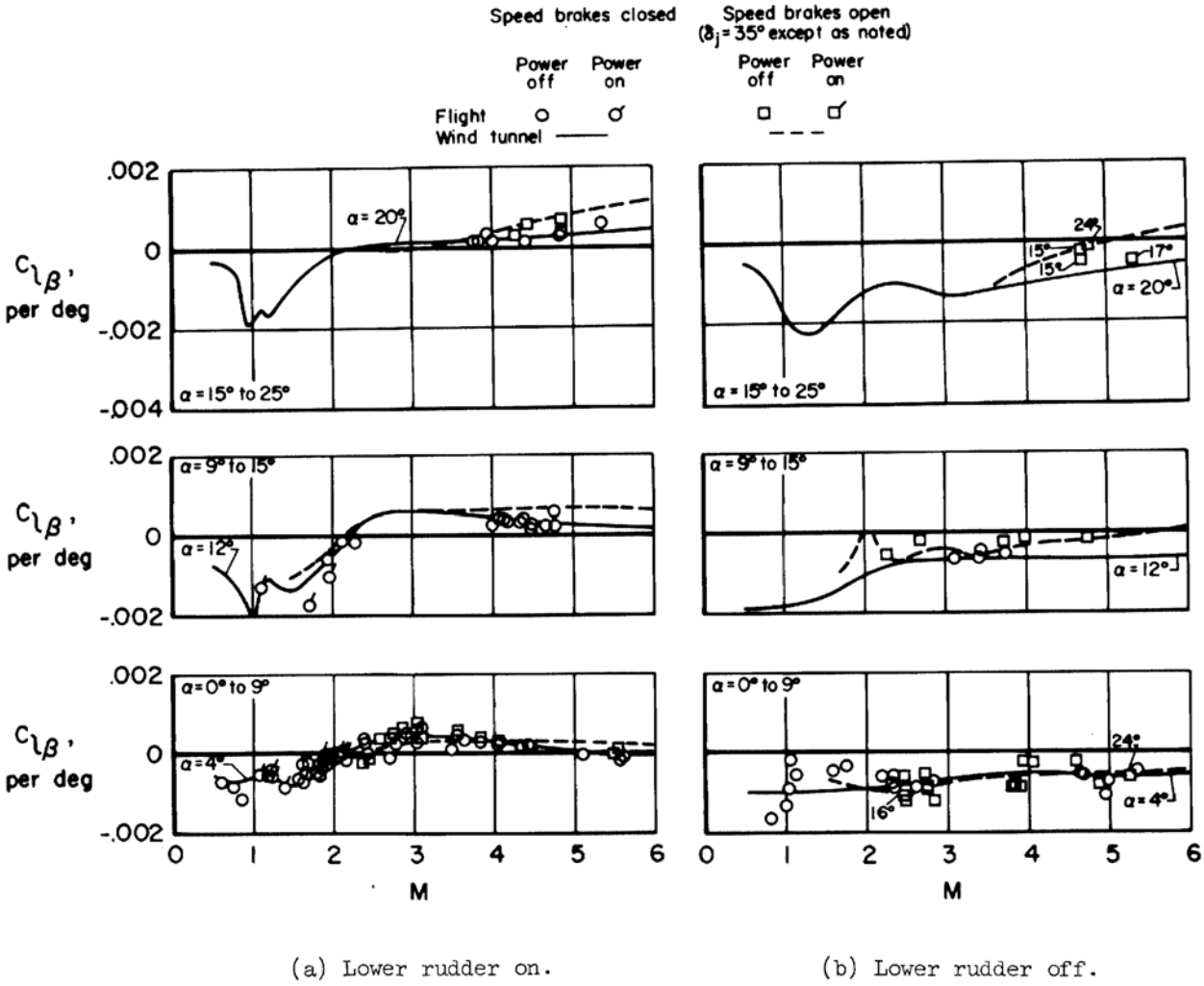


Figure 10-10: Variation of effective-dihedral derivative with Mach number. *From R. B. Yancy. "Flight Measurements of Stability and Control Derivatives of the X-15 Research Airplane to a Mach Number of 6.02 and an Angle of Attack of 25°." NASA. Public domain.*

Specifically, look at the $\alpha = 15°$ to 25° areas of figures 10-9 and 10-10. Leaving the lower portion of the ventral off reduces $C_{n\beta}$ compared to when it is on. At a Mach number below 3, $C_{n\beta}$ goes negative. However, at this speed, the angle of attack can be reduced and $C_{n\beta}$ becomes positive. In exchange for sacrificing strongly positive $C_{n\beta}$ (directional stability), figure 10-10 shows that $C_{l\beta}$ is now at least slightly negative. The pilots found this acceptable. *These figures should be studied very carefully*. This is an important example of configuration aerodynamics understanding that is necessary to achieve a viable configuration.

10.3 Aerodynamic Heating

We are now ready to address what is probably the most challenging consideration in developing hypersonic vehicles. This is illustrated by looking at the relationship between stagnation temperature and static temperature:

$$\frac{T_0}{T} = 1 + \frac{\gamma - 1}{2} M_\infty^2 \qquad (10\text{-}16)$$

For the adiabatic wall temperature,

$$T_{\text{adiabaticwall}} = \left(1 + r\frac{\gamma - 1}{2}M_\infty^2\right)T_e \qquad (10\text{-}17)$$

where *r* is the recovery factor. Equation 10-17 describes a wall temperature with no heat transfer (adiabatic). For many hypersonic vehicles, the surface will have to be cooled and the heating needs to be estimated. For adiabatic wall temperatures, the limit for an aluminum structure is around Mach 2, which was the Concorde's cruise Mach number. The SR-71 was made of titanium, and temperature limited the speed to slightly over Mach 3. Some sources indicate that this limit was actually the temperature limit on the wiring inside the airplane and that is the condition that limited the speed.

Hypersonic aerodynamic configuration design means that you must always deal with heating. In general, at sustained high speeds, surfaces must be cooled, and since heating is a critical concern, this means that viscous effects are crucial immediately. Unlike normal airplane aerodynamics, hypersonic vehicles fly at very high altitudes and the Reynolds number may be low enough that the flow is laminar, meaning that laminar flows are also often of interest. Recall that the heat transfer is much lower when the flow is laminar. In fact, a critical requirement in hypersonic vehicle design is the ability to estimate the transition location (for these cases, transition occurs over a region and can't be assumed to occur at a "location"), making this ability the subject of much research.[16] (*Note*: ignore the error in the first line of the abstract that has the wrong date and pilot for the Mach 6.7 flight.) A description of the aerodynamic heating on the SR-71 is available in the excellent paper by Ben Rich.[17] An appendix in his paper provides the equations used to estimate the heat transfer coefficients.

In the 1950s, the problem of aerodynamic heating was a problem of national focus. The ability of ICBMs to reenter the atmosphere and accurately deliver the payload was a critical requirement. Initially it had been assumed that the nose shape should consist of a sharply pointed tip. However, H. Julian Allen and A. J. Eggers at NACA Ames found that a blunt shape would be much better. A blunt nose forces a detached shock wave, and most of the heat goes off the surface and into the flow field, not the vehicle. This insight enabled practical reentry vehicles. Thus, a nose or leading edge radius large enough to prevent the nose from melting had to be used. The analysis by H. Julian Allen and A. J. Eggers convinced the aerodynamic design community that blunt bodies were required to survive entry from orbit.[18]

The maximum value of the heat transfer, *q*-dot, is proportional to the leading-edge radius, as shown in this relation:

$$\dot{q}_{\text{max, laminar}} = \frac{1}{\sqrt{R_{LE}}} \qquad (10\text{-}18)$$

where R_{LE} is the leading-edge radius at the stagnation point. Clearly, a larger R_{LE} is desirable.

This result led to the choice of the manned space capsule shapes for the Mercury, Gemini, and Apollo programs. The Space Shuttle entered the atmosphere at a very high angle of attack so that it was in effect a blunt body. Figure 10-11 show a photo of Harvey Allen demonstrating the concept.

Figure 10-12 shows an example of the flow field over a sphere at a Mach number of 7.6. The shock standoff distance was critically important and its estimation was one of the most important efforts at the time.

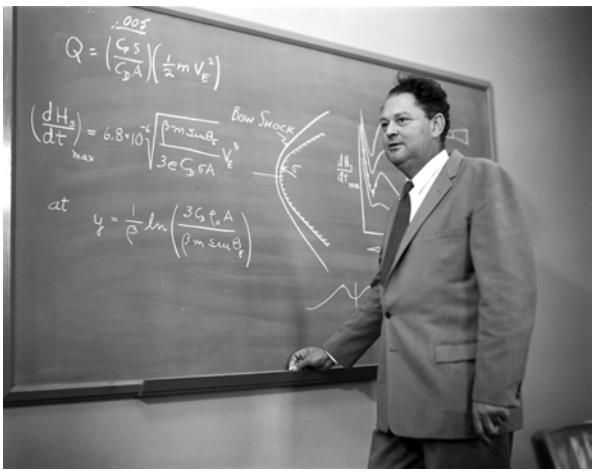


Figure 10-11: NASA Ames Engineer H. Julian "Harvey" Allen explaining blunt nose principle. From NASA. Public domain.

Even when using a blunt-body reentry shape, the heating problem is severe. The Mercury, Gemini, and Apollo vehicles used an ablative heat shield, where portions of the shield actually burn off. The Space Shuttle, which reentered from a relatively low Earth orbit, used special heat-resistant tiles, a number of which had to be replaced after each flight. Details of the Apollo capsule thermal protection system can be found in the NASA report by Pavlosky and Leger.[19]

This was the first great challenge problem for CFD (though this was in the 1960s, and the computational solution of the flow field wasn't called CFD until the early 1970s). This challenge, known as the blunt-body problem, was particularly difficult because the flow is subsonic behind the strong normal, or nearly normal, shock wave. The flow then accelerates quickly to supersonic/hypersonic speed. Thus, this is the reverse of the transonic flow problem. In this case, the freestream is supersonic/hypersonic rather than subsonic. We want to know the shock standoff distance, the shock shape, and the flow properties at the nose, where the aerodynamic heating is the highest. The shape of the shock determines the distribution of flow properties such as entropy, which vary as the shock slope changes.

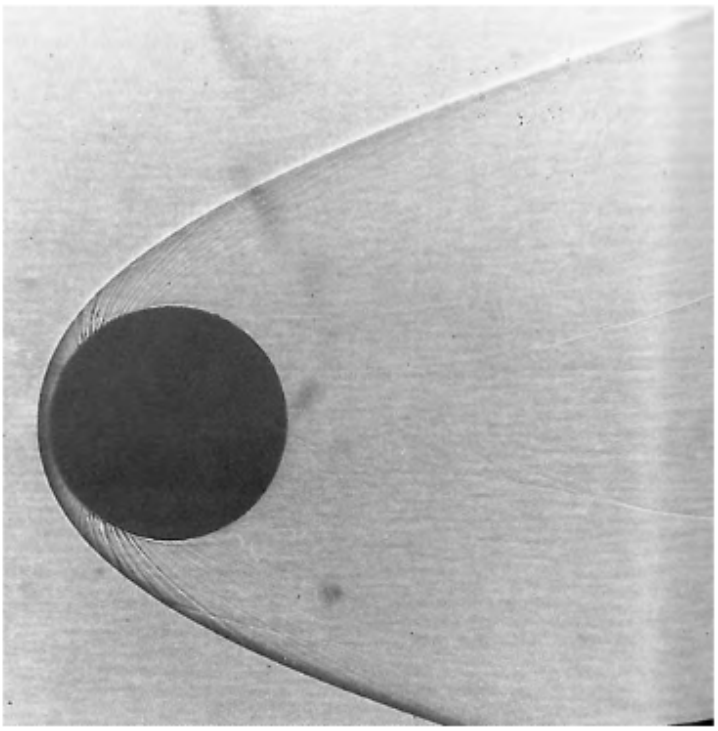


Figure 10-12: Photo of M = 7.6 flow over a sphere. From M. Van Dyke. "An Album of Fluid Motion." Attributed to US Navy Naval Surface Weapons Center. Public domain.

The problem was solved by computing the unsteady flow field, which is always mathematically hyperbolic. If the solution is steady, the computation will converge to the steady state result while overcoming the difficulty of the mixed elliptic-hyperbolic equation type that describes the steady-state problem. The successful approach invented to obtain a practical blunt-body calculation method is generally attributed to Moretti.[20]

In case the issue of aerodynamic heating seems academic, consider the $M = 6.7$ flight of the X-15. It turned out to be the last flight of that airplane. A dummy scramjet* installation was tested by placing the scramjet mockup below the airplane. The shocks from the front of the scramjet inlet impinged on the pylon supporting the scramjet. The shock interference heating was so severe that the shocks acted as a blowtorch, cutting through the structure and effectively slicing off the scramjet. The internal damage to the airplane from the heating led to the scrapping of this high-speed version of the airplane and to the termination of the program. Figure 10-13 below shows the scramjet hanging below the airplane.

*A scramjet is similar to a ramjet, but the flow through the combustion chamber is supersonic. This has been a difficult technology to develop, but it has been demonstrated in flight (see the discussion later in this chapter).

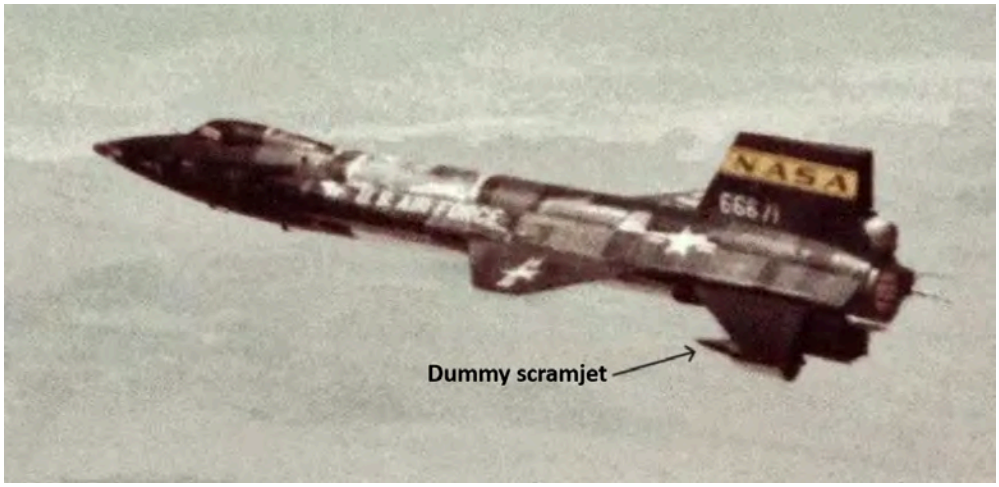


Figure 10-13: X-15 with dummy scramjet. From NASA. Public domain. Label added.

Figure 10-14 shows a schematic representation of the scramjet installation. Apparently, this was done in an ad hoc fashion without serious analysis. Figure 10-15 shows the result. This was an indication of the seriousness of the aerodynamic heating problem. Both of these figures are contained in the paper by Iliff and Shafer,[21] who had taken the figures directly from NASA TM X-1669.[22]

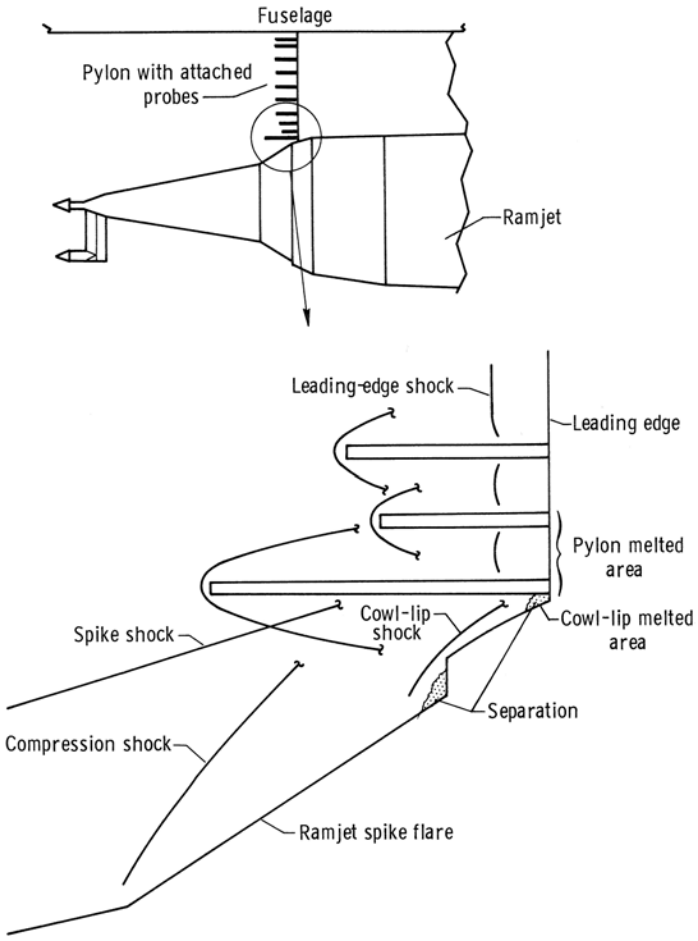


Figure 10-14: Schematic of assumed shock patterns in shock impingement and cowl-lip interference zones for the scramjet installation. From J. D. Watts. "Flight Experience with Shock Impingement and Interference Heating on the X-15-2 Research Airplane." NASA. Public domain.

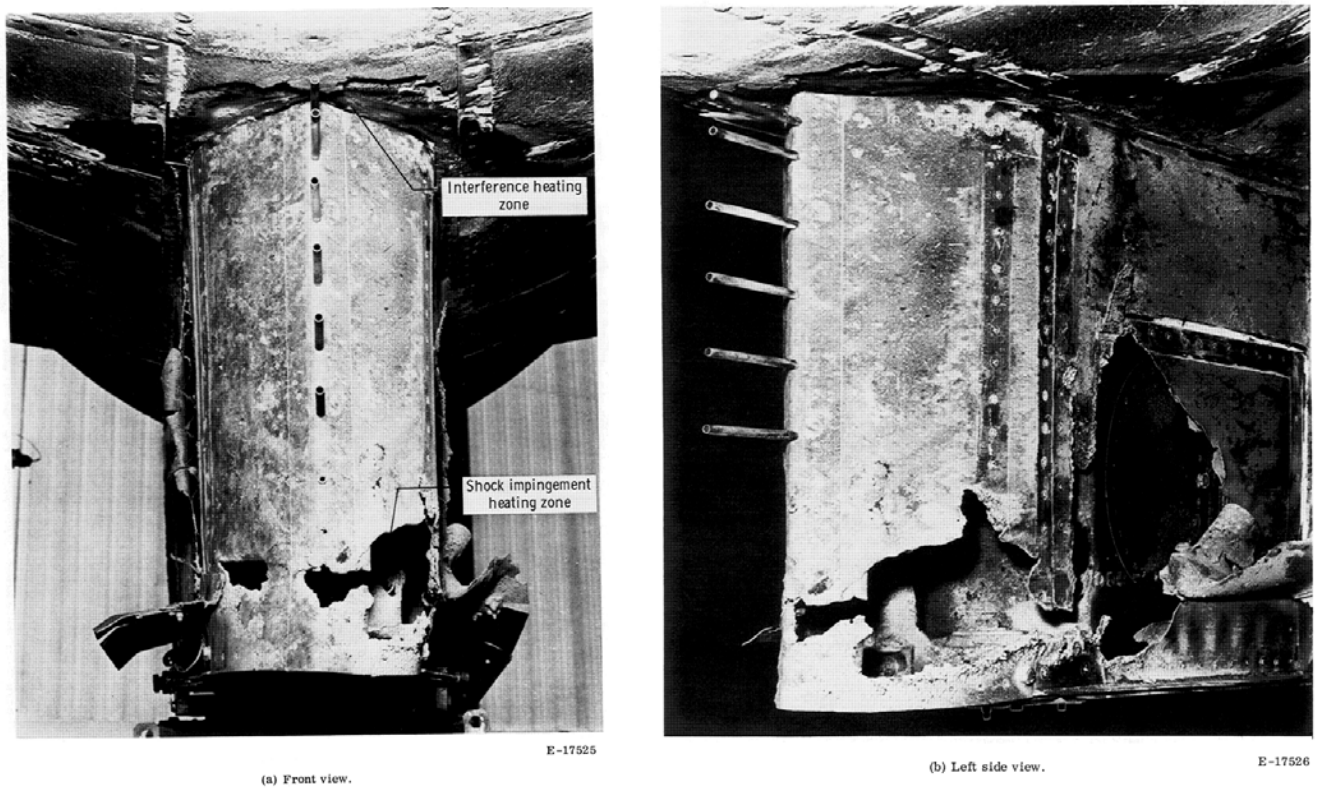


Figure 10-15: Post-flight condition of dummy engine pylon due to aerodynamic heating at M = 6.7. From J. D. Watts. "Flight Experience with Shock Impingement and Interference Heating on the X-15-2 Research Airplane." NASA. Public domain.

The message from this "incident," as it was described, is that shock impingement on a surface at hypersonic speed leads to extreme heating. Special care must be taken when developing a hypersonic configuration to avoid shock impingement heating.

Recall that the Space Shuttle Columbia was destroyed by the breakdown of the thermal protection system on February 1, 2003. In that case, a piece of insulating foam from the external tank broke off during ascent and damaged the leading edge of the Space Shuttle, exposing the internal structure to the heating during reentry. There was essentially nothing left to see when debris was found, in contrast to the X-15 case we've shown. Some of the recent flight test vehicles have also been lost due to adverse effects of aerodynamic heating.

10.4 Additional Considerations for Gas Dynamics

Because of the extreme conditions in hypersonic flows, many somewhat unique and distinctive gas dynamics effects become important. These effects are the result of a difference in the viscous effects at hypersonic speeds. Specifically, flight at high altitudes leads to a significant extent of laminar flow. In addition, Mach number effects (heating in particular) result in a thicker boundary layer. Figure 10-16 from Hayes and Probstein[23] illustrates the situation.

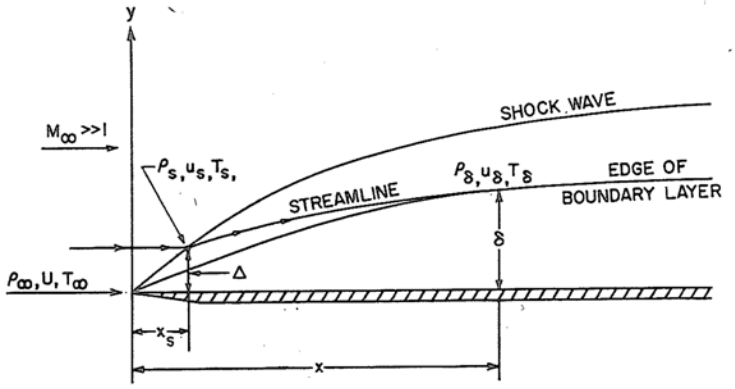


Figure 10-16: Sketch of boundary layer induced flow on a flat plate at hypersonic speed and zero angle of attack. *From W. D. Hayes and R. F. Probstein. "Hypersonic Flow Theory." Fair use.*

The thicker hypersonic boundary layer means that it immediately affects the pressure distribution compared to the low-speed case where the flow over a flat plate surface in line with the freestream flow will not change the pressure distribution significantly. An example of this effect on pressures is shown in figure 10-17, where pressures were measured on a plate at $\alpha = 0°$ and $M = 6.86$.[24] At low speeds, we would expect $p_2 - p_1$ to be zero (here, p_2 is the static pressure at some point on the surface and p_1 is the freestream static pressure). Especially near the leading edge, there is an effect of the boundary layer on the pressures. This effect is known as viscous-inviscid interaction and can be characterized as either "strong" or "weak." An extensive description is available in Hayes and Probstein.[25] Once again, modern CFD methods need to be used in design, and this flow feature should arise without having to be deeply involved in the theory.

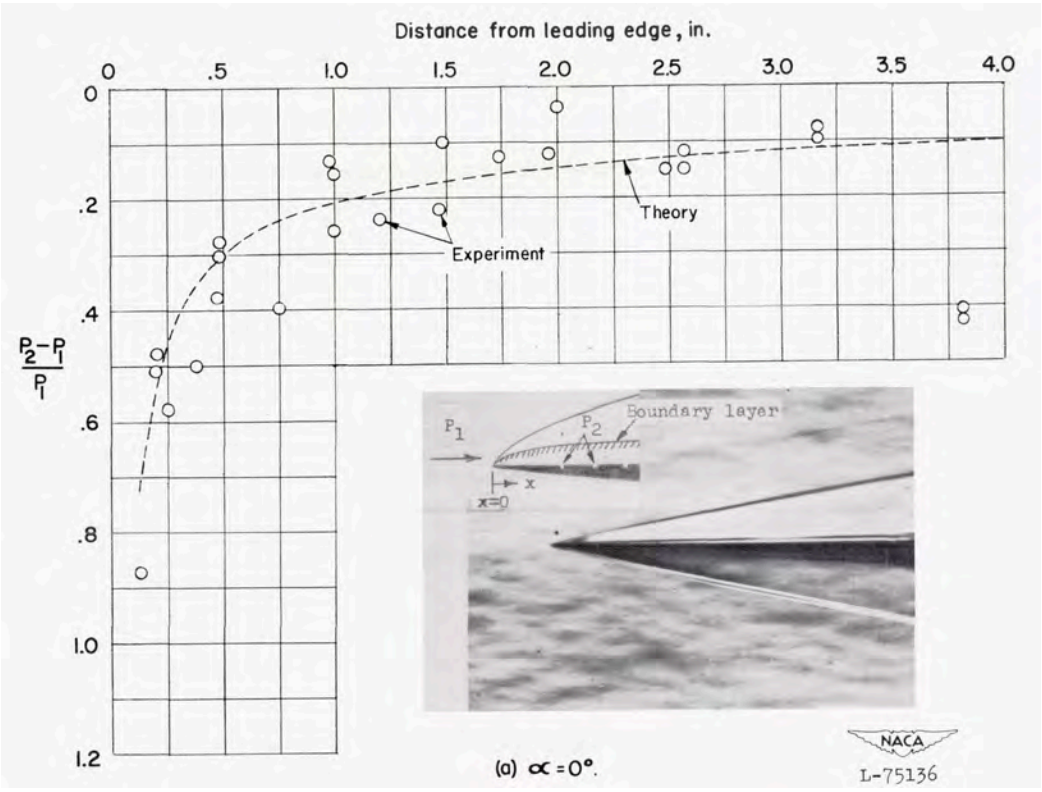


Figure 10-17: A comparison between theoretical and experimental pressures over a flat plate at zero angle of attack, M = 6.86, and Re = 0.98 million. *From M. H. Bertram. "An Approximate Method for Determining the Displacement Effects and Viscous Drag of Laminar Boundary Layers in Two-Dimensional Hypersonic Flow." NACA. Public domain.*

As shown above, viscous compressibility effects can be important. We illustrate this by looking at the change in the skin friction drag coefficient on a flat plate with increasing Mach number. The code FRICTION can be used to study this effect; see section E.5.1. As posted on the website, the code assumes that the wall is at the adiabatic wall temperature (no heat transfer). This is the usual assumption for typical aircraft aerodynamics, up to around a Mach number of 2. However, the hardwired value of the ratio of the wall temperature to the adiabatic wall temperature, TWTAW, can be easily changed. Figure 10-18 shows the variation of skin friction drag coefficient for an adiabatic wall in laminar flow for values of the wall-temperature-to-freestream-temperature ratios (T_W/T_e) of 0.25, 1.0, and 4.0. These laminar flow results use the Eckert reference temperature method to incorporate Mach number and wall temperature effects.[26]

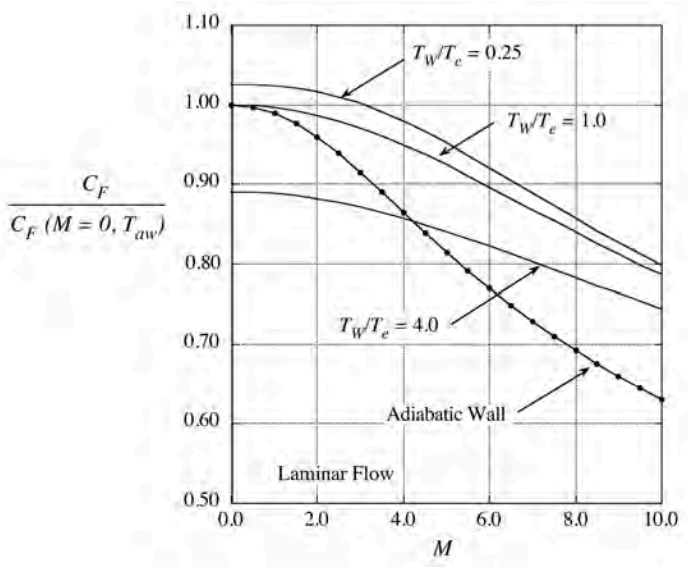


Figure 10-18: Compressibility effects on flat-plate skin friction drag coefficient for laminar flow.

Figure 10-19 shows the compressibility effects for turbulent flows for a flap plate using the Van Driest II method.[27] The values are given normalized by the zero Mach number adiabatic wall value, T_{aw}. In general, the skin friction coefficient decreases with increasing Mach number and wall temperature.

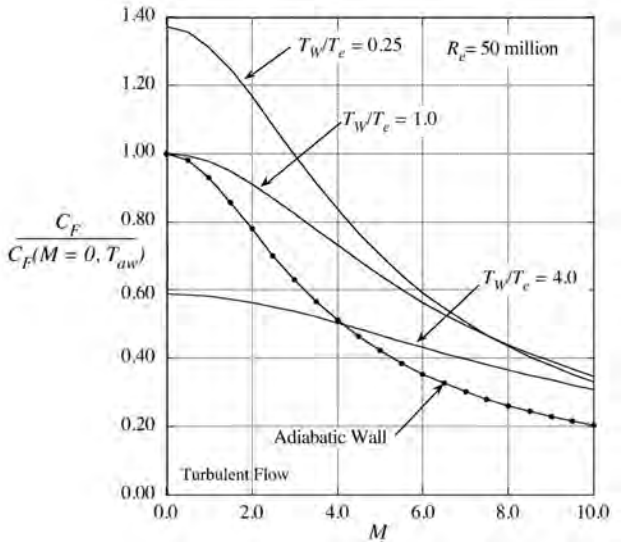


Figure 10-19: Compressibility effects on flat-plate skin friction drag coefficient for turbulent flow.

At one time, theoretical aerodynamicists devoted a large part of their efforts to developing prediction methods to predict viscous-inviscid interaction effects. Today, we can use CFD to find the hypersonic flow field. A good overview of CFD for hypersonic flow appeared in a special issue of the *Journal of Spacecraft and Rockets*.[28] This paper is an overview of all the papers contained in this issue of the journal. Finally, an excellent chart shown in figure 10-20 was sent to me by Chris Johnston at NASA Langley. It illustrates the range of considerations that might be important when making hypersonic aerothermodynamic predictions.[29]

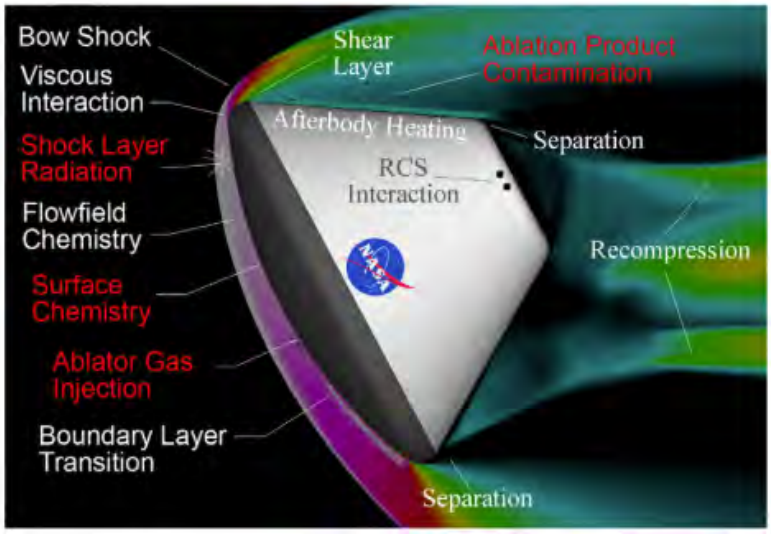


Figure 10-20: The range of gas dynamic consideration required to predict reentry flowfields. *From National Academies of Sciences, Engineering and Medicine. "Plasma Science: Enabling Techology Sustainability, Secuity, and Exploration." Attributed to NASA/Jet Propusion Laboratory. Public domain.*

For a much more thorough description of these effects, study the books by Bertin[30] and Hirschel and Weiland.[31] An excellent discussion of aerothermodynamics is available in the survey paper by Hollis and Borrelli.[32] This paper includes a discussion of radiation effects. These also have to be included when the entry velocities become extremely high.

10.5 Considerations for High-Temperature Gas Dynamics

We now briefly discuss the effects of high temperatures on gas dynamic properties. From the classic subsonic viewpoint through the supersonic aerodynamic viewpoint, we almost always assume a calorically and thermally perfect gas. This means that the ratio of specific heats, γ, is a constant. At high temperatures, this is no longer the case. According to Anderson,[33] γ is not constant above about 980°F (800 K). Oxygen starts to dissociate above about 3,140°F (2000 K) and is completed at 6,740°F (4000 K). Nitrogen dissociation begins at 15,740°F (9000 K). Above 15,740°F (9000 K), gas starts to ionize and become a plasma. Clearly these are temperatures more closely connected to reentry vehicles than any atmospheric flight vehicles. Anderson also makes the point that this effect should be called "high-temperature gas dynamics." It is very common in the community and in the literature to describe this as a "real gas" effect, which is not precisely correct. In addition, the gas can be in equilibrium or "reacting" in time and space. If the flow composition varies in time, additional equations must be added to the governing equation set. This situation involves finite-rate chemistry. Here we will present the difference between our classical constant-γ gas dynamics and air that is in equilibrium, using the values from tables generated at the Cornell Aeronautical Lab.[34] An engineering applet is available to compute the same information,[35] making use of that is known as the Tannehill curve fits.[36]

Figure 10-21 shows the difference between calorically perfect gas and equilibrium air values for the temperature behind a normal shock wave. In this case, we present results for two different altitudes as a function of freestream Mach number. The equilibrium air results also depend on the freestream value of pressure. It is clear that the Mach number is not necessarily an appropriate reference value for equilibrium and finite-rate chemistry flows, and you will not necessarily see results presented in this fashion. However, from a low-speed perspective, it is useful in trying to understand the effects. We see that there is an extremely large difference between the calorically perfect and equilibrium gas values. For flow behind the shock, a significant amount of energy goes into dissociation of the gas instead of raising the temperature.

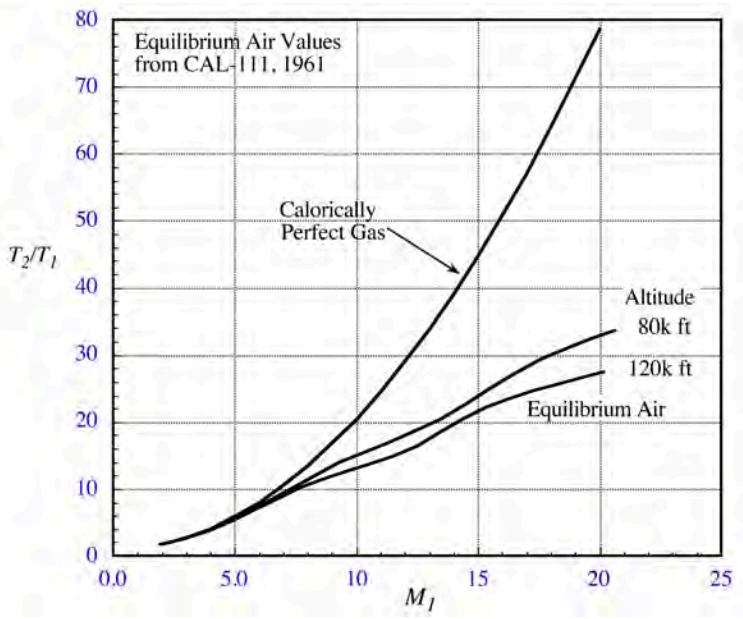


Figure 10-21: Temperature jump across a normal shock wave with increasing upstream Mach number considering air as perfect gas and using equilibrium air assumption. From W. H. Mason. Data from US Department of Defense.

We next present the values for the change in pressure and density across the normal shock. The density jump is presented in figure 10-22, and pressure jump is presented in figure 10-23. The density is strongly affected by the strong shock. Conversely, there is just a small pressure difference between equilibrium air and the calorically perfect gas case. Anderson[37] shows that the pressure is more closely connected to the fluid mechanics of the shock jump, while the temperature and density are the result of the thermodynamics of the shock jump.

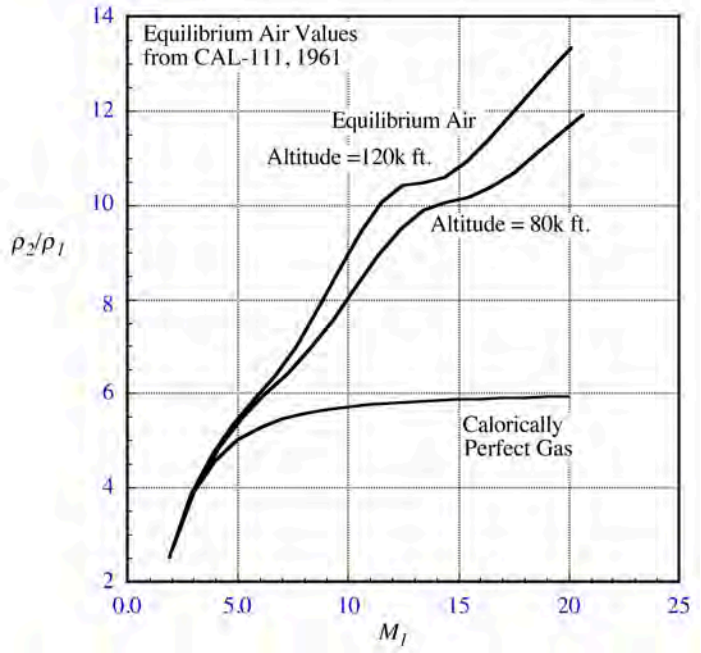


Figure 10-22: Density jump across a normal shock wave with increasing upstream Mach number, considering air as perfect gas and using equilibrium air assumption. From W. H. Mason. Data from US Department of Defense.

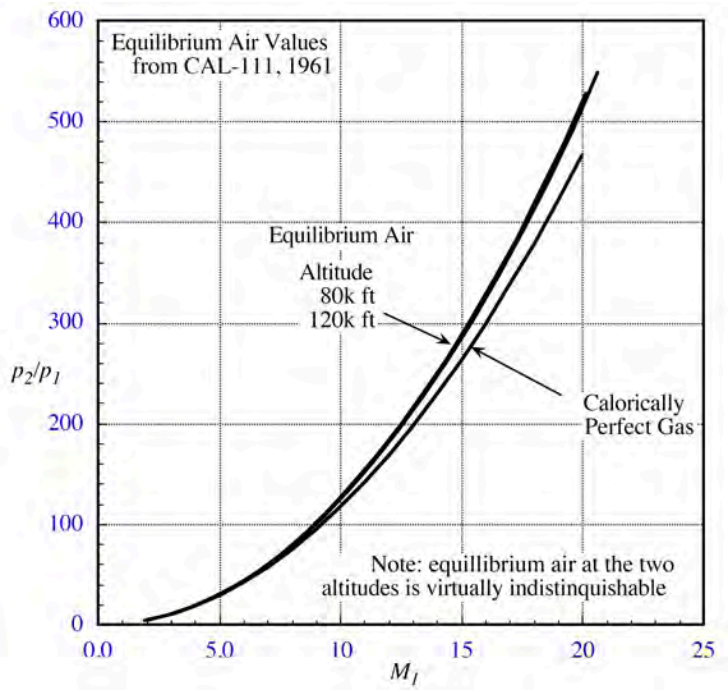


Figure 10-23: Pressure jump across a normal shock wave with increasing upstream Mach number, considering air as perfect gas and using equilibrium air assumption. From W. H. Mason. Data from US Department of Defense.

To illustrate the importance of including high-temperature effects, we describe a situation where the space shuttle was almost lost during the first reentry, apparently because the high-temperature gas effects were not included in the predictions. The difference between the perfect gas and equilibrium air simulation for the pitching moment is shown in figure 10-24.[38] There is a significant difference between the two.

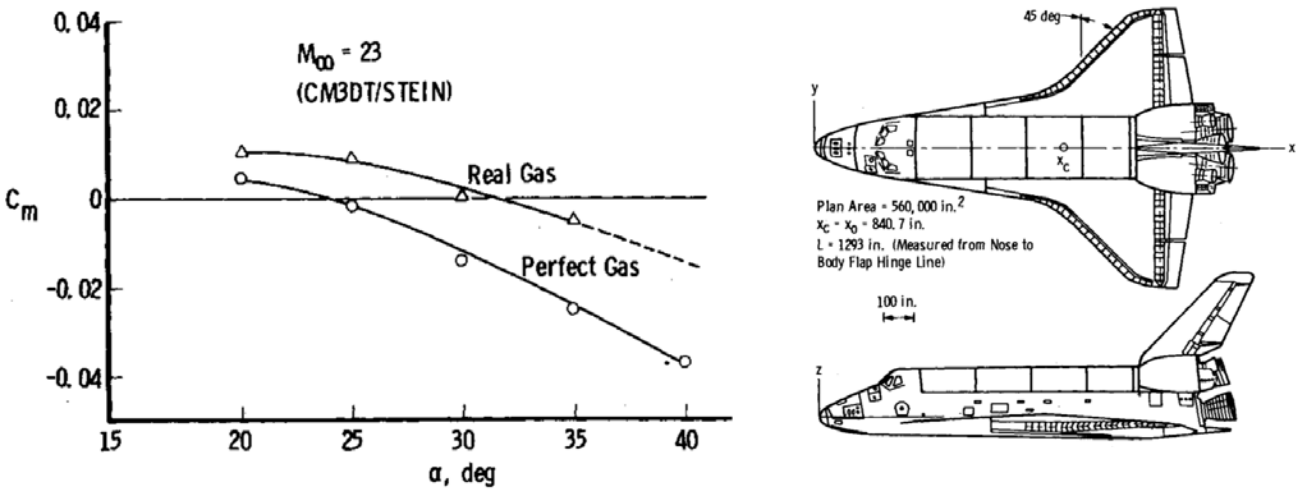


Figure 10-24: Space Shuttle pitching moment estimates for perfect-gas and real-gas models; note that CM3DT and STEIN are the names of the inviscid CFD codes used for simulations. From J. R. Maus, B. J. Grifith, K. Y. Szema, and J. T. Best, "Hypersonic Mach Number and Real Gas Effects on Space Shuttle Orbiter Aerodynamics." Reprinted by permission of the American Institute of Aeronautics and Astronautics, Inc.

One of the controls on the space shuttle is the body flap used to trim the shuttle. It is barely visible in figure 10-24 in the side view of the shuttle, located below the rocket nozzle. Figure 10-25 shows the flap in more detail. It has a limited deflection range. At a Hypersonics Short Course given at the State University of New York at Buffalo in August 1986, a speaker said that the predicted body-flap deflection required to trim was 11°. It turned out they needed a 16° deflection to trim in flight, which was nearly all that was available! The pressure distributions didn't look very different between the two simulations, but the integrated effect was extremely important.

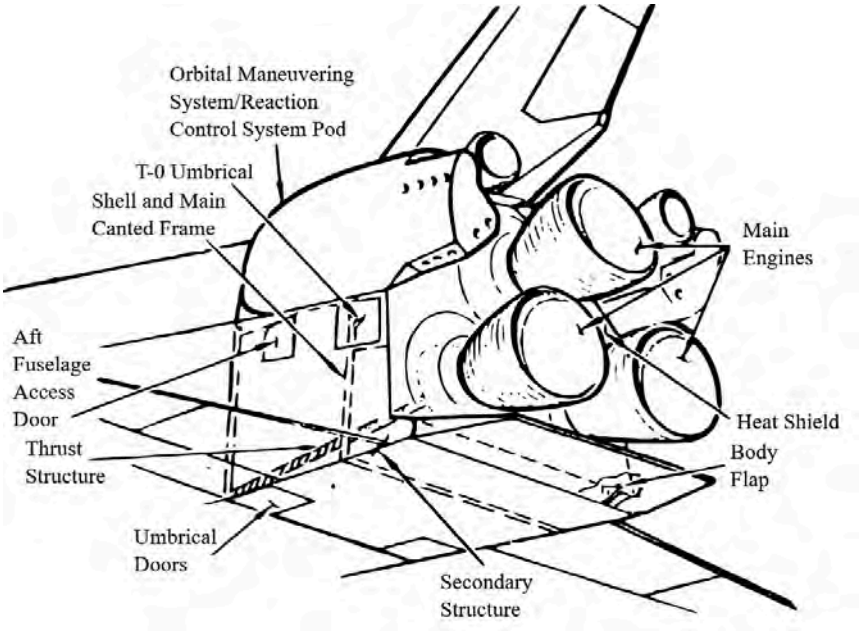


Figure 10-25: Sketch of the Space Shuttle aft fuselage structure illustrating the body flap. From NASA. Wikimedia. Public domain.

Figure 10-26 is a photo of the body flap on the Space Shuttle Discovery, as displayed at the Smithsonian National Air and Space Museum at the Udvar-Hazy Center. Discovery made thirty-nine flights, with the last one on February 24, 2011. It is worth visiting the museum to see Discovery. If you do, you'll notice that the surface is not at all smooth. This is in contrast to the previous shuttle on display, Enterprise. That shuttle never flew into space and therefore never reentered the atmosphere. Its surface is very smooth. (*Note*: Enterprise is currently on display on the Intrepid Sea, Air and Space Museum in the New York City Harbor.)



Figure 10-26: Space Shuttle Discovery body flap. Mason took this photo of the Discovery at the National Air and Space Museum Udvar-Hazy Center. From W. H. Mason.

Although this explanation of the pitching moment discrepancy seems completely plausible, there have been other explanations. More details of the problem are contained on pages 141 to 147 of the book by Bertin.[39] This variety of opinions illustrates the importance of studying problems independently and developing judgment as a configuration aerodynamicist.

10.6 Hypersonic Vehicle Design

Hypersonic flight vehicles encompass a wide variety of applications. Rockets and missiles have become routine. Above, we described the evolution of the shape required to survive the aerodynamic heating environment for entry where the use of blunt shapes enabled success. Although hypersonic transports have been the dream of aerodynamicists for many years, we are still a long way from achieving them. Good histories of hypersonic efforts have been written by Hallion[40] and Heppenheimer;[41] the latter is available as a free PDF file that can be downloaded. As histories, they focus on vehicle efforts as well as the associated technology development.

10.6.1 Minimum Drag Axisymmetric Shapes at Hypersonic Speeds

Before discussing flight vehicles, it is worth reviewing the shapes of minimum drag bodies of revolution at hypersonic speeds. Using the Newtonian pressure formula, equation (10-2), the minimum forebody drag can be found for a variety of constraints using the calculus of variations. Eggers et al. presented this analysis together with wind tunnel test verification results.[42] They considered five cases: given (i) forebody length and base diameter, (ii) length and volume, (iii) length and wetted surface area, (iv) diameter and wetted surface area, and (v) diameter and volume. Surprisingly, they found that when the body length is fixed, the body has a blunt nose. If the length is not fixed, the body has a sharp nose. They also found that, when the diameter and wetted surface area are specified, the minimum drag forebody shape is a cone. When the length and diameter are given, the minimum drag forebody shape has "as much as" 20% less forebody drag than a cone of the same fineness ratio. Although the theoretical results lead to a blunt nose, the radius at the nose is actually very small. Furthermore, the forebody shape is very closely approximated by the power law shape:

$$\frac{r}{r_{\text{base}}} = \left(\frac{x}{l}\right)^n \qquad (10\text{-}19)$$

where the value of n is 0.75 for the minimum drag body of given length and diameter. Many other variations of minimum drag bodies have been found and collected in a book edited by Angelo Miele.[43]

Because of the interest in minimum drag shapes, work has been done using CFD to verify the results found from Newtonian theory. Mason and Lee[44] studied a power law body with various values of n. The CFD results found the minimum drag exponent have an n of very nearly 0.69, and the drag was indeed about 20% less than a cone with the same length and diameter. The results of the computational study are shown in figure 10-27.

Power law bodies with an n greater than 0.50 have a peculiar property. The slope at the nose is 90°, but there is no longer a leading-edge radius. So the shape could be described as "blunt," but only weakly![45]

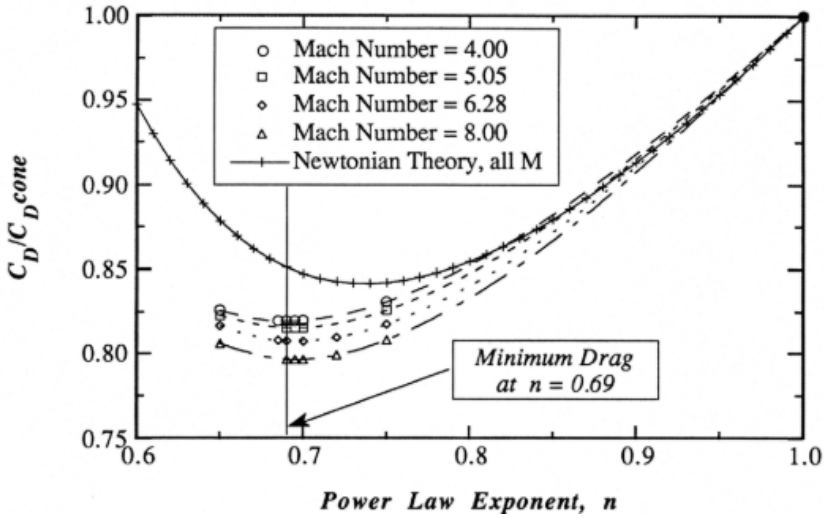


Figure 10-27: Numerical determination of the optimum n for power law shapes. From W. H. Mason and J. Lee. "Minimum-Drag Axisymmetric Bodies in the Supersonic/Hypersonic Flow Regimes." Reprinted by permission of the American Institute of Aeronautics and Astronautics, Inc.

10.6.2 Brief Review of Hypersonic Flight Vehicles

NASP. A description of "recent" efforts should probably start with NASP. This was the acronym for the National Aero-Space Plane concept, although considerable work had been done previously.[46,47,48] Based on hopes and dreams, this program was announced publicly by President Ronald Reagan in his 1986 State of the Union address. It was to be a single-stage-to-orbit (SSTO) vehicle and a passenger plane capable of a two-hour flight from Washington to Tokyo. Anyone who has taken a propulsion course and studied the staging equations understands the difficulty of developing a successful SSTO. Nevertheless, a large government program was started. An artist's conception of the plane is given in figure 10-28. Recall that rockets have to carry both the oxidizer and the fuel.

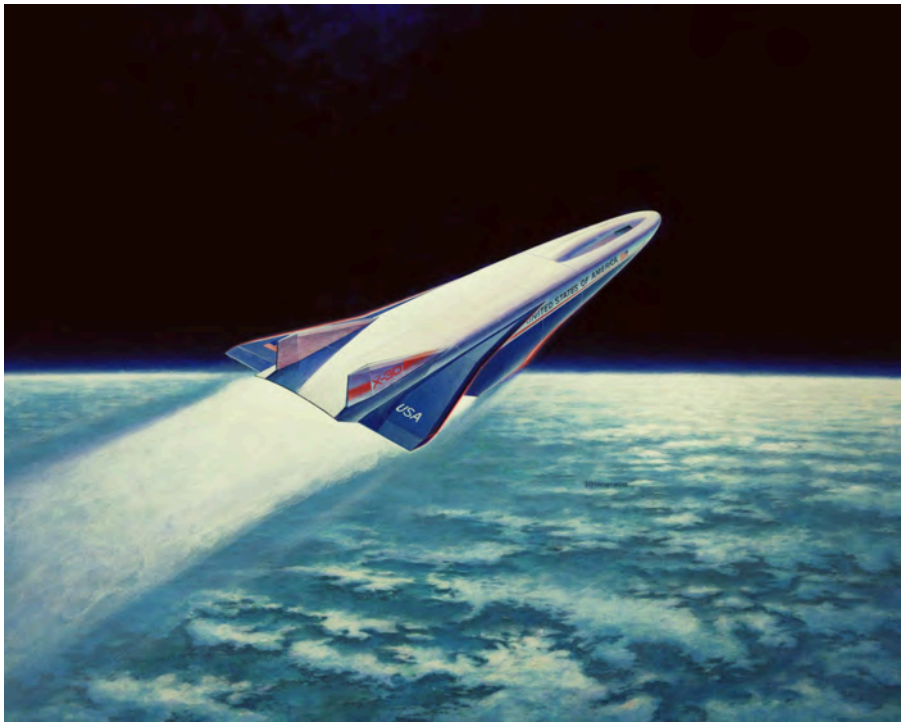


Figure 10-28: Artist's concept of the National Aero-Space Plane (NASP) concept. From James Schultz. NASA. Public domain.

The first step was to create the X-30 demonstrator. It was hoped that the X-30 would be viable because it would employ a propulsion system that used atmospheric air for most of the oxidizer. This would result in a large weight savings. The propulsion system envisioned is known as a scramjet (remember the X-15 fiasco with the dummy scramjet engine described previously). This is a ramjet where the incoming flow is only slowed to supersonic speed in the combustor. Details of scramjet propulsion systems can be found in a book by Segal.[49] When the NASP program was initiated, no scramjet had been demonstrated! The development of such a system is ongoing, clearly very slowly. The NASP program was cancelled in 1993.

10.6.3 Engine-Airframe Integration and Modern Vehicle Development

X-43. Efforts since the NASP have been much more modest. Clearly the first step had to be a successful demonstration of a scramjet propulsion system. This requires flight demonstration because no ground-based facilities have the capability to simulate the flight environment. This requirement led to a concept known as Hyper-X, which became the X-43. A description of the evolution of this concept is described in a highly readable book by Curtis Peebles.[50] As we saw above in figure 10-5, all of the important forces are on the lower surface of a hypersonic vehicle. Therefore, it had become clear that the airframe and engine would rely on controlling the lower surface flow field. In effect, the forebody became the inlet and the aft body became the nozzle. Figure 10-29 illustrates the concept.

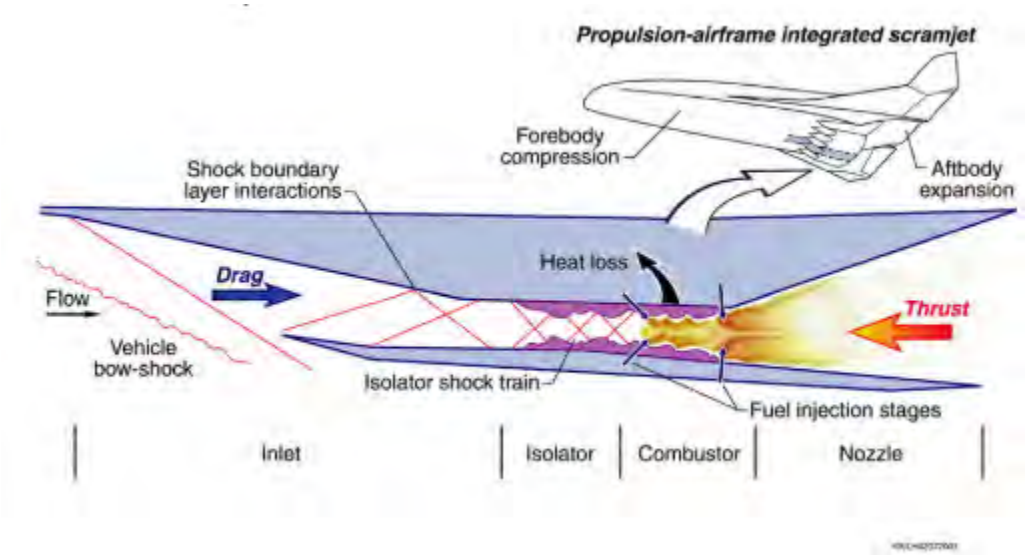


Figure 10-29: Example of engine-airframe integration for a hypersonic aircraft. *From J. C. Ross, M. N. Rhode, B. Falman, K. T. Edquist, M. Schoenenberger, G. J. Brauckmann, B. L. Kleb, T. K. West, S. J. Alter, and D. W. Witte. "Evaluation of CFD as a Surrogate for Mach 2.4 to 4.6 Wind-Tunnel Testing – Project Overview." NASA. Courtesy of Walt Engelund. Public domain.*

The X-43 was mounted on the Orbital Sciences rocket-powered Pegasus vehicle that was dropped from a B-52. It boosted the X-43 to the speed where it could be separated from the Pegasus and undergo scramjet-powered propulsive flight. The first attempt resulted in a Pegasus failure on June 2, 2001. Subsequently there were two successful flights of the X-43. The second flight occurred on March 27, 2004, achieving a Mach number of 6.83 after 10 seconds of powered flight (the q was 980psf at 110,000 feet of altitude). The third flight, on November 16, 2004, reached a Mach number of 9.68 with 11 seconds of powered flight (also at 110,000 feet of altitude). In each case, the vehicle came down in the Pacific Ocean and was never recovered. All the results were obtained from onboard telemetry. Figure 10-30 provides an idea of what the X-43 actually looked like.

The November-December 2001 issue of the *Journal of Spacecraft and Rockets* had a special section devoted to the Hyper-X, and the 2006 AIAA Dryden Lecture was given on the X-43 by McClinton.[51] The McClinton paper shows that a surface temperature as high as 2,000°F was measured.



Figure 10-30: Artist conception of the X-43 in flight. *From Steve Lighthill. NASA. Public domain.*

X-51. The next step in the evolution of hypersonic air-breathing vehicles is the X-51. This is known as a Waverider concept. Waveriders provide efficient hypersonic flight. The designs can be thought of as a shape placed in the streamline of a body-generated flow field so that the bottom surface is "resting" on the pressure field generated by the shock wave of this flow field. The arrangement is designed to obtain lift with very low drag. See Bertin and Cummings[52] for a good, detailed description of waveriders. At one time, waveriders had a precise definition, but the term now appears to refer to any concept that exploits lower surface lift. The application of the X-51 type vehicle is likely a missile. The X-51 concept is shown in figure 10-31. It is 25 feet long and weighs 4,000 pounds.

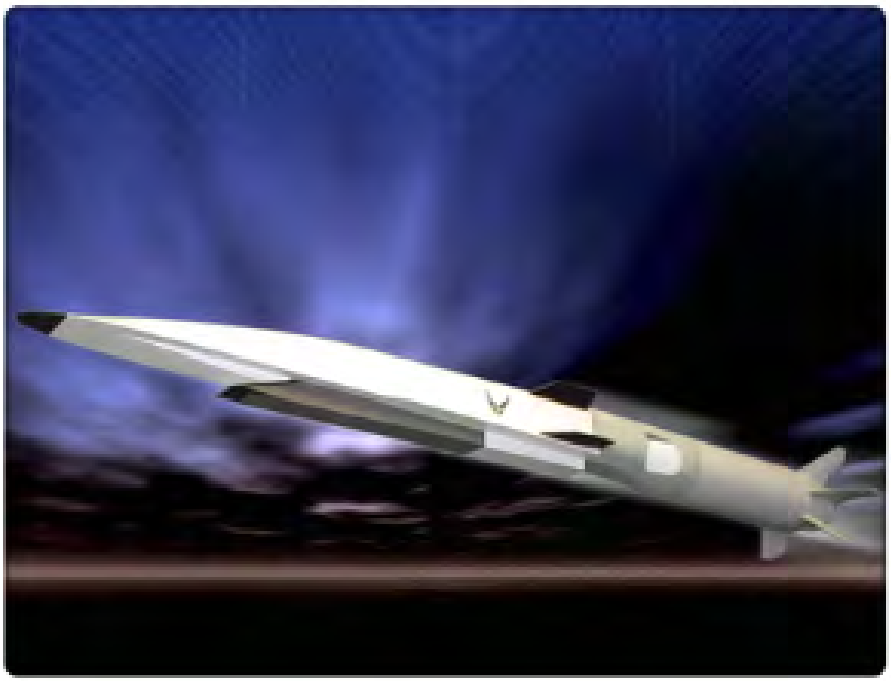


Figure 10-31: Artist rendition. The X-51 Waverider. From US Airforce. Courtesy of Karen Berger of NASA Langley. Public domain.

The first flight of the X-51 took place on May 26, 2010, achieving 200 seconds of powered flight and reaching a speed of Mach 5 at 70,000 feet. The second flight had a problem, as the scramjet had an "unstart" when they tried to switch from ethylene to JP-7 as fuel. On the third flight, a control fin locked up and the vehicle went out of control. On the fourth flight, May 1, 2013, they had success with 210 seconds of flight at a Mach number of 5.21.

Clearly, significant progress was made between the X-43 and X-51. This also illustrates the importance of maturing a technology before undertaking a vehicle development program. Any air-breathing hypersonic vehicle will have a highly integrated engine and airframe. To reiterate, in these concepts, the hypersonic propulsion is provided by a scramjet engine, which obtains thrust with a combustion chamber in which the flow is supersonic. This can be seen in figure 10-29, which is based on a presentation to the class by Walt Engelund of NASA Langley. The entire forebody of the vehicle underside is used as an external inlet to provide flow at just the right conditions to the engine. The entire underside afterbody is the exhaust nozzle. The successful design of an air-breathing hypersonic vehicle is an excellent example of the need for multidisciplinary optimization methods. This is a very hard problem, and the structure, aerodynamics, aerothermodynamics, aeroservoelasticity, and propulsion systems are very tightly integrated. Two reviews are available with more details.[53,54]

With further maturation of scramjet technology, we can expect to see hypersonic vehicle designs proposed using this technology. However, the vehicle must still be boosted to a high enough Mach number for the scramjet propulsion system to start. It will be interesting to see how these concepts are developed in the future.

Chapter 10 Exercises

10.1 Derive expressions for the lift-curve slope of a flat plate and a wedge using linear supersonic theory and Newtonian theory. Comment on the differences and implications for aircraft design.

10.2 Derive the expression for $C_{p\max}$ used in the modified Newtonian theory formula. Show that with $\gamma = 1.4$, the value for $M = \infty$ is 1.84, and at $M = 4$, $C_{p\max}$ is 1.79.

10.3 Using the estimate given below for the adiabatic wall temperature, what is the surface temperature at Mach 2 for an airplane flying at an altitude of 60,000 feet? What is it if the airplane is flying at M =3?

$$T_{AW} = \left(1 + r\frac{\gamma - 1}{2}M_\infty^2\right)T_e$$

where r = 0.85 for laminar flow and 0.88 for turbulent flow.
What is your conclusion? (This should be less than one page of analysis.)

10.4 Consider a wedge with a half-angle of θ. Find $C_{L\alpha}$ assuming both linear supersonic theory and hypersonic Newtonian theory for the pressure coefficients. How does the lift-curve slope vary with θ and Mach number for the two different flow models? What are the configuration implications?

10.5 Read Ben Rich's Paper: Rich, B. R., "F-12 Series Aircraft Aerodynamic and Thermodynamic Design in Retrospect," Journal of Aircraft, Vol.11, No. 7, Jul. 1974, pp. 401–406. Turn in the usual one-page summary of what you learned.

Figure References

Figure 10-1: NASA. X-15 aircraft, ship #1 (56-6670). 1960. Public domain. https://www.nasa.gov/image-article/x-15-1-rocket-powered-aircraft

Figure 10-3: W. H. Mason. Data from Jackson, C. M., Jr., and Sawyer, W. C., "A Method for Determining Surface Pressures on Blunt Bodies of Revolution at Small Angles of Attack in Supersonic Flow," NASA TN D4865, 1968.

Figure 10-4: W. H. Mason. Data from Sims, J. L., "Tables for Supersonic Flow around Right Circular Cones at Zero Angle of Attack," NASA SP-3004, Jan. 1964. https://ntrs.nasa.gov/citations/19640009035

Figure 10-8: Figure 1 from Yancy, R. B., "Flight Measurements of Stability and Control Derivatives of the X-15 Research Airplane to a Mach Number of 6.02 and an Angle of Attack of 25°," NASA TN D2532, 1964. Public domain. https://ntrs.nasa.gov/citations/19650001037

Figure 10-9: Figure 19 from Yancy, R. B., "Flight Measurements of Stability and Control Derivatives of the X-15 Research Airplane to a Mach Number of 6.02 and an Angle of Attack of 25°," NASA TN D2532, 1964. Public domain. https://ntrs.nasa.gov/citations/19650001037

Figure 10-10: Figure 20 from Yancy, R. B., "Flight Measurements of Stability and Control Derivatives of the X-15 Research Airplane to a Mach Number of 6.02 and an Angle of Attack of 25°," NASA TN D2532, 1964. Public domain. https://ntrs.nasa.gov/citations/19650001037

Figure 10-11: Portrait of NASA Ames Engineer H. Julian "Harvey" Allen explaining blunt nose principle. ARC-1957-A-22664. Public domain. https://images.nasa.gov/details/ARC-1957-A-22664

Figure 10-12: US Navy Naval Surface Weapons Center. In Van Dyke, M., An *Album of Fluid Motion*, Parabolic Press, 1982. Public domain. https://ia903109.us.archive.org/20/items/ScientificBooks/An_Album_of_Fluid_Motion_text.pdf

Figure 10-13: NASA. X-15A #2 with Dummy Ramjet Engine Attached. 1967. Public domain. https://www.nasa.gov/image-article/x-15a-2-with-dummy-ramjet-engine-attached

Figure 10-14: Figure 9 from Watts, J. D., "Flight Experience with Shock Impingement and Interference Heating on the X15-2 Research Airplane," NASA TM X-1669, 1968. Public domain.

Figure 10-15: Figure 7 from Watts, J. D., "Flight Experience with Shock Impingement and Interference Heating on the X15-2 Research Airplane," NASA TM X-1669, 1968. Public domain.

Figure 10-16: Hayes, W. D., and Probstein, R. F., *Hypersonic Flow Theory*, Academic Press, 1959. Fair use.

Figure 10-17: Figure 11 from Bertram, M. H., "An Approximate Method for Determining the Displacement Effects and Viscous Drag of Laminar Boundary Layers in Two-Dimensional Hypersonic Flow," NACA 2773, 1952. Public domain. https://ntrs.nasa.gov/citations/19930083558

Figure 10-20: Figure 5.16 in National Academies of Sciences, Engineering, and Medicine, *Plasma Science: Enabling Technology Sustainability, Security, and Exploration*, National Academies Press, 2021, p. 253. Attributed to NASA/Jet Propulsion Laboratory. Public domain. https://nap.nationalacademies.org/read/25802/chapter/7#253

Figure 10-21: W. H. Mason. Data from Wittliff, C. E., and Curtis, J. T., "Normal Shock Wave Parameters in Equilibrium Air," AD-270-202, 1961. Armed Services Technical Information Agency. US Department of Defense. Public domain. https://apps.dtic.mil/sti/tr/pdf/AD0270202.pdf

Figure 10-22: W. H. Mason. Data from Wittliff, C. E., and Curtis, J. T., "Normal Shock Wave Parameters in Equilibrium Air," AD-270-202, 1961. Armed Services Technical Information Agency. US Department of Defense. Public domain. https://apps.dtic.mil/sti/tr/pdf/AD0270202.pdf

Figure 10-23: W. H. Mason. Data from Wittliff, C. E., and Curtis, J. T., "Normal Shock Wave Parameters in Equilibrium Air," AD-270-202, 1961. Armed Services Technical Information Agency. US Department of Defense. Public domain. https://apps.dtic.mil/sti/tr/pdf/AD0270202.pdf

Figure 10-24: Maus, J. R., Grifith, B. J., Szema, K. Y., and Best, J. T., "Hypersonic Mach Number and Real Gas Effects on Space Shuttle Orbiter Aerodynamics," Journal of Spacecraft and Rockets, Vol. 21, No. 2, Mar.-Apr. 1984, pp. 136–141. https://doi.org/10.2514/3.8624

Figure 10-25: NASA. OMS-RCS Pod. Public domain. https://commons.wikimedia.org/wiki/File:OMS-RCS_Pod.svg

Figure 10-26: W. H. Mason. Space shuttle Discovery body flap. Udvar-Hazy Center. National Air and Space Museum. Mason personal collection.

Figure 10-27: Figure 7(a) in Mason, W. H., and Lee, J., "Minimum-Drag Axisymmetric Bodies in the Supersonic/Hypersonic Flow Regimes," Journal of Spacecraft and Rockets, Vol. 31, No. 3, May-June 1994, pp. 406–412. https://doi.org/10.2514/3.26453

Figure 10-28: J. Schultz. Artist conception of X-30 aerospace plane. *Winds of Change: Expanding the Frontiers of Flight*, p. 117. Public domain. https://commons.wikimedia.org/wiki/File:X-30_NASP_3.jpg and https://ntrs.nasa.gov/citations/19930001912

Figure 10-29: Ross, J. C., Rhode, M. N., Falman, B., Edquist, K. T., Schoenenberger, M., Brauckmann, G. J. Kleb, B. L, West, T. K., Alter, S. J., and Witte, D. W., "Evaluation of CFD as a Surrogate for Mach 2.4 to 4.6 Wind-Tunnel Testing—Project Overview," 2007, p. 7. NASA Ames Research Center. Public domain. https://ntrs.nasa.gov/citations/20210017797

Figure 10-30: S. Lighthill. Artist conception of the X-43A Hypersonic Experimental Vehicle or "Hyper-X" in flight. NASA. 1998. Public domain. https://www.nasa.gov/image-article/artists-conception-x-43a-dual-mode-ramjet-scramjet-propulsion-system

Figure 10-31: US Air Force. The X-51 Waverider. Public domain. https://commons.wikimedia.org/wiki/File:X51waverider.jpg

Notes

1. Bertin, J. J., and Cummings, R. M., *Aerodynamics for Engineers*, Pearson Prentice Hall, Upper Saddle Brook, 2009.
2. Anderson, J., *Hypersonic and High Temperature Gas Dynamics*, McGraw-Hill, New York, 1989. (*Note*: Now published by the AIAA.)
3. Thompson, M. O., *At the Edge of Space: The X-15 Flight Program*, Smithsonian Institution Press, Washington, 1992.
4. Bertin, J. J., and Cummings, R. M., *Aerodynamics for Engineers*, Pearson Prentice Hall, Upper Saddle Brook, 2009.
5. Anderson, J., *Hypersonic and High Temperature Gas Dynamics*, McGraw-Hill, New York, 1989.
6. Anderson, J., *Hypersonic and High Temperature Gas Dynamics*, McGraw-Hill, New York, 1989.
7. Jackson, C. M., Jr., and Sawyer, W. C., "A Method for Determining Surface Pressures on Blunt Bodies of Revolution at Small Angles of Attack in Supersonic Flow," NASA TN D-4865, 1968.
8. DeJarnette, F. R., Ford, C. P., and Young, D. E., "A New Method for Calculating Surface Pressures on Bodies at an Angle of Attack in Supersonic Flow," AIAA 1979-1552, 12th Fluid & Plasma Dynamics Conference, Williamsburg, VA, Jul. 23-25, 1979.
9. Sims, J. L., "Tables for Supersonic Flow Around Right Circular Cones at Zero Angle of Attack," NASA SP-3004, 1964.
10. DeJarnette, F. R., Ford, C. P., and Young, D. E., "A New Method for Calculating Surface Pressures on Bodies at an Angle of Attack in Supersonic Flow," AIAA 1979-1552, 12th Fluid & Plasma Dynamics Conference, Williamsburg, VA, Jul. 23-25, 1979.
11. Carmichael, R., Public Domain Aeronautical Software. http://www.pdas.com
12. McLellan, C., "A Method for Increasing the Effectiveness of Stabilizing Surfaces at High Supersonic Mach Numbers," NACA RM-L54F21, Aug. 1954. (*Note*: Declassified in 1958.)
13. Yancy, R. B., "Flight Measurements of Stability and Control Derivatives of the X-15 Research Airplane to a Mach Number of 6.02 and an Angle of Attack of 25°." NASA TN D-2532, 1964.
14. Hoey, B., "X-15 Ventral Off," in *Flight Testing at Edwards, Flight Test Engineers' Stories 1946–1975*, edited by F. Stoliker, B. Hoey, and J. Armstrong, Flight Test Historical Foundation, 1996.
15. Yancy, R. B., "Flight Measurements of Stability and Control Derivatives of the X-15 Research Airplane to a Mach Number of 6.02 and an Angle of Attack of 25°." NASA TN D-2532, 1964.
16. Bertin, J. J., and Cummings, R. M., "Fifty years of hypersonics: Where we've been, where we're going," Progress in Aerospace Sciences, Vol. 39, 2003, pp. 511–536.
17. Rich, B. R., "F-12 Series Aircraft Aerodynamic and Thermodynamic Design in Retrospect," Journal of Aircraft, Vol. 11, No. 7, Jul. 1974, pp. 401–406.
18. Allen, H. J., and Eggers, A. J., Jr., "A Study of the Motion and Aerodynamic Heating of Ballistic Missiles Entering the Earth's Atmosphere at High Supersonic Speeds," NACA R-1381, 1958. (*Note*: 1958 is when the work was declassified.)
19. Pavlosky, J. E., and St. Leger, L. G., "Apollo Experience Report – Thermal Protection Subsystem," NASA TN D-7564, 1974.

20. Moretti, G., and Abbett, M., "A Time Dependent Computational Method for Blunt Body Flows," AIAA Journal, Vol. 4, No. 12, 1966, pp. 2136–2141.
21. Iliff, K. W., and Shafer, M. F., "A Comparison of Hypersonic Flight and Prediction Results," AIAA Paper 93-0311, 31st Aerospace Sciences Meeting and Exhibit, Reno, NV, January 11-14, 1993.
22. Watts, J. D., "Flight Experience with Shock Impingement and Interference Heating on the X-15-2 Research Airplane," NASA TM X-1669, 1968.
23. Hayes, W. D., and Probstein, R. F., *Hypersonic Flow Theory*, Academic Press, New York, 1959.
24. Bertram, M. H., "An Approximate Method for Determining the Displacement Effects and Viscous Drag of Laminar Boundary Layers in Two Dimensional Hypersonic Flow," NACA 2773, 1952.
25. Hayes, W. D., and Probstein, R. F., *Hypersonic Flow Theory*, Academic Press, New York, 1959.
26. White, F. M., *Viscous Fluid Flow*, McGraw-Hill, New York, 1974, pp. 589–590.
27. Hopkins, E. J., "Charts for Predicting Turbulent Skin Friction from the Van Driest Method (II)," NASA TN D-6945, Oct. 1972.
28. Cummings, R. M., "Numerical Simulation of Hypersonic Flows," Journal of Spacecraft and Rockets, Vol. 52, No. 1, Jan.-Feb. 2015, pp. 15–16.
29. Johnston, C., NASA Langley Research Center, personal communication.
30. Bertin, J. J., *Hypersonic Aerothermodynamics*, AIAA, Washington, 1994.
31. Hirschel, E. H., and Weiland, C., *Selected Aerothermodynamic Design Problems of Hypersonic Flight Vehicles*, Springer, Berlin, 2009.
32. Hollis, B. R., and Borrelli, S., "Aerothermodynamics of Blunt Body Entry Vehicles," Progress in Aerospace Sciences, Vol. 48-49, Jan.-Feb. 2012, pp. 42–56.
33. Anderson, J., *Hypersonic and High Temperature Gas Dynamics*, McGraw-Hill, New York, 1989.
34. Wittliff, C. E., and Curtis, J. T., "Normal Shock Wave Parameters in Equilibrium Air," CAL Report CAL-111, Nov. 1961.
35. Devenport, W., Kapania, R., Rojiani, K., and Singh, K., *engAPPLETS*. http://www.engapplets.vt.edu
36. Srinivasan, S., Tannehill, J. C., and Weilmuenster, K. J., "Simplified Curve Fits for the Thermodynamic Properties of Equilibrium Air," NASA RP-1181, Aug. 1987.
37. Anderson, J. *Hypersonic and High Temperature Gas Dynamics*, McGraw-Hill, New York, 1989.
38. Maus, J. R., Grifith, B. J., Szema, K. Y., and Best, J. T., "Hypersonic Mach Number and Real Gas Effects on Space Shuttle Orbiter Aerodynamics," Journal of Spacecraft and Rockets, Vol. 21, No. 2, Mar.-Apr. 1984, pp. 136–141.
39. Bertin, J. J., *Hypersonic Aerothermodynamics*, AIAA, Washington, 1994.
40. Hallion, R. P., "The History of Hypersonic: Or, Back to the Future—Again and Again", AIAA Paper 2005-0329, 43rd Aerospace Sciences Meeting and Exhibit, Reno, NV, Jan. 10-13, 2005.
41. Heppenheimer, T. A., "Facing the Heat Barrier: A History of Hypersonics," NASA SP-2007-4232, 2007.
42. Eggers, A. J., Jr., Resnikoff, M. M., and Dennis, D. H., "Bodies of Revolution Having Minimum Drag at High Supersonic Airspeeds," NACA R-1306, 1958.
43. Miele, A. (ed.), *Theory of Optimum Aerodynamic Shapes*, Academic Press, New York, 1965.
44. Mason, W. H., and Lee, J., "Minimum-Drag Axisymmetric Bodies in the Supersonic/Hypersonic Floe Regime," Journal of Spacecraft and Rockets, Vol. 31, No. 3, May-Jun. 1994, pp. 406–412.
45. Mason, W. H., and Lee, J., "Aerodynamically Blunt and Sharp Bodies," Journal of Spacecraft and Rockets, Vol. 31, No. 3, May-Jun. 1994, pp. 378–382.
46. Gregory, T. J., Petersen, R. H., and Wyss, J. A., "Performance Tradeoffs and Research Problems for Hypersonic Transports," Journal of Aircraft, Vol. 2, No. 4, Jul.-Aug. 1965, pp. 266–271.
47. Petersen, R. H., Gregory, T. J., and Smith, C. L., "Some Comparisons of Turboramjet-Powered Hypersonic Aircraft for Cruise and Boost Missions," Journal of Aircraft, Vol. 3, No. 5, Sept.-Oct. 1966, pp. 398–405.
48. Fetterman, D. A., McLellan, C. H., Jackson, L. R., Henry, B. Z., Jr., and Henry, J. R., "A Review of Hypersonic Cruise Vehicles," NASA TM X-1276, 1966.
49. Segal, C., *The Scramjet Engine – Processes and Characteristics*, Cambridge University Press, New York, 2009.
50. Peebles, C., *Road to Mach 10 – Lessons Learned from the X-43A Flight Research Program*, AIAA, Reston, 2008. (Note: The book includes a DVD with videos and a collection of AIAA and NASA Reports.)
51. McClinton, C. R., "X-43 – Scramjet Power Breaks the Hypersonic Barrier, Dryden Lectureship in Research for 2006," AIAA Paper 2006-1, 44th Aerospace Sciences Meeting and Exhibit, Reno, NV, Jan. 9-12, 2006.
52. Bertin, J. J., and Cummings, R. M. *Aerodynamics for Engineers*, Pearson Prentice Hall, Upper Saddle Brook, 2009.
53. Lockwood, M. K., Petley, D., Martin, J. G., and Hunt, J. L., "Airbreathing hypersonic vehicle design and analysis methods and interactions," Progress in Aerospace Sciences, Vol. 35, pp. 1–32, 1999.
54. Bowcutt, K. G., "Multidisciplinary Optimization of Airbreathing Hypersonic Vehicles," Journal of Propulsion and Power, Vol. 17, No. 6, Nov.-Dec. 2001, pp. 1184–1190.

11. End Note

Most textbooks come to an abrupt ending. This seems strange considering most papers and reports end with a conclusions section. Here we need to finish with a few brief comments. This text covers just the tip of the iceberg of configuration aerodynamics. I've included lots of citations to references that can lead your further studies in the field. And of course the papers keep coming, so stay up to date by following the literature.

Be curious.

> As new concepts and theories are proposed, think about why they might be good ideas. What physics are exploited? How can you connect new requirements and technological advances? Consider examples such as UAVs and various proposed autonomous vehicles. When do they make sense? When don't they make sense?

Be skeptical.

> Similarly, all the results presented in papers and textbooks aren't necessarily correct. Be skeptical, and be prepared to do some calculations for yourself to look further into the assertions. You will be rewarded with a deeper understanding of the work.

Most of all, be creative.

> Use your understanding of aerodynamics to invent new configurations. You have the tools. You've seen the physics supporting Whitcomb's *Area Rule, Supercritical Airfoil,* and *Winglets*. You saw why R. T. Jones's *Oblique Wing Concept* should continue to be considered. And you saw the basis for Werner Pfenninger's *High Aspect Ratio Truss-Braced Wing Concept,* Rudy Meyer's *Supercritical Conical Camber,* and Glenn Spacht's *Forward-Swept Wing Concept*. These are just a few of the innovative ideas arising from an understanding of aerodynamics.

Use these notes as a basis to keep exploring. As technology changes, concepts that were ridiculous may become practical! Talk to anyone who has been through the process. There are fewer and fewer of these people around. I always tried to talk to experienced configuration aerodynamicists. I was lucky to be able to chat with many of the famous aerodynamicists. This exposed me to so much information, since a lot of the key issues were never written down in the literature.

Appendix A: Geometry for Aerodynamicists

Aerodynamicists control the flow field by defining the configuration geometry, and they are always interested in geometric shapes that could possibly be useful in design. Though this appendix provides the detailed definition of many of the classic shapes frequently specified in aerodynamics, it is *not* encyclopedic.

We discuss airfoil geometry in section A.1, followed by classic bodies of revolution in section A.2. In section A.3, we present a class of cross-sectional shapes that can be used to develop more realistic models than bodies of revolution. Planform properties of interest in aerodynamic analysis are presented in section A.4. Sources for information on conical camber and 3D wing geometry are highlighted in sections A.5 and A.6, respectively.

A.1 Airfoil Geometry

This section is divided into two subsections. In section A.1.1, we discuss NACA airfoils, which are generally based on simple geometrical definitions of the section shapes described by equations. Most modern airfoils are defined only by a table of coordinates, not equations. A long list of the tabulated airfoils is presented in section A.1.2. A number of references are included to allow the reader to study both the older NACA literature and new airfoil design ideas. As a whole, this literature provides a means of obtaining a rather complete understanding of the ways in which airfoils can be shaped to obtain desired performance characteristics.

A.1.1 The NACA Airfoils

The NACA airfoils were designed between 1929 and 1947 under the direction of Eastman Jacobs at the NACA's Langley Field Laboratory. Most of the airfoils were based on simple geometrical descriptions of the section shape, although the 6 and 6A series were developed using theoretical analysis and don't have simple shape definitions. Although a new generation of airfoils has emerged as a result of improved understanding of airfoil performance and the ability to design new airfoils using computational methods, the NACA airfoils are still useful in many aerodynamic design applications.

The NACA airfoils are constructed by combining a thickness envelope with a camber or mean line. The equations that describe these shapes are

$$\begin{aligned} x_u &= x - y_t(x)\sin\theta \\ y_u &= y_c(x) + y_t(x)\cos\theta \end{aligned} \qquad \text{(A-1)}$$

and

$$\begin{aligned} x_l &= x + y_t(x)\sin\theta \\ y_l &= y_c(x) - y_t(x)\cos\theta \end{aligned} \qquad \text{(A-2)}$$

where $y_t(x)$ is the thickness function, $y_c(x)$ is the camber line function, and

$$\theta = \tan^{-1}\left(\frac{dy_c}{dx}\right) \qquad \text{(A-3)}$$

is the camber line slope. It is not unusual to neglect the camber line slope terms in equations (A-1) and (A-3). This simplifies the equations and makes the reverse problem of extracting the thickness envelope and mean line for a given airfoil quite straightforward.

The primary reference for all the NACA subsonic airfoil studies is 1959's *Theory of Wing Sections* by Abbott and von Doenhoff (Dover Publications, Inc.). A brief history of the evolution of the NACA Airfoils is presented in the table below. We also provide references to the development of the NASA advanced airfoils from 1966 to approximately 1977. The original NACA Reports cited below are now available online as PDF files through NASA and are well worth reading.

Evolution of the NACA airfoils	Primary NACA report	Authors	Date
The 4-digit foils: According to Abbott, Pinkerton found that the thickness distribution of the Clark Y and Gottingen 398 airfoils were similar, and Jacobs selected a function to describe this thickness distribution. The mean lines were selected to be described by two parabolic arcs which were tangent at the position of maximum camber.	R-460	Jacobs, Ward, and Pinkerton	1993
The 4-digit modified foils: The camber lines were identical to the 4-digit series, and a more general thickness distribution was defined which allowed variations in the leading edge radius and position of maximum thickness to be investigated.	R-492	Stack and von Doenhoff	1934
The 5-digit foils: The thickness distribution was kept identical to the 4-digit series, and a new camber line was defined which allowed for camber to be concentrated near the leading edge. A reflexed camber line was designed to produce zero pitching moment, but it has generally not been used. These foils were derived to get good high lift with minimum C_{m0}.	R-537 R-610	Jacobs, Pinkerton, and Greenberg	1935 1937
The 6-series foils: The foils were designed to maintain laminar flow over a large portion of the chord by delaying the adverse pressure gradient. The thickness envelope was obtained using exact airfoil theory, and no simple formulas are available to describe the shapes. The camber lines were designed using thin airfoil theory, and simple formulas are available to describe their shape.	R-824*	Abbott, von Doenhoff, and Stivers	1945
The 6A-series foils: To improve the trailing edge structurally, the 6-series foils were redesigned to provide sections with simple (nearly straight) surface geometry near the trailing edge while maintaining the same general properties as the original foils. The camber line can be described by a simple alteration of the standard 6-series mean line.	R-903*	Loftin	1948

*Table A-1: Evolution of the NACA airfoils. (*Additional section data for NACA 6- and 6A-series airfoils is in NASA Technical Report R-84 authored by Patterson and Braslow and published in 1958.)*

These airfoils, regardless of the combination of camber lines and thickness envelopes, can be constructed using program FOILGEN, described in appendix E.

Historical accounts of the NACA airfoil program are contained in the following sources:

Abbott, I. H., "Airfoils," in "Evolution of Aircraft Wing Design," AIAA Dayton Section Symposium, Mar. 1980, AIAA Paper 80-3033. https://doi.org/10.2514/6.1980-3033

Jones, R. T., "Recollections From an Earlier Period in American Aeronautics," Annual Review of Fluid Mechanics, Vol. 9, pp. 1–11, 1977. https://doi.org/10.1146/annurev.fl.09.010177.000245

NASA has published two reports describing computer programs that produce the NACA airfoil ordinates:

Ladson, C. L., and Brooks, C. W., Jr., "Development of a Computer Program to Obtain Ordinates for the NACA 4-Digit, 4-Digit Modified, 5-Digit, and 16-Series Airfoils," NASA TM X-3284, Nov. 1975. https://ntrs.nasa.gov/citations/19760003945

Ladson, C. L., and Brooks, C. W., Jr., "Development of a Computer Program to Obtain Ordinates for the NACA 6- and 6A-Series Airfoils," NASA TM X-3069, Sept. 1974. https://ntrs.nasa.gov/citations/19740025318 (*Note:* This program is included in the utility programs described in App. E, as LADSON. It is not extremely accurate for sections less than 6% thick or greater than 15% thick.)

An extensive and excellent survey of the older airfoils is contained in:

Riegels, F. W., *Airfoil Sections* (English-language version), Butterworths, London, 1961.

NASA supercritical airfoil development is described in the following references:

Whitcomb, R. T., "Review of NASA Supercritical Airfoils," ICAS Paper 74-10, 9th Congress of the International Council of the Aeronautical Sciences, Haifa, Israel, Aug. 25-30, 1974. https://www.icas.org/icas_archive/ICAS1974/Page%208%20Whitcomb.pdf

Harris, C. D., "NASA Supercritical Airfoils," NASA TP-2969, Mar. 1990. https://ntrs.nasa.gov/citations/19900007394

Becker, J. V., "The High-Speed Airfoil Program," in *The High Speed Frontier*, NASA SP-445, 1980. https://www.nasa.gov/wp-content/uploads/2024/01/sp-445.pdf

A.1.1.1 The NACA 4-Digit Airfoil

The numbering system for these airfoils is defined by NACA as *MPXX*, where

XX is the maximum thickness, t/c, in percent chord,

M is the maximum value of the mean line in hundredths of chord, and

P is the chordwise position of the maximum camber in tenths of the chord.

Note that although the numbering system implies integer values, the equations can provide 4-digit foils for arbitrary values of *M*, *P*, and *XX*.

An example: NACA 2412

It is a 12-percent-thick airfoil with a max value of the camber line of 0.02, at $x/c = 0.4$.

The NACA 4-digit thickness distribution is given by

$$\frac{y_t}{c} = \left(\frac{t}{c}\right)\left[a_0\sqrt{x/c} - a_1(x/c) - a_2(x/c)^2 + a_3(x/c)^3 - a_4(x/c)^4\right] \qquad \text{(A-4)}$$

where

$a_0 = 1.4845$; $a_1 = 0.6300$; $a_2 = 1.7580$; $a_3 = 1.4215$; and $a_4 = 0.5075$.

The maximum thickness occurs at $x/c = 0.30$, and the leading edge radius is

$$\left(\frac{r_{LE}}{c}\right) = 1.1019\left(\frac{t}{c}\right)^2. \qquad \text{(A-5)}$$

The included angle of the trailing edge is

$$\delta_{TE} = 2\tan^{-1}\left\{1.16925\left(\frac{t}{c}\right)\right\}. \qquad \text{(A-6)}$$

It is important to realize that the airfoil has a finite thickness at the trailing edge. The equation (A-4) definition of the thickness distribution results in a small but finite trailing edge thickness. Many computational methods require a zero-thickness trailing edge, and the coefficient definitions are frequently modified to produce a zero-thickness trailing edge. This can lead to the wrong value of drag from calculations. Van Dam[1] cites a value of wave drag at M = 0.78, which is 15.3% too high for the 0012 airfoil modified to zero trailing edge thickness!

The camber line is given by

$$\left.\begin{array}{ll} \frac{y_c}{c} & = \frac{M}{(p)^2}\left[2P(x/c) - (x/c)^2\right] \\ \frac{dy_c}{dx} & = \frac{2M}{(p)^2}(P - (x/c)) \end{array}\right\} \left(\frac{x}{c}\right) \text{ less than } P \qquad \text{(A-7)}$$

and

$$\left.\begin{array}{ll} \frac{y_c}{c} & = \frac{M}{(1-P)^2}\left[1 - 2P + 2P(x/c) - (x/c)^2\right] \\ \frac{dy_c}{dx} & = \frac{2M}{(1-P)^2}(P - (x/c)) \end{array}\right\} \left(\frac{x}{c}\right) \geq P. \qquad \text{(A-8)}$$

The camber line slope is found from equation (A-3) using equations (A-7) and (A-8), and the upper and lower surface ordinates resulting from the combination of thickness and camber are then computed using equations equations (A-1) and (A-2).

A.1.1.2 The NACA 5-Digit Airfoil

This airfoil is an extension of the 4-digit series that provides additional camber lines. The numbering system for these airfoils is defined by NACA as *LPQXX*, where:

XX is the maximum thickness, t/c, in percent chord,

L is the amount of camber; the design lift coefficient is (3/2) *L*, in tenths,

P is the designator for the position of maximum camber, x_f, where $x_f = P/2$, and *P* is given in tenths of the chord, and

Q = 0 standard 5-digit foil camber, and Q = 1 "reflexed" camber.

An example: NACA 23012

For a 12-percent-thick airfoil, the design lift coefficient is 0.3 [(3/2)2 in tenths], the position of max camber is located at *x*/*c* = 0.15, and the "standard" 5-digit foil camber line is used.

The thickness distribution is the same as that of the NACA 4-digit airfoil described above in equation (A-4).

The standard 5-digit series camber line is given by

$$\left.\begin{array}{ll} \frac{y_c}{c} & = \frac{K_1}{6}\left[(x/c)^3 - 3m(x/c)^2 + m^2(3-m)(x/c)\right] \\ \frac{dy_c}{dx} & = \frac{K_1}{6}\left[3(x/c)^2 - 6m(x/c) + m^2(3-m)\right] \end{array}\right\} \quad 0 \leq (x/c) \leq m \qquad \text{(A-9)}$$

and

$$\left.\begin{array}{ll} \frac{y_c}{c} & = \frac{K_1}{6} m^3 [1 - (x/c)] \\ \frac{dy_c}{dx} & = -\frac{K_1}{6} m^3 \end{array}\right\} \quad m < (x/c) \leq 1 \qquad \text{(A-10)}$$

where m is not the position of maximum camber, but is related to the maximum camber position by

$$x_f = m\left(1 - \sqrt{\frac{m}{3}}\right), \qquad \text{(A-11)}$$

and m is found from a simple fixed-point iteration for a given x_f. To avoid the leading edge singularity for a prescribed C_{l_i} and m, K_1 is defined as

$$K_1 = \frac{6 C_{l_i}}{Q} \qquad \text{(A-12)}$$

where

$$Q = \frac{3m - 7m^2 + 8m^3 - 4m^4}{\sqrt{m(1-m)}} - \frac{3}{2}(1 - 2m)\left[\frac{\pi}{2} - \sin^{-1}(1 - 2m)\right]. \qquad \text{(A-13)}$$

Note that K_1 is a linear function of C_{l_i} and the K_1's were originally tabulated for $C_{l_i} = 0.3$. The tabulated K_1's are multiplied by $(C_{l_i}/0.3)$ to get values at other C_{l_i}. To compute the camber line, the values of Q and K_1 must be determined. In some cases, the computed values of K_1 and Q differ slightly from the official tabulated values (remember these were computed in the 1930s). The tabulated values should be used to reproduce the official ordinates. Table A-2 illustrates the differences.

Mean line	x_f	m tabulated	m computed	tabulated	K_1 using tabulated m	K_1 using computed m
210	0.05	0.0580	0.0581	361.4	351.56	350.332
220	0.10	0.1260	0.1257	51.65	51.318	51.578
230	0.15	0.2025	0.2027	15.65	15.955	15.920
240	0.20	0.2900	0.2903	6.643	6.641	6.624
250	0.25	0.3910	0.3913	3.230	3.230	3.223

Table A-2: Difference between computed and tabulated values

Once the camber line parameters are chosen, the airfoil is constructed using the equations given above.

Camber lines designed to produce zero pitching moment

The reflexed mean line equations were derived to produce zero pitching moment about the quarter chord:

$$\frac{y_c}{c} = \frac{K_1}{6}\left[\{(x/c) - m\}^3 - \frac{K_2}{K_1}(1-m)^3(x/c) - m^3(x/c) + m^3\right] \quad 0 \leq (x/c) \leq m \qquad \text{(A-14)}$$

$$= \frac{K_1}{6}\left[\frac{K_2}{K_1}\{(x/c) - m\}^3 - \frac{K_2}{K_1}(1-m)^3(x/c) - m^3(x/c) + m^3\right] \quad 0 < (x/c) \leq 1 \qquad \text{(A-15)}$$

where

$$\frac{K_2}{K_1} = \frac{3(m - x_f)^2 - m^3}{(1 - m)^3}. \qquad \text{(A-16)}$$

The parameters are defined as follows:

1. given x_f, find m to give $C_{mc/4} = 0$ from thin airfoil theory; and
2. given x_f and m, calculate K_1 to give $C_{li} = 0.3$.

The tabulated values for these camber lines are described in table A-3 below.

Mean line	(P/2) x_f	m	K_1	K_1/K_2
211	.05	-	-	-
221	.10	0.1300	51.99	0.000764
231	.15	0.2170	15.793	0.006770
241	.20	0.3180	6.520	0.030300
251	.25	0.4410	3.191	0.135500

Table A-3: Tabulated values for camber lines designed to produce zero pitching moment

A.1.1.3 The NACA Modified 4-Digit Airfoil

This airfoil is an extension of the 4-digit series that allows for a variation of leading edge radius and location of maximum thickness. The numbering system is defined by NACA as *MPXX-IT*, where MPXX is the standard 4-digit designation and the IT appended at the end describes the modification to the thickness distribution. They are defined as:

I = designation of the leading edge radius, and

T = chordwise position of maximum thickness in tenths of chord.

These are implemented as:

$$\frac{r_{le}}{c} = 1.1019\left(\frac{I}{6} \cdot \frac{t}{c}\right)^2 \quad \text{for I} \leq 8 \qquad \text{(A-17)}$$

and

$$\frac{r_{\text{le}}}{c} = 3 \times 1.1019\left(\frac{t}{c}\right)^2 \quad \text{for I} = 9. \qquad \text{(A-18)}$$

$I = 6$ produces the leading edge radius of the standard 4-digit airfoils.

One example of the modified 4-digit airfoil is NACA 0012-74. It is an uncambered 12-percent-thick airfoil, with a maximum thickness at $x/c = 0.40$ and a leading edge radius of 0.0216, which is 36% larger than the standard 4-digit value.

The NACA 16-series is a special case of the modified 4-digit airfoil with a leading edge radius index of $I = 4$ and the maximum thickness located at $x/c = 0.5$ ($T = 5$). As an example, the NACA 16-012 is equivalent to an NACA 0012-45.

The thickness distribution is given by

$$\frac{y_t}{c} = 5\left(\frac{t}{c}\right)\left[a_0\sqrt{\frac{x}{c}} + a_1\left(\frac{x}{c}\right) + a_2\left(\frac{x}{c}\right)^2 + a_3\left(\frac{x}{c}\right)^3\right] \quad 0 \text{ less than } \frac{x}{c} \text{ less than } T \qquad \text{(A-19)}$$

and

$$\frac{y_t}{c} = 5\left(\frac{t}{c}\right)\left[.002 + d_1\left(1 - \frac{x}{c}\right) + d_2\left(1 - \frac{x}{c}\right)^2 + d_3\left(1 - \frac{x}{c}\right)^3\right] \quad T \text{ less than } \frac{x}{c} \leq 1 \qquad \text{(A-20)}$$

The coefficients are determined by solving for the d's first, based on the trailing edge slope and the condition of maximum thickness at $x/c = T$. Once these coefficients are found, the a's are found by relating a_0 to the specified leading edge radius, the maximum thickness at $x/c = T$, and the condition of continuity of curvature at $x/c = T$. These constants are all determined for t/c = 0.2 and then scaled to other t/c values by multiplying by 5(t/c). The value of d_1 controls the trailing edge slope and was originally selected to avoid reversals of curvature. In addition to the tabulated values, Riegels[2] has provided an interpolation formula. The official (tabulated) and Riegels approximate values of d_1 are given in table A-4.

T	Tabulated d_1	Approximate d_1
0.2	0.200	0.200
0.3	0.234	0.234
0.4	0.315	0.314
0.5	0.465	0.464
0.6	0.700	0.722

Table A-4: Riegels approximate values of d_1

In this table, the Riegels approximate d_1 is defined by

$$d_1 \cong \frac{\left(2.24 - 5.42T + 12.3T^2\right)}{10(1 - 0.878T)}. \qquad \text{(A-21)}$$

Once the value of d_1 is known, d_2 and d_3 are found from the relations given by Riegels:

$$d_2 = \frac{0.294 - 2(1 - T)d_1}{(1 - T)^2} \qquad \text{(A-22)}$$

and

$$d_3 = \frac{-0.196 + (1 - T)d_1}{(1 - T)^3}. \qquad \text{(A-23)}$$

With the d's determined, the a's can be found. a_0 is based on the leading edge radius:

$$a_0 = 0.296904 \cdot \chi_{LE} \qquad \text{(A-24)}$$

where

$$\chi_{LE} = \begin{array}{ll} \dfrac{I}{6} & \text{for} \quad I \leq 8 \\ 10.3933 & \text{for} \quad I = 9 \end{array} \quad . \qquad \text{(A-25)}$$

Define the following:

$$\rho_1 = \left(\frac{1}{5}\right) \frac{(1-T)^2}{[0.588 - 2d_1(1-T)]} \quad , \qquad \text{(A-26)}$$

then the rest of the *a*'s can be found from:

$$a_1 = \frac{0.3}{T} - \frac{15}{8} \cdot \frac{a_0}{\sqrt{T}} - \frac{T}{10\rho_1} \qquad \text{(A-27)}$$

$$a_2 = -\frac{0.3}{T^2} + \frac{5}{4} \cdot \frac{a_0}{T^{3/2}} + \frac{1}{5\rho_1} \qquad \text{(A-28)}$$

$$a_3 = \frac{0.1}{T^3} - \frac{0.375 a_0}{T^{5/2}} - \frac{1}{10\rho_1 T} \quad . \qquad \text{(A-29)}$$

The camber lines are identical to the standard 4-digit airfoils described previously. The upper and lower ordinates are then computed using the standard equations.

A.1.1.4 The NACA 6 and 6A-Series Mean Lines

For these airfoils, only the mean lines have analytical definitions. The thickness distributions are the result of numerical methods which produced tabulated coordinates. In addition to the values tabulated in the NACA reports, the closest approximation for the thickness distributions is available in the program LADSON (see appendix E).

The 6-series mean lines were designed using thin airfoil theory to produce a constant loading from the leading edge back to *x*/*c* = *a*, after which the loading decreases linearly to zero at the trailing edge. Theoretically, the loading at the leading edge must be either zero or infinite within the context of thin airfoil theory analysis. The violation of the theory by the assumed finite leading edge loading is reflected by the presence of a weak singularity in the mean line at the leading edge, where the camber line has an infinite slope. Therefore, according to Abbott and von Doenhoff,[3] the 6-series airfoils were constructed by holding the slope of the mean line constant in front of *x*/*c* = 0.005, with the value at that point. For round leading edges, the camber line values are essentially not used at points ahead of the origin of the leading edge radius. The theory is discussed by Abbott and von Doenhoff on pages 73–75, 113, and 120. Tabulated values are contained on pages 394–405. The derivation of this mean line is a good exercise in thin airfoil theory. By simply adding various mean lines together, other load distributions can be constructed.

To quote from Abbott and von Doenhoff:

> The NACA 6-series wing sections are usually designated by a six-digit number together with a statement showing the type of mean line used. For example, in the designation NACA 65,3-218, a = 0.5, the 6 is the series designation. The 5 denotes the chordwise position of minimum pressure in tenths of the chord behind the leading edge for the basic symmetrical section at zero lift. The 3 following the comma (sometimes this is a subscript or in parenthesis) gives the range of lift coefficient in tenths above and below the design lift coefficient in which favorable pressure gradients exist on both surfaces. The 2 following the dash gives the design lift coefficient in tenths. The last two digits indicate the thickness of the wing section in percent chord. The designation a = 0.5 shows the type of mean line used. When the mean line is not given, it is understood that the uniform-load mean line (a = 1.0) has been used.

The 6A series airfoils employed an empirical modification of the $a = 0.8$ camber line to allow the airfoil to be constructed of nearly straight line segments near the trailing edge. This camber line is described by Loftin in NACA R-903.

Basic camber line equations

When $a = 1$ (uniform loading along the entire chord),

$$\frac{y}{c} = -\frac{C_{l_i}}{4\pi}\left[\left(1-\frac{x}{c}\right)\ln\left(1-\frac{x}{c}\right)+\frac{x}{c}\ln\left(\frac{x}{c}\right)\right] \qquad \text{(A-30)}$$

and

$$\frac{dy}{dx} = \frac{C_{l_i}}{4\pi}\left[\ln\left(1-\frac{x}{c}\right)-\ln\left(\frac{x}{c}\right)\right] \qquad \text{(A-31)}$$

where C_{l_i} is the "ideal" or design lift coefficient, which occurs at zero angle of attack.

For $a < 1$,

$$\frac{y}{c} = \frac{C_{l_i}}{2\pi(1+a)}\left\{\begin{array}{c}\frac{1}{1-a}\left[\begin{array}{c}\frac{1}{2}\left(a-\frac{x}{c}\right)^2\ln\left|a-\frac{x}{c}\right|-\frac{1}{2}\left(1-\frac{x}{c}\right)^2\ln\left(1-\frac{x}{c}\right)\\ +\frac{1}{4}\left(1-\frac{x}{c}\right)^2-\frac{1}{4}\left(a-\frac{x}{c}\right)^2\end{array}\right]\\ -\frac{x}{c}\ln\left(\frac{x}{c}\right)+g-h\frac{x}{c}\end{array}\right\} \qquad \text{(A-32)}$$

with

$$g = \frac{-1}{(1-a)}\left[a^2\left(\frac{1}{2}\ln a-\frac{1}{4}\right)+\frac{1}{4}\right], \qquad \text{(A-33)}$$

$$h = (1-a)\left[\frac{1}{2}\ln(1-a)-\frac{1}{4}\right]+g, \qquad \text{(A-34)}$$

and

$$\frac{dy}{dx} = \frac{C_{l_i}}{2\pi(1+a)}\left\{\frac{1}{1-a}\left[\left(1-\frac{x}{c}\right)\ln\left(1-\frac{x}{c}\right)-\left(a-\frac{x}{c}\right)\ln\left(a-\frac{x}{c}\right)\right]-\ln\left(\frac{x}{c}\right)-1-h\right\}. \qquad \text{(A-35)}$$

The associated angle of attack is

$$\alpha_i = \frac{C_{l_i}h}{2\pi(1+a)} \qquad \text{(A-36)}$$

a = .8 (modified), the 6A-series mean line

For $0 < x/c < .87437$, use the basic $a = .8$ camber line, but with a modified value of the ideal lift coefficient, $C_{l_{imod}} = C_{l_i}/1.0209$. For $.87437 < x/c < 1$, use the linear equation:

$$\frac{y_c/c}{C_{l_i}} = 0.0302164 - 0.245209\left(\frac{x}{c}-0.87437\right) \qquad \text{(A-37)}$$

and

$$\frac{dy}{dx} = -0.245209C_{l_i}. \qquad \text{(A-38)}$$

Note that at $x/c = 1$, the foregoing approximate relation gives $y/c = -0.000589$, indicating an α shift of 0.034° for $C_{l_i} = 1$.

A.1.1.5 Other airfoil definition procedures

Interest in defining airfoils by a small number of parameters for use in numerical optimization has led to several recent proposed parametric representations that might be useful. In particular, works by Verhoff et al.[4] and Stookesberry et al.[5] use Chebyshev functions to obtain functions with can represent very general airfoil shapes requiring five to twenty coefficients.

Ventkataraman.[6,7] employed another approach that uses Bezier methods frequently featured in CAD surface representation software. This approach uses fourteen design variables to represent the airfoil. Sadrehaghighi et al.[8] have used a similar approach based on nonuniform rational B-splines (NURBS).

A.1.2 Tabulated Airfoil Definition and the Airfoil Library

Most modern airfoils are not described by equations; instead, they are defined by a table of coordinates. Frequently, these coordinates are the results of a computational aerodynamic design program, and simple algebraic formulas cannot be used to define the shape. This was the case with the NACA 6-series airfoils described above.

The following table provides a list of the tabulated airfoils currently available that you can obtain as a ZIP file by accessing https://archive.aoe.vt.edu/mason/Mason_f/foils.zip. The subsequent tables provide a guide to these airfoils. A standard 2F10 format (the Jameson input format) is used with each set of coordinates. The values are given from leading edge to trailing edge, top followed by bottom.

Airfoils	File name	Comments
NACA 4 digit airfoils		
NACA 0010	N0010.DAT	
NACA 0010-35	N001035.DAT	(Abbott & VonDoenhoff)
NACA 0012	N0012.DAT	
NACA 4412	N44122.DAT	
NACA 6 and 6A airfoils		
NACA 63(2)-215	N632215.DAT	NASA TM 78503
NACA 63(2)-215 mod B	N632215m.DAT	
NACA 64A010	N64A010.DAT	
NACA 64A410*	N64A410.DAT	
NACA 64(3)-418	N643418.DAT	
NACA 65(1)-012	N651012.DAT	
NACA 65(1)-213	N651213.DAT	

Airfoils	File name	Comments
NACA 65(1)A012	N65A012.DAT N658299M.DAT N658299R.DAT	
NACA 65(2)-215	N652215.DAT	
NACA 66(3)-018	N663018.DAT	
NASA General Aviation Series		
LS(1)-0417	GAW1.DAT	Originally known as GA(W)-1
LS(1)-0417 mod	LS10417M.DAT	
LS(1)-0413	GAW2.DAT	Originally known as GA(W)-2
LS(1)-0013	LS10013.DAT	
NASA Medium Speed Series		
MS(1)-0313	MS10313.DAT	
MS(1)-0317	MS10317.DAT	
NASA Laminar Flow Series		
NLF(1)-1215F	NL11215F.DAT	
NLF(1)-0414F	NL10414F.DAT	
NLF(1)-0416	NL10416.DAT	
NLF(1)-0414Fmod	NL0414FD.DAT	Drooped le
NLF(2)-0415	NL20415.DAT	
HSNLF(1)-0213	HSN0213.DAT	
HSNLF(1)-0213mod	HSN0213D.DAT	Drooped le
NASA Supercritical Airfoils*		
SC(2)-0402	SC20402.DAT	
SC(2)-0403	SC20403.DAT	
SC(2)-0503	SC20503.DAT	
SC(2)-0404	SC20404.DAT	
SC(2)-0406	SC20406.DAT	
SC(2)-0606	SC20606.DAT	
SC(2)-0706	SC20706.DAT	
SC(2)-1006	SC21006.DAT	
SC(2)-0010	SC20010.DAT	
SC(2)-0410	SC20410.DAT	
SC(2)-0610	SC20610.DAT	

Airfoils	File name	Comments
SC(2)-0710	SC20710.DAT	Also known as Foil 33
SC(2)-1010	SC21010.DAT	
SC(2)-0012	SC20012.DAT	
SC(2)-0412	SC20412.DAT	
SC(2)-0612	SC20612.DAT	
SC(2)-0712	SC20712.DAT	
SC(2)-0712(B)	SC20712B.DAT	
SC(2)-0414	SC20414.DAT	
SC(2)-0614	SC20614.DAT	
SC(2)-0714	SC20714.DAT	Raymer, Ref. NASA TP 2890
SC(2)-0518	SC20518.DAT	
FOIL31	FOIL31.DAT	
SUPER11	SUPER11.dat	11% thick, from ICAS paper
SUPER14	super14.dat	14% thick, NASA TM X-72712
NYU Airfoils		
82-06-09	K820609.DAT	
79-03-12	K790312.DAT	
72-06-16	K720616.DAT	
71-08-14	K710814.DAT	
70-10-13	K701013.DAT	
65-14-08	K651408.DAT	
65-15-10	K651510.DAT	
75-06-12	KORN.DAT	The "Korn" airfoil
75-07-15	K750715.DAT	
Miscellaneous Transonic Airfoils		
CAST 7	CAST7.DAT	
DSMA 523	DSMA523.DAT	From AIAA paper 75-880
NLR HT 731081	NLRHT73.DAT	From AGARD AR-138
ONERA M6	ONERAM6.DAT	
RAE 2822	RAE2822.DAT	
WILBY A	WILBYA.DAT	
WILBY B	WILBYB.DAT	

Airfoils	File name	Comments
WILBY C	WILBYC.DAT	
WILBY R	WILBYR.DAT	
SUPER10	NASA10SC.DAT MBB-A3.DAT	AGARD AR-138 AGARD AR-138
Eppler Airfoils		
EPPLER 662	EPP662.DAT	Raymer's book, ref NASA CP 2085
EPPLER 746	EPP746.DAT	Raymer's book, ref NASA CP 2085
Wortman Airfoils		
FX-63-137-ESM	FX63137.DAT	
FX-72-MS-150A	FX72M15A.DAT	
FX-72-MS-150B	FX72M15B.DAT	
Miscellaneous Foils		
Clark Y	CLARKY.DAT	
Early Liebeck High Lift	RHLHILFT.DAT	
NLR-1	NLR1.DAT	Rotorcraft foil (NASA CP 2046, V.II)
RAE 100	RAE100.DAT	
RAE 101	RAE101.DAT	
RAE 102	RAE102.DAT	
RAE 103	RAE103.DAT	
RAE 104	RAE104.DAT	
VariEze Airfoils		
VariEze wing bl23	VEZBL32.DAT	
VariEze winglet root	VEZWLTR.DAT	
VariEze winglet tip	VEZWLTT.DAT	
VariEze canard	VEZCAN.DAT	
Human powered aircraft airfoils		
DAE 11	DAE11.DAT	Daedalus airfoils (Mark Drela)
DAE 21	DAE21.DAT	
DAE 31	DAE31.DAT	
DAE 51	DAE51.DAT	(Propeller foil?)
Lissaman 7769	LISS769DAE11.DAT	Gossamer Condor airfoil

Table A-5: Airfoil library files

The coordinates for the NACA 64A410 airfoil, widely used as a test case, are found on page 356 of the book by Abbott and von Doenhoff; be aware that this page contains some typos. In particular, the value of y at $x = 7.5$ is supposed to be 2.805. Also, it is obvious that the x value between 30 and 40 is 35. Finally, the table is mislabeled. The y typo was responsible for the widely circulated story that the coordinates contained in Abbott and von Doenhoff were not accurate enough to be used in modern computational airfoil codes.

It is also noteworthy that coordinates for the NASA Supercritical Airfoils were typed in by students when NASA TP-2969 was issued. The coordinates are exactly the values printed in the TP. It turns out that those values were developed by taking the original set of coordinates and enhancing them to 100 points upper and lower using straight-line interpolation. As such, they are not really usable. Our experience is that we can identify the original values and weed out the straight-line interpolated values. This works.

Many other airfoils are available on the World Wide Web. In particular, the Applied Aerodynamics group at the University of Illinois, under the direction of Prof. Michael Selig, has established a massive online source for airfoil definitions and includes data from wind tunnel tests on the airfoils available at https://m-selig.ae.illinois.edu/ads/coord_database.html. Their focus is directed toward airfoils designed for low speeds and low Reynolds numbers. Finally, Richard Eppler has published an entire book of his airfoils, *Airfoil Design and Data*, published by Springer-Verlag in 1990.

The NASA low- and medium-speed airfoils, including natural laminar flow airfoils, are listed in the table below.

Airfoil designation	Design lift	Design thickness	Design mach	Test?	Ordinates in airfoil library?	Ref.	Comments
GA(W)-1	0.4/1.0	0.17		Yes	Yes	TN D-7428	Low speed
LS(1)-0417mod		0.17			Yes		Low speed
GA(W)-2		0.13		Yes	Yes	TM X-72697	Low speed
mod		0.13		Yes	Yes	TM X-74018	Low speed
?		0.21		Yes		TM 78650	Low speed
LS(1)-0013		0.13		Yes	Yes	TM-4003	Low speed
MS(1)-0313		0.13		Yes	Yes	TP-1498	Medium speed
MS(1)-0317	0.30	0.17	0.68	Yes	Yes	TP-1786	Medium speed
mod		0.17		Yes		TP-1919	Medium speed
NLF(1)-0215F	0.20?	0.15			Yes	Raymer's book	Natural laminar flow
NLF(1)-0414F					Yes		Natural laminar flow
NLF(1)-0416					Yes		Natural laminar flow
NLF(1)-0414F drooped L.E.					Yes		Natural laminar flow
NLF(2)-0415	0.40?	0.15?	?	Yes	Yes	Raymer's book	Natural laminar flow
HSNLF(1)-0213	0.20?	0.13?	?		Yes	TM-87602	Natural laminar flow
HSNLF(1)-0213 mod					Yes		

Table A-6: NASA low speed, medium speed, and natural laminar flow airfoil

The NASA Phase 2 supercritical airfoils are listed in the following table.

Airfoil designation	Design lift	Design thickness	Design mach	Test?	Ordinates in airfoil library?	Ref.	Comments
SC(2)-0402	0.40	0.02			Yes		
SC(2)-0403	0.40	0.03			Yes		
SC(2)-0503	0.50	0.03			Yes		
SC(2)-0404	0.40	0.04			Yes		
SC(2)-0406	0.40	0.06			Yes	Unpublished	
SC(2)-0606	0.60	0.06			Yes		
SC(2)-0706	0.70	0.06	0.795	Yes	Yes	Unpublished	
SC(2)-1006	1.00	0.06		Yes	Yes	Unpublished	
SC(2)-0010	0.00	0.10			Yes		
SC(2)-0410	0.40	0.10	0.785		Yes		
SC(2)-0610	0.60	0.10	0.765		Yes		
SC(2)-0710	0.70	0.10	0.755	Yes	Yes	TM X-72711	Airfoil 33
SC(2)-1010	1.00	0.10	0.700		Yes		
SC(2)-0012	0.00	0.12		?	Yes	TM-89102	
SC(2)-0412	0.40	0.12			Yes		
SC(2)-0612	0.60	0.12			Yes		
SC(2)-0712	0.70	0.12	0.735	?	Yes	TM-86370	TM-86371
SC(2)-0414	0.40	0.14			Yes		
SC(2)-0614	0.60	0.14			Yes		
SC(2)-0714	0.70	0.14	0.715	Yes	Yes	TM X-72712	Low speed TM-81912
SC(2)-0518	1.00	0.18			Yes		

Table A-7: NASA supercritical airfoils—Phase 2, from NASA TP 2969, March 1990, by Charles D. Harris

Several transonic airfoils were developed at New York University by a group led by Paul Garabedian. The following table provides a list of the airfoils they published.

Airfoil designation	Design lift	Design thickness	Design mach	Test?	Ordinates in airfoil library?	Pages in Ref., Korn II book	Comments
79-03-12	0.293	0.123	0.790		Yes	37, 41–43	
72-06-16	0.609	0.160	0.720		Yes	48, 52–54	
71-08-14	0.799	0.144	0.710		Yes	55, 59–61	
70-10-13	0.998	0.127	0.700		Yes	62, 66–68	
65-14-08	1.409	0.083	0.650		Yes	73, 77–79	
65-15-10	1.472	0.104	0.650		Yes	80, 84–86	
82-06-09	0.590	0.092	0.820		Yes	91, 95	
75-06-12	0.629	0.117	0.750	Yes	Yes	96, 99–101	The "Korn"
75-07-15	0.668	0.151	0.750		Yes	102, 106	

Table A-8: Garabedian and Korn airfoil chart

Their airfoils are included in the following references:

Bauer, F., Garabedian, P., and Korn, D., *A Theory of Supercritical Wing Sections with Computer Programs and Examples*, Lecture Notes in Economics and Mathematical Systems, Vol. 66, Springer-Verlag, 1972.

Bauer, F., Garabedian, P., Jameson, A., and Korn, D., *Supercritical Wing Sections II, A Handbook*, Lecture Notes in Economics and Mathematical Systems, Vol. 108, Springer-Verlag, 1975.

Bauer, F., Garabedian, P., and Korn, D., *Supercritical Wing Sections III*, Lecture Notes in Economics and Mathematical Systems, Vol. 150, Springer-Verlag, 1977.

A.2 Classic Bodies of Revolution

Bodies of revolution form the basis for a number of shapes used in aerodynamic design and are also often used in comparing computational methods. The bodies defined in this section are generally associated with supersonic aerodynamics.

A.2.1 Summary of Relations

The body radius *r* is given as a function of *x*, *r/l = f(x/l)*. Once *r* is known, a number of other values characterizing the shape can be determined.

The cross-sectional area and derivatives are

$$S(x) = \pi r^2, \qquad \text{(A-39)}$$

$$\frac{dS}{dx} = 2\pi r \frac{dr}{dx} \quad , \qquad \text{(A-40)}$$

and

$$\frac{d^2S}{dx^2} = 2\pi \left[\left(\frac{dr}{dx} \right)^2 + r \frac{d^2r}{dx^2} \right]. \qquad \text{(A-41)}$$

Basic integrals for volume, surface area, and length along the contour are

$$V = \int_0^l S(x) dx, \qquad \text{(A-42)}$$

$$S_{wet} = 2\pi \int_0^l r(x) dx, \qquad \text{(A-43)}$$

and

$$p(\bar{x}) = \int_0^l \sqrt{1 + \left(\frac{dr}{dx} \right)^2} dx. \qquad \text{(A-44)}$$

Note that the incremental values can be found by changing the lower limit of the integrals.

The local longitudinal radius of curvature is given by

$$R(x) = \frac{\left[1 + \left(\frac{dr}{dx} \right)^2 \right]^{3/2}}{\left| \frac{d^2r}{dx^2} \right|}. \qquad \text{(A-45)}$$

Several simple shapes are also of interest in addition to those presented in detail in the subsections below. These simple shapes are: parabolic spindle, equation (A-46); ellipsoid of revolution, equation (A-47); and the power law body, equation (A-48):

$$\frac{r}{l} = 4 \frac{r_{\text{mid}}}{l} \frac{x}{l} \left(1 - \frac{x}{l} \right) \qquad \text{(A-46)}$$

$$\frac{r}{l} = 2 \frac{r_{\text{mid}}}{l} \sqrt{\frac{x}{l} \left(1 - \frac{x}{l} \right)} \qquad \text{(A-47)}$$

$$\frac{r}{l} = \frac{r_0}{l} \left(\frac{x}{x_N} \right)^n \qquad \text{(A-48)}$$

In equation (A-48), x_N is the nose length, and r_0 is the radius at $x = x_N$. The nose is blunt for $0 < n < 1$.

Two references that discuss geometry of bodies of revolution are listed below. Krasnov's reference discusses the spherical nose cap, which is another common shape.

Krasnov, N. F., *Aerodynamics of Bodies of Revolution*, edited and annotated by D. N. Morris, American Elsevier, New York, 1970.

Johns Hopkins University Applied Physics Laboratory. *Handbook of Supersonic Aerodynamics*, Vol. 3, Sec. 8, "Bodies of Revolution," NAVWEPS Report 1488. October 1961.

A.2.2 Tangent/Secant Ogives

The tangent or secant ogives are frequently used shapes in supersonic aerodynamics. The nomenclature is illustrated in figure A-1.

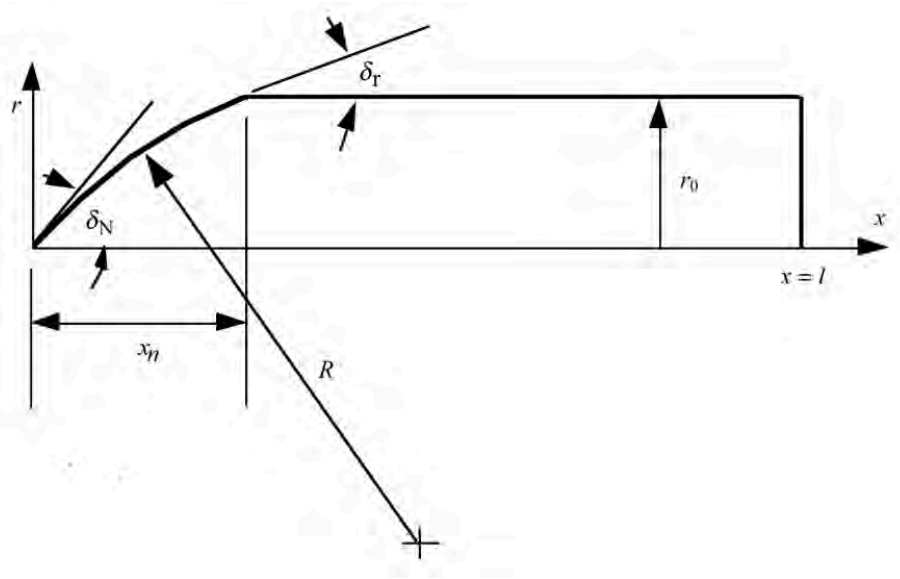


Figure A-1: Tangent or secant ogive shapes. *From W. H. Mason. Adapted by P. Raj.*

Note that the ogive is actually the arc of a circle, and when $\delta_r = 0$, the ogive ends tangent to the body, meaning that $\delta_r = 0$ represents the tangent ogive body. If $\delta_r = \delta_N$, the cone-cylinder is recovered. If $\delta_r = 0$ and $\delta_N = 90°$, the spherical cap case is obtained.

The expression for the radius *r* is determined using three basic constants for a particular case:

$$A = \frac{r_0}{l}\left(\frac{\cos\delta_N}{\cos\delta_r - \cos\delta_N}\right) \qquad \text{(A-49)}$$

$$B = 2\frac{r_0}{l}\left(\frac{\sin\delta_N}{\cos\delta_r - \cos\delta_N}\right) \qquad \text{(A-50)}$$

$$C = \frac{r_0}{l} \qquad \text{(A-51)}$$

The radius is then given by

$$\frac{r}{l} = \sqrt{A^2 + B\left(\frac{x}{l}\right) - \left(\frac{x}{l}\right)^2} - A \qquad 0 \text{ less than } \frac{x}{l} \text{ less than } \frac{x_N}{l}$$
$$= C \qquad \frac{x_N}{l} \text{ less than } \frac{x}{l} \text{ less than } 1 \qquad \text{(A-52)}$$

Next, x_N must be determined. For a tangent ogive ($\delta_r = 0$), the ogive can be defined by specifying either x_N/r_0 or δ_N. The other value can then be found as follows.

Given δ_N,

$$\frac{x_N}{r_0} = \frac{\sin\delta_N}{1 - \cos\delta_N}. \qquad \text{(A-53)}$$

Or given x_N/r_0,

$$\delta_N = \cos^{-1}\left[\frac{\left(\frac{x_N}{r_0}\right)^2 - 1}{\left(\frac{x_N}{r_0}\right)^2 + 1}\right]. \qquad \text{(A-54)}$$

For the secant ogive, the simplest analytical procedure is to define the ogive in terms of δ_N and δ_r and then to find x_N/l from

$$\frac{x_N}{l} = \frac{r_0}{l}\left(\frac{\sin\delta_N - \sin\delta_r}{\cos\delta_r - \cos\delta_N}\right). \qquad \text{(A-55)}$$

If x_N/l is not satisfactory, δ_N and δ_r can be adjusted by trial and error to obtain the desired nose length. A program can be set up to handle this process quite simply.

The first and second derivatives are then given by

$$\frac{d(r/l)}{d(x/l)} = \frac{B - 2(x/l)}{2[(r/l) + A]} \qquad \text{(A-56)}$$

and

$$\frac{d^2(r/l)}{d(x/l)^2} = -\frac{[B - 2(x/l)]^2}{4[(r/l) + A]^3} - \frac{1}{[(r/l) + A]}. \qquad \text{(A-57)}$$

The relationships between radius and area derivatives given in section A.2.1 are then used to complete the calculation.

A.2.3 The Von Kármán Ogive

This shape produces minimum wave drag for a specified base area and length, according to slender body theory. This ogive has a very slightly blunted nose, and it is described in a book by Ashley and Landahl.[9]

In this case, it is convenient to work with the cross-sectional area and a new independent variable:

$$\theta = \cos^{-1}\left[2\left(\frac{x}{x_N}\right) - 1\right] \qquad \text{(A-58)}$$

or

$$\frac{x}{x_N} = \frac{1}{2}(1 + \cos\theta) \qquad \text{(A-59)}$$

where the nose is at $\theta = \pi$ and the base is located at $\theta = 0$.

Here we use x_N to denote the "nose length" or length of the ogive and allow this shape to be part of an ogive-cylinder geometry. The shape is then given as

$$\frac{S(x)}{l^2} = \frac{S_B}{l^2}\left[1 - \frac{\theta}{\pi} + \frac{\sin 2\theta}{2\pi}\right] \qquad \text{(A-60)}$$

and

$$\frac{r}{l} = \sqrt{\frac{S/l^2}{\pi}} \qquad \text{(A-61)}$$

where S_B is the prescribed base area and l is the total length.

Defining nondimensional area and distance from the nose as:

$$\bar{S} = \frac{S}{l^2}, \quad \bar{x} = \frac{x}{l}, \qquad \text{(A-62)}$$

we have

$$\frac{d\bar{S}}{d\theta} = -\frac{\bar{S}_B}{\pi}[1 - \cos 2\theta], \qquad \text{(A-63)}$$

$$\frac{d^2\bar{S}}{d\theta^2} = -\frac{2}{\pi}\bar{S}_B \sin 2\theta, \qquad \text{(A-64)}$$

and

$$\begin{aligned} \frac{d\bar{S}}{d\bar{x}} &= \bar{S}' = \frac{4}{\pi}\left(\frac{l}{x_N}\right)\bar{S}_B \sin\theta \\ \frac{d^2\bar{S}}{d\bar{x}^2} &= \bar{S}'' = -\frac{8}{\pi}\left(\frac{l}{x_N}\right)^2 \frac{\bar{S}_B}{\tan\theta} \end{aligned} \qquad \text{(A-65)}$$

The radius derivatives are then computed by

$$\frac{d\bar{r}}{d\bar{x}} = \frac{\bar{S}'}{2\pi\bar{r}}, \quad \frac{d^2\bar{r}}{d\bar{x}^2} = \frac{\bar{S}''}{2\pi\bar{r}} - \frac{\bar{r}'^2}{\bar{r}}. \qquad \text{(A-66)}$$

A.2.4 The Sears–Haack Body

This is the minimum wave drag shape for a given length and volume according to slender body theory as discussed in Chapter 9. The body is closed at both ends, has a very slightly blunted nose, and is symmetric about the mid-point. It is described by Ashley and Landahl.[10]

Although the notation used in the previous section A.2.3 for the Von Kármán Ogive could be used, it is more common to describe the Sears-Haack body in the manner presented below. This form uses the fineness ratio, $f = l/d_{max}$ to scale the shape. However, it is important to realize that the Sears-Haack shape is the minimum drag body for a specified volume and length, not for a specified fineness ratio. The minimum drag body for a specified fineness ratio is described in section A.2.5 below.

In defining

$$\varsigma = 1 - 2\left(\frac{x}{l}\right), \qquad \text{(A-67)}$$

the Sears–Haack body is defined as

$$\frac{r}{l} = \frac{1}{2f}\left(1 - \varsigma^2\right)^{3/4}. \qquad \text{(A-68)}$$

The derivatives are given by

$$\frac{d(r/l)}{d(x/l)} = \frac{3\varsigma}{1 - \varsigma^2}\left(\frac{r}{l}\right) \qquad \text{(A-69)}$$

and

$$\frac{d^2(r/l)}{d(x/l)^2} = -\left(\frac{1}{1-\varsigma^2}\right)\left[\varsigma\frac{d(r/l)}{d(x/l)} + 6\left(\frac{r}{l}\right)\right]. \qquad \text{(A-70)}$$

The fineness ratio is related to the length and volume by

$$f = \sqrt{\frac{3\pi^2}{64}\frac{l^3}{V}}. \qquad \text{(A-71)}$$

In terms of *f* and either *V* or *l*, the other value can be found based on the following givens.

Given *f* and *l*:

$$V = \frac{3\pi^2}{64}\frac{l^3}{f^2} \qquad \text{(A-72)}$$

Given *f* and *V*:

$$l = \left[V\frac{64}{3\pi^2}f^2\right]^{1/3} \qquad \text{(A-73)}$$

The relationships between radius and area derivatives given in section A.2.1 are then used to complete the calculation.

A.2.5 The Haack–Adams Bodies

The Haack–Adams bodies define a number of minimum drag shapes, as described by M.C. Adams.[11] These bodies correspond to the following cases:

I. Given length, base area, and contour passing through a specifically located radius
II. Given length, base area, and maximum area
III. Given length, base area, and volume

In case I, the specified radius will not necessarily be the maximum radius.

The notation used in TN-2550 is employed in the equations, leading to the following definitions:

$$S = 4\frac{\bar{S}(x)}{l^2}, \quad B = 4\frac{S_{BASE}}{l^2}, \quad A = 4\frac{S_A}{l^2}, \quad V = 8\left(\frac{\bar{V}}{l^3}\right) \qquad \text{(A-74)}$$

where *S(x)* is the area, S_A corresponds to either the specified area at a given location or the maximum area, and *V* is the volume. The independent variable is defined with its origin at the body midpoint, as seen in equation (A-75).

$$\varsigma = 2\left(\frac{x}{l}\right) - 1 \qquad \text{(A-75)}$$

The location of the specified radius (case I) and maximum radius (case II) is designated *C* and given in ζ coordinates. When referring to the *x* coordinate, this value is designated C_x.

What follows are the standard forms of equations for each case.

Case I: Given S_{BASE}, S_A, and C_x

$$\begin{aligned}\frac{\pi S}{B} =& \left[\frac{\pi A}{B} - \cos^{-1}(-c)\right]\frac{\sqrt{1-\varsigma^2}(1-c\varsigma)}{(1-c^2)^{3/2}} + \frac{\sqrt{1-\varsigma^2}(\varsigma-c)}{(1-c^2)} \\ &+ \left[\frac{\pi A}{B} - \cos^{-1}(c) - c\sqrt{1-c^2}\right]\frac{(\varsigma-c)^2}{(1-c)^2}\ln N + \cos^{-1}(-\varsigma)\end{aligned} \tag{A-76}$$

where

$$N = \frac{1 - c\varsigma - \sqrt{1-c^2}\sqrt{1-\varsigma^2}}{|\varsigma - c|} \tag{A-77}$$

Case II: Given S_{BASE} and S_{MAX}

First, find the location of the maximum thickness from the implicit relation.

$$f(c) = 0 = \frac{\pi A}{R}c - \sqrt{1-c^2} - c\cos^{-1}(-c) \tag{A-78}$$

Use Newton's iteration

$$c^{i+1} = c^i - \frac{f\left(c^i\right)}{f'\left(c^i\right)} \tag{A-79}$$

where

$$f'(c) = \frac{\pi A}{B} - \cos^{-1}(-c). \tag{A-80}$$

An initial guess of $c = 0$ is sufficient to start the iteration. Given c, the relation for the area is

$$\frac{\pi S}{B} = \frac{\sqrt{1-\varsigma^2}}{c} + \frac{(\varsigma-c)^2}{c\sqrt{1-c^2}}\ln N + \cos^{-1}(-\varsigma) \tag{A-81}$$

where N is the same function as given in case I.

Case III: Given S_{BASE} and V

$$\frac{\pi S}{B} = \frac{8}{3}\left[\frac{V}{B} - 1\right]\left(1-\varsigma^2\right)^{3/2} + \varsigma\sqrt{1-\varsigma^2} + \cos^{-1}(-\varsigma) \tag{A-82}$$

The maximum thickness for this case is located at

$$e = \frac{1}{4(V/B - 1)} \quad , \tag{A-83}$$

and in x coordinates, it is located at:

$$e_x = \frac{1}{2}(1 + e). \qquad \text{(A-84)}$$

Note that if $S_{BASE} = 0$, the Sears–Haack body is recovered.

A.3 Cross-Section Geometries for Bodies

The axisymmetric bodies described above can be used to define longitudinal lines for aerodynamic bodies. However, many aerodynamic bodies are not axisymmetric because the fuselage cross section is not typically round. In this section, we define a class of cross section shapes that can be used to develop more realistic aerodynamic models. In particular, they have been used to study geometric-shaping effects on forebody aerodynamic characteristics using an analytical forebody model with the ability to produce a wide variation of shapes. This generic model makes use of the equation of a superellipse to define cross-sectional geometry. The superellipse, used previously to control flow expansion around wing leading edges, can recover a circular cross section and can produce elliptical cross sections and chine-shaped cross sections. Thus it can be used to define a variety of different cross-sectional shapes.

The superellipse equation for a cross section is

$$\left(\frac{z}{b}\right)^{2+n} + \left(\frac{y}{a}\right)^{2+m} = 1 \qquad \text{(A-85)}$$

where n and m are adjustable coefficients that control the surface slopes at the top and bottom planes of symmetry and the chine leading edge. The constants a and b correspond to the maximum half-breadth (the maximum width of the body) and the upper or lower centerlines, respectively. Depending on the value of n and m, the equation can be made to produce all the shapes described above. The case $n = m = 0$ corresponds to the standard ellipse. The body is circular when $a = b$.

When $n = -1$, the sidewall is linear at the maximum half-breadth line, forming a distinct crease line. When $n < -1$, the body cross section takes on a cusped or chine-like shape. As n increases, the cross section starts to become rectangular.

The derivative of z/b with respect to y/a is

$$\frac{d\bar{z}}{dy} = -\frac{\left(\frac{2+m}{2+n}\right)}{\left[1 - \bar{y}^{(2+m)}\right]^{\left(\frac{1+n}{2+n}\right)}} \qquad \text{(A-86)}$$

where $z = z / b$ and $y = y / a$. As $y \to 1$, the slope becomes

$$\frac{d\bar{z}}{d\bar{y}} = \begin{cases} \infty & n > -1 \\ 0 & n < -1 \\ -(2+m)\bar{y}^{1+m} & n = -1 \end{cases} \qquad \text{(A-87)}$$

Figure A-2 shows a quadrant of the cross section for various values of *n* ranging from a chine to a rectangle.

Different cross sections can be used above and below the maximum half-breadth line. Even more generality can be provided by allowing *n* and *m* to be functions of the axial distance *x*. The parameters *a* and *b* can also be functions of the planform shape and can be varied to study planform effects. Notice that when *n* = -1, the value of *m* can be used to control the slope of the sidewall at the crease line. Observe that large positive values of *n* drive the cross-sectional shape to approach a rectangular or square shape.

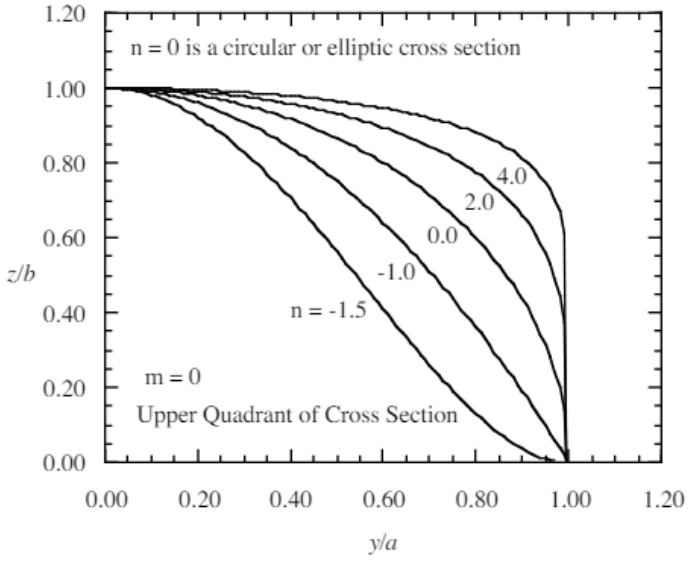


Figure A-2: Quadrant of the cross section for various values of n ranging from a chine to a rectangle. From W. H. Mason. Adapted by P. Raj.

Connecting various cross-sectional shapes is part of the subject of lofting. A good discussion of lofting can be found in the book by Raymer,[12] who worked at North American Aviation (actually part of Rockwell), where Liming literally wrote the book[13] on the analytic definition of aircraft lines. Liming's book emphasizes conic sections, and the examples in the book are for the P-51 Mustang.

A.4 Planform Analysis

Several local and integral planform properties are of interest in aerodynamic analysis. They are summarized in this section. (Note: Biplanes use the total area of both wings as the reference area.) For a more complete presentation, see DATCOM (https://www.pdas.com/datcom.html).

Figure A-3 illustrates the standard nomenclature. The local values are the leading- and trailing-edge locations, $x_{LE}(y)$ and $x_{TE}(y)$, the local chord, $c(y)$, and the leading- and trailing-edge sweep angles: $\Lambda_{LE}(y)$ and $\Lambda_{TE}(y)$.

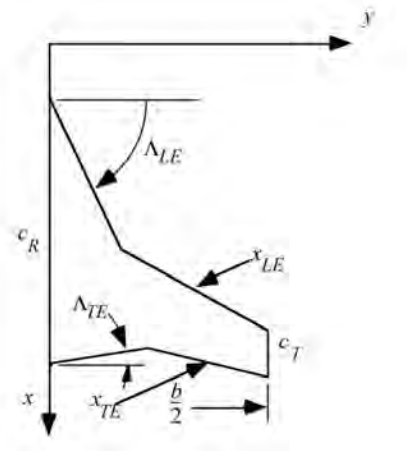


Figure A-3: Standard nomenclature for a wing planform. From W. H. Mason. Adapted by P. Raj.

Assuming the planform is symmetric, the integral properties are as follows.

(1) Planform Area, *S*

$$S = 2\int_0^{b/2} c(y)dy \qquad \text{(A-88)}$$

(2) Mean aerodynamic chord (*mac*)

$$\bar{c} = \frac{2}{S}\int_0^{b/2} c^2(y)dy \qquad \text{(A-89)}$$

(3) *X* position of centroid of area, x_{cen}

$$x_{cen} = \frac{2}{S}\int_0^{b/2} c(y)\left\{x_{LE}(y) + \frac{c(y)}{2}\right\}dy \qquad \text{(A-90)}$$

(4) Spanwise position of *mac*

$$y_{\text{mac}} = \frac{2}{S}\int_0^{b/2} yc(y)dy \qquad \text{(A-91)}$$

(5) Leading-edge location of *mac*

$$x_{LE_{\text{mac}}} = \frac{2}{S}\int_0^{b/2} x_{LE}(y)c(y)dy \qquad \text{(A-92)}$$

In addition, the following derived quantities are often of interest.

Aspect ratio:

$$AR = \frac{b^2}{S_{ref}} \qquad \text{(A-93)}$$

Average chord:

$$c_A = \frac{S_{ref}}{b} \qquad \text{(A-94)}$$

Taper ratio:

$$\lambda = \frac{c_T}{c_R} \qquad \text{(A-95)}$$

S_{ref} is usually chosen to be equal to the area of a basic reference trapezoidal planform, and thus the actual planform area, *S*, may not equal S_{ref}.

When considering two areas, recall that the centroid of the combined surfaces is

$$\begin{aligned} S\bar{x} &= S_1\bar{x}_1 + S_2\bar{x}_2 \\ S\bar{y} &= S_1\bar{y}_1 + S_2\bar{y}_2 \end{aligned}. \qquad \text{(A-96)}$$

For a standard trapezoidal wing planform, it is convenient to collect a set of formulas related to its geometric characteristics using a standard nomenclature for geometric parameters shown in figure A-4.

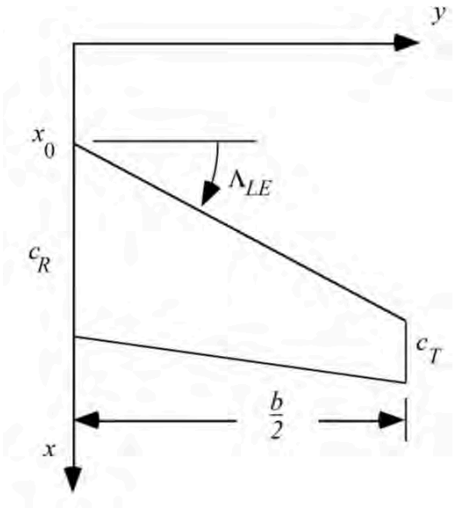


Figure A-4: Nomenclature for standard trapezoidal wing planform. From W. H. Mason. Adapted by P. Raj.

For a wing section at span station y, the leading and trailing edge *x* coordinates are given by equation (A-97).

$$\begin{aligned} x_{LE}(y) &= x_{LE_0} + y\tan\Lambda_{LE}(y) \\ x_{TE}(y) &= x_{TE_0} + y\tan\Lambda_{TE}(y), \end{aligned} \qquad \text{(A-97)}$$

and the local chord is

$$\frac{c(y)}{c_R} = 1 - (1-\lambda)\eta \qquad \text{(A-98)}$$

where

$$y = \frac{b}{2}\eta \quad \text{or} \quad \eta = \frac{y}{b/2} \quad \text{and} \quad \lambda = \frac{c_T}{c_R}. \qquad \text{(A-99)}$$

The sweep at any element line can be found in terms of the sweep at any other by

$$\tan\Lambda_n = \tan\Lambda_m - \frac{4}{AR}\left[(n-m)\left(\frac{1-\lambda}{1+\lambda}\right)\right] \qquad \text{(A-100)}$$

where *n* and *m* are fractions of the local chord. An alternate formula is available using the trailing-edge sweep angle:

$$\tan\Lambda_n = (1-n)\tan\Lambda_{LE} + n\tan\Lambda_{TE}. \qquad \text{(A-101)}$$

The integral and other relations are given by

$$
\begin{aligned}
S &= \frac{b}{2} c_R (1+\lambda) \\
c_{\text{ave}} &= \frac{S}{b} \\
\frac{\bar{c}}{c_R} &= \frac{2}{3}\left(\frac{1+\lambda+\lambda^2}{1+\lambda}\right) \\
AR &= \frac{b^2}{S} = \frac{b/2}{c_R}\left(\frac{4}{1+\lambda}\right) \qquad . \qquad \text{(A-102)} \\
y_{\text{mac}} &= \frac{b}{6}\left(\frac{1+2\lambda}{1+\lambda}\right) \\
\frac{x_{LE_{\text{mac}}}}{c_R} &= \frac{x_{LE_0}}{c_R} + \left(\frac{1+2\lambda}{12}\right) AR \tan\Lambda_{LE} \\
x_{cen} &= x_{LE_{\text{mac}}} + \frac{\bar{c}}{2}
\end{aligned}
$$

When computing the projected planform area of an entire configuration, the following formula is useful:

$$
S = \sum_{k=1}^{k=N} \left(y_{k+1} + y_k\right)\left(x_{k+1} - x_k\right) \qquad \text{(A-103)}
$$

where the standard nomenclature is shown in figure A-5.

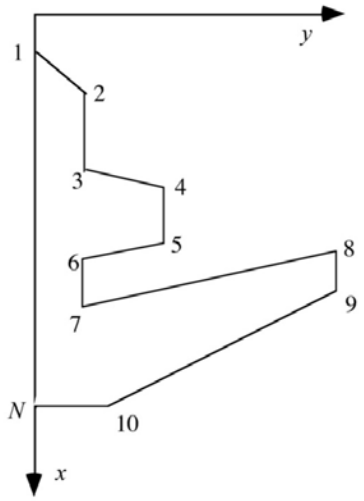


Figure A-5: Nomenclature for projected planform area of an entire configuration. From W. H. Mason. Adapted by P. Raj.

At $k = N$, y_{k+1}, x_{k+1} refer to the initial points y_1, x_1. For normal planforms, $y_{n+1} = y_1 = 0$, so that the summation can be terminated at $N-1$. This formula assumes planform symmetry and provides the total planform area with only one side of the planform used in the computation.

A.4.1 A Note on Reference Chords and Aerodynamic Center Location

Looking at the aerodynamics literature, especially the older literature and textbooks, you find that the nomenclature for reference chords is not uniform. However, there is a standard in use today in the US industry. The issue is what value to use when nondimensionalizing the pitching moment:

$$C_m = \frac{M}{qS_{ref}c_{ref}}. \qquad \text{(A-104)}$$

The USAF DATCOM defines the standard. They define c_{ref} to be the mean aerodynamic chord or *mac*:

$$\bar{c} = \frac{2}{S}\int_0^{b/2} c^2(y)dy \qquad \text{(A-105)}$$

which, for a straight tapered wing, is

$$\frac{\bar{c}}{c_r} = \frac{2}{3}\left(\frac{1+\lambda+\lambda^2}{1+\lambda}\right). \qquad \text{(A-106)}$$

The use of the symbol $\bar{c}$ to represent the mean aerodynamic chord is confusing because $\bar{c}$ is sometimes used to represent the average chord, $c_a = S/b$, in other literature. For example, ESDU Item 76003 uses $\bar{c}$ to be the standard (or geometric) mean chord, which I have defined here as the average chord. They use c (with two overlines) as the *mac* defined by equation (A-89). The main problem occurs when the report or paper does not specifically define the terms used. For example, Lamar and Alford[14] use equation (A-89) to nondimensionalize the pitching moment, but they call it the "mean geometric chord."

Another issue to consider is that the *mac* does not necessarily lie on the actual planform if the wing is not a simple straight tapered configuration.

A.5 Conical Camber

An important class of camber distributions is associated with the planform and not the airfoil. Conical camber has been widely used, and many forms can be found in the literature. However, the NACA defined a specific type of conical camber that is known as NACA conical camber. The most recent example of NACA conical camber is the F-15 wing. It improves the drag characteristics of wings in the subsonic and transonic flow region, even though it was developed to reduce the drag at supersonic speeds!

The key references on this topic are listed below.

Hall, C. F., "Lift, Drag, and Pitching Moment of Low Aspect Ratio Wings at Subsonic and Supersonic Speeds," NACA RM-A53A30, 1953. https://ntrs.nasa.gov/citations/19930086624

> This report provided the original mathematical definition of NACA conical camber. It also provided a large range of test conditions for which the camber was effective.

Boyd, J. W., Migotsky, E., and Wetzel, B. E., "A Study of Conical Camber for Triangular and Swept Back Wings," NASA RM-A55G19, Nov. 1955. https://ntrs.nasa.gov/citations/19930090334

> This report provided more details of the derivation of the formulas for NACA conical camber, and it corrected errors in the equations presented in the first report. Additional experimental results were also presented.

An advanced form of conical camber addressing cases of so-called supercritical crossflows is supercritical conical camber (SC3). It is described in a report by Mason[15] and in Mason's AIAA paper.[16]

A.6 Three-Dimensional Wing Geometry

Wing geometry is often defined by interpolating between airfoil sections specified at particular spanwise stations. Some care should be taken to interpolate properly. Program WNGLFT provides an example of a lofting scheme to provide wing ordinates at any desired location. It can be used to provide wing ordinates for a wide class of wings. In fact, it will produce a very good approximation of the wing design employed by a successful Navy airplane.

Notes

1. Van Dam, C. P., "Recent experience with different methods of drag prediction," Progress in Aerospace Sciences, Vol. 35, No. 8, Nov. 1999, pp. 751–798.
2. Riegels, F. W., *Airfoil Sections*, Butterworths, London, 1961.
3. Abbott, I. H., and Von Doenhoff, A. E., *Theory of Wing Sections*, Dover Publications, Inc., 1959.
4. Verhoff, A., Stookesberry, D., and Cain, A., "An efficient approach to optimal aerodynamic design. I - Analytic geometry and aerodynamic sensitivities," AIAA Paper 1993-0099, 31st Aerospace Sciences Meeting, Reno, NV, Jan. 11-14, 1993.
5. Stookesberry, D., Verhoff, A., and Cain, A., "An efficient approach to optimal aerodynamic design. II - Implementation and evaluation," AIAA Paper 1993-0100, 31st Aerospace Sciences Meeting, Reno, NV, Jan. 11-14, 1993.
6. Venkataraman, P., "A New Procedure for Airfoil Definition," AIAA Paper 1995-1875, 13th Applied Aerodynamics Conference, San Diego, CA, Jun. 19-22, 1995.
7. Venkataraman, P., "Optimum Airfoil Design in Viscous Flows," AIAA Paper 1995-1876, 13th Applied Aerodynamics Conference, San Diego, CA, Jun. 19-22, 1995.
8. Sadrehaghighi, I., Smith, R. E., and Tiwari, S. N., "Grid and Design Variables Sensitivity Analysis for NACA Four-Digit Wing-Sections," AIAA Paper 1993-0195, 31st Aerospace Sciences Meeting, Reno, NV, Jan. 11-14, 1993.
9. Ashley, H., and Landahl, M., *Aerodynamics of Wings and Bodies*, Addison-Wesley, 1965, pp. 178–181.
10. Ashley, H., and Landahl, M., *Aerodynamics of Wings and Bodies*, Addison-Wesley, 1965, pp. 178–181.
11. Adams, M. C., "Determination of Shapes of Boattail Bodies of Revolution for Minimum Wave Drag," NACA TN-2550, Nov. 1951.
12. Raymer, D., *Aircraft Design: A Conceptual Approach*, 5th ed., AIAA Education Series, Reston, VA.
13. Liming, R., *Practical Analytic Geometry with Applications to Aircraft*, MacMillan, New York, 1944.
14. Lamar, J. E., and Alford, W. J., Jr., "Aerodynamic-Center Considerations of Wings and Wing-Body Combinations," NASA TN D-3581, Oct. 1966.
15. Mason, W. H., "A Wing Concept for Supersonic Maneuvering," NASA CR-3763, Dec. 1983. https://ntrs.nasa.gov/citations/19840007047
16. Mason, W. H., "SC3 — A Wing Concept for Supersonic Maneuvering," AIAA Paper 83-1858, Applied Aerodynamics Conference, Danvers, MA, Jul. 13-15, 1983.

Appendix B: Fifteen Minutes of Stealth in Aircraft Design

There is not much point in considering military aerodynamic configuration development without including stealth. It plays a key role in the configuration layout. A few government planners want to ignore the fundamental importance of stealth to survivability. This is fanciful and nostalgic thinking. The fact is that missiles are finally becoming reliable, and there is no such thing as too much stealth. Although the details are classified, certain basic principles have been described.

Stealth is usually considered to consist of several elements (often referred to as signatures):

- radar cross section (RCS)
- infrared
- visual
- aural

For aerodynamic configuration design, the key element is radar cross section, RCS, with some consideration of infrared, mainly from the back of the aircraft. In the mid-1980s, I actually took the graduate sequence in electromagnetic theory at a local university. Any aerodynamicist working in military configuration design will have to add this topic to his plan for continuing education.

Although complete information on this technology is not available, there are numerous references that define the public's knowledge of stealth. To get insight into how stealth emerged to influence airplane design, read the book by Ben Rich.[1] This book tells the story of stealth configuration development at the Skunk Works. Not particularly technical, but a good read, providing insight into aircraft development programs. Rich succeeded Kelly Johnson, the founder of the Skunk Works. Rich headed the Lockheed Skunk Works during the development of the F-117 but passed away much too soon. More details on the F-117 design are given by Alan Brown.[2] The B-2 development is described in part of the 1991 Wright Brothers Lecture by Waaland.[3] The paper describes experiences at Northrop, including the B-2 development, along with many other programs. The author received the AIAA Aircraft Design Award for the B-2.

Explicit discussions of stealth in airplane design have been given by Raymer.[4] The section on RCS is found on pages 191 to 201 of Raymer's book. Infrared, visual and aural aspects of stealth are discussed in the following sections on pages 201 to 203. This is a good direct unclassified source of accurate shaping information. A very good SAE paper by Whitford[5] was adapted by the author in "Fundamentals of Fighter Design, Part 10 – Stealth" (in Sept. 1997's *Air International*) and his book, *Fundamentals of Fighter Design* (published by Airlife in 2000). Somewhat more theoretical treatments of the theory underlying stealth have been given by Ball.[6] More insight into electromagnetic theory can be obtained from the handwritten charts from lectures by Prof. Fuhs.[7] These were developed in 1982, but there are no date or copyright markings. The synopsis given here is supported by these references. A good overview of the survivability issues has been given by Patterson,[8] who discusses the question of how much stealth is enough.

B.1 How RCS Works

(1) A radar site transmits a signal and measures the signal that is returned from the target (in this case, an airplane).

When the sending and receiving antennas are colocated, the radar is known as monostatic, as shown in figure B-1(a). This is the usual case. If the receiving antenna is located somewhere else, the radar is bistatic, shown in figure B-1(b). Bistatic systems may be able to detect aircraft designed to operate stealthily against monostatic systems. This is a fundamental consideration in stealth.

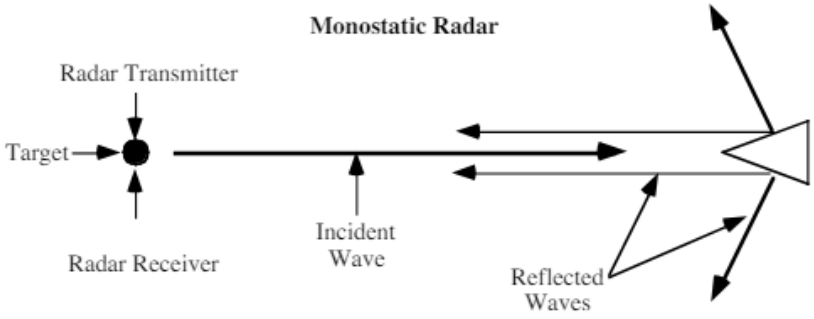


Figure B-1(a): Radar cross section: monostatic radar

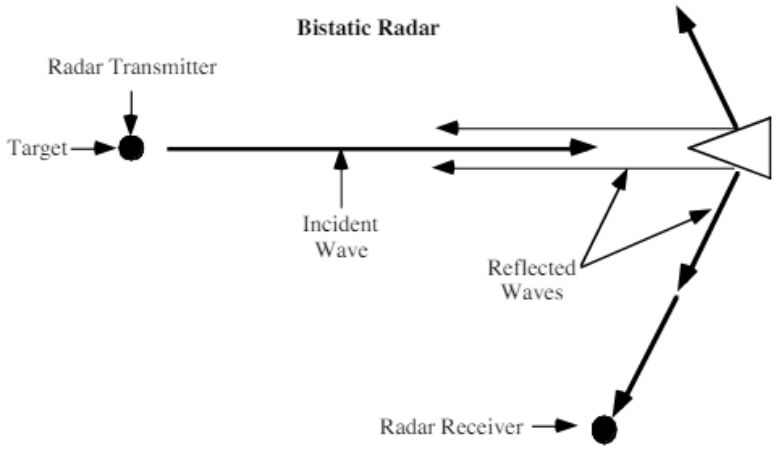


Figure B-1(b): Radar cross section: bistatic radar

(2) There is a length scale associated with radar:

$$\underset{\text{wavelength}}{\lambda} \cdot \underbrace{f}_{\text{frequency}} = \underset{\substack{\text{speed of}\\ \text{light}}}{c} \qquad \text{(B-1)}$$

The ratio of the wavelength to key length scales on the vehicle,

$$\frac{\lambda}{l_{ref}}, \qquad \text{(B-2)}$$

is important in understanding the physics of the radar reflectivity. Several different mechanisms exist, and these ratios can be thought of (very) loosely as analogous to the Reynolds number and Knudson number for use in aerodynamics, where values of these parameters are used to decide which physical phenomena dominate the flow field. The wavelength also determines the size of the antenna required.

(3) The signature is expressed as an area.

One square meter is the reference area, and the value of the RCS is usually expressed as a relative value using decibels:

$$\sigma\left(db_{sm}\right) = 10 \cdot \log_{10}\left(\frac{\sigma_{\text{meters}}}{1\text{meter}}\right) \qquad \text{(B-3)}$$

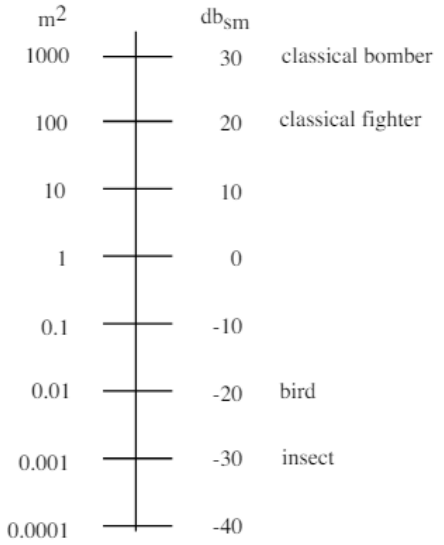


Figure B-2: Typical stealth values

Ben Rich loved to tell the story of his test range experience, where the operator claimed that the model, a precursor of the F-117, wasn't "on the pole" until a bird landed on the model and he could pick up a reflection. That should tell you something about the signature level of the F-117.

For a lot of the work in aerodynamic configurations, specular reflection dominates, making physical optics useful. Figure B-3 is a sketch based on Fuhs's notes that illustrates the situation. It is perhaps obvious, but to avoid large radar returns, there should be no surfaces normal to the radar signal.

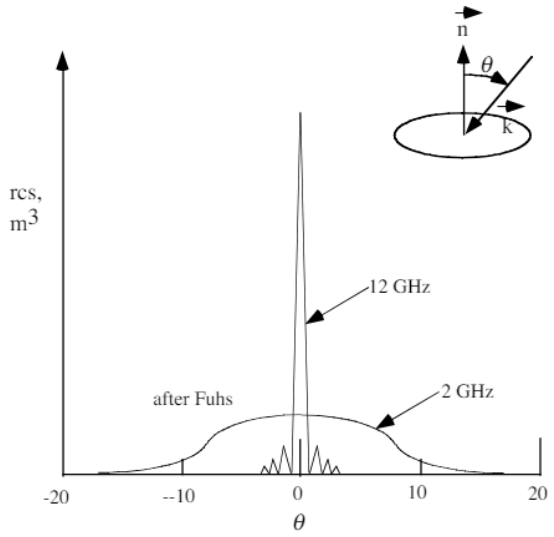


Figure B-3: Radar return from a circular plate

Clearly, flat surfaces normal to the incoming waves are bad and reflect strongly back to the transmitter, thus surfaces should be angled to reflect the waves in other directions, as illustrated in figure B-4.

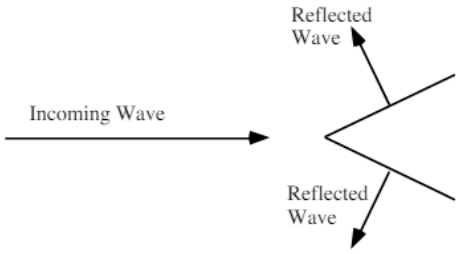


Figure B-4: A way to reduce radar returns

Designers work to different RCS target values (levels) in different sectors. A typical division is shown here in figure B-5.

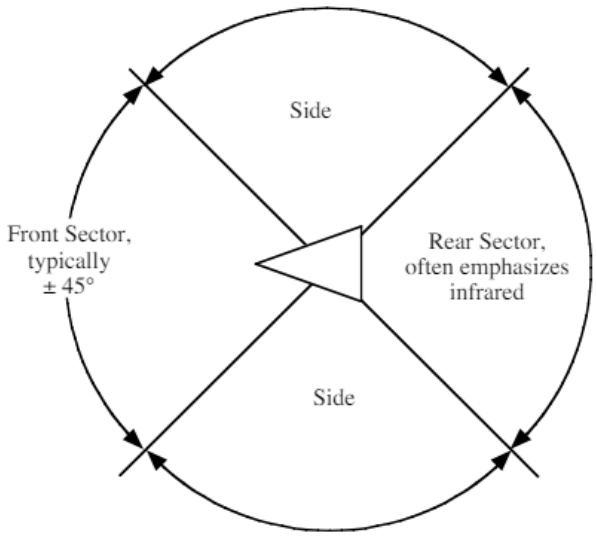


Figure B-5: Typical divisions of radar returns around an airplane

The front sector typically has the lowest allowable RCS value. This means that wings are swept and cavities are bad. The worst case is the inlet and engine front face.

The F-14 and F-15 aircraft turned out to have terrible inlets from a stealth point of view. This was ironic. The designers had worked hard to design these intakes since they were excellent aerodynamically. Figure B-6 illustrates this situation.

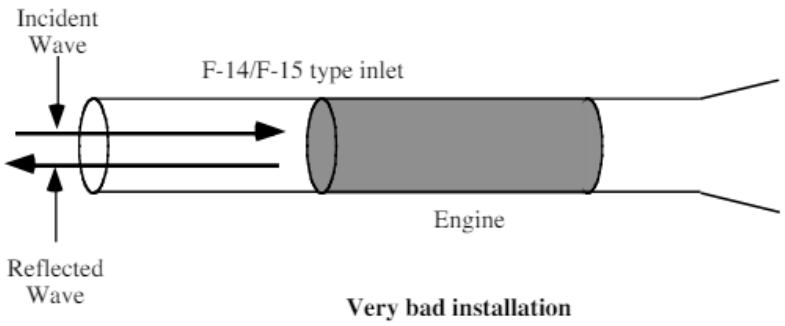


Figure B-6: Example of the inlet situation on some modern fighters

Instead of the F-15 type inlets, the engine front face has to be shielded by an offset inlet, as shown below in figure B-7. Observe the extreme effort devoted to hiding the engine in the F-117 and B-2. This also provides an opportunity to take full advantage of radar absorbing material (RAM) treatments in the duct. Thus modern military inlets use S-shaped inlets; figure B-7 provides an example. More information and new approaches to inlet design appeared in *Aviation Week*.[9]

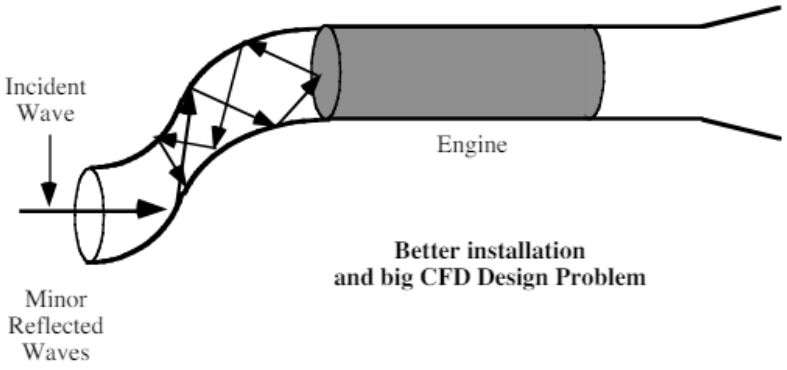


Figure B-7: Inlet design to reduce radar return

Cockpits and radomes are also bad, passing electromagnetic waves to the surfaces inside them, which are often huge reflectors. Thus special design procedures and materials are required to reduce the radar cross section.

From the side, vertical surfaces are eliminated, introducing canted tails and chine-sided fuselages. However, corner reflectors are terrible, so the angle shown in the front view is only acceptable if it doesn't line up in the side view. Figure B-8(a) illustrates the poor shaping situation where the configuration is prone to reflecting lots of incident waves.

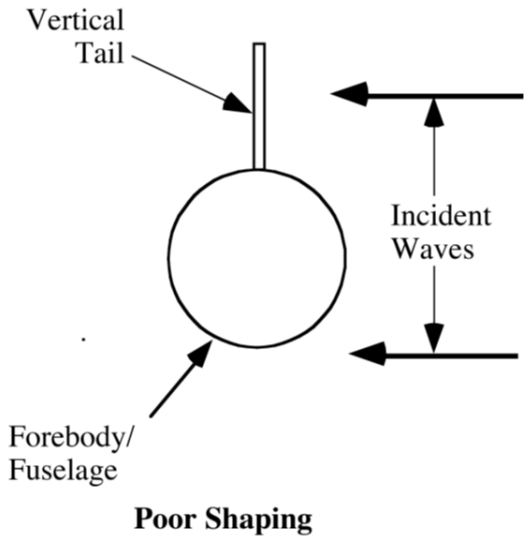


Figure B-8(a): Poor shaping practice to reduce radar returns. From W. H. Mason. Adapted by P. Raj.

Figure B-8(b) is the good shaping situation since incident waves will be scattered in different directions and only a small portion will be returned in the direction of the incident waves. Note that care must be taken to ensure that the vertical tails do not form a corner in the side view since this is even worse than the arrangement shown in figure B-8(b).

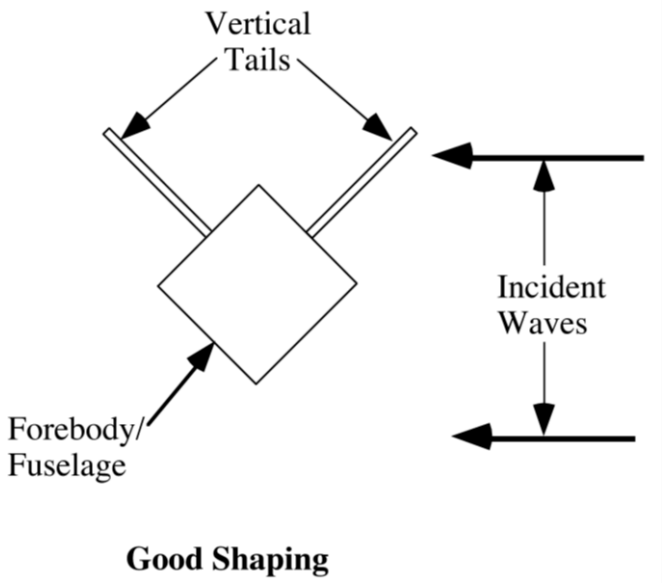


Figure B-8(b): Good shaping practice to reduce radar returns. *From W. H. Mason. Adapted by P. Raj.*

This also explains the sawtooth landing gear doors and access panels illustrated in figure B-9.

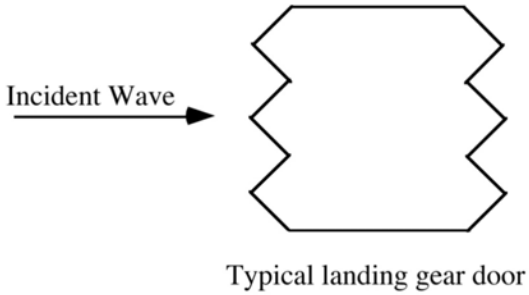


Figure B-9: Example of doors used on stealth airplanes showing no edges normal to the incident wake. *From W. H. Mason. Adapted by P. Raj.*

Finally, in addition to shaping, the vehicles are treated with coatings and special materials to reduce the radar return.

B.2 Computations

The second edition of Ball's book on aircraft combat survivability[10] provides some sources to start making RCS estimates. Sefer et al.[11] describe MATLAB-based methods for RCS analysis. An article by Joy and Singh[12] provides hybrid approaches incorporating low-frequency and high-frequency methods to solve electromagnetic problems.

Notes

1. Rich, B. R., and Janos, L., *Skunk Works*, Little, Brown, and Co., 1994.
2. Brown, A., "Fundamentals of Low Radar Cross-Sectional Aircraft Design," Journal of Aircraft, Vol. 30, No. 3, May-Jun. 1993, pp. 289–290.
3. Waaland, I. T., "Technology in the Lives of an Aircraft Designer," AIAA Paper 91-3069, 1991 Wright Brothers Lecture, AIAA Aircraft Design and Operations Meeting, Baltimore, MD, Sept. 23-25, 1991.
4. Raymer, D., *Aircraft Design: A Conceptual Approach*, 3rd ed., AIAA, Washington, 1999.
5. Whitford, R., "Designing for Stealth in Fighter Aircraft (Stealth from the Aircraft Designer's Viewpoint)," SAE Paper 965540, Oct. 1996.
6. Ball, R. E., *The Fundamentals of Aircraft Combat Survivability: Analysis and Design*, 2nd ed., AIAA, Washington, 2003.
7. Fuhs, A., *Radar Cross Section Lectures*, AIAA.
8. Patterson, J., "Overview of Low Observable Technology and Its Effects on Combat Aircraft Survivability," Journal of Aircraft, Vol. 36, No. 2, Mar.-Apr. 1999, pp. 380–388.
9. Fulghum, D. A., "Stealth Engine Advances Revealed in JSF Designs," Aviation Week, Mar. 2001, pp. 90–99.
10. Ball, R. E., *The Fundamentals of Aircraft Survivability: Analysis and Design*, 2nd ed., AIAA Education Series, American Institute of Aeronautics and Astronautics, Inc., 2003. https://doi.org/10.2514/4.862519
11. Sefer, A., Uslu, M. A., and Sevgi, L., "MATLAB-Based 3-D MoM and FDTD Codes for the RCS Analysis of Realistic Objects [Testing Ourselves]," IEEE Antennas and Propagation Magazine, Vol. 57, No. 4, Aug. 2015, pp. 122–148. https://ieeexplore.ieee.org/document/7274814
12. Joy, V., and Singh, H. "Radar Cross-Section (RCS) Estimation and Reduction," in *Handbook of Metrology and Applications*, edited by D. K. Aswal, S. Yadav, T. Takatsuji, P. Rachakonda, H. Kumar, Springer, Singapore, 2023. https://doi.org/10.1007/978-981-99-2074-7_83

Appendix C: Government Regulations Affecting Configuration Aerodynamics

A number of government regulations affect the aerodynamic design of airplanes. The goal is to ensure safe flight. The government is not interested in sacrificing safety for improved economics. For example, the second segment climb requirement described below often determines the engine thrust requirement for twin-engine transports. Other examples include reserve fuel requirements, emergency exits, and flight in icing conditions.

The specific safety-related regulations for commercial aircraft are made in the US by the Federal Aviation Administration (FAA) and have been known as the Federal Aviation Regulations (FARs) from 1958 onwards. However, FAR is also an acronym for "Federal Acquisition Regulations," and this has led to confusion at times. To avoid this confusion, the term "14 CFR" has been formally adopted for the Federal Aviation Regulations. The United States Code of Federal Regulations (CFR), Title 14, contains rules and regulations issued by the US Department of Transportation and Federal Aviation Administration for Aeronautics and Space, hence the term "14 CFR." These regulations can be found online in the Code of Federal Regulations, or eCFR, at the following URL: https://www.ecfr.gov/current/title-14. As an example, Part 25, Subchapter C, Chapter I contains Airworthiness Standards for Transport Category Airplanes: https://www.ecfr.gov/current/title-14/chapter-I/subchapter-C/part-25. Examples of regulations include the takeoff and landing distances, engine-out performance, noise limits, icing performance, and emergency evacuation to name a few.

In Europe, the equivalent Joint Aviation Requirements (JARs) are managed by Joint Aviation Authorities and by the European Union Aviation Safety Agency (EASA). Military aircraft also have numerous requirements. In both situations, the emphasis is on safety, including the handling qualities.

Note that many aerospace engineers continue to use the term FAR when referencing the 14 CFR regulations. You should be aware that this is the case with the material in this appendix that was initially prepared when FAR was a much more widely used and accepted term.

The interpretation of the requirements is often complicated. The summary given in this appendix is based on summaries given in appendix F in the aircraft design books by Raymer,[1] Torenbeek,[2] and Roskam.[3] Table C-1 summarizes the various FAR Parts that most directly influence configuration aerodynamics work. The specific requirements depend on the particular type of airplane.

Category	Various	Normal	Transport
Airworthiness standards airplanes	Part 23	Part 23	Part 25
Airworthiness standards engines	Part 33	Part 33	Part 33
Airworthiness standards propellers	Part 35	Part 35	Part 35
Noise (prop driven: App. F)	Part 36	Part 36	Part 36
General operating & flight rules	Part 91	Part 91	Part 91
Operations: Domestic, large a/c	-	-	Part 121
Air travel clubs using large a/c	-	-	Part 123
Air taxi & commuter operators	-	Part 121*	-
Agricultural aircraft	Part 137	-	-

*Table C-1: FAR parts directly applicable to design. (*Formerly Part 135; from Torenbeek, then Raymer, p. 803)*

Characteristic	Small		Generally large
	Various (normal, utility, acrobatic and agricultural; from Torenbeek, then Raymer, App. F; see FARs for details.) **Part 23**	**Normal** **Part 23**	**Transport** **Part 25**
Max TOGW	≤ 12,500 lb	≤ 12,500	-
No. of engines	one or more	two or more	two or more
Type of engine	all types	props only	all types
Flight crew	one or more	two	two or more
Cabin attendants	none	< 20 pass: none ≥ 20 pass: one	< 10 pass: none ≥ 10 pass: ≥ 1
Max no. of pass.	10	11-23	unlimited
Max altitude	25,000 ft	25,000 ft	unlimited

Table C-2: Categorizing aircraft—FAA criteria synopsis

With the type of airplane defined above, the various requirements are summarized in the following tables.

Table C-3 defines takeoff requirements, and table C-4 defines the so-called "balanced field length" requirement. For early design studies, the balanced field length is usually determined without allowing for a stop way past the end of runway.

Item	MIL-C5011A	FAR Part 23	FAR Part 25
Velocity	$V_{TO} \geq 1.1\ V_s$ $V_{CL} \geq 1.2\ V_s$	$V_{TO} \geq 1.1\ V_s$ $V_{CL} \geq 1.1\ V_s$	$V_{TO} \geq 1.1\ V_s$ $V_{CL} \geq 1.2\ V_s$
Climb gradient	Gear up: 500 fpm @SL (AEO) 100 fpm @ SL (OEI)	Gear up: 300 fpm @SL (AEO)	Gear up: 3% @ V_{CL} (OEI) Gear down: 1/2% @ V_{TO}
Field-length definition	Takeoff distance over 50-ft obstacle	Takeoff distance over 50-ft obstacle	115% of takeoff distance with AEO over 35-ft obstacle or balanced field length (see discussion in table C-4)
Rolling coef.	$\mu = 0.025$	not specified	not specified

V_s: stall speed
V_{TO}: takeoff velocity
V_{CL}: climb velocity
AEO: all engines operating
OEI: one engine inoperative
From Nicolai and Carichner,[4] p. 257; see also Raymer, App. F., p. 804.

Table C-3: Takeoff requirements

Following engine failure, at decision speed V_1 ($1.1V_{stall}$) either:

1. Continue the takeoff (including obstacle clearance), or
2. Stop.

If $V > V_1$, takeoff

If $V < V_1$, stop

- V1 chosen such that distance for both is equal
- Details require precise takeoff speed definitions (see Sean Lynn's report, "Aircraft Takeoff Analysis in the Preliminary Design Phase," on our website or the FARs)
- Assume a smooth, hard, dry runway

Table C-4: Balanced field length (takeoff) (called critical field length for military aircraft)

Table C-5 defines the second segment climb and the associated one-engine inoperative (OEI) requirement, which applies to climbs from 35 feet to 400 feet above ground level for engine failure at V_2, the airspeed at the 35-feet height point, with flaps in the takeoff position and landing gear retracted. Note that $V_2 > 1.2$ Vs in takeoff configuration or $V_2 > 1.1\ V_{mc}$ where V_{mc} represents the minimum control speed in the engine-out condition.

# of engines	Climb gradient (CGR)
4	3%
3	2.7%
2	2.4%

Table C-5: Second segment climb requirement

Table C-6 defines the requirements for landing, which are similar to the takeoff requirements. Table C-7 defines the requirements for a missed approach. Table C-8 defines typical reserve fuel requirements used in design. Note that the ATA standards are actually more rigorous than the FARs. Table C-9 provides a brief summary of the stability and control issues. In certifying an airplane, the stability and control requirements and handling quality requirements are extremely rigorous and are becoming more so with every accident that occurs on existing airplanes.

Item	MIL-C5011A (Military)	FAR Part 23 (Civil)	FAR Part 25 (Commercial)
Velocity	$V_{App} > 1.2\ V_S$ $V_{TD} > 1.1\ V_S$	$V_{App} > 1.3\ V_S$ $V_{TD} > 1.15\ V_S$	$V_{App} > 1.3\ V_S$ $V_{TD} > 1.15\ V_S$
Field-length definition	Landing distance over 50-ft obstacle	Landing distance over 50-ft obstacle	Landing distance over 50-ft obstacle divided by 0.6
Braking coefficient	$\mu = 0.30$	not specified	not specified
Also note that the max stall speed for a Part 23 airplane is 61 kts.			
From Nicolai and Carichner[5]; see also Raymer, App. F., p. 804.			

Table C-6: CTOL landing requirements

# of engines	Climb gradient (CGR)
4	2.7%
3	2.4%
2	2.1%

Table C-7: Missed approach requirement

FAR part 121 and ATA standards (more stringent than part 121)

- Domestic operations
    - Fly one hour at end of cruise fuel flow for 99% max range.
    - Execute missed approach, climb out, and fly to alternate airport 200 NM away.
- International operations
    - Fly 10% of trip time at normal cruise altitude at fuel flow for 99% max range.
    - Execute a missed approach, climb out, and fly to alternate airport 200 NM away.
- Flight to alternate airport
    - Cruise thrust for 99% max range, then hold at greater of max. endurance or min. speed for comfortable handling.
    - Cruise at BCA unless greater than climb/descent distance.
- Approximation often used in very early stages of design studies:
    - Add 400 to 600 NM to design range.

Table C-8: Reserve fuel requirements

FAR requirements are qualitative only.

MIL-STD-1797A (was MIL-SPEC-8785) is used to establish quantitative guidelines for control power requirements and handling qualities.

Good flying qualities depend on good nonlinear aerodynamics (stall characteristics):

- In early design, before wind tunnel and flight test, draw on lessons from the past (Stinton's *Flying Qualities* book is a good place to start).
- Expect a lot of effort to go into getting this right.

Table C-9: Stability and control

You must carefully examine FAR Part 25 (https://www.ecfr.gov/current/title-14/chapter-I/subchapter-C/part-25) for more complete requirements.

C.1 Light Sport Aircraft (LSA)

Another category of aircraft are now governed by the FAA. Light sport aircraft are intended to make it easier for people to fly airplanes for fun. These aircraft have much simpler, but restrictive, certification requirements. In particular, the max stall speed is 45 kts (52 mph). The maximum weight is 1,320 pounds for land-based airplanes and 1,430 pounds for seaplanes (although several companies seem to have gotten waivers to allow for slightly higher weights). See https://www.ecfr.gov/current/title-14/chapter-I/subchapter-C/part-23 for more details.

Notes

1. Raymer, D. P., *Aircraft Design: A Conceptual Approach*, 4th ed., AIAA, Reston, 2006.
2. Torenbeek, E., *Synthesis of Subsonic Airplane Design*, Kluwer, Dordrecht, 1982.
3. Roskam, J., *Airplane Design: Part VII. Determination of Stability, Control, and Performance Characteristics: FAR and Military Requirements*, DARCorp, Lawrence, KS, 1988.
4. Nicolai, L. M., and Carichner, G. E., *Fundamentals of Aircraft Design*, AIAA, Reston, 2010.
5. Nicolai, L. M., and Carichner, G. E., *Fundamentals of Aircraft Design*, AIAA, Reston, 2010.

Appendix D: Examples of Aerodynamic Design

D.1 Overview of Case Studies

This appendix provides examples of the procedures and computational aerodynamics tools for aerodynamic design. We include three case studies: (i) the B-2 in section D.2; (ii) comparisons of the Beech Starship and the Grumman X-29 in section D.3; and (iii) the YF-22 and YF-23 ATF candidate designs in section D.3 that were performed by student teams. The case studies illustrate many of the issues facing configuration aerodynamicists, tying together a number of aspects of aerodynamic theory and applications that are covered in the course. The results obtained in the term projects described in this appendix have been highly instructive to both student and teacher. They provided the students with an opportunity to examine real-world problems. Portions of these examples have been discussed previously in the AIAA paper, "Applied Computational Aerodynamics Case Studies."[1] A key component of these case studies is the need to gather information. Students must read the literature and get to know the sorts of reports that are available. This means using NASA and AIAA literature, as well as AGARD and news-type publications (*Aviation Week*, *Interavia*, *Air International*, etc.).

The examples are provided in considerable detail. We show use of the simple tools listed in appendix E because our focus is on aerodynamic analyses typical of early conceptual and preliminary design work. The input datasets for the simple computational tools almost always mimic the old "punched card" input styles, *requiring* that the values in the datasets be placed in specific fields. Although students aren't used to this style, I don't see a problem; it's any easy adjustment. When making calculations, it is always important to assess whether the code is giving the "right" answer by conducting the infamous "sanity check." These examples should help students examine results in their own work. Finally, many aerospace engineers are heavy users of computational methods. While some will modify existing codes, only a handful of graduates will develop entirely new algorithms and codes. The examples contained here depict the typical work of an aerodynamic engineer/designer.

The case studies presented in this appendix show that a significant number of issues associated with configuration aerodynamics can be resolved without expensive CFD calculations. Students can get considerable insight and make good sanity checks against much more sophisticated codes using a PC. However, other aspects of the problem require the use of sophisticated CFD methods. Still other aspects require wind tunnels or flight tests at present. The role of each is identified through the use of these projects. These projects require an assessment intended to improve the student's ability for "critical thinking."

D.2 The B-2 Study

The B-2 was unveiled in late November of 1988. This example was used as a class project in spring 1989. The statement of the assignment is given in table D-1.

Using the best available information (*Aviation Week*, *Flight International*, *Popular Science*, etc.), analyze the B-2 and provide an evaluation of the aircraft. Complete at least the following:

1. Develop a geometry model of the B-2 for use in analysis and design.
2. Estimate C_{D0} for the B-2.
3. Find and plot the spanload assuming an untwisted wing. What is the span *e* for this case?
4. Plot the section C_l distribution. Where will the wing stall first? Do you see a problem?
5. What would you do to improve the spanload? Plot and analyze a twist distribution that will improve *e*. Plot the new spanload and compute "*e*."
6. Estimate L/D_{max} and the C_L required to fly at L/D_{max}. Comment on the implications for the operation of the B-2. What can you say about the B-2 in comparison with conventional aircraft?
7. Determine the neutral point of the B-2. Examine the available information, and estimate the static margin. Does your conclusion make sense?

Table D-1: B-2 study questions

Several other aspects of the design are required. For example, it also requires an estimate of the CG of the B-2, although this wasn't explicitly stated. Some students were surprised that the static margin required both the neutral point and the CG, since they weren't given the CG.

D.2.1 Develop a Geometry Model of the B-2 for Use in Analysis and Design

Initial specific sources of information included the *Aviation Week* story[2] and the first three-view of the B-2 which appeared in *Air International*.[3] The three-view was important. The side view allowed the students to estimate the CG by assuming a 15° angle from the landing gear ground contact to the CG location. Figure D-1 shows a three-view from Wikipedia. However, students used one from *Janes All the World Aircraft* that Jane's had created based on the information available at that time. The lecture by Waaland[4] and the Aerofax book[5] were not yet available when this example was done.

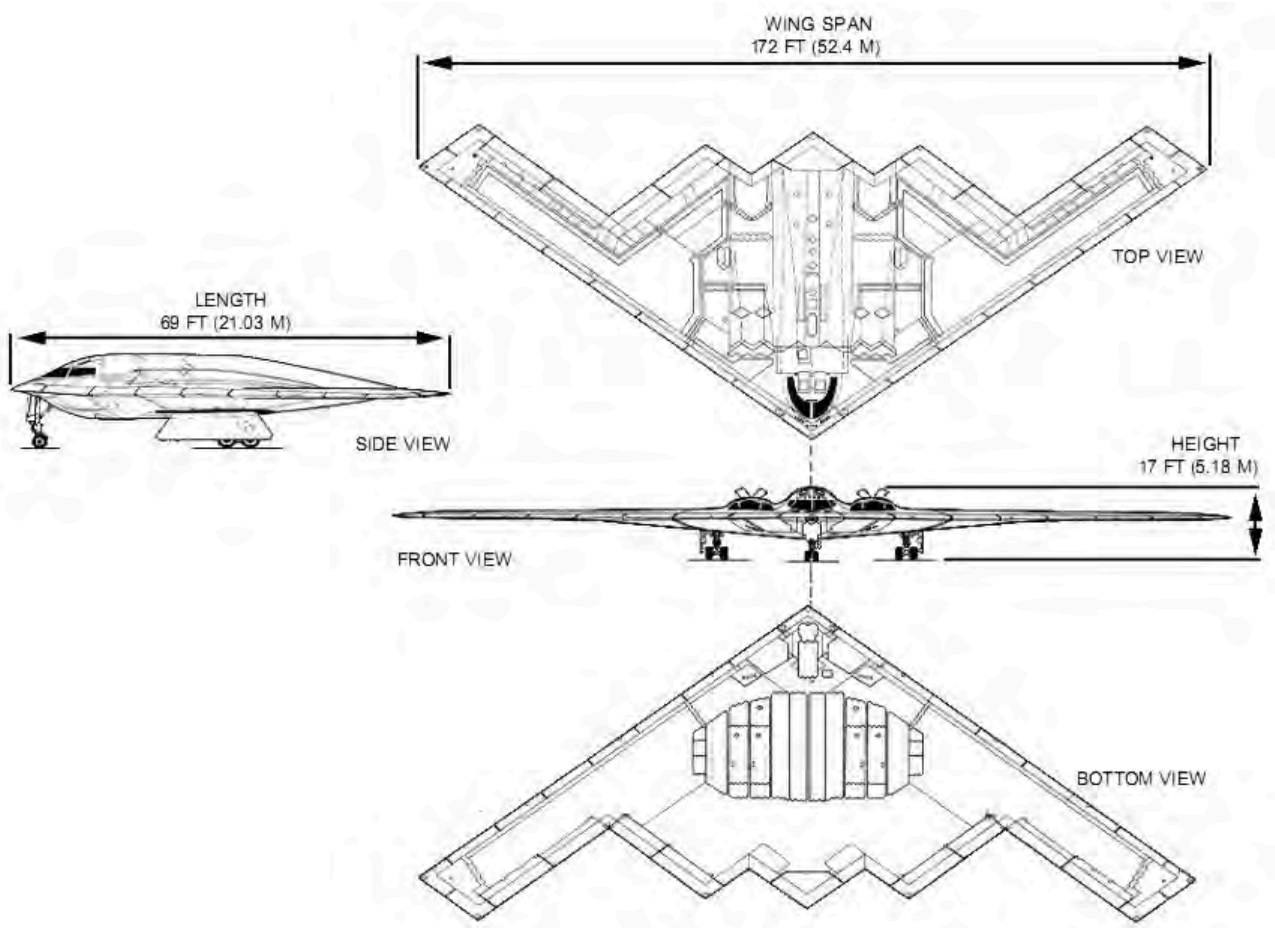


Figure D-1: Drawing of the B-2A. From US Army. Wikimedia. Public domain.

The numerical values of the so-called corner points measured from the top view are shown in figure D-2. Many students can't quite believe that engineers would be expected to scale a drawing to get quantitative values to develop a computational model. The integral properties were then found using the WingPlanAnal code. Table D-2 contains the input dataset, and table D-3 contains the output from the code.

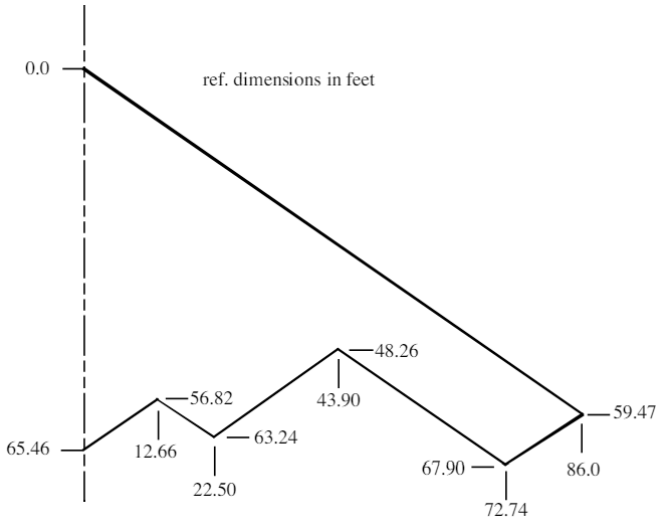


Figure D-2: Idealization of B-2 for aerodynamic analysis

```
B-2 Planform
2.0  Number of LE pts
 YL          XL
  0.0         0.00
 86.0        59.47
 6.0          Number of TE pts
 YT          XT
 0.00        65.46
 12.66       56.82
 22.50       63.24
 43.90       48.26
 72.74       67.90
 86.00       59.47
end of data
```

Table D-2: Input data set for WingPlanAnal

```
   WingPlanAnal
   Wing Planform Geometry Analysis
   Virginia Tech Aircraft Design Software Series
   W.H. Mason, Department of Aerospace and Ocean Engineering
   Virginia Tech, Blacksburg, VA 24061, email: whmason@vt.edu
   version: January 22, 2006
   Planform Properties

Enter name of data set:

B2plan.inp

   Input Case Title:  B-2 Planform
   Planform Points

       Leading Edge     iLM =  2

         i        YLE            XLE
         1        0.0000         0.0000
         2       86.0000        59.4700

       Trailing Edge     iTM =  6

         i        YTE            XTE
         1        0.0000        65.4600
         2       12.6600        56.8200
         3       22.5000        63.2400
         4       43.9000        48.2600
         5       72.7400        67.9000
         6       86.0000        59.4700

    Interpolated LE and TE points and sweep

      i       eta        y       XLE  LE sweep(deg)   XTE  TE sweep(deg)
      0     0.000    0.000     0.000     34.664     65.460    -34.312
      1     0.050    4.300     2.974     34.664     62.525    -34.312
      2     0.100    8.600     5.947     34.664     59.591    -34.312
. . . Intermediate values omitted to keep table to a single page . . .
     19     0.950   81.700    56.497     34.664     62.204    -32.446
     20     1.000   86.000    59.470     34.664     59.470    -32.446

    Integral Quantities
        Planform Area            =  5039.31300
        Mean Aerodynamic Chord   =    39.24220
        X-Centroid               =    39.75905
        Spanwise position of MAC =    29.12163
        X-Leading Edge of MAC    =    20.13795
        Quarter Chord of MAC     =    29.94850
        Aspect Ratio             =     5.87064
        Average Chord            =    29.29833
        Taper Ratio              =     0.00000
```

Table D-3: WingPlanAnal output

Note that the results based on measuring the published drawing are very close to the values for leading- and trailing-edge sweep angles given in the literature, which are 35°. Recall that this is a stealth airplane using parallel edge alignment; see appendix B, section "Fifteen Minutes of Stealth."

D.2.2 Estimate C_{D_0} for the B-2

To estimate C_{D_0}, the planform is broken up into strips, as shown in figure D-3. The average chord of each strip and the associated wetted area is then estimated. To obtain this data, we can use the option in the WingPlanAnal computer program to get the leading- and trailing-edge *x* values at a prescribed value of the span (span locations not explicitly shown above in figure D-2).

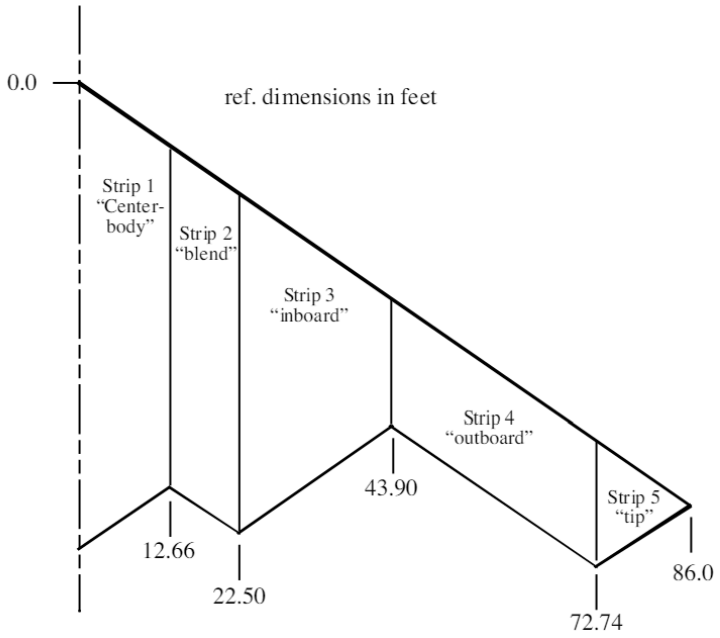


Figure D-3: Strips used in estimating the skin friction drag

As each of the strips is a trapezoid, some side calculations were made to find the area of each strip. This was then multiplied by four to include the top and bottom of the surface as well as the area of the "other" side of the planform. The results are contained in the input dataset for the FRICTION computer program, as shown in table D-4. It would be illustrative for students to compute the values contained in the table for themselves.

```
 B-2 airplane
5046.4    1.          5.          0.0
 CenterBody           2916.11     56.763     .25000     0.0        0.0
 Blending section     1903.20     47.873     .160       0.0        0.0
 Inboard Wing         2834.91     32.792     .12000     0.0        0.0
 Outboard Wing        2068.12     17.751     .12000     0.0        0.0
 Tip section           471.33     11.733     .080       0.0        0.0
     0.400    00.000
     0.780    20.000
     0.780    37.000
     0.780    40.000
     0.000     0.000
```

Mach number

altitude in Kft.

wetted area top/bottom both planform sides

reference length

t/c

klue for "wing" type surface

transition at LE (all turbulent)

see **FRICTION** manual for details

Table D-4: Input for program FRICTION

Using table D-4 as the input to the FRICTION program, table D-5 contains the output of the program.

```
Enter name of data set:
B2friction.inp
     FRICTION - Skin Friction and Form Drag Program
     W.H. Mason, Department of Aerospace and Ocean Engineering
     Virginia Tech, Blacksburg, VA 24061 email:whmason@vt.edu
     version:   Jan. 28, 2006
     CASE TITLE: B-2 airplane
     SREF =  5046.40000  MODEL SCALE =  1.000  NO. OF COMPONENTS = 5
     input mode =  0  (mode=0: input M,h;  mode=1: input M, Re/L)
    COMPONENT TITLE    SWET (FT2)  REFL(FT)   TC  ICODE FRM FCTR FTRANS
     CenterBody        2916.1101   56.763   0.250   0   2.0656   0.0000
     Blending sectio   1903.2000   47.873   0.160   0   1.4975   0.0000
     Inboard Wing      2834.9100   32.792   0.120   0   1.3447   0.0000
     Outboard Wing     2068.1201   17.751   0.120   0   1.3447   0.0000
     Tip section        471.3300   11.733   0.080   0   1.2201   0.0000

TOTAL SWET =   10193.6700

REYNOLDS NO./FT =0.284E+07   Altitude =      0.00   XME =  0.400

COMPONENT        RN         CF      CF*SWET   CF*SWET*FF    CDCOMP
     CenterBody      0.161E+09  0.00191  5.58320    11.53280   0.00229
     Blending sectio 0.136E+09  0.00196  3.73024     5.58617   0.00111
     Inboard Wing    0.931E+08  0.00207  5.85818     7.87771   0.00156
     Outboard Wing   0.504E+08  0.00226  4.66880     6.27831   0.00124
     Tip section     0.333E+08  0.00240  1.13164     1.38071   0.00027
                                  SUM =20.97207    32.65570   0.00647

    FRICTION DRAG: CDF = 0.00416          FORM DRAG: CDFORM = 0.00232

  REYNOLDS NO./FT =0.308E+07   Altitude =  20000.00   XME =  0.780

    COMPONENT        RN         CF      CF*SWET   CF*SWET*FF    CDCOMP
  CenterBody      0.175E+09  0.00183  5.33262    11.01519   0.00218
  Blending sectio 0.148E+09  0.00187  3.56296     5.33565   0.00106
  Inboard Wing    0.101E+09  0.00197  5.59596     7.52510   0.00149
  Outboard Wing   0.547E+08  0.00216  4.46050     5.99820   0.00119
  Tip section     0.362E+08  0.00229  1.08127     1.31925   0.00026
                               SUM =20.03331    31.19339   0.00618

  FRICTION DRAG: CDF = 0.00397          FORM DRAG: CDFORM = 0.00221

  REYNOLDS NO./FT =0.172E+07   Altitude =  37000.00   XME =  0.780

    COMPONENT        RN         CF      CF*SWET   CF*SWET*FF    CDCOMP
  CenterBody      0.979E+08  0.00198  5.78279    11.94508   0.00237
  Blending sectio 0.825E+08  0.00203  3.86697     5.79093   0.00115
  Inboard Wing    0.565E+08  0.00215  6.08509     8.18284   0.00162
  Outboard Wing   0.306E+08  0.00235  4.86635     6.54396   0.00130
  Tip section     0.202E+08  0.00251  1.18243     1.44268   0.00029
                               SUM =21.78364    33.90549   0.00672

  FRICTION DRAG: CDF = 0.00432          FORM DRAG: CDFORM = 0.00240


  REYNOLDS NO./FT =0.149E+07   Altitude =  40000.00   XME =  0.780

    COMPONENT        RN         CF      CF*SWET   CF*SWET*FF    CDCOMP
  CenterBody      0.848E+08  0.00202  5.90243    12.19220   0.00242
  Blending sectio 0.715E+08  0.00207  3.94782     5.91200   0.00117
  Inboard Wing    0.490E+08  0.00219  6.21538     8.35805   0.00166
  Outboard Wing   0.265E+08  0.00241  4.97476     6.68974   0.00133
  Tip section     0.175E+08  0.00257  1.20950     1.47571   0.00029
                               SUM =22.24990    34.62771   0.00686

  FRICTION DRAG: CDF = 0.00441          FORM DRAG: CDFORM = 0.00245
```

```
SUMMARY
 J    XME      Altitude      RE/FT       CDF      CDFORM    CDF+CDFORM
 1   0.400   0.000E+00    0.284E+07   0.00416   0.00232    0.00647
 2   0.780   0.200E+05    0.308E+07   0.00397   0.00221    0.00618
 3   0.780   0.370E+05    0.172E+07   0.00432   0.00240    0.00672
 4   0.780   0.400E+05    0.149E+07   0.00441   0.00245    0.00686

END OF CASE
```

Table D-5: FRICTION output for the B-2.

The values of skin friction are relatively low, reflecting the small multiplier of wetted to reference area, and rather large Reynolds numbers. Note that the value changes with altitude, where the Reynolds number decreases as the altitude increases, so that the skin friction increases.

D.2.3 Find and Plot the Spanload Assuming an Untwisted Wing

To find the untwisted spanload and the span efficiency, *e*, for this case, we start by using the VLMpc program to compute the spanload. This calculation also provides other useful information. Table D-6 contains the input dataset. The output of this code is rather lengthy, and we will provide only the key parts of it in table D-7, which is split in three parts: Geometry Data (Part 1), Aerodynamic Data (Part 2), and Complete Configuration Characteristics (Part 3) .

```
ANALYSIS OF THE B-2: AIR INTERNATIONAL GEOMETRY
1.        1.        1.0000    5040.1    0.0
 6.       0.        0.        -0.00
  0.00      0.00    0.0       1.
-59.47    -86.00    0.        1.
-67.90    -72.74    0.        1.
-48.26    -43.90    0.        1.
-63.24    -22.50    0.        1.
-56.82    -12.66    0.        1.
-65.46      0.00
  1.   8. 20.   .30 1.   0.   0.   0.            0.
end of data
```

Table D-6: Input to VLMpc for the B-2

vortex lattice aerodynamic computation program
nasa-lrc no. a2794 by j.e. lamar and b.b. gloss

modified for watfor77 with 72 column output

ANALYSIS OF THE B-2: AIR INTERNATIONAL GEOMETRY

geometry data

reference planform has 6 curves

center of gravity = 0.00000
root chord height = 0.00000
variable sweep pivot position x(s) = 0.00000 y(s) = 0.00000

break points for the reference planform

point	x ref	y ref	sweep angle	dihedral angle	move code
1	0.00000	0.00000	34.66431	0.00000	1
2	-59.47000	-86.00000	-32.44602	0.00000	1
3	-67.90000	-72.74000	34.25482	0.00000	1
4	-48.26000	-43.90000	-34.99203	0.00000	1
5	-63.24000	-22.50000	33.12201	0.00000	1
6	-56.82000	-12.66000	-34.31215	0.00000	1
7	-65.46000	0.00000			

configuration no. 1.

curve 1 is swept 34.66431 degrees on planform 1

break points for this configuration

point	x	y	z	sweep angle	dihedral angle	move code
1	0.00000	0.00000	0.00000	34.66431	0.00000	1
2	-59.47000	-86.00000	0.00000	-32.44603	0.00000	1
3	-67.90000	-72.74000	0.00000	34.25482	0.00000	1
4	-48.26000	-43.90000	0.00000	-34.99203	0.00000	1
5	-63.24000	-22.50000	0.00000	33.12201	0.00000	1
6	-56.82000	-12.66000	0.00000	-34.31215	0.00000	1
7	-65.46000	0.00000	0.00000			

160 horseshoe vortices used on the left half of the configuration

planform	total	spanwise
1	160	20

8. horseshoe vortices in each chordwise row

aerodynamic data

configuration no. 1.

static longitudinal aerodynamic coefficients are computed

panel no.	x c/4	x 3c/4	y	z	s
1	-58.07243	-58.25077	-83.85000	0.00000	2.15000
2	-58.42913	-58.60748	-83.85000	0.00000	2.15000
3	-58.78583	-58.96418	-83.85000	0.00000	2.15000
4	-59.14253	-59.32088	-83.85000	0.00000	2.15000
5	-59.49923	-59.67758	-83.85000	0.00000	2.15000
6	-59.85593	-60.03428	-83.85000	0.00000	2.15000
7	-60.21263	-60.39098	-83.85000	0.00000	2.15000
8	-60.56933	-60.74768	-83.85000	0.00000	2.15000
9	-55.27727	-55.81232	-79.55000	0.00000	2.15000
10	-56.34737	-56.88243	-79.55000	0.00000	2.15000

details for panels 11 – 150 omitted

151	-48.76898	-52.32695	-6.21000	0.00000	2.15000
152	-55.88493	-59.44291	-6.21000	0.00000	2.15000
153	-3.36223	-7.27916	-2.03000	0.00000	2.03000
154	-11.19608	-15.11301	-2.03000	0.00000	2.03000
155	-19.02994	-22.94687	-2.03000	0.00000	2.03000
156	-26.86379	-30.78072	-2.03000	0.00000	2.03000
157	-34.69764	-38.61457	-2.03000	0.00000	2.03000
158	-42.53149	-46.44842	-2.03000	0.00000	2.03000
159	-50.36535	-54.28228	-2.03000	0.00000	2.03000
160	-58.19920	-62.11613	-2.03000	0.00000	2.03000

panel no.	x	c/4 sweep angle	dihedral angle	local alpha in rad	delta cp at cl=
1	-58.07243	33.02525	0.00000	0.00000	6.76335
2	-58.42913	25.83288	0.00000	0.00000	3.38737
3	-58.78583	17.65210	0.00000	0.00000	2.47320
4	-59.14253	8.66031	0.00000	0.00000	1.92850
5	-59.49923	-0.77887	0.00000	0.00000	1.49911
6	-59.85593	-10.17633	0.00000	0.00000	1.12121
7	-60.21263	-19.05540	0.00000	0.00000	0.77637
8	-60.56933	-27.08142	0.00000	0.00000	0.44514
9	-55.27727	33.02528	0.00000	0.00000	4.80733
10	-56.34737	25.83291	0.00000	0.00000	2.30310

details for panels 11 – 150 omitted

151	-48.76898	-20.90222	0.00000	0.00000	0.27079
152	-55.88493	-28.97129	0.00000	0.00000	0.15599
153	-3.36223	32.96642	0.00000	0.00000	1.78805
154	-11.19608	25.49311	0.00000	0.00000	1.04392
155	-19.02994	16.96595	0.00000	0.00000	0.78870
156	-26.86379	7.59467	0.00000	0.00000	0.61722
157	-34.69764	-2.19983	0.00000	0.00000	0.48021
158	-42.53149	-11.86856	0.00000	0.00000	0.36029
159	-50.36535	-20.90221	0.00000	0.00000	0.24756
160	-58.19920	-28.97129	0.00000	0.00000	0.13405

ref. chord	c average	true area	reference area
1.00000	29.30300	5040.11620	5040.10000

b/2	ref. ar	true ar	mach number
86.00000	5.86972	5.86971	0.30000

complete configuration

cl	computed alpha	lift cl(wb)	induced drag(far field solution) cdi at cl(wb)	cdi/(cl(wb)**2)
1.0000	14.3369	1.0000	0.0569	0.0569

complete configuration characteristics

cl per rad	alpha per deg	cl(twist)	alpha at cl=0	y cp	cm/cl	cmo
3.99639	0.06975	0.00000	0.00000	-0.40049	-32.70269	0.00000

additional loading with cl based on s(true) -at cl des-

stat	2y/b	sl coef	cl ratio	c ratio	load dueto twist	add. load at cl = 0.000	basic load at cl = 0	span load at cl desir	x loc of local cent of press
1	-0.975	0.224	2.299	0.097	0.000	0.000	0.000	0.224	-58.722
2	-0.925	0.439	1.504	0.292	0.000	0.000	0.000	0.439	-57.045
3	-0.873	0.598	1.208	0.495	0.000	0.000	0.000	0.598	-55.211
4	-0.821	0.695	1.156	0.601	0.000	0.000	0.000	0.695	-52.827
5	-0.771	0.750	1.243	0.603	0.000	0.000	0.000	0.750	-50.026
6	-0.721	0.789	1.305	0.604	0.000	0.000	0.000	0.789	-47.160
7	-0.671	0.822	1.356	0.606	0.000	0.000	0.000	0.822	-44.263
8	-0.621	0.853	1.404	0.608	0.000	0.000	0.000	0.853	-41.360
9	-0.571	0.887	1.456	0.609	0.000	0.000	0.000	0.887	-38.476
10	-0.528	0.927	1.519	0.610	0.000	0.000	0.000	0.927	-36.068
11	-0.485	0.998	1.400	0.713	0.000	0.000	0.000	0.998	-34.280
12	-0.435	1.097	1.196	0.917	0.000	0.000	0.000	1.097	-32.620
13	-0.385	1.186	1.058	1.121	0.000	0.000	0.000	1.186	-30.966
14	-0.335	1.263	0.953	1.326	0.000	0.000	0.000	1.263	-29.311
15	-0.286	1.326	0.868	1.527	0.000	0.000	0.000	1.326	-27.677
16	-0.237	1.367	0.839	1.630	0.000	0.000	0.000	1.367	-25.683
17	-0.179	1.392	0.850	1.637	0.000	0.000	0.000	1.392	-22.972
18	-0.122	1.417	0.814	1.741	0.000	0.000	0.000	1.417	-20.779
19	-0.072	1.443	0.743	1.943	0.000	0.000	0.000	1.443	-19.562
20	-0.024	1.460	0.683	2.139	0.000	0.000	0.000	1.460	-18.598

induced drag,leading edge thrust , suction coefficient characteristics computed at the desired cl from a near field solution

section coefficients

station	2y/b	l.e. sweep angle	cdii c/2b	ct c/2b	cs c/2b
1	-0.97500	34.66431	-0.00300	0.00777	0.00945
2	-0.92500	34.66431	-0.00216	0.01153	0.01402
3	-0.87291	34.66431	-0.00114	0.01386	0.01685
4	-0.82081	34.66431	-0.00070	0.01547	0.01880
5	-0.77081	34.66431	-0.00049	0.01645	0.02000
6	-0.72081	34.66431	-0.00058	0.01739	0.02114
7	-0.67081	34.66431	-0.00077	0.01828	0.02222
8	-0.62081	34.66431	-0.00094	0.01913	0.02325
9	-0.57081	34.66431	-0.00090	0.01983	0.02411
10	-0.52814	34.66431	0.00028	0.01952	0.02374
11	-0.48547	34.66431	0.00128	0.02005	0.02438
12	-0.43547	34.66431	0.00282	0.02053	0.02496
13	-0.38547	34.66431	0.00465	0.02059	0.02503
14	-0.33547	34.66431	0.00641	0.02047	0.02488
15	-0.28605	34.66431	0.00804	0.02014	0.02449
16	-0.23663	34.66431	0.00994	0.01913	0.02325
17	-0.17942	34.66431	0.01238	0.01728	0.02101
18	-0.12221	34.66431	0.01519	0.01501	0.01825
19	-0.07221	34.66431	0.01800	0.01274	0.01549
20	-0.02360	34.66431	0.02590	0.00522	0.00634

```
                total coefficients
cdii/cl**2=   0.05620     ct=   0.19392     cs=   0.23577
 end of file encountered after configuration     1.
```

Table D-7: Output of VLMpc for the B-2

The spanload results are shown in figure D-4; for comparison, the elliptic spanload at the same lift coefficient is included in the figure. A useful relation is

$$\frac{cc_l}{c_{\text{avg}}} = \frac{4}{\pi}\sqrt{1-\eta^2}C_L$$

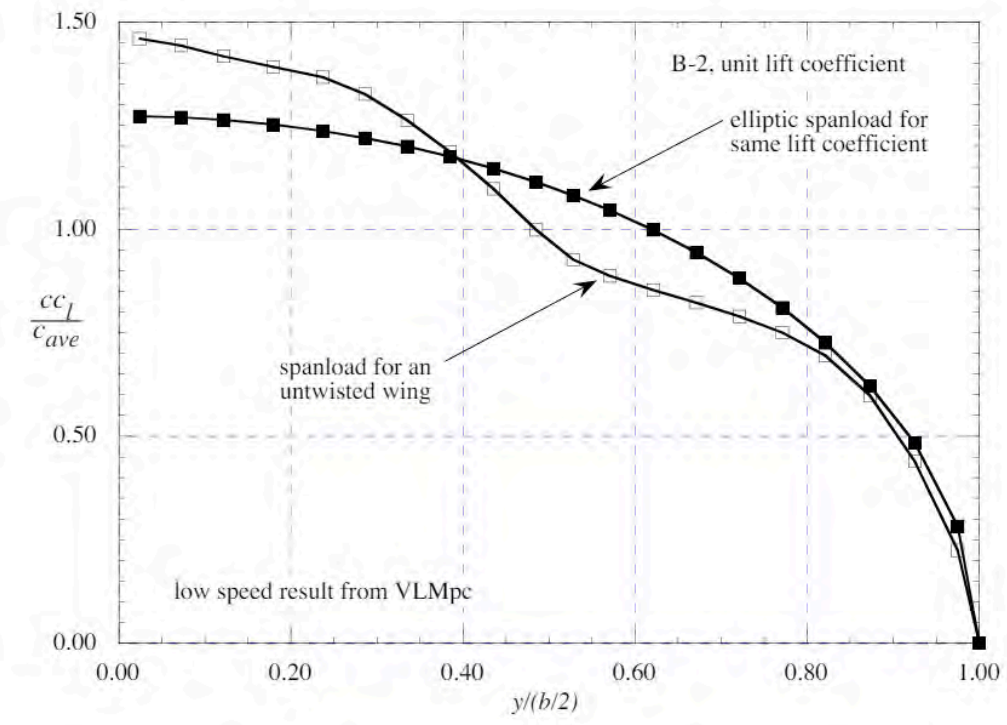


Figure D-4: B-2 untwisted wing spanload compared with an elliptic (minimum induced drag) spanload

With the basic spanload determined, we use the LIDRAG computer code to compute the span efficiency, *e*. This code does a Fourier series analysis. Table D-8 contains the input dataset, and table D-9 provides the output of the program.

```
22.
  0.000    1.461
  0.024    1.460
  0.072    1.443
  0.122    1.417
  0.179    1.392
  0.237    1.367
  0.286    1.326
  0.335    1.263
  0.385    1.186
  0.435    1.097
  0.485    0.998
  0.528    0.927
  0.571    0.887
  0.621    0.853
  0.671    0.822
  0.721    0.789
  0.771    0.750
  0.821    0.695
  0.873    0.598
  0.925    0.439
  0.975    0.224
  1.0      0.000
```

Table D-8: LIDRAG input for the B-2

```
          Program LIDRAG
   enter name of input data file
          B2LIDRAG.inp
LIDRAG - LIFT INDUCED DRAG ANALYSIS

          INPUT SPANLOAD
        N      Y/(B/2)       CCLCA
        1      0.00000      1.46100
        2      0.02400      1.46000
        3      0.07200      1.44300
        4      0.12200      1.41700
        5      0.17900      1.39200
        6      0.23700      1.36700
        7      0.28600      1.32600
        8      0.33500      1.26300
        9      0.38500      1.18600
       10      0.43500      1.09700
       11      0.48500      0.99800
       12      0.52800      0.92700
       13      0.57100      0.88700
       14      0.62100      0.85300
       15      0.67100      0.82200
       16      0.72100      0.78900
       17      0.77100      0.75000
       18      0.82100      0.69500
       19      0.87300      0.59800
       20      0.92500      0.43900
       21      0.97500      0.22400
       22      1.00000      0.00000

Span e =    0.94957     CL =    1.000

Press RETURN to quit the program.
```

Table D-9: LIDRAG output for the B-2

Using the results for the spanload shown in figure D-4 that were obtained using the VLMpc vortex lattice code, a span *e* of 0.95 was found using LIDRAG (see table D-9). Considering the unusual planform and the non-elliptic shape of the spanload, this is a surprisingly high value. Figure D-4 also contains the minimum induced drag (elliptic) spanload.

D.2.4 Plot the Section C_l Distribution. Where will the wing stall first? Do you see a problem?

The output from VLMpc also provides the section lift coefficient distribution. This distribution is presented in figure D-5. This shows what happens when the planform has breaks leading to variations in the chord distribution. Because the spanload naturally tends toward a smooth distribution, the section lift coefficients vary to compensate for smaller chords by increasing C_l. In addition, a pointed tip, where the chord goes to zero, results in the local section lift coefficient becoming large. Locations where section C_l values are high would be locations where the wing would tend to stall first.

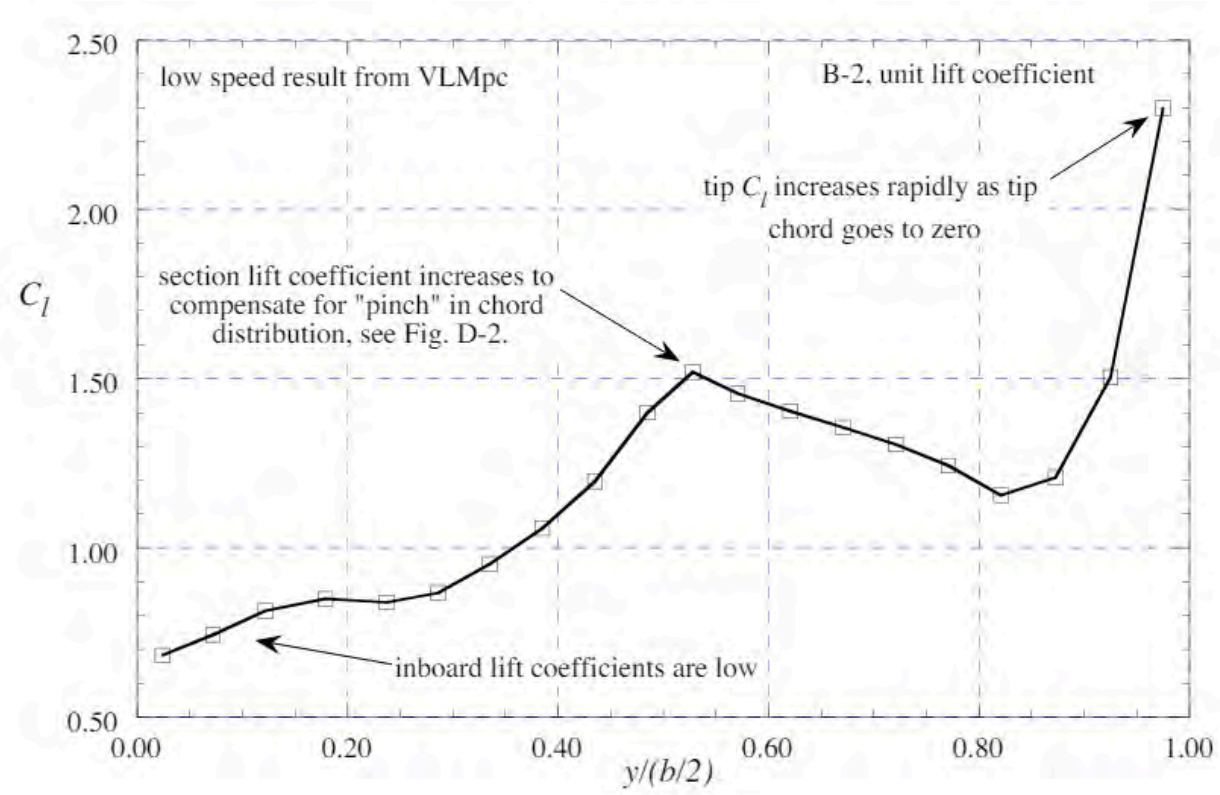


Figure D-5: Spanwise section lift coefficient distribution for the B-2

D.2.5 What would you do to improve the spanload? Plot and analyze a twist distribution that will improve *e*. Plot the new spanload and compute *e*.

The LAMDES program can be used to find the twist distribution required to improve the spanload. Table D-10 contains the LAMDES input dataset, which is quite similar to the VLMpc input.

```
LamarDesign Program - B-2 Planform -
  1.000    -0.000    39.24     5040.0    0.0       0.0       0.0
 6.       0.        0.        -0.00
  0.00      0.00    0.0       1.
-59.47    -86.00    0.        1.
-67.90    -72.74    0.        1.
-48.26    -43.90    0.        1.
-63.24    -22.50    0.        1.
-56.82    -12.66    0.        1.
-65.46      0.00
1.0  16.0 22.  0.78 0.34 40.0  0.0006
 0.65      0.65      1.0       -0.00     1.0
 0.030     1.0       0.0        0.0      0.0       0.0
```

Table D-10: LAMDES input for the B-2

Table D-11 contains the corresponding output. Once again, the output is a lengthy text file, and relatively unimportant portions have been deleted.

```
 enter name of input file:

B2LamDes.inp

  Lamar Design Code     mods by W.H. Mason

  LamarDesign Program - B-2 Planform -

  plan   = 1.0  xmref =   0.0000   cref   = 39.2400
  tdklue = 0.0  case  =   0.0      spnklu = 0.0
  sref   =    5040.0000

           REFERENCE PLANFORM HAS  6 CURVES
         ROOT CHORD HEIGHT =      0.0000

         POINT   X        Y       SWEEP    DIHEDRAL
                 REF      REF     ANGLE     ANGLE
           1   0.0000   0.0000  34.66431   0.00000
           2 -59.4700 -86.0000 -32.44602   0.00000
           3 -67.9000 -72.7400  34.25482   0.00000
           4 -48.2600 -43.9000 -34.99202   0.00000
           5 -63.2400 -22.5000  33.12201   0.00000
           6 -56.8200 -12.6600 -34.31215   0.00000
           7 -65.4600   0.0000

         scw    = 16.0      vic = 22.0
         xitmax = 40.0   epsmax =  0.00060

  CONFIGURATION NO.      1.
  delta ord shift for moment =     0.0000

  CURVE  1 IS SWEPT 34.6643 DEGREES ON PLANFORM  1

   BREAK POINTS FOR THIS CONFIGURATION

 POINT   X        Y        Z       SWEEP  DIHEDRAL
                                   ANGLE    ANGLE
   1   0.0000   0.0000   0.0000  34.6643   0.0000
   2 -59.4700 -86.0000   0.0000 -32.4460   0.0000
   3 -67.9000 -72.7400   0.0000  34.2548   0.0000
   4 -48.2600 -43.9000   0.0000 -34.9920   0.0000
   5 -63.2400 -22.5000   0.0000  33.1220   0.0000
   6 -56.8200 -12.6600   0.0000 -34.3121   0.0000
   7 -65.4600   0.0000   0.0000

     a = 0.000     clmin =  0.000     cd0 =0.0000

     336 HORSESHOE VORTICES USED
    PLANFORM     TOTAL        SPANWISE
       1          336           21

     16. HORSESHOE VORTICES IN EACH CHORDWISE ROW
```

```
      xcfw  = 0.65     xcft   =  0.65      fkon   =   1.00
      ficam = 1.00     punch  =  0.00      crbmnt =   0.000
      cmb   = 0.00     iflag  =   1

      relax = 0.03     fioutw =  1.00      cd0    =   0.0000
      firbm = 0.00     yrbm   =  0.0000    zrbm   =   0.0000


LM = 50  IL = 51  JM = 51  IM = 53  TSPAN = -86.000    TSPANA =   0.000
BOTL =  86.000    BOL  =  0.000     SNN    =  0.8600    DELTYB =  1.7200
NMA(KBOT) = 50    KBOT = 1          NMA(KBIT) =  0     KBIT   =  2

        induced drag cd = 0.00621     pressure drag cdpt = 0.00000

induced drag alone was minimized on this run

ref. chord =    39.240  c average   =    29.3023  true area =   5040.115
ref. area  =  5040.000  b/2         =    86.0000  ref ar    =  5.8698
true ar    =    5.8697  Mach number =     0.7800

      first  planform   cl =   0.34000  cm =  -0.33786  cb =  -0.07251

1st planform   CL = 0.3401   CDP = 0.0000   CM = -0.3381   CB = -0.0726
2nd planform   CL = 0.0000   CDP = 0.0000   CM =  0.0000   CB =  0.0000

no pitching moment or bending moment constraints
      CL DES  = 0.34000    CL COMPUTED =  0.3401    CM = -0.3381
      CD I    = 0.00621    E           =  1.0106
      CDPRESS = 0.00000    CDTOTAL     =  0.00621
```

first planform

Y	CL*C/CAVE	C/CAVE	CL	CD
-84.0455	0.09965	0.08854	1.12552	0.00000
-80.1364	0.16140	0.26559	0.60769	0.00000
-75.4609	0.20992	0.47737	0.43974	0.00000
-70.7854	0.24711	0.60132	0.41094	0.00000
-66.8764	0.27281	0.60272	0.45264	0.00000
-62.9673	0.29506	0.60412	0.48841	0.00000
-59.0582	0.31449	0.60552	0.51936	0.00000
-55.1491	0.33163	0.60693	0.54641	0.00000
-51.2400	0.34686	0.60833	0.57019	0.00000
-46.5927	0.36277	0.60999	0.59472	0.00000
-41.9455	0.37662	0.70378	0.53513	0.00000
-38.0364	0.38678	0.88942	0.43487	0.00000
-34.1273	0.39574	1.07505	0.36811	0.00000
-30.2182	0.40357	1.26069	0.32012	0.00000
-25.3818	0.41176	1.49035	0.27628	0.00000
-20.5455	0.41840	1.62981	0.25672	0.00000
-16.6364	0.42271	1.63503	0.25853	0.00000
-13.6709	0.42533	1.63898	0.25951	0.00000
-10.7055	0.42745	1.73198	0.24680	0.00000
-6.7964	0.42943	1.91527	0.22422	0.00000
-2.4209	0.43063	2.12044	0.20309	0.00000

mean camber lines to obtain the spanload

(subsonic linear theory)

y= -84.0455 y/(b/2) = -0.9773 chord= 2.5943

slopes, dz/dx, at control points, from front to rear

x/c	dz/dx
0.0469	0.2086
0.1094	0.1308
0.1719	0.0843
0.2344	0.0521
0.2969	0.0281
0.3594	0.0090
0.4219	-0.0074
0.4844	-0.0233
0.5469	-0.0412
0.6094	-0.0655
0.6719	-0.1123
0.7344	-0.1436
0.7969	-0.1644
0.8594	-0.1777
0.9219	-0.1812
0.9844	-0.1643

mean camber shape (interpolated to 41 points)

x/c	z/c	delta x	delta z	(z-zle)/c
0.0000	-0.0297	0.0000	-0.0772	0.0000
0.0250	-0.0350	0.0649	-0.0908	-0.0060
0.0500	-0.0403	0.1297	-0.1045	-0.0120
0.0750	-0.0451	0.1946	-0.1171	-0.0176
0.1000	-0.0492	0.2594	-0.1276	-0.0224
0.1250	-0.0524	0.3243	-0.1359	-0.0264
0.1500	-0.0550	0.3891	-0.1427	-0.0297
0.1750	-0.0572	0.4540	-0.1485	-0.0327
0.2000	-0.0591	0.5189	-0.1534	-0.0353
0.2250	-0.0607	0.5837	-0.1575	-0.0376
0.2500	-0.0620	0.6486	-0.1608	-0.0397
0.2750	-0.0630	0.7134	-0.1634	-0.0414
0.3000	-0.0638	0.7783	-0.1654	-0.0429
0.3250	-0.0643	0.8432	-0.1669	-0.0443
0.3500	-0.0647	0.9080	-0.1679	-0.0454
0.3750	-0.0649	0.9729	-0.1684	-0.0463
0.4000	-0.0650	1.0377	-0.1685	-0.0471
0.4250	-0.0648	1.1026	-0.1682	-0.0477
0.4500	-0.0646	1.1674	-0.1675	-0.0482
0.4750	-0.0641	1.2323	-0.1663	-0.0485
0.5000	-0.0635	1.2972	-0.1648	-0.0486
0.5250	-0.0627	1.3620	-0.1627	-0.0486
0.5500	-0.0618	1.4269	-0.1602	-0.0484
0.5750	-0.0606	1.4917	-0.1573	-0.0480
0.6000	-0.0593	1.5566	-0.1537	-0.0474
0.6250	-0.0576	1.6214	-0.1493	-0.0464
0.6500	-0.0554	1.6863	-0.1438	-0.0450
0.6750	-0.0528	1.7512	-0.1369	-0.0431
0.7000	-0.0497	1.8160	-0.1290	-0.0408
0.7250	-0.0464	1.8809	-0.1203	-0.0382
0.7500	-0.0428	1.9457	-0.1109	-0.0353
0.7750	-0.0389	2.0106	-0.1009	-0.0322
0.8000	-0.0349	2.0754	-0.0904	-0.0289
0.8250	-0.0307	2.1403	-0.0795	-0.0255
0.8500	-0.0263	2.2052	-0.0683	-0.0219
0.8750	-0.0219	2.2700	-0.0567	-0.0181
0.9000	-0.0173	2.3349	-0.0449	-0.0143
0.9250	-0.0128	2.3997	-0.0331	-0.0105
0.9500	-0.0083	2.4646	-0.0216	-0.0068
0.9750	-0.0041	2.5294	-0.0107	-0.0034
1.0000	0.0000	2.5943	0.0000	0.0000

y= -80.1364 y/(b/2) = -0.9318 chord= 7.7825

slopes, dz/dx, at control points, from front to rear

x/c	dz/dx
0.0469	0.1194
0.1094	0.0777
0.1719	0.0524
0.2344	0.0340
0.2969	0.0193
0.3594	0.0067
0.4219	-0.0049
0.4844	-0.0165
0.5469	-0.0292
0.6094	-0.0450
0.6719	-0.0725
0.7344	-0.0910
0.7969	-0.1033
0.8594	-0.1110
0.9219	-0.1131
0.9844	-0.1042

mean camber shape (interpolated to 41 points)

x/c	z/c	delta x	delta z	(z-zle)/c
0.0000	-0.0204	0.0000	-0.1587	0.0000
0.0250	-0.0234	0.1946	-0.1821	-0.0035
0.0500	-0.0264	0.3891	-0.2056	-0.0070
0.0750	-0.0292	0.5837	-0.2273	-0.0104
0.1000	-0.0316	0.7783	-0.2456	-0.0132
0.1250	-0.0335	0.9728	-0.2604	-0.0156
0.1500	-0.0351	1.1674	-0.2728	-0.0177
0.1750	-0.0364	1.3619	-0.2835	-0.0196
0.2000	-0.0376	1.5565	-0.2928	-0.0213
0.2250	-0.0386	1.7511	-0.3006	-0.0228
0.2500	-0.0395	1.9456	-0.3071	-0.0242
0.2750	-0.0401	2.1402	-0.3123	-0.0254
0.3000	-0.0407	2.3348	-0.3165	-0.0264
0.3250	-0.0411	2.5293	-0.3196	-0.0273
0.3500	-0.0413	2.7239	-0.3218	-0.0281
0.3750	-0.0415	2.9184	-0.3230	-0.0288
0.4000	-0.0415	3.1130	-0.3232	-0.0293
0.4250	-0.0415	3.3076	-0.3226	-0.0297
0.4500	-0.0413	3.5021	-0.3211	-0.0300
0.4750	-0.0409	3.6967	-0.3187	-0.0302
0.5000	-0.0405	3.8913	-0.3153	-0.0303
0.5250	-0.0400	4.0858	-0.3110	-0.0303
0.5500	-0.0393	4.2804	-0.3057	-0.0301
0.5750	-0.0385	4.4750	-0.2994	-0.0298
0.6000	-0.0375	4.6695	-0.2920	-0.0294
0.6250	-0.0364	4.8641	-0.2829	-0.0287
0.6500	-0.0349	5.0586	-0.2718	-0.0278
0.6750	-0.0332	5.2532	-0.2585	-0.0266
0.7000	-0.0313	5.4478	-0.2433	-0.0251
0.7250	-0.0291	5.6423	-0.2266	-0.0235
0.7500	-0.0268	5.8369	-0.2088	-0.0217
0.7750	-0.0244	6.0315	-0.1899	-0.0198
0.8000	-0.0219	6.2260	-0.1701	-0.0178
0.8250	-0.0192	6.4206	-0.1496	-0.0157
0.8500	-0.0165	6.6152	-0.1285	-0.0134
0.8750	-0.0137	6.8097	-0.1068	-0.0112
0.9000	-0.0109	7.0043	-0.0847	-0.0088
0.9250	-0.0080	7.1988	-0.0626	-0.0065
0.9500	-0.0053	7.3934	-0.0410	-0.0043
0.9750	-0.0026	7.5880	-0.0203	-0.0021
1.0000	0.0000	7.7825	0.0000	0.0000

The similar results at each spanwise station are omitted here

y= -2.4209 y/(b/2) = -0.0282 chord= 62.1337

slopes, dz/dx, at control points, from front to rear

x/c	dz/dx
0.0469	-0.0098
0.1094	-0.0248
0.1719	-0.0325
0.2344	-0.0367
0.2969	-0.0390
0.3594	-0.0402
0.4219	-0.0406
0.4844	-0.0407
0.5469	-0.0410
0.6094	-0.0422
0.6719	-0.0476
0.7344	-0.0509
0.7969	-0.0533
0.8594	-0.0554
0.9219	-0.0569
0.9844	-0.0554

mean camber shape (interpolated to 41 points)

x/c	z/c	delta x	delta z	(z-zle)/c
0.0000	-0.0410	0.0000	-2.5464	0.0000
0.0250	-0.0407	1.5533	-2.5318	-0.0008
0.0500	-0.0405	3.1067	-2.5173	-0.0016
0.0750	-0.0402	4.6600	-2.4978	-0.0023
0.1000	-0.0397	6.2134	-2.4684	-0.0028
0.1250	-0.0391	7.7667	-2.4291	-0.0032
0.1500	-0.0384	9.3201	-2.3834	-0.0035
0.1750	-0.0376	10.8734	-2.3341	-0.0038
0.2000	-0.0367	12.4267	-2.2819	-0.0039
0.2250	-0.0358	13.9801	-2.2270	-0.0041
0.2500	-0.0349	15.5334	-2.1697	-0.0042
0.2750	-0.0340	17.0868	-2.1107	-0.0043
0.3000	-0.0330	18.6401	-2.0504	-0.0043
0.3250	-0.0320	20.1935	-1.9892	-0.0044
0.3500	-0.0310	21.7468	-1.9273	-0.0044
0.3750	-0.0300	23.3001	-1.8648	-0.0044
0.4000	-0.0290	24.8535	-1.8020	-0.0044
0.4250	-0.0280	26.4068	-1.7390	-0.0044
0.4500	-0.0270	27.9602	-1.6759	-0.0044
0.4750	-0.0260	29.5135	-1.6127	-0.0044
0.5000	-0.0249	31.0669	-1.5495	-0.0044
0.5250	-0.0239	32.6202	-1.4860	-0.0044
0.5500	-0.0229	34.1735	-1.4224	-0.0045
0.5750	-0.0219	35.7269	-1.3588	-0.0045
0.6000	-0.0208	37.2802	-1.2946	-0.0044
0.6250	-0.0198	38.8336	-1.2287	-0.0044
0.6500	-0.0187	40.3869	-1.1597	-0.0043
0.6750	-0.0175	41.9403	-1.0870	-0.0042
0.7000	-0.0163	43.4936	-1.0114	-0.0040
0.7250	-0.0150	45.0470	-0.9337	-0.0038
0.7500	-0.0137	46.6003	-0.8543	-0.0035
0.7750	-0.0124	48.1536	-0.7735	-0.0032
0.8000	-0.0111	49.7070	-0.6912	-0.0029
0.8250	-0.0098	51.2603	-0.6076	-0.0026
0.8500	-0.0084	52.8137	-0.5227	-0.0023
0.8750	-0.0070	54.3670	-0.4365	-0.0019
0.9000	-0.0056	55.9204	-0.3489	-0.0015
0.9250	-0.0042	57.4737	-0.2607	-0.0011
0.9500	-0.0028	59.0270	-0.1728	-0.0007
0.9750	-0.0014	60.5804	-0.0861	-0.0004
1.0000	0.0000	62.1337	0.0000	0.0000

twist table

i	y	y/(b/2)	twist
1	-84.04546	-0.97727	1.70360
2	-80.13635	-0.93182	1.16809
3	-75.46091	-0.87745	0.30947
4	-70.78545	-0.82309	-0.00569
5	-66.87636	-0.77763	0.68299
6	-62.96726	-0.73218	1.08198
7	-59.05817	-0.68672	1.41865
8	-55.14908	-0.64127	1.77459
9	-51.23998	-0.59581	2.21565
10	-46.59272	-0.54178	3.50599
11	-41.94546	-0.48774	3.90543
12	-38.03636	-0.44228	2.57660
13	-34.12727	-0.39683	2.07071
14	-30.21818	-0.35137	1.70050
15	-25.38182	-0.29514	1.16032
16	-20.54545	-0.23890	1.13859
17	-16.63636	-0.19345	2.12305
18	-13.67091	-0.15896	3.17933
19	-10.70545	-0.12448	2.84199
20	-6.79636	-0.07903	2.37425
21	-2.42091	-0.02815	2.34680

STOP

Table D-11: LAMDES output for the B-2

Figure D-6 shows the twist distribution required to obtain the minimum drag spanload. This was found using the constant chord-loading approach in LAMDES, which may not be a good assumption for this planform. However, the results are consistent with the changes in spanload required to achieve the $e = 1$ elliptic spanload shown in figure D-4.

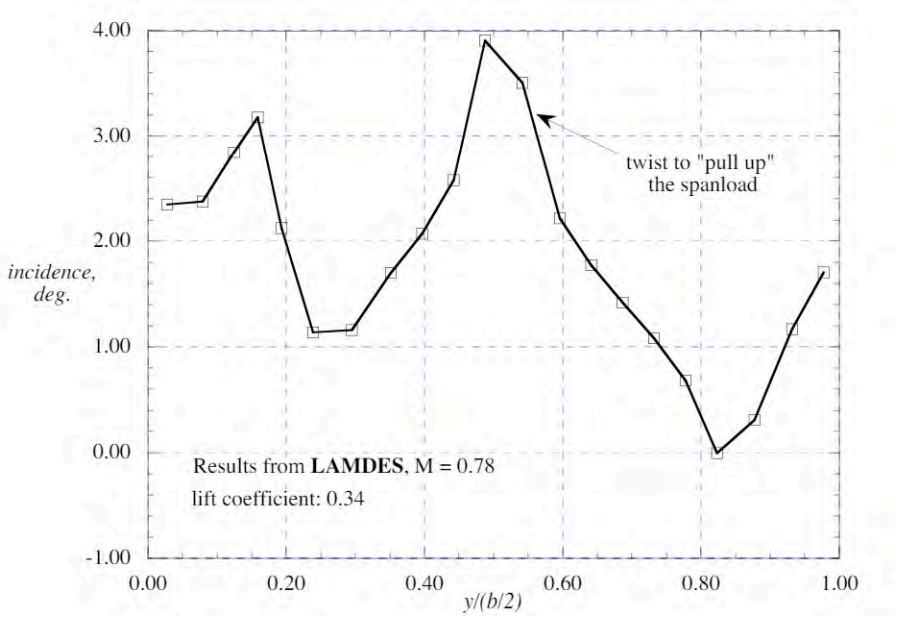


Figure D-6: B-2 Incidence distribution required for minimum induced drag

Assuming that the small chord tip section C_l values shown in figure D-5 will be dominated by viscous effects in general, we see from figure D-6 that wing stall will also occur in the midspan area. To fill in the hole in the spanload for the untwisted wing, the optimized twist distribution actually increases the local lift coefficient. The potential stall problem would be a good reason to accept the $e = .95$ spanload without attempting to completely fill in the spanload distribution.

D.2.6 Estimate L/D_{max} and the C_L required to fly at L/D_{max}. Comment on the implications for the operation of the B-2. What can you say about the B-2 in comparison with conventional aircraft?

Using the results from FRICTION and the spanload data analysis results from LIDRAG, we can make an estimate of the L/D variation with altitude. First, we estimate the C_L requirement as the altitude increases as shown in figure D-7 for $M = 0.78$ and the weight corresponding to the published value of 336,000 lbs. The lift coefficients in the cruise altitude range of 30,000 to 40,000 feet are relatively low compared to typical commercial transports. This is typical of flying wing aircraft.

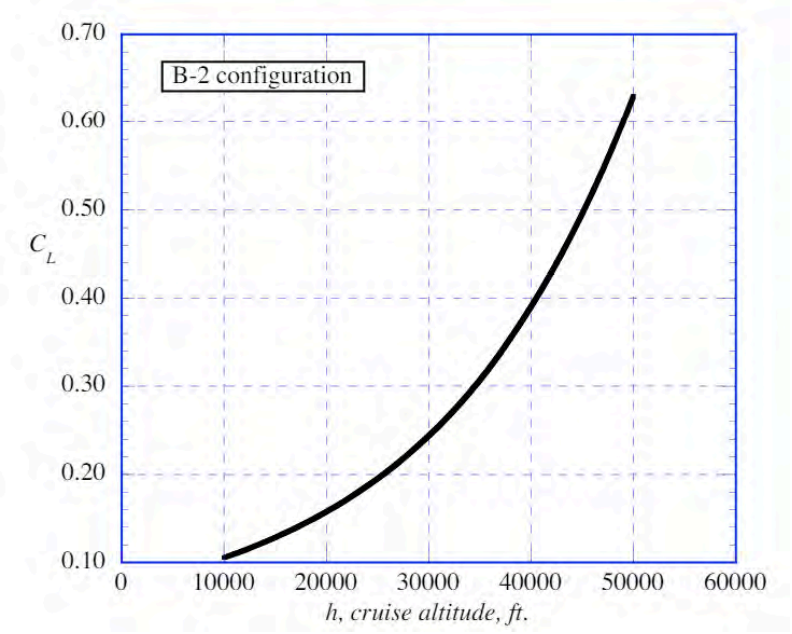


Figure D-7: C_L variation with altitude

Figure D-8 shows the L/D variation with altitude or two different values of C_{D0}, 0.0060 and 0.0080. These plots assume $M = 0.78$ and the weight of 336,000 pounds, which are the same values used for data in figure D-7. Based on the results presented in table D-5, the C_{D0} value of eighty counts is likely close to the value for the B-2 and agrees with the published result of a cruise altitude of 37,000 feet. The value of $(L/D)_{max}$ is slightly greater than twenty-one, which is higher than typical commercial transonic transports. Indeed the B-2 is a very efficient airplane.

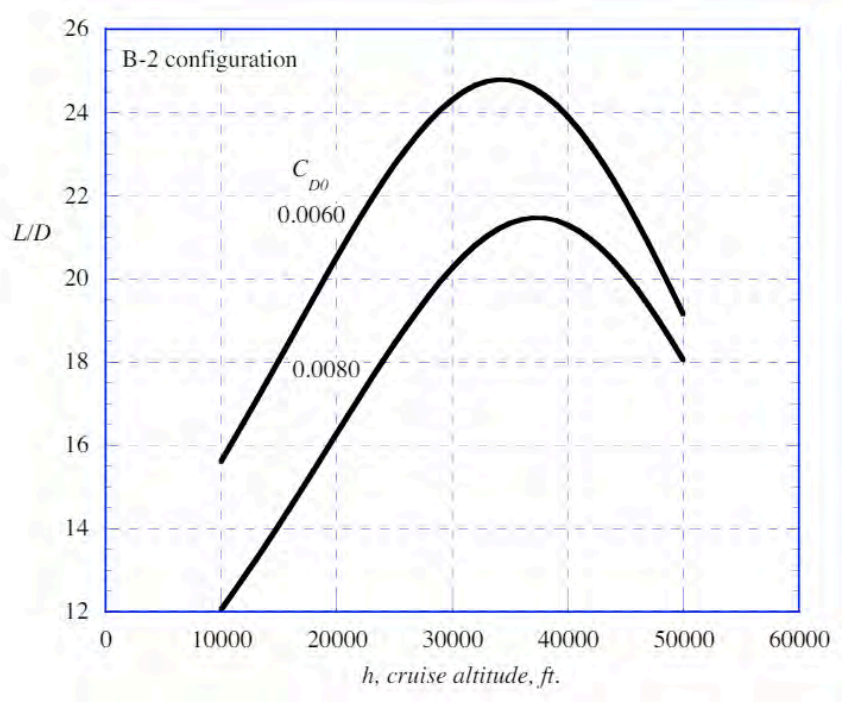


Figure D-8: L/D variation with altitude

D.2.7 Determine the neutral point of the B-2. Examine the available information, and estimate the static margin. Does your conclusion make sense?

Using the side view in figure D-1, the CG location was estimated to be between 32.25 and 36 feet aft of the nose. This was done assuming a 15° angle between the landing gear and the CG location. With the neutral point determined from the vortex lattice method to be 32.7 feet aft of the nose, the low-speed static margin ranges from 1.1% stable to 8.4% unstable. This is in the range that would be expected for an advanced flying wing design.

Using these values, the C_m-C_L curves presented in figures D-9 and D-10 were used to illustrate the setup and advantages of near-neutral or negative static margins compared to classically stable designs. The figures show that the use of modern control system technology, allowing an unstable airplane, plays an important part in the reemergence of the flying wing concept. These figures are based on the paper by Sears.[6]

Figure D-9 illustrates pitching moment trim for a classical stable airplane. We can see that (i) the trim requirements are highly restrictive on C_{Lmax}; (ii) reflexed trailing edges and upward deflection of devices to trim with increasing lift are inefficient; and (iii) sweep with washout of tips is good for both stability and aerodynamic characteristics.

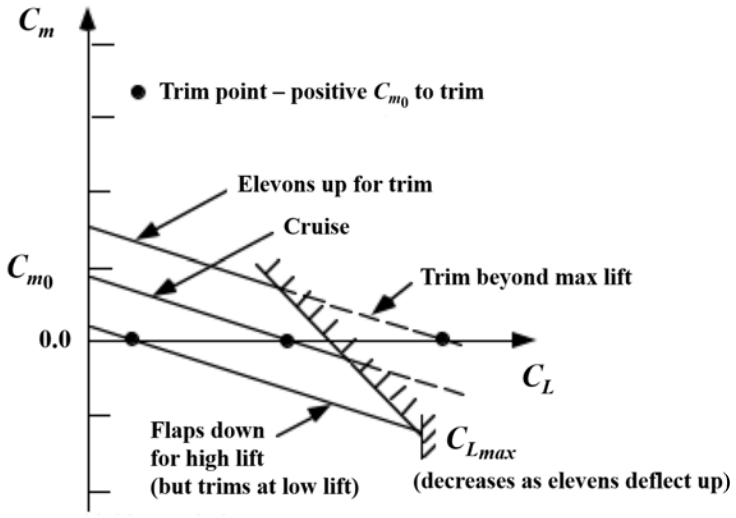


Figure D-9: Pitching moment trim for a classical stable airplane. *From W. H. Mason. Adapted by P. Raj.*

Figure D-10 illustrates pitching moment trim for a neutral-to-unstable airplane, like a flying wing. Note that (i) near-neutral stability means almost self-trimming; (ii) we can use airfoils with negative C_{m0}; and (iii) unstable balance (relaxed static stability) and flying wing concepts are highly complementary, as the trailing edge devices work in the "natural" direction.

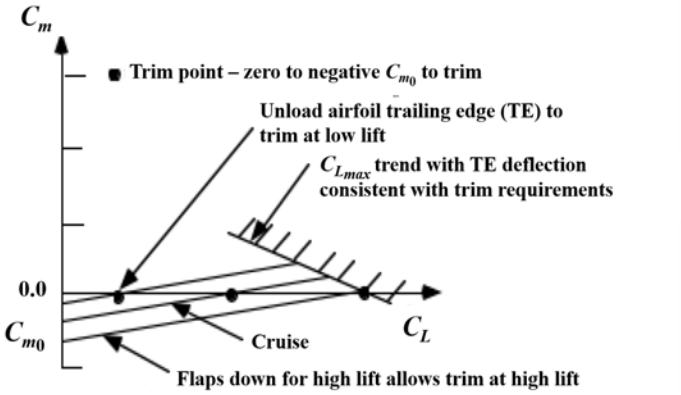


Figure D-10: Pitching moment trim for a neutral-to-unstable airplane. *From W. H. Mason. Adapted by P. Raj.*

The important outcome of studying figures D-9 and D-10 is that a slightly unstable flying wing can trim at higher lift coefficients by deflecting the trailing edges down. This is in the right direction for achieving high lift for takeoff and landing. Thus relaxed static stability plays an important role in making the flying wing a practical concept.

Key Lessons Learned From This Study

- Aerodynamically, the B-2 spanload is surprisingly good considering the unusual planform.
- The students did not revisit the literature of the XB-35/YB-49 program[7,8,9,10] once the project was completed. As a result, they missed an opportunity to fully appreciate the concept and the role of modern technology in improving the feasibility of the concept.

D.3 Comparison of the Beech Starship and X-29

During the period from the late 1970s through the 1990s, canard concepts were popular. Burt Rutan was involved with Beech in developing the Starship. It had been certified when this project was carried out by the students. The objective was to try to understand the configuration concept and canard concepts in general. The Grumman X-29 was a good example of a potential military canard configuration and was used for comparison. The tools used for the B-2 study could be applied to these configurations. Table D-12 summarizes the work. Students were expected to consider available sources of information as needed. Item 6 is representative of a question that your boss might ask, expecting an answer in "a day or so."

1. Compare your estimate of the static margins for both the Beech Starship and the X-29.
2. Compare the load sharing between the canard and wing for the X-29 and the Starship. Consider a range of CGs. What are the implications for selection of canard and wing airfoils?
3. Examine the control effectiveness of the canard. What is $C_{m\delta c}$, $C_{L\delta c}$? How do these numbers compare with a conventional layout competitor of the Starship?
4. With an untwisted wing, what is the span e of the Starship? The X-29?
5. What is the twist distribution required to obtain a minimum drag spanload for the Starship? The X-29? Consider both the isolated wing case and the wing in the presence of the canard.
6. Make your assessment. Is the Starship a better idea than other equivalent current aircraft (the Piaggio Avanti in particular)? How is the Starship concept different than the X-29? Why? Does that make the Starship a better or worse idea than the X-29? What do you advocate as the future trend for business aviation configurations from an aerodynamics standpoint?

Table D-12: Starship and X-29 Study Questions

The format is similar to that of the B-2 project, but the configuration now contains two lifting surfaces. In this case, the key resource for geometry was Jane's.[11] The students were able to conduct their investigation without any additional information. The schematic of the Starship planform used for analysis in this project is shown in figure D-11. The estimates of center of gravity and neutral point are included.

In the case of the Starship, the basic configuration was estimated to be about 10% stable. The aerodynamic analysis result is consistent with the operation of this aircraft. The Starship does not use an advanced fly-by-wire flight control system, and it is statically stable.

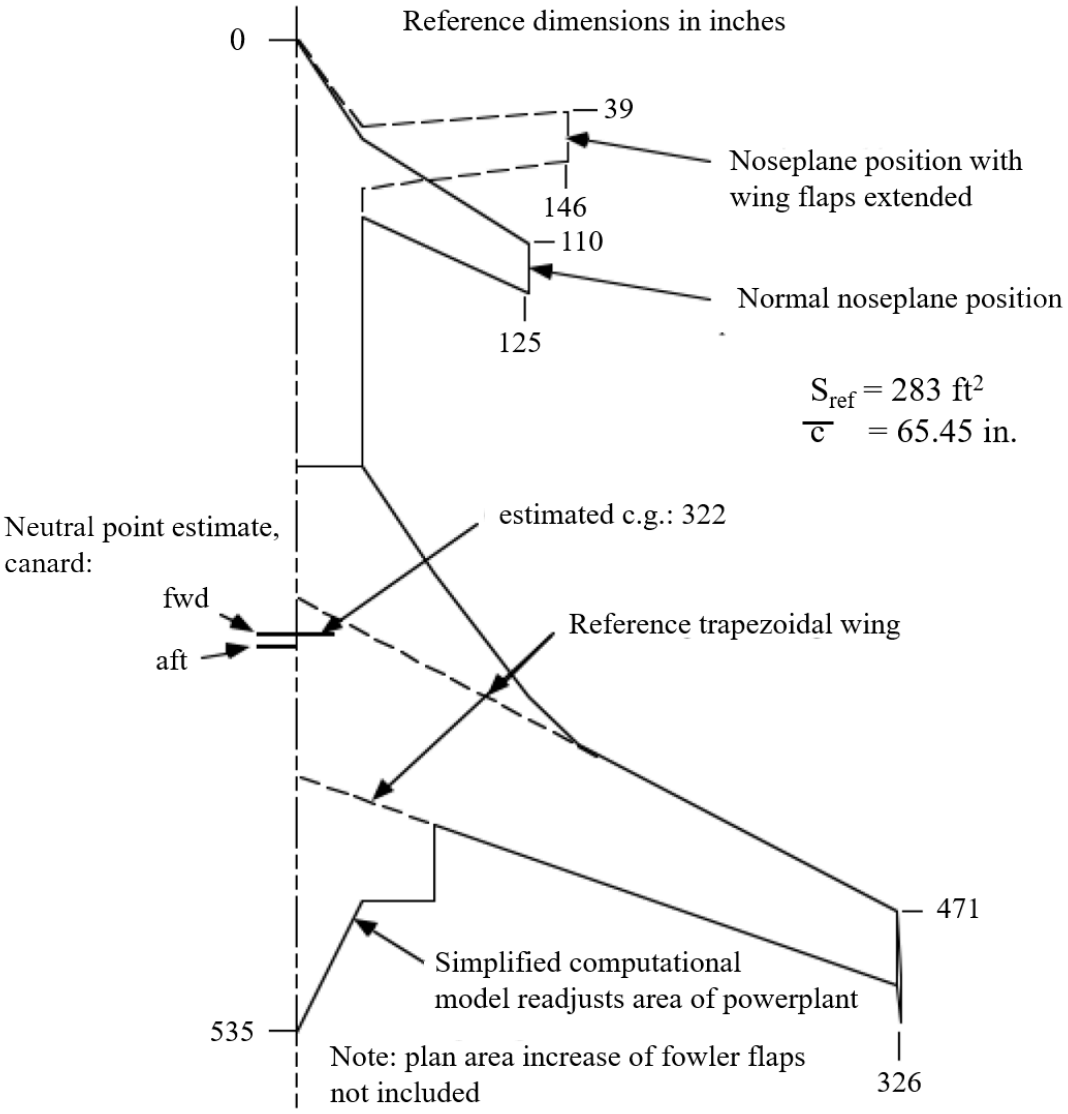


Figure D-11: Starship planform used for analysis

Figure D-12 shows the schematic of the X-29 planform used for analysis in this project. The X-29 was found to be about 32% unstable. Thus the aerodynamic analysis result is consistent with the operation of this aircraft. In contrast to the Starship, the X-29 exploits the advantages of an advanced flight control system to balance the aircraft at a significant level of static instability.

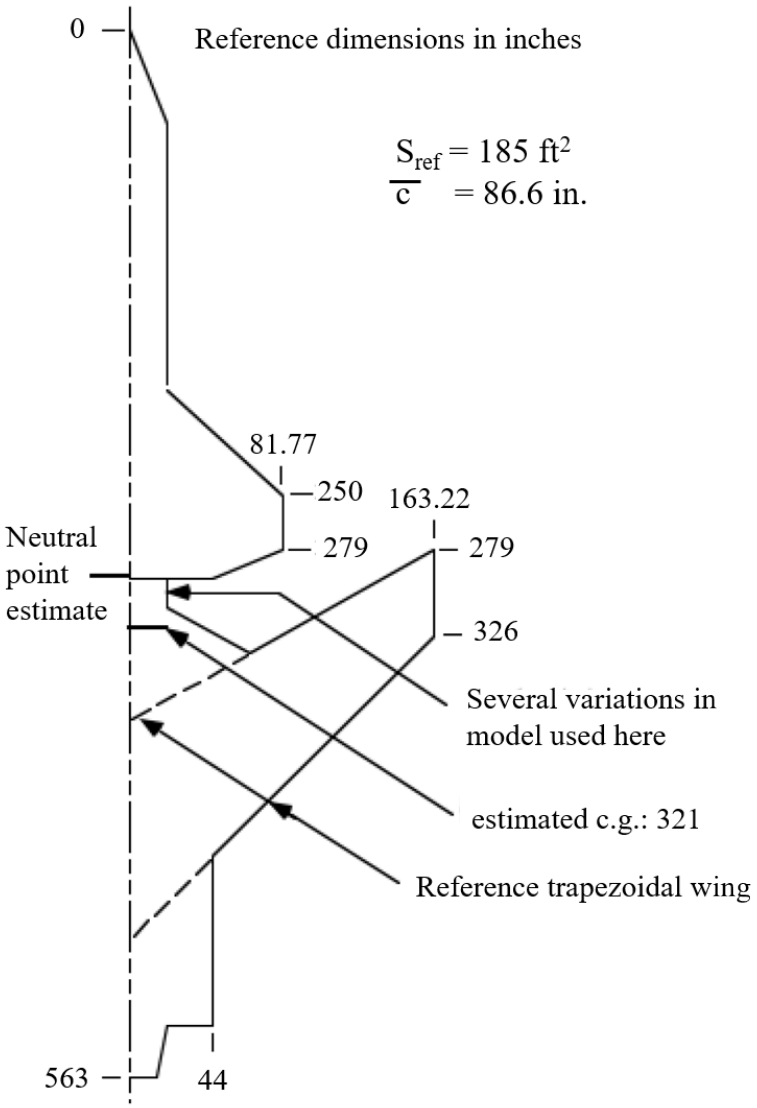


Figure D-12: Grumman X-29 planform used for analysis

Table D-13 contains the VLMpc dataset developed using the information in figure D-11. Table D-14 is the VLMpc dataset for the X-29, created using figure D-12.

```
Starship model
2.        1.        1.0000    27193.
6.        0.        0.        0.00
0.0       0.0       0.0       1.
  -54.    -35.
 -110.    -125.
 -137.    -125.
  -96.    -35.
 -230.    -35.
 -230.    0.0
12.
 -230.    0.0
 -230.    -35.
 -288.    -74.
 -355.    -125.
 -381.    -152.
 -471.    -324.       85.
 -506.    -326.        0.
 -531.    -326.       85.
 -510.    -324.
 -424.    -74.
 -465.    -74.
 -465.    -35.
 -535.     0.0
1.   9. 15.   .20 1.   0.   0.   0.          0.            0.
```

Table D-13: VLMpc model of the Starship

```
X-29 vlm model
2.          1.          1.0000      27193.
6.          0.          0.          0.00
0.0         0.0         0.0         1.
  -50.      -20.
 -194.      -20.
 -250.      -81.771
 -279.      -81.771
 -295.      -44.0
 -295.      0.0
10.
 -295.      0.0
 -295.      -20.
 -311.      -20.
 -335.      -64.
 -279.      -163.22
 -326.      -163.22
 -444.      -44.
 -535.      -44.
 -535.      -20.
 -563.      -14.
 -563.       0.0
  1.    9. 13.    .20 1.    0.    0.    0.          0.              0.
```

Table D-14: VLMpc model of the X-29

The forward position of the Starship canard, or foreplane, is connected to the extension of the Fowler flaps. The additional area of the flaps was not estimated by students in this project, and the forward position leads to an approximately neutral static margin. According to Swanborough,[12] the area of the Fowler flap ensures the stability level stays the same as the canard moves forward. This feature illustrates the sophistication required to develop an aircraft concept. Figure D-13 show a photo of the Starship taken by Mason at the Virginia Tech airport in the early 1990s.



Figure D-13: Beech Starship at the Virginia Tech Airport

Figures D-14(a) and D-14(b) provide the load-sharing requirements for trim between the canard and the wing for Starship and X-29, respectively. The results change with the center of gravity position. In the case of the Beech Starship, the requirement for a stable aircraft means the canard must always operate at a lift coefficient higher than the wing. When designed properly, this results in an airplane where the canard will always stall before the main wing. In the case of the X-29, the canard is at a significantly lower lift coefficient than the wing.

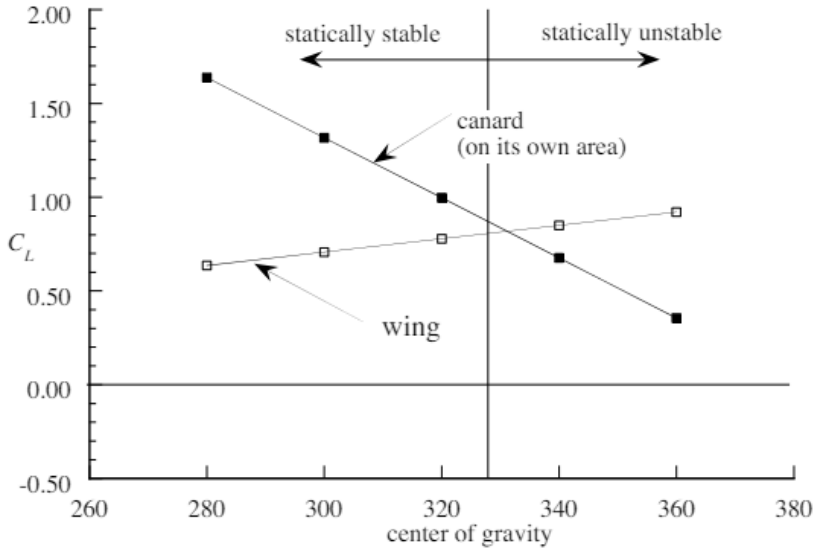


Figure D-14(a): Beech Starship: Load-sharing requirements between the canard and wing

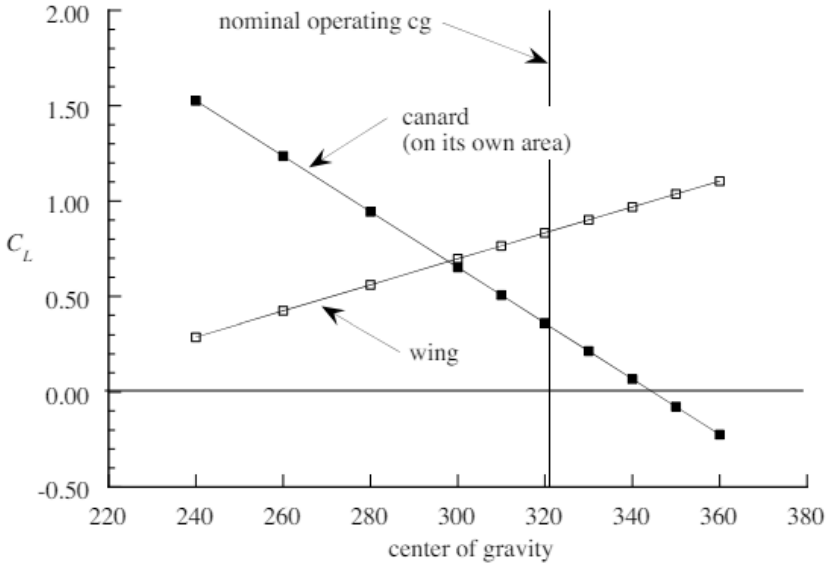


Figure D-14(b): X-29: Load-sharing requirements between the canard and wing

The choice of center of gravity location is important in obtaining the minimum trimmed induced drag. In figure D-15(a), the Starship is shown to be limited by stability requirements from reaching the highest cruise efficiency available for the configuration. Figure D-15(b) shows the benefit of relaxed static stability technology. The center of gravity for minimum induced drag corresponds to a negative static margin. The X-29 is balanced at the edge of the minimum drag bucket. These approximate calculations were made using Lamar's design code LAMDES,[13] ignoring the limits to airfoil performance, which are also important.[14] This example requires that the induced drag be calculated considering the multiple lifting surfaces and nonplanar effects. LAMDES can be used as an extended version of LIDRAG to account for these effects.

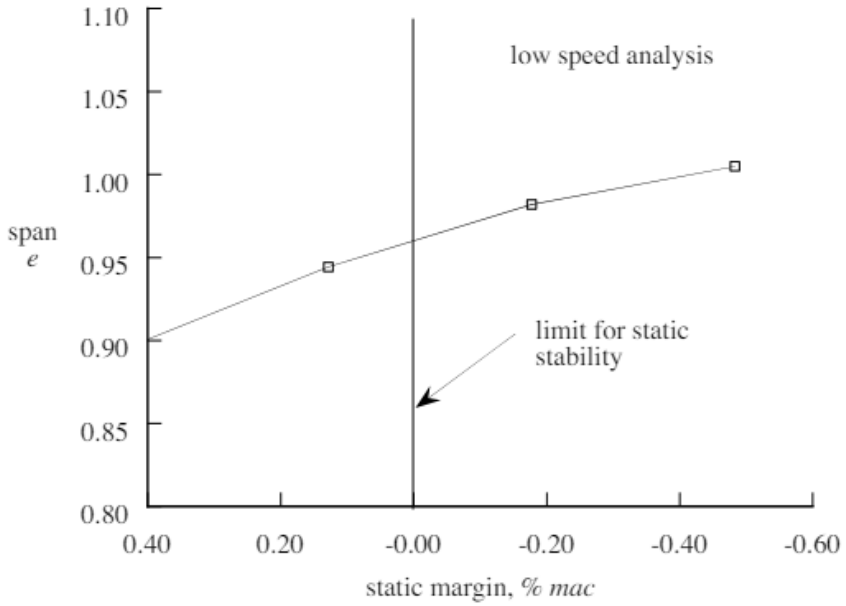


Figure D-15(a): Beech Starship: Effect of trim requirement on life-induced drag using vortex lattice analysis

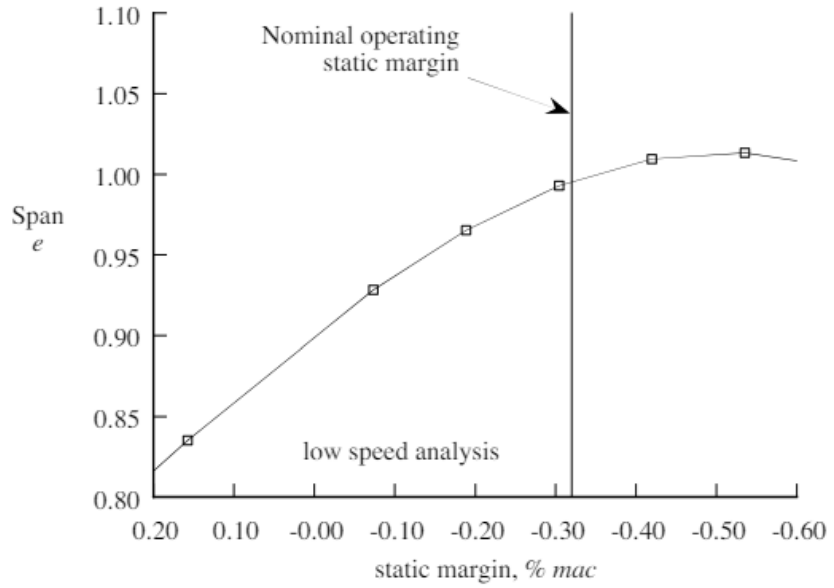


Figure D-15(b): Beech Starship: Effect of trim requirement on life-induced drag using vortex lattice analysis

Canard effectiveness as a control is slightly unusual. The canard is an effective moment generator, but increasing the canard incidence does not produce an equivalent increase in configuration lift. In cases where linear aerodynamic theory is valid, the increased lift on the canard produces additional downwash on the wing. The result is a loss of lift on the wing roughly equal to the canard lift. In transonic and separated flow situations, the linear aerodynamic flow field model is not valid and improved calculations or testing are required. Figure D-16 shows the X-29 in high-angle-of-attack research flight on September 10, 1991, by NASA research pilot Rogers Smith (https://www.nasa.gov/image-detail/amf-ec91-491-07). Smoke generators in the nose of the aircraft were used to help researchers see the behavior of the air flowing over the aircraft. The smoke here is demonstrating forebody vortex flow.



Figure D-16: X-29 in high-angle-of-attack flight with smoke generators in the nose of the aircraft.
From NASA. Public domain.

Figures D-17(a) and D-17(b) show the spanloads that correspond to the operation of the Starship and X-29 at their design points, respectively. Because the canard and wing are nearly coplanar, it is appropriate to combine them. Essentially, the vertical separation of the surfaces results in two distinct limits. In the first, the canard is coplanar with the wing, and the sum of the spanloads should be elliptic. As the vertical separation grows larger, individual spanloads should become ellipctic. Most canard designs correspond to the first case, and this is evidenced in the results of an optimization, as shown in figures D-17(a) and D-17(b).

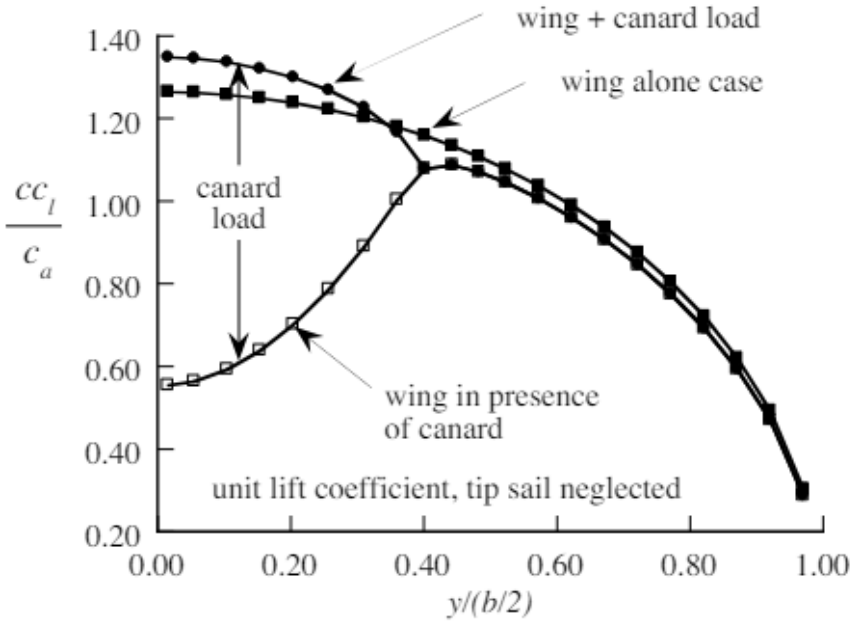


Figure D-17(a): Beech Starship: Minimum trimmed drag spanloads

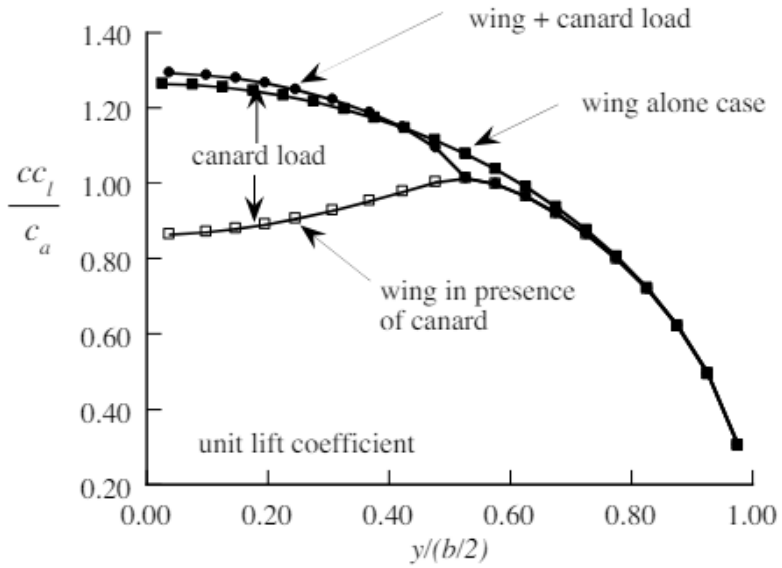


Figure D-17(b): Grumman X-29: Minimum trimmed drag spanloads

Figures D-18(a) and D-18(b) show the wing incidence distribution required to achieve the spanloads shown in figures D-17(a) and D-17(b), respectively. This includes the basic angle of attack and additional twist. The design wing twist will change when the wing is in the wake of the canard. In this case, the canard wake is held flat and fixed, resulting in the most extreme condition. This shows how you need to compensate for flow nonuniformity in interacting flow fields. It is also noteworthy that the trends in twist between aft- and forward-swept wings are exactly opposite. In particular, the presence of the canard reduces the twist variation required across the wing in the case of the X-29.

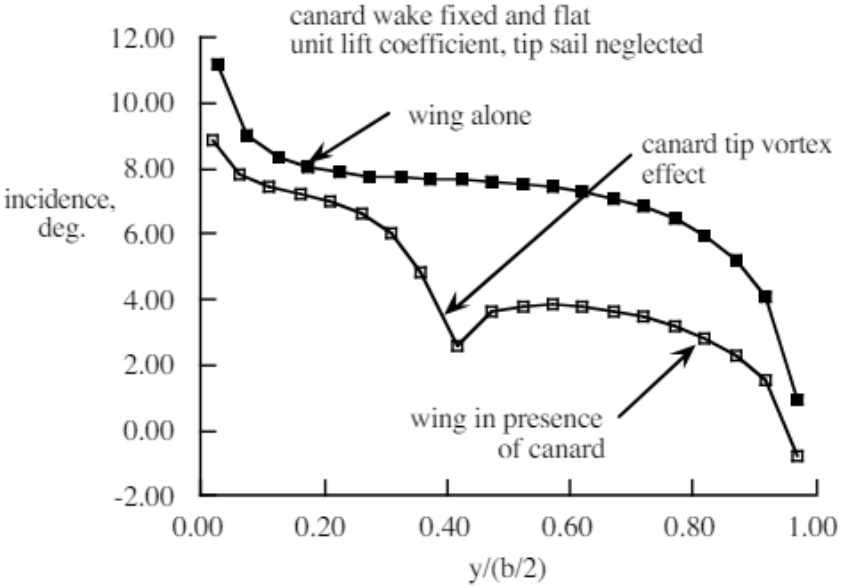


Figure D-18(a): Beech Starship: Incidence distribution required to achieve minimum drag spanloads presented in figure D-17(a)

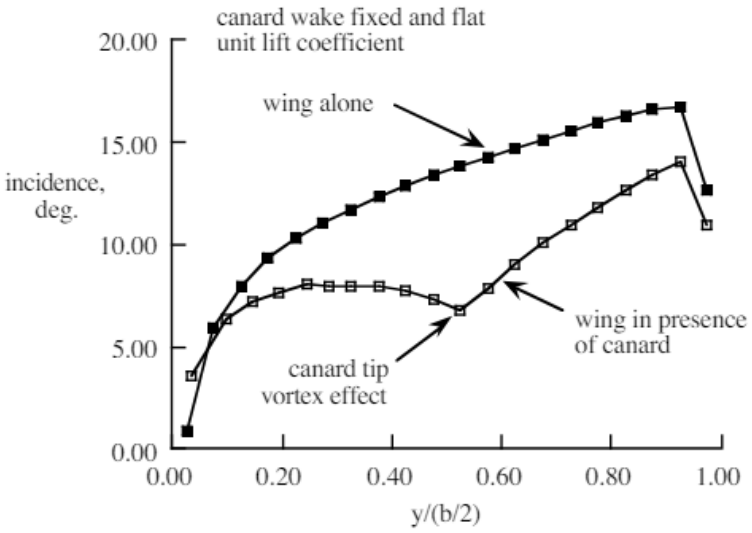


Figure D-18(b): Grumman X-29: Incidence distribution required to achieve minimum drag spanloads presented in figure D-17(b)

Additional information on the X-29 aerodynamic design is given in several papers.[15,16,17,18] Many comparisons of forward/aft-swept wings and canard/tail configurations have also been published. Key reading should include McKinney and Dollyhigh,[19] Landfield and Rajkovic,[20] and McGeer and Kroo.[21]

For this case study, the assessment also required consideration of a competitor aircraft, the Piaggio Avanti. In this case, the *Aviation Week*[22] article provided a useful analysis of the Starship and Avanti. Some confusion exists within the literature on the aerodynamics of three-surface configurations. The definitive analysis has been given in a NASA TP,[23] and the code is now available to students for future projects. The key benefit of a three-surface configuration is the reduction in the trim drag variation with balance location.

Key Lessons Learned From This Study

- Canard configurations go most naturally with unstable designs.
- If a canard aircraft is balanced to be stable, the canard airfoil design will likely be critical.
- Trim is an important issue in the aerodynamic layout of aircraft.

D.4 Term Project: Examine the YF-22 and YF-23

The US Air Force was in the process of selecting its new Advanced Tactical Fighter (ATF) when this project was assigned. Therefore, this was a timely project. The selection was scheduled to be announced about the time the assignment was due. As luck would have it, the announcement was made on the exact day that the assignment was due. The objective was to make an assessment of the aerodynamic design of the YF-22 and YF-23.

D.4.1 The Assignment

Use recent aviation magazines to establish a geometric model of each aircraft. Aviation Week & Space Technology magazine articles during Fall 1990 are a good source. Turn in an engineering report, including copies of input data sets as appendices. Use all the tools we have from class, and explain how you used them. Reference other data sources used.

1. Compare your estimate of the low-speed static margins for both candidates. (Review your notes from stability and control to recall definitions of SM and aircraft trim requirements.)
2. Compare the load sharing between the tail and wing for the YF-22 and YF-23. Do this for both up and away flight and the approach condition. Consider a range of CGs. What are the implications for selection of wing and tail airfoils?
3. Examine the control effectiveness of the tail. What is $C_{m\delta t}$, $C_{L\delta t}$?
4. What is the span e for each plane with an untwisted wing?
5. What is the twist distribution required to obtain an elliptic spanload for each airplane? Consider both the isolated wing case and the wing-tail case.
6. Using the analysis performed above, examine and discuss the trim drag issues. What if you used thrust vectoring to help trim?
7. Estimate the skin friction drag on each airplane.
8. Make your assessment. Would you pick the YF-22 or YF-23? Explain your choice, and comment on any refinements you would make.

The students used the *Aviation Week & Space Technology*[24] and *Air International*[25] analyses and the book by Sweetman.[26] Again, the requirements were similar to the previous projects, with the addition of a requirement to consider the estimation of friction drag. This allowed the students to estimate the L/D of the airplanes. Although interesting, without explicit requests, this had not been done previously.

Since the due date coincided with the Air Force announcement of the selection, student interest was extreme. Interestingly enough, a number of their parents turned out to be employed by the DOD and were able to supply an extraordinary amount of propaganda that was distributed by lobbyists.

Key Lessons Learned From This Study

- Using the methods available in the course, both airplanes were nearly equal. Supersonic and low-speed high-angle-of-attack aerodynamic evaluations are required to make a selection. The student use of nonlinear analysis of the configurations through airfoil design and analysis continued to produce disappointing results.

D.5 Discussion

Let me reiterate that the case studies presented in this appendix show that a significant number of issues associated with configuration aerodynamics can be resolved without expensive CFD calculations. Students can get considerable insight and conduct good sanity checks against much more sophisticated codes using a PC. However, other aspects of the problem require the use of sophisticated CFD methods.

Still other aspects require wind tunnels or flight tests at present. The role of each is identified with the use of these projects. These projects require an assessment intended to improve the student's ability for "critical thinking."

Figure References

Figure D-1: US Army. Northrop B-2 3-view line drawing. Public domain. https://commons.wikimedia.org/wiki/File:Northrop_B-2_3-view_line_drawing.png

Figure D-16: NASA. X-29 during a 1991 research flight. Public domain. https://commons.wikimedia.org/wiki/File:X-29_at_High_Angle_of_Attack_with_Smoke_Generators.jpg

Notes

1. Mason, W. H., "Applied Computational Aerodynamics Case Studies," AIAA Paper 92-2661, 1992.
2. Dornheim, M., "USAF, Northrop Unveil B-2 Next-Generation Bomber," Aviation Week & Space Technology, Nov. 1988, pp. 20–27.
3. *Air International*, Feb. 1989, p. 104.
4. Waaland, I. T., "Technology in the Lives of an Aircraft Designer," AIAA 1991 Wright Brothers Lecture, Sept. 1991, Baltimore, MD.
5. Miller, J., *Northrop B-2 Stealth Bomber*, Aerofax Extra 4, Specialty Press, Stillwater, 1991.
6. Sears, W. R., "Flying-Wing Airplanes: The XB-35/YB-49 Program," AIAA Paper 80-3036, Evolution of Aircraft Wing Design Symposium, Dayton, OH, Mar. 18-19, 1980.
7. Sears, W. R., "Flying-Wing Airplanes: The XB-35/YB-49 Program," AIAA Paper 80-3036, Evolution of Aircraft Wing Design Symposium, Dayton, OH, Mar. 18-19, 1980.
8. Northrop, J. K., "The Development of the All-Wing Aircraft," 35th Wilbur Wright Memorial Lecture, The Royal Aeronautical Society Journal, Vol. 51, 1947, pp. 481–510.
9. Wooldridge, E. T., *Winged Wonders*, Smithsonian Institution Press, Washington, 1983.
10. Coleman, T., *Jack Northrop and the Flying Wing*, Paragon House, New York, 1988.
11. Taylor, J. W. P. (ed.), *Jane's All the World's Aircraft* 1988-89, Jane's Group, Surrey, 1988.
12. Swanborough, G., "Starship ...bright newcomer in a conservative firmament," *Air International*, Apr. 1991.
13. Lamar, J. E., "Application of Vortex Lattice Methodology for Predicting Mean Camber Shapes of Two-Trimmed-Noncoplanar-Complex Planforms with Minimum Induced Drag at Design Lift," NASA TN D-8090, Jun. 1976.
14. Mason, W. H., "Wing-Canard Aerodynamics at Transonic Speeds - Fundamental Considerations on Minimum Drag Spanloads," AIAA Paper 82-0097, 20th Aerospace Sciences Meeting, Orlando, FL, Jan. 11-14, 1982.
15. Spacht, G., "The Forward Swept Wing: A Unique Design Challenge," AIAA Paper 80-1885, AIAA Aircraft Systems Meeting, Anaheim, CA, Aug. 4-6, 1980.
16. Moore, M., and Frei, D., "X-29 Forward Swept Wing Aerodynamic Overview," AIAA Paper 83-1834, Applied Aerodynamics Conference, Danvers, MA, Jul. 13-15, 1983.
17. Raha, J., "The Grumman X-29 Technology Demonstrator: Technology Interplay and Weight Evolution," SAWE Paper 1665, 44th Annual Conference, Society of Allied Weight Engineers, Arlington, TX, May 20-22, 1985.
18. Frei, D., and Moore, M., "The X-29—A Unique and Innovative Aerodynamic Concept," SAE Technical Paper 851771, Aerospace Technology Conference and Exposition, Oct. 1985.
19. McKinney, L. W., and Dollyhigh, S. M., "Some Trim Drag Considerations for Maneuvering Aircraft," Journal of Aircraft, Vol. 8, No. 8, Aug. 1971, pp. 623–629.
20. Landfield, J. P., and Rajkovc, D., "Canard/Tail Comparison for an Advanced Variable-Sweep-Wing Fighter," Journal of Aircraft, Vol. 23, No. 6, Jun. 1986, pp. 449–454.
21. McGeer, T., and Kroo, I., "A Fundamental Comparison of Canard and Conventional Configurations," Journal of Aircraft, Vol. 20, No. 11, Nov. 1983, pp. 983–992.
22. "Piaggio Avanti, Beech Starship Offer Differing Performance Characteristics," Aviation Week & Space Technology, Oct. 2, 1989, pp. 75–78.
23. Goodrich, K. H., Sliwa, S. M., and Lallman, F. J., "A Closed-Form Trim Solution Yielding Minimum Trim Drag for Airplanes with Multiple Longitudinal Control Effectors," NASA TP-2907, May 1989.
24. Dornheim, M. A., "ATF Prototypes Outstrip F-15 in Size and Thrust," Aviation Week and Space Technology, Sept. 1990, pp. 44–50.
25. Braybrook, R., "ATF: The USAF's future fighter programme," Air International, Vol. 40, No. 2, Feb. 1991, pp. 65–70.
26. Sweetman, B., *YF-22 and YF-23: Advanced Tactical Fighters*, Motorbooks, Osceola, 1991.

Appendix E: Software for Aerodynamic Analysis and Aircraft Design

This appendix contains programs that may prove useful to students of configuration aerodynamics and aircraft design classes. These are mostly old-fashioned codes without graphical user interfaces. Originally they were all FORTRAN source code. However, I've added some executables since the FORTRAN source files typically can't be used by current undergraduates. In addition, some methods are given as MATLAB m-files.

Important Note

Many of these programs require a text file as input. DO NOT embed tabs in these files. The location of the input on each line is critical. The input instructions are often given as "cards," a holdover from the days when the text files were physical decks of computer cards. The spacing definitions use FORTRAN terminology. Do yourself a favor and learn what this means. For example, F10 means a real number (with a decimal point) taking ten spaces. Study the sample input files for examples of how this works (in fact, ALWAYS run the sample case before doing anything else with these codes). For pointers on running codes, read "Computer, Codes, and Engineering," Chapter 2 in Applied Computational Aerodynamics by Cummings et al.[1]

Note that files here may be posted in various formats. For example, consider carriage return (CR) and line feed (LF). When using PCs (Windows), the lines are terminated with a CR/LF; for a "classic" Mac, the lines end with a CR, while for unix (and modern Macs), the lines are terminated by an LF. Add dealing with these variations to your computational engineering toolbox.

Students often have permissions issues with windows .exe files: All .exe files are run as user; however, the default file output location is usually C, which is an administrator directory and will create an error at run time due to permissions issues. Always use a folder with user permissions to output data files to such as documents.

A student has further suggestions and tips for using the codes:

1. Do not have any spaces in the directory name. (Example: *C:\User\Documents\VT 2016*. The space between *VT* and *2016* will not be recognized by the code.)
2. The input file must match the example input file exactly. The number of spaces between the columns and before the first column of numbers must match the example code.

Finally, the programs and manuals change as students suggest clarifications and other improvements. And these codes are of course for educational use only.

Other useful online Java-based programs are available at www.engapplets.vt.edu.

Another source of classic aerodynamics codes is Ralph Carmichael's Public Domain Aeronautical Software (PDAS). These codes can now be downloaded for free.

E.1 Aerodynamic Relations

E.1.1 Aerocal Pak #1: Basic Aerodynamic Relations

This software is a BASIC program that implements the old Aerocal Pak #1, *Basic Aerodynamic Relations*. It has the NACA 1135 tables, Prandtl–Meyer angle and inverse, properties of oblique shocks, the Rayleigh/Fanno line table, and the 1976 standard atmosphere. Originally written for a programmable calculator, the code is in QuickBASIC and runs as is on a Mac with QuickBASIC. A one-line change is required to run it on an IBM-type PC. The file is standard ASCII text.

Aerocal Pak #1

E.1.2 Standalone NACA 1135: Compressible Flow Functions

These codes compute the compressible flow functions given in NACA 1135, plus a few more useful relations. These are executables that replace the NACA 1135 portions of Aerocal Pak #1 above, which doesn't run on many computers anymore.

- NACA1135.sit – The Macintosh version (stuffed)
- NACA1135.exe – The PC version

E.1.3 Standard Atmosphere Routines

Originally a FORTRAN subroutine (actually TI-59 and then Applesoft), a MATLAB file is also provided. stdatmtest.m is the driving script file for the MATLAB function file. The subroutine can be used in other programs. It is the same routine used in Pak #1 above. The units are listed in the subroutine header. A sample main program is included to illustrate the use of the program, and it should run using any FORTRAN compiler or in MATLAB. Note that the MATLAB version was originally converted from FORTRAN by Paul Buller.

- stdatm.f
- stdatmf.m
- stdatmtest.m

The following web-based standard atmosphere calculators have been suggested by students:

- Digital Dutch
- AerospaceWeb – Can also can provide Reynolds number
- ConvertIt Calculator

E.2 Airplane Design and Sizing

E.2.1 Nicolai's Sizing Program(s)

I've included four files here. They implement Nicolai's aircraft sizing algorithm in QuickBASIC and more recently, REALBasic. Acsize provides the size, while the second code, acsweep, covers a range of takeoff gross weights, showing the empty weight required and available. They should run on either Macs or IBM-type PCs. In the QuickBASIC versions, data values are set in the program with the hope that the users will look at the code and see what is going on. The files are standard ASCII text. The REALBasic programs are executables for both Mac and PC. The only modification to Nicolai's notation is a supersonic mission leg.

- acsize.QB – The QuickBASIC listing
- acsweep.QB
- ACsize.exe – A PC code
- ACsizeMac.sit – A Mac code

E.2.2 The OpenVSP Tools

OpenVSP (Vehicle Sketch Pad) is an open source vehicle design suite. The origin of this work is the NASA Langley Research Center.

- The OpenVSP website

E.2.3 Dan Raymer's Aircraft Design Pages

Dan Raymer has a good collection of aircraft design tools, including a description of design software.

- Dan Raymer's website

E.2.4 CEASIOM

CEASIOM is a European aircraft design project. Some of its capabilities are free, and some require joining the consortium.

- CEASIOM website

E.2.5 Landing Gear Integration Codes

These programs allow the designer to assess the configuration against the landing gear requirements and also against the pavement thickness requirements. Finally, there is a code that will estimate the landing gear weight. The report and codes are available on a separate page that is accessible by looking at the HTML cover page for the report and software for MAD 96-09-01, "Landing Gear Integration in Aircraft Conceptual Design."

E.2.6 Takeoff Distance Calculation

This program computes the takeoff distance, including the balanced field length. The program uses the method of Krenkel and Salzman. Two versions are available. The original FORTRAN program was written by Sean Lynn as an undergraduate research project. After gathering some initial experience, a few improvements to the numerics were made by Pete MacMillin, who felt compelled to convert the code to C. For the test case, there is very little difference between the answers from the two different codes. The input files are also slightly different between the FORTRAN and C verisons. The basic theory is contained in Sean Lynn's final report, which is available as a PDF file.

- Takeoff theory – Sean Lynn's final report
- TAKEOFF2manf.pdf
- takeoff2.f
- takeoff2.exe
- TAKEOFF2.IN – The sample input
- TAKEOFF2.OUT – The sample output
- DC9.IN – A sample DC-9 case
- 747.IN – A sample 747 case
- takeoff2.c
- TAKEOFF2cman.pdf
- takeoff.in – The sample input
- takeoff.out – The sample output

E.2.7 Propulsion

The best source of propulsion information and software is Prof. Jack Mattingly's books. He is a co-author of the AIAA *Aircraft Engine Design* book and the software that goes with it.

- AEDSys code – Includes many useful programs

E.3 Geometry

E.3.1 Airfoil Generation: NACA 4 & 5 Series

FOILGEN is an interactive FORTRAN program that allows the user to construct airfoils using the NACA 4-digit or modified 4-digit airfoil thickness distributions and the NACA 4-digit, 5-digit or 6- and 6A-series camber lines. A variety of output options are available on the screen. It can also create a file for use as input to airfoil analysis programs. This file is in the so-called "Jameson format." The file is standard ASCII text. It should run using any FORTRAN compiler. Please see appendix A in this book for a theoretical description of the equations used.

- FOILGENMan.pdf
- foilgen.f
- foilgen.exe

E.3.2 Airfoil Generation: NACA 6 & 6A Series

This is a FORTRAN program that allows the user to obtain (approximately) the NACA 6-digit or 6A-digit airfoils. The program was written at NASA by Cuyler Brooks and Charles Ladson. It appears to be in the public domain. The file is standard ASCII text. It should run using any FORTRAN compiler. The theoretical description of the equations for the camber lines is available in appendix A of this book. Note that the thickness distribution of these airfoils is not described by a single equation.

- LADSON Manual (PDF)
- LADSONpc.f
- LADSONpc.exe
- LADSON.inp
- LADSON.out

E.3.3 Planform Analysis

This software includes a BASIC program that implements the old Aerocal Pak #2, *Basic Geometry for Aerodynamics*. I put it up for the little planform and wing analysis programs, which I still find useful, although today it should be on a spreadsheet. It also generates the shapes for several of the classic bodies of revolution and features the BASIC (original) version of the FORTRAN program FOILGEN given above for the NACA airfoils. Originally written for a programmable calculator and then translated to Applesoft, the code is in QuickBASIC and runs as is on a Mac with QuickBASIC. A one-line change is required to run it on an IBM-type PC. The file is standard ASCII text. The theoretical description is available as a PDF file in appendix A of this book. An executable of a FORTRAN program in also posted here, together with the manual, sample input, and sample output.

- Aerocal Pak #2 – A BASIC program
- WingPlanAnal.f – A FORTAN source file for the planform analysis portion of Pak #2
- WingPlanAnal.exe – An executable

- WingPlanAnal.pdf – The manual for WingPlanAnal
- B2Plan.inp – A sample input
- B2Plan.out – A sample output

E.4 Lifting-Line Theory

E.4.1 Simple Lifting-Line Theory

This is an interactive FORTRAN program that solves the classical Prandtl lifting-line theory using the monoplane equation. The file is standard ASCII text. It should run using any FORTRAN compiler.

- llt.f – The source code
- llt.exe – An executable for PCs

E.4.2 Utah State Lifting-Line and Analysis Codes

Utah State has a page of aero analysis codes, and their lifting-line method is called MachUpX. Their group has been working on improved lifting-line methods for many years.

- MachUp

E.5 Drag

E.5.1 Skin Friction/Form Factor Drag Estimation

This program can be used to estimate the basic friction drag of an airplane. It should run using any FORTRAN compiler. Along with the manual and code, a sample input and the resulting sample output are provided. In November of 2002, an executable version was added.

- friction.f – The source code
- friction.exe – The executable
- FRICTman.pdf
- F15frict.inp
- F15frict.out

We also have a MATLAB version made by Paul Buller in 1998.

- friction.m – The main program
- finput.m – The input routine
- lamcf.m – The laminar skin friction routine
- turbcf.m – The turbulent skin friction routine
- stdatm.m – The standard atmosphere

E.5.2 Induced Drag

E.5.2.1 Induced Drag for a Single Planar Wing

Computation of the induced drag of a single planar surface given the spanload distribution. You get a value of the span *e* as output. The coefficients of the assumed Fourier series are computed using a fast Fourier transform. The program was written by Dave Ives and used in numerous programs developed for the government by Grumman.

- LIDRAG Manual (PDF)
- lidrag.f
- lidrag.exe
- lidragB2.inp
- lidrag.out

E.5.2.2 Induced Drag for Nonplanar Lifting Systems

This program can be used to find the induced drag of a system of nonplanar lifting elements. It was written by Joel Grasmeyer. It has both design and analysis capabilities. This means that you can either find the spanload required to obtain the minimum induced drag or you can input a spanload and find the induced drag. The program also prints out the span efficiency factor *e*. This program does not give you the twist and camber required to generate the spanloads. Three FORTRAN programs are required and must be linked to run the program.

- idrag.f
- idragin.f
- math77.f
- idrag.exe
- idragman.pdf – The program manual
- dsample.in – A winglet design example input file
- dsample.idrag – A winglet design example output file
- asample1.in – An analysis example input file (linear load distribution)
- asample1.idrag – An analysis example output file
- asample2.in – An analysis example input file (elliptic load distribution)
- asample2.idrag – An analysis example output file

E.5.2.3 Induced Drag for Simple Nonplanar Lifting Systems, With Camber Line Design

John Lamar's design program, LAMDES, is a more capable version of LIDRAG. It can be used to find the span *e* for two nonplanar lifting surfaces given the spanload on each surface. This code also finds the wing camber and twist required to obtain this spanload at subsonic speeds. The code will also do an optimization analysis, finding the minimum trimmed drag and spanload required to achieve it. Three samples are included. The first is the sample case in the NASA TN, the second is an isolated wing with an aspect ratio of ten, taper ratio of 0.5, and a sweep of thirty degrees. Both of those cases neglect airfoil contributions. The third case is for a wing canard and includes airfoil properties in the optimization.

- LAMDES Manual (PDF)
- LamDes2.f
- LamDes2.exe
- LamDesTNsamp.inp
- LamDesTNsamp.out
- ar1030.inp
- ar1030.out
- WCfoildes.inp
- WCfoildes.out

E.5.2.4 Minimum Drag and Area Distribution (Supersonic Flow)

The MinDrag program computes the minimum value of the supersonic wave drag and the area distribution required to attain this value for a given length, *XL*, volume, nose area [Snose] and base area [Sbase], and another area specified at a given location along the body [XSgiven, Sgiven]. It uses the formulas published by Lord and Eminton in their article "Slender Bodies of Minimum Wave Drag" for *The Journal of the Aeronautical Sciences* (August 1954, pp. 569–570).

- MinDrag.exe

E.5.2.5 Harris Wave Drag Computation

AWAVE is a version of the Harris wave drag code. You can get a copy from the PDAS site described above, http://www.pdas.com. We have put the manual (essentially a description of the Craiden geometry dataset), and a sample input and output here.

- awave.man – The user's manual
- awaveFileMake.m – A Matlab script file to help make the input file and make sure that the numbers are in the correct columns. The directions on use are contained as comments in the script. Todd Lowe (a professor in VT AOE) wrote this script for us (version updated 2-7-06).
- AWAVEIN.DAT – The sample input file
- AWAVEOUT.DAT – The sample output to check your results

E.6 Vortex Lattice Methods

E.6.1 Vortex Lattice Analysis and Design: VLMpc

VLMpc is John Lamar's two-surface vortex lattice program developed at NASA Langley. The program treats two lifting surfaces using up to 200 panels. Vortex flows are estimated using the leading-edge suction analogy. This program was typed in from the NASA TN D, which contained the listing, by students in the Applied Computational Aerodynamics course. John Lamar didn't have a copy of the code anymore. It has been modified to run in WATFOR and to produce 80-column output. Now it runs in Compaq Visual FORTRAN. In November 2002, an executable was added. The source now includes PC directory code specific to PCs.

- VLMpc Manual (PDF) – *Note*: This code has many check cases.
- VLMpcv3.f – The source code
- VLMpc.exe – The executable
- vlm.dat
- vlm.out
- vlm2.dat
- vlm2.out
- B767.dat
- B767.out
- YF23.inp
- YF23.out
- YF23.in2
- YF23.out2

E.6.2 Vortex Lattice Analysis and Design: VLM 4.997 Manual

VLM 4.997 is a NASA Langley vortex lattice program which can handle four planforms and up to 400 panels. It is an extension and improvement of the two-surface code discussed above. This is an Acrobat manual only. If you want the code, you need to contact NASA Langley. A version is available for student use in the VT Design Lab.

- VLM 4.997 Manual
- A7wing.inp – An A-7 with a different wing, wing alone case input
- A7wing.out – The output for this input
- A7wingfus.inp – An A-7 with a different wing, wing-fuselage case
- A7wingfus.out – The output for this input
- A7full.inp – An A-7 with a different wing, wing-fuselage-tail case
- A7full.out – The output for this input

E.6.3 Vortex Lattice Analysis Code in MATLAB: Tornado

Tornado is a Vortex Lattice Program, written in MATLAB. It comes from KTH, the Royal Institute of Technology, in Stockholm, Sweden. Tomas Melin wrote the program, and Professor Arthur Rizzi was his advisor. It is a very flexible program, and can handle a wide range of geometries. Also, it is still being developed, so check the site for updated versions.

- Tornado The location for the code and related manuals

E.6.4 A General Vortex Lattice Code: AVL

AVL is a very general Vortex Lattice Program developed by Mark Drela and Harold Youngren from MIT. Drela is the author of the widely used XFOIL airfoil analysis and design code. It is a very flexible program, and can handle a wide range of geometries.

- AVL The location for the code and related manuals

E.6.5 A General Vortex Lattice Code: VSPAERO

VSPAERO is a potential flow aerodynamics tool developed by Dave Kinney at NASA Ames. It is a very flexible program, and can handle a wide range of geometries.

E.7 Airfoil Aerodynamics

E.7.1 Subsonic Airfoil Analysis and Design: XFOIL

XFOIL is an airfoil analysis and design program from Prof. Mark Drela at MIT. It is for essentially incompressible single element airfoils. However, it includes viscous effects, and can be used in an inverse mode, where the pressure distribution is input and the required geometry found. It runs on workstations and win32 PC systems. Some very good airfoil work has been done by design class students with this code.

- Xfoil The location for the code, which is available under the GNU licensing rules, and related manuals and discussion groups
- Some notes by Tim Miller on using XFOIL
- Some more notes by Tim Miller on using XFOIL
- A sample airfoil, clarky.dat demonstrating the format for inputting coordinates into XFOIL (Tim Miller attributes this data file to JD Jacob at the University of Kentucky)

E.7.2 Subsonic Airfoil Analysis and Design: Pablo

Pablo is a subsonic airfoil analysis and design program. It comes from KTH, the Royal Institute of Technology, in Stockholm, Sweden. Christian Wauquiez wrote the program, and Professor Arthur Rizzi was his advisor. Pablo stands for "Potential flow around Airfoils with Boundary Layer coupled One-way." It is a MATLAB code, so you need to have MATLAB to run it. Eventually, this url will go away, and when it does, Prof. Rizzi has given us permission to put this up on our site at Virginia Tech.

- pablo The location for the code and related manuals

E.7.3 Subsonic Airfoil Analysis and Design: JavaFoil

JavaFoil is a subsonic airfoil analysis and design program. It comes from Germany, and is by Martin Hepperle. It does a panel method solution and a boundary layer calculation. Our students like this program.

- JavaFoil The location for the code and related manuals

E.7.4 Vortex Lattice Design for a 2D Camber Line for a Given Chord Load

The camber line required to produce a specified chord load distribution is computed using the quasi-vortex lattice method by Prof. Lan of the University of Kansas. The method is valid for two dimensional incompressible flow, and is an original (and very simple) program. Thanks to Tom Zeiller for improvements and bug fixes.

- DESCAM Manual (pdf)
- descam.f
- descam.exe
- descam.inp

E.7.5 Transonic Airfoil Analysis: TSFOIL2

TSFOIL2 provides a finite difference solution of the transonic small disturbance equation. The source code is provided as standard ascii text. The code was written by Earll Murman and co-workers, and includes wind tunnel wall effects. It originated at NASA Ames. It's very old, but appears to be in the public domain. The listing was included in a NASA CR which is referenced in the mini-manual provided here as a pdf file. The NASA CR (3064) is also now available as a pdf file from the NASA Technical Reports Server.

- TSFOIL2 Manual (pdf)
- tsfoil2.f The source code
- tsfoil2.exe The executable
- bicon.inp Sample input for a biconvex airfoil
- bicon.out Sample output for the biconvex airfoil input

- n2412.inp Sample input for an NACA 2412 airfoil
- n2412.out Sample output for the NACA 2412 airfoil
- N0012.inp Sample input for an NACA 0012 airfoil
- N0012.out Sample output for the NACA 0012 airfoil
- SC20610.inp Sample input for a NASA SC(2)-0610 airfoil
- SC20610.out Sample output for the NASA SC(2)-0610 airfoil

E.8 Supersonic Aerodynamics

E.8.1 Minimum Drag and Area Distribution (supersonic flow)

See section E.5.2.4 above.

E.8.2 Harris Wave Drag computation

See section E.5.2.5 above.

E.8.3 Supersonic Aerodynamics of Arrow Wings

Arrow is a code to compute the linear theory lift curve slope, aerodynamic center and drag due to lift of arrow wings at supersonic speed.

- arrow.f The source code
- arrow.exe The PC executable

E.8.4 Supersonic Cone at Zero Angle of Attack

This is a link to a JAVA code that finds the pressure on a circular cone at supersonic speed at zero angle of attack. I checked it with the famous Sims Table (NASA SP-3004). It doesn't give the pressure coefficient, but you can find *Cp* from the simple relation between pressure and pressure coefficient.

- Supersonic Cone Program

Sims also made tables for circular cones at small angle of attack, see NASA SP 3007.

E.9 Stability and Control

E.9.1 Control Power Assessment

This is a collection of codes that may be useful in aircraft conceptual design. There are two main components, a vortex lattice code to provide at least a rough estimate of the stability and control derivatives, and a spreadsheet to evaluate a design using specified aircraft characteristics. We also have codes that implement the methods of NASA TP 2907 to find the best way to trim the aircraft when you have multiple possibilities. This includes three surfaces, and two surfaces with thrust vectoring.

- VPI-Aero-200.pdf (the complete report, including the user's manuals for the codes)
- JKayVLM.f This is the original "small" code. It might fit on a PC.
- JKaydblp.f This is the double precision version with more panels.
- JKsamp.inp This is the sample input file
- JKlata.tst This is the sample input file for the lateral geometry
- JKlonga.tst This is the sample input file for the longitudinal geometry
- JKsampoutref This is the sample output to check your results.

For the executable of JKayVLM, use these files:

- JKayVLM.exe This is the executable
- f18samp.inp This is the sample input file
- f18lata.tst This is the sample input file for the lateral geometry
- f18longa.tst This is the sample input file for the longitudinal geometry
- f18samp.out This is the sample output to check your results.

The rest of the material is available below:

- CPRCheck.sit CPRCheck (the spreadsheet in Lotus 1-2-3 format, in Stuffit format from a Macintosh)
- VPINASACPC.sit VPI-NASA-CPC (the spreadsheet in EXCEL format and improved by Marty Waszak at NASA Langley, in Stuffit format from a Macintosh.)
- VTnascpc.zip VPI-NASA-CPC (the spreadsheet in EXCEL format and improved by Marty Waszak at NASA Langley, zipped so that an IBM can download and unzip. It is the same file format from a Macintosh as the .sit file above. EXCEL on IBM should be able to import the file – let me know if there is a problem.)
- fltcond.f A program to establish various flight conditions to assess the configuration.
- FLTcondSetup.sit This is a spreadsheet in Lotus 1-2-3 format, in Stuffit format from a Macintosh, to setup the input for the fltcond.f code.
- trim3s.f (FORTRAN program implementing NASA TP 2907, the version for 3 surfaces)
    - 3SURFACE.DAT (input file that reproduces the case in the manual)
- trimTV.f (FORTRAN program implementing NASA TP 2907, the version for 2 surfaces and thrust vectoring)
    - 2SURFACE.DAT (input file that reproduces the case in the manual)

E.9.2 Lateral/Directional Estimates and Engine Out

These are codes that can be used to estimate some of the key lateral directional analysis, including stability and control derivatives for use in estimating aircraft characteristics. LDstab is basically an implementation of the DATCOM method, with adjustments to match published B-747 data. It should be used in place of lateral-directional estimates from Jacob Kay's code given above, which are on shaky theoretical grounds. This code was developed by Joel Grasmeyer for the truss-braced wing project. The report covers an engine out analysis, but the
program doesn't provides the complete analysis. Use VMCA below to do the engine out analysis.

- LDstabdoc.pdf This report describes the methods, including the user's manual
  Note: on March 26, 2004 we have revised the calculation, adding the estimation of the $C_{n\beta}$ contribution from the wing as described in DATCOM and added two more inputs to the code, not described in the user's manual (for which we only have the pdf file). See the sample input file for the additional input description, previously not required.
- LDstab.f This is the FORTRAN source
- LDstab.exe The executable
- 747LDs.in This is the sample input file
- 747LDs.out This is the sample output to check your results

E.9.3 DigitalDATCOM Stability and Control Estimation

(sample input files only)

Digital DATCOM is a code that can be used to estimate stability and control derivatives. It is on the VT design lab computers. It is an industrial strength code that has a non-trivial learning curve. However, it has the capability to estimate stability and control characteristics at supersonic speeds. This information is not available in Roskam's volumes, so we needed to add it to our computing library.

- DATCOM.IN This is the sample input file
- DATCOM.OUT This is the sample output to check your results

E.9.4 Single Engine Minimum Control Speed, VMCA

VMCA is a MATLAB file to calculate the single engine minimum control speed of a jet powered airplane. It was written by Mike Cavanaugh and uses the stability and control derivatives estimated from the lateral/direction program by Joel Grassmeyer, listed above.

- VMCAUserMan.pdf This is the manual
- VMCAv1.m This is the m-file

E.10 Cryogenic Wind Tunnel Testing

Wind tunnel testing, especially at transonic speeds and cryogenic temperatures requires some planning. Information and a spreadsheet calculator are provided here (for educational purposes). This allows you to find the test Reynolds number and dynamic pressure.

- CryogenicTesting.pdf The background info for the spreadsheet
- CryoCalculator.xlsb The spreadsheet

Notes

1. Russell M. Cummings, William H. Mason, Scott A. Morton and David R. McDaniel. "Applied Computational Aerodynamics: A Modern Engineering Approach," Cambridge University Press, 2015.

Appendix F: Configuration Aerodynamics Reading List

In our courses, we read and have class discussions about a few key papers in configuration aerodynamics. We don't have time to read and discuss all the classic papers in class, so these are a few papers that fit the primary themes of the course. I wish we could discuss more. References in the various chapters provide citations to many of the other classic configuration aerodynamics papers.

To get oriented to the attitude of a successful configuration aerodynamicist:

Waaland, I. T., "Technology in the Lives of an Aircraft Designer," AIAA Paper 91-3069, AIAA Wright Brothers Lecture, Aircraft Design and Operations Meeting, Baltimore, MD, Sept. 23-25, 1991. https://doi.org/10.2514/6.1991-3069

These sources can be discussed together to compare and contrast different solutions for similar missions:

Shevell, R. S., and Schaufele, R. D., "Aerodynamic Design Features of the DC-9," Journal of Aircraft, Vol. 3, No. 6, Nov.-Dec. 1966, pp. 515–523. https://doi.org/10.2514/3.43770

Olason, M. L., and Norton, D. A., "Aerodynamic Design Philosophy of the Boeing 737," Journal of Aircraft, Vol. 3, No. 6, Nov.-Dec. 1966, pp. 524–528. https://doi.org/10.2514/3.43771 (Note: Also known as AIAA Paper 65-739.)

Read together to consider the role of CFD:

Shevell, R. S., "Aerodynamic Bugs, Can CFD Spray Them Way?" AIAA Paper 85-4067, Oct. 1985. https://doi.org/10.2514/6.1985-4067 (*Note*: Later published in the Journal of Aircraft, Vol. 23, No. 8, Aug. 1986, as "Aerodynamic Anomalies: Can CFD Prevent or Correct Them?" pp. 641–649.) https://doi.org/10.2514/3.45356

Although some of the "CFD" methods discussed are slightly dated, the aerodynamic thinking, insight and approach to understanding aerodynamic flow fields is unsurpassed.

Tinoco, E. N., "The Impact of Computational Fluid Dynamics in Aircraft Design," Canadian Aeronautics and Space Journal, Vol. 44, No. 3, Sept. 1998, pp. 132–144.

Additional CFD resources:

Rubbert, P. E., "CFD and the Changing World of Airplane Design," AIAA Wright Brothers Lecture, Sept., 1994. https://www.icas.org/icas_archive/ICAS1994/ICAS-94-0.2.pdf

Tinoco, E. N., "The Changing Role of Computational Fluid Dynamics in Aircraft Development," AIAA Paper 98-2512, Jun. 1998. https://doi.org/10.2514/6.1998-2512

Jameson, A., "Re-Engineering the Design Process through Computation," AIAA Paper 97-0641, Jan. 1997. https://doi.org/10.2514/6.1997-641

A paper describing transonic transport aerodynamic design:

Lynch, F. T., "Commercial Transports—Aerodynamic Design for Cruise Performance Efficiency," Douglas Paper 7026, Feb. 1981. https://doi.org/10.2514/5.9781600865558.0081.0147 (*Note*: This is also included as Chapter 2 in *Transonic Aerodynamics*, edited by D. Nixon, AIAA Progress in Astronautics & Aeronautics, Vol. 81, 1982, pp. 81–147.)

The key paper on the physics of high lift:

Smith, A. M. O., "High-Lift Aerodynamics," AIAA Wright Brothers Lecture, AIAA Paper 74- 939, Aug. 1974. https://doi.org/10.2514/6.1974-939 (*Note*: Also published in Journal of Aircraft, Vol. 12, No. 6, Jun. 1975, pp. 501–530 https://doi.org/10.2514/3.59830.)

We have to have a case study of the SR-71, one of the most remarkable airplanes ever:

Rich, B. R., "F-12 Series Aircraft Aerodynamic and Thermodynamic Design in Retrospect," Journal of Aircraft, Vol. 11, No. 7, Jul. 1974, pp. 401–406. https://doi.org/10.2514/3.60356

Garrison, P. "Desert Blackbirds," Flying, Oct. 1994, pp. 96–99. https://books.google.com/books?id=qn20_NrLHC8C&lpg=PP1&pg=PA96#v=onepage&q&f=false

Appendix G: The Configuration Aerodynamicist's Bookshelf

Throughout the text, we've referenced many, many papers, reports, and books. Here is a short summary of the references that a configuration aerodynamicist should keep handy.

A basic aerodynamics book:

Bertin, J. J., and Cummings, R. M., *Aerodynamics for Engineers*, 6th. ed., Pearson Prentice Hall, 2014 (Note: The third edition, published in 1998, is by J. J. Bertin and M. L. Smith.)

Airfoils:

Abbott, I. H., and Von Doenhoff, A. E., *Theory of Wing Sections*, Dover, 1949.

See also the PDF file of Abbott, I. H., Von Doenhoff, A. E., and Stivers, L., Jr., "Summary of Airfoil Data," NACA R-824, 1945. Although I had been told the book was the same as this NACA Report, it is not. They are very similar but highly complementary. Beware that the Dover book has numerous typos.

Harris, C. D., "NASA Supercritical Airfoils," NASA TP-2969, Mar. 1990.

This report describes the Whitcomb airfoil work and the thinking and experience behind the design work. Watch out for the tables of airfoil coordinates. See my comments in appendix A.

General aerodynamic information:

Hoerner, S. F., *Fluid-Dynamic Drag*, published by the author, 1965. https://archive.org/details/FluidDynamicDragHoerner1965

Hoerner, S. F., and Borst, H. V., *Fluid Dynamic Lift*, published by Mrs. Lisselotte A. Hoerner, 1985. https://archive.org/details/FluidDynamicLiftHoerner1985

These books are well worth perusing as a great source of aerodynamic information and knowledge.

Essential thinking for transonic transport design:

Lynch, F. T., "Commercial Transports—Aerodynamic Design for Cruise Performance Efficiency," Douglas Paper 7026, Feb. 1981. (*Note*: Also included as Chapter 2 in *Transonic Aerodynamics*, edited by D. Nixon, Progress in Astronautics & Aeronautics, Vol. 81, 1982, pp. 81–147. https://doi.org/10.2514/5.97816008655558.0081.0147)

See also Shevell's Aerodynamic Bugs paper (https://doi.org/10.2514/6.1985-4067) listed in appendix F. Read for the design philosophy and thinking.

Best recent surveys of high lift:

Van Dam, C. P., "The aerodynamic design of multi-element high-lift systems for transport airplanes," Progress in Aerospace Sciences, Vol. 38, pp. 101–144, 2002. https://doi.org/10.1016/S0376-0421(02)00002-7

Rudolph, P. K. C., "High-Lift Systems on Commercial Subsonic Airliners," NASA CR-4746, Sept. 1996.

These references examine the high-lift systems used on transonic transports.

High-alpha aerodynamics:

Chambers, J. R., and Grafton, S. B., "Aerodynamics of Airplanes at High Angles of Attack," NASA TM-74097, Dec. 1977.

Invaluable lessons related to configuration stability and control issues:

Abzug, M. J., and Larrabee, E. E., *Airplane Stability and Control: A History of the Technologies that Made Aviation Possible,* Cambridge University Press, 1997. https://search.worldcat.org/title/34513500

For computational considerations:

Cummings, R. M., Mason, W. H., Morton, S., A., and McDaniel, D. R., *Applied Computational Aerodynamics: A Modern Engineering Approach*, Cambridge University Press, New York, NY, 2015. https://search.worldcat.org/title/881146298

Quick estimation methods:

Most aerodynamics textbooks aren't aimed at providing handbook-type methods to use in aerodynamic configuration development. There are several reasons that handbook-oriented collections of aerodynamic methods are useful. First, they almost always identify the key parameters that contribute to the estimate and generally show the functional form. Second, you can take a shortcut by making a big calculation to get a quick estimate, and finally, they can provide a sanity check for your calculated estimates. In this section, we list a few handy resources:

Brandt, S. A., Post, M. L., Hall, D., Gilliam, F., Jung, T., and Yechout, T., "The Value of Semi-Empirical Analysis Methods in Aircraft Design," AIAA Paper 2015-2486, 16th AIAA/ISSMO Multidisciplinary Analysis and Optimization Conference, Dallas, TX, Jun. 22-26, 2015. (*Note*: A good recent collection.)

The next set of reports, from the US Air Force, are available for free download:

The mother of all handbook methods is DATCOM (short for "data compendium"). This was originally a multi-volume paper handbook with an emphasis on stability and control. It was eventually replaced with a computer program, the so-called Digital DATCOM. I suggest using the original paper version (https://search.worldcat.org/title/605998083) or print. It gives more insight into the methods and has numerous references supporting the methods. In particular, many references are to reports of wind tunnel tests. There is also a Missile DATCOM. The handbook is formally called *USAF Stability and Control DATCOM*. There are at least two versions available in electronic form. They are the 1965 and 1978 revisions.

Schemesky, R. T., and Howell, G., "Aerodynamic Accounting Technique for Determining Effects of Nuclear Damage to Aircraft, – Volume I – Empirical Methods," DNA 4531F-1, Feb. 1978. https://apps.dtic.mil/sti/tr/pdf/ADA064134.pdf

> DNA stands for Defense Nuclear Agency. This is the basic General Dynamics Fort Worth Division aero methods code with blast damage added. It describes the basic aerodynamic estimation methods as well as damaged aircraft methods, including illustration of the accuracy for the F-16, the FB-111, and a number of NASA models. The basic program is described in "Development of an Empirically Based Computer Program to Predict the Aerodynamic Characteristics of Aircraft, Vol. I, Empirical Methods," AFFDL TR-73-144, 1973. (*Note*: Also available on the web for download: https://apps.dtic.mil/sti/pdfs/AD0780100.pdf.)

Jobe, C. E., "Prediction of Aerodynamic Drag," AFWAL TM-84-203, July 1984. https://apps.dtic.mil/sti/pdfs/ADA326842.pdf

This report formed the basis for Chuck Jobe's chapter in the AIAA book, *Thrust and Drag* (https://search.worldcat.org/title/922978774). Again, this is a good practical summation of methods.

Sieron, T. R., Fields, D., Baldwin, A. W., and Adamczak, D. W., "Procedures and Design Data for the Formulation of Aircraft Configurations," WL-TR-93- 3068, Aug. 1993. https://apps.dtic.mil/sti/citations/ADA270150

This report includes lots of data from existing aircraft and includes supersonic cases. The title is a little misleading, as it's actually an aerodynamics report.

Next, several aircraft design textbooks have excellent collections of aerodynamic methods:

Nicolai, L. M., and Carichner, G. E., *Fundamentals of Aircraft and Airship Design, Volume I – Aircraft Design*, AIAA, Reston, VA, 2010. https://arc.aiaa.org/doi/book/10.2514/4.867538

This book contains a wealth of aerodynamics methods and data. There is also a second volume covering airships and including case studies.

Raymer, D. P., *Aircraft Design: A Conceptual Approach*, AIAA, Reston, 2018 (https://search.worldcat.org/title/1048659355); 2024 (https://search.worldcat.org/title/1492940499)

Dan shares lots of info and explanations of aerodynamic configuration issues and geometry.

Torenbeek, E., *Synthesis of Subsonic Airplane Design*, Delft University Press, 1982. (*Note*: Now available for free electronically at https://resolver.tudelft.nl/229f2817-9be9-49b6-959a-d653b5bac054)

Although the book covers many aircraft design topics, it has a very good collection of aerodynamics material, including many references. As the title suggests, the emphasis is on subsonic transport aircraft. He also wrote a second book, *Advanced Aircraft Design* (https://onlinelibrary.wiley.com/doi/book/10.1002/9781118568101), which covers modern design procedures and configuration studies.

Jan Roskam has written numerous books with aerodynamic methods and configuration information. These include the eight-volume *Airplane Design* series, an *Aerodynamics and Performance* book, and a *Flight Dynamics and Automated Flight Controls* book. All of these are available through DARCorporation: https://shop.darcorp.com/index.php?route=product/category&path=85_60.

From a quick methods perspective, Roskam compiled two relatively short paperback books: *Methods for Estimating Drag Polars of Subsonic Airplanes* (https://search.worldcat.org/title/201953) and *Methods for Estimating Stability and Control Derivatives of Conventional Subsonic Airplanes* (https://search.worldcat.org/title/200202), both initially printed in 1971. These are quite handy and were largely compiled from DATCOM.

When using estimates from these sources, remember to be sure to compare the estimates with existing data before using them for your project of interest. Sometimes the methods aren't very accurate (if they were really good, we wouldn't need CFD!). But it is also possible you don't understand exactly how they are supposed to be used.

Performance methods:

Doing configuration aerodynamics frequently requires performance estimates. The aircraft design books include this information. Books I use for performance include:

Shevell, R. S., *Fundamentals of Flight*, 2nd ed., Prentice-Hall, 1989. https://search.worldcat.org/title/17678498

> This book contains a couple of good chapters on performance, especially for transonic transports.

Roskam, J., and Lan, C.-T. E., *Airplane Aerodynamics and Performance*, DARcorporation, Kansas, 1997; revised 2016. https://search.worldcat.org/title/38463817

> This includes detailed procedures for computing performance, emphasizing general aviation and the FAR requirements associated with performance. The book also includes details on propellers, a topic that has become much more important with the widespread emphasis on drones.

Takahasi, T., *Aircraft Performance and Sizing, Volume I: Fundamentals of Aircraft Performance*, Momentum Press, 2016. https://search.worldcat.org/title/945097483

> This book covers a lot of extremely useful practical aspects of operating an airplane. Tim primarily covers commercial transports. There is also a second volume, *Applied Aerodynamic Design* (https://search.worldcat.org/title/945180130). The second volume could be considered an aircraft design book, but it also covers field performance and issues with stability and control.

So far, I haven't seen good text material for the emerging electric and electric-hybrid airplane propulsion systems. Check the latest edition of Brandt (https://search.worldcat.org/title/910239571), as he said he would be including it.

Another good source of aerodynamic reference material is the website by Brenda Kulfan, http://www.brendakulfan.com [stable link]. Many of her reports and papers are collected here, and most can be downloaded. Her work is notable for its insight and the superior figures and illustrations.

Note: I was hoping to make this a one-page summary. I ran over!

Acknowledgments

I have been fortunate to meet and work with many of the key contributors in both computational methodology and aircraft configuration development. After I formed a strong fundamental base at Virginia Tech, I had a chance to work with a wide variety of experts at Grumman. I was able to learn a lot from them. I was also able to talk with experts at national meetings, as well as NASA, WPAFB, and Pax River. Moving back to Virginia Tech, I was able to collaborate with more experts. And I was able to spend a year at the Air Force Academy, where, as might be expected, the Aeronautics Department has a very strong emphasis on aircraft aerodynamics. In the last decade, Russ Cummings has been a great collaborator. It has been a fantastic experience and hasn't stopped yet. If I try to name all the aerodynamicists that I've learned from, it will be a book-length list in itself, and I will offend someone by omitting them. Finally, I appreciate former students in the class sending me info that they know I will appreciate.

– W. H. Mason (1947–2019)

Production Acknowledgments

Anita Walz, *Acquisitions, Developmental, and Managing Editor*

Anita Walz is Associate Professor, Assistant Director of Open Education, and Scholarly Communication Librarian in the University Libraries at Virginia Tech. She received her MS in library and information science from the University of Illinois at Urbana-Champaign and has worked in university, government, school, and international libraries for over twenty years. She is the founder of the Open Education Initiative at Virginia Tech and the managing editor of over twenty open textbooks adapted or created at Virginia Tech, many of which may be found by visiting the Open Textbook Collection. She has provided overall planning, project consulting, coaching, guidance, developmental assistance, and technical assistance for this book.

Kindred Grey, *Publishing Coordinator*

Kindred Grey is the Graphic Design and Production Specialist in the University Libraries at Virginia Tech. She joined University Libraries after receiving her BS in statistics and psychology from Virginia Tech. Kindred has contributed to over twenty open textbooks, providing technical support on layout and design. Her main focus is publishing open textbooks that are visually appealing, accessible, student oriented, and technologically advanced. She led production efforts involving accessibility and formatting for the PDF, EPUB, print, and HTML versions of the text.

Pranay Patel, *Production and Technical Assistance*

Pranay Patel earned his BS and MS in aerospace engineering at Virginia Tech. His research focused on the commissioning of a new wind tunnel at Virginia Tech for use in dust separation experiments for turboshaft engines. Pranay's focus throughout his undergraduate and graduate degrees centered around aircraft propulsion and design. He served as a subteam lead on the Design, Build, Fly team at Virginia Tech for three years and served as the team's project manager for the spring 2024 semester. He worked to import all equations and images into the text, ensuring that they had proper numbering and formatting.

Special thanks to **Sullivan Madden**, **Joseph Brooks**, and **Pranay Patel,** who worked on alternative text and figure review. Acknowledgments and gratitude are also extended to Dr. Mason's former students, some of which allowed use of their graphics in this book.

Thank you to **Dr. Jason M. Merret**, **Dr. Russell M. Cummings**, **Mr. Jason R. Riopelle**, and two other peers who took time out of their days to review this text.

About the Author

Author

William H. Mason (1947–2019) developed a deep passion for airplanes quite early in his life. Growing up in Southwest Virginia, he spent countless hours building and flying model airplanes as a teenager. When he was an undergraduate student at Virginia Tech, he seized upon opportunities to gain practical experience, working summers at McDonnell Douglas in St. Louis, Missouri, where he was involved with various F-4 aircraft projects, including the swing-wing F-4, and at the Edwards Air Force Base, California, working on US Army Huey Cobra helicopters. In 1974, he began his fifteen-year professional aerospace engineering career with Grumman, where he made valuable contributions to many high-profile projects, such as: (i) the X-29, an experimental aircraft with a forward-swept wing and canard; (ii) the NASA/Grumman Research Fighter Configuration with supercruise and maneuvering capabilities; and (iii) the SC3 Wing Concept, which set a record for low drag at high-lift supersonic performance. From 1989 until his passing in 2019, he was a dedicated educator at Virginia Tech. Right after returning to VT in 1989, he devoted himself to sharing his knowledge and insights with students and colleagues. His legacy lives on with a large number of students who either took the courses he offered in aircraft design, applied computational aerodynamics, and configuration aerodynamics or performed research in aerospace systems design and multidisciplinary optimization. He co-authored *Applied Computational Aerodynamics: A Modern Engineering Approach*—one of the first textbooks on this topic for undergraduates—published by Cambridge University Press in 2015. He also authored or co-authored more than 100 technical papers and reports. He was a lifelong Hokie, having earned his BS degree in 1971, a MS in 1972, and a PhD in 1975, all in aerospace engineering from Virginia Tech. Mason was an Associate Fellow of the American Institute of Aeronautics and Astronautics (AIAA).

Editor

Pradeep Raj is a Collegiate Professor Emeritus at Virginia Tech and spent twelve years serving as a faculty advisor of student capstone aircraft design teams and conducting collaborative research in simulation driven design to enable development of quality affordable aerial vehicles. He joined VT in 2012 after thirty-two years (1979–2011) with Lockheed Martin, a premier aerospace and defense corporation. For the first twenty years there, he held key technical leadership positions and made noteworthy contributions to advancing the effectiveness of computational simulation capabilities for meeting aircraft design needs. For the next twelve years, he held executive leadership and management positions before retiring from the Advanced Development Programs organization commonly known as the Skunk Works®, which is world renowned for creating breakthrough technologies and landmark aircraft. He is a Fellow of the American Institute of Aeronautics and Astronautics and of the Royal Aeronautical Society (RAeS). He earned a PhD in aerospace engineering from Georgia Institute of Technology in 1976 after earning a master's degree in aeronautical engineering and a bachelor's in electrical technology, both from the Indian Institute of Science in Bangalore, India.